October 1996 • NREL/CP-430-21968-Vol.1

CONF-9605795--Vol.1

Proceedings of the 1996 U.S. DOE Hydrogen Program Review

Volume I

May 1–2, 1996
Miami, Florida

RECEIVED
NOV 26 1996
OSTI

Sponsored by the
Office of Solar Thermal, Biomass
Power and Hydrogen Technologies
U.S. Department of Energy

MASTER

DISTRIBUTION OF THIS DOCUMENT IS UNLIMITED

National Renewable Energy Laboratory
1617 Cole Boulevard
Golden, Colorado 80401-3393
A national laboratory of the U.S. Department of Energy
Managed by Midwest Research Institute
for the U.S. Department of Energy
under Contract No. DE-AC36-83CH10093

NREL/CP-430-21968 • UC Category: 1360 • DE97000053

Proceedings of the 1996 U.S. DOE Hydrogen Program Review

Volume I

May 1–2, 1996
Miami, Florida

Sponsored by the
Office of Solar Thermal, Biomass
Power and Hydrogen Technologies
U.S. Department of Energy



National Renewable Energy Laboratory
1617 Cole Boulevard
Golden, Colorado 80401-3393
A national laboratory of
the U.S. Department of Energy
Managed by Midwest Research Institute
for the U.S. Department of Energy
under Contract No. DE-AC36-83CH10093

Prepared under Task No. HY611010

October 1996

NOTICE: This report was prepared as an account of work sponsored by an agency of the United States government. Neither the United States government nor any agency thereof, nor any of their employees, makes any warranty, express or implied, or assumes any legal liability or responsibility for the accuracy, completeness, or usefulness of any information, apparatus, product, or process disclosed, or represents that its use would not infringe privately owned rights. Reference herein to any specific commercial product, process, or service by trade name, trademark, manufacturer, or otherwise does not necessarily constitute or imply its endorsement, recommendation, or favoring by the United States government or any agency thereof. The views and opinions of authors expressed herein do not necessarily state or reflect those of the United States government or any agency thereof.



Printed on paper containing at least 50% wastepaper, including 20% postconsumer waste

TABLE OF CONTENTS

Volume I

Systems Analysis

Supporting Analysis and Assessments Quality Metrics: Utility Market Sector, J. Ohi, National Renewable Energy Laboratory 1

H Scan/AHP Advanced Technology Proposal Evaluation Process, S. Mack, Energetics, Inc., M.R. Szoka deValladares, National Renewable Energy Laboratory 13

Systems Analysis - Independent Analysis and Verification, J.P. DiPietro, E. Skolnik, J. Badin, Energetics, Inc. 31

System Comparison of Hydrogen with Other Alternative Fuels in Terms of EPAct Requirements, F. Barbir, K Özay, T.N. Veziroglu, University of Miami 41

Integrated Analysis of Transportation Demand Pathway Options for Hydrogen Production, Storage, and Distribution, C.E.Thomas, Directed Technologies, Inc. 51

Comparative Costs and Benefits of Hydrogen Vehicles, G. Berry, Lawrence Livermore National Laboratory 77

Hydrogen Energy Systems Studies, J. Ogden, T. Kreutz, A. Cox, J. White, Princeton University 125

Coupling Renewables Via Hydrogen Into Utilities: Temporal and Spatial Issues, and Technology Opportunities, J. Iannucci, S. Horgan, J. Eyer, Distributed Utility Associates, S. Schoenung, Longitude 122 West, Inc.. 185

Modeling of Hydrogen Production Methods: Single Particle Model and Kinetics Assessment, R. Miller, J. Bellan, Jet Propulsion Laboratory 197

Technicoeconomic Analysis of Renewable Hydrogen Production, Storage, and Detection Systems, M. Mann, P. Spath, K. Kadam, National Renewable Energy Laboratory 249

Hydrogen Storage and Delivery System Development: Analysis, J. Handrock, Sandia National Laboratory 273

Production

Development of an Efficient Algal H_2-Producing System, M. Ghirardi, S. Markov, M. Seibert, National Renewable Energy Laboratory 285

Hydrogen Production By Photosynthetic Water Splitting, E. Greenbaum, J. Lee, C. Tevault, Oak Ridge National Laboratory 303

In Vitro Hydrogen Production by Glucose Dehydrogenase and Hydrogenase, J. Woodward, Oak Ridge National Laboratory 313

Biological H_2 from Syngas and from H_2O, P. Weaver, P.-C. Maness, S. Markov, S. Martin, National Renewable Energy Laboratory 325

Photoelectrochemical Based Direct Conversion Systems for Hydrogen Production, S. Kocha, M. Peterson, D. Arent, H. Scott, A. Frank, J. Turner, National Renewable Energy Laboratory 333

Photoelectrochemical Hydrogen Production, R. Rocheleau, E. Miller, A. Misra, University of Hawaii 345

Photovoltaic Hydrogen Production, H. Hiser, S. Memory, T.N. Veziroglu, J. Padin University of Miami 359

Solar Photocatalytic H, Production from Water Using a Dual Bed Photosystem, C. Linkous, Florida Solar Energy Center 389

International Marine Biotechnology Culture Collection (IMBCC), O. Zaborsky, K. Baker, University of Hawaii 397

Biological Hydrogen Photoproduction, L. Brand, Y.-H. Luo, T. Tszuki, University of Miami 405

Development of Solid Electrolytes for Water Electrolysis at Higher Temperature, C. Linkous, University of Central Florida 443

Solar Photochemical Production of HBr for Off-Peak Electrolytic Hydrogen Production, H. Heaton, Solar Reactor Technologies, Inc. 449

Biomass-to-Hydrogen via Fast Pyrolysis and Catalytic Steam Reforming, E. Chornet, D. Wang, S. Czernik, D. Montané, M. Mann, National Renewable Energy Laboratory 457

Hydrogen Production from Municipal Solid Waste, P. Wallman, J. Richardson, C. Thorsness, Lawrence Livermore National Laboratory, T. Leininger, J. Klein, J. Winter, A. Robin, Montebello Technology Center, Texaco, Inc.. 481

Hydrogen Production from High-Moisture Content Biomass in Supercritical Water, M. Antal, T. Adschiri, T. Ekbom, A. Garcia, Y. Matsumura, T. Minowa, F. Nuessle, M. Sakurai, X. Xu, University of Hawaii 499

DISCLAIMER

Portions of this document may be illegible in electronic image products. Images are produced from the best available original document.

Production of Hydrogen by Thermocatalytic Cracking of Natural Gas, N. Muradov, Florida Solar Energy Center 513

Sorption Enhanced Reaction Process (SERP) for Production of Hydrogen, M. Anand, J. Hufton, S. Mayorga, S. Nataraj, S. Sircar, Air Products and Chemicals, Inc. 537

Hydrogen Manufacturing Using Plasma Reformers, L. Bromberg, Massachusetts Institute of Technology 553

Volume II

Utilization

Hydrogen Safety Analysis, M. Swain, B. Sievert, University of Miami, M. Swain, Analytical Technologies, Inc. 569

Design and Development of a Low-Cost Fiber-Optic Sensor for Hydrogen Detector, D. Benson, C. Tracy, C. Bechinger, National Renewable Energy Laboratory 605

Chemical Kinetic Modeling of H_2 Applications, C. Westbrook, N. Marinov, W. Pitz, H. Curran, Lawrence Livermore National Laboratory 625

Hydrogen Engine Development: Experimental Program, P. Van Blarigan, Sandia National Laboratory 639

Numerical Modeling of Hydrogen-fueled Internal Combustion Engines, N. Johnson, A. Amsden, T. Butler, Los Alamos National Laboratory 665

Analysis of Experimental Hydrogen Engine Data and Hydrogen Vehicle Performance and Emissions Simulation, S. Aceves, Lawrence Livermore National Laboratory 691

Development of a Lean Premixed Burner for Hydrogen Utilization, J. Keller, Sandia National Laboratory 711

City of Chula Vista, Hydrogen Fuel Cell Bus Demonstration Project, B. Gustafen, B. Bamberger, City of Chula Vista 717

A Polymer Electrolyte Fuel Cell Stack for Stationary Power Generation from Hydrogen Fuel, C. Zawodzinski, M. Wilson, S. Gottesfeld, Los Alamos National Laboratory 727

The Palm Desert Renewable Hydrogen Transportation System, P. Lehman, Humboldt State University 737

Storage

Carbon Nanotube Materials for Hydrogen Storage, A. Dillon, K. Jones, M. Heben, National Renewable Energy Laboratory 747

Hydrogen Transport and Storage in Engineered Glass Microspheres, G. Rambach, Lawrence Livermore National Laboratory, C. Hendricks, W. J. Schafer Associates 765

Hydrogen Storage and Delivery System Development: Fabrication, J. Handrock, M. Malinowski, K. Wally, Sandia National Laboratories 773

Hydrogen Storage via Polyhydride Complexes, C. Jensen, University of Hawaii 787

Thermodynamic Characterization of Polyhydride Complexes, R. Zidan, R. Rocheleau, C. Jensen, University of Hawaii 795

Hydride Development for Hydrogen Storage, G. Thomas, S. Guthrie, W. Bauer, N. Yang, Sandia National Laboratories, G. Sandrock, SunaTech, Inc. 807

Thermal Management Technology for Hydrogen Storage: Fullerene Option, J. Wang, F. Chen, R. Murphy, Oak Ridge National Laboratory. 819

Supporting Analysis and Assessments
Quality Metrics: Utility Market Sector

Jim Ohi
National Renewable Energy Laboratory
Golden, CO 80401

Abstract

In FY96, NREL was asked to coordinate all analysis tasks so that in FY97 these tasks will be part of an integrated analysis agenda that will begin to define a 5-15 year R&D roadmap and portfolio for the DOE Hydrogen Program. The purpose of the Supporting Analysis and Assessments task at NREL is to provide this coordination and conduct specific analysis tasks. One of these tasks is to prepare the Quality Metrics (QM) for the Program as part of the overall QM effort at DOE/EERE. The Hydrogen Program one of 39 program planning units conducting QM, a process begun in FY94 to assess benefits/costs of DOE/EERE programs. The purpose of QM is to inform decisionmaking during budget formulation process by describing the expected outcomes of programs during the budget request process. QM is expected to establish first step toward merit-based budget formulation and allow DOE/EERE to get "most bang for its (R&D) buck." In FY96. NREL coordinated a QM team that prepared a preliminary QM for the utility market sector. In the electricity supply sector, the QM analysis shows hydrogen fuel cells capturing 5% (or 22 GW) of the total market of 390 GW of new capacity additions through 2020. Hydrogen consumption in the utility sector increases from 0.009 Quads in 2005 to 0.4 Quads in 2020. Hydrogen fuel cells are projected to displace over 0.6 Quads of primary energy in 2020. In future work, we will assess the market for decentralized, on-site generation, develop cost credits for distributed generation benefits (such as deferral of transmission and distribution investments, uninterruptible power service), cost credits for by-products such as heat and potable water, cost credits for environmental benefits (reduction of criteria air pollutants and greenhouse gas emissions), compete different fuel cell technologies against each other for market share, and begin to address economic benefits, especially employment. NREL will also develop and integrated QM analysis for the transportation market in cooperation with the DOE Office of Transportation Technologies.

Approach/Rationale

The Hydrogen Program one of 39 program planning units conducting QM, a process begun in FY94 to assess benefits and costs of DOE/EERE programs. The purpose of QM is to inform decisionmaking during budget formulation process by describing the expected outcomes of programs. QM is expected to establish first step toward merit-based budget formulation and allow DOE/EERE to get "most bang for its (R&D) buck." QM is also expected to provide an analytic framework to estimate longer-term benefits of DOE/EERE programs by standardizing data, analysis models, outreach to key stakeholders, and the "metrics" used to estimate benefits (e.g., energy savings, economic productivity, and environmental quality). In FY97 the DOE/EERE QM will begin to address technical and market risk of R&D programs in an effort to develop and present a balanced DOE/EERE portfolio. In FY96. NREL coordinated a QM team that prepared a preliminary QM for the utility market sector as part of the overall DOE/EERE effort.

The analysis process to project market share of total new installed capacity for electricity generation is shown in Figure 1. Fuel cells are competed against other generating technologies on the basis of the levelized cost of electricity (LCE), which, in turn, is calculated from capital cost, operation and maintenance cost, heat rate (efficiency), and fuel cost. The market share is estimated by the Renewable Energy Penetration (REP) model developed by Princeton Economic Research, Inc., based on the LCEs of the competing technologies. The new installed capacity of hydrogen fuel cells is estimated by multiplying its market share by the total capacity addition.

The scope of the QM for the Hydrogen Program is limited to electricity supply additions and considers only grid-connected electricity generation by phosphoric acid (PAFC) and proton exchange membrane (PEM) fuels cells. Energy storage is not considered. Key assumptions include: PAFCs, which are commercially available using natural gas feed and have a total worldwide installed capacity of about 13 MW today, will continue to penetrate the market and be joined by PEM fuel cells using hydrogen gas by 2005; natural gas prices for utilities will remain low (<$3.50/MMBtu in 2020) as projected by the Energy Information Administration's *Annual Energy Outlook 1996*; and capital costs of PAFCs and PEM fuel cells will decline to $850/kW and $300/kW, respectively, by 2020.[1]

Past Results

In FY95, NREL prepared a preliminary QM analysis for the light-duty transportation market sector and began QM planning for utility market sector. The results of the QM analysis and were presented at 1995 Hydrogen Program annual review.

---

[1] Assumptions and calculations are documented in *1995/96 DOE Hydrogen Program Quality Metrics Analysis: Supporting Information.*

Current Year Results

In the electricity supply sector, the QM analysis shows hydrogen fuel cells capturing 5% (or 22 GW) of the total market of 390 GW of new capacity additions through 2020. As shown in Figure 2, most of the market for new capacity additions, 348 GW or almost 90%, is captured by natural gas combustion turbines and combined cycle systems due to the projected low cost of natural gas and the high efficiency of these systems. Hydrogen consumption in the utility sector increases from 0.009 Quads in 2005 to 0.4 Quads in 2020 (Figure 3). Hydrogen fuel cells are projected to displace over 0.6 Quads of primary energy in 2020.

For the light-duty vehicle market sector, NREL began refining market penetration projection by working with DOE/OTT to apply its Vehicle Choice Model to hydrogen vehicles. Results for this market sector will be presented in 1997.

Plans for Future Work

In 1997, NREL and the QM team will refine the analysis for the utility market sector by:

- assessing market for decentralized, on-site generation
- establishing cost credits for distributed generation benefits (transmission and distribution, uninterruptible power supply)
- establishing cost credits for by-products (heat, water)
- establishing cost credits for environmental benefits (GHG, criteria pollutants)
- competing fuel cell technologies (PAFC, PEM, molten carbonate, solid oxide)
- addressing economic benefits, including employment.

NREl will also develop an integrated QM for the light-duty transportation market sector by:

- working with DOE/OTT to expand its vehicle choice model to account for market penetration of hydrogen vehicles
- continuing analysis of transportation pathways
- coordinating with DOE/OTT on development of a national fuel strategy for advanced vehicles.

The 1997 QM analysis will attempt to integrate transportation and hydrogen production strategies by examining regional and niche markets. NREL will also begin to integrate QM into the overall analysis agenda of the Hydrogen Program.

Status of Economic Evaluation/Systems Analysis

One of the parameters of LCE is capital cost, and, as one would expect, any projection of market penetration is very sensitive to capital costs. Fuel cell capital costs are difficult to project, especially for PEM fuel cells, which are still in a pre-commercial development stage. The capital cost projections for PEM fuel cell systems are consistent with capital cost projections made by Arthur D. Little, Inc., Daimler Benz, and Energy Partners, Ltd., for PEM fuel cell stacks based on large-volume production. Capital cost projections for PAFCs are based on information received from International Fuel Cells, Inc., which produces the only commercially available PAFCs. Mid- to long-term cost fuel cell capital cost projections are also highly sensitive to production volume, and the market penetration projections try to account for production volume constraints.

While the REP model addresses the market for only grid-connected capacity additions, the on-site generation market may represent a more significant market for fuel cells. Furthermore, the impending deregulation of the electricity market will have major and, as yet, unknown impacts on the market as a whole and on the decentralized, on-site generation market in particular. Because cost advantage will be particularly important in a deregulated electricity market, cost credits for transmission and distribution deferral and on-site generation of by-product heat should improve the market attractiveness of fuel cells.

For programmatic systems analysis, the QM analysis must be integrated into overall analysis agenda so that results can be factored into the R&D portfolio analysis. The QM analysis can then contribute to the development of a balanced portfolio for the Hydrogen Program and for DOE/EERE.

Projected Goals/Basis for Goals

The projected goals are based on attaining cost-competitive use of hydrogen in the utility and transportation sectors. The market penetration goals in utility sector are based on reducing the LCE from hydrogen by increasing the energy efficiency of fuel cells, reducing the capital and O&M costs of fuel cells, and by reducing the cost of hydrogen fuel. A sensitivity analysis showed the importance of meeting goals for PEM capital cost and hydrogen fuel cost. The Hydrogen Program's QM goals are consistent with the data and analysis models used in the QM analysis process of the Office of Utility Technologies in DOE/EERE.

Barriers to Meeting Goals: Strategic Questions

The key barrier to meeting goals can be stated in terms of the key strategic issue raised by the QM analysis: what are the implications for hydrogen use in the utility market sector if natural gas is abundant and inexpensive through 2020 as projected by the EIA? What are the

implications of a plentiful and inexpensive domestic supply of natural gas for:

- renewable hydrogen production
- a transition strategy based on reforming fossil fuels in the near-term
- other "metrics" such as environmental quality and "energy security"

Other strategic questions raised by the abundance of inexpensive natural gas include:

- technological and economic implications of on-site reforming of natural gas to liquid hydrocarbons as a competitor for hydrogen and other alternative fuels
- the implications of anticipated regulatory and institutional changes in the electricity supply (services) industry?

Finally, the implications of these strategic questions must be assessed and integrated the Hydrogen Program's QM effort and its overall analysis agenda, especially R&D portfolio planning and management.

Conclusion

The QM analysis is a critical component of "merit-based" DOE budget formulation and defense that is based on determining competitive market share of technologies and estimating national strategic benefits accruing from this market share. The QM analysis is also an important component of the Hydrogen Program's analysis agenda. The contributions of QM analysis to the Hydrogen Program include:

- development of data and analysis for budget formulation and defense
- development and integration of market penetration information and data
- coordination of analysis and modeling within DOE/OUT and DOE/EERE
- identification and bounding critical market penetration parameters
- identification of strategic issues for portfolio analysis and planning

The value of QM analysis will be strengthened as it is integrated into the overall analysis agenda of the Hydrogen Program.

Acknowledgements

The QM analysis was developed by DOE Hydrogen QM Team:

Frank Brock, Princeton Economic Research, Inc.
Daryl Brown, Pacific Northwest Laboratory
Phil DiPietro, Energetics, Inc.
Jim Ohi, National Renewable Energy Laboratory

The QM team appreciates information from or review by:

Arthur D. Little, Inc.
Dupont (Nafion)
Energy Partners, Ltd.
Hydrogen Technical Advisory Panel
International Fuel Cells, Inc.
Los Alamos National Laboratory

Figure Captions

Figure 1: Analysis Process for QM

Figure 2: Projected Market Share in Electricity Supply Sector

Figure 3: Projected Hydrogen Consumption in the Utility Sector

Levelized Cost of Electricity

The levelized cost of electricity (LCE) from various generation technologies is calculated based on: capital cost, O&M, heat rate, and fuel cost.

Generation Technologies considered include:

- Fuel cell
- Combustion turbine
- Steam turbine
  - Coal
  - Geothermal
  - Nuclear
- Combined Cycle
- Wind turbine



Installed Capacity

The Renewable Energy Penetration (REP) model developed by Princeton Economic Research, Inc. estimates the market share garnered by each technology based on a comparison of the LCE's.

The total new capacity additions for baseload, intermediate, and peaking applications are estimated based on economic growth and retirements.

The new installed capacity of each technology equals its market share multiplied by the total capacity additions.



National Benefits

National benefits are quantified in terms of specific quality metrics based on the installed capacity of renewable-based technologies.

EERE Quality Metrics

- Displaced fossil energy
- Reduced carbon emissions
- Energy cost savings
- Non-energy cost savings
- Private sector investment

FIGURE 1

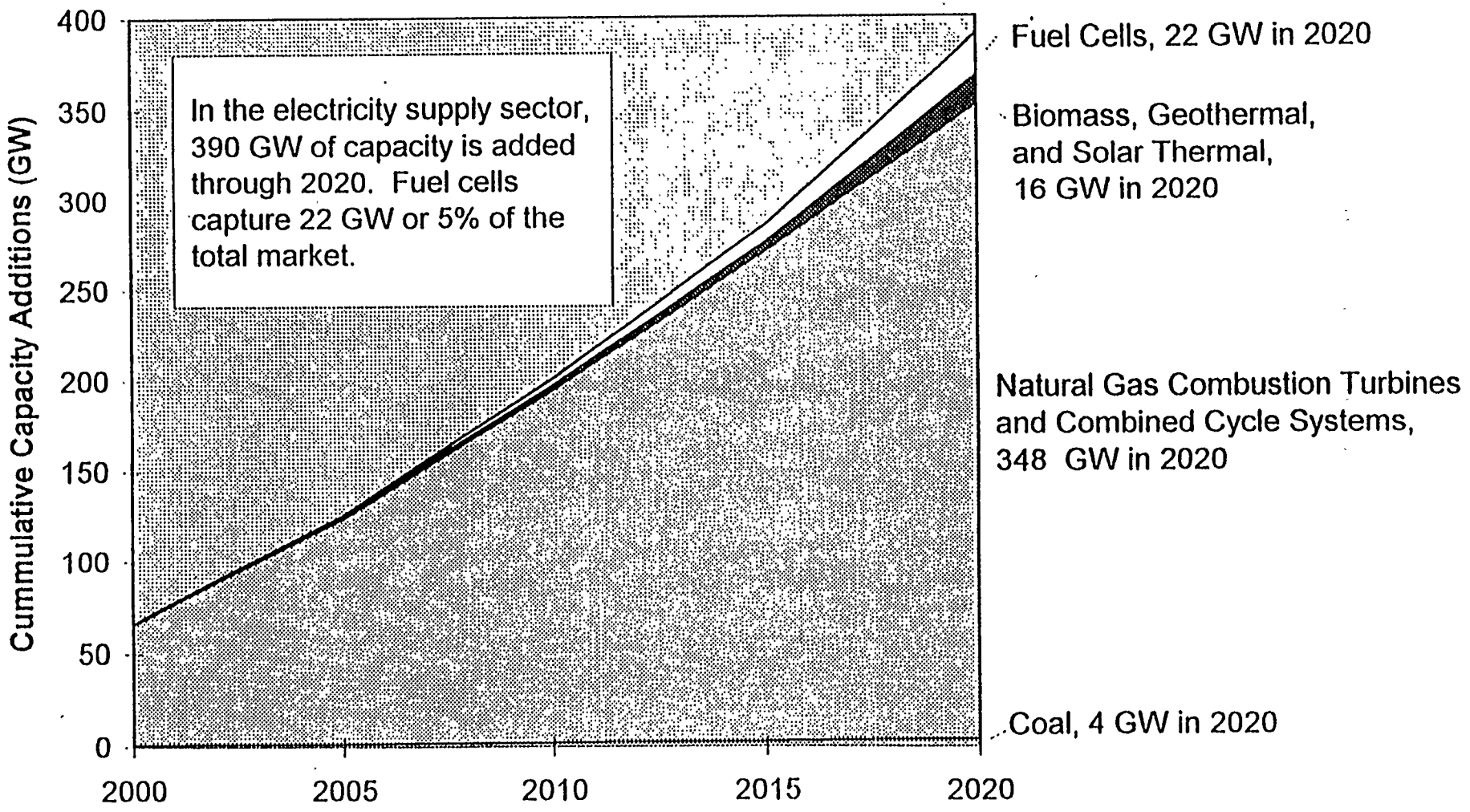

Cummulative Capacity Additions (GW)
400
350
300
250
200
150
100
50
0
2000
2005
2010
2015
2020
In the electricity supply sector, 390 GW of capacity is added through 2020. Fuel cells capture 22 GW or 5% of the total market.
Fuel Cells, 22 GW in 2020
Biomass, Geothermal, and Solar Thermal, 16 GW in 2020
Natural Gas Combustion Turbines and Combined Cycle Systems, 348 GW in 2020
Coal, 4 GW in 2020

FIGURE 2

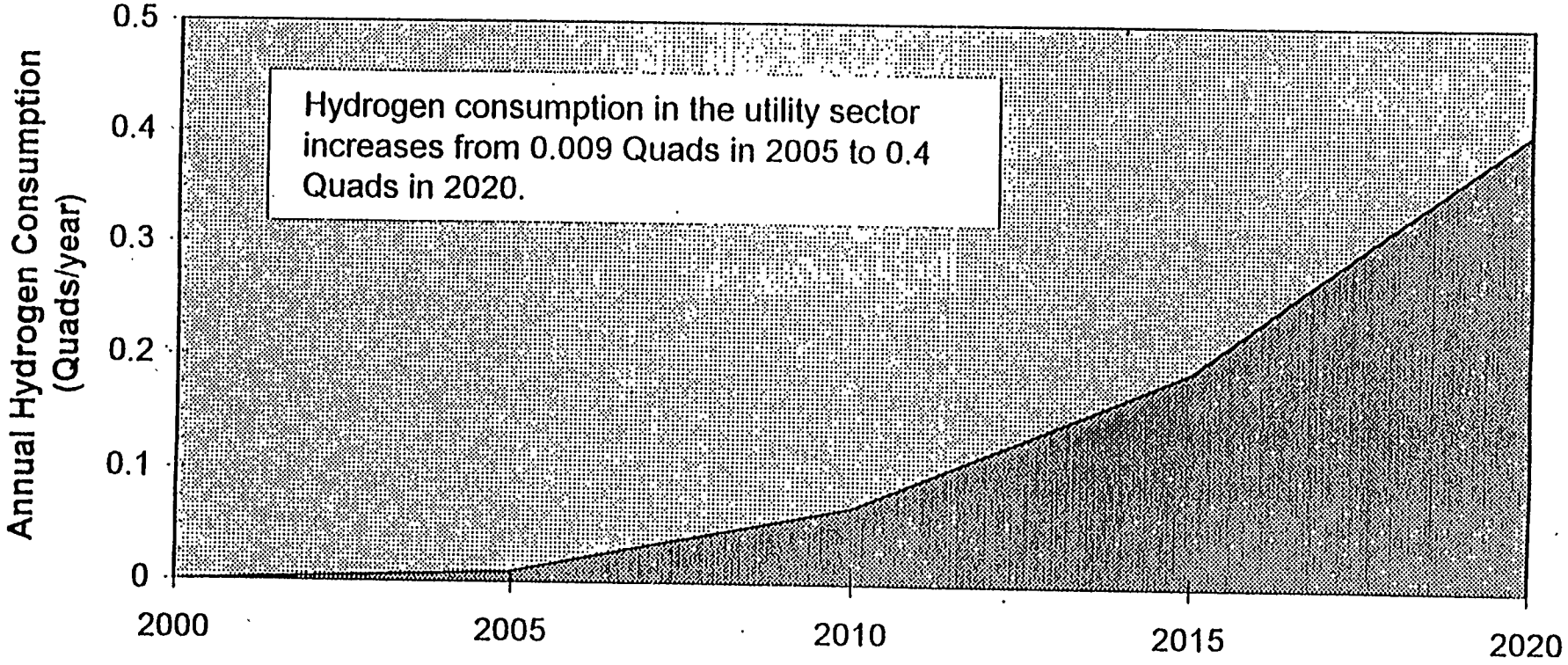

Annual Hydrogen Consumption (Quads/year)
0.5
0.4
0.3
0.2
0.1
0
2000
2005
2010
2015
2020
Hydrogen consumption in the utility sector increases from 0.009 Quads in 2005 to 0.4 Quads in 2020.

FIGURE 3

H Scan/AHP
Advanced Technology
Proposal Evaluation Process

Stephen Mack
Energetics, Incorporated
Columbia, MD 21046

Mary Rose Szoka deValladares
National Renewable Energy Laboratory
409 12th Street, S.W.
Washington, D.C. 20024

Background

It is anticipated that a family of high value/impact projects will be funded by the Hydrogen Program to field test hydrogen technologies that are at advanced stages of development. These projects will add substantial value to the Program in several ways, by: demonstrating successful integration of multiple advanced technologies, providing critical insight on issues of larger scale equipment design, construction and operations management, yielding cost and performance data for competitive analysis, refining and deploying enhanced safety measures.

These projects will be selected through a competitive proposal evaluation process. Because of the significant scope and funding levels of projects at these development phases, Program management has indicated the need for an augmented proposal evaluation strategy to ensure that supported projects are implemented by capable investigative teams and that their successful completion will optimally advance programmatic objectives. These objectives comprise a complex set of both quantitative and qualitative factors, many of which can only be estimated using expert judgment and opinion.

To meet the above need, the National Renewable Energy Laboratory (NREL) and Energetics Incorporated have jointly developed a proposal evaluation methodology called H Scan/AHP. The H Scan component of the process was developed by NREL. It is a two-part survey instrument that substantially augments the type and scope of information collected in a traditional proposal package. The AHP (Analytic Hierarchy Process) component was developed by Energetics. The AHP is an established decision support methodology that allows the Program decision makers to evaluate proposals relatively based on a unique set of weighted criteria that they have determined. For this exercise, H Scan and AHP were developed around a common criteria set which provided a strong link between the two products yielding more informed project recommendations. The augmented information collected in H Scan provided an information source that explicitly addressed the criteria defined by management. The proposal reviewers were therefore able to

directly reference H Scan feedback when actually comparing the proposals using the AHP decision model. This linking of information and evaluation provided important benefits in ranking competing proposals:

1) Organization of complex technical, market and economic issues.

2) Incorporation of qualitative as well as quantitative information into the evaluation.

3) Explicit consideration of the tradeoffs between competing criteria and the allowance for sensitivity analysis.

4) Identification of value differences among reviewers.

5) Generation of an audit trail as to why a winning proposal was selected.

Approach

The fundamental approach of H Scan/AHP was the development for proposal reviewers of an information collection instrument that links a project's potential to complex programmatic needs, and an evaluation device that reviewers can use to discriminate among proposals regarding their potential risk and value to the Program. The individual products were joined into a single process by the use of common evaluation criteria that constituted an expansive set of quantitative and qualitative selection factors.

H Scan

The H Scan part of the proposal evaluation process provides a framework in which a project proposer can fully describe their candidate technology system and its components. The H Scan supplements traditional methods of capturing cost and technical data in a standard format. In H Scan, a more comprehensive set of management defined evaluation and selection criteria are explicitly incorporated into an augmented survey form. H Scan is designed to elicit supplementary information on: relevant markets; energy efficiency and economic impacts; environmental impacts; applicable regulations; operations and maintenance; and proposer capabilities, experience and commitment. H Scan is a flexible information gathering device and the actual index of factors addressed depends on the proposed technologies and their level of development.

Since H Scan is a very comprehensive survey instrument, it is selectively distributed only to proposers who have met baseline quality requirements in their original proposal. Completed H Scans are forwarded to proposal reviewers who use the supplementary information to make clearer, more informed judgments about the potential value of candidate projects. Along with the completed proposer H Scan forms, the reviewers are supplied with their own, related H Scan form that allows each reviewer to provide a very detailed evaluation in a standard format. A completed H Scan, along with the original proposal serve as primary information sources for competitively evaluating candidate proposals.

The Analytic Hierarchy Process (AHP)

The AHP process is an intuitive evaluation methodology that captured and quantified the expert opinions of the proposal reviewers and of the Hydrogen Program manager. This process works by decomposing the proposal decision environment into the important criteria that have been identified by Program management. Sub-criteria were then defined for each major criterion to provide a finer level of attribute detail. Weights were then derived for each criterion and sub-criterion. In the AHP calculations, each sub-criteria weight is a function of its relative importance to other sub-criteria in the same branch of the hierarchy and the relative importance of the major criteria that it is associated with. The candidate proposals were competitively evaluated against each of the sub-criteria to deliver a rank ordering of the alternatives based on their relative[1] potential contribution and risk to Program objectives. The goal of the process is an incremental ranking of the proposal candidates consistent with the institutional needs of the Hydrogen Program.

The criteria weights and the relative rankings of candidate alternatives were derived in a special pairwise comparison process unique to the AHP. In the H Scan/AHP exercise, the evaluation criteria are those factors that the Program has determined must be considered in selecting projects to fund. These criteria include technical, market, financial and other factors. The H Scan and AHP components of the process are linked by explicitly building those evaluation criteria into their structures. With these criteria, a completed H Scan provides a concise information source for evaluating proposals using the decision model generated with the AHP. The underlying mathematical calculations of the AHP pairwise comparison process are managed by supporting software and are transparent to the decision maker. The reviewer uses H Scan and AHP in tandem to synthesize conclusions about the relative value of competing project proposals.

Implementation

The H Scan/AHP methodology for proposal evaluation was implemented as a multi-step process (Table 1.) Two unsolicited proposals were selected as evaluation candidates. Both proposed transportation end-use applications of Hydrogen and consisted of total energy pathways. Two reviewers were recruited to first evaluate the proposals themselves and then evaluate the candidate projects using the H Scan/AHP methodology. For this study, the evaluation criteria and sub-criteria (Table 2) were elicited from the Hydrogen Program manager through two directed interviews. The AHP decision model (Figure 1) was constructed from this criteria set. However, the criteria and sub-criteria were not initially weighted by the Program manager. To gauge value consistency among the reviewers, they were asked to not only evaluate the alternative proposals relatively against the criteria, but to also compare the criteria themselves to determine their relative importance. The AHP pairwise comparisons were analyzed and weights calculated using the *Expert Choice*® software package. The Program manager also participated in this part of the

[1] Relative evaluation is a powerful feature of the AHP because it allows very subjective assessments to be validly made even when no absolute standards may exist.

exercise, (note that he did not pairwise evaluate the candidate proposals.) His relative criteria weights were compared against those of the reviewers for further indications of value consistency from technical experts inside and outside the Program office.

Table 1. Implementation Steps

H Scan/AHP Implementation Steps	
Step 1	Program management was interviewed to determine what important criteria were to be considered in selecting an advanced technology proposal. The factors were both quantitative and qualitative to account for technical, economic market and other issues. Through extended discussion the primary criteria were further refined into sub-criteria so that finer distinctions could be made among the proposal candidates.
Step 2	The criteria defined in Step1 were structured into a decision hierarchy that reflected the selection criteria and sub-criteria relationships. This allowed them to be weighted as to their importance.
Step 3	Using the evaluation criteria for reference, a customized H-Scan was designed to augment the basic proposal evaluation. The H-Scan was structured so that proposer responses coincided with the criteria used to build the decision hierarchy.
Step 4	The H Scan was distributed to the two development teams who had submitted unsolicited proposals. The proposer H Scans were completed by the teams and returned for review and analysis. Guidance was provided as required.
Step 5	The completed H Scans along with the actual proposals were sent to two expert reviewers for evaluation. The reviewers were supplied with a complementary H Scan evaluation form that allowed them to evaluate the proposals based on the content of the proposer H Scans and original information in the proposals.
Step 6	The reviewers were supplied with an AHP proposal evaluation package. Using special elicitation forms, the reviewers derived unique criteria weights using the pairwise comparison technique that forms the basis for the AHP. The reviewers supplied judgements using the elicitation forms, first on criteria importance and then proposal merit. This exercise served as a valuable cross check of value consistency among different reviewers.
Step 7	The Program manager evaluated the decision model to generate his set of criteria weights.
Step 8	The proposal rankings and the criteria weighting outcomes were presented to the Program manager.

Results and Discussion

Figures 2.1 through 2.9 present a synopsis of the H Scan/AHP process. Implementation of the H Scan/AHP prototype indicated the feasibility and value of the process. Both the proposers and the reviewers were able to complete the H Scan/AHP sections with minimal assistance. The returned H Scans section were analyzed for content and information gaps. Valuable feedback was received from the reviewers about the structure of the process and the form and content of the H Scan and AHP components. Both reviewers had strong preferences for one of the proposed projects across virtually all dimensions. However H Scan/AHP was developed to help discriminate among proposals that are more evenly matched, so the actual proposal evaluation was less instructive than the comparison of criteria preferences among the reviewers and Program manager.

The criteria weighting exercise indicated some noticeable differences in criteria importance among the reviewers and the Program manager. Figures 2.7 and 2.8 indicate the variance from the viewpoint of the Program manager. In a decision model that is value driven, there are no "right" or "wrong" answers. But the quantification of these value differences presents a basis for discussion and collaboration in defining and prioritizing the Program's needs and objectives. This interactive process will ensure that all participants who support the Program are "on the same page" when assisting in resource allocation exercises.

Conclusions and Future Work

Both the H Scan and AHP components of the process will be refined based on feedback from the reviewers and Program management. The H Scan will be reformatted as a word processing document for easier entry. The decision model will be reevaluated for completeness and congruence with Program objectives. Contributions from other stakeholders, e.g. business, the Hydrogen Technical Advisory Panel (HTAP), the Industry Advisory Group (IAG), may be solicited for added perspective. An assessment of the differences in criteria weights among the reviewers will also be made with the objective of generating a stable evaluation model that most closely reflects the Program's multi-criteria focus. Application of the AHP decision process to other planning exercises will be investigated. These may include a decision structure for the development of a formalized strategic plan and a prioritization model to help manage the technology portfolio supported by the Program. This experiment provided valuable feedback about the homogeneity of criteria importance inside of the Hydrogen technical community. Noting value differences are instructive, because the recognition of such differences indicates why some Program activities enjoy varying support.

Acknowledgments

The authors wish to thank David Nahmias and Sandy Thomas for serving as reviewers for this H Scan/AHP evaluation test. We also want to thank Jim Ohi of NREL and Joe Badin of Energetics for providing guidance in developing a decision model that is consistent with the objectives of the Hydrogen Program.

References

Boschi, Roberto A.A., Balthasar, Hans Ulrich and Menke, Michael M. September 1979. "Quantifying and Forecasting Exploratory Research Success." *Research Management, 14-21*

Golden, B.L., Wasil, E.A. and Harker, P.T., editors, 1989. The Analytic Hierarchy Process: Applications and Studies. New York: Springer-Verlag

Hamalainen, Raimo P., June 1992. "Politics and Policy: Decision analysis makes its way into environmental policy in Finland." *OR/MS Today, 40-43*

Liberatore, Matthew J. 1988, "A Decision Support System Linking Research and Development Project Selection with Business Strategy." *Project Management Journal, XIX, Number 5:14-21*

Rajasekera, Jay R. August 1990. "Outline of a Quality Plan for Industrial Research and Development Projects." *IEEE Transactions on Engineering Management, 191-197*

Saaty, T.L. 1980. *The Analytic Hierarchy Process.* New York: Mcgraw Hill.

Saaty, T.L. 1982. *Decision Making for Leaders.* California: Wadsworth

Saaty, T.L. and Kearns, K.P. 1985. *Analytical Planning: The Organization of Systems.* Pergamon Press.

Short, Walter, Packey, Daniel J., and Holt, Thomas. 1995. *A Manual for the Economic Evaluation of Energy Efficiency and Renewable energy Technologies.* DE-AC 36-83CH10093. Golden, CO: National Renewable Energy Laboratory.

U.S. Department of Energy, Office of Conservation and Renewable Energy. 1993. The Hydrogen Program Implementation Plan, FY 1994-1998. Washington, D.C.: U.S. D.O.E.

U.S. Department of Energy, Office of Conservation and Renewable Energy. 1994. The FY 1995 Hydrogen Program Annual Operating Plan. Washington, D.C.: U.S. D.O.E.

U.S. Department of Energy, Office of Conservation and Renewable Energy. 1994. The Hydrogen Program Summary, FY 1994. Washington, D.C.: U.S. D.O.E.

Figures and Tables

Figure 1. H Scan/AHP Proposal Evaluation Hierarchy

Figures 2.1 - 2.9. H Scan/AHP Presentation and Results

Table 1. H Scan/AHP Stepwise Implementation

Table 2.1 - 2.3. H Scan/AHP Proposal Evaluation Criteria Definitions

H2 Proposal Evaluation Hierarchy

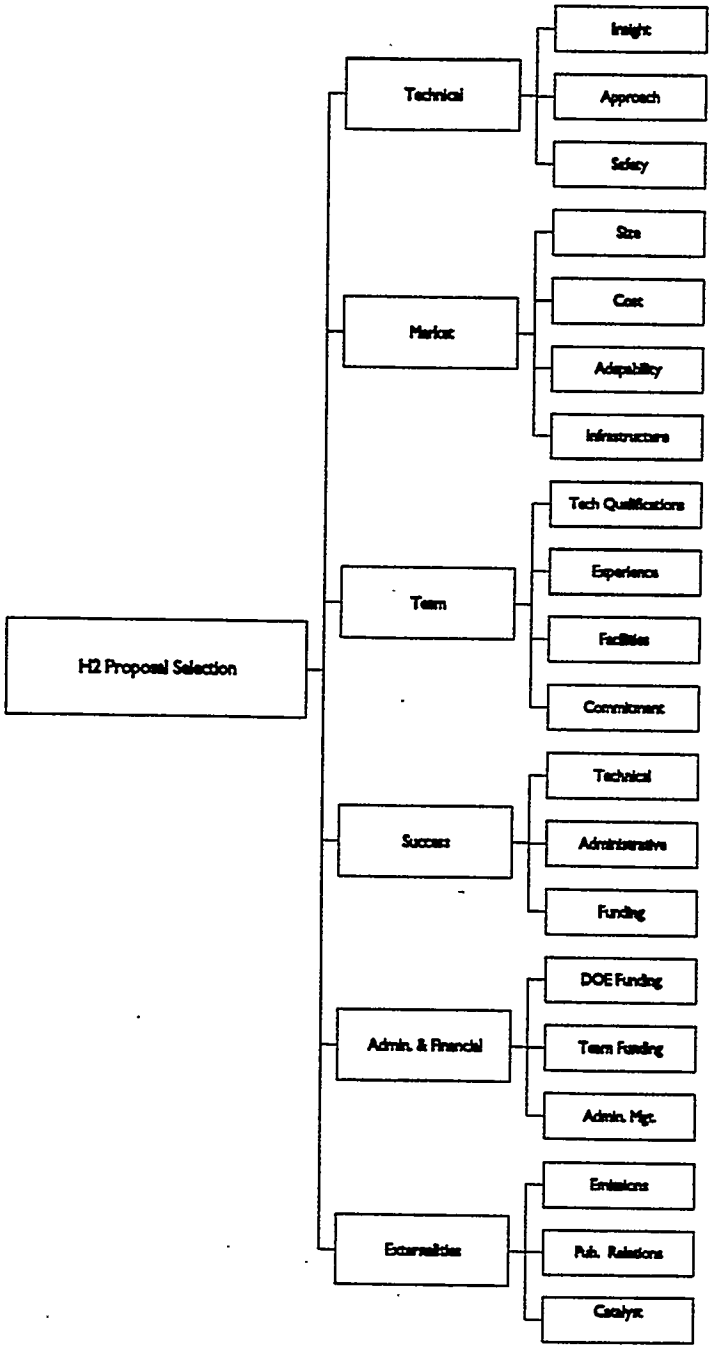


Figure 1

Proposal Evaluation Criteria and Sub-Criteria		
Major Criteria	**Sub-Criteria**	**Definition**
Technical		The technical aspects of a proposal that indicate that the project is technically feasible, will add substantive value to the H2 Program development and can be constructed and operated in a safe manner.
	Insight	The engineering and scientific insight evidenced by the unique design and operational characteristics of the project. Insight includes the expected contributions to the H2 Program technological knowledge base.
	Approach	Indicates how well the technological aspects of the project conform to the RFP's statement of work. The technical proposal should be largely consistent with programmatic objectives at the validation level.
	Safety	The real and perceived safety of the operating equipment. Safety includes fault level monitoring and error correction equipment, operator training and contingency planning for emergencies.
Market		The market promise of the proposed technologies. Market characterization includes the size of the market directly related to the project, the cost of the product versus a conventional technology and the potential adaptation directed to an alternative application.
	Size	Represents the size of the market directly related to the technologies being validated.
	Cost	Indicates the relative cost of the technology being validated versus a conventional technology. It is proper to consider probable advances in the proposed technologies that will make them more cost competitive in the future.
	Adaptability	Indicates how adaptive a project's energy pathway is to alternative end-uses or component substitution.
	Infrastructure	The availability of the infrastructure required to support the commercialized technology pathway.

Table 2.1 Criteria Definitions

Proposal Evaluation Criteria and Sub-Criteria		
Team		The quality and commitment of the investigating team.
	Capabilities	The technical capabilities of the project team. Capabilities include levels of education and training of participating engineers and scientists. They also include training and experience of equipment operators and technicians
	Experience	The direct experience of the project team with the technologies being proposed.
	Commitment	Extent of corporate and personal commitment to the project including a breakout of proposed hours dedicated by senior staff..
	Facilities	Adequacy of the proposed facilities and physical plant to safely construct and operate the equipment specified in the proposal.
Success		Probability that specified technical and administrative hurdles will be overcome.
	Technical	The probability that the project will meet the major technical objectives specified in the proposal.
	Administration	The probability that licencing, permitting, government and public opinion hurdles will be met.
	Funding	The probability that the project will be successfully funded throughout its expected life length.
Finance and Administration		Indications of financial commitment by the proposing team, the expected commitment from DOE and the quality of the administrative team that will oversee the project.
	DOE Cost	The expected contribution to the project by DOE.
	Team Cost	The financial contribution supplied by the proposing team.
	Admin. Mgt.	The quality of the administrative management team.

Table 2.2 Criteria Definitions

Proposal Evaluation Criteria and Sub-Criteria		
Externalities		Aspects of the project that demonstrate the positive benefits of hydrogen technologies, disseminate information about hydrogen technologies to the public and catalyze interest in the Program by influential stakeholder groups.
	Emissions	The relative reduction in emissions compared to a conventional technology pathway.
	Public Relations	The visibility and attractiveness of the technologies to the general public.
	Catalyst	The potential for the project to catalyze future interest in and funding of the Hydrogen Program.

Table 2.3 Criteria Definitions

H Scan/AHP

A decision support methodology for proposal evaluation

Developed by NREL and Energetics, Incorporated
Presented by Stephen Mack, Energetics

The Annual Hydrogen Program Review, April 1996

Rationale

A consistent, explainable process is needed to select high value projects that are part of a progressive Hydrogen portfolio

- The Hydrogen Program will fund high cost/impact projects through a competitive bidding process
- The decision environment in which to select projects of this scope is complex
- Program management has recognized the need to develop a formal proposal evaluation process that integrates both quantitative and qualitative factors into the selection process

Figure 2.1

Team Approach

H Scan/AHP is a two-phased methodology for evaluating proposals

- The H Scan, developed by NREL, is a survey instrument that extends beyond a traditional proposal
- H Scan collects 5 categories of additional supporting information from the proposer
  - Technology System and Market
  - Energy Efficiency and Economics
  - Environmental Impacts
  - Regulation, Safety and Reliability
  - Capabilities, Experience and Commitment

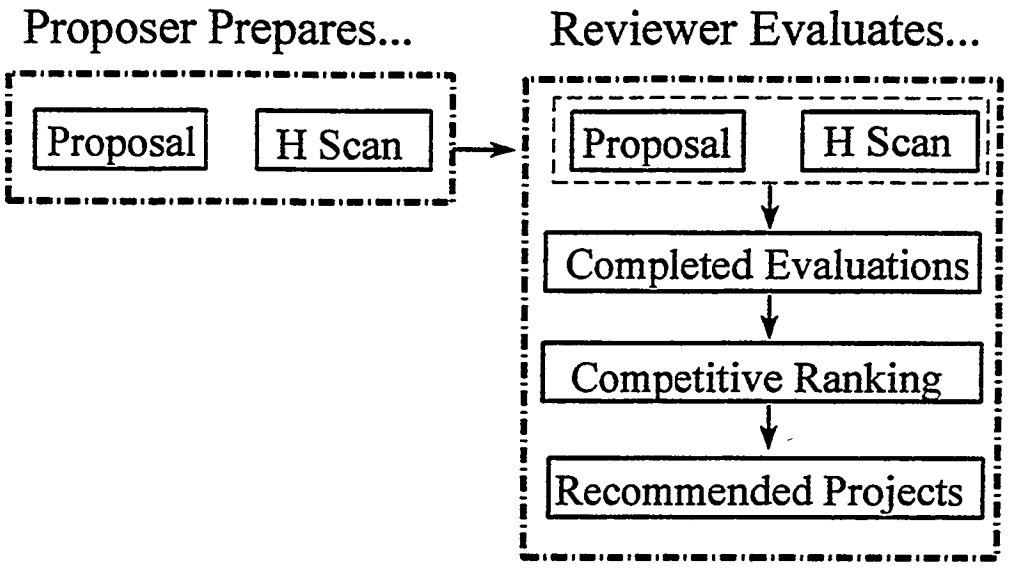
Team Approach cont'd

The evaluation model, developed by Energetics, is linked with H Scan to rank competing proposals

- The Analytic Hierarchy Process (AHP) serves as the decision platform for the competitive evaluation process
- Program management defines the important criteria for evaluating candidate proposals with an AHP decision model
- The AHP pairwise comparison process is used to weigh decision criteria for importance
- Candidate proposals are competitively evaluated against the criteria of the decision model.
- H Scan results are a primary information source for the evaluation

Figure 2.2

Proposal Evaluation Process

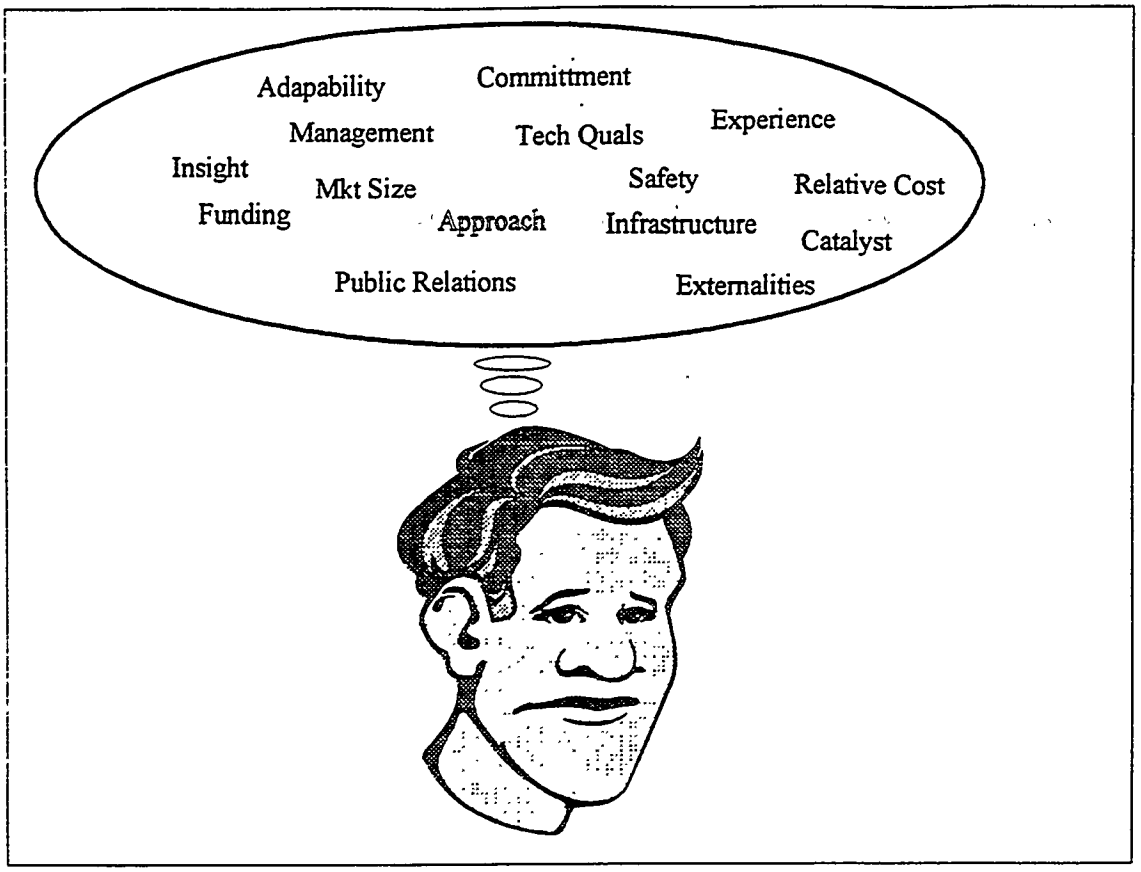


H Scan Sample (Section 5)

Component and Pathway Details

- Describe the components of the pathway for technology development
- Is H2 technology system a substitute for an existing product or process? If so describe
- Is it a whole or partial substitute? Explain
- Is the component an enabling technology? Explain
- Is this a "redesign" issue? Explain

Figure 2.3



Hydrogen Proposal Decision Hierarchy

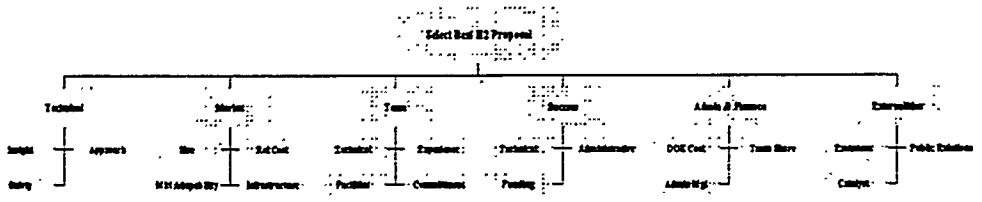


Figure 2.4

Benefits

An H Scan/AHP decision support system for proposal/project evaluation will add tangible benefits

- Builds a structured, focused decision environment
- Assembles augmented proposal information critical to a thorough evaluation
- Incorporates qualitative factors into the evaluation process
- Considers tradeoffs between conflicting criteria
- Induces collaboration in the evaluation process
- Supports the Program in oversight by documenting how project selections are made
- Helps ensure that selected projects closely reflect programmatic objectives
- Can serve as an analytical platform for the management of a robust Hydrogen technology portfolio

Past Results

Conceptual Development of H Scan/AHP Strategy

- Work was initiated in the 1995 planning year
- Premise of the decision strategy was outlined
- Evaluation criteria were defined by Program management
- Sample decision hierarchies were constructed
- H Scan prototype was developed using the defined criteria as its structural framework

Figure 2.5

Current Year Results

H Scan/AHP Implementation

- The H Scan/AHP methodology was successfully tested using two unsolicited proposals as candidates.
- The proposal information was sent to two reviewers for H Scan evaluation and ranking using the AHP decision model
- The reviewers completed the complementary H Scan form, generated criteria weights and ranked the candidate proposals competitively
- Completed H Scan/AHP packages were analyzed for content, completeness and comparison of the reviewers evaluations

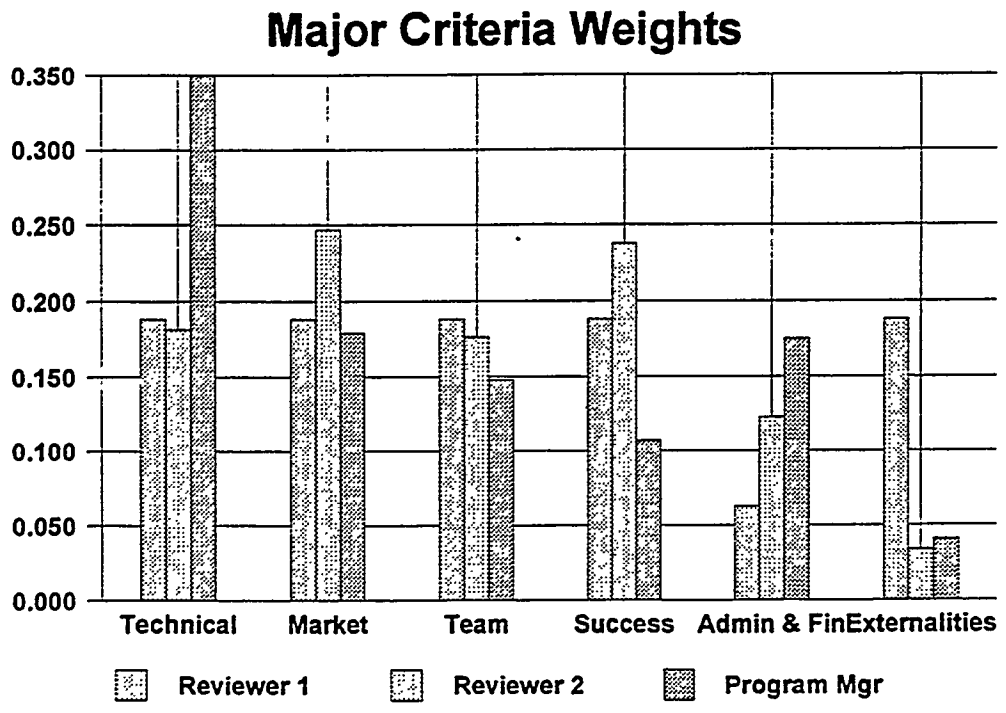
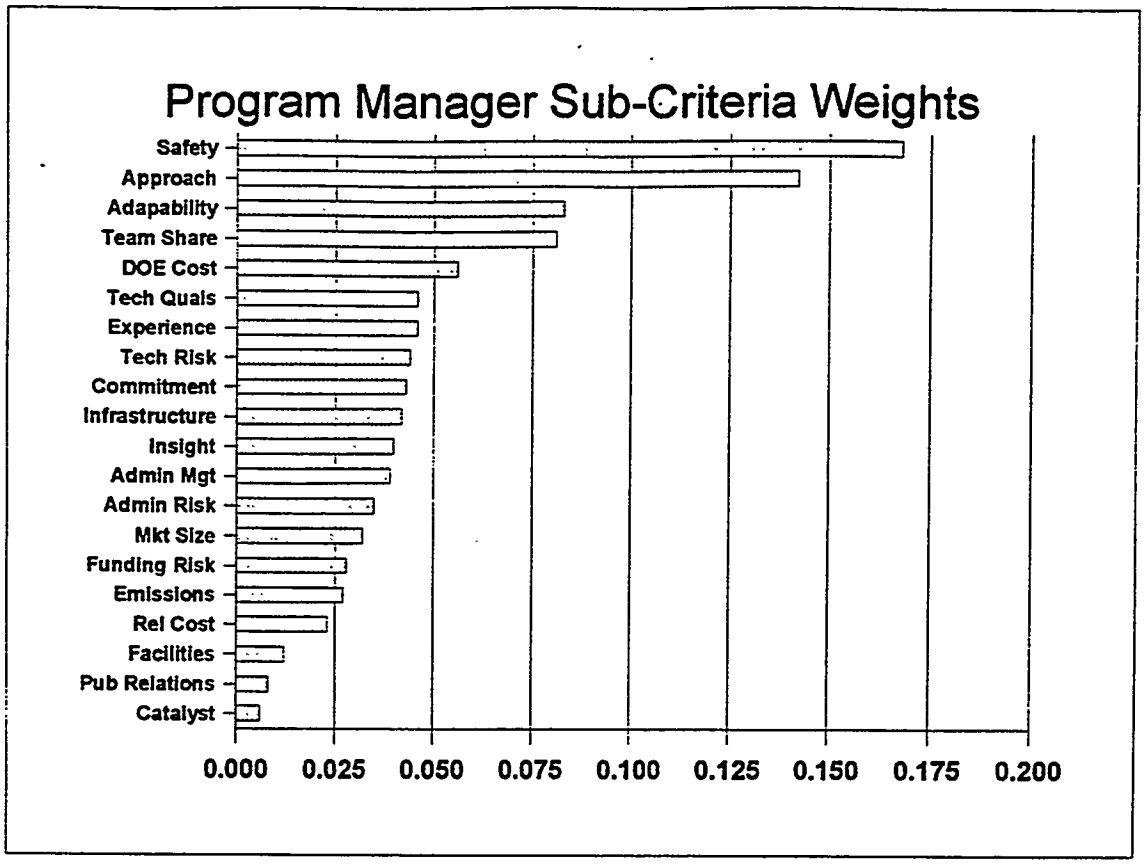


Figure 2.6


Program Manager Sub-Criteria Weights
Safety
Approach
Adapability
Team Share
DOE Cost
Tech Quals
Experience
Tech Risk
Commitment
Infrastructure
Insight
Admin Mgt
Admin Risk
Mkt Size
Funding Risk
Emissions
Rel Cost
Facilities
Pub Relations
Catalyst
0.000
0.025
0.050
0.075
0.100
0.125
0.150
0.175
0.200

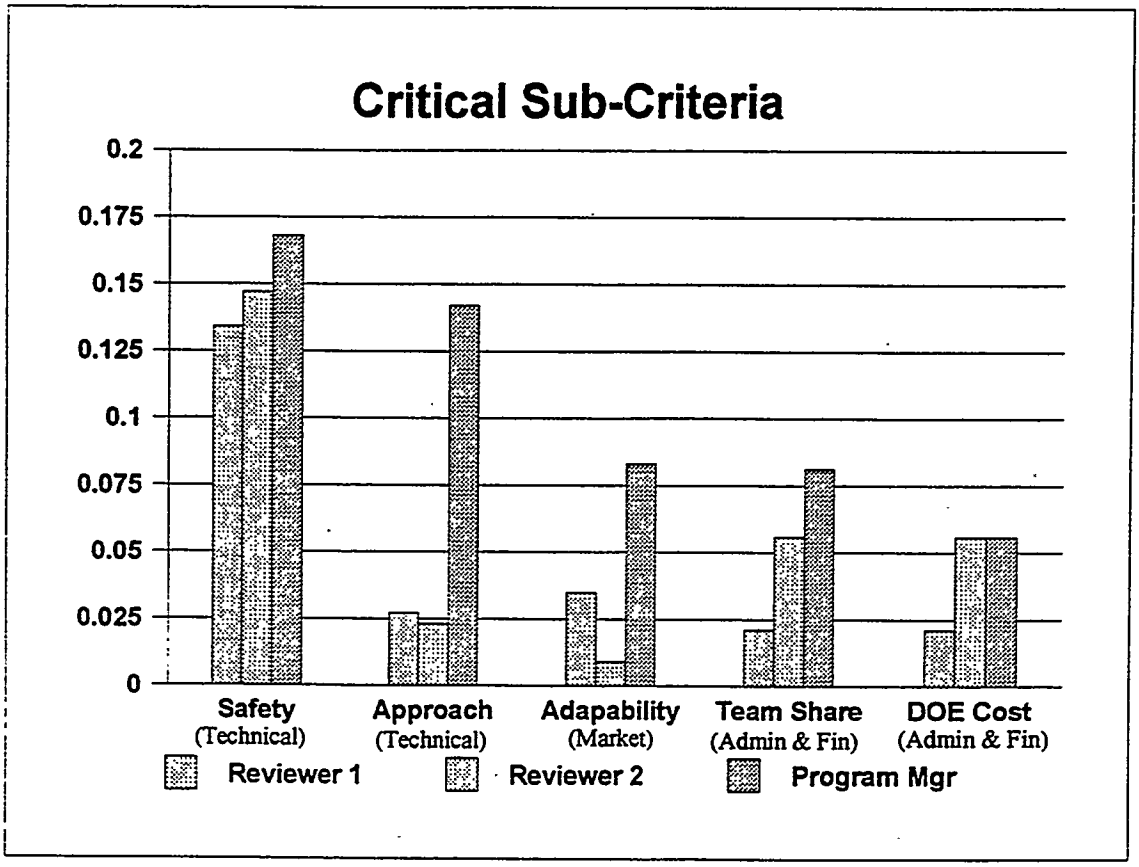

Critical Sub-Criteria
0.2
0.175
0.15
0.125
0.1
0.075
0.05
0.025
0
Safety (Technical)
Approach (Technical)
Adapability (Market)
Team Share (Admin & Fin)
DOE Cost (Admin & Fin)
Reviewer 1
Reviewer 2
Program Mgr

Figure 2.7

Plans for Future Work

Implementation Protocol

- Develop protocol for AHP criteria definition and weighting
- Generate a revised H Scan that reflects feedback and recommendations
- Validate the H Scan/AHP outcomes with Program management
- Implement H Scan/AHP methodology for projected portfolio analysis
- Investigate other value added applications of the methodology

Projected Goals

Full Implementation

- Implement modified H Scan/AHP framework for next round of proposals
- Extend modeling paradigm to other Program decision environments

Figure 2.8

Barriers/Lessons Learned

Needed Steps to Full Implementation

- ☐ Inclusion of additional stakeholders in the process
  - IAG
  - HTAP
  - Industry outreach participants
  - Business representatives
- ☐ H Scan/AHP training session for reviewers
- ☐ Seek to minimize the complexity of the process

Figure 2.9

SYSTEMS ANALYSIS - INDEPENDENT ANALYSIS AND VERIFICATION

J.P. DiPietro, E.G. Skolnik, and J.S. Badin
Energetics, Inc.
Columbia, MD 21046

Introduction

The Hydrogen Program of the U.S. Department of Energy (DOE) funds a portfolio of activities ranging from conceptual research to pilot plant testing. The long-term research projects support DOE's goal of a sustainable, domestically based energy system, and the development activities are focused on hydrogen-based energy systems that can be commercially viable in the near-term. Energetics develops analytic products that enable the Hydrogen Program Manager to assess the potential for near- and long-term R&D activities to satisfy DOE and energy market criteria.

Our work is based on a pathway analysis methodology. We consider an energy component (e.g., hydrogen production from biomass gasification, hybrid hydrogen internal combustion engine (ICE) vehicle) within a complete energy system. The work involves close interaction with the principal investigators to ensure accurate representation of the component technology. Comparisons are made with the current cost and performance of fossil-based and alternative renewable energy systems, and sensitivity analyses are conducted to determine the effect of changes in cost and performance parameters on the projects' viability.

Past Results

Energetics developed the E-3 Pathway Analysis Model in 1994. The model shows users the levelized cost and full life-cycle emissions of a set of hydrogen-based and fossil-based energy pathways. It allows users to conduct sensitivity analyses with respect to component capital costs, efficiencies, operations and maintenance costs, and financial parameters.

Building upon the pathway analysis methodology, in 1995 we initiated more detailed analyses of specific hydrogen energy concepts. In these analyses, each pathway component was discussed and the basis for the size and cost estimates defined. Screening analyses were developed to identify the component variables that produced the most significant effect on the overall pathway cost, and

selected sensitivity analyses were performed on the most important factors. Table 1 lists the detailed analyses completed in 1995 and summarizes the results.

Table 1. Detailed Pathway Analyses Completed in FY 1995

Energy System Concept	Pathway Analysis Results
An integrated electricity storage and hydrogen production system incorporating a solar-powered HBr reactor and a reversible HBr cell.	The benefits of the system include a high utilization of capital equipment and the proven low electricity consumption of the HBr cell. The HBr production reactor must be proven, and the cost of the HBr cell must be estimated. Also, industrial facilities into which the SRT process can be integrated must be identified.
Dedicated switchgrass crops are gasified, the hydrogen-rich effluent is purified by an iron-bed system, and the pure hydrogen product is fed to a proton exchange membrane fuel cell for baseload electricity generation.	The iron-bed system takes the place of conventional hydrogen purification, compression, and buffer storage. The cost of dedicated biomass feedstock and potential problems with alkali slagging limit the attractiveness of this concept. Low-cost proton exchange membrane (PEM) fuel cells and indirect gasification must be proven.
A small-scale (1-2 kW) electrolyzer located at a residence supplies hydrogen to a personal-use hybrid hydrogen ICE vehicle.	The electrolyzer avoids the large investment in hydrogen transport infrastructure. Although the levelized cost of hydrogen is high, it is a small portion of the total cost of the transportation system. A low-cost, small-scale electrolyzer and an on-board storage system must be developed.
Several small (50-kW) wind turbines are used to supply electricity to a remote Alaskan village. A hydrogen-based energy storage system is used to match wind turbine generation and load from the village.	The high cost of electricity from a diesel generator and the high-quality wind resources in Alaska favor the hydrogen-based system. The low utilization of the electrolyzer (33%) and the low round-trip efficiency of the hydrogen-based storage system (40%) limit the viability of this concept.

Additional work in 1995 included development of the first version of the Hydrogen Technology Cost and Performance Database. The database contains cost and performance data for hydrogen production, storage, and end-use technologies from the technical literature and industry sources.

Current Year Results

In FY 1996, we continued the detailed analysis of hydrogen energy concepts. Table 2 lists the analyses completed in 1996 and summarizes the results.

As an example of our analytic efforts, consider the HBr-based hydrogen production process being developed by Solar Reactor Technologies, Inc. The process uses sunlight energy to produce HBr from bromine and steam. The HBr is then electrolyzed to produce hydrogen. Figure 1 is a block flow diagram of the process. Our first step was to create a heat and material balance for the process, which identifies the relative sizes of the various process equipment. The capital cost of each piece of equipment was then estimated based on its size, and the cost of hydrogen was calculated based on the total system's capital cost, the operation and maintenance charges, and the credit for by-product oxygen and peak electricity.

We developed a spreadsheet model that contains all the analytical expressions that contribute to the

heat and material balance, the system's capital cost, and the cost of hydrogen from the system. This model contains 55 discrete inputs (e.g., hours per day of usable sunlight, amount of heat re-radiated from the reactor, cost of off-peak electricity). This model has been transferred to the investigators at Solar Reactor Technologies for use in tracking the economics of the process as technical progress is made, and to evaluate the process in specific applications where location-specific factors are known.

Table 2. Detailed Pathway Analyses Completed in FY 1996

Energy System Concept	Pathway Analysis Results
Municipal solid waste (MSW) is suspended in a water-based slurry and charged to a gasifier producing hydrogen-rich gas. The gasifier effluent is shifted and purified, producing hydrogen gas.	The low base-case cost of hydrogen ($8/MBtu) is due to the low-value feedstock. Economics are strongly dependent on a sustained tipping fee for MSW and the degree to which raw MSW must be classified (i.e., the range of materials that can be suspended in the slurry).
A large-scale (100-MW) geothermal electricity generation unit supplies full electricity service (both peak and baseload) to a load center. The geothermal unit is operated at a level rate, and surplus electricity fuels an electrolyzer. Hydrogen is used to fuel zero-pollution vehicles in the Los Angeles basin.	Large amounts of waste heat from a geothermal unit make it a good match with HTS electrolysis. However, geothermal sites are far from population centers and the cost of transporting hydrogen from the geothermal site is significant. The scale of the project is high compared to vehicle penetration forecasts.
A hydrogen-based energy storage system (electrolyzer/hydrogen/storage/fuel cell) stores surplus off-peak electricity on the island of Hawaii and releases it during peak hours.	The island's fossil fuel costs are high and the utility has a significant surplus of baseload capacity. Also, location of the fuel cells at the load center can reduce peak-time reliance on transmission lines, improving reliability. The avoided cost of peak electricity set by the local utility is low (6 cents/kWh) limiting this concept's viability.
Golf carts are retrofitted with a 4-kW PEM fuel cell and used for personal transportation in the city of Palm Desert, California. Hydrogen for the golf carts is produced by a wind-turbine/electrolysis system.	Low-pressure PEM technology eliminates the need for the on-board air compressor, which is important for small vehicles. Golf cart-sized vehicles are easier to build than buses or full-size passenger cars, but a battery-powered electric vehicle is well suited for the low-range golf cart application.
A more detailed analysis was undertaken of the integrated electricity storage and hydrogen production system incorporating a solar-powered HBr reactor and a reversible HBr cell.	The size of the solar field is large relative to the amount of hydrogen produced (a 100,000-scfd plant would require a 6-acre solar field), and the low conversion in the reactor (9 mole % of HBr in the reactor effluent) greatly increases the size of the product recovery and heat exchange equipment. Significant technical improvements must be achieved before the process is commercially viable.

The MSW gasification concept provides an example of a more preliminary analysis. MSW is received from solid waste haulers and it is assumed they pay the facility a tipping fee that is comparable to what they would pay at a landfill. The MSW is sorted to remove glass, metal, and other non-gasifiable materials (rejected material is estimated to represent 15 percent of the total

mass), and put into a water-based slurry. The slurry is mixed with oxygen, gasified, and the resulting syngas is purified using a pressure swing adsorption (PSA) system. In Figure 2, we present a block diagram of the MSW gasification pathway as well as pathways for biomass gasification and steam reforming of natural gas.

A standard question we ask when evaluating a pre-commercial process is, "Are the feedstock supplies and/or the by-product markets large enough to support large-scale commercialization of the technology?" In the case of MSW gasification, the supply of MSW is the key question. In 1993, 130 MM tons of MSW were landfilled in the domestic United States. If this entire amount had been slurried and gasified, it would have produced 0.7 quads of hydrogen or enough to fuel 50 million fuel cell vehicles. Thus, we found that the domestic MSW supply is large enough to justify development of the slurry and gasification technology.

The tipping fee that a facility can expect to receive for MSW varies widely with geographic region and the type of contract (i.e., many large haulers receive a significant discount from the posted tipping fee). Figure 3 illustrates the sensitivity of the cost of hydrogen to changes in the tipping fee. (Figure 3 also shows the base case cost of hydrogen from a steam methane reformer and from a biomass gasifier. Significantly, the base case cost of hydrogen from biomass gasification and steam reforming is estimated based on the same financial parameters as those used for the MSW gasifier. Figure 3 demonstrates our conclusion that MSW gasification is competitive with steam reforming of natural gas at a tipping fee of $44 ton.)

In 1996, Energetics also revised the Hydrogen Technology Cost and Performance Database to include more data from equipment manufacturers, improved units of measure, enhanced definitions of efficiencies and capital cost bases, segregation of data based on capacity, and additional data categories (e.g., membranes). In addition, the database was moved to a Paradox platform to facilitate evaluation and updating of data, and to enable future linkage with the E-3 pathway model.

We studied existing, mandated, wind turbine generation fields to determine the economics of coupling them with hydrogen-based energy storage to create a dispatchable peak electricity generation system. Figures 4 through 7 are a series of nomographs that enable utility professionals to quickly assess the cost of peak electricity based on different assumptions such as the value of electricity from the wind field and the capacity factor of the electrolyzer. The nomographs show that a peak electricity generation cost of 22 cents/kWh is achievable with a PEM fuel cell cost of $500/kW.

The following are other analysis tasks completed this year.

- In an additional effort, we supported the development of the Hydrogen Program Utility Sector Quality Metrics analysis, led by NREL. This involved developing projections for the cost of hydrogen production, the capital cost and efficiency of phosphoric acid and proton exchange membrane fuel cells, and emissions reductions in carbon dioxide and nitric oxides resulting from market penetration of fuel cells.

- Energetics also performed a study of the use of licensing as a means of forming partnerships to develop and commercialize novel technologies. The study is based on telephone interviews with licensing industry professionals and provides a discussion of typical negotiation issues and heuristics governing the value of licensing agreements.

- We developed a draft framework that would incorporate environmental-impact considerations into the pathway selection and ranking process. This study reviews the various approaches used to quantify environmental externalities and presents the ranges of values. We have not endorsed a particular set of estimates; however, we have provided a methodology to calculate an environmental performance index (EPI) based on emissions reductions for CO_2, SO_2, NO_x, and differential life cycle costs from a conventional benchmark technology/system. By plotting these two values, technologies can be ranked for their environmental value.

- We recently initiated a study to survey and interview utility industry representatives in order to construct feasible scenarios for utility sector participation in the development of hydrogen energy systems in a restructured utility industry. To date, we have identified a list of industry contacts and drafted a questionnaire for use during the interviews.

We have made an effort to disseminate the results of our analytic activities. We submitted Independent Analysis and Verification of Key Hydrogen Energy Concepts, a compendium of eight pathway analysis reports, to the Hydrogen Technical Advisory Panel. We also presented a paper on the coupling of hydrogen-based energy storage and wind turbine electricity generation at the 7th Annual Canadian Hydrogen Workshop, and are scheduled to present a poster session at the 11th Annual World Hydrogen Energy Conference. In addition, the E-3 Pathway Analysis Model was distributed to the IEA Executive Committee.

Plans for Future Work

In 1997, we plan to finalize the Hydrogen Technology Cost and Performance Database. We will also publish the final report on the "Utility Restructuring Research and the Environmental Externalities" studies, and will perform additional analyses in a coordinated effort with the NREL process analysis group.

Figure 1. SRT Hydrogen/Electricity Generation System

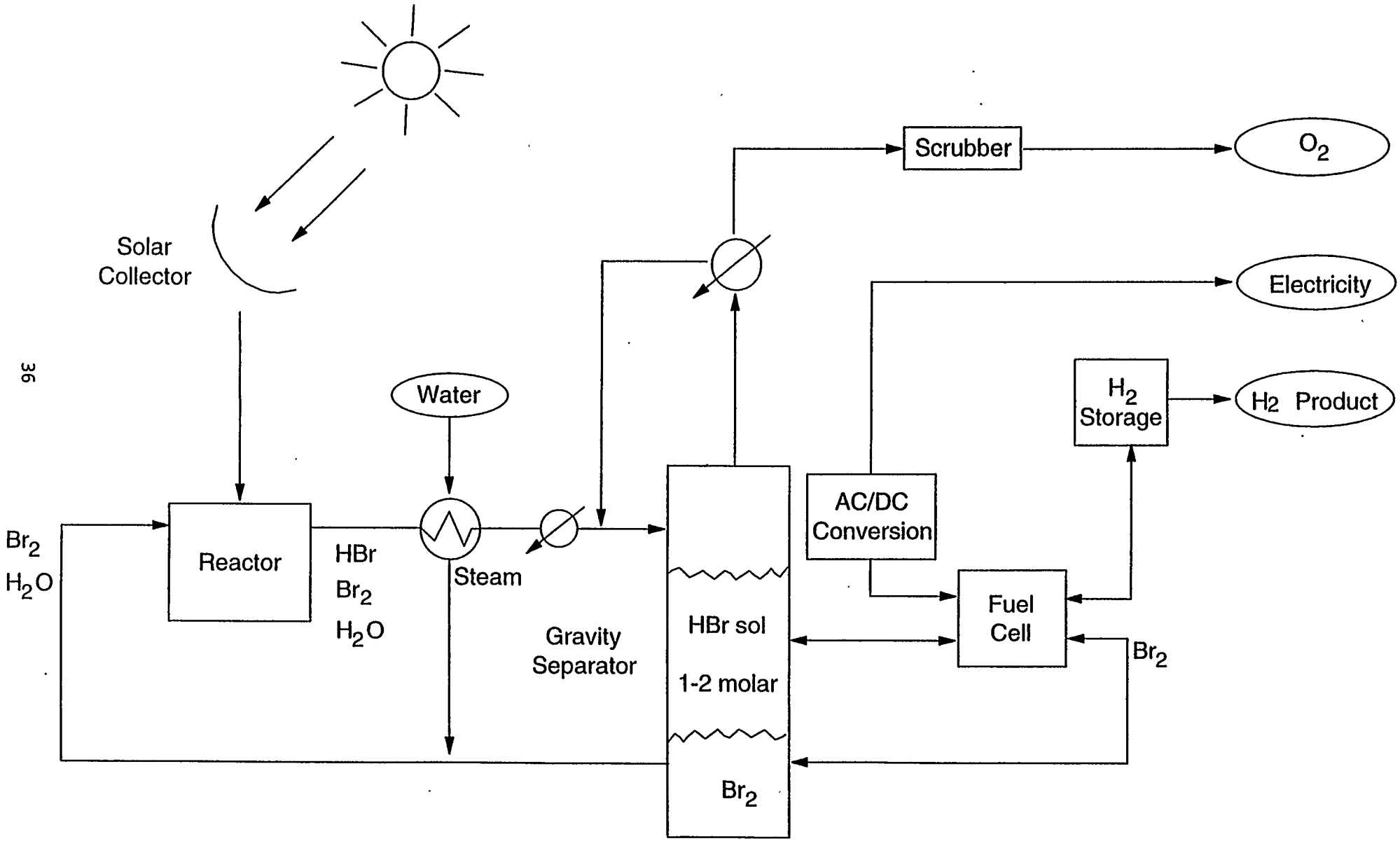
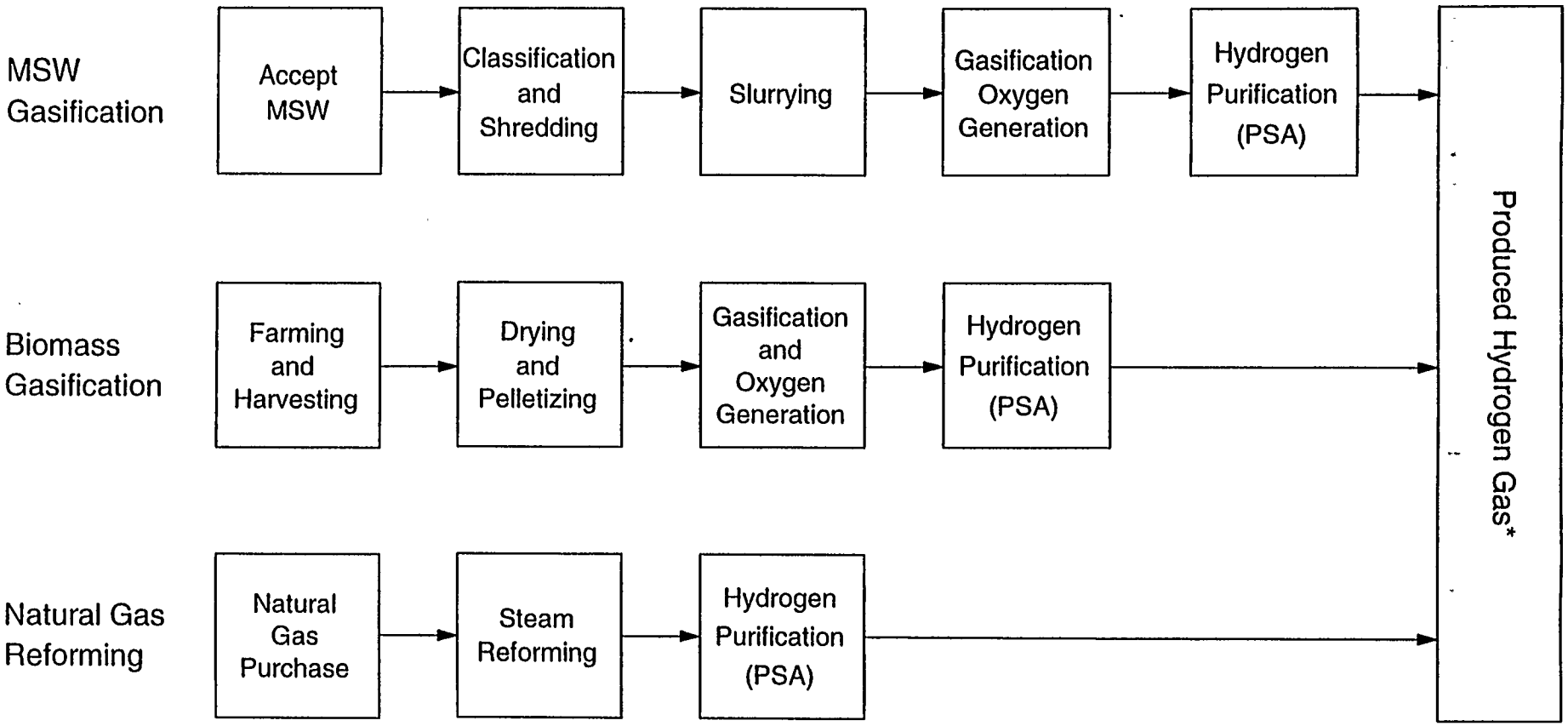
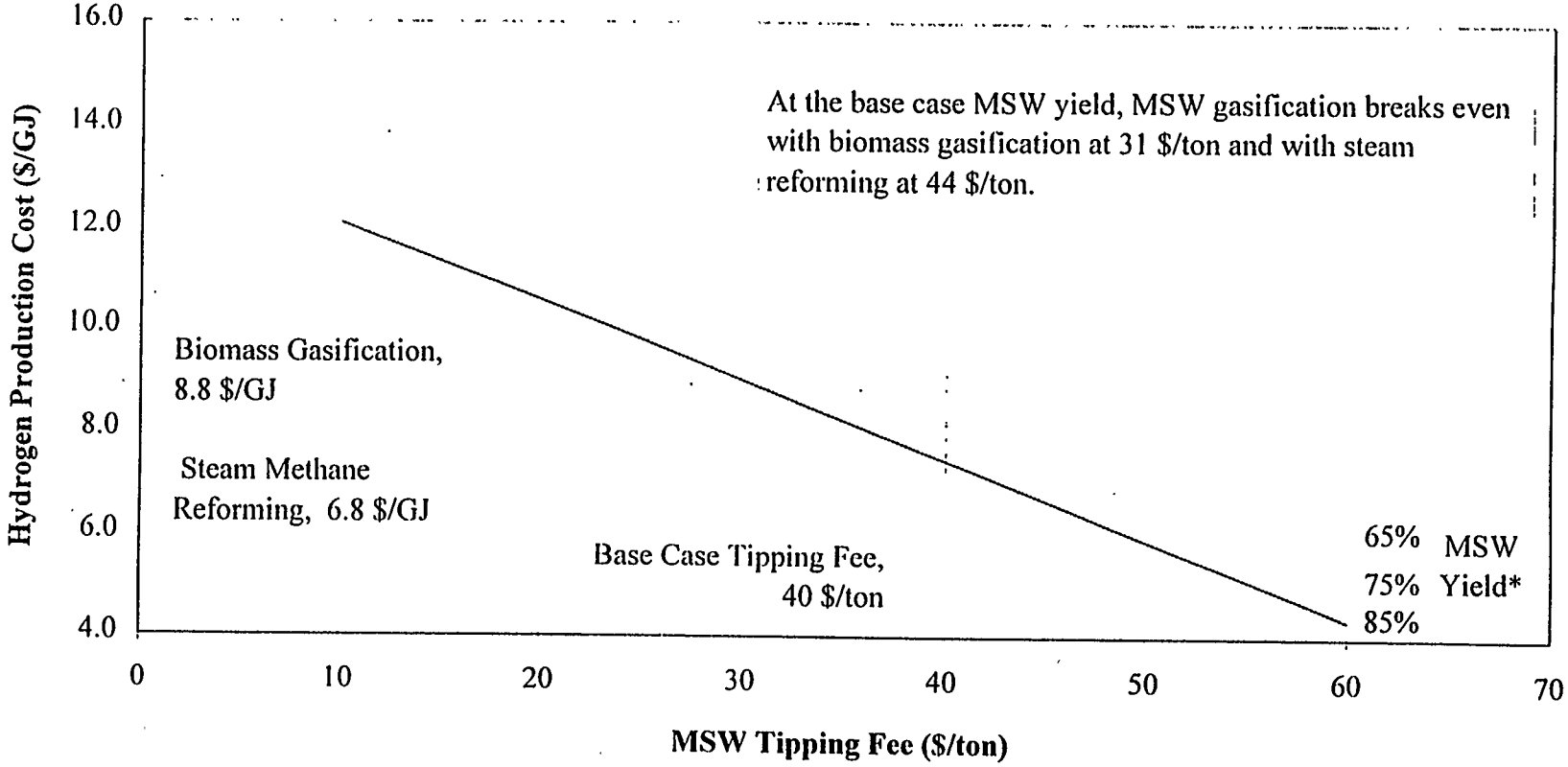


Figure 2. MSW Gasification Analysis: Hydrogen Production Pathways



*The pathway analyses and costs do include the compression and storage of hydrogen product.

Figure 3. MSW Gasification Sensitivity Analysis with Respect to MSW Tipping Fee and MSW Yield



* The MSW yield is defined as the GJ of MSW charged to the slurry unit per GJ of unclassified MSW received by the facility.
Costs based on a unit capacity of 66 MMSCFD.

Figure 4

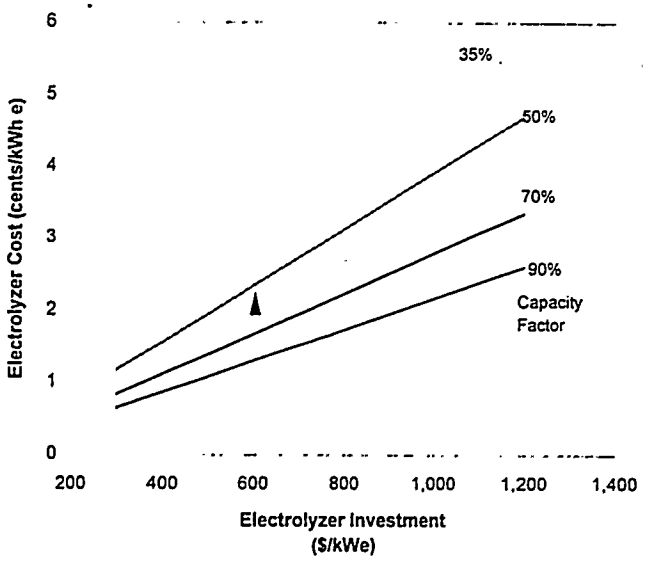


Figure 5

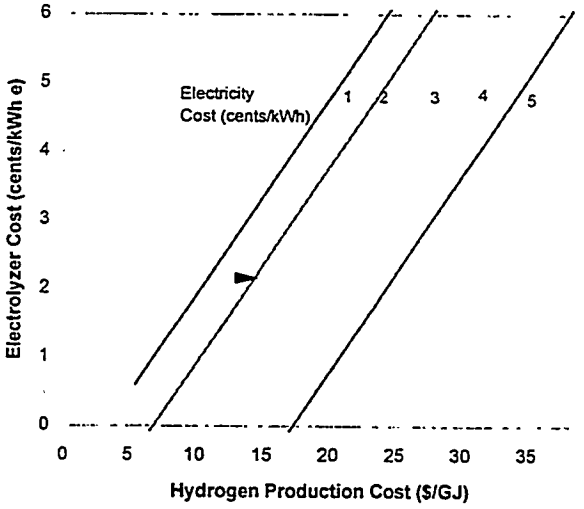


Figure 7

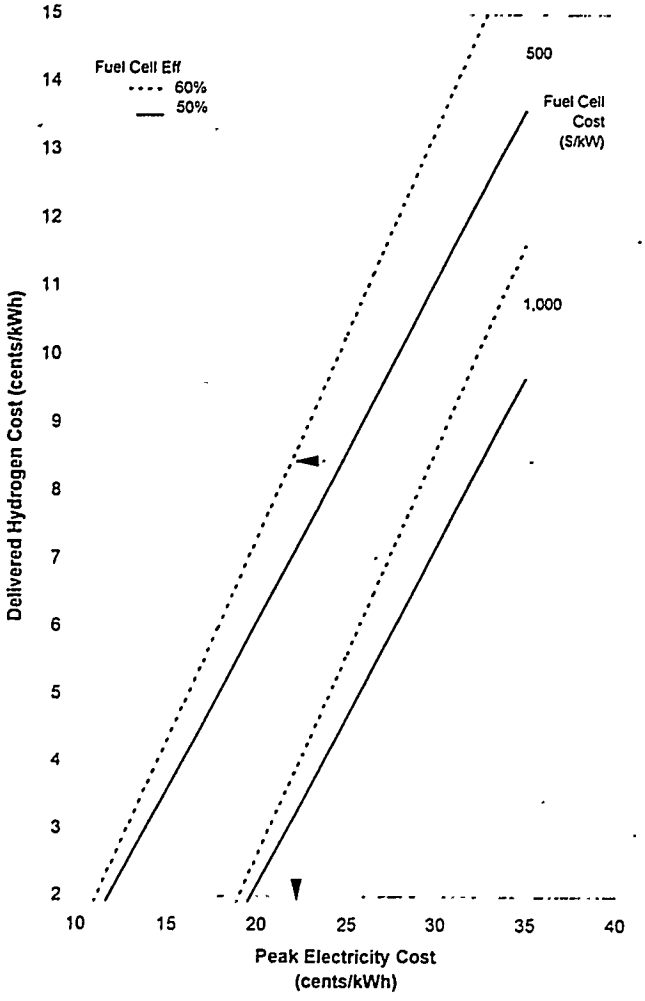
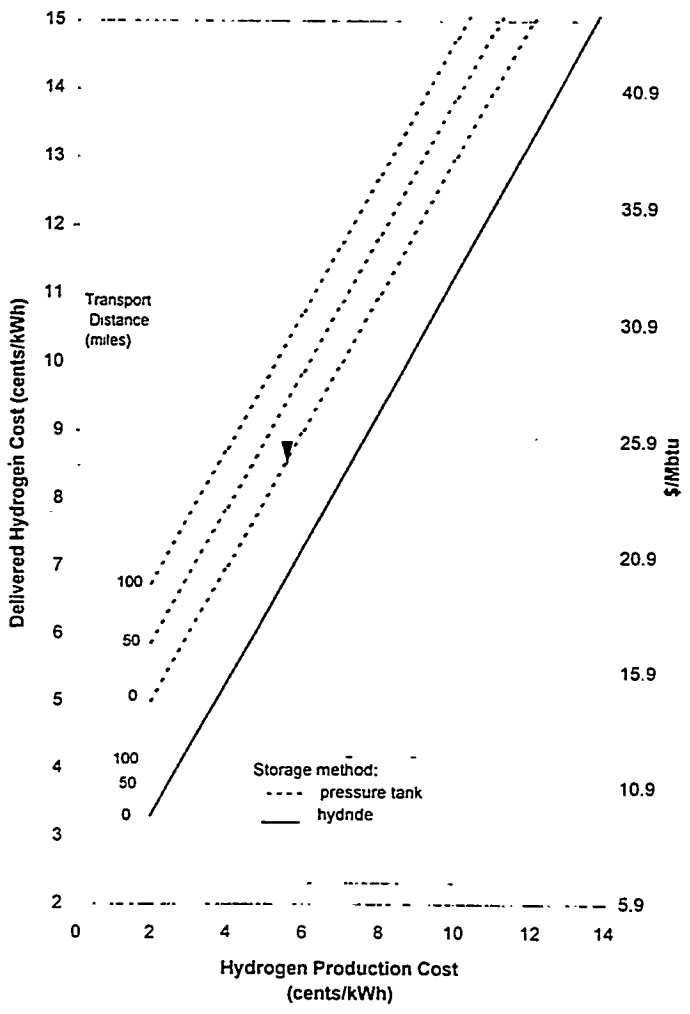


Figure 6



SYSTEM COMPARISON OF HYDROGEN WITH OTHER ALTERNATIVE FUELS IN TERMS OF EPACT REQUIREMENTS

F. Barbir, K. Özay and T.N. Veziroglu
Clean Energy Research Institute
University of Miami
P.O. Box 248294
Coral Gables, FL 33124

Abstract

The feasibility of several alternative fuels, namely natural gas, methanol, ethanol, hydrogen and electricity, to replace 10% of gasoline by the year 2000 has been investigated. The analysis was divided in two parts: (i) analysis of vehicle technologies, and (ii) analysis of fuel production storage and distribution, from the primary energy sources to the refueling station. Only technologies that are developed to at least demonstration level were considered. The amount and type of the primary energy sources have been determined for each of the fuels being analyzed. A need for a common denominator for different types of energy has been identified.

Project Rationale

Section 502(a) of the Energy Policy Act (EPACT) of 1992, requires a program promoting domestic replacement fuels in light duty motor vehicles which will have the greatest impact in reducing oil imports, improving the health of our Nation's economy and reducing greenhouse gas emissions. It sets the goals of achieving 10% replacement by 2000 and 30% replacement by 2010. Energy Policy Act defines alternative fuels as: methanol (or mixtures of >85% of methanol), ethanol (or mixtures of >85% of ethanol), natural gas, liquefied petroleum gas, electricity, **hydrogen**, coal derived liquids and fuels derived from biological materials. Each of these fuels is derived from different primary sources and has different efficiencies associated with its processing, delivery, storage and end use. Different processes involved imply different

economic requirements and different emissions. Consequently, the impact each of these fuels may have on the health of our nation's economy and environment would be different as well.

The objectives of this project were:

- determine technical and economic feasibility of each of the replacement fuels to meet the EPACT goals;
- determine the potential effects of such replacement on economy and environment;
- examine and highlight hydrogen's potential as compared with other replacement fuels.

Transportation Fuel Requirements

Gasoline is the primary transportation fuel in the U.S. Curent gasoline consumption is 315 million gallons per day (over 100 billion gallons per year) [1]. DOE projects that gasoline consumption will continue to increase in spite of increasing vehicle efficiency (Table 1) [1]. This forecast is based on an assumption of uninterrupted oil supply and relatively steady prices [2].

Table 1 Current and future gasoline consumption

		1995	2000	2010
gasoline consumption	10^6 gallons/day	315	340	353
avg. vehicle efficiency	mpg	19.3	20.3	21.8
new vehicle efficiency	mpg	27.8	28.9	32.8
vehicle-miles	10^{12} miles/yr	2.22	2.52	2.81
gasoline price*	1993 $/gallon	0.727	0.815	0.867

* taxes not included

In order to achieve 10% fuel savings by 2000 (34 million gallons of gasoline per day) it would be necessary to introduce vehicles powered by alternative fuels and traveling 2.52×10^{11} miles/yr. This may be achieved by replacing 10% of vehicles with average efficiency (20.3 mpg in 2000) or 6% of the most inefficient (older) vehicles (with 13.5 mpg fuel efficiency on average). The later is a more likely scenario.

Alternative fuels make unsignificant contribution today (less than 1% of total vehicle fuels) [3]. However, large amount of methanol and ethanol are added to gasoline as oxygenates (either directly or indirectly), as shown in Table 2. This is still much less than required 10%. In order to determine the amount of each alternative fuel needed to replace 10% of gasoline, it is important to determine the efficiency of the alternative fuel vehicles first, i.e., to determine the amount of fuel needed to travel distance of 1 mile (or 1 km).

Table 2 Consumption of vehicle fuels in U.S. (1995)
(million gallons of gasoline equivalent)

	consumption	percentage
Alternative Fuels		
LPG	260.0	0.23
CNG	43.6	0.04
LNG	3.1	
Methanol (85%)*	2.4	
Methanol (100%)	3.1	
Ethanol (85%)*	0.1	
Ethanol (95%)*	0.1	
Electricity	0.6	
Subtotal	312.9	0.28
Oxygenates		
MTBE	2,973.3	2.57
Ethanol in gasohol	919.3	0.79
Other alcohols & ethers	201.2	0.17
Subtotal	4,093.8	
Diesel	26,739.6	
Gasoline**	115,809.0	

* includes gasoline
** includes oxygenates

Vehicle Efficiency Analysis

Several vehicle propulsion technologies are available and applicable for alternative fuels. Almost each of the alternative fuels (except electricity) may be used in internal combustion engines with minor modifications mainly in fuel supply components. Another technology which is currently being developed is fuel cell/electric vehicle technology. Fuel cells, particularly proton exchange fuel cells, are very promising because of their high conversion efficiency, simplicity, high power density, and zero emissions. Hydrogen is the fuel of choice for fuel cells. However, due to lack of hydrogen infrastructure some car manufacturers are developing on-board reforming systems that enable the use of more conventional fuels such as methanol and natural gas. Direct methanol fuel cells are being developed, but are far from being developed even to a demonstration level. Electricity is also considered to be an alternative fuel. The only way to use it as fuel is to store in on-board in batteries. A variety of battery technologies are being developed with a common goal to reduce the weight and increase vehicle range [4].

The amount of each of the alternative fuels analyzed (hydrogen, CNG, electricity, methanol and ethanol) needed to meet the EPACT goals have been determined based on a detailed analysis of vehicle technologies available in given time frame. In order to compare all the fuel on an equal basis the following assumptions were made:

Vehicle mass:	800 kg
Payload:	136 kg
Engine power:	100 hp (75 kW)
Range:	300 miles (483 km) except or battery electric vehicles where 100 miles (161 km) range was considered

The mass of the power plant, specific energy of the fuel tank (in kWh_{fuel}/kg), and the power plant efficiency in FUDS cycle (in terms of J of energy delivered to the wheels per J of energy in fuel consumed) was calculated based on various published data [4-11] for each of the fuels and vehicle power plant technologies. Fuel economy (in kWh_{fuel}/km) was then calculated from the following equation:

$$Fe = \frac{(M_v + M_e + M_p)e_c}{\eta_m - \frac{R \cdot e_c}{S}}$$

where:

M_v = mass of vehicle (kg)
M_e = mass of engine (kg)
M_p = payload (kg)
e_c = average traction energy = kWh/km/kg
η_m = overall mechanical efficiency
R = range (km)
S = storage specific energy (kWh/kg)

The results are shown in Tables 3, 4 and 5 for internal combustion engine, fuel cell, and battery electric vehicles respectively. The results indicate that the hydrogen fuel cell electric vehicles are the most efficient (~70 mpg gasoline equivalent) and will thus require the least amount of fuel (on energy basis) to meet the EPACT goals. Battery vehicles are also very efficient, but their range is limited to approximately 100 miles, due to their heavy weight.

Table 3 Results of vehicle efficiency analysis for internal combustion engine vehicles (FUDS cycle)

	kWh*/km	mpg**
Gasoline	0.734	28.6
CNG	0.661	31.8
LPG	0.650	32.3
Methanol	0.578	36.3
Ethanol	0.567	37.0
GH_2	0.707	29.7
LH_2	0.624	33.6

* lower heating value (1 kWh = 3,412 Btu) ** gasoline equivalent

Table 4 Results of vehicle efficiency analysis for fuel cell vehicles (FUDS cycle)

	100 miles range		300 miles range	
	kWh*/km	mpg**	kWh*/km	mpg**
GH_2	0.306	68.6	0.327	64.2
LH_2	0.301	69.8	0.311	67.5
CNG	0.464	45.3	0.478	43.9
Methanol	0.470	44.7	0.483	43.5

* lower heating value of fuel (1 kWh = 3,412 Btu)
** gasoline equivalent

Table 5 Results of vehicle efficiency analysis for battery electric vehicles (FUDS cycle)

	100 km range	
type of battery	kWh*/km	mpg**
Na/Sulfur	0.256	82.0
Lead-Acid	0.516	40.7
Li-Ion	0.230	91.3
Li-AlS or Li-FeS	0.276	76.1
Nickel/Iron	0.533	39.4
Nickel/MeH	0.250	84.0
Zn/Bromine	0.281	74.7

*charging included
** gasoline equivalent

Fuel Production Analysis

Table 6 summarizes the results of the above analysis and shows the amount of each fuel needed to achieve 10% of gasoline replacement. However, the analysis has been expanded further to include fuel production, processing, storage and delivery technologies, in order to determine possible obstacles (in terms of quantitative and qualitative primary energy requirements, costs, technology availability, infrastructure issues, etc.) and benefits (in terms of reduced greenhouse gas emissions throughout the analyzed pathways).

Table 6 Summary of vehicle efficiency analysis: Ammount of fuel needed to replace 10% of gasoline

	kWh/km	10^9 kWh/yr (10%)	10^9 kWh/yr (10%)	current production
Internal combustion engine				
CNG	0.661	271.0	162.6	5,600
LPG	0.650	266.5	159.9	644
Methanol	0.578	237.0	142.2	28
Ethanol	0.567	232.5	139.5	31
GH_2	0.707	289.9	173.9	~300
LH_2	0.624	255.8	153.5	
Fuel cells				
GH_2	0.327	134.1	80.5	~300
LH_2	0.311	127.5	76.5	
CNG	0.478	196.0	117.6	5,600
Methanol	0.483	198.0	118.8	28
Battery electric vehicles				
Electricity	0.260	106.6	64.0	3,000

For each of the fuels there are several possible pathways from primary energy sources to the fuel. In this pathway typically one or more energy conversions are included, such as for example, solar energy into electricity (e.g. photovoltaic conversion) and then electricity into hydrogen (e.g. water electrolysis). The efficiencies of these conversions were taken into account when calculating primary energy requirement. In addition, other forms of energy, typically electricity (but in some cases fuels), are needed in process of fuel transportation, storage or delivery. For example, in case of hydrogen, electricity is needed for hydrogen compression to a desired pressure needed for pipeline transport, or for liquefaction. For harvesting biomass, fuels are needed (gasoline, diesel or biomass based fuels). This type of energy (electricity and already processed fuels) represents high quality inputs and have to be accounted separately. Therefore, primary energy and high quality inputs were quantitatively and qualitatively determined. Figure 1 shows a typical pathway analysis (a) and corresponding system analysis (b) that shows energy conversions and high quality inputs. High quality inputs do not necessarily have to be energy; they may be goods and services.

Tables 7 and 8, show the results of these pathway analysis. The amounts and types of both primary energy and high quality inputs are shown.

Table 7 Primary energy and high quality feedback for fuel production and distribution (internal combustion engine vehicles)

	primary energy 10^9 kWh/yr	primary energy type	high quality feedback 10^9 kWh/yr	high quality feedback type
natural gas (CNG)	271.0	natural gas	54.5	electr./nat. gas
LPG	266.5	nat. gas/oil	30.9	LPG/nat gas
methanol from natural gas	381.0	natural gas	34.7	el./fuel
methanol from biomass	11,200.0	solar	56.0	fuel/el.
ethanol from corn	12,900.0	solar	65.0	fuel/el.
gaseous hydrogen from nat. gas	402.6	natural gas	87.4	nat. gas/electr.
GH_2 from biomass	12,000.0	solar	82.0	fuel/electr.
GH_2 from electricity mix	828.3	mix	63.2	electr.
GH_2 from solar electricity	2,636.0	solar	63.2	electr.
GH_2 from wind electricity	1,530.0	wind	63.2	electr.
liquid hydrogen from nat. gas	355.4	natural gas	104.0	nat. gas/electr.
LH_2 from biomass	10,600.0	solar	99.2	fuel/electr.
LH_2 from electricity mix	731.0	mix	82.6	electr.
LH_2 from solar electricity	2,326.0	solar	82.6	electr.
LH_2 from wind electricity	1,347.0	wind	82.6	electr.

Table 8 Primary energy and high quality feedback for fuel production and distribution (fuel cell vehicles)

	primary energy 10^9 kWh/yr	primary energy type	high quality feedback 10^9 kWh/yr	high quality feedback type
natural gas (CNG)	196.0	natural gas	39.4	electr./nat. gas
methanol from natural gas	318.0	natural gas	30.0	el./fuel
methanol from biomass	9,360.0	solar	46.8	fuel/el.
gaseous hydrogen from nat. gas	186.2	natural gas	40.4	nat. gas/electr.
GH_2 from biomass	5,550.0	solar	37.9	fuel/electr.
GH_2 from electricity mix	383.1	mix	29.2	electr.
GH_2 from solar electricity	1,220.0	solar	29.2	electr.
GH_2 from wind electricity	708.0	wind	29.2	electr.
liquid hydrogen from nat. gas	177.1	natural gas	51.8	nat. gas/electr.
LH_2 from biomass	5,280.0	solar	49.4	fuel/electr.
LH_2 from electricity mix	364.0	mix	41.2	electr.
LH_2 from solar electricity	1,160.0	solar	41.2	electr.
LH_2 from wind electricity	671.0	wind	41.2	electr.

Discussion of Results

It would be impossible to draw any conclusions from Tables 7 and 8 unless a common denominator is applied that would allow combining primary energy sources and high quality inputs. Possible candidate for a common denominator is money, or costs of fuels. However money is only paid for high quality services, actually goods and services. No money goes for the primary energy sources - money only goes for the goods ands services needed to extract and utilize those services. It has therefore been proposed to use emergy as a common denominator in such analyses. Term "eMergy" has been introduced by Odum [12-13]. It stands for embodied energy, and it is energy of one type (typically solar) required in transformations to generate flow of energy, materials, goods and services, or money. Emergy is therefore a more complete unit than money, because it does include primary energy sources. The system that maximizes the power with minimum use of the primary energy sources is therefore preferable. Emergy analysis has yet to be performed. A complete analysis should include all the inputs, not only energy, such as goods and services which can also be expressed in terms of embodied energy, i.e., emergy. Emergy therefore combines energy and economic analysis. Environmental effects could be expressed in terms of monetary value of environmental damage [14], and could eventually be added to this analysis.

Another common denominator that may be used for comparisons between different fuels and their production pathways is land requirement. For any energy activity land is required. Table 9 shows the results of land requirement analysis, based on data in [15]. Surprisingly, solar hydrogen (photovoltaics to electricity to hydrogen) results in the least amount of land area being used. It requires 12 times less area than alcohols, and this area does not have to be good quality agricultural land, thus competing with food production. On the contrary, the highest insolation is in dry desert areas in the south which are not being used for agriculture.

Table 9 Land area requirement for various fuels

	fuel required 10^9 kWh	land area required km^2
Internal combustion engine vehicles		
Gasoline	301.0	4,800
Methanol	237.0	87,300
Ethanol	232.5	192,000
GH_2 from biomass	289.9	52,200
GH_2 from hydropower	289.9	11,500-500,000
GH_2 from solar PV el.	289.9	2,516
GH_2 from wind el.	289.9	3,700-26,900
Fuel cell vehicles		
Methanol	198.0	73,000
GH_2 from biomass	134.1	24,100
GH_2 from hydropower	134.1	5,300-240,000
GH_2 from solar PV el.	134.1	1,200
GH_2 from wind el.	134.1	1,710-12,400

Conclusions and Plans for Future Work

Several energy pathways were defined for each of the fuels being considered, namely, hydrogen, compressed natural gas, electricity, methanol and ethanol. The analysis was divided in two parts: (i) analysis of vehicle technologies, and (ii) analysis of fuel production storage and distribution, from the primary energy sources to the refueling station. Only technologies that are developed to at least demonstration level were considered. The efficiencies of individual steps as well as the efficiencies of the overall pathways were calculated. The amount of each of the alternative fuels analyzed needed to meet the EPACT goals have been determined.

In the subsequent phases of this project the results of individual step analyses will be synthesized. For each alternative fuel a steady state model will be compiled, that will then be used to assess economic and environmental impacts per unit of services delivered, which in this case is the vehicle-mile. Both emergy and money will be used as common denominators and the results of these two analyses will be compared mutually compared.

At the end of the projects the conclusions will be reached regarding the feasibility of each alternative fuels to meet the EPACT goals and recommendations will be given regarding, not only the fuel, but also the specific technologies that would meet the EPACT requirements with optimal benefits to national economy and to the environment.

Various technologies being evaluated are at different stages of development, which makes comparisons very difficult. A carefully and objectively selected set of assumptions is needed in order to compare the technologies on an equal basis. Development of key technologies will have to be monitored and the set of assumptions constantly updated.

References

1. Annual Energy Outlook 95, Energy Information Administration, U.S. Department of Energy, Washington DC, 1995
2. *Petroleum Marketing Monthly*, June 1995
3. Alternatives to Traditional Transportation Fuels 1994, Volume I, Energy Information Administration, U.S. Department of Energy, Washington DC, 1996
4. F.R. Kalhammer, A. Kozawa, C.B. Moyer, and B.B. Owens, Electric Vehicle Batteries, *Interface*, Vol. 5, No. 1, pp. 32-37, 1996
5. J.M. Ogden, M. Steinbugler, E. Dennis, S. Kartha, L. Iwan, and A. Jones, Hydrogen Energy System Studies, Proc. 1995 U.S. DOE Hydrogen Program Review, Vol. 1, pp. 1-46, 1995
6. M.A. DeLuchi, Hydrogen Vehicles: An Evaluation of Fuel Storage, Performance, Safety, Environmental Impacts, and Costs, *Int. J. Hydrogen Energy*, Vol. 14, No. 2, pp. 81-130, 1989
7. W.L. Kohl, Methanol as Transportation Fuel Choice: An Assessment, The Johns Hopkins Foreign Policy Institute, Washington, DC, pp. 440, 1990
8. J.S. Cannon, Harnessing Hydrogen, Inform, 1995

9. R. Wurster, Clean Energy Sources, Hydrogen and Other Alternative Fuels for Air and Ground Transportation, John Wiley & Sons, New York, 1995

10. R.H. Williams, E.D. Larson, R.E. Katofsky, and J. Chen, Methanol and Hydrogen from Biomass for Transportation, with Comparisons to Methanol and Hydrogen from Natural Gas and Coal, PU/CEES Report No. 292, Center for Environmental Studies, Princeton University, 1995

11. D. Sperling, *The Future Drive: Electric Vehicles and Sustainable Energy*, Island Press, Washington, DC, 1995

12. H.T. Odum, Self-Organization, Transformity, and Information, *Science*, Vol. 242, pp. 1132-1139, 1988

13. H.T. Odum, *Emergy Analysis for Public Policy*, manuscript for J. Wiley, (published in 1995 as *Environmental Accounting*), 1989

14. F. Barbir, T.N. Veziroglu and H.J. Plass, Jr., Environmental Damage Due to Fossil Fuel Use, *Int. J. Hydrogen Energy*, Vol. 15, No. 10, pp. 739-750, 1990

15. T. Johansson, H. Kelly, A.K.N. Ready, and R.H. Williams, *Renewable Energy: Fuels and Electricity from Renewable Sources*, Island Press, Washington, DC, 1993

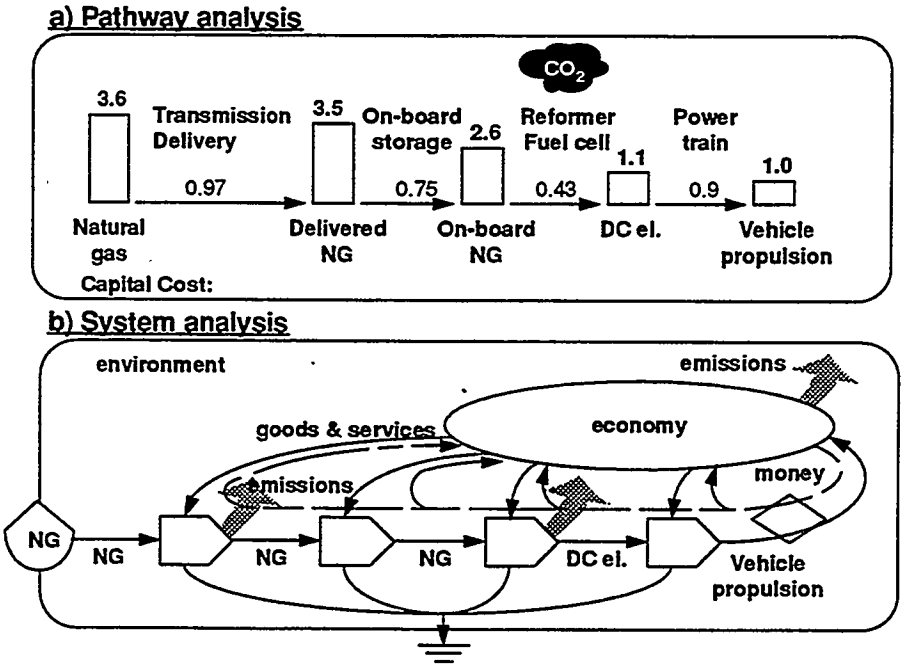


Figure 1 Comparison between pathway analysis and proposed system analysis

Integrated Analysis of Transportation Demand Pathway Options for Hydrogen Production, Storage, and Distribution

C. E. (Sandy) Thomas
Directed Technologies, Inc.
4001 North Fairfax Drive, Suite 775
Arlington, Virginia 22203

Abstract

Directed Technologies, Inc. has begun the development of a computer model with the goal of providing guidance to the Hydrogen Program Office regarding the most cost effective use of limited resources to meet national energy security and environmental goals through the use of hydrogen as a major energy carrier. The underlying assumption of this programmatic pathway model is that government and industry must work together to bring clean hydrogen energy devices into the marketplace. Industry cannot provide the long term resources necessary to overcome technological, regulatory, institutional and perceptual barriers to the use of hydrogen as an energy carrier, and government cannot provide the substantial investments required to develop hydrogen energy products and increased hydrogen production capacity.

The computer model recognizes this necessary government/industry partnership by determining the early investments required by government to bring hydrogen energy end uses within the time horizon and profitability criteria of industry, and by estimating the subsequent investments required by industry. The model then predicts the cost/benefit ratio for government, based on contributions of each hydrogen project to meeting societal goals, and it predicts the return on investment for industry. Sensitivity analyses with respect to various government investments such as hydrogen research and development and demonstration projects will then provide guidance as to the most cost effective mix of government actions. The initial model considers the hydrogen transportation market, but this programmatic pathway methodology will be extended to other market segments in the future.

Project Rationale

Previous studies by various organizations have individually assessed fuel cell vehicle technology, fuel infrastructure issues and, to a limited degree, fuel cell vehicle market penetration scenarios. Some studies have estimated the efficiency, cost and pollution of particular transportation pathways at one particular time. Others have assessed the cost of hydrogen using current merchant hydrogen technology.

The Department of Energy needs to estimate which hydrogen technologies are most likely to help meet department and societal goals such as reduced oil imports, reduced greenhouse gas emissions and reduced urban air pollution. Given limited resources to support hydrogen energy research and development, the department needs to allocate funding on the basis of those elements of the program with the best chances of success.

Previous studies of the existing costs of hydrogen compared to alternative energy carriers are helpful but not sufficient to predict future market penetration. Current costs of hydrogen are based on large production plants dedicated to a few large customers. The hydrogen transportation market will, however, be dependent on thousands or millions of dispersed customers. Technologies and marketing strategies that have worked historically may not be appropriate for tomorrow's hydrogen markets. Similarly, estimates of fuel cell vehicle costs based on current technology is insufficient to predict what costs might be in large manufacturing volumes.

A new methodology is required to integrate the various aspects of hydrogen production and utilization over time, and to predict which markets are most likely to lead to significant hydrogen penetration and therefore to making a significant contribution to meeting DOE and societal goals, while at the same time bringing reasonable return on investment to industry.

Approach

The primary approach of this analysis is to integrate the past hydrogen energy systems analysis results along with new analyses as needed to provide a coherent, realistic , time-dependent and defensible projection or "programmatic pathway" for possible fuel cell vehicle market penetration in the future. This dynamic model will incorporate changing technology and evolving prices over time as new R&D lowers costs, which increases market penetration. As sales increase, production costs drop, creating more market penetration.

The resulting time-dependent model of vehicle, fuel infrastructure and market potential will help to identify critical R&D needs, and to assess the impacts of R&D and other government actions on the successful deployment of hydrogen transportation technologies. The model will estimate the cost/benefit ratio from both the industry and government perspective. For government, the figure of merit will be meeting societal objectives such as reduced oil imports, reduced air pollution and reduced greenhouse gas emissions. For industry, the figure of merit will be return on investment.

The end goal of any hydrogen project must eventually be success in the marketplace, free of any government involvement. The intent is to show how small government investments now in R&D can lead, over time, to a much larger investment by industry as companies are able to project profitable

business ventures. It will also serve as input to industry to illustrate potential return on investment for both hydrogen infrastructure companies as well as vehicle manufacturers.

Past Results

This is a new project for fiscal year 1996. Directed Technologies, Inc. has previously analyzed the efficacy of using off-peak electricity and small electrolyzers to provide hydrogen for fuel cell vehicles (Thomas 1995). We are currently under contract to the Ford Motor Company to provide technical guidance under the Department of Energy direct hydrogen fuel cell vehicle development program. DTI is coordinating the hydrogen infrastructure, on-board hydrogen storage and hydrogen safety aspects of that contract, and also provides technical assistance to Ford on the fuel cell system.

Key Results

Literature Search

We have completed a preliminary literature search in three transportation areas: fuel cell vehicle technology, hydrogen infrastructure studies, and fuel cell vehicle market penetration analysis. We have also identified major reports regarding the environmental impact of fuel cell vehicles.

General Description of Programmatic Pathway Model

We have started to develop the actual programmatic pathway computer model for the transportation sector. This is definitely a work in progress. We have entered some real data regarding fuel cell vehicle (FCV) and hydrogen costs as described below, but all data should be considered preliminary and subject to change after peer review. The data presented here are intended mainly to show potential relationships and to illustrate the capability of the model, rather than to constitute actual projections or conclusions at this time.

The basic structure of the programmatic pathway model is illustrated by the four overlapping circles of Figure 1 (vehicle technology, fuel, market scenarios and government actions). Examples of elements of these four components are shown in Figure 2. This initial programmatic pathway model is based on the direct hydrogen fuel cell vehicle designed under the Ford contract. Not all of the elements of Figure 2 will be analyzed during this contract, particularly under the government actions category. We will limit the analysis at this time to the effects of government R&D and demonstration projects, although the model will be suitable for evaluating other quantifiable government actions such as incentives, mandates or taxes. Some government actions such as education, regulatory relief and establishment of codes and standards will undoubtedly be essential for success of the program, but are difficult to quantify. How does one measure the need for or the effectiveness of public education to overcome possible perceptions of hydrogen as a hazardous fuel? Obviously the programmatic pathway model cannot replace sound judgment in these soft areas of the hydrogen domain. But the model could provide guidance on the efficacy of a vehicle feebate or other incentive system versus additional technology R&D.

The functional relationships of the model are shown in Figure 3. As currently written, the primary inputs are one or more market penetration scenarios and a set of government actions such as a particular group

of relevant R&D or demonstration projects. The model converts these inputs into a series of eight industry time functions and two government time functions, extending from the present to 2030:

* Cumulative number of fuel cell vehicles sold over time
* FCV price over time
* FCV industry investment over time
* Industry profit over time
* Hydrogen production required over time
* Hydrogen cost over time
* Hydrogen investment over time
* Hydrogen industry profits over time

* Government investment over time
* Societal benefits over time.

These various functions are inter-dependent. For example, the model assumes that the number of FCVs sold each year depends on the FCV price relative to the competition. The FCV price depends on the current price, the degree of R&D investment (input parameter) in fuel cell systems, and the cumulative number of FCVs sold. Initially the FCV price is too high for any significant sales, so the model assumes government-industry cost shared demonstration projects to bring the price down. A manufacturing "learning curve" is assigned to each element of the FCV, such that the price falls as more units are produced. Where possible, these learning curves are determined by estimating the fully mature component cost in very large, automobile industry mass production, and linking these high volume costs to current costs. As more FCVs are sold, the price falls further, simulating yet more sales.

We have entered reliable data on hydrogen costs, based primarily on the extensive hydrogen gas industry study conducted by the Ford Motor Company as part of the DOE direct hydrogen fuel cell vehicle project. The amount of hydrogen is linked to the cumulative number of FCVs on the road. As with the FCV cost, the cost of the hydrogen hardware is assumed to fall as more production systems are manufactured.

The primary outputs from the model (Figure 3) are the return on investment for both the automobile and the gas supply industries, and, for government, the cost/benefit ratio. These figures of merit will determine whether industry and government will make the necessary investments.

Potential Fuel Cell Vehicle Markets

We have incorporated three potential fuel cell vehicle markets into the initial model:

* Bus demonstrations
* Centrally fueled fleets of light duty vehicles
* Zero emission vehicles.

The bus demonstrations are assumed to be 50/50 government/industry cost shared projects to help reduce the cost of the fuel cell and related equipment. This project would expand on the PEM fuel cell buses being purchased by Chicago, helping to mature the technology and drive down the cost. It would also provide an opportunity to develop hydrogen fueling devices. The current model assumes that 110 fuel

cell buses are produced between 1997 and 2001.

Fuel cell light duty vehicles will undoubtedly be sold initially to fleet owners, both to provide central fueling and to take advantage of fleet maintenance capabilities and control. Centrally fueled fleets are also the subject of two major government fleet mandates: both the Clear Air Act Amendments (CAAA) of 1990 and the Energy Policy Act (EPACT) of 1992 require that a growing percentage of centrally fueled fleet sales be alternatively fueled vehicles(AFVs). The EPACT specifically designates hydrogen as an alternative fuel, along with natural gas, LPG, biofuels, ethanol, methanol and electricity. Figure 4 illustrates the number of AFVs required to be sold each year if the EPACT program is fully implemented by the Secretary of Energy. As shown in Figure 5, however, the major increase in AFVs after 1998 would come from privately owned fleets (dashed line), and the Secretary of Energy must make a decision to include private fleets. Otherwise the program will stabilized at about 30,000 vehicles sold per year for the combined state and federal fleets.

While the EPACT mandates that a growing percentage of government fleets must be AFVs, this program may have begun too early for FCVs. The AFV mandate will be well established by the time FCVs are mass produced in the 2005-2010 time period. By that time, fleet owners will have acquired large numbers of natural gas vehicles (NGVs), electric vehicles (EVs), and possibly alcohol-fueled vehicles. While hydrogen-powered FCVs will have significant environmental and energy security advantages over these other AFVs, it may be too difficult to force fleet owners to make another change in vehicle and fuel technology. The model default value is zero for AFVs -- we assume no FCVs are sold as AFVs.

The California Zero Emission Vehicle (ZEV) mandate may be more applicable to FCVs. Although the 2% ZEV requirement for 1998 and the 5% ZEV mandate for 2001 have recently been abandoned by the California Air Resources Board (CARB), they have left the 10% requirement intact, providing a residual pressure on the automobile industry to continue the development of ZEVs. In one sense, abandoning the 1998 standards may be a boost for FCVs, since the auto companies would have been forced to provide battery powered EVs to meet a 1998 deadline. This would have diverted resources into heavy and expensive batteries, possibly at the expense of developing more promising alternatives such as FCVs. In any case, the ZEV requirements recommended by the South Coast Air Quality Management District in their latest plan (SCAQMD 1994) are as follows:

2003	10% ZEV
2005	35% ZEV
2009 & later:	50% ZEV

In addition, six other states of opted in to the California ZEV plan. While they may also postpone the introduction of ZEVs, the total potential ZEV sales could grow to over 2 million per year by 2010, as illustrated in Figure 6. The model does not assume that these will all be FCVs, however, as described in the next section.

Fuel Cell Vehicle Market Share

The model estimates the fraction of ZEVs that will be FCVs based on the price of the FCVs and the price of hydrogen. Normally vehicle choice models also depend on other vehicle attributes such as range and acceleration. However, we have assumed that all FCVs will have equal performance to their ICE

counterparts. The FCV will have the same range and acceleration as the ICE.[1]

The assumed market share as a function of FCV price is shown in Figure 7. We assume that the FCV would capture 50% of the ZEV market if its cost was equal to the competition. This is probably too conservative, given the advantages of FCV's over EVs, but the publics possible fear of or reluctance to use hydrogen may cancel some of its physical advantages. As the price of the FCV increases, the market share drops nonlinearly, as shown in Figure 7. The model has a term to adjust the slope of this price elasticity curve. The parameter essentially sets the market share at 1.5 times the competitor's price, or $30,000 in this example. The two curves in Figure 7 illustrate the market share factor when the FCV market share is set to 10% and 20% at $30,000. These curves have a very long tail in the high price direction, representing the "early adopters" who will pay much more than the average person for new technology.

The FCV market share also depends on the price of hydrogen. We have assumed a multiplicative function shown in Figure 8. This function is unity as long as the price of hydrogen (in $/gallon of gasoline equivalent -- meaning that the cost per mile driven is equal to that of an ICE powered by gasoline at that price/gallon) is less than the price of gasoline. As the price of hydrogen increases above the price of gasoline, the market share declines. The tail on the fuel price elasticity curve is even more pronounced than the vehicle market share tail to take into account the relatively minor importance of fuel price relative to vehicle price. That is, not only will you have early adopters who will agree to pay the higher fuel price for a clean technology, but also the average driver tends to discount the cost of fuel relative to the price of the vehicle. In effect, the typical vehicle owner has a very high discount rate, discounting the future costs of fuel consumption relative to the initial purchase price.

Manufacturing Learning Curves

The price of the vehicle is determined by a thorough analysis of the expected price in mass production, coupled to the known current price of each vehicle component. These two prices are tied together in the model by manufacturing learning curves. This model is based on the observation in many industries that the cost of a new product follows a logarithmic curve as a function of the total cumulative number of items produced. For example, Figure 9 shows the price of the Model T Ford from its introduction in 1909 through 1923. On a log-log plot, these prices fall approximately on a straight line. In effect, the price of the Model T dropped about 13.4% for every doubling of production -- an 86.6% learning curve. This learning curve covers all aspects of manufacturing improvements: new materials, new manufacturing processes, reduced labor input, innovation, etc. Other examples of learning curve experience include:

---

[1]However, the FCV will not be competing with the ICE. Rather, the FCV will be competing with battery-powered EVs for the ZEV market. Since FCV's will most likely have longer range than a battery-powered EV, we should add a factor favoring the FCV in future versions of this model.

Radios	83.2%
Black & White TV	90.0%
Color TV	94.0%
Video Cassettes	87.8%
Photovoltaics (solar cells)	66.0%
Model T Ford	86.6%

In the model, we have assumed this logarithmic dependence between the initial cost of a product and the cost of the "Nth" item off the production line:

$$\log(C_N) = \frac{\log(A) * \log(N)}{\log(2)} + \log(C_1)$$

where C_N = the cost of the Nth item,

A = the learning curve factor (eg, 0.866 for the Model T), and

C_1 = the cost of the first item off the production line.

We estimate the cost of the FCV by essentially stripping out all of the ICE components (gasoline engine, transmission, radiator, exhaust pipe, muffler, catalytic converter, gasoline tank) and replacing them with the 5,000 psi storage tank, fuel cell system, peak power augmentation device (if any) and electric motor. We then project the cost of each of the unique FCV components in large scale mass production. The results of this exercise are summarized in Table 1 for two steps: the bus demonstration program and the actual FCV manufacturing program. That is, we assume an initial cost for each of the four major FCV components. We then estimate a learning curve during the course of the bus demonstration program, which produces a final cost after the bus program for each component. This final bus component cost then becomes the initial cost of the FCV program. Finally, the model calculates the necessary learning curve factor to produce the estimated final component price at the one million unit mark.

Table 1. Fuel Cell Vehicle Component Cost and Learning Curve Assumptions

	Initial Component Price at Start of Bus Program (Input)	Bus Program Component Learning Curve Factor (Input)	Bus Component Final Price (Calculated, based on 110 buses)	Vehicle Component Learning Curve Factor (Calculated)	Vehicle Component Price at One Million Production Volume (Input)
Fuel Cell Stack ($/kW)	1,000	0.9	489.40	0.875	33.90
Peak Power Battery ($/kW)	80	0.9	39.20	0.922	7.8
Motor & Controller ($)	35,000	0.81	8,384.40	0.894	900
High Pressure Tank ($)	3,150	0.95	2,224.60	0.95	800

This process is conservative in one sense: the learning curve is intended to take into account unforeseen innovation. During the course of long manufacturing runs, engineers and scientists will invent new materials, new manufacturing techniques or even entirely new systems to accomplish a given function. We have based our final component price on the basis of the existing fuel cell system design. This process essentially looks at the materials in the existing design, and estimates (with the help of the Ford costing department) the expected cost of materials and production costs in large scale mass production. The end cost is therefore limited by our inability to envision as yet uninvented breakthroughs that could reduce costs even more. The fuel cell cost is limited by the cost of platinum, for example, but one cannot rule out the development of noncatalytic or a least low cost catalytic reactions in the future.[2]

This process resulted in calculated learning curves over the FCV production process between 87.5% for the fuel cell system to 95% for the hydrogen tank. This is close to but higher (more pessimistic) than the 86.6% learning curve experienced by the Model T Ford over its 14 year life. Overall, this projection seems reasonable, but we will continue to explore other relevant industries and make corrections based on peer review and new information as it becomes available.

Fuel Cell Vehicle Projections

Sample projections of FCV market penetration, price, investments and profits are shown in Figure 10.

---

[2]For example, General Motors has been assigned Patent No. 5,240,893on August 31, 1993 (R. R. Witherspoon, inventor) for non-precious metal catalyst fuel cells.

These data do not represent our conclusions, but merely illustrate the types of information that can be produced by the model. This example includes only ZEV market penetration in addition to the initial 110-bus demonstration project. There are no AFV fleet vehicles under the EPACT mandate on the grounds that all AFVs will be supplied by NGVs or alcohol fueled vehicles, and this example assumes no substitution for conventional (non-ZEV) vehicles.

As shown in Figure 10, the price of the FCV under these assumptions falls from $105,000 initially to become roughly competitive with ICE's soon after mass production begins in 2005.

This simulation shows that the federal investment grows to about $60 million per year (compared to $20 million per year now for the fuel cell vehicle program) in 1999, tapering off after the bus demonstration project is completed. But the bus project has the intended effect of lowering costs and demonstrating practical feasibility, so that industry begins making significant investments in vehicle manufacturing equipment beginning in 2003 rising to over $200 million in 2006. Profits (assumed initially here to be 10% of revenues) rapidly outpace investments by 2007 in this scenario, with a total project internal rate of return of 23.9%. That is, the total project cash flow would have a net present worth of zero with a discount rate of 23.9%.

Hydrogen Production Requirements

The quantity of hydrogen required is determined directly by the number of fuel cell vehicles on the road. We assume here that all FCVs are midsize passenger vehicles, based on the Ford AIV Sable fuel cell vehicle design. At the projected fuel cell system weight in mass production, this vehicle would consume hydrogen at the rate equivalent to about 85 mpg (LHV) on the EPA Federal Urban Driving Schedule, but only 68.6 mpg on the more realistic 55% urban and 45% highway combined cycles with each speed step in the EPA driving cycle multiplied by 1.25. That is, the EPA driving cycles are too anemic to represent real driving habits. As an example, the average EPA highway speed is only 48.6 mph, and the maximum speed in only 60 mph. Clearly this is not representative of actual highway driving conditions. Unfortunately fuel cell efficiency decreases as higher power is required, so the fuel economy of a FCV drops for the 1.25 times faster speed cycles. The model is based on the more demanding fuel economy of 68.6 mpg (LHV), so a FCV traveling 12,000 miles per year would consume 177 kg of hydrogen each year.

The economic viability of hydrogen sales will depend on the number of FCVs that are within range of a fueling station. Initially FCVs will undoubtedly be sold to fleet operators with central fueling, as discussed previously. The average number of vehicles in a commercial fleet varies between 32 to 231, depending on the category , while government fleets average 569 vehicles and utility fleets 310 cars per fleet (Miaou 1992). However, not all these vehicles are refueled at one central site. Even though a given fleet operator might own 500 vehicles, they may be fueled at 10 or 20 different centers, or they may all be fueled commercially and garaged at the homes of employees. For commercial fleets, about 44% to 65% do have on-site fueling capability for existing gasoline and diesel powered vehicles.

To determine the economic viability of hydrogen fuel sales to the general (non-fleet) population, the model must assume some type of FCV geographic distribution. For example, the Los Angeles metropolitan area includes about 5,000 square kilometers. If we assume that a driver would prefer one hydrogen fueling station every 5 kilometers, then we would need to install at least 200 stations in the L.A. area. Extrapolating to the six other states that have opted in to the ZEV program on the basis of

population, about 900 stations would be required. If each of these stations could support 300 FCVs, then 270,000 FCVs would have to be on the road in order for the hydrogen vendors to make a reasonable economic return on their investment.

We conclude from these considerations that hydrogen dispensers should be very small, ideally beginning with systems that could economically supply just a few vehicles. While centrally fueled fleets might require hydrogen dispensing systems for several hundred vehicles, most public stations will begin with far fewer customers.

Hydrogen Cost Estimates

The model assumes two types of hydrogen fueling appliances: small scale electrolyzers and small scale steam methane reformers. This choice is based on an extensive hydrogen infrastructure study conducted by the Ford Motor Company as part of its cost shared project with the Department of Energy to develop direct hydrogen fuel cell vehicles. Four subcontractors (Air Products and Chemicals, BOC Gases, Electrolyser Corporation and Praxair) provided in-depth analysis of the likely cost of hydrogen for the transportation market under a wide variety of production modes, including very large remote plants with liquid hydrogen delivery by tanker truck, regional plants with pipeline delivery, and on-site hydrogen production plants, both steam methane reformers and electrolyzers.

The preliminary results from this program are summarized in Figure 11. The price of hydrogen ($/kg)[3] is shown as a function of the size of the production plant in terms of the total number of FCVs supported.[4] The hydrogen cost includes full capital recovery of both the production facility, transportation pipelines (if used) and the dispensing equipment, all operation and maintenance costs and all fuel costs. This analysis assumes 10 percent after-tax real rate of return (effective annual capital recovery rate of 18.54%). The data in Figure 11 therefore represent the delivered cost of hydrogen. The costs shown in Figure 11 do not include retail labor for dispensing, however, so they are greater than gasoline wholesale prices (which do not include capital recovery for dispensing equipment), but less than full retail markup. The computer model does include retail markup, however (default value is five percent retail markup.)

For reference the equivalent price of gasoline is shown for both taxed and wholesale gasoline for oil selling at $15/barrel and $20/barrel. The dashed lines represent the cost of hydrogen that would be equivalent to fully taxed gasoline per mile driven, assuming that the FCV has an on-board fuel economy of 68.6 mpg on the 1.25 times faster speed EPA combined driving schedules, while the same vehicle powered by a gasoline ICE would achieve 25.8 mpg, all based on lower heating values of the fuel. Thus

---

[3]$1/kg = $0.454/lb = $8.80/MBTU (LHV) = $8.35/GJ (LHV) = $7.43/GJ (HHV) = $7.05/GJ (HHV) = $0.236/thousand SCF.

[4]The number of FCVs supported should not be confused with the number of vehicles fueled per day. On the average, a vehicle traveling 12,000 miles per year with a 350-mile range on one tank of hydrogen would stop at a hydrogen fueling station once every eight days, assuming an average purchase of three fourths of a tank. So a station supporting 800 FCVs would service about 100 FCVs per day.

the FCV is 2.67 times more energy efficient per mile driven than the gasoline ICE vehicle.[5]

The dashed lines of Figure 11 therefore represent the cost of hydrogen necessary to compete with fully taxed gasoline, assuming that the hydrogen is not required to pay highway taxes. This may be valid initially, when hydrogen vehicles are rare and both state and federal governments are trying to encourage the use of clean fuels. For example, natural gas vehicles currently are taxed at a lower rate than gasoline, and no road taxes are (yet) paid by those charging electric vehicles at home.

Eventually hydrogen would have to become competitive with untaxed gasoline, represented by the solid lines in Figure 11. By the time enough FCVs were on the road to necessitate taxing zero emission vehicles, however, we presume that the price of oil may have risen above $20/barrel.

Figure 11 illustrates that hydrogen would be competitive per mile with taxed gasoline from very large steam methane reformer plants, those supporting over 50,000 FCVs. Since it will take many years to reach these levels of FCVs, we need an alternative fueling approach for the transition phase of FCV market deployment.

Two sets of multiple data in Figure 11 show options for producing hydrogen in small quantities from factory-built appliances. The open triangles are estimates of a 1.36 kg/day electrolyzer system hydrogen cost, assuming that these electrolyzers are built in the quantities shown, assuming off peak electricity costs 3 cents/kWh. Production volumes would have to reach 100,000 before these electrolyzer systems could compete with fully taxed gasoline. Nonetheless, these electrolyzer systems could be economic, particularly for "early adopters," those consumers who would be willing to pay more per mile for the convenience of home refueling and the novelty of a truly zero emission vehicle.

The other factory-built option would be to fabricate small-scale steam methane reformers, much like International Fuel Cells now builds steam reformers as part of each of the PC-25 200-kW phosphoric acid fuel cell systems it sells. The set of data in Figure 11 (open circles) at the 300 FCV level show our estimate of the hydrogen costs from such factory built steam methane reformers. Based on extrapolations of IFC data, we estimate that even the first of these smaller SMR systems would be competitive with gasoline. Hydrogen could be competitive with wholesale gasoline once 1,000 units were manufactured, according to these estimates.

Even these reformers, although considered very small by the hydrogen merchant hydrogen industry, are really too big for initial transportation markets. We would really prefer on-site dispensers that could support 50 to 100 FCVs, likely for early fleet users. The model therefore extrapolates downward to these smaller units to fill in the gap between electrolyzers for just one or two FCVs, and the IFC size reformer that can support 300 FCVs. The cost assumptions for these smaller units are summarized in Table 2.

---

[5]Many analysts use the EPA Federal Urban Driving Schedule (FUDS) to compare alternative vehicles. On FUDS, the gasoline ICE would achieve about 24.1 mpg, while the FCV would reach 85 mpg, or 3.5 times higher efficiency. The price of hydrogen could therefore be 31% higher than on the 1.25 times faster cycle. However, the FUDS driving cycle is not considered realistic, as discussed previously, and should not be used to compare real life economics.

Table 2. Capital Cost Assumptions for Small Scale Steam Methane Reformers

	300-FCV Size (Input)	Scaling (Input)	Learning Curve (Input)	100-FCV Size (Calculated)	50-FCV Size (Calculated)
Reformer	208,000	0.6	0.85	123,588	103,394
PSA	40,800	0.5	0.85	27,000	23,700
PSA Compressor	60,300	0.4	0.85	43,985	40,082
H_2 Compressor	36,000	0.4	0.85	26,260	23,930
H_2 Storage	60,000	0.8	0.95	27,534	19,767
Dispensers	42,000	0	0.85	42,000	42,000
Totals	447,100			290367	252873

The model selects the appropriate hydrogen dispenser by assuming a normal geographic distribution of FCVs. Initially, we assume that FCVs are all constrained to areas (centrally fueled fleets) with up to 20 vehicles -- no new hydrogen fuel stations are introduced until a region has at least 20 FCVs. After each region has at least 20, then the model assumes a random distribution across the 900 fueling regions. Fueling appliances are added to match the number of FCVs as closely as possible. Steam methane reformers replace electrolyzers whenever possible (once the region has more than 50 FCVs, the smallest SMR assumed here). This leads to cost increases due to mismatch between hydrogen capacity and customer demand. Once a region reaches 51 FCVs, for example, then two 50-car stations are installed, producing a capacity for 100 FCVs but demand for only 51 -- the capacity factor falls to 51% for this particular region until more vehicles are added in subsequent years.

The projected hydrogen production, cost, and revenue for the hydrogen companies is shown in Figure 12. Initially, the hydrogen cost is exorbitant, equivalent to over $25/gallon of gasoline. As more vehicles are added during the demonstration and early market phases, the fuel cost drops, reaching parity with gasoline by the year 2009, or four years after mass production begins.

From industry perspective, the investments and revenues are much more closely matched than for the vehicle industry. While the automobile companies must invest many hundreds of millions of dollars to start mass production, we project that the gas companies can incrementally add capacity as demand rises. With these preliminary data, the estimated return on investment for the gas companies would be about 22%, just slightly lower than the 23% predicted for the auto companies.

In summary, preliminary indications, based primarily on cost data developed in conjunction with the Ford Motor Company contract with DOE, indicates that both the automobile industry and the hydrogen gas suppliers could make a viable business producing and selling hydrogen and fuel cell vehicles. These data are very preliminary, and subject to considerable revision as this analysis undergoes peer review.

Definitions of Success

We will consider this programmatic pathway model a success over the next few years when it:

* Is accepted as the standard methodology to evaluate all hydrogen energy projects.
* Receives sufficient credibility to be used by DOE, elected officials and industry.
* Begins to impact DOE choices for various hydrogen R&D and demonstration projects.
* Begins to convince elected officials to continue and expand support for the hydrogen energy program relative to other alternatives.
* Begins to convince some segments of industry to begin their own planning to invest in hydrogen technologies.

Plans for Future Work

The hydrogen transportation programmatic pathway options explored this year will include fuel cell vehicles powered by hydrogen, methanol and gasoline. In addition to projecting the return on investment for the hydrogen industry and the vehicle industry, the model will be expanded to include projections of societal benefits, including oil, air pollution and greenhouse gas reductions over time.

We also propose extending this analysis to other alternative fueled vehicles such as natural gas vehicles, hybrid vehicles and possibly battery powered vehicles, so that DOE and industry will have a uniform basis for comparing the cost/benefit ratios from investing in these various alternatives.

The primary government input to the model as developed this year is R&D investment. But other government actions such as education, establishment of codes and standards, plus numerous market incentives can also contribute to successful market penetration. We propose extending the model to include these other government actions.

While this particular analysis is limited to the light duty hydrogen transportation market, the methodology of programmatic pathway analysis developed under this contract can serve as a template for evaluating other hydrogen markets and other hydrogen R&D projects. We expect that the programmatic pathway analysis will be extended to other hydrogen areas next year as part of the integrated hydrogen systems analysis team organized by Jim Ohi. We propose extending the programmatic pathway model to stationary utility fuel cell systems, biomass hydrogen and remote village renewable energy systems. Other options may be explored by the systems analysis team members.

Acknowledgments

This work was supported by the National Renewable Energy Laboratory under Modification 1 to subcontract No. ACF-4-14266-01. Much appreciation goes to Jim Ohi, the NREL technical monitor for his support, and for suggesting the term "programmatic pathway" to describe this analysis. We also thank Bob Moore of Air Products, Anne Kotar of BOC Gases, Tom Halvorson of Praxair and Matthew Fairlie of Electrolyser Corporation for their contributions to the hydrogen infrastructure work under the Ford Contract with DOE, and we thank Ron Sims of Ford for his guidance and help throughout that work. Al Meyer and Paul Farris of International Fuel Cells were most helpful in discussing their small scale steam methane reformer. Finally, I thank George Baum, Brian James, Ira Kuhn, and Frank Lomax of Directed Technologies, Inc. for their assistance.

References

Miaou, S.P., S.H. Hu and J.R. Young, *Fleet Vehicles in the United States: Composition, Operating Characteristics, and Fueling Practices*, Report ORNL-6717. Oak Ridge, Tennessee: Oak Ridge National Laboratory

SCAQMD - South Coast Air Quality Management District. 1994. *1994 Air Quality Management Plan: Meeting the Clean Air Challenge*. Los Angeles

Thomas, C.E. and I.F. Kuhn, Jr. 1995. *Electrolytic Hydrogen Production Infrastructure Options Evaluation*, National Renewable Energy report NREL/TP-463-7903. Arlington, Virginia: Directed Technologies, Inc.

Figure 1

DIRECTED TECHNOLOGIES, INC.

Programmatic Pathway Components

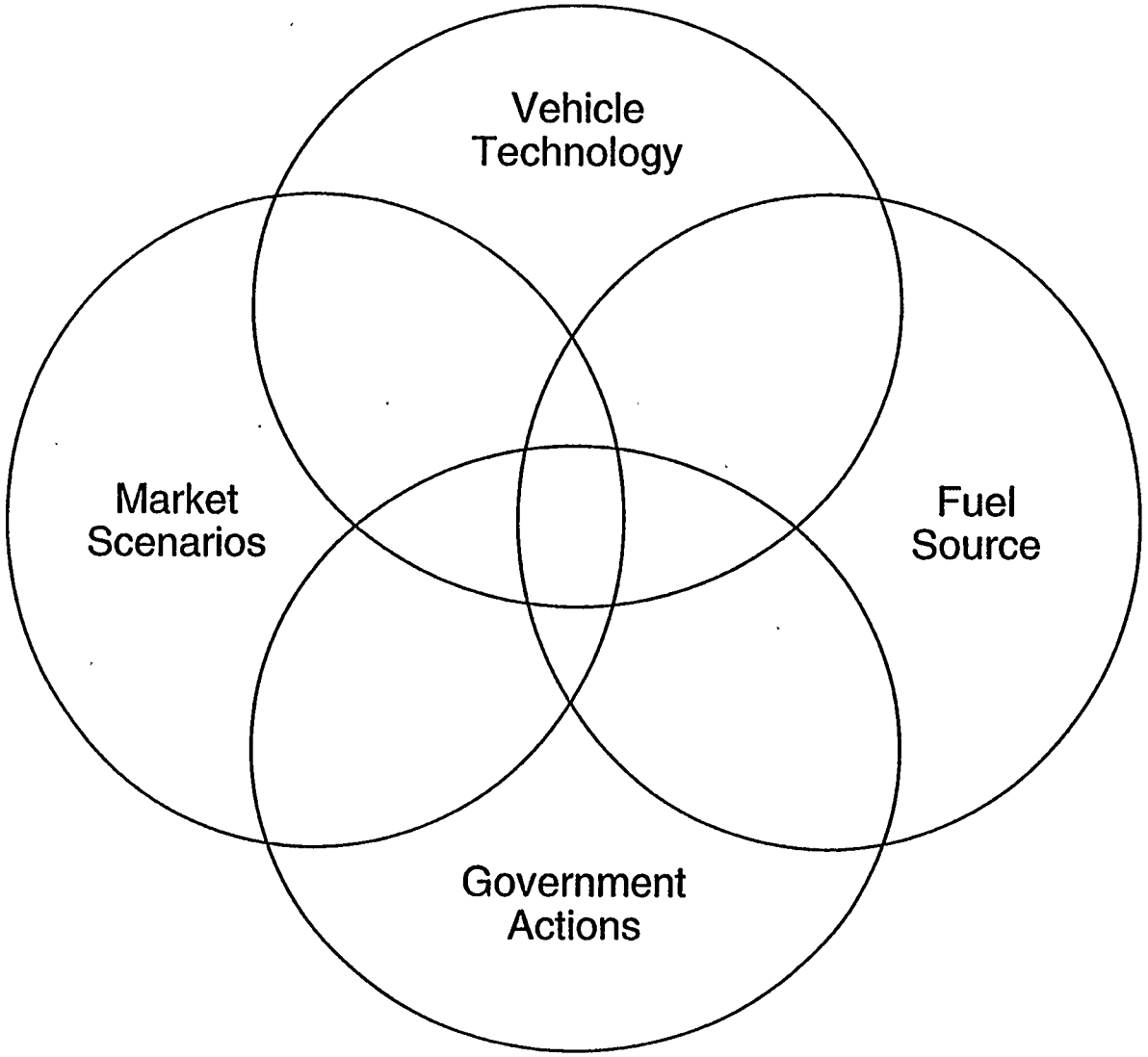


Figure 2

DIRECTED TECHNOLOGIES, INC.

Components of Hydrogen Transportation Programmatic Pathways

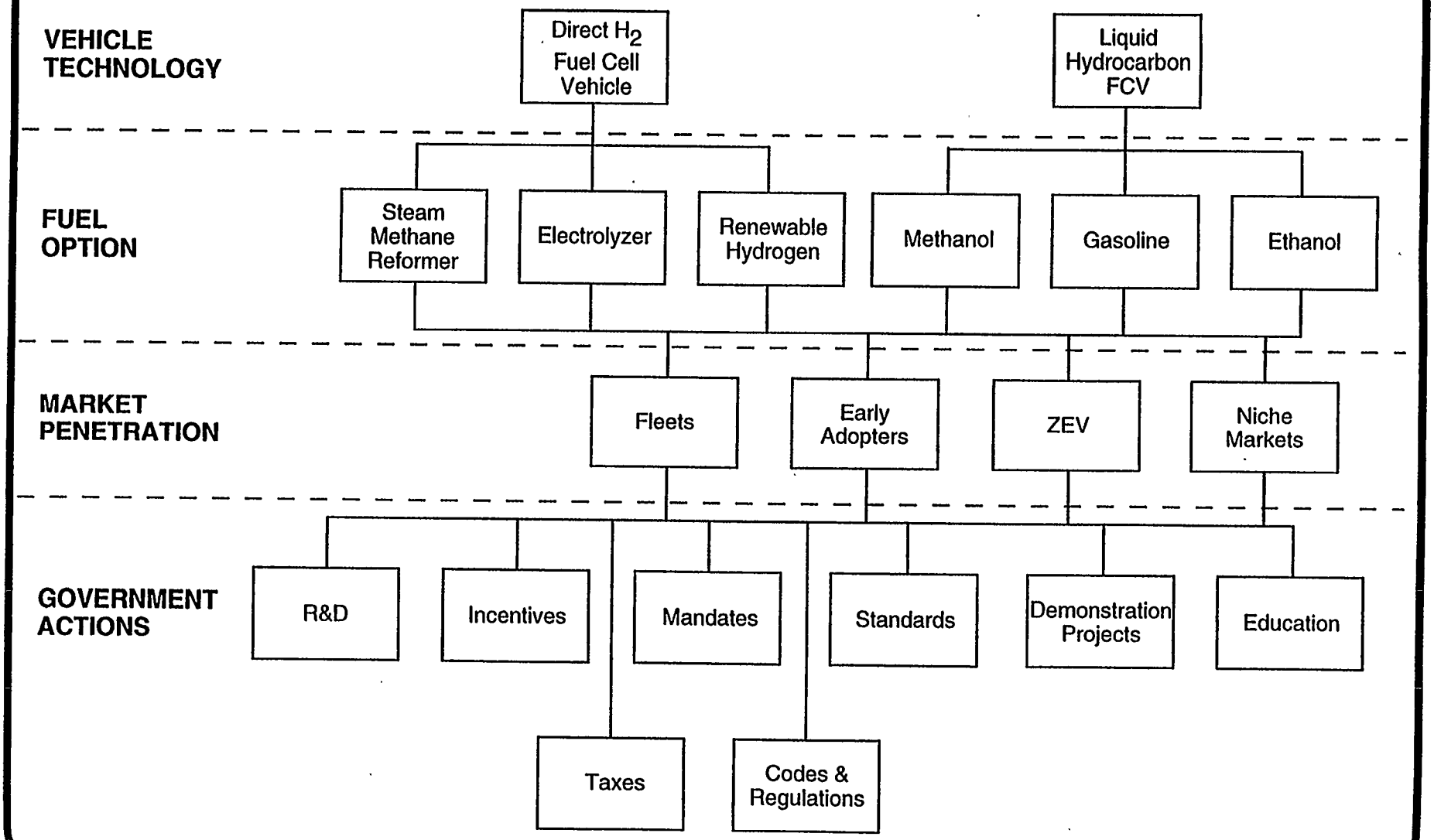


Figure 3

DIRECTED TECHNOLOGIES, INC.

Major Functional Relationships for Proposed Hydrogen Programmatic Pathway Analysis

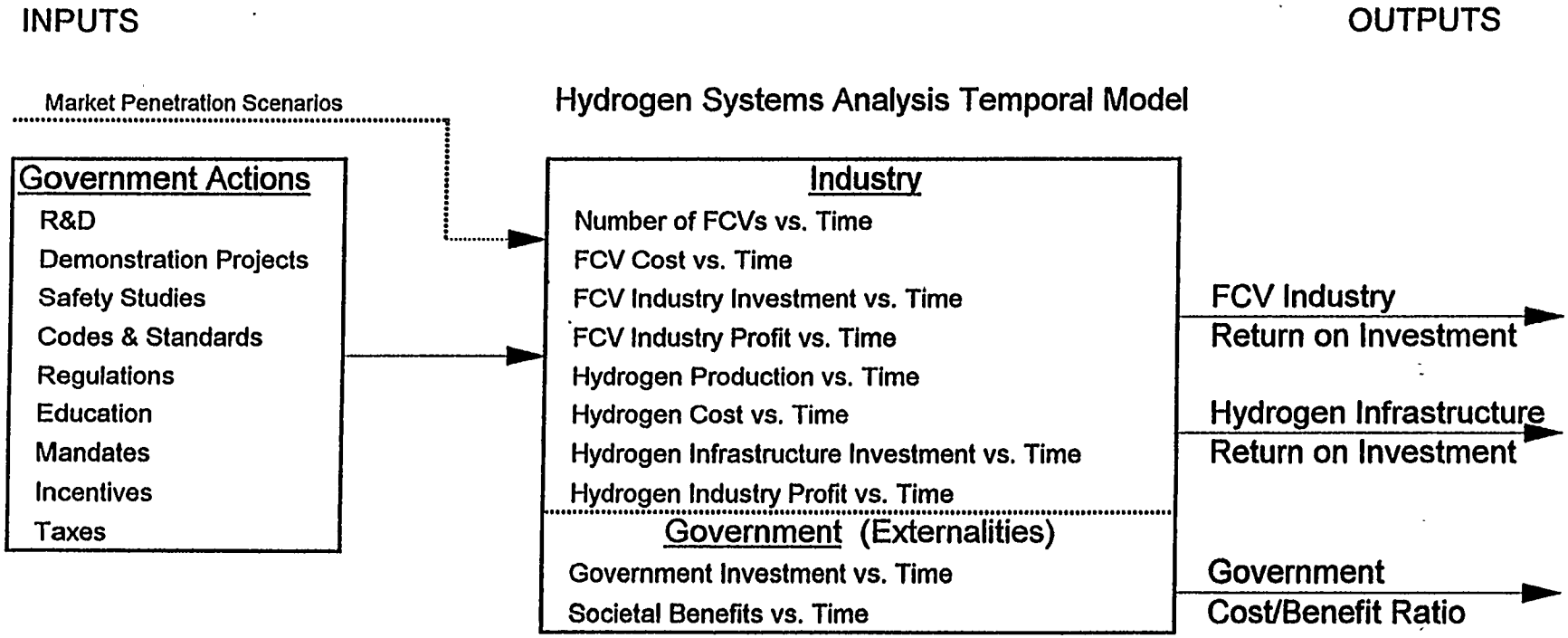
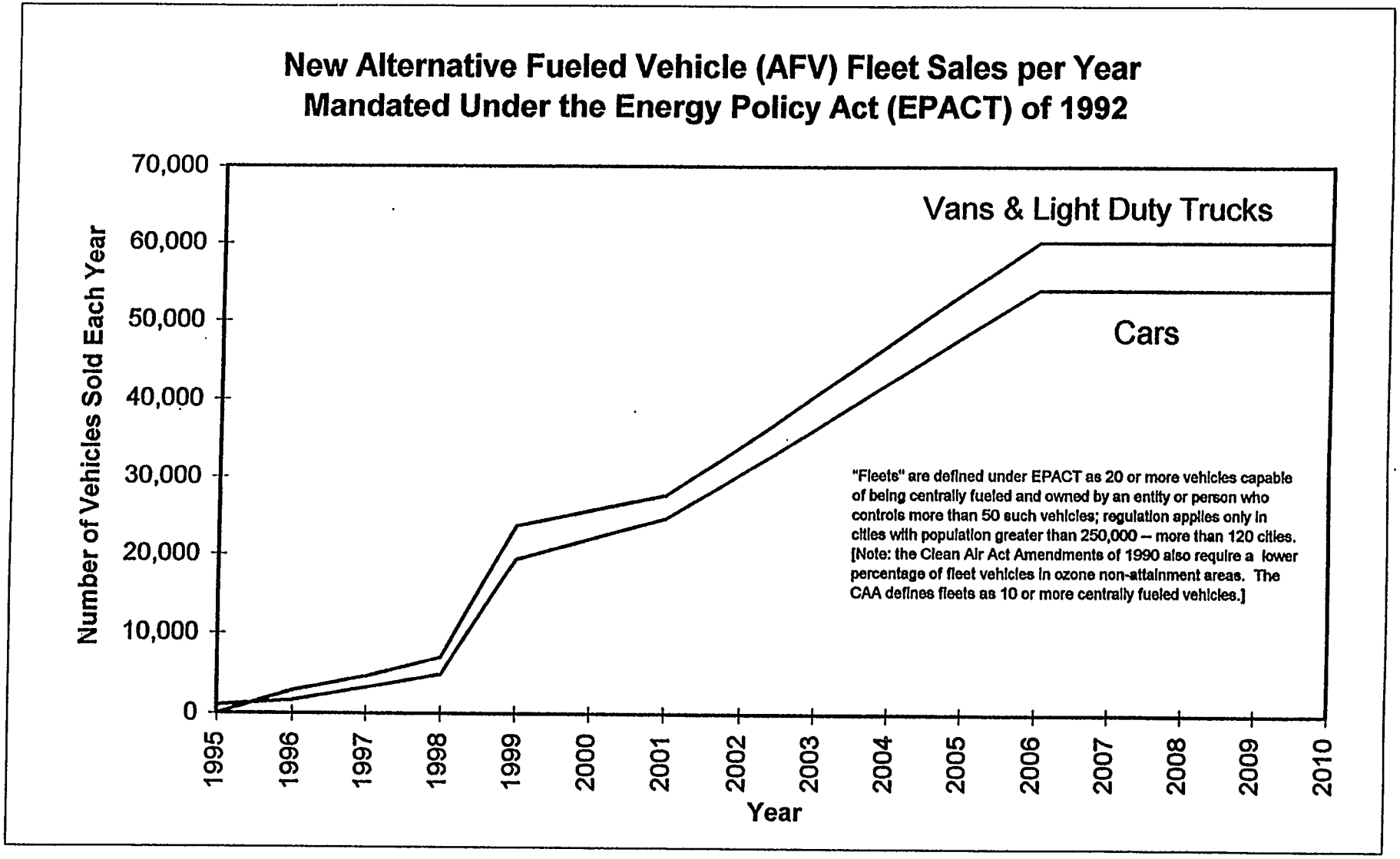


Figure 4


New Alternative Fueled Vehicle (AFV) Fleet Sales per Year
Mandated Under the Energy Policy Act (EPACT) of 1992
Number of Vehicles Sold Each Year
70,000
60,000
50,000
40,000
30,000
20,000
10,000
0
Vans & Light Duty Trucks
Cars
"Fleets" are defined under EPACT as 20 or more vehicles capable of being centrally fueled and owned by an entity or person who controls more than 50 such vehicles; regulation applies only in cities with population greater than 250,000 -- more than 120 cities. [Note: the Clean Air Act Amendments of 1990 also require a lower percentage of fleet vehicles in ozone non-attainment areas. The CAA defines fleets as 10 or more centrally fueled vehicles.]
1995
1996
1997
1998
1999
2000
2001
2002
2003
2004
2005
2006
2007
2008
2009
2010
Year

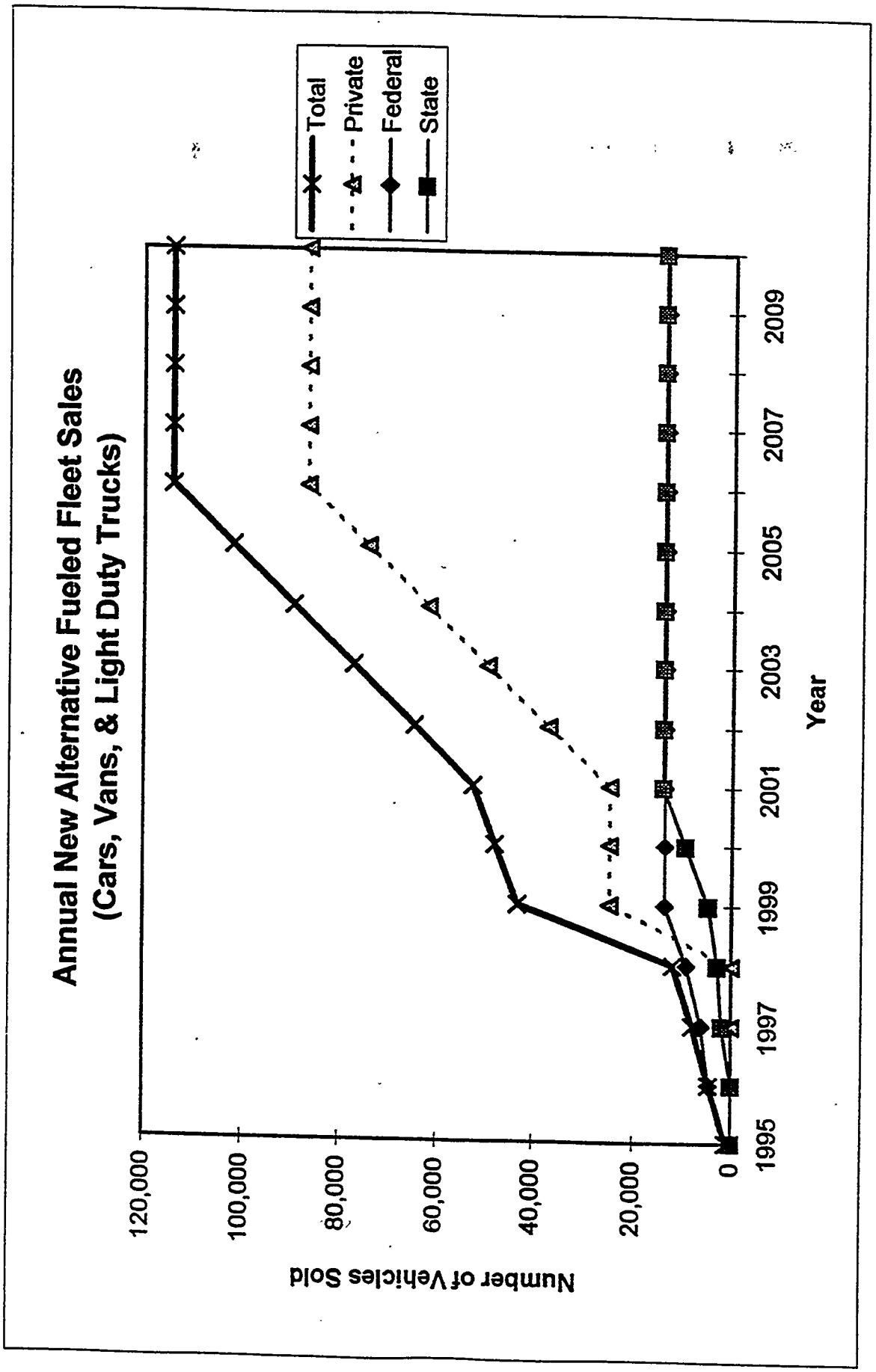

Annual New Alternative Fueled Fleet Sales
(Cars, Vans, & Light Duty Trucks)
Total
Private
Federal
State
Number of Vehicles Sold
120,000
100,000
80,000
60,000
40,000
20,000
0
1995
1997
1999
2001
2003
2005
2007
2009
Year

Figure 5

Figure 6

DIRECTED TECHNOLOGIES, INC.

Projected Annual Sales of Zero Emission Vehicles

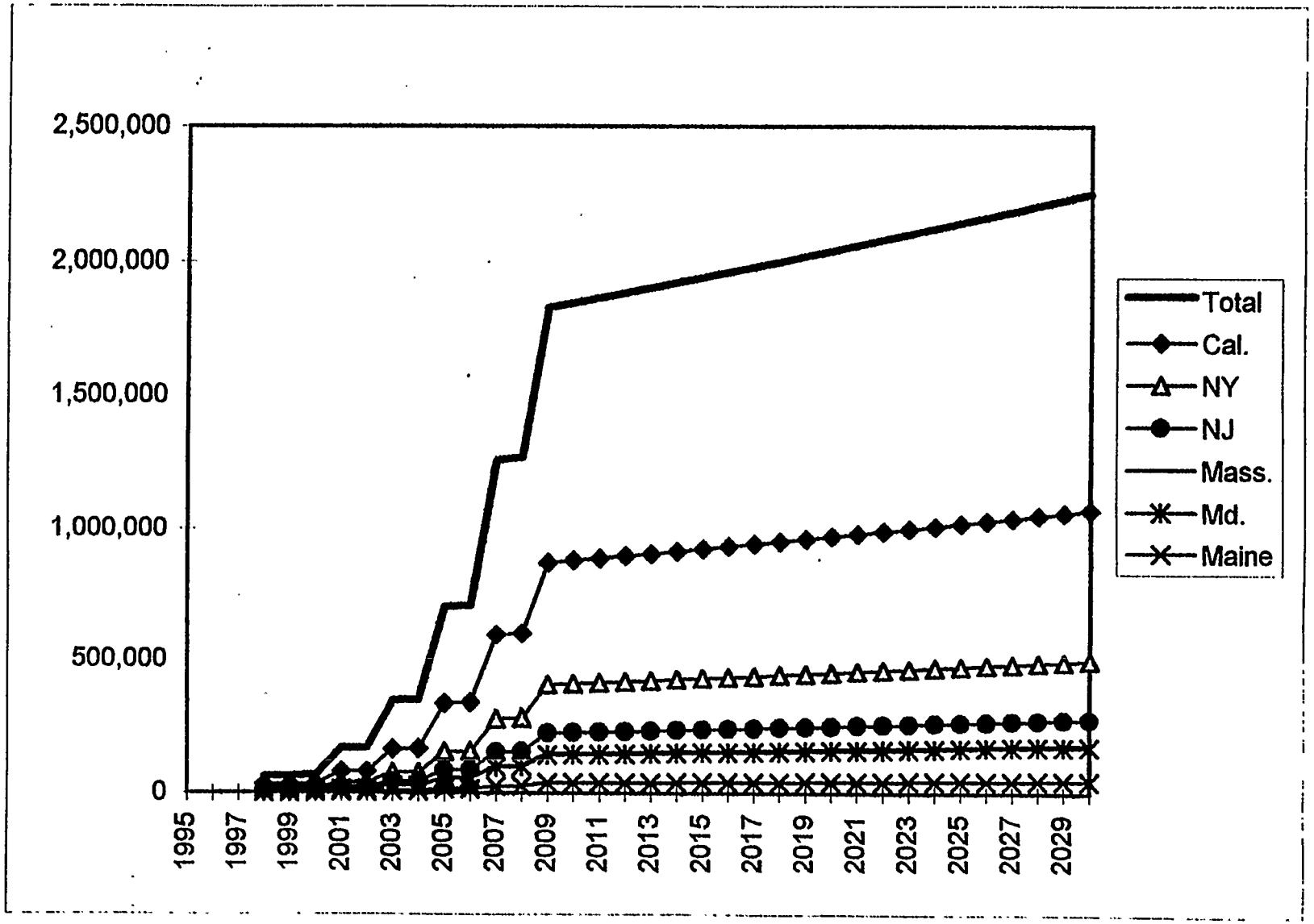


Figure 7

DIRECTED TECHNOLOGIES, INC.

Fuel Cell Vehicle Market Share vs. Vehicle Price

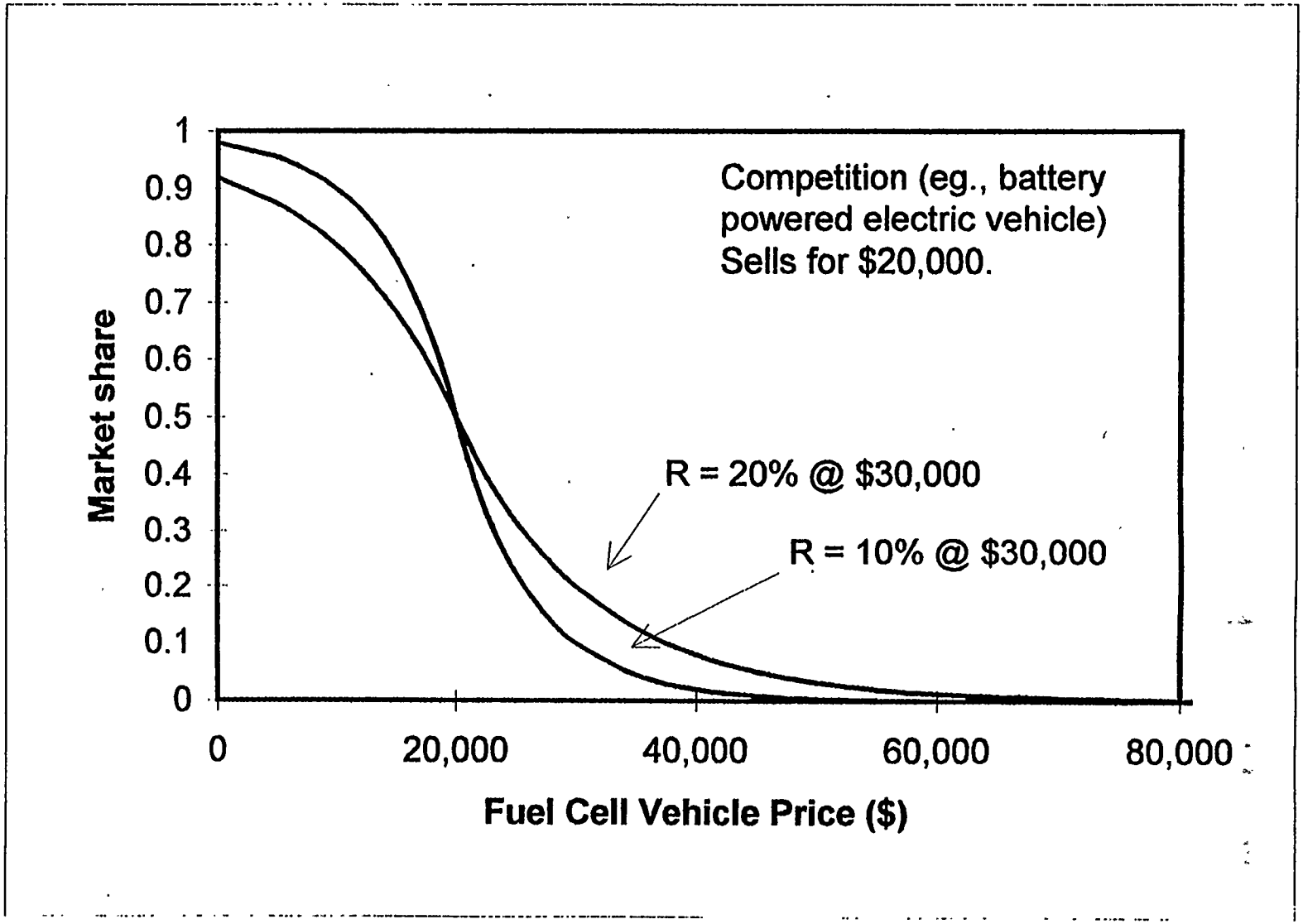


Figure 8

DIRECTED TECHNOLOGIES, INC.

Vehicle Market Share Multiplier Due to Hydrogen Price Relative to Gasoline Price

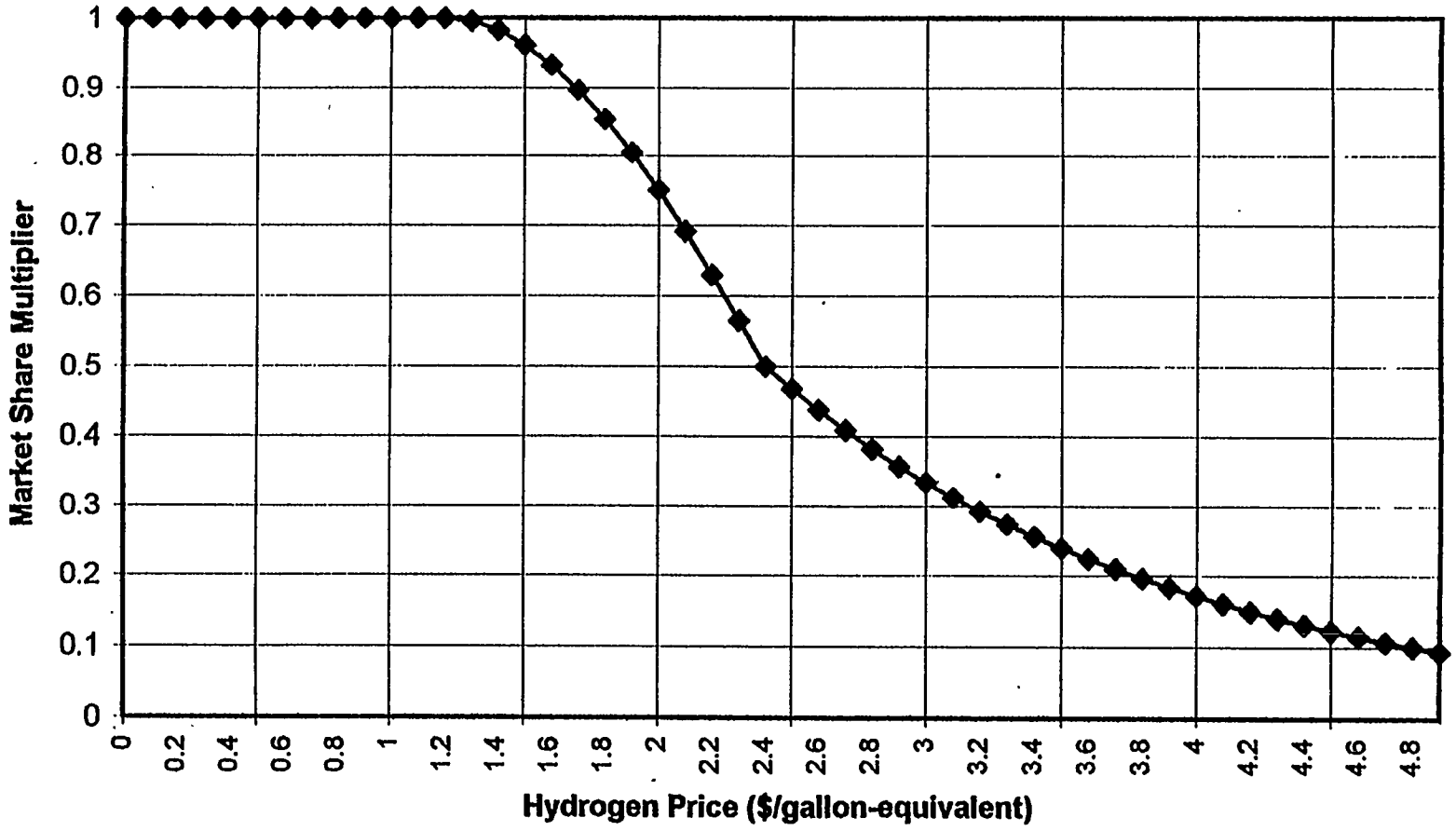


Figure 9

Ford Model T: Price Versus Cumulative Production, 1909-23

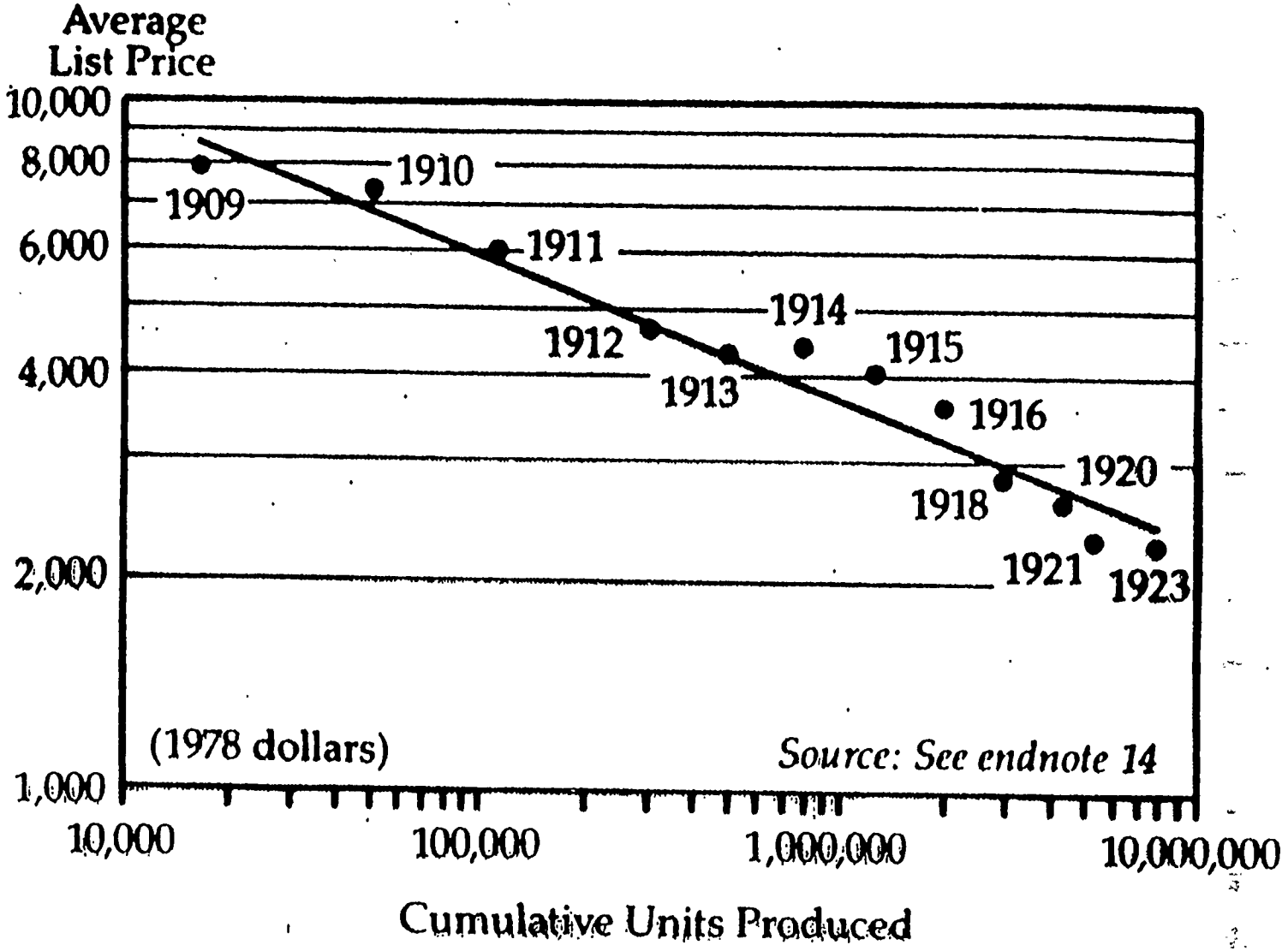


Figure 10

DIRECTED TECHNOLOGIES, INC.

Fuel Cell Vehicle Data

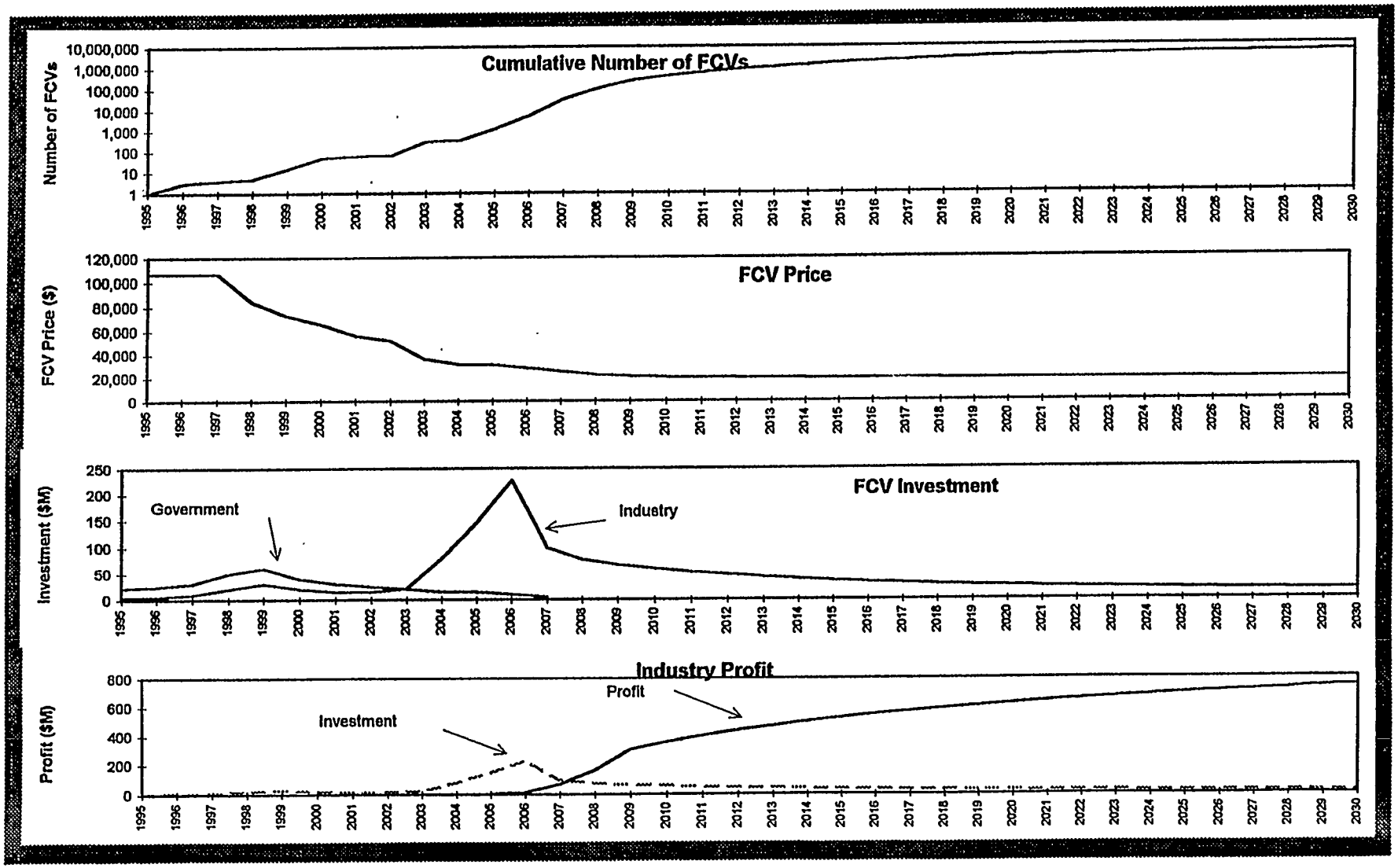


Figure 11

DIRECTED TECHNOLOGIES, INC.

Dispensed Hydrogen Cost
(Including 85% Learning Curve Volume Manufacturing)

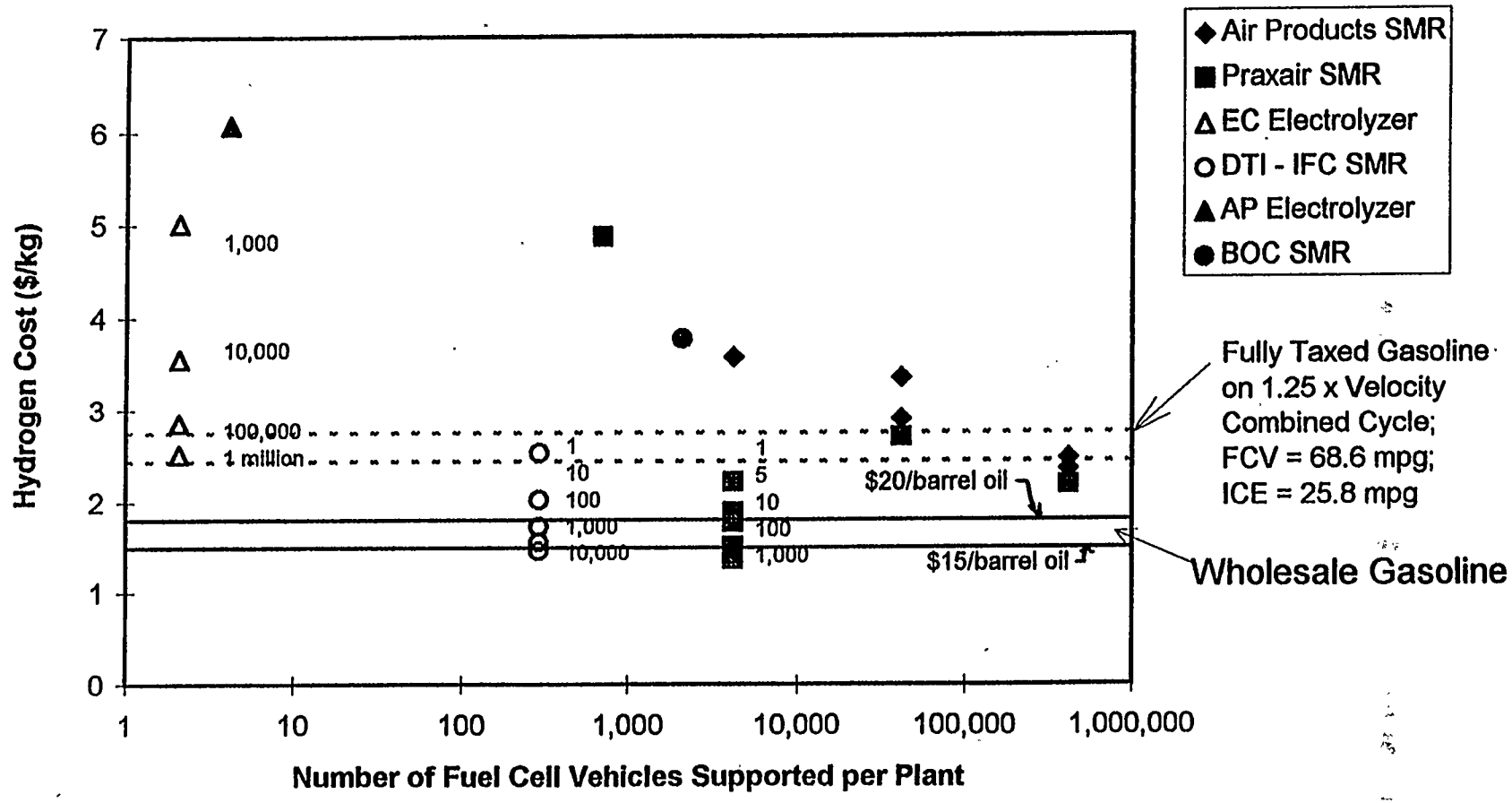
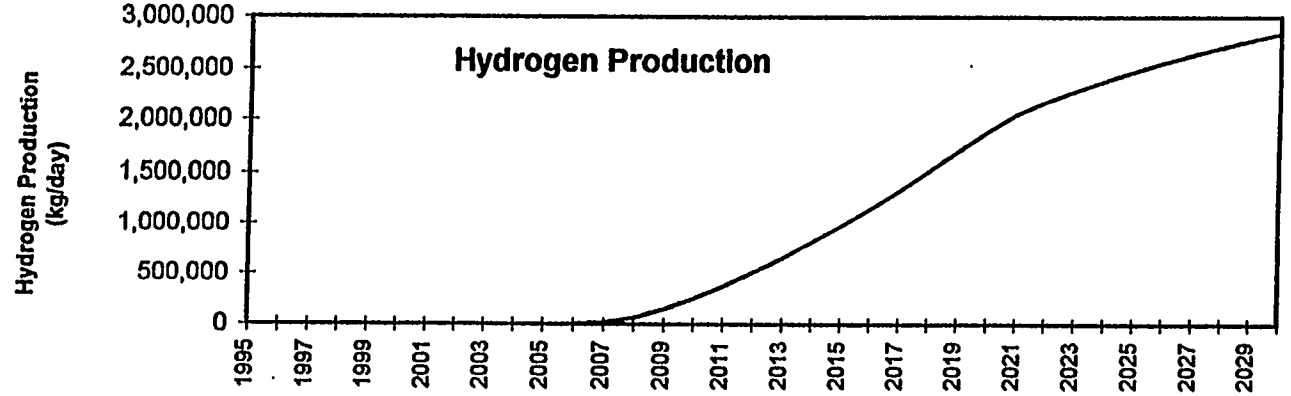
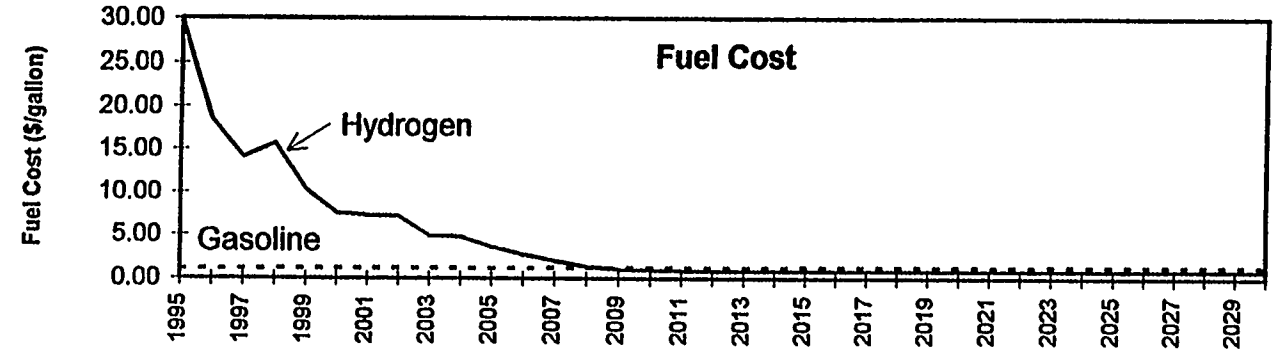


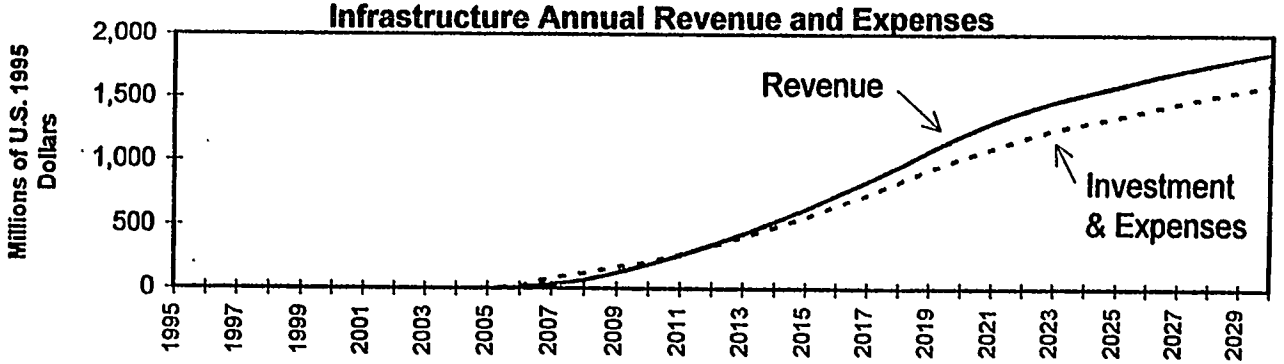
Figure 12

DIRECTED TECHNOLOGIES, INC.

Hydrogen Data







Comparative Costs and Benefits of Hydrogen Vehicles

Gene D. Berry
Energy Analysis, Policy, and Planning
Energy Program, Lawrence Livermore National Laboratory
Livermore, CA 94550

Abstract

The costs and benefits of hydrogen as a vehicle fuel are compared to gasoline, natural gas, and battery-powered vehicles. Costs, energy, efficiency, and tail-pipe and full fuel cycle emissions of air pollutants and greenhouse gases were estimated for hydrogen from a broad range of delivery pathways and scales: from individual vehicle refueling systems to large stations refueling 300 cars/day. Hydrogen production from natural gas, methanol, and ammonia, as well as water electrolysis based on alkaline or polymer electrolytes and steam electrolysis using solid oxide electrolytes are considered. These estimates were compared to estimates for competing fuels and vehicles, and used to construct oil use, air pollutant, and greenhouse gas emission scenarios for the U.S. passenger car fleet from 2005-2050. Scenarios include transitions to hydrogen vehicles fueled from a range of pathways and other fuels/vehicles, including potential changes in the U.S. primary electricity generation mix and emissions.

Fuel costs need not be an overriding concern in evaluating the suitability of hydrogen as a fuel for passenger vehicles. Even under conservative economic assumptions (20% discount rate, $0.05/kwh off-peak electricity, and $4.00/GJ natural gas) Hydrogen fuel can be expected to be affordable (4-10 cents/mile) at delivery scales ranging from individual vehicles to 300 car/day filling station using any of the technology pathways examined for hydrogen vehicles which achieve fuel efficiency similar to PNGV goals (~80 mpg equivalent).

The combined emissions and oil import reduction benefits of hydrogen cars are estimated to be significant, valued at up to ~$400/yr for each hydrogen car when primarily clean energy sources are used for hydrogen production. These benefits alone, however, become tenuous as the basis supporting a compelling rationale for hydrogen fueled vehicles, if efficient, advanced fossil-fuel hybrid electric vehicles (HEV's) can achieve actual on-road emissions at or below ULEV standards in the 2005-2015 timeframe. It appears a robust rationale for hydrogen fuel and vehicles will need to also consider unique, strategic, and long-range benefits of hydrogen vehicles which can be achieved through the use of production, storage, delivery, and utilization methods for hydrogen which are unique among fuels: efficient use of intermittent renewable energy sources, (e,g, wind, solar), small-scale feasibility, fuel production at or near the point of use, electrolytic production, diverse storage technologies, and electrochemical conversion to electricity.

Introduction

Hydrogen possesses the greatest diversity of production, storage, and utilization methods of any fuel. This diversity creates strategic versatility in achieving the scale, overall efficiency, environmental quality, and economic objectives necessary to justify a transition to hydrogen vehicles. This is especially true from a strategic perspective because significant and perhaps rapid, technological, market, and regulatory change can be expected over the next 20 to 30 years. Unparalleled flexibility, however, means a larger number of possible tradeoffs exist for hydrogen than other fuels. Fuel costs, emissions, fuel supply infrastructure scale and scope, as well as hydrogen vehicle use and requirements are all crucial factors in determining an overall balance which provides a robust rationale and feasible, marketable, hydrogen vehicles.

Issues for Hydrogen-Fueled Vehicles

Considering vehicles and fuel supply infrastructure issues can put cost and emission estimates and comparisons in context, showiing their implications for a sound transition strategy. Crucial issues for hydrogen are competing fuels and vehicles, hydrogen vehicle utilization and,onboard storage systems, and fuel supply infrastructure scale, shape, and feasibility.

Competing Alternative Fuels and Vehicles

No fuel, including hydrogen, is the clear alternative to gasoline on the basis of all relevant criteria. Even when a consensus is reached that current gasoline-powered vehicles are no longer the best option, a new debate emerges among the alternative fuels and the vehicles competing to replace gasoline. Figure 1 is a schematic representation of the elements composing the rationale for hydrogen cars. A sound rationale must balance (1) the private costs for hydrogen fuel, infrastructure, and onboard storage to provide a vehicle of sufficient value to consumers, (2) the public benefits (emissions, energy security, improved economic efficiency of potential fuel suppliers, environmental impact, sustainability), and (3) alternative fuel transition criteria, such as a smooth, flexible transition (involving fuel infrastructure scale and shape, and assured fuel availability). These three components of a rationale, in turn, depend on a range of technical, economic, and policy factors and are interconnected. Various alternative-fuel/vehicle choices can each be compelling under a different set of priorities and reasons for moving away from the problems of gasoline. The rationale for each alternative-fuel vehicle depends upon these priorities, vehicle technology, and market demands.

The rationale for hydrogen vehicles is most compelling when high priority is given to the public benefits of alternative-fuel vehicles, and moderate vehicle range is demanded. Hydrogen is a high cost—but high value—fuel. Hydrogen can be more sustainable, cleaner, and more efficiently utilized than natural gas or methanol; but among alternative fuels, only batteries are heavier and more expensive than the on-board storage systems for hydrogen. The best niche for hydrogen fuel exists for vehicles with range and performance similar to today's vehicles (200–400 miles). If range or performance requirements are relaxed, battery-powered electric vehicles (BPEVs) begin to compete with hydrogen vehicles, both on consumer cost and policy criteria (energy security, urban air pollution, and sustainability). For vehicles with very long range (>400 miles), hydrogen compares unfavorably to higher-energy-density fuels such as natural gas and methanol. Consequently, a major premise of hydrogen vehicles is that consumers will require and be satisfied with a 200–400 mile range.

Hydrogen-Powered Vehicles: Utilization systems

Not all classes of hydrogen vehicles compete well with other alternatives. There are three major ways to employ hydrogen in vehicles. (1) Hydrogen burned in internal combustion engine vehicles (ICEVs) essentially as gasoline vehicles operate today. (2) Eectricity generated onboard in a fuel cell electric vehicle (FCEV) at very high efficiency. (3) A hybrid-electric vehicle (HEV), which burns hydrogen only at peak efficiency in a small internal combustion engine to generate electricity when needed.

Of the three options, FCEVs are the ideal technical choice for hydrogen-powered vehicles, and fuel cells should eventually replace the hydrogen combustion engine-generator in HEVs. Fuel cell vehicles operate at the highest efficiencies, producing zero emissions. However, until fuel cells are low cost, the piston-engine hybrid vehicle can be the near-term forerunner of the FCEV's, providing a mass market and developing the infrastructure for FCEVs earlly.

Since HEVs can eneable viable hydrogen vehicles without awaiting the development of cost-effective fuel cells, the baseline hydrogen vehicle used in our analysis is a five-passenger hybrid-electric vehicle, with peak power electrical storage for acceleration. It achieves 80-mpg equivalent energy efficiency on the combined federal driving cycle, with a range of 300 miles. Stored onboard are 3.75 kg of hydrogen (125 kWh or 0.45 GJ on a lower heating value basis). Iincreasing the onboard hydrogen to 4.75 kg would provide a 380-mile range. Figure 3 displays the volumes, weights, and energy requirements of various onboard hydrogen storage systems. Figure 4 shows fueling costs as a function of gasoline-energy-equivalent mileage. These figures demonstrate the feasibility of onboard storage and the importance of fuel efficiency in hydrogen vehicles. High fuel efficiency is necessary to reduce fuel costs and the size, weight, and cost of on-board hydrogen storage to reasonable levels. High fuel efficiency is likely the single most important factor in creating a hydrogen vehicle with sufficient consumer value and appeal.

Hydrogen-Powered Vehicles: Onboard storage systems

A product's value usually depends upon how well it is used. For hydrogen fuel, the value of a transition to hydrogen vehicles and the relative advantages of various hydrogen pathways revolve around how well and easily vehicles can use hydrogen. This depends upon onboard storage in addition to fuel efficiency. Onboard storage is crucial, not only because of the vehicle performance and production/delivery pathway consequences, but also in comparing hydrogen vehicles to other alternative-fuel vehicles. All hydrogen storage choices involve greater bulk, weight, cost, and/or energy requirements than for other alternative fuels (e.g., natural gas or methanol). Compressed hydrogen is more expensive, and three times bulkier, than compressed natural gas. Liquefying hydrogen can increase storage density but raises questions of the dormancy and energy efficiency of liquid hydrogen (LH_2). Fortunately, the diversity of hydrogen storage technologies practical in high-efficiency vehicles can enhance hydrogen vehicles. For example, metal hydride storage can likely make hydrogen fuel safer than any other alternative fuel, especially compressed gaseous fuels such as natural gas.

Vehicles Influence Infrastructure Scale, Shape and Feasibility

In addition to fuel cost and efficiency, onboard storage choices can strongly influence the feasibility of starting a transition to hydrogen vehicles and can perhaps even shape the evolution of the final hydrogen production and delivery infrastructure. Early on, a few dispersed hydrogen vehicles necessitate small-scale fuel production, storage, and refueling. Off-peak electrolysis with low-pressure hydrogen storage can achieve this easily with vehicles that use hydrides for storage. Hydrides support the broadest range of hydrogen production anddelivery options, especially at small scales, with the clear advantage of safety and low energy requirements. Compressed gas storage offers a transition to filling stations with fast refueling and potential blending of natural gas and hydrogen, at the filling station or in the current pipeline system. Liquid hydrogen filling stations could support a transition to a centralized fuel delivery system similar to gasoline today and best support hydrogen use by heavy-duty vehicles, such as trucks, trains, and aircraft.

In summary high efficiency, sufficient vehicle range (200–400 miles), and an assured fuel supply infrastructure are necessary for consumer acceptance. The likelihood of an assured fuel supply infrastructure depends, in turn, on the vehicle's fuel efficiency, range, and onboard hydrogen storage. This circular and reinforcing link between vehicles and infrastructure can strengthen the rationale for hydrogen vehicles and forms the heart of infrastructure considerations for alternative fuels.

Approach, Methodology, and Model Description

Approach: Examine Fuel Costs, Estimate Benefits, and Build Scenarios

The value of various possible transitions to hydrogen fuel depends fundamentally on the efficiency, emissions, and costs of two basic approaches:

(1) Hydrogen production at large plants using a centralized distribution and storage infrastructure.

(2) On-site hydrogen production and storage at fuel stations, fleets, or homes.

This study addresses a broad range of factors influencing the costs and benefits of a transition to hydrogen vehicles. An extended range of production, storage, and delivery pathways, are examined, even if fuel costs are somewhat higher than for other options, to assess a wide range of possibilities in the search for the strongest overall rationale for hydrogen vehicles. In addition to hydrogen delivery by truck, we consider on-site hydrogen production using electricity, natural gas, methanol, and ammonia. We also included for consideration a spectrum of hydrogen delivery scales, down to the individual vehicle level, and fuel cycle emissions in addition to tailpipe emissions.

The results of this examination are used to compare hydrogen vehicles to competing alternatives which were assumed to be capable of meeting ULEV emission standards. A "best case" value of the benefits of hydrogen vehicles is estimated. Scenarios of oil use and full fuel cycle emissions of air pollutants and greenhouse gases for the U.S passenger car fleet are the constructed as well. These scenarios to show the range of emission benefits achievable over 2005-2050 by a transition to hydrogen cars and competing alternatives.

Methodology: Conservative Assumptions (and Units)

Conservative assumptions were used throughout the analysis. Competing fossil fuel vehicles vehicles were assumed capable of achieving high fuel efficiency and actual "on-road" tail-pipe emissions emissions at or below ULEV levels (Green Car Journal 1995). Energy costs for hydrogen production were conservatively hgh as well as disount rates.

Hydrogen cost estimates depend in large measure on energy or feedstock costs, capital equipment discount rates, and off-peak electrolysis schedules. Throughout, this study uses conservatively high discount rates and these electrolysis schedules and energy costs:

Electricity (off-peak)	\$0.05/kWh (\$14/GJ)
Natural gas	\$4.00/GJ (stations) \$2.50/GJ (large central plants)
Methanol	\$0.66/gallon (\$11/GJ)
Ammonia	\$250/ton (\$13/GJ)
Discount rate	20%
Off-peak electrolysis schedule	
Filling stations	128 h/week (76%)
Home or commercial electrolysis	88 h/week (52%)

Cost estimates have been escalated to 1996 dollars. Byproduct credits, taxes, and other financial adjustments have been excluded for clarity and simplicity. Efficiency calculations use input energy divided by the output hydrogen energy (or the lower heating value [LHV] of hydrogen carrier compounds) evaluated at the LHV of 33.3 kWh or 120 MJ/kg of hydrogen. For reference, the LHV of a kilogram of hydrogen is nearly equal to the energy equivalent of 1 gallon of reformulated gasoline.

The volumes used for hydrogen were 2.372 grams per standard cubic foot (1 atmosphere and 68°F) and 89.895 grams per normal cubic meter (Nm^3) (1 atmosphere and 0°C). It should be noted that a normal cubic meter is 7% denser than a standard cubic foot. Ambiguity is avoided by using mass units (kilograms) for hydrogen and $/kW of hydrogen energy LHV output for capital equipment costs. When original sources were in other units, any ambiguities were resolved conservatively (i.e., higher costs, lower production or storage capacity, etc.). The Compressed Gas Association's *Handbook of Compressed Gases,* Third Edition (1990), was used as the definitive reference for hydrogen and other substances when possible.

Model Description: consistency, versatility, and breadth.

A consistent set of technical, economic, and market assumptions was necessary throughout, while still maintaining the flexibility to explore the impact of alternative assumptions, hydrogen pathways, competing gasoline and alternative-fuel vehicles, changes in electric-generation mix, emissions, and other factors, especially over the 40-year timeframe of a transition from conventional gasoline vehicles.

Consequently, the costs, energy use, emissions, and other information for each hydrogen production, storage, and delivery option—as well as assumptions about vehicle fuel efficiency, transportation demand, alternative-fuel-vehicle market penetration, electric-generation mixes, and various other data assembled during this study—were incorporated into a relational database computer model, allowing scenario construction and sensitivity analysis. The result is consideration of a representative set of hydrogen pathways over a wide range of assumptions.

The software used to construct the database, pathway analyses, and scenarios is commercially available (STELLA II from High Performance Systems Inc. of Hanover, NH) and employs a graphical interface. This enables simple visualization, conceptualization, and interconnection of technical, economic, or market variables. Importantly, the value of each factor and its relationship to other factors are easily modified, allowing exploration of strategic parameter spaces such as production and storage scale, efficiency, discount rate, equipment lifetimes, vehicle fuel efficiency, and transportation demand. The model therefore allows more dynamic analysis, and data can be easily updated to include new information. For this report, the model was used in calculating costs, emissions, and energy use of hydrogen production and delivery pathways and in comparing hydrogen vehicles to other alternative-fuel and gasoline vehicles, and then in extending this comparison to consider the changes that will occur over the time required for a transition, both in terms of a changing electricity mix and of vehicle population and use.

Results

Cost Estimates for Hydrogen Pathways and Refueling Scenarios for Stations, Fleets, and Individual Vehicles

Six on-site hydrogen production technologies mentioned earlier and and LH_2 delivery by truck from a central steam-reforming plant form a representative set of hydrogen production/storage/delivery pathways, spanning a broad range of technoeconomic characteristics (energy requirements, scale economies, capital intensity, emissions) and strategic character (centralization, flexibility, and synergy with the existing energy infrastructure). The results of this report are an estimate of the costs, emissions, and benefits of using these pathways to fuel high-efficiency hydrogen cars and comparison with the benefits achievable with other alternatives to today's gasoline vehicles.

Hydrogen delivery costs are a strong function of scale because of the scale economies of not only production pathways but also of storage pathways. Compressors and cryogenic or compressed gas storage, in addition to hydrogen-dispensing equipment, are significant elements of delivered hydrogen cost, particularly at small scales. Four refueling scenarios were chosen to explore these cost changes, with production, storage, and delivery equipment sized accordingly, as listed below. Vehicles were assumed to refuel when a 3.75-kg tank was 80% empty (requiring 3 kg of hydrogen).

(1) Filling station scale: 900 kg H_2/day (300 cars/day).
(2) Small station: 180 kg H_2/day (60 cars/day).
(3) Fleet: 30 kg H_2/day (10 cars/day).
(4) Home refueling: 0.4 kg H_2/12 hr, (refueling 1 car with 3 kg every 8 days).

The station scenarios allow for 60% recovery of a full day's worth of hydrogen compressed gas from on-site storage in a high-pressure (8400 psi) cascade (Ogden *et al.* 1995) For the home refueling case, hydrogen from the electrolyzer is either produced at pressure or compressed using a small hot-water-driven hydride bed (30–40 grams H_2/hr capacity). The hydrogen can then be stored in a low-pressure tank at 500 psi (resulting in a volume of 100 gallons per kilogram of hydrogen storage capacity).

The home refueling scenario is distinct from the other scenarios in a number of ways. First, to save on capital costs, buffer storage is small and at low pressure (500 psi). This eliminates the need for a compressor but requires hydride storage onboard the vehicle. Second, the electrolyzer is sized to meet average demand using a 50% duty cycle to allow for off-peak electricity rates. These two factors mean that, although the vehicle has a driving range of 300 miles, it will need to be "topped off" every other night, similar to EV home-recharging schemes. There is, however, some flexibility to adjust to higher-than-average home hydrogen needs. Buffer storage (I kg) at home will be sufficient for an 80-mile driving range. The electrolyzer can produce 0.4 kg of hydrogen every 12 hours. Using off-peak electricity only, this can fuel 32 miles of driving per day (or 64 miles every two days). However, if the customer is willing to pay peak electricity prices, running the electrolyzer around the clock will produce enough hydrogen for 64 miles of driving per day (or 128 miles every two days). This is constraining but is a strategy that allows a single hydrogen-fueled vehicle to be driven in a community well before a hydrogen filling station is justified.

Delivered Hydrogen Cost Estimates for Stations, Fleets, and Homes

Our cost estimates of producing, delivering (in the case of LH_2), storing, and dispensing hydrogen for each of the seven pathways and four scales are presented by different categories in Fig. 5–7. Relatively high energy costs ($4.00/GJ natural gas, $11.00/GJ methanol, $13.00/GJ ammonia, and $0.05/kWh electricity) and discount rates (20%) were used. Detailed cost and technical assumptions used for each scenario are given in a more comperehensive report (Berry 1996)

Production equipment capital costs were taken from industry (Richter 1995) when available. Some costs were drawn from literature sources, adjusted for inflation, and scaled approximately in some cases. Cost estimates in mass production were used in the case of solid polymer electrolysis (Molter 1994), steam electrolysis (Quandt and Streicher 1986), and home alkaline electrolysis (Kincaide 1995). The electrolysis pathways operate with a duty cycle of 76% to allow off-peak electricity pricing. In general, the thermochemical production methods can be expected to have greater cost certainty but less potential for cost reductions in comparison to electrolysis technologies.

The on-site storage costs used were also conservatively chosen (see Fig. 6). Storage economics were based on compressed gas storage (for on-site production scenarios) from Ogden in her recent examination of on-site steam reforming (Ogden *et al.* 1995) Current industrial equipment prices could probably be reduced somewhat if compressors and storage tanks were manufactured in greater quantities. Hydrogen was assumed to be delivered to vehicles at 6000 psi.

Non-hydrogen-related operating costs of $720/day for a 300 car/day station were assumed, to account for factors such as labor, utilities, and land (Berry *et al.* 1995) This equates to $2.40 per car, which was used for smaller-scale scenarios.

Figure 5 shows delivered hydrogen cost broken down by pathway step (production, delivery, storage, and overhead). Hydrogen will cost roughly $30–50/GJ at filling stations refueling 300 cars/day. Costs increase to $35–60/GJ at 60 cars/day, and $60–75/GJ at 10 cars/day. Refueling an individual vehicle from a very small (~2 kW electrical) electrolyzer system costs $60–70/GJ. Assuming an 80-mpg-equivalent hydrogen vehicle, this $30–75/GJ range correspond to 4.5–11 cents/mile (see Fig. 4). Figure 5 shows that, even with high energy costs and discount rates, at stations hydrogen refueling costs are comparable with per-mile gasoline costs today.

Some conclusions about hydrogen storage costs can be drawn from Fig. 5. Liquid storage at stations is a small (10–20%) fraction of total costs, while compressed gas is more expensive (15–25%). But at very small scales (10 cars/day), both systems have comparable costs. Storage costs rise far faster than production costs with decreasing scale, becoming roughly equal to production costs at 10 cars/day. Figure 7 also shows that steam electrolysis can produce hydrogen for costs comparable to the lowest-cost thermochemical methods at stations of 300 and 60 cars/day (on-site steam-reforming at 300 cars/day, and methanol decomposition at 60 cars/day). Alkaline and polymer membrane electrolysis costs are roughly equivalent to the highest-cost thermochemical methods at each scale. Liquid hydrogen delivery by truck achieves lower costs than any on-site production method down to 10 cars/day, but its greatest cost savings is actually at higher scales (60 cars/day).

Costs are disaggregated financially into capital, interest, energy, operating, and station overhead costs in Fig. 6. The most striking feature of this comparison is the increasing share for interest below the 300 car/day station scale. Interest accounts for the majority of cost increases in delivering hydrogen at small scales. This is driven both by the high discount rate (20%) used in these estimates and by the increasing share of costs for storage equipment, which has shorter operating life (10 years) than production equipment (20 years). Interest alone is more than repayment of the capital investments in all cases except the individual-vehicle scale, where interest is lower because consumers are assumed to use a 10% discount rate. Figure 6 also shows that, except for steam- reforming, all on-site hydrogen production pathways have a large component of energy and feedstock (including water for electrolysis) costs (40–50%), making these pathways sensitive to changes in methanol, ammonia, or electricity prices. The energy costs of ammonia and methanol decomposition pathways are roughly comparable to electricity costs for the electrolysis pathways.

Figure 7 gives the detailed cost breakdown of the hydrogen pathways, principally for reference in determining the largest cost driver in the categories displayed in Fig. 5 and 6. Costs are disaggregated both by pathway step and cost type. Figure 7 shows that the majority

of production costs are dominated by energy, except in the case of steam-reforming, which is capital- intensive. Cost increases at smaller scales are due more to increasing capital costs of storage rather than production-related costs. For fleets (10 cars/day), hydrogen costs are $65–75/GJ, with storage and dispensing capital costs becoming dominant. Residential electrolysis costs of $60–70/GJ are roughly split between capital and energy costs. Figure 9 shows that the 20% discount rate on hydrogen pathways sharply increases the cost penalties of storage at scales below 60 cars/day. Non-hydrogen-related overhead is significant ($6–7/GJ), even at 300 cars per day. A major conclusion of Fig. 7 is that LH_2 is a cheaper pathway for all scales than it was previously considered to be.

At smaller scales, capital equipment for production and especially storage becomes a larger share of total costs. These costs have the potential to be reduced through higher-volume production techniques. Small-scale costs may also be reduced as alternative technologies develop. One possibility is the use of magnesium-hydride stationary storage in combination with a phase change material to replace or augment compressed gas storage at a refueling facility. Alternatives to compressed gas storage are especially attractive if hydride storage is used onboard the vehicles. The cost of hydrogen storage would be roughly $3–5/GJ at scales as low as 35 kg H_2 storage (Hynek and Fuller 1994) Another, more speculative possibility is on-site storage using microspheres. If material costs were low, savings over compressed gas storage might be $5/GJ at $300/cars day and $10/GJ at 60 cars/day, making on-site steam-reforming and steam-electrolysis station costs comparable to LH_2 delivery by truck.

Electricity Generation Mix Changes and Emission Scenarios (2005-2050)

As long as natural gas (or any fossil fuel) is used as the primary energy source for hydrogen pathways, hydrogen cars will have higher or comparable greenhouse gas, NOx, and hydrocarbon emissions than natural-gas hybrid cars. The emission benefits of hydrogen vehicles can be improved significantly with pathways fueled from a cleaner, more efficient primary energy mix that contains a larger proportion of renewable or nuclear electricity. Figure 8(a–c) shows three scenarios chosen for use in the fuel cycle emissions estimates of hydrogen vehicles. The scenarios include an electricity-generation primary energy mix and the corresponding emissions of CO_2 and NOx per kWh of electricity generated from 2005 to 2050. In choosing the scenarios, it was important to encompass the spectrum of possibilities over the time required for full implementation of hydrogen vehicles. Three scenarios were adapted from the "reference," "market," and "climate" electricity-generation mixes constructed in *America's Energy Choices: Investing in a Strong Economy and a Clean Environment* (Union of Concerned Scientists 1992). Full-fuel-cycle emission factors were adapted from a study for the Gas Research Institute (Darrow 1994)examining full-fuel-cycle emissions of alternative-fuel vehicles, including BPEVs. The "reference" scenario results in a clean-coal-based (75%) mix in 2035. The "market" scenario embodies an electricity mix using efficient advanced technologies, pollution abatement, and renewable energy when it is economically competitive, with 40% of electricity coming from non-fossil sources by 2035. The "climate" case uses all available supply and efficiency options to replace coal-generated electricity, resulting in only 5% of electricity coming from coal in 2035. These scenarios are used later to build estimates of U.S. passenger hydrogen car emissions over a transition period from 2005-2050

Oil Use and Emission Benefits of a Transition from Today's Gasoline Vehicles

Chrarting a Transition

In an earlier detailed report (Berry 1996) energy use, and full-fuel-cycle emissions for hydrogen production, storage, and delivery for hydrogen vehicles were estimated for a representative set of hydrogen pathways. These estimates were used to explore the benefits of different pathways for a transition to hydrogen vehicles, and to compare these benefits with those of other alternative-vehicle transitions from conventional gasoline vehicles. Transition scenarios were constructed with common transportation demand and market penetration assumptions for the decades from 2005 to 2050. The oil use and emissions for each case were then calculated and compared to a base case in which the U.S. passenger vehicle fleet meets ULEV emissions standards and achieves an average fuel efficiency of 30 mpg.

A relatively simple transportation-demand scenario was adapted from an analysis in *America's Energy Choices* (Union of Concerned Scientists 1992) based on growth in U.S. driving-age population, saturation in vehicle ownership, and moderate growth in average annual driving to the distances driven by average male drivers today. These assumptions result in a scenario in which the U.S. passenger car fleet grows slowly from 169 million vehicles in 2005 to saturate at 200 million in 2050.. Growth in vehicle miles traveled is moderate also: rising 30% from 1.83 trillion miles/year to 2.4 trillion miles/year over the same period.

Alternative vehicles fueled by hydrogen, electricity, or natural gas are introduced using an aggressive schedule to replace gasoline cars by 2040, as shown in Table 1. A 10-year vehicle life is assumed for all vehicles.

Table 1. Production schedule for alternative vehicles.

Year traveled	Production rate (10^6 vehicles/yr)	Total alternative vehicles in fleet (millions)	Vehicle miles (trillion miles)
2005	0.1	0	1.832
2015	3	1	2.074
2025	13	50	2.248
2030	18	110	2.328
2050	20	200	2.400

For clarity, constant vehicle fuel efficiencies are assumed of 30 mpg for conventional internal-combustion-gasoline-powered fleet, 65 mpg forgasoline HEVs, 70 mpg for natural-gas HEVs, and 80 mpg for hydrogen HEVs. BPEVs are assumed to perform as well as hydrogen HEVs, requiring 0.16 kWh/mile. It is optimistically assumed that ULEV tailpipe emission standards are met nationally by the gasoline automobile fleet by 2005.

Reduced Oil Use

The conventionally cited benefits of a transition to alternative-fuel vehicles include reduced oil consumption, reduced urban air-pollutant emissions, and reduced greenhouse-gas emissions. Of these, reducing oil use enjoys the broadest consensus as a worthwhile benefit and also the broadest range of methods to achieve the benefit. Any alternative-fuel vehicle displaces oil use. Oil use reductions achievable by alternative-fuel cars under the market penetration assumptions described previously are shown in Fig. 9. The associated passenger fleet population, average annual mileage, and replacement of gasoline cars with alternative-fuel cars are also shown. The most striking point about oil-use reductions and alternative-fuel vehicles is the *very long lead times necessary for large-scale change.* Alternative-fuel cars introduced in 2005 do not begin to materially influence aggregate oil use for another decade, and two decades more (2035) are required to replace gasoline vehicles. This points out the

need for an assured, single transition to an enduring, and essentially permanent, alternative fuel—arguably a position that hydrogen vehicles alone can claim among the alternatives. It also points out the necessity of a long-term perspective, infrastructure flexibility, and advanced technology in formulating a rationale for hydrogen vehicles.

The second point from Fig. 9 is the sheer amounts of oil and money involved. The transition shown would save an average 2 billion barrels annually over the 20 years from 2030 to 2050. Assuming an average price of $30/barrel, that would represent a $1.2 trillion savings in imports.

This large benefit is achievable with any alternative fuel, however, and therefore supports moving away from today's gasoline vehicles more than moving towards hydrogen vehicles.

Air-Pollutant and Greenhouse Gas Emission Reductions

Air-pollutant and greenhouse-gas emissions support hydrogen vehicles more directly than oil import reductions. A range of vehicle/pathway combinations were used to assess the emission benefits of hydrogen and other vehicles. Total emissions for the U.S. passenger car fleet are calculated, combining the electricity-mix assumptions and market penetration of Fig. 8 and 9. Eight transition scenarios were chosen.

- Conventional (30-mpg) gasoline cars.
- High-efficiency (65-mpg) gasoline HEVs.
- High-efficiency (70-mpg) natural gas HEVs.
- Hydrogen HEVs (80-mpg) fueled by steam reforming.
- Hydrogen HEVs (80-mpg) fueled by steam electrolysis (with "reference" electricity-generation mix).
- Hydrogen HEVs (80-mpg) fueled by steam electrolysis (with "market" electricity-generation mix).
- Hydrogen HEVs (80-mpg) fueled by steam electrolysis (with "climate" electricity-generation mix).
- Advanced (0.16 kWh/mile) BPEVs (with "market" electricity-generation mix).

These options encompass the range of emissions reductions possible from using efficiency, alternative fuels, fossil-fuels, BPEVs, and hydrogen vehicles (for which the hydrogen fuel is made from natural gas and a wide range of electric-generation mixes).
10 (a–d) displays the effect of a transition to each option in terms of U.S. passenger car annual emissions of CO_2-equivalent greenhouse gases, NOx, hydrocarbons, and CO. Figure 11 (a–d) presents the same options and scenarios in terms of cumulative emissions from U.S. passenger cars.

These figures show that, depending upon the relevant criteria, other advanced/alternative vehicles can deliver a large portion of the benefits of hydrogen vehicles. For example, 65-mpg gasoline vehicles reduce oil consumption by more than half, with greenhouse-gas emissions similar to those of 80-mpg steam-reformed hydrogen vehicles. And 70-mpg natural-gas vehicles can eliminate oil consumption completely, with even lower greenhouse-gas emissions (with the caveat that methane leakage must be eliminated on the vehicle). Natural-gas vehicles would also produce lower hydrocarbon and NOx emissions than steam-reformed hydrogen vehicles. The only criteria on which steam-reformed-based hydrogen vehicles compare favorably to fossil-fueled HEVs are CO tailpipe emissions. BPEVs produce lower pollution and greenhouse-gas emissions than any of the fossil or hydrogen-powered vehicles. Electrolytic hydrogen vehicles can provide lower emissions than most other options only under largely non-fossil electric-generation mixes (i.e., the "climate" mix). Even though hydrogen vehicles can produce fewer emissions than other alternative-fuel vehicles, the vast majority of emission reductions (from the levels of conventional 30-mpg gasoline vehicles) can be achieved with natural-gas HEVs.

"Best Case" Estiamte of Oil Use and Emission Reductions for Hydrogen Vehicles

An upper estimate of the emissions and oil import reduction benefits of hydrogen vehicles can be made from Fig. 17 and 19, using the transition scenario in which hydrogen vehicles are fueled by steam electrolysis using the most favorable electricity mix (the "climate" scenario).

The value of emission and oil-use reductions can be approximated using control costs for emissions obtained from an Office of Technology Assessment background paper (OTA 1994) summarizing the Tellus study. The benefits of a transition from 30-mpg ULEV gasoline cars to 200 million hydrogen cars can be approximated as shown in Table 2.

Table 2. Estimated Emissions benefits from hydrogen vehicles.

Externality	Annual savings/benefit	Price (billion)	Annual value ($ billion)
Carbon monoxide	4.0 million tons	$900/ton	3.6
Nitrogen oxides	0.5 million tons	$7500/ton	3.8
Hydrocarbons	0.4 million tons	$5500/ton	2.2
Carbon dioxide	600 million tons	$24/ton	14.4
Emissions total			24.0
Oil imports	2.0 billion barrels	$30/bbl	60
Total annual value of benefit		$84.0 billion	
Total annual benefits per hydrogen vehicle		~$420/yr	

This valuation is only approximate, and refinements in the analysis or evaluation process are possible, but two important qualitative results from these calculations are clear:

First, only a tiny fraction, roughly 5% (in a monetary context), of the emission and oil-use-reduction benefits of hydrogen vehicles are uniquely achievable by hydrogen vehicles (CO emission elimination). Even fuel-cell hydrogen vehicles (with zero tailpipe emissions) would only raise the fraction of benefits unique to hydrogen vehicles to 15% at most.

Second, greenhouse-gas-emissions reductions will be of greater benefit than air-pollution-emission reductions below ULEV gasoline vehicles.

In summary, a strong rationale for hydrogen vehicles requires more than the conventional benefits of air-pollution, greenhouse-gas, and oil-import reductions. Hydrogen vehicles need to offer emissions benefits beyond gasoline or natural-gas HEVs and will only do so when the hydrogen is derived from renewable or nuclear energy (because greenhouse-gas emissions from gasoline and natural gas are lower than steam-reformed hydrogen vehicles).

Discussion

Unique Strategic Benefits Needed for Robust Rationale

The preceding emissions and benefit estimates for vehicles using hydrogen produced from a range of possible electricity-generation mixes and thermochemical production methods make it likely that other benefits are necessary for a robust rationale for hydrogen vehicles. This is especially true in comparison to other vehicle/fuel combinations. At least three additional major potential benefits of hydrogen fuel are unique:

- A smooth, flexible, and enduring transition from gasoline vehicles.
- A flexible, new, value-added market for electricity, improving the economic efficiency of electricity generation and enabling an electricity-generation mix based in large part on renewables, capturing their environmental and sustainability advantages without the intermittent or fluctuating supply disadvantages of these sources.
- Real and perceived safety advantages of hydrogen vehicles using hydride storage, especially in comparison to compressed storage of alternative fuels.

These advantages are difficult to measure and value precisely, but they can be quite large.

A smooth, flexible, *and* single transition from today's gasoline vehicles is the strategic goal of every alternative fuel, but hydrogen is superior to other fuels in this regard, because it can be made and used in all of the same ways as other fuels but can also be used and stored more safely (in hydrides) at small scales and is more sustainable. This is the root of both the long-term reliability of a transition to hydrogen vehicles and the short-term low investment risk of starting the transition. To crudely estimate the potential value of this benefit, consider that 2–10 million alternative fuel vehicles (1–5% market penetration of the 2050 passenger car fleet) are built and that these vehicles later become stranded without a fuel supply (due to any of a number of environmental, economic, or technological changes). This would correspond to a loss of $40–200 billion, sufficient perhaps to build the hydrogen-fuel-supply infrastructure for 100 million passenger vehicles.

Electrolytic hydrogen vehicles could dramatically improve the economic efficiency of the nation's utilities and electricity supply system by 2030. Adding new electricity-generating capacity (and replacing retired capacity) requires a large investment. Forty gigawatts of new capacity is projected to be added by 2010, by which time U.S. generating capacity will reach 722 GW. More than $400–700 billion will probably be required between 2010 and 2050 to replace this capacity as it ages. Projected electricity production of 3.2 trillion kWh in 2010 represents only a 50% capacity utilization of this investment. Electrolytic hydrogen vehicles can make fuller use of this underutilized investment by creating a very large market tolerant of intermittent or off-peak service. Thirty billion kilograms of electrolytic hydrogen would be needed annually to fuel 200 million vehicles traveling 2.4 trillion miles/yr in 2050. The additional 1.6 trillion kWh/yr electricity demand would increase utilization of the giant investment in generating capacity to 70%. Estimating the total capital investment of U.S. electric generation in 2035 at $1 trillion, and discounting at 10% over 30 years, the extra benefit of efficiently utilizing generating capacity would be perhaps $20 billion annually or $100/vehicle. For reference, the electricity cost (at $0.05/kWh) for hydrogen fuel would be roughly $75 billion annually.

In addition to possible fuel and energy-infrastructure benefits of hydrogen, vehicle characteristics can benefit from hydrogen fuel. Hydrogen's most unique characteristic in this respect is a diversity of storage technologies. The potential safety benefit of hydrogen vehicles with hydride storage is not easily quantified, but there are inherently lower risks than with vehicles using cryogenic and/or high-pressure compressed gas storage, and these lower risks can be readily understood, perceived, and valued by consumers.

Conclusions

Examining and estimating the costs, emissions, and benefits of a transition to hydrogen vehicles has led to a number of conclusions.

Efficiency and Economics

High-efficiency (~80 mpg) vehicles are crucial to the competitiveness of hydrogen fuel. An efficient vehicle reduces sensitivity to fuel and onboard storage cost, allowing the full range of possible onboard storage, production, and delivery infrastructures, while reducing the fuel-cycle energy requirements and associated emissions. Internal-combustion-engine HEVs can achieve the necessary fuel efficiency and lead to development of the infrastructure and market for hydrogen fuel cells without requiring automotive fuel cells.

Given ~80-mpg-equivalent hydrogen vehicles, all of the options we examined were economically feasible in terms of fuel cost, with conservative economic assumptions ($4.00/GJ natural gas, $0.05/kWh off-peak electricity, $250/ton ammonia, $11/GJ methanol, and 20% discount rates). Cost differences among hydrogen production methods at similar delivery scales were almost negligible (1–2 cents/mile) in comparison to vehicle lifecycle costs (45 cents/mile).

Hydrogen fuel costs were $35–75/GJ (4.5–11 cents/mile), depending principally upon scale. At stations, hydrogen will cost $30–50/GJ, with roughly $15/GJ for overhead and compressed gas storage. Production costs are dominated by energy costs except in the case of steam-reforming. Liquid hydrogen delivery was generally cheaper than other options because of on-site storage costs. Among on-site production technologies at the station scale, steam electrolysis and steam reforming could have comparable hydrogen production costs. At smaller production/delivery scales (60 cars/day), the capital costs of storage increase, raising hydrogen costs to $35–65/GJ. Small fleets that refuel approximately 10 vehicles/day would have hydrogen costs of $65–75/GJ. Residential electrolysis for a single vehicle is estimated to cost $60–70/GJ.

The greatest potential for cost savings is probably in storage technologies (perhaps hydrides or glass microspheres) to replace compressed gas, especially at small scales. Off-peak electricity rates lower than $0.05/kWh would also be significant.

Urban Air Pollution

Hydrogen vehicles have much lower tailpipe emissions and total CO emissions than ULEV fossil-fueled HEVs, but full-fuel-cycle emissions estimates (with natural gas as the primary energy source of hydrogen and electricity) indicate that a rationale based on NOx and hydrocarbon emission reductions below ULEV vehicles is weak. To support a rationale for hydrogen vehicles based on full-fuel-cycle emissions requires sustainable sources as a necessary part of the primary energy used to produce hydrogen.

Steam-reformed hydrogen vehicles (with hydride storage) can achieve emissions levels comparable to BPEVs using natural-gas-fired power plants.

Based upon the control costs used in the Tellus study, the benefits from automotive emission reductions below ULEV levels are relatively small for hydrogen vehicles, given the already low air pollutant emission levels of ULEV vehicles in the near future. Other benefits of hydrogen vehicles—such as reducing oil consumption and greenhouse gases or increasing the use of electric generation capacity—are much larger.

Greenhouse Gas Emissions

High-efficiency gasoline and natural-gas vehicles can achieve lower greenhouse-gas emissions (CO_2 equivalent) than hydrogen vehicles using natural gas as a primary energy

high; storage media that are filled directly from hydrogen production equipment (e.g., low-pressure gas, glass microspheres, or hydride storage), eliminating additional compression, are needed.

If range requirements beyond hydride storage (300 miles) are desired, onboard storage using hydrides combined with either LH_2 or cryogenic compressed hydrogen would allow greater range and refueling flexibility, without the full emissions and energy penalties of compressed gas or LH_2. A combination vehicular storage system should be developed.

Systems Analysis Needs

Vehicle issues, providing fuel supply reliability, and providing benefits from hydrogen fuel that other alternative vehicles cannot supply, should drive the fueling infrastructure—NOT fuel cost. System studies should focus on strategic issues, rather than on fuel cost. These issues need to be addressed to develop a robust rationale for hydrogen fuel and vehicles.

One candidate for study is the feasibility of a hydrogen vehicle with supplementary electricity storage, onboard photovoltaic panels, and recharging capability from the grid at home or work. There are potentially dramatic implications for vehicle drivetrain life, hydrogen demand, and infrastructure development, as well as for the utility sector, depending upon driving patterns.

Another issue is to ascertain the degree to which the size and flexibility of demand for electrolytic hydrogen enable the large-scale use of intermittent and renewable resources in the utility sector. Electrolyzing hydrogen for vehicles should be examined and compared with other approaches to enable large-scale renewable implementation and for utility load-leveling using hydrogen.

Acknowledgments

I am grateful to the following for their helpful suggestions in an earlier stage of this work: J.M. Ogden, M. DeLuchi, P.K. Takahashi, and W. Van Vorst. I have benefited greatly from discussions with J. Birk, K. Davis, M. Fairlie, W. Kincaide, D. Sperling, V. Raman, P. Campos, and M. Schalef on infrastructure issues dealing with the introduction of hydrogen into the marketplace. I thank J.R. Smith, R.N. Schock, and G.V. Kaiper for reviewing a draft of this report. This work performed under the auspices of the U.S. Department of Energy by the Lawrence Livermore National Laboratory under Contract No. W-7405-ENG-48.

References

Note: This report is based on a larger, more detailed and comprehensive final report submitted in March 1996. Additional references and background material can be found in:

Berry, Gene D. March 1996. *Hydrogen as a Transportation Fuel: Costs and Benefits.* Final Report Presented at the DOE Hydrogen Annual Review Meeting Miami, FL, Apr. 29-May 3, 1996; Lawrence Livermore National Laboratory Report UCRL-ID-1231465.

Other Cited References

Berry, G. D. J. Ray Smith, and Robert N. Schock. Apr. 19-21, 1995. *A Smooth Transition to Hydrogen Transportation Fuel,* presented at the DOE Hydrogen Program Review Coral Gables, FL, ; Lawrence Livermore National Laboratory Report UCRL-JC-120152.

Darrow, Kenneth G. 1994 *Light-Duty Vehicle Full Fuel Cycle Emissions Analysis.* Energy International Report No. 9333R440, prepared for Gas Research Institute under Contract No. 5093-294-2573. Energy International Inc., Bellevue, WA.

"Behind the Wheel in Honda's New Gasoline-Powered ULEV Accord EX," *Green Car Journal* 4 (Apr. 1995) pp. 37–39.

Hynek, Scott and W. Fuller, (1994) A. D. Little, Inc., "Hydrogen Storage Within the Infrastructure,"*Hydrogen '94; the 10th World Hydrogen Energy Conference* (Cocoa Beach, FL,) Vol. 2, pp. 1341–1353.

Kincaide, W.C. June 1995. Teledyne Brown Engineering, Energy Systems, Hunt Valley, MD, private communication.

Molter, T. 1994. *SPE Water Electrolyzers for Commercial Hydrogen Production.* Hamilton Standard Division of United Technologies, Space and Sea Systems, Windsor Locks, CT .

Ogden, Joan M., E. Dennis, M. Steinbugler, and J. Strohbehn. Jan. 18, 1995. *Hydrogen Energy Systems Studies,* Final Report to NREL for Contract No. XR-11265-2, Center for Energy and Environmental Studies, Princeton University, Princeton, NJ.

Office of Technology Assessment, U.S. Congress, "Studies of the Environmental Costs of Electricity," OTA-ETI-134 (U.S. Government Printing Office, Washington DC, Sept. 1994).

Quandt, K.H. and R. Streicher, 1986."Concept and Design of a 3.5 MW Pilot Plant for High Temperature Electrolysis of Water Vapor," *International Journal of Hydrogen Energy* **11,** No. 5 pp. 309–315.

Richter, Neal. 1995. Research Fellow, Texaco Montebello Research Center, Montebello, CA, private communication.

Union of Concerned Scientists 1992. *America's Energy Choices: Investing in a Strong Economy and a Clean Environment,* (Cambridge, MA, 1992).

Figure 1. Elements of a Robust Rationale for Hydrogen-Vehicles. Hydrogen competes with today's gasoline vehicles on a rationale composed of a balance of (1) consumer costs, (2) public benefits, and (3) feasibility of a smooth, flexible transition. Hydrogen has many attractive public policy benefits (secure, domestic, sustainable fuel production; clean air; and new markets that enhance the economic efficiency of utilities) that depend mostly upon the primary energy source. But to achieve these benefits, hydrogen vehicles must be successful in the market. Hydrogen vehicles must deliver greater value (cost, range, vehicle life, refueling time, acceleration, etc.) to consumers than other alternative-fuel vehicles. Technical issues and choices of fuel efficiency, onboard storage, delivery infrastructure, and production scale determine to a large extent the value of hydrogen vehicles to consumers. In addition to a high-value vehicle, consumers want assured fuel availability, which at least initially is a major issue involving both technical and business risk aspects of hydrogen infrastructure. Hydrogen is already produced today in industry, and synergies exist with potential fuel suppliers (utilities, chemical industry) who can invest in delivery infrastructure and capture a new fuel market. The development of a reliable hydrogen fuel supply is helped by the diverse domestic sources of hydrogen production and the wide array of possible production, storage, and delivery scales, which allows market entry and decentralization. These provide hydrogen vehicles a unique flexibility and potential for a smooth transition through changes in the mix of primary energy sources used to produce hydrogen fuel in response to market, economic, or regulatory changes.

Figure 1. Elements of a Robust Rationale for Hydrogen Vehicles

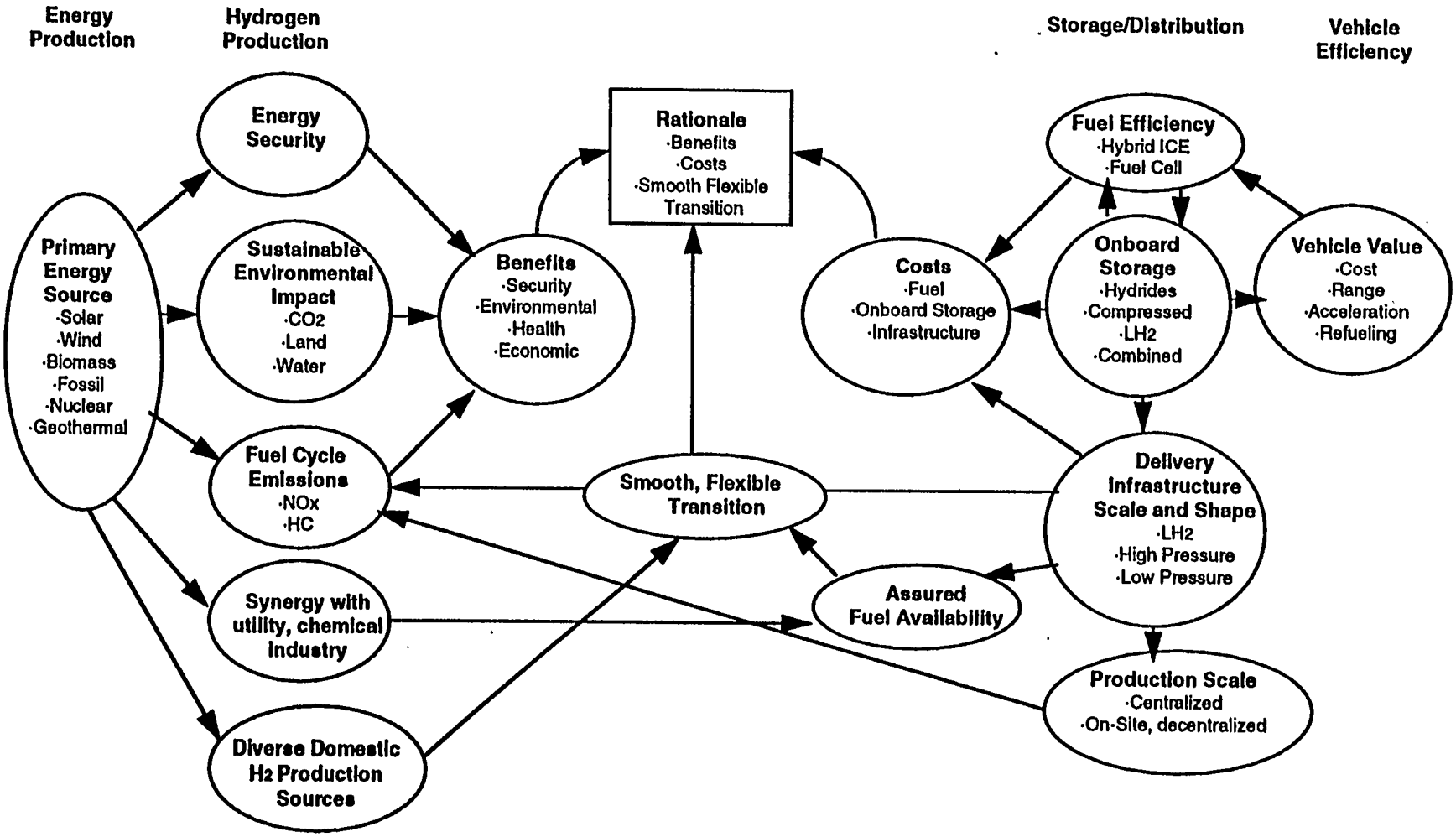


Figure 2. Conceptual design of a hydrogen-powered five-passenger hybrid-electric vehicle that can travel 300 miles using only 3.75 kg of hydrogen fuel, achieving 80-mpg-energy-equivalent mileage. This high fuel efficiency is possible because of a low drag coefficient and high drivetrain efficiency. A small internal combustion engine (or ultimately a fuel cell), optimized for hydrogen, generates electricity at peak efficiency to charge a secondary electrical energy storage device (batteries, a flywheel, or capacitors) that delivers electricity to the electric motor and has sufficient power for peak accelerations and energy recovery from regenerative braking. Hydrogen is stored onboard in a hydride bed, in compressed gas tanks at 5000 psi and room temperature, or cryogenically as a compressed gas (80 K, 3600 psi), or as a liquid (20 K, 5 atm).

Figure 2. Conceptual hydrogen powered vehicle

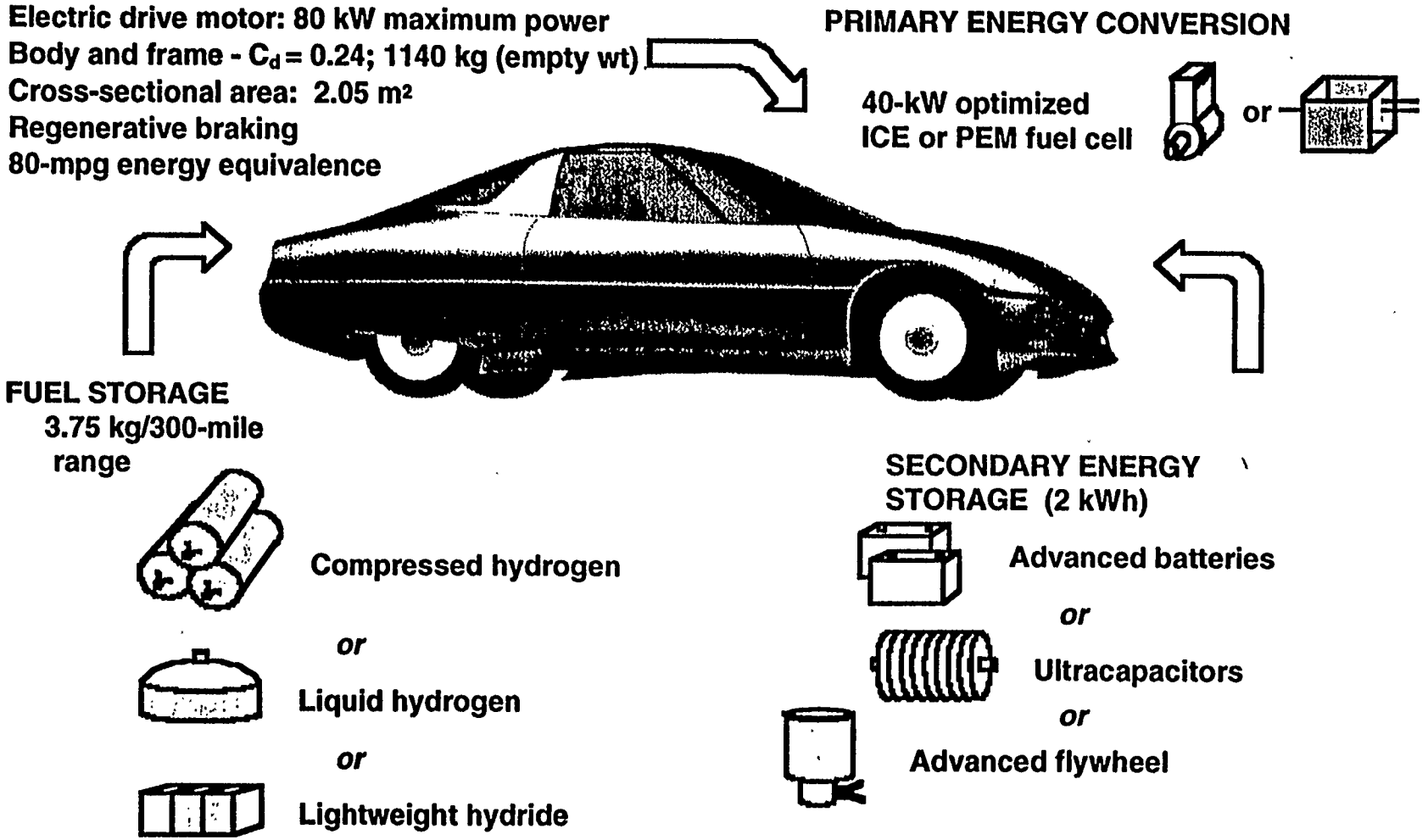


Figure 3. To provide enough fuel for a 300-mile range in an 80-mpg-equivalent hydrogen vehicle, 3.75 kg of hydrogen must be stored onboard. The weight, volume, and storage energy required to store 3.75 kg of H_2 is shown for (1) an Fe-Ti-based hydride (15% energy penalty), (2) carbon-fiber-wrapped aluminum pressure vessels storing hydrogen between 3600 and 9000 psi with a safety factor of 2.25 (5–10% energy penalty), (3) a cryogenic pressure tank storing hydrogen at 3600 psi and 80 K (25% energy penalty), and (4) a low-pressure (1–5 atm) liquid hydrogen tank (40% energy penalty). The system volumes and weights shown are all feasible (although room-temperature compressed gas tanks may require pressures of 5000 psi or above). Compact, lightweight storage technologies require generally large increases in energy requirements.

Figure 3. Storage systems for 3.75 kg hydrogen (300 mile range at 80 mpg)

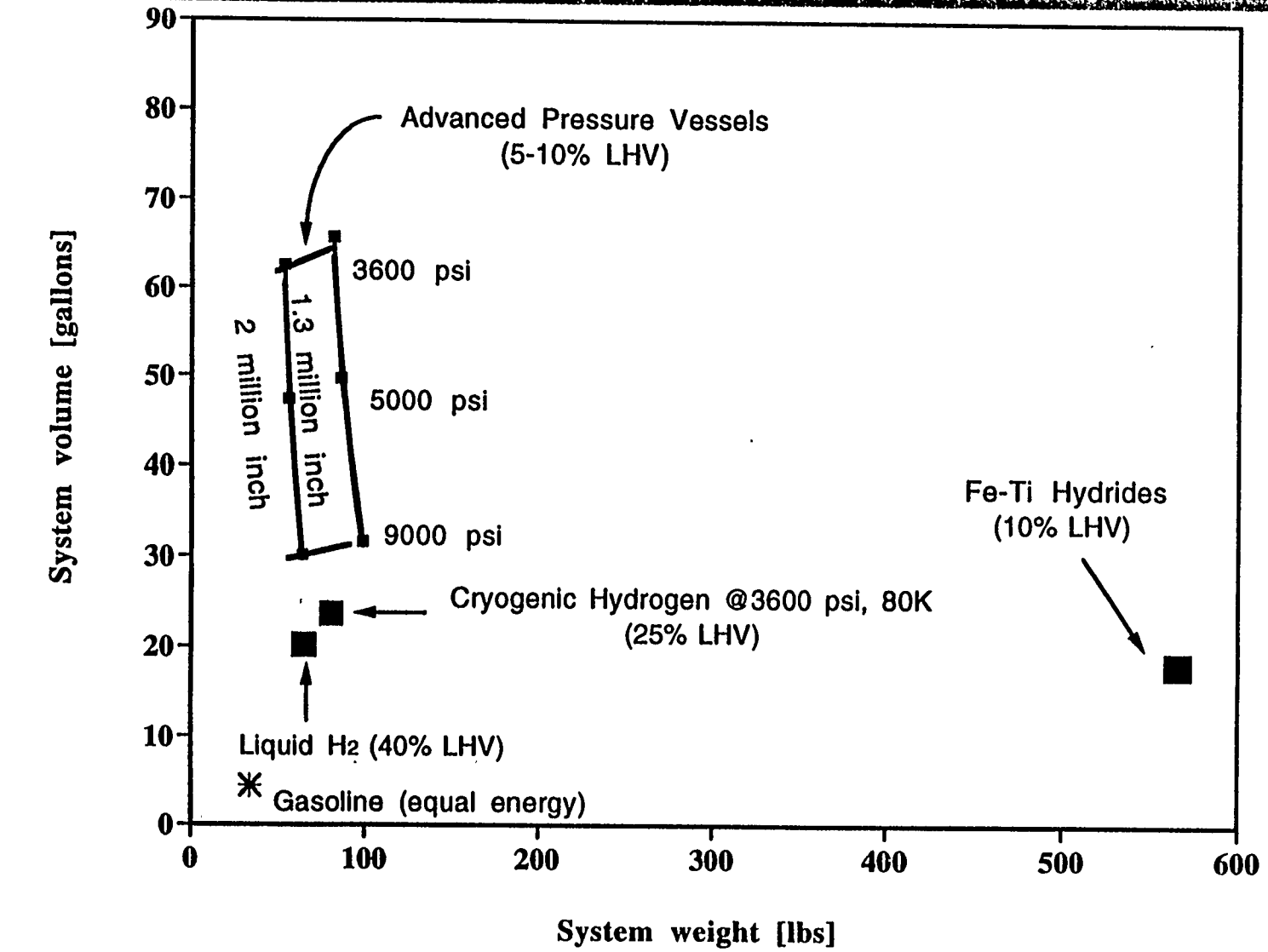


Figure 4. Fuel cost in cents per mile is shown for hydrogen vehicles ranging in fuel efficiency from 70 to 100-mpg gasoline energy equivalent. Hydrogen in filling stations is conservatively estimated to cost at most $50/GJ (off-peak electrolysis at $0.05/kWh for electricity). Hydrogen costing $40/GJ (equivalent to $5.00/gallon gasoline) corresponds to only $0.06/mile, comparable to gasoline fueling costs in today's vehicles.

Figure 4. Hydrogen from natural gas or off-peak electricity is an affordable fuel in 70-100 mpg vehicles

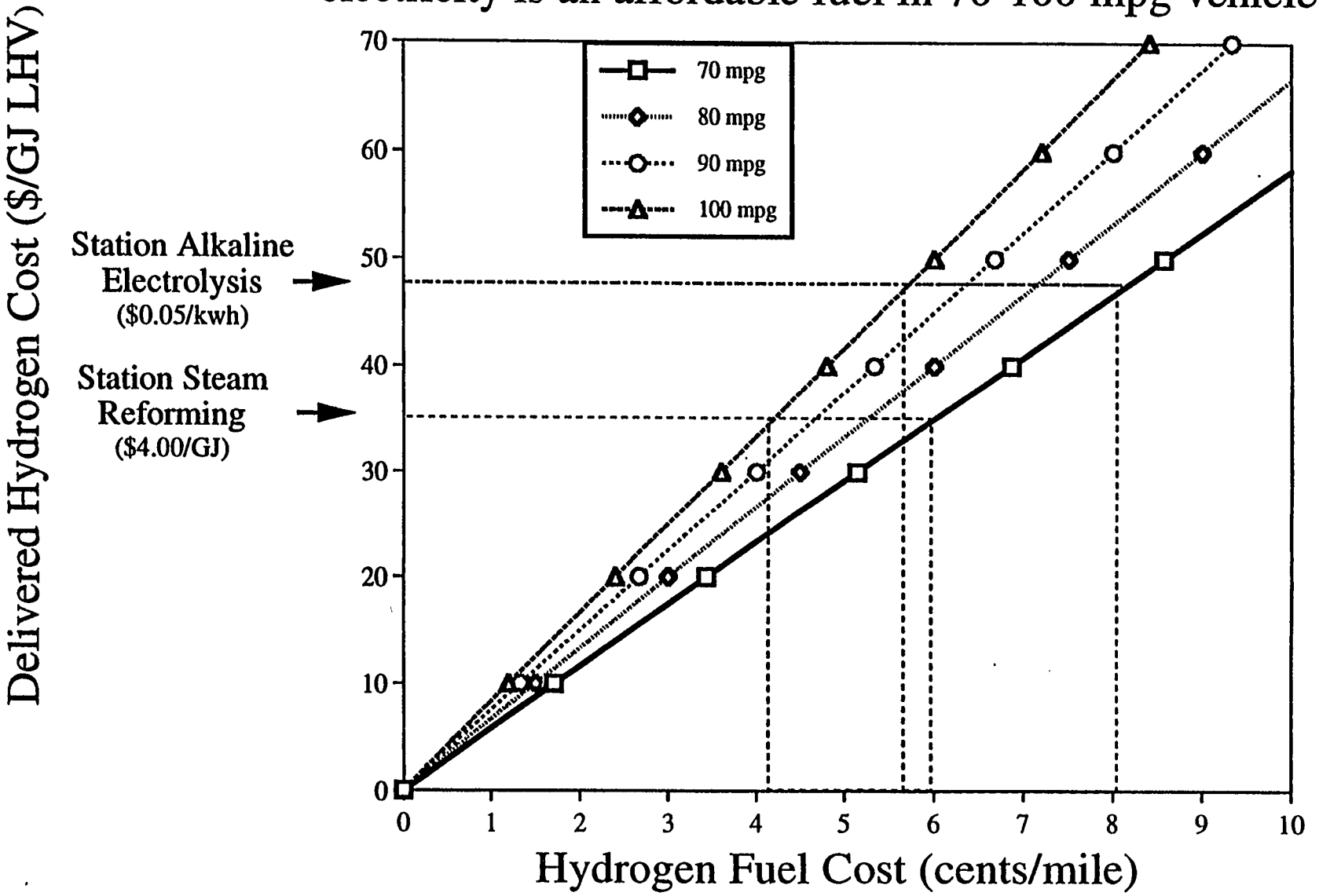


Figure 5. The costs of production, storage, and delivery of hydrogen at four scales, broken down by process steps, are shown for seven hydrogen pathways: (1) LH_2 delivery by truck, (2) on-site steam-reforming from $4.00/GJ natural gas, (3) on-site methanol reforming from $0.66/gallon methanol, (4) on-site ammonia cracking from $250/ton ammonia, (5) conventional alkaline electrolysis, (6) polymer membrane electrolysis, and (7) steam electrolysis. Off-peak electricity costs are $0.05/kWh. Discount rates are 20% for stations, 10% for individual vehicle systems. Note that individual-vehicle refueling using home electrolysis has compressed gas storage for 1 kg of hydrogen.

Figure 5. Cost Breakdown of 7 Hydrogen Pathways for Stations, Fleets, and Homes (broken down by pathway step)

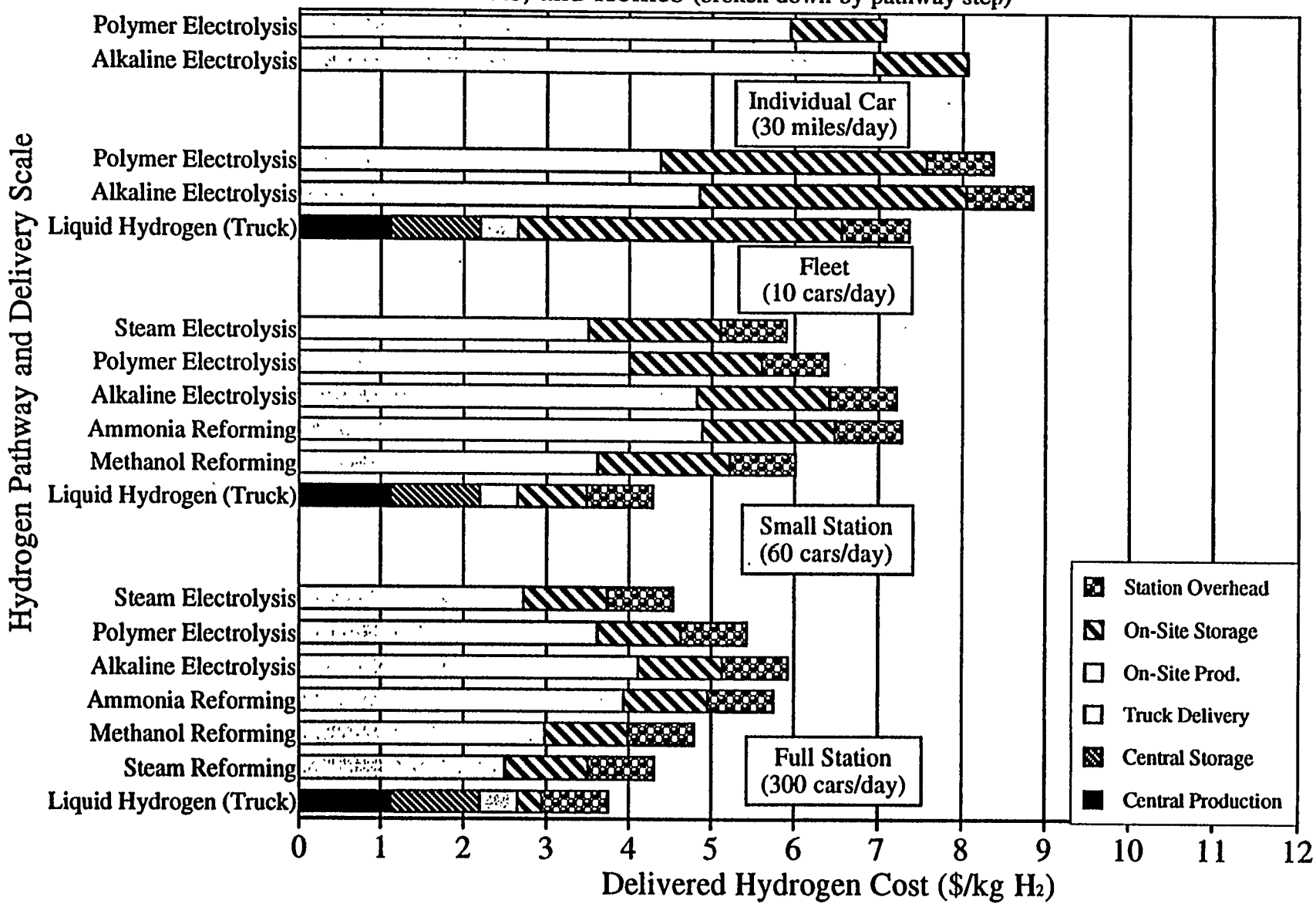


Figure 6. The costs of production, storage, and delivery of hydrogen at four scales—broken down into capital recovery, interest, energy, overhead, and operations and maintenance costs—are shown for seven hydrogen pathways: (1) LH_2 delivery by truck, (2) on-site steam reforming from $4.00/GJ natural gas, (3) on-site methanol reforming from $0.66/gallon methanol, (4) on-site ammonia cracking from $250/ton ammonia, (5) conventional alkaline electrolysis, (6) polymer membrane electrolysis, and (7) steam electrolysis. Off-peak electricity costs are $0.05/kWh. Discount rates are 20% for stations, 10% for individual vehicle systems. Equipment life is 20 years for production and 10 years for storage.

Figure 6. Cost Breakdown of 7 Hydrogen Pathways for Stations, Fleets, and Homes (broken down by cost element)

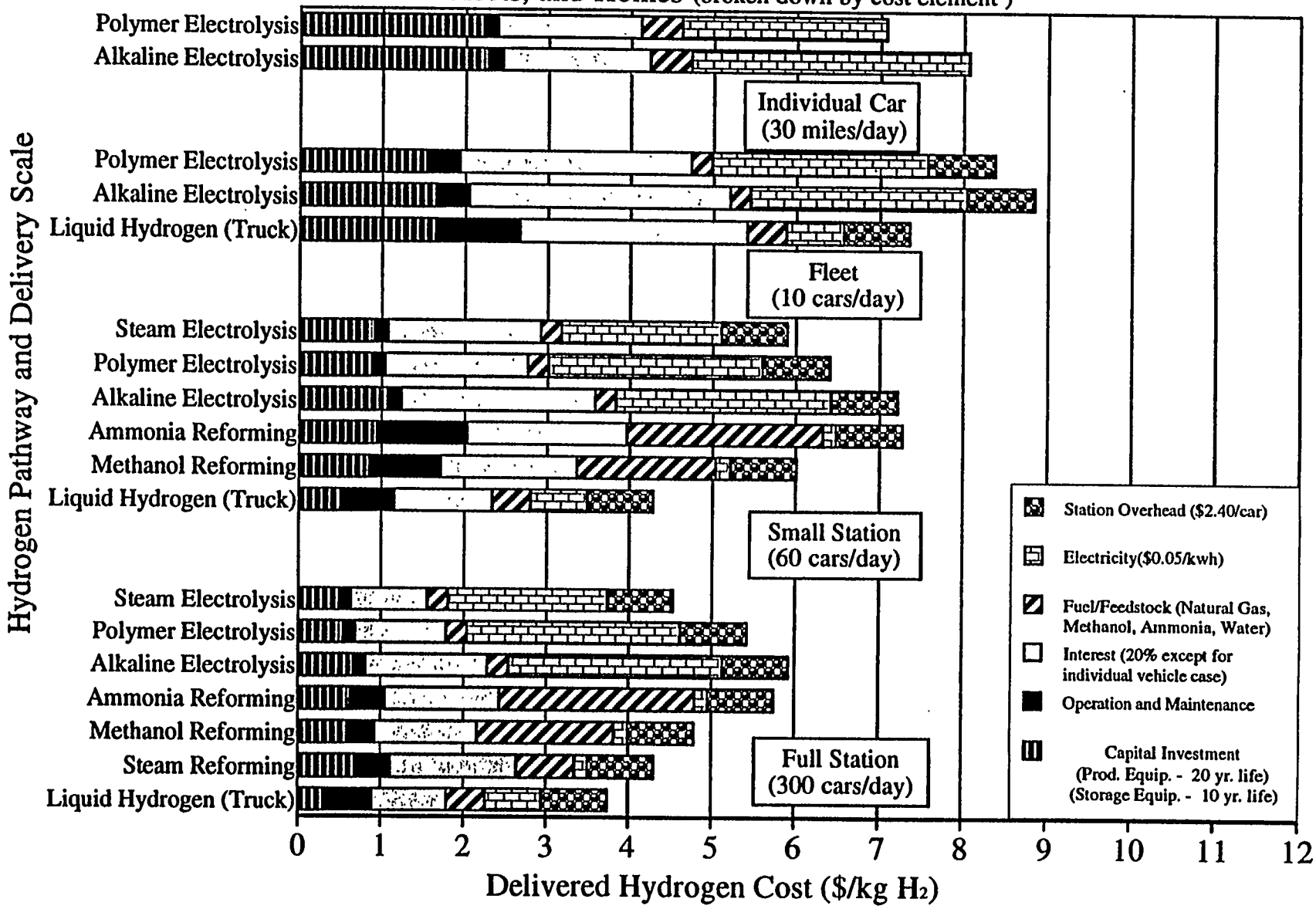


Figure 7. Detailed cost breakdown for production, storage, and delivery of hydrogen at four scales—broken down into capital recovery, interest, energy, overhead, and operations and maintenance costs of each process step—are shown for seven hydrogen pathways: (1) LH_2 delivery by truck, (2) on-site steam reforming from $4.00/GJ natural gas, (3) on-site methanol reforming from $0.66/gallon methanol, (4) on-site ammonia cracking from $250/ton ammonia, (5) conventional alkaline electrolysis, (6) polymer membrane electrolysis, and (7) steam electrolysis. Off-peak electricity costs are $0.05/kWh. Discount rates are 20% for stations, 10% for individual vehicle systems. Equipment life is 20 years for production and 10 years for storage. Note that $/kg of hydrogen can be changed to $/GJ by an 8.33 multiplier.

Figure 7. Cost Breakdown of 7 Hydrogen Pathways for Stations, Fleets, and Homes (broken down by pathway step and cost type)

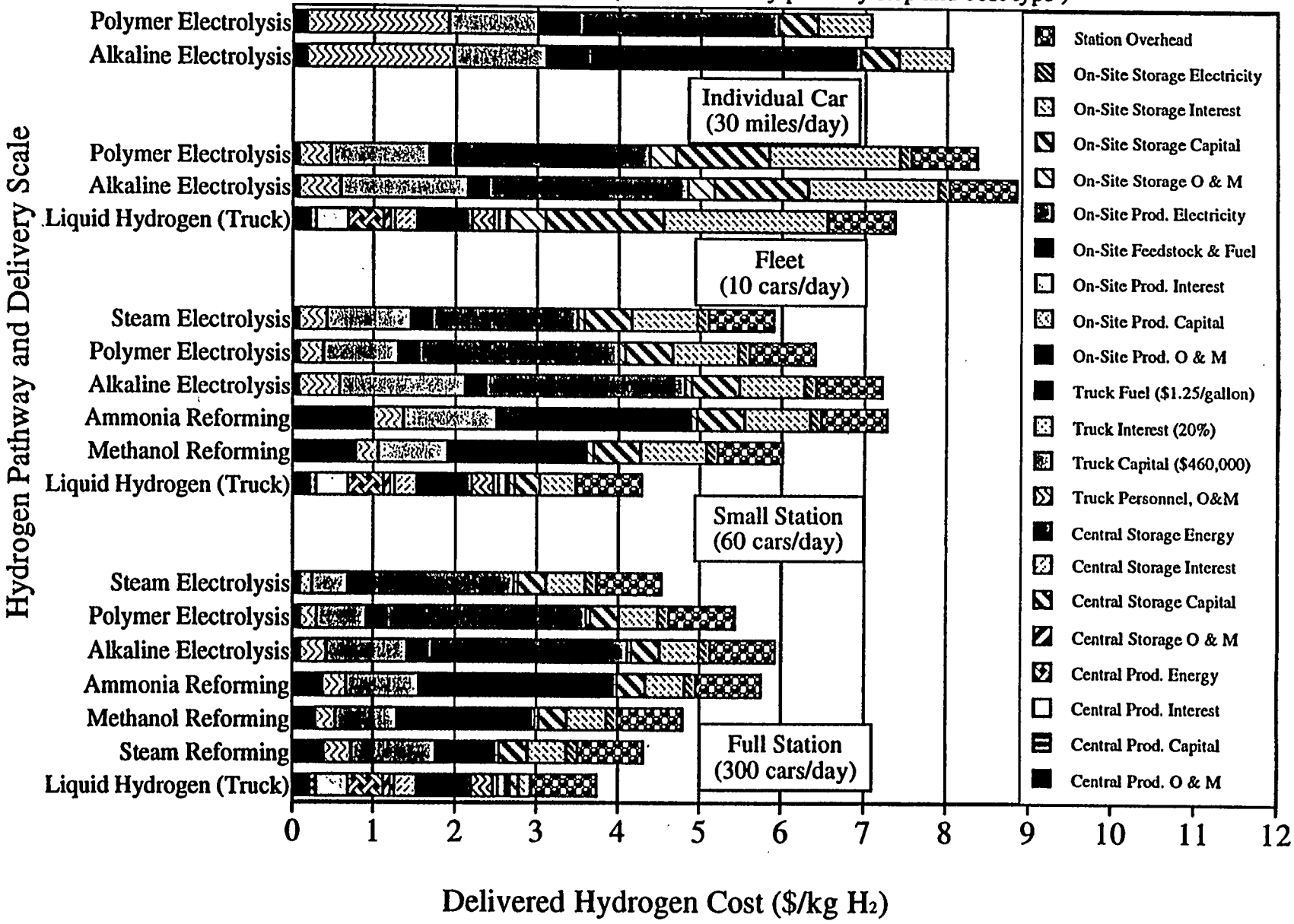


Figure 8(a-c). Electricity-generation primary energy supply mix and associated average full-fuel-cycle emissions of greenhouse gases (kg of CO_2 equivalent) and NOx are shown for three electricity-mix scenarios spanning the period 2005 to 2050. The scenarios were adapted from Ref. 36. Figure 14(a) describes a "reference" scenario in which the share of coal-based generation grows from 55% to 70% from 2005 to 2030 at the expense of oil-based and non-fossil generation, with natural-gas-based generation retaining a steady share of 15%. Figure 14(b) describes a "market" scenario in which market barriers to non-fossil generation are diminished, increasing the share of non-fossil generation from 30% to 40%, reducing gas-based generation, and eliminating oil-based generation, while coal remains steady. Figure 14(c) describes a "climate" scenario in which greenhouse-gas emission reductions are a long-term driver. Coal-based generation is eliminated by 2040, initially replaced by retaining oil generation, but ultimately by increasing natural-gas generation from 10% to 30% and non-fossil generation from 40% to 70% of electricity production.

Emissions for all three scenarios were based chiefly on Ref. 35 and 36 and on the Department of Energy's "Hydrogen Program Plan, FY1993–FY1997" (DOE/CH10093-147 DE92010556, 1992), using conventional steam generation for each fuel type but phasing in cleaner and more efficient combined-cycle plants between 2020 and 2035. NOx and CO_2 emissions for non-fossil generation were assumed to be essentially zero. Average NOx emission rates drop from roughly 1/3 to 1/10 of emissions in 2005 by the 2035–2040 timeframe, depending upon scenario. Average CO_2 emission rates increase slightly between 2005 and 2050 or drop by up to 75%, depending upon scenario.

Figure 8(a). Electric Generating Supply Mix and Average CO_2 and NO_x Emissions for "Reference" Scenario (2005-2050)

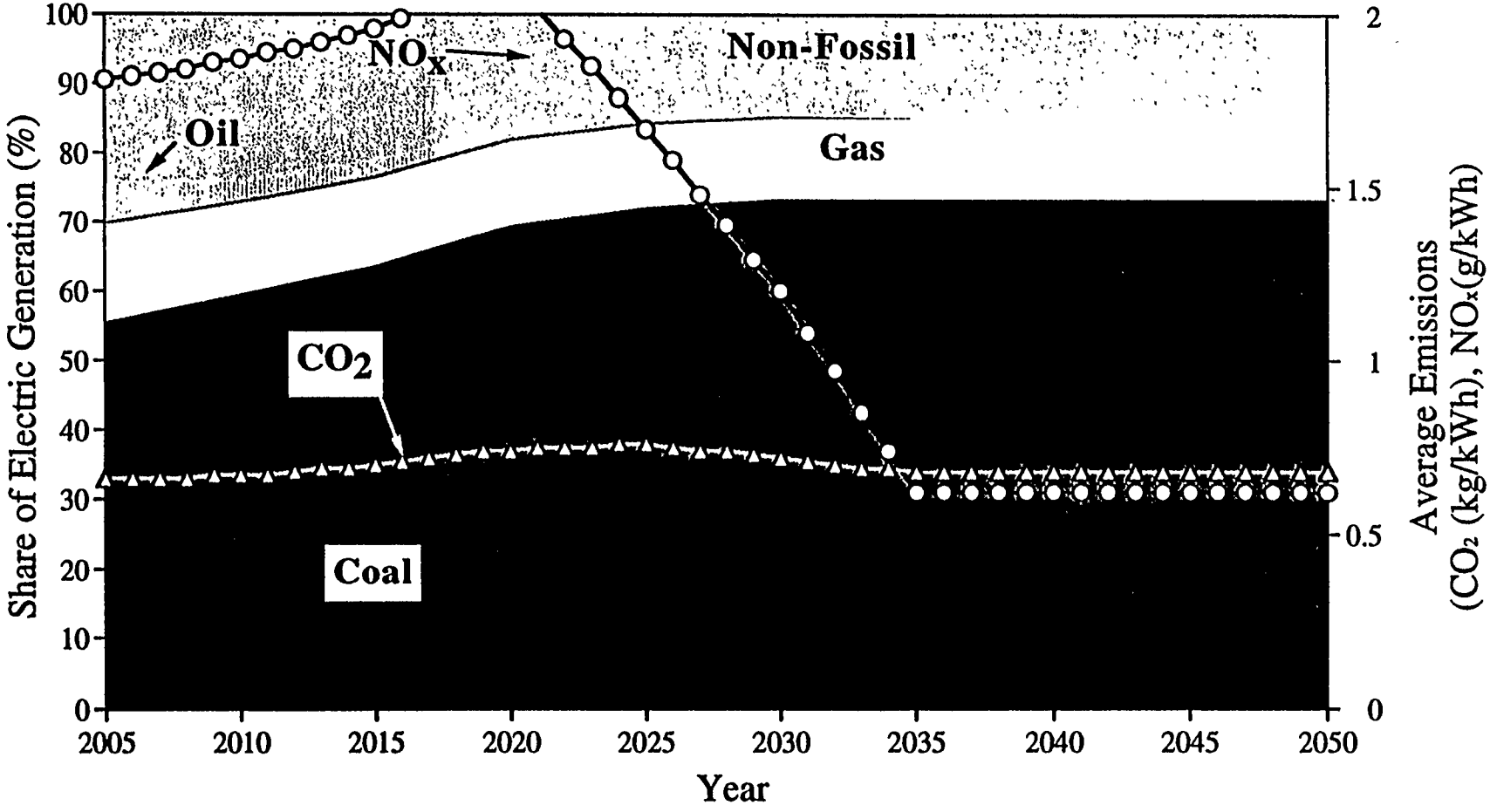


Figure 8(b). Electric Generating Supply Mix and Average CO_2 and NO_x Emissions for "Market" Scenario (2005-2050)

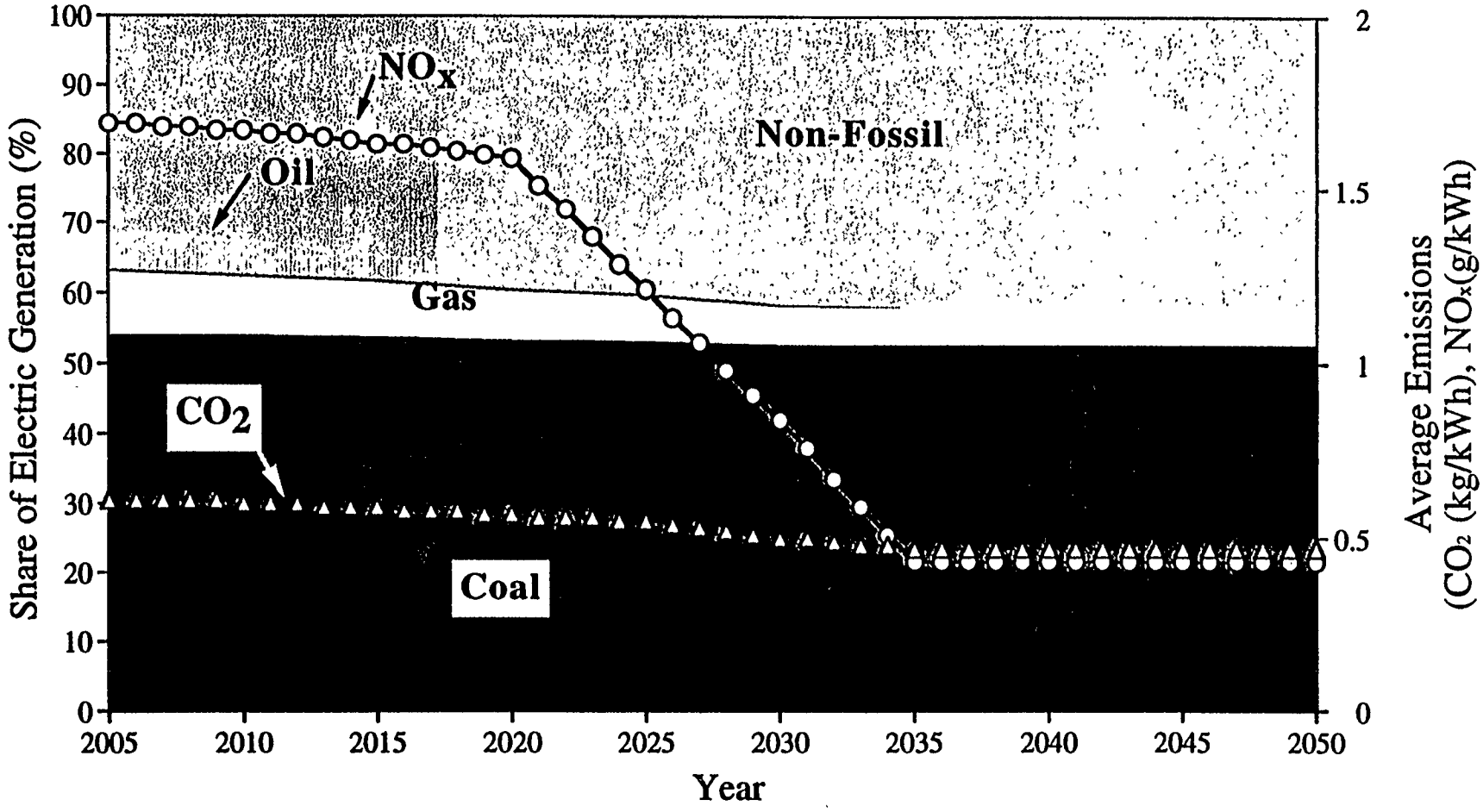


Figure 8(c). Electric Generating Supply Mix and Average CO_2 and NO_x Emissions for "Climate" Scenario (2005-2050)

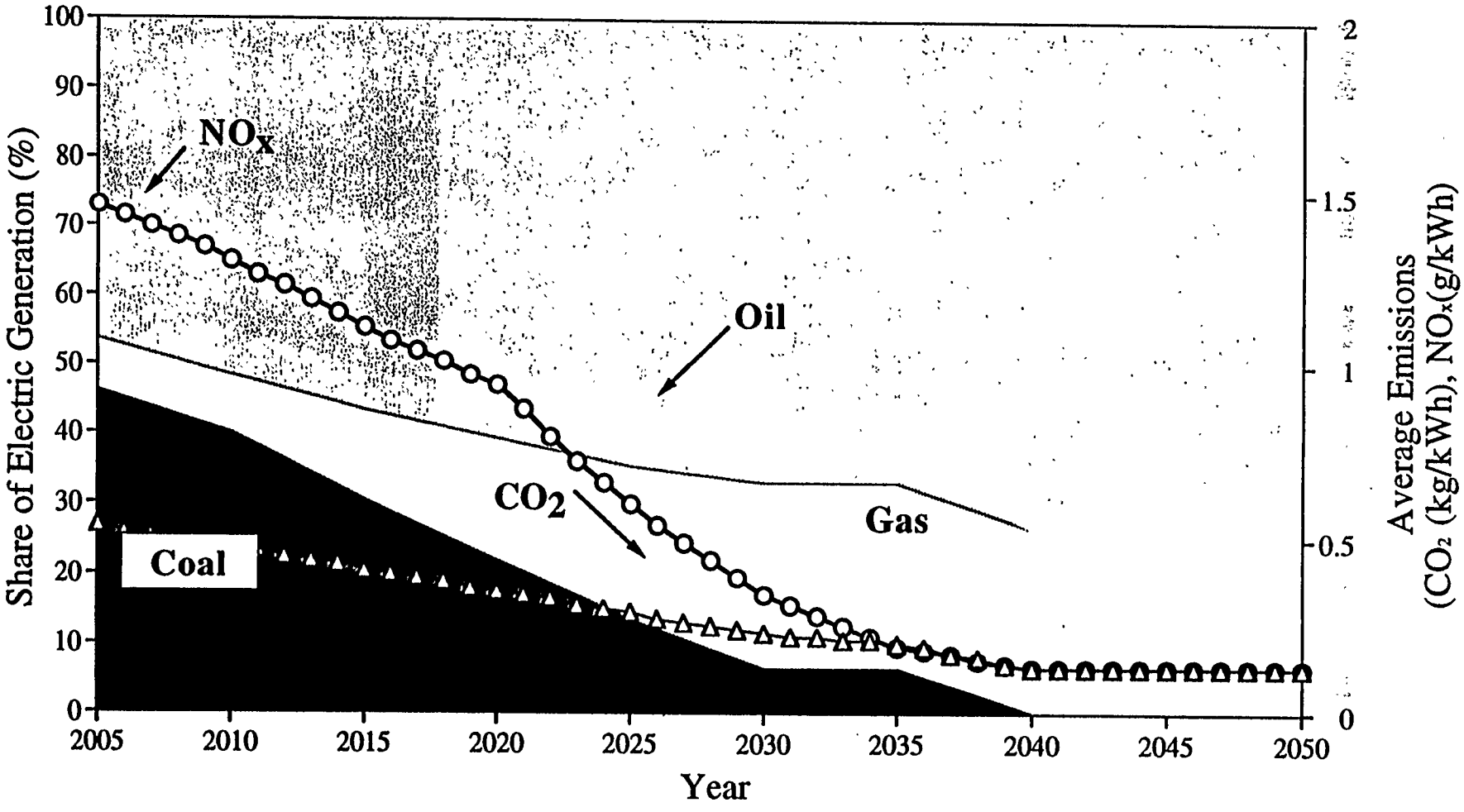


Figure 9. This figure sketches a scenario for converting the fleet from conventional 30-mpg gasoline vehicles to advanced vehicles (i.e., HEVs and BPEVs). This scenario is used to estimate the overall impacts of a transition from conventional gasoline vehicles to a variety of alternatives. Between 2005 and 2050, the U.S. passenger car fleet is expected to increase from 170 million to 200 million vehicles (left axis). Assuming vehicles are driven more as well, increasing from 10,000 to 12,000 miles/year, annual vehicle miles traveled will grow from 1.9 to 2.4 trillion/year by 2050 (right axis). As the figure indicates, to sharply reduce oil imports (also right axis) by 2025–2030 will require introducing alternative-fuel vehicles by at least two decades earlier (e.g., 2005) and dramatically increasing the number of alternative-fuel vehicles thereafter.

Figure 9. U.S. Passenger Car Transportation Demand Scenario (2005-2050): Alternative Fuel Market Penetration and Oil Import Displacement

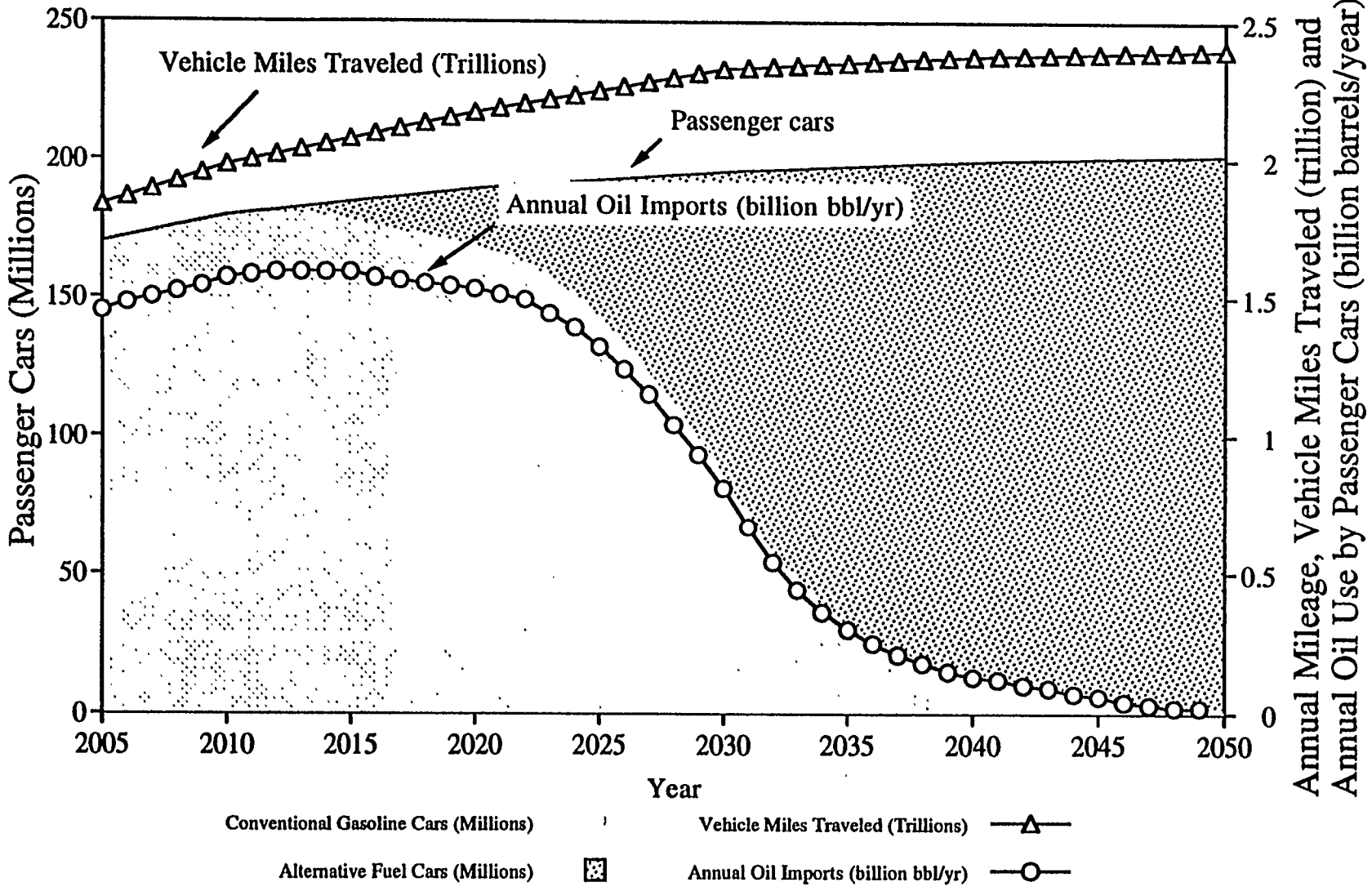


Figure 10(a-d). Annual CO_2, NOx, HC, and CO emissions for U.S. Passenger Car Fleet (2005-2050). Using the full-fuel-cycle vehicle emissions in Fig. 15 and 16 and the passenger car fleet size and use assumptions shown in Fig. 17, the total emissions from fueling U.S. passenger cars has been estimated under eight scenarios to demonstrate the emission impacts of continuing to use conventional gasoline vehicles or of a transition to a number of alternative vehicles, fuels, electricity mixes, and hydrogen production pathways. Figure 18(a) shows that hydrogen vehicles will require electrolysis under the "climate" electricity mix to provide the greatest reduction in CO_2 emissions. If hydrogen fuel is electrolyzed under more fossil-intensive mixes (on average), then greater emission reduction can be achieved by every other fuel/vehicle combination. If hydrogen is produced at stations by steam-reforming natural gas, then hydrogen vehicles are comparable to gasoline HEVs. Figure 18(b) shows that, in the case of NOx emissions, hydrogen vehicles again require the largely non-fossil "climate" electricity mix to achieve emissions reduction comparable to natural-gas HEVs or BPEVs, although steam-reformed hydrogen can provide emission reductions over gasoline HEVs. Figure 18(c) shows that for hydrocarbon emissions hydrogen vehicles provide large and similar emission reduction benefits whether the fuel is made electrolytically or by steam-reforming. However, natural-gas HEVs approach the emissions levels of steam-reformed hydrogen cars, and BPEVs provide lower emissions than hydrogen vehicles. Figure 18(d) shows that for CO emissions hydrogen vehicles provide large emission reductions over gasoline, but natural gas can achieve 75% of these emissions reductions as well. Note that, in Fig. 18(d), all of the lines are superimposed on each other, except for the 30-mpg gasoline car and the 70-mpg natural-gas hybrid.

Figure 10(a). Carbon Dioxide Emissions Estimates for U.S. Cars (2005-2050)

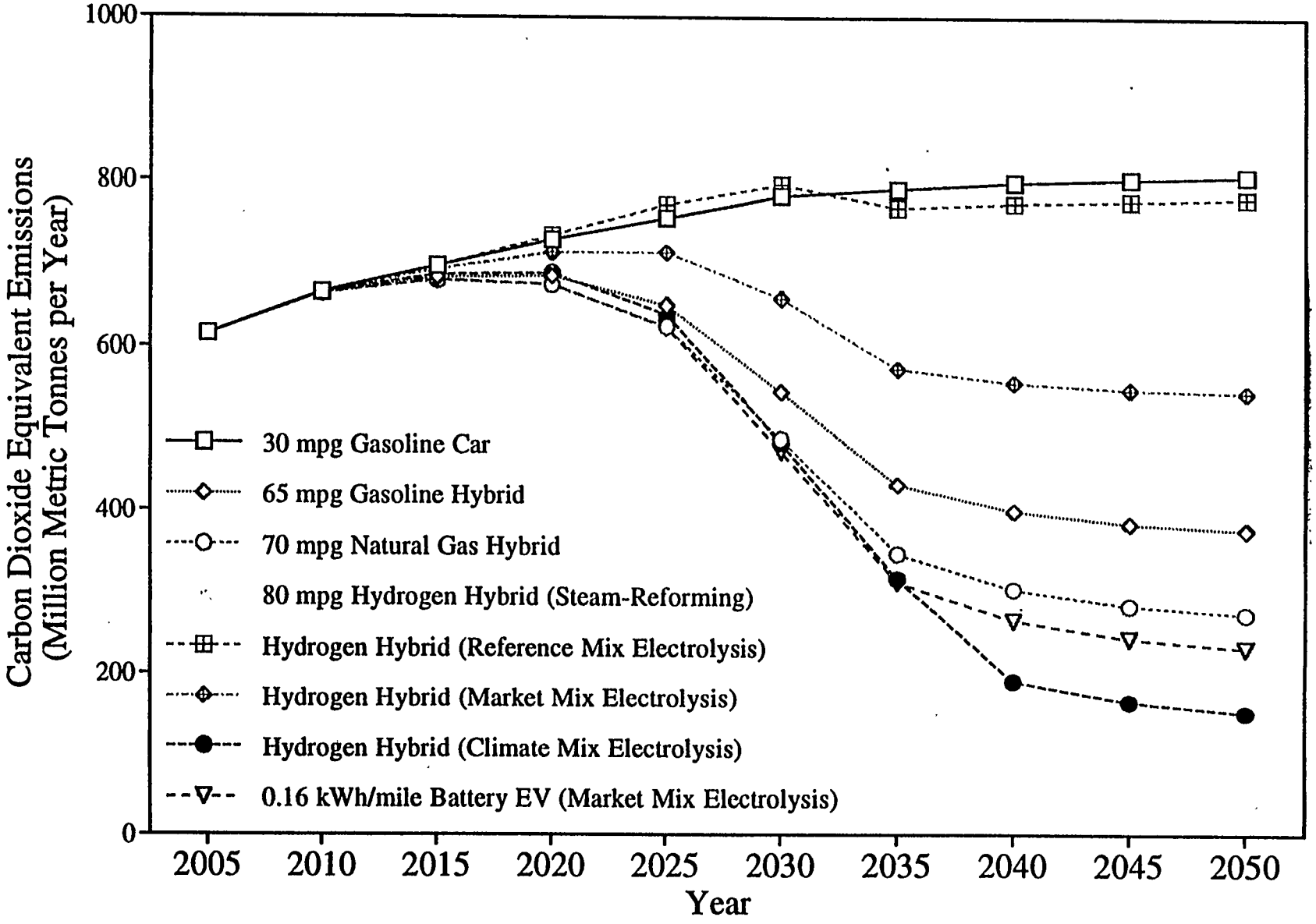


Figure 10(b). Nitrogen Oxide (NOx) Emissions Estimates for U.S. Cars (2005-2050)

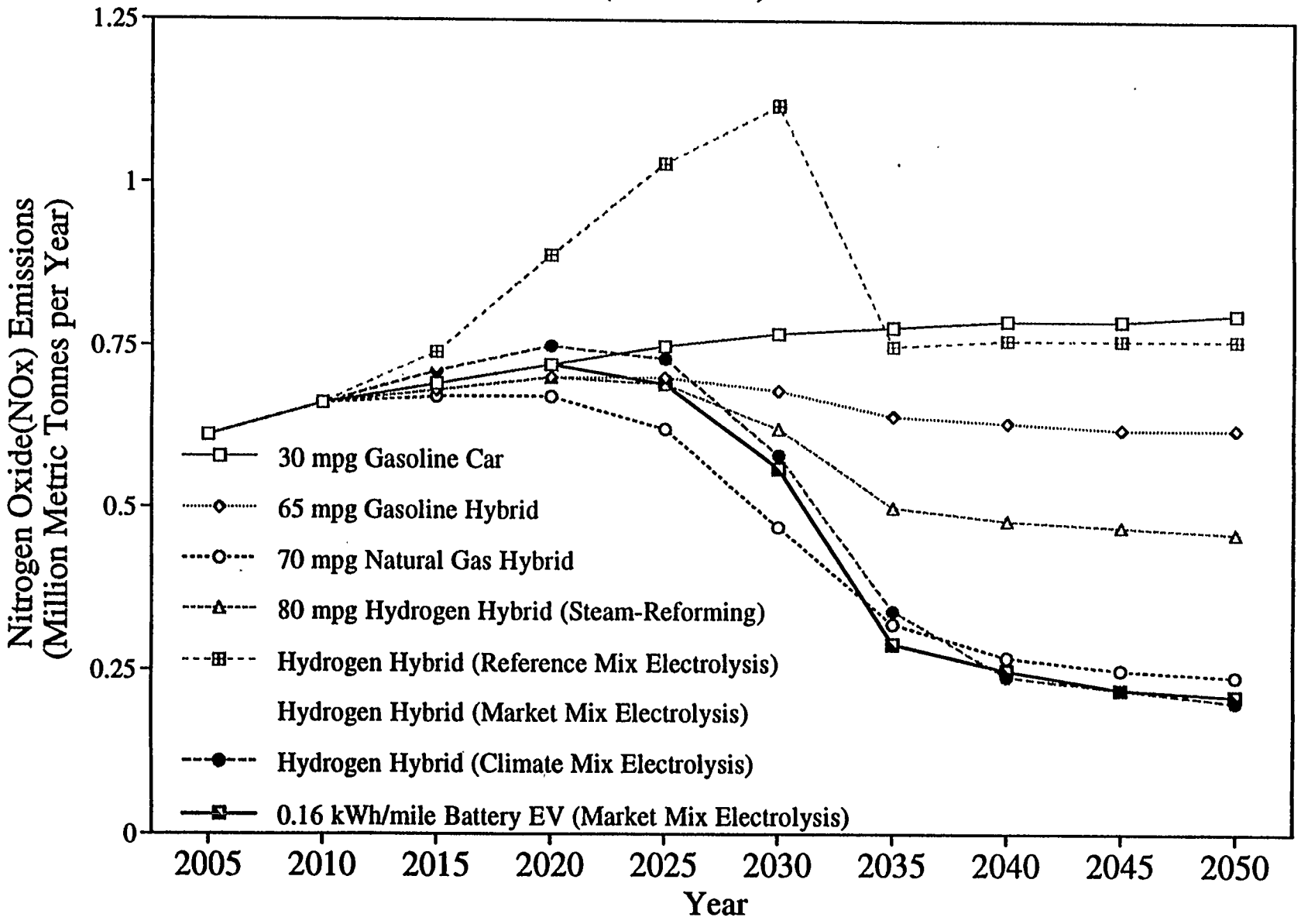


Figure 10(c). Hydrocarbon Emissions Estimates for U.S. Cars (2005-2050)

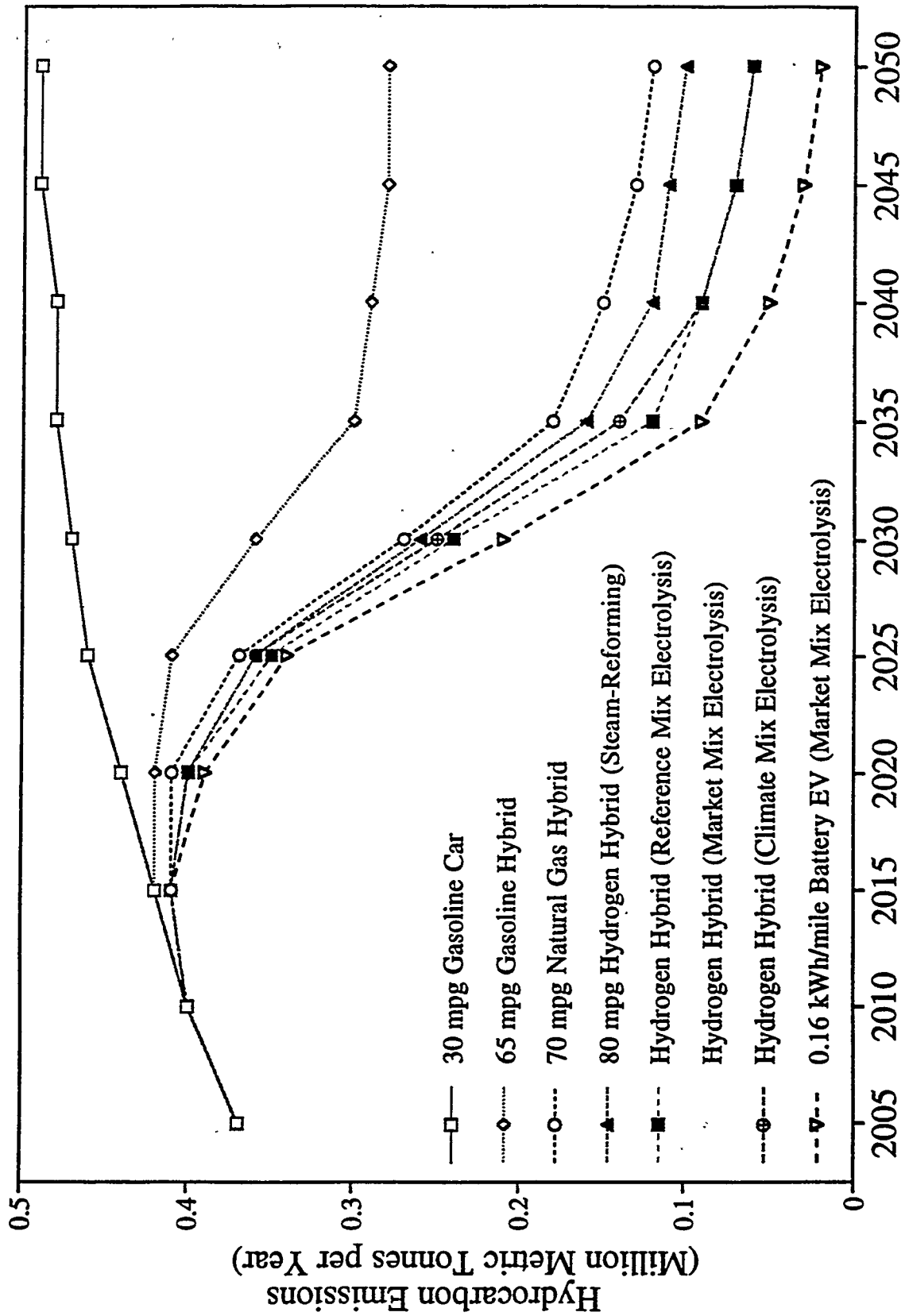


Figure 10(d). Carbon Monoxide (CO) Emissions Estimates for U.S. Cars (2005-2050)

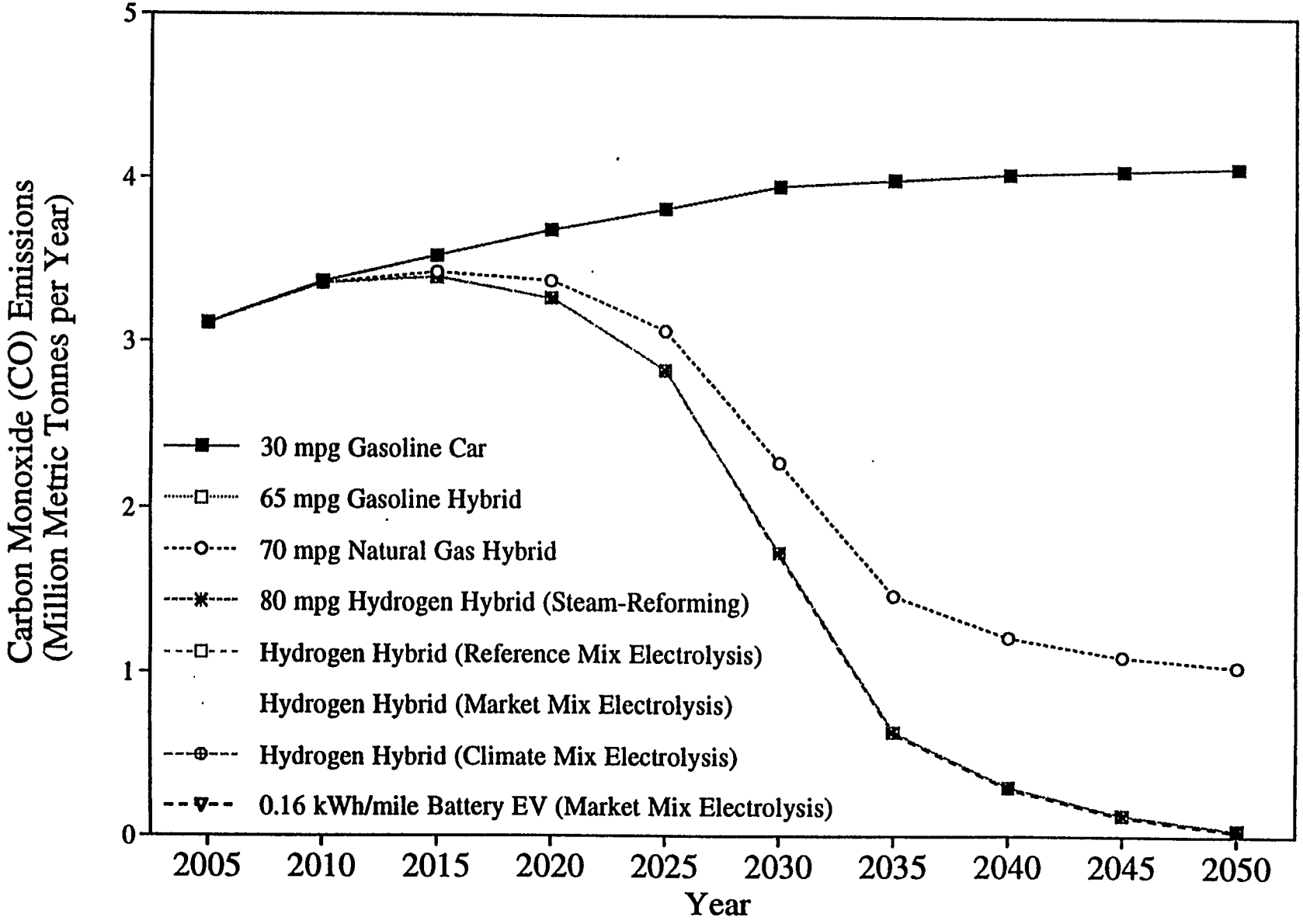


Figure 11 (a-d). Cumulative full-fuel-cycle emissions for U.S. passenger cars over the period 2005–2050 are shown for same eight scenarios presented in Fig. 18, based on the electricity mixes, emissions factors, and passenger car fleet assumptions of Fig. 14, 15–16 and 17, respectively. Figure 19(a) shows that emissions savings of roughly 15 billion tons of CO_2-equivalent greenhouse gases through 2050 are achievable by natural-gas HEVs, BPEVs, and electrolytic hydrogen vehicles under a largely non-fossil electric-generating mix (the "climate" mix). Steam-reformed hydrogen vehicles and 65-mpg gasoline HEVs achieve comparable emission reductions. Fossil- intensive electricity mixes limit and possibly eliminate emission reductions with electrolytic hydrogen vehicles over conventional 30-mpg gasoline cars. Figure 19(b) shows that, in the case of NOx emissions, roughly 12 million metric tons can be saved by 2050 by a transition from 30-mpg gasoline vehicles to natural-gas or hydrogen HEVs, using steam-reformed hydrogen or electrolytic hydrogen under the "climate" electric generation mix. Fossil (particularly coal) electric generation eliminates the potential emission savings of electrolytic hydrogen cars. Figure 19(c) shows that roughly 10 million metric tons of hydrocarbon emissions can be saved by a transition from 30-mpg gasoline vehicles to hydrogen or natural-gas HEVs or to BPEVs, relatively independent of changes in the electricity mix. Figure 19(d) shows that approximately 100 million metric tons of CO emissions can be eliminated by a transition from gasoline to hydrogen HEVs or BPEVs, but 80% of these savings can be achieved by natural-gas HEVs.

Figure 11(a). Cumulative Carbon Dioxide (CO_2) Emissions for U.S. Cars (2005-2050)

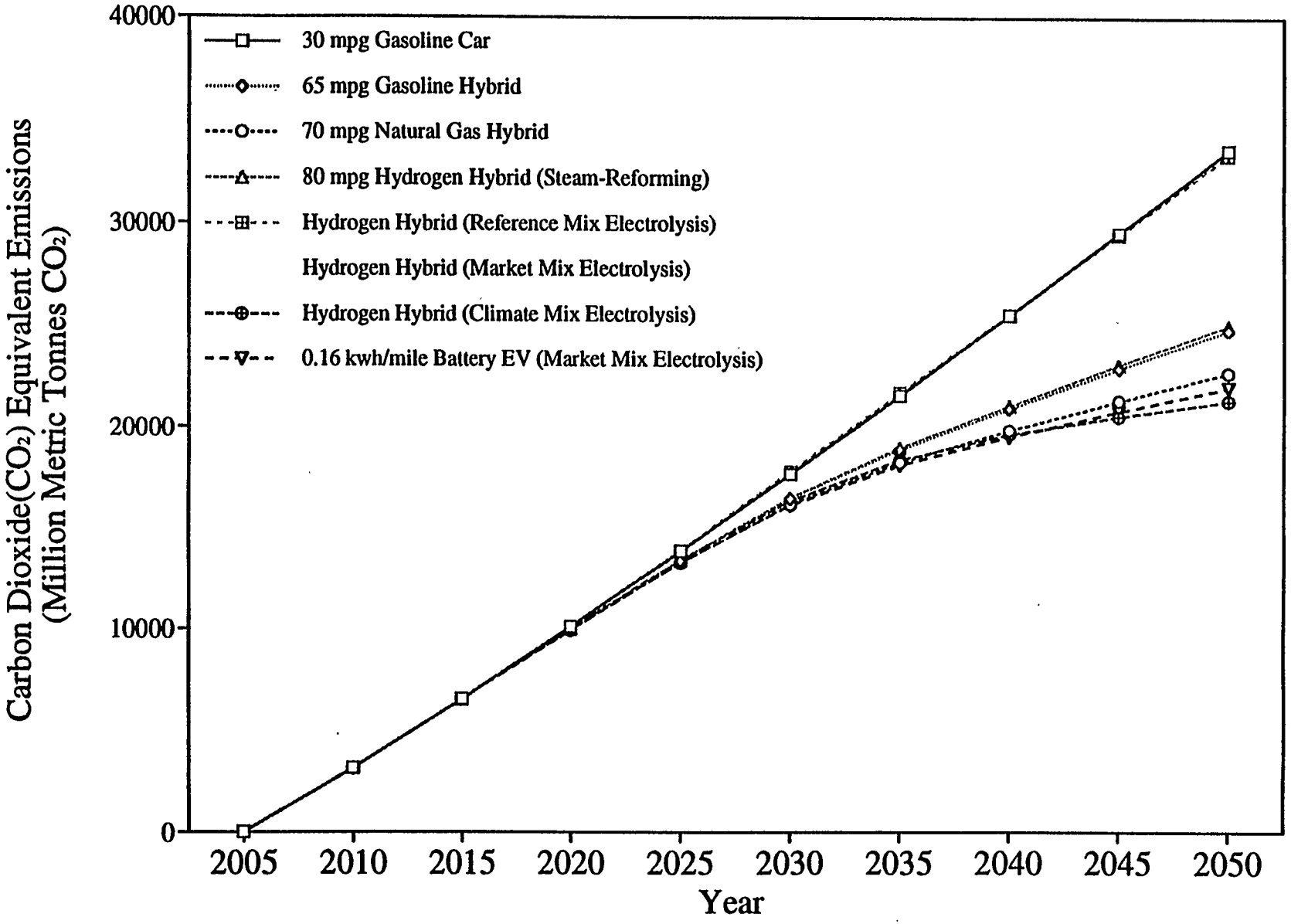


Figure 11(b). Cumulative Nitrogen Oxide (NOx) Emissions for U.S. Cars (2005-2050)

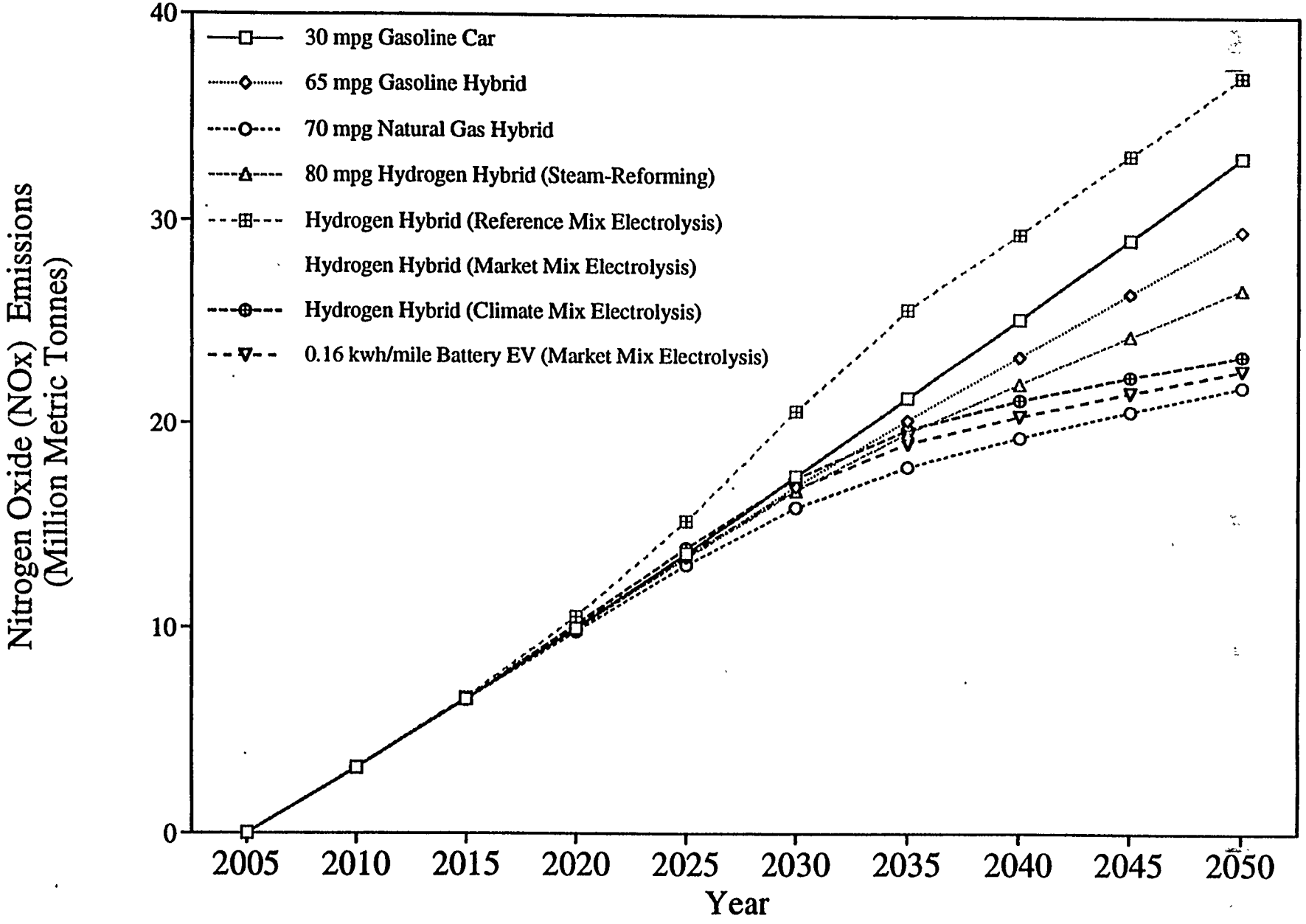


Figure 11(c). Cumulative Hydrocarbon Emissions for U.S. Cars (2005-2050)

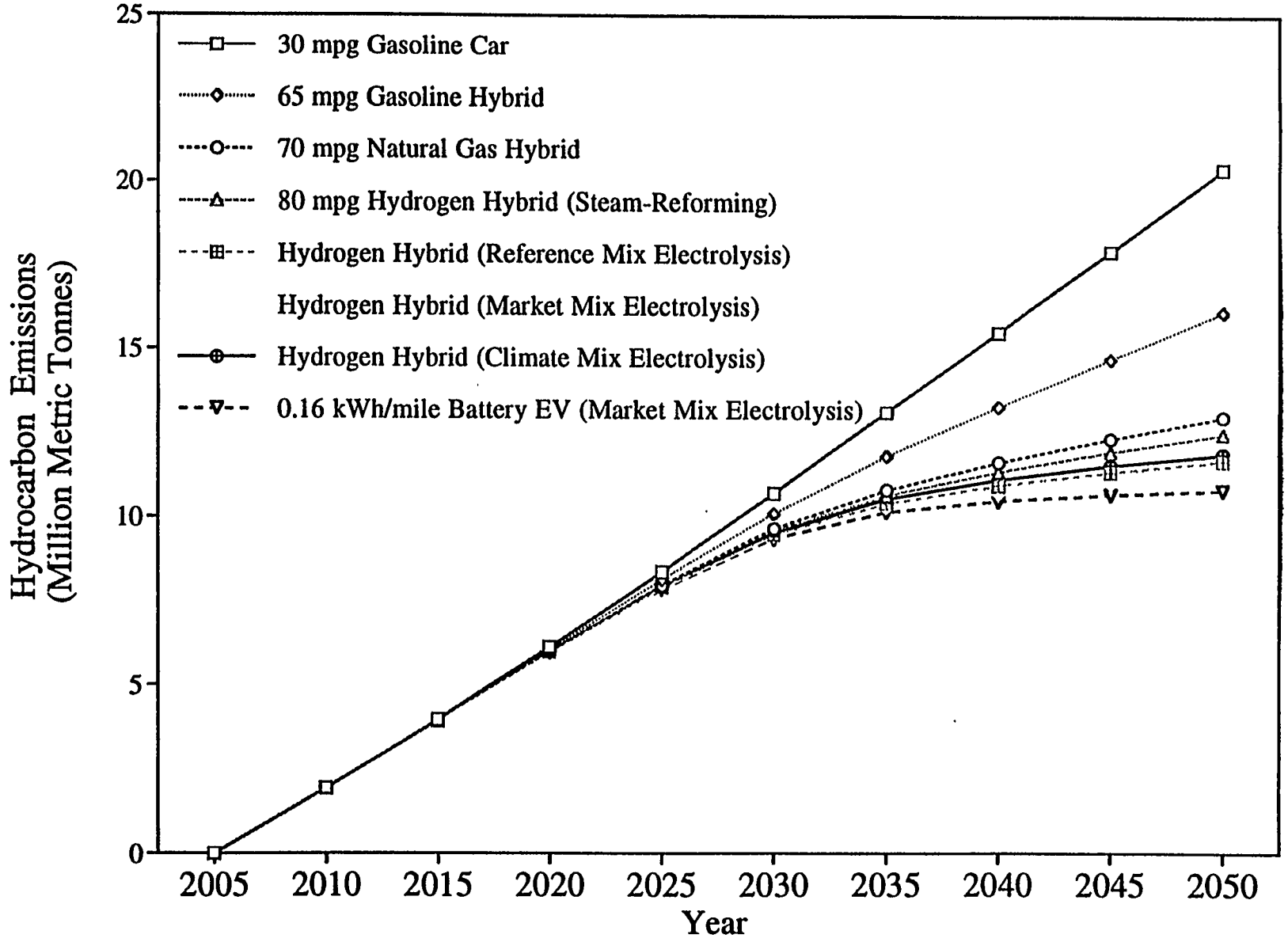
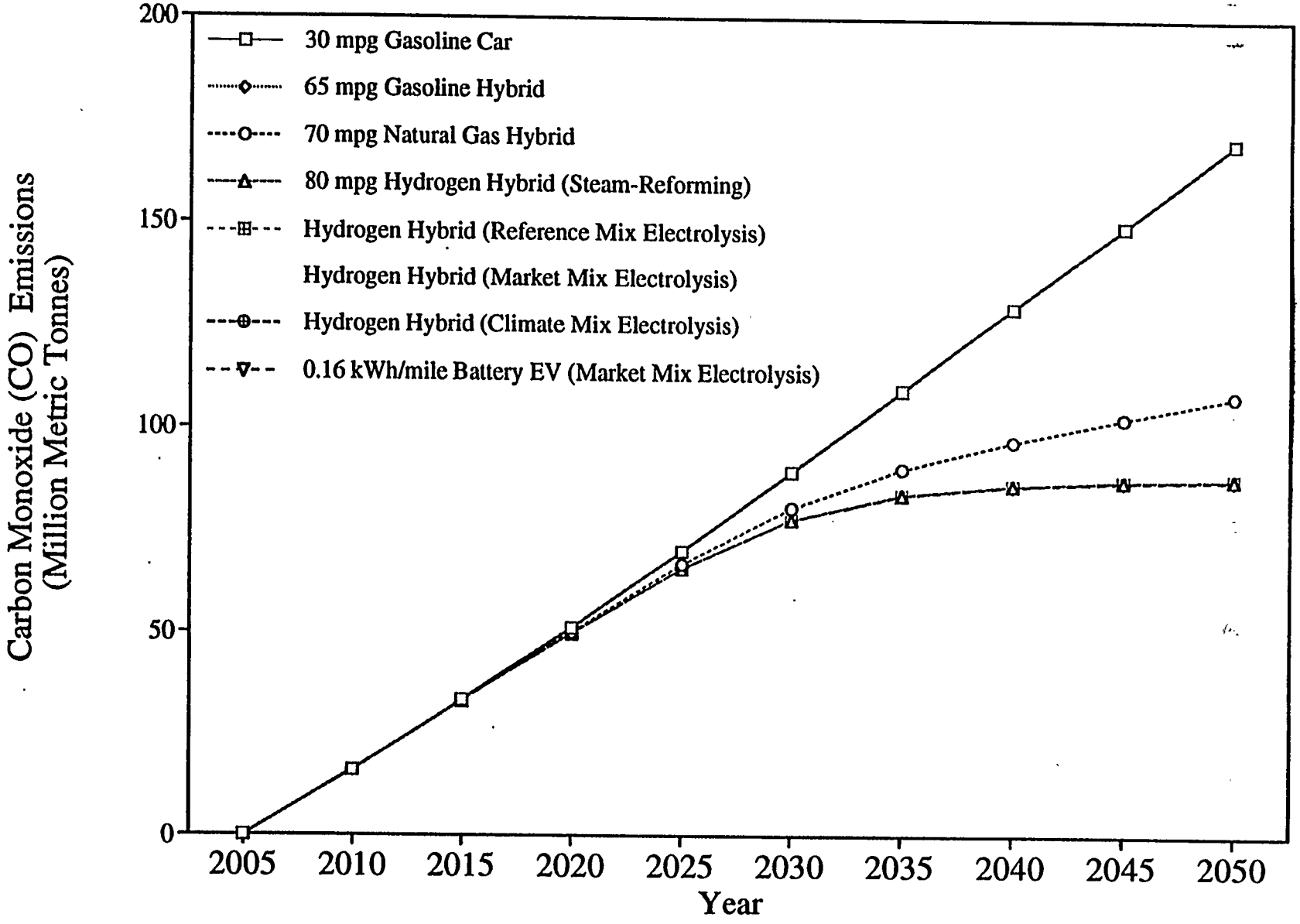


Figure 11(d). Cumulative Carbon Monoxide (CO) Emissions for U.S. Cars (2005-2050)



HYDROGEN ENERGY SYSTEMS STUDIES

Joan M. Ogden, Thomas G. Kreutz, Margaret Steinbugler,
Adam B. Cox and Jason W. White
Center for Energy and Environmental Studies
Princeton University
Princeton, NJ 08544

Abstract

In this report we describe results from technical and economic assessments carried out during the past year with support from the USDOE Hydrogen R&D Program.

1) *Assessment of technologies for small scale production of hydrogen from natural gas.* Because of the cost and logistics of transporting and storing hydrogen, it may be preferable to produce hydrogen at the point of use from more readily available energy carriers such as natural gas or electricity. In this task we assess near term technologies for producing hydrogen from natural gas at small scale including steam reforming, partial oxidation and autothermal reforming.

2) *Case study of developing a hydrogen vehicle refueling infrastructure in Southern California*
Many analysts suggest that the first widespread use of hydrogen energy is likely to be in zero emission vehicles in Southern California. Several hundred thousand zero emission automobiles are projected for the Los Angeles Basin alone by 2010, if mandated levels are implemented. Assuming that hydrogen vehicles capture a significant fraction of this market, a large demand for hydrogen fuel could evolve over the next few decades. Refueling a large number of hydrogen vehicles poses significant challenges. In this task we assess near term options for producing and delivering gaseous hydrogen transportation fuel to users in Southern California including: 1) hydrogen produced from natural gas in a large, centralized steam reforming plant, and delivered to refueling stations via liquid hydrogen truck or small scale hydrogen gas pipeline, 2) hydrogen produced at the refueling station via small scale steam reforming of natural gas, 3) hydrogen produced via small scale electrolysis at the refueling station, and 4) hydrogen from low cost chemical industry

sources (e.g. excess capacity in refineries which have recently upgraded their hydrogen production capacity, etc.).

1. Project Rationale/Summary of Approach

In this report, we discuss technical and economic assessments of hydrogen energy systems carried out during the past year. The motivation for our work is to illuminate possible near term pathways leading from present hydrogen markets and technologies toward eventual wide scale use of hydrogen as an energy carrier, highlighting important technologies for research, development and demonstration. Our focus has been on technologies and markets which might be important in the early stages of a hydrogen economy. This year's work includes an assessment of small scale reformer technologies for producing hydrogen from natural gas, and a study of technical and supply issues involved in developing an infrastructure for refueling hydrogen vehicles in Southern California. Our approach has been to assess the entire hydrogen energy system from production through end-use from several perspectives (fuel producer, consumer, society) considering technical performance, economics (e.g. capital cost, delivered hydrogen cost, cost of energy services), infrastructure, environmental and resource issues.

This work is part of the systems analysis activity of the DOE Hydrogen R&D Program.

2. Past Results

Since 1986, researchers at Princeton University's Center for Energy and Environmental Studies have carried out technical and economic assessments of hydrogen energy systems. Initially, we focussed on assessing the long term potential of renewable hydrogen as an energy carrier. These studies suggested that renewable hydrogen used in energy efficient end-use devices (e.g. fuel cells) could become economically competitive, beginning in the early part of the next century (Ogden and Williams 1989, Ogden and Williams 1991; Ogden and Nitsch 1993; Ogden et.al 1993; Ogden, Larson and Delucchi 1994, Larson, Williams, Katofsky and Chen 1995).

More recently we have explored how a transition to renewable hydrogen might begin. The goal of this work is to identify promising strategies leading from near term hydrogen markets and technologies toward eventual large scale use of renewable hydrogen as an energy carrier. Since steam reforming of natural gas is currently the least expensive method of hydrogen production over a wide range of plant sizes, we concentrated on natural gas as the initial feedstock for hydrogen production. We have emphasized zero emission vehicles and cogeneration in our studies, as two potentially large markets for hydrogen, which might open over the next decade or so.

In the past few years, we have carried out technical and economic assessments of various near term options for providing hydrogen transportation fuel to vehicles, including steam reforming of natural gas and electrolysis using off-peak power (Ogden, Dennis, and Montemayor 1995, Ogden et. al. 1995). We have also investigated the feasibility of using

the existing natural gas system with hydrogen and hydrogen blends. In another recent study, we assessed the feasibility of using PEM fuel cells in residential cogeneration (Ogden et.al 1995).

Our current year's work continues our exploration of near term paths toward large scale use of hydrogen energy.

3. Current Year Results

3.1 Assessment Of Small Scale Reformer Technologies for Producing Hydrogen from Natural Gas

Introduction

It is apparent from our previous studies that small scale reforming of natural gas could be an important technology in the early stages of a hydrogen economy (Ogden et.al. 1995). Unless pipeline hydrogen is available, onsite reforming could be the best option for applications such a distributed power generation with fuel cells or hydrogen refueling stations.

In this task, we assess the technical options for low cost, small scale production of hydrogen from natural gas, considering a) steam reforming, b) partial oxidation and c) autothermal reforming.

Our focus is on stationary hydrogen production systems (rather than onboard vehicle reformers), in the range 0.1-2.0 million scf H2/day. This is about the size range needed for hydrogen vehicle refueling stations or cogeneration systems in commercial buildings. [For example, a refueling station serving a fleet of 200 Ballard type PEM fuel cell buses might require about 1.4 million scf H2/day. A 200 kW, natural gas fueled, fuel cell cogeneration system might require about 140,000 scf H2/day.]

We have addressed the following questions:

* What are the performance and cost of small scale steam reformers now on the market? How does this compare to partial oxidation and autothermal reformer systems?

* How do the performance and cost of reformer technologies depend on scale? What critical technologies limit cost and performance of small scale hydrogen production systems? What are the prospects for potential cost reductions and performance improvements as these technologies advance?

* How would reductions in the reformer capital cost impact the delivered cost of hydrogen transportation fuel?

Approach

* We gathered cost and performance data on commercially available reformer technologies and those now under development. These include small scale steam reformer systems for industrial and fuel cell applications, partial oxidation

systems and autothermal reforming systems. Table 1 summarizes cost and performance data gathered for small scale hydrogen production systems.

* To better understand the fundamentals of small scale reforming, we carried out computer modelling of
  a) equilibrium and kinetics of reformer reactions,
  b) conversion of methane in a single steam reformer tube, and
  c) hydrogen plants based on steam reforming, including upstream and downstream processing and heat recovery.

* We held discussions with reformer manufacturers and developers (Howe-Baker, KTI/Air Products and Chemicals, Inc., Haldor-Topsoe), fuel cell developers (International Fuel Cells, Ballard Power Systems, H-Power), developers of partial oxidation (POX) systems (Arthur D.Little, Hydrogen Burner Technology) and industrial gas companies (Air Products and Chemicals Inc., Praxair) focussing on cost and design issues for small scale reformers.

Catalytic Steam Reforming

Catalytic steam reforming of natural gas is a well known, commercially available process for hydrogen production (Rostrup-Nielsen 1984, Twigg 1989). Most steam reforming units built to date have larger capacities than the 0.1-2.0 million scf/day needed for refueling stations or fuel cell cogeneration applications. Typical applications are for refineries or ammonia production, where 25-100 million scf/day might be needed. However, a number of smaller reformers have been built for chemical processing needs.

Hydrogen production is accomplished in several steps: steam reforming, water gas shift reaction, and hydrogen purification. (Figure 1 shows material flows for a typical hydrogen production plant based on steam reforming of natural gas.)

The steam reforming reaction

$$CH_4 + H_2O \leftrightarrow CO + 3\,H_2 \qquad \Delta h = +206.16 \text{ kJ/mol } CH_4 \quad (1)$$

is endothermic and is favored at higher temperatures, and lower pressures. (This is illustrated in Figure 3, which shows how the equilibrium conversion of methane varies with temperature and pressure.) Typical reformers operate at anywhere from 3 atm, 700°C to 15-25 atm, 850°C. External heat needed to drive the reaction is often provided by the combustion of 20% of the incoming natural gas feedstock (exhaust from fuel cell anode or purge gas from the hydrogen purification system are often used in addition). Heat transfer to the reactants is accomplished indirectly through a heat exchanger. Methane and steam react in catalyst filled tubes (typically the "steam-to-carbon" ratio is about 3 or more to avoid coking).

After reforming, the resulting syngas is sent to one or more shift reactors, where the hydrogen output is increased via the water-gas shift reaction:

$$CO + H_2O \leftrightarrow CO_2 + H_2 \qquad \Delta h = -41.15 \text{ kJ/mol CO} \quad (2)$$

This reaction is favored at temperatures of less than about 600°C, and can take place as low as 200°C, with sufficiently active catalysts. The gas exiting the shift reactor contains CO_2, H_2O, CH_4, and CO as well as H_2.

Hydrogen is then purified. The degree of purification depends on the application. For industrial hydrogen, pressure swing absorption (PSA) systems or palladium membranes are used to produce hydrogen at up to 99.999% purity. For PEM or phosphoric acid fuel cells closely coupled to reformers, diluents such as CO_2 and CH_4 are tolerable. However, CO must be reduced to less than about 10 ppm for PEM fuel cells, so a CO removal system such as preferential oxidation must be used.

In a preferential oxidation system, the gas is passed over a catalyst bed, with added air. At certain temperature and stoichiometry conditions, the reaction

$$CO + 1/2\ O_2 \rightarrow CO_2$$

is strongly favored over hydrogen oxidation, so that CO is removed to the level of several ppm.

"Conventional " small scale steam methane reformers vs. fuel cell steam reformers

In surveying the design of small methane steam reformers, we found that there were two general types:

* "conventional" steam methane reformers, which are commercially available today and are used in chemical applications

* fuel cell steam reformers, which are now under development and have just been commercialized for stand-alone hydrogen production.

"Conventional" small scale reformers

Conventional designs are used to make high purity hydrogen for chemical applications. They are essentially small versions of the systems used in refineries. Generally, the methane feed plus steam are introduced into high alloy nickel chromium tubes containing nickel based catalysts. In most designs, heat tranfer is largely radiative, with tubes heated via radiation from a flame. Because the heat flux (and, thus, the reaction kinetics) are limited by the need for indirect heating, heat exchangers in steam reformers have relatively large surface areas, and can be quite bulky. (Typical tube lengths for commercially available reformers are 12 meters. See Figure 2.)

The most important design considerations for chemical hydrogen plants are long tube lifetime, long catalyst lifetime, reliability, and production at a particular set of pressure, temperature and purity requirements. Compactness is not generally an issue. These systems are custom designed, and, not surprisingly, at small size (less than 1 million scf H2/day), engineering costs are quite important. Because hydrogen purification systems such as pressure swing adsorption (PSA) allow a higher recovery of hydrogen at high inlet pressure (several hundred psi), high pressure (15-25 atm) operation of the reformer is common, which means higher cost reformer tube materials. Because of the thermodynamics of the steam reforming reaction, acheiving good conversion of methane to hydrogen at higher pressure requires higher temperature operation (c. 800-850°C) (Figure 3) .

Manufacturers of commercially available, "conventional" small scale reformers commented that these systems had not yet been optimized for cost or compactness. They agreed that it

was likely that the cost might be brought down by standardizing the design. This had not occured since conventional reformers are customed designed for particular chemical plants.

Fuel cell reformers

A number of groups are developing small scale methane reformers as part of fuel cell cogeneration packages (Table 2). Fuel cell reformers are designed for low cost and compactness. Acheiving these goals is largely a problem of designing the heat exchange system. A number of low cost designs have been proposed for small scale steam methane reformers, where the heat flow path is made more compact (Sederquist 1978, Stahl et.al. 1989, Ohsaki 1993, Buswell 1994, Sederquist 1995, Buswell 1996, Haldor-Topsoe 1988, Haldor-Topsoe 1993) Instead of radiative heat transfer, which requires large heat exchanger areas, fuel cell reformers rely on convective heat exchange. The hot gases travel through several catalyst beds to assure efficient heat transfer (Figure 4). The design is standardized to reduce engineering costs.

A key point influencing the design of fuel cell reformers is that fuel cells [even proton exchange membrane (PEM) fuel cells] require lower purity hydrogen than many chemical applications. Diluents like CO_2, CH_4, H_2O, and N_2, which would be removed by the PSA in a conventional steam methane reformer, are acceptable input for a PEM fuel cell (although the fuel cell performance may suffer somewhat because of diluents). For use in PEM fuel cells, CO must be reduced to less than about 10 ppm. This is accomplished in a preferential oxidation system. The downstream hydrogen purification equipment required is less for fuel cell reformers; only CO must be removed, after the last shift reactor stage.

Also the operating pressure of a PEM or PAFC fuel cell is at most a few atmospheres. So low pressure reformers (1-5 atm) with a shift stage and minimal purification are acceptable for coupling to a fuel cell. Lower pressure operation means less expensive materials can be used for the reformer. The reformer can also operate at lower temperature.

Some important performance and design features of conventional and fuel cell reformers are contrasted in Table 3.

In summary:

* Conventional reformers produce hydrogen at relatively high pressure (so that downstream purification equipment such as PSAs will work well), and temperature (so that methane conversion to hydrogen will be high), and high purity. They are custom designed.

* Fuel cell reformers produce hydrogen at relatively low pressure (and temperature) and low purity (only CO is removed), as required by fuel cells. They are a standardized design.

Cost and performance of small scale steam reforming systems

Cost of "conventional" steam reformer systems

Data on commercially available "conventional" steam methane reforming plants were gathered from several vendors (Howe-Baker, Hydrochem, Haldor-Topsoe, KTI/Air Products and Chemicals, Inc.). In discussions with vendors, we found that the minimum commercially available size is about 100,000 scf H_2/day. Below this size, plant capital

costs decrease very little, and other sources of hydrogen (such as truck delivery or electrolysis) are usually less expensive (King 1993).

Manufacturers' installed capital cost data for steam reforming plants in the range 0.1 to 2.0 million scf H_2/day are shown in Figure 5 (costs include the reformer, shift reactor, PSA system, and NOx control). The capital cost of commercially available small scale "conventional" steam reformers ranges from about $1,500,000 for a plant producing 100,000 scf H_2/day to $3,000,000 for a plant producing 1 million scf/day. There are strong scale economies in this size range, with installed capital costs varying as

$$\text{Installed cost} = \$3 \times 10^6 \times (\text{plant capacity in million scf/day})^{0.3}.$$

One of the main capital cost drivers for commercially available steam reformers is the reformer tubes. Because of the high temperatures and pressures and long lifetime required for chemical plant applications, tube materials are expensive.

The energy efficiency (=hydrogen energy out/methane in) of small scale reformers is quite high, typically about 80-85%.

To achieve long equipment lifetime, good performance and low emissions, manufacturers indicated that the reformer should be run continuously, preferably at constant output. The reformer start-up time is 4 to 6 hours, and the response time to changes in load is relatively slow, so that following a rapidly varying hydrogen demand would be difficult. Small scale reformers are designed for automated operation, with occasional monitoring.

The only significant pollutants emitted from a steam reforming system would be nitrogen oxides (NOx). NOx can be controlled through a low NOx burner design or with selective catalytic reduction (SCR) to levels that meet stringent California air quality standards.

Reformer manufacturers contacted stressed that commercially available small scale "conventional" steam reforming systems had not yet been optimized for cost or compactness, nor have they been standardized to the degree that fuel cell reformers would be, since chemical applications are more individual.

Cost of fuel cell reformers

Small scale natural gas reformers are also being developed for fuel cell cogeneration systems in the 200-250 kWe range (see Table 2). Fuel cell reformers contribute about one third of the total capital cost of a fuel cell cogeneration system (Prater 1994, Wheeler 1995). (The fuel cell stack and power conditioning equipment /electronics each contribute another third).

Current prices for phosphoric acid fuel cell cogeneration packages in the 200 kWe size range are about $3000/kWe, or about $1000/kWe for the reformer. In the near term, with modest increases in production volume costs for PAFC or PEM fuel cell cogeneration systems in the 200 kW range are projected to reach $1500/kWe or $500/kWe for the reformer.

A steam reformer for a 200 kWe fuel cell produces about 120,000 scf H2/day and costs about $200,000 assuming $1000/kW for the reformer contribution (or $100,000 if the refomer costs $500/kW). Using a scaling factor of 0.7 over the range 0.1-2.0 million scf H2/day, the capital cost for a fuel cell reformer is given by

$0.44 - 0.88 million x (capacity in million scf H2/day)$^{0.7}$

Comparing these costs to those for conventional reformers (Fig 6), we see that fuel cell reformers appear to be considerably less costly. However, as discussed above, the pressure, temperature and purity requirements for conventional reformers are quite different than for fuel cell reformers. This is illustrated in Figures 7a and 7b, where a conventional small scale steam reformer and a fuel cell reformer are compared. The conventional reformer produces 99.999% pure hydrogen, whereas the fuel cell reformer produces a gas which is only about 70% hydrogen.

Figure 6 is somewhat misleading, as the hydrogen purity is lower from the fuel cell reformer. To make the two systems comparable, the output of the fuel cell reformer would have to be purified to 99.999%. This could be accomplished with a PSA unit or membranes. To make either of these alternatives work well, an additional compression stage would be needed (Figure 7c) after the shift reactor. This is the approach taken by Praxair and IFC, which recently announced a new small scale hydrogen production system based on the reformer from IFC's 200 kW fuel cell coupled with a PSA purification system (Farris 1996).

We now investigate whether it might be possible to reduce the cost of small scale hydrogen systems by adopting some of the design features of fuel cell reformers. This involves a trade-off between lower cost, low pressure fuel cell reformers with more expensive PSA purification vs. higher pressure higher cost conventional reformers with less expensive purification.

Potential for low cost, small scale hydrogen production using fuel cell reformers

We now estimate the capital cost of a small scale hydrogen plant with a fuel cell reformer plus compression and a PSA clean-up system.

To get a rough idea of the relative costs of various components in a conventional steam reformer plant, we show the contributions of the reformer (43%), the shift reactors (7%) the PSA (39%), and compressors (11%) (Figure 8). The reformer vessel and the PSA are the dominant costs in a conventional system.

Capital cost of the a fuel cell steam reformer

As discussed above the reformer cost depends on the type of heat transfer, and the operating pressure and temperature. We found a number of reasons why fuel cell reformers are less expensive than today's conventional small scale steam reformers.

*Convective heat transfer (rather than radiative) => less heat exchanger area

* Lower pressure operation => lower cost steels for reformer tubes (stainless steel can be used instead of alloy steels)

* Standardized design for fuel cell reformers vs. specialized conditions for chemical applications => lower engineering costs. (It is possible that standardized design might bring down the cost of conventional reformers, as well, if a large enough market existed for a particular small scale model.)

The capital cost of the reformer plus shift reactors is taken to be

$0.44 million x (capacity in million scf H2/day)$^{0.7}$

This assumes that fuel cell reformers are produced in quantities of tens to hundred per year and have costs of $500/kWe

Capital cost of small scale PSA units

The cost for small scale PSA units is shown in Figure 9 as a function of plant size (Ernst Ecker UOP 1996). Comparing the cost of the PSA to the total plant cost, we see that the capital cost of the PSA is roughly 30-40% of the total capital cost of a conventional hydrogen plant in the range 0.1-4 million scf H2/day. The capital cost for a first of a kind PSA system capable of removing CO, CO_2, CH_4, and H_2O would be about

$500,000, for PSA inlet total gas flow rates of 1 million scf/day or less

$500,000 x (gas flow rate in million scf/day)$^{0.7}$,
for gas flow rates > 1 million scf/day

The PSA inlet gas flow rate is related to the hydrogen flow rate based on the composition of the gas leaving the shift reactor, and the hydrogen recovery in the PSA system. For example, for a gas having 70% hydrogen by volume at the PSA inlet, and a hydrogen recovery of 80%,

the PSA inlet gas flow rate = hydrogen flow rate out of PSA/(0.7 x 0.8)

The PSA capital cost might be reduced by 50%, if the engineering costs could be spread over a number of units (say 10 or more). If nitrogen removal is required, the cost of the PSA would be approximately doubled, as more expensive adsorbent materials are needed.

Capital cost of small scale hydrogen compressors

After the last shift reactor stage, the hydrogen rich gas must be compressed prior to the PSA. Because the gas is about 70% hydrogen, we have assumed that a hydrogen compressor is used. The cost of small scale hydrogen compressors has been estimated by various authors. We have used a figure of $2000/kW (where kW refers to the electrical input to the compressor) for multi-stage compressors and $1000/kW for single stage compressors (see Ogden et.al 1995 and Dennis 1994). It is assumed that there is no scale economy for compressors in this size range. The cost of compression can be estimated based on the power input requirement. This is

$$P_{cm} = Q_{MMscfd} \times 114/n_C \times N \times [(P_2/P_1)^{0.291/N} - 1]/(n_{PSA} \times f_{H2})$$

where:

P_{cm} = compressor power requirement (kW)
Q_{MMscfd} = hydrogen flow rate in million scf/day
P_1=inlet pressure
P_2=outlet pressure
N = number of compressor stages
n_C = compressor efficiency = 55%
n_{PSA} = H2 recovery in the PSA = 80%
f_{H2} = fraction H2 by volume at the PSA inlet = 70%

The compressor capital cost is then (assuming that each stage has a compression ratio of 4.):

Capital cost for a single stage compressor =
$1000/kW x Pcm = $184,000 x (hydrogen plant capacity in million scf/day)

Capital cost for a multi-stage compressor =
$2000/kW x Pcm = $368,000 x N x (hydrogen plant capacity in million scf/day)

Fuel cell reformers operate at anywhere from 1 atm to 5 atm pressure. To get a high recovery of hydrogen (80%) in the PSA, we assume that the PSA inlet pressure is 250 psia (about 17 atm). Pre-PSA compressor power requirements and costs are quite sensitive to the reformer operating pressure. If the reformer operates at 5 atm (as shown in some fuel cell reformer designs e.g. Stahl 1993, Buswell 1994) it may be possible to use a single stage compressor. If the reformer operates at atmospheric pressure, 2 stages will be needed. With two stages, the compressor power requirement is about doubled, and the capital cost is quadrupled.

Approximate estimate of the capital cost of a small scale hydrogen plant with a fuel cell reformer and a PSA

The total capital cost of a fuel cell reformer with 1-stage compression and a PSA would be about:

$1 million x [(0.44+0.375) x (million scf H2/day)$^{0.7}$ + 0.184 x (million scf H2/day)],
for a hydrogen flow rate of more than 0.56 million scf/day

and

$1 million x [(0.44 x (million scf H2/day)$^{0.7}$ + 0.25 + 0.184 x (million scf H2/day)],
for a hydrogen flow rate of less than 0.56 million scf/day

For a plant producing 1 million scf H2/day, the capital cost would be about $1 million, one third that of a conventional SMR plant, which would cost about $3 million. [This assumes that several tens of units are built so that the cost of fuel cell reformer is $500/kWe and the cost of the PSA is $0.25 million x (gas flow rate in million scf/day)$^{0.7}$, for gas flow rates > 1 million scf/day]

If a 2 stage compressor were needed, the total capital cost would be

$1 million x [(0.44+0.375) x (million scf H2/day)$^{0.7}$ + 0.736 x (million scf H2/day)],
for a hydrogen flow rate of more than 0.56 million scf/day

and

$1 million x [(0.44 x (million scf H2/day)$^{0.7}$ + 0.25 + 0.736 x (million scf H2/day)],
for a hydrogen flow rate of less than 0.56 million scf/day

For a plant producing 1 million scf H2/day, the capital cost would be about $1.6 million, about half that of a conventional SMR plant.

Figure 10 compares the cost of fuel cell reformer with 1-stage compression and PSA cleanup versus a conventional SMR system vs. hydrogen production capacity. The capital cost for a fuel cell reformer based system is about 30-75% that of a comparable conventional SMR system over the range 0.1-2.0 million scf H2/day.

Effect of small scale steam reformer cost reductions on the delivered cost of hydrogen transportation fuel

Figure 11 shows the potential impact of reducing the small scale reformer capital cost on the delivered cost of hydrogen transportation fuel. Assuming that the reformer capital cost followed the curve shown in Figure 10, the delivered cost of hydrogen transportation fuel could be significantly reduced, especially at small station size. For example, the delivered cost of hydrogen would be reduced from about $40/GJ to about $25/GJ for a hydrogen refueling station dispensing 100,000 scf/day, (enough for perhaps 8 Ballard PEMFC buses/day or 80 fuel cell automobiles).

Partial Oxidation

Small scale partial oxidation systems have recently become commercially available, but are still undergoing intensive R&D (Moard 1995, Loftus 1994, Mitchell et.al. 1995). In partial oxidation reforming, methane is oxidized to produce carbon monoxide and hydrogen according to

$$CH_4 + 1/2\ O_2 \rightarrow CO + 2\ H_2, \qquad \Delta h^\circ = -36\ MJ/kmol\ CH_4$$

The reaction is exothermic and no indirect heat exchanger is needed. No catalyst is required because of the high temperature. However, the hydrogen yield per mole of methane input (and the system efficiency) can be significantly enhanced by use of catalysts (Loftus 1994). The reactor is more compact than a steam reformer, where heat must be added indirectly via a heat exchanger. The efficiency of the partial oxidation unit is relatively high (70-80%). However, partial oxidation systems are typically less energy efficient than steam reforming because of the higher temperatures involved (and the problem of heat recovery). A hydrogen plant based on partial oxidation would include a shift reactor and hydrogen purification equipment. Partial oxidation systems have a fast response time, making them attractive for following rapidly varying loads. Partial oxidation systems can handle a variety of fuels.

Partial oxidation systems are under development by Arthur D. Little (Loftus 1994, Mitchell et.al. 1995) and by Hydrogen Burner Technology (Moard 1995). Because they are more compact, and do not require heat exchangers, it is likely that partial oxidation systems could be lower cost than steam reformers.

Stationary Hydrogen Production from Methane with POX

Partial oxidation systems could potentially offer low capital cost and good conversion efficiency. Hydrogen Burner Technology has estimated capital costs for a range of stationary hydrogen production systems, which include a POX, shift reactor and PSA (Moard 1995) The costs for POX hydrogen plants are plotted vs. plant size, and contrasted with the costs of a hydrogen production plant based on fuel cell steam reformers and conventional small scale steam reformers (Figure 12). The capital costs for POX-based hydrogen plants in the 0.1-0.5 million scf/day range are less than those for a

conventional SMR system, but similar to those for a fuel cell SMR system. At larger plant capacities, the POX capital costs appear to be slightly lower.

The cost of the PSA unit is an important issue for POX systems. In a POX system, where the reaction takes place in air, nitrogen is a major diluent. In HBT's POX system, N_2 is perhaps 47% of the input to the PSA. This drives up PSA costs in two ways. First, the adsorbent materials needed to separate nitrogen from hydrogen are about twice as expensive as those used to separate CO_2, CO, CH_4, and H_2O. Second, since hydrogen is only about 45% of the PSA inlet gas (as compared to 70% for a SMR system), the PSA must be larger to accomodate the larger total gas flow. One would expect the PSA for a POX based hydrogen production system to cost several times more than a PSA for a SMR based system (Figure 12). Our very rough estimate for the cost of a mass produced PSA needed for a POX is comparable to the total system cost estimated by HBT in Figure 12.

Developing low cost purification technologies is key if POX systems are to be used for stationary hydrogen production. Another approach is using pure oxygen feed to the POX, which incurs high capital costs for small scale oxygen production, but eliminates the need to deal with nitrogen downstream. Oxygen enrichment of incoming air is another way of reducing, but not eliminating the amount of nitrogen.

Autothermal Reforming

In autothermal reformers, some fuel undergoes partial oxidation, which supplies heat to drive a catalytic steam reforming reaction. The autothermal reformer requires no external heat source and no indirect heat exchangers. This system has a higher efficiency than partial oxidation, and is only slightly more bulky. Autothermal reforming systems are not commercially available at present, but are now being developed by Rolls Royce, (Shoesmith 1992) International Fuel Cells, and Chiyoda. Because they are more compact and less costly, this approach may eventually offer lower cost than steam reforming.

Other Approaches to Small Scale Reforming

Sorbent enhanced steam reforming

Recently several authors have investigated the possibility of sorbent enhanced steam methane reforming (Lyon 1996, Sircar 1996, Han and Harrison 1994). Here an absorbent (such as calcium oxide) is mixed with the steam reforming catalyst, removing the CO and CO_2 as the steam reforming reaction progresses. The resulting syngas has a substantially higher fraction of hydrogen than that produced in a catalytic steam reforming system. This reduces the need for downstream processing and purification, which can be expensive in a small scale steam reformer. Moreover, the reaction can take place at lower temperature and pressure, reducing heat losses and material costs. These systems are still at the laboratory stage, and show promise for low cost. Issues include catalyst and sorbent lifetime and system design.

Thermocatalytic cracking

In this approach, methane is broken down into carbon and hydrogen at high temperature (Muradov 1996). The primary issues here are low energy efficiency of conversion and coking.

Conclusions

We found that appear to be real opportunities to reduce the capital cost of small scale steam reformers.

* Fuel cell steam methane reformers offer several design features which could reduce the costs as compared to "conventional" small scale steam reforming: use of convective rather than radiative heat transfer which reduces heat exchanger area; lower pressure operation, which reduces the cost of reformer steels; standardized design, which reduces engineering costs.

* Operating pressure of the steam reformer is an important issue. At higher pressure (15-25 atm), the cost of the reformer materials is higher (alloys rather than stainless steel must be used for tubes), but there is no need for costly dowstream compression prior to the PSA. There are system trade-offs between lower pressure, less costly reformers and more costly downstream clean-up and compression equipment. Even among fairly low pressure reformers, reforming at 5 atm rather than 1 atm appeared to offer advantages in terms of reduced compression power requirements and costs.

* Adapting fuel cell steam methane reformers for stationary hydrogen production looks promising. The capital cost of small scale steam reformer systems might be reduced by 25-70%. as compared to conventional small scale SMR systems. Some of the savings

* By using lower cost fuel cell reformers, the delivered cost of hydrogen transportation fuel produced via onsite reforming might be significantly reduced at small station size (less than 500,000 scf H2/day).

* Hydrogen purification technologies at small scale are an important part of the cost of a small scale reformer system (especially for POX). According to our preliminary estimates the cost of the PSA may account for a large majority of the system capital cost for a POX system, and about 1/3-1/2 of that for a small scale steam reformer.

Recommendations for Future Work

We recommend that demonstrations of small scale hydrogen production systems based on fuel cell reformers be undertaken in parallel with demonstrations of fuel cell vehicles.

It would be interesting to look in more detail at how reformer pressure effects hydrogen production system cost and design .

Clean-up systems for partial oxidation reactors are an interesting area for future work.

3.2 Case Study Of Developing A Hydrogen Vehicle Refueling Infrastructure In Southern California

Introduction

Many analysts suggest that the first widespread use of hydrogen energy is likely to be in zero emission vehicles in Southern California. Several hundred thousand zero emission automobiles are projected for the Los Angeles Basin alone by 2010, if mandated levels are implemented. Assuming that hydrogen vehicles capture a significant fraction of this market, a large demand for hydrogen fuel could evolve over the next few decades. Refueling a large number of hydrogen vehicles poses significant challenges. In this task we assess near term options for producing and delivering gaseous hydrogen transportation fuel to users in Southern California including:

* hydrogen produced from natural gas in a large, centralized steam reforming plant, and truck delivered as a liquid to refueling stations,

* hydrogen produced in a large, centralized steam reforming plant, and delivered via small scale hydrogen gas pipeline to refueling stations,

* hydrogen produced at the refueling station via small scale steam reforming of natural gas,

* hydrogen produced via small scale electrolysis at the refueling station,

* hydrogen from low cost chemical industry sources (e.g. excess capacity in refineries which have recently upgraded their hydrogen production capacity, etc.).

To compare these alternatives, we are addressing the following questions:

* What are projected hydrogen demands for ZEVs in the LA Basin?

* What are existing and potential hydrogen supplies in the LA Basin?

* What is the refueling system capital cost and delivered cost of hydrogen transportation fuel for various supply options and levels of demand?

* What is the lifecycle cost of transportation for hydrogen vehicles fueled with hydrogen from these sources?

* How might a hydrogen infrastructure evolve to meet projected demands for hydrogen for ZEVs in Southern California?

* What are the synergisms between near term options and phasing in longer term supplies such as hydrogen from renewables?

Hydrogen As A Fuel For Zero Emission Vehicles In Southern California

California's zero emission vehicle mandate requires that starting in 2003, 10% of all new light duty vehicles must be zero emission vehicles (ZEVs.) The only zero emission vehicle technologies likely to be ready in this time frame are electric battery vehicles and fuel cell vehicles. Because of their potential for longer range, faster refueling time and lower cost in mass production, fuel cell vehicles are among the leading contenders in the emerging market for zero emission vehicles.

All fuel cells currently considered for road vehicles use hydrogen as fuel. While hydrogen can be produced onboard the vehicle by reforming methanol or gasoline, direct storage of

compressed gaseous hydrogen also has attractions. The design of the vehicle is much simpler, the vehicle is more energy efficient, refueling can be accomplished rapidly, and hydrogen can be produced from many sources. Several experimental fuel cell vehicles such as the Ballard bus and the Daimler-Benz mini-van employ compressed hydrogen gas storage. Although the energy density of compressed hydrogen gas is lower than liquid fuels, it is higher than that of electric batteries (Arthur D. Little 1994). With high efficiency fuel cell vehicles, a travelling range of 400 km should be possible for a fuel cell automobile (Delucchi 1992).

The relative simplicity of the hydrogen fuel cell vehicle design must be weighed against the added complexity of a gaseous hydrogen refueling infrastructure. Unlike gasoline, natural gas or electricity, hydrogen is not widely distributed to consumers today. The question is often asked "Where is the hydrogen going to come from?" In this paper we attempt to answer that question for a specific region, the Los Angeles Basin. We focus on the near term (1996-2010), our estimates are based on commercial or near commercial technologies for hydrogen production, storage, and distribution.

Estimated Hydrogen Demand for Refueling Hydrogen Vehicles

Data and projections were obtained from the South Coast Air Quality Management District for populations of passenger cars, light duty trucks and buses in the LA Basin (R. George 1995). Based on the schedule for implementing the zero emission vehicle mandate (Table 4), we estimated the mandated number of ZEV passenger cars sold each year and the cumulative number of ZEVs in operation in the LA Basin (Figure 14). We see that despite recent changes in the zero emission vehicle mandate in California, postponing the introduction of ZEVs from 1998 to 2003, over 700,000 ZEV cars are mandated for the LA Basin by 2010.

It is possible that hydrogen fuel cell vehicles could capture a significant fraction of the ZEV automobile market. Many analysts believe that fuel cell cars could be commercialized sometime between 2003 and 2010. In our base case, we assume that hydrogen fuel cell cars capture 50% of the ZEV market starting in 2003, e.g. 5% of all new cars sold in the LA area are fuel cell vehicles. We further assume that 10% of all new buses will be fuel cell buses.

The hydrogen demand for fuel cell vehicles is then calculated based on assumptions about the vehicle performance (Table 5). The assumptions for PEM fuel cell buses are based on data from the Ballard PEMFC Phase II bus (Larson, Worrell and Chen 996). The assumptions for PEM fuel cell cars are based on studies by Delucchi (Delucchi 1992; Ogden, Larson and Delucchi 1994).

Hydrogen demand for buses and cars is shown in Figure 15. The total hydrogen demand in 2010 for our base case (350,000 cars and 300 buses) is about 55 million standard cubic feet per day (scf/day), almost all for cars. For reference, based on Los Angeles driving patterns, one million scf/day of hydrogen would be enough to fuel 800 PEM fuel cell passenger cars per day (or a total fleet of 6500 FCVcars) or 80 PEMFC buses per day (or a total fleet of 140 PEMFC buses) (Table 6).

We now consider how the projected hydrogen demand might be met in the near term (1996-2010) from existing hydrogen supplies and potential future supplies in the LA Basin.

Existing and Potential Hydrogen Supplies in the Los Angeles Basin

Existing Supplies Of Hydrogen

Industrial gas companies

At present, the primary suppliers of hydrogen in Southern California are the industrial gas companies Praxair, Inc. and Air Products and Chemicals, Inc.

Praxair has a hydrogen plant in Ontario, CA (see Figure 16) which currently produces 15 ton/day of liquid hydrogen (15 ton/day is equivalent in energy to about 5.3 million scf/day of gaseous hydrogen.) This plant supplies liquid hydrogen to the aerospace industry and to chemical industry users. Although most of the current output of this plant is already committed, there may be a million scf/day or so available today for transportation fuel.

The Praxair plant was originally designed to produce 28 ton/day, using two reformers. With lowered demand from aerospace companies, one reformer was shut down several years ago. The output could be returned fairly easily to 28 ton/day by restarting the second reformer. There is also room for further expansion beyond 28 ton/day if the market warranted (Kerr 1995). If an additional 13 ton/day of liquid hydrogen were produced, this could fuel a fleet of about 30,000 fuel cell cars or about 600 Ballard type PEMFC urban transit buses. The price of liquid hydrogen in the LA area at demand levels of 0.1-2.0 million scf/day is currently about $1.1-1.5/lb or $17-23/GJ (Lenci 1995). A liquid hydrogen refueling station might add several $/GJ to this cost.

Air Products and Chemicals recently completed a new 80 million scf/day hydrogen plant (based on steam reforming of natural gas) in Wilmington, CA to provide gaseous hydrogen to nearby oil refineries. The plant may still have some uncommitted capacity, which could be used for vehicle fuel. If 5 million scf/day were available, this could fuel a fleet of about 33,000 fuel cell cars or 700 fuel cell buses. The cost of hydrogen at a large reformer plant might be $7-9/GJ. With gaseous hydrogen, a pipeline distribution system would have to be built (or refueling might be done at the hydrogen plant). The delivered cost of transportation fuel would depend on the type of pipeline distribution system needed.

Excess hydrogen from refineries

In addition, a number of oil refineries are located in the Torrance/Wilmington area. Typically oil refineries produce large amounts of gaseous hydrogen (25-100 million scf/day) using most or all of it onsite. Historically some excess hydrogen has been available, and some refineries have sold a few million scf/day of hydrogen "over the fence" to other refineries or chemical users, delivering the hydrogen by small scale pipeline. To meet 1996 requirements for Phase II reformulated gasoline, significantly more hydrogen will be required by refineries. Thus, the refiners expect to be "hydrogen short" in the near future. To meet increased demands for hydrogen, several refineries are now building extra reformer capacity or planning to buy hydrogen from the new Air Products plant.

It may be possible to purchase a few million scf/day from refineries, especially those with newly expanded reformer capacity. This could be economically attractive, as the cost (at the plant site) would be quite low. If the reformer capital cost is considered to be a "sunk" cost, gaseous hydrogen might be sold for as little as $1/1000 scf ($2.8/GJ). If the reformer capital costs are counted, the price for gaseous hydrogen would be $2.5-3.0/1000 scf ($6.9-8.3/GJ) The delivered cost to the user would depend on how long a pipeline was required, as well as the cost of the refueling station.

Summary: total hydrogen available from existing sources

Hydrogen from existing sources could be significant in getting hydrogen fuel cell vehicles started. Even without building any new hydrogen production capacity, the total available from all existing sources might be 5-15 million scf/day or enough for 30,000-100,000 fuel cell cars or 700-2000 fuel cell buses. (Of course, there would be costs to build new distribution systems and refueling stations to bring the "excess hydrogen" available in the LA Basin today to consumers' vehicles.)

Other Potential Near Term Sources Of Hydrogen in Southern California

If fuel cell vehicles capture a significant fraction of the ZEV passenger car market, demand would soon outstrip these existing sources of hydrogen. (Recall that by 2010, fueling all 50% of ZEVs with hydrogen would require 55 million.) In this case, other near term supplies would have to be developed.

Expansion of industrial gas supplies

If a large market for hydrogen transportation fuel were to develop, industrial gas suppliers indicated that they could build a new, large hydrogen plant based on steam reforming in 2-3 years. A plant producing 80 million scf/H2 per day could serve a fleet of 500,000 fuel cell passenger cars. Hydrogen from such a plant could be liquified for truck delivery or delivered via a small scale pipeline system.

Hydrogen from onsite steam reforming of natural gas

It is also possible to produce hydrogen onsite at the refueling station via small scale steam reforming of natural gas or partial oxidation. The natural gas flow through Southern California Gas's distribution system averages about 3×10^9 scf of natural gas/day (David Crain, private communications 1995). Fueling a fleet of 1 million fuel cell cars with LA driving patterns would require about 150 million scf H2/day. This amount of hydrogen could be produced via steam reforming from about 60 million scf of NG or about 2% of the total flow in the natural gas utility system. Natural gas is widely available throughout the LA Basin. Based on experence with installing CNG stations (which would require a similar natural gas flow to hydrogen stations based on onsite reforming), pipelines of sufficient capacity are easily tapped (Wayne Tanaka, Southern California Gas, private communications 1995). The natural gas distribution system would not have to be modified to bring natural gas to refueling stations for onsite hydrogen production for ZEVs.

Hydrogen from onsite electrolyis using off-peak power

There is a large potential for using off-peak power in Southern California. Southern California Edison estimated that some 4000-6000 MW of off-peak power might available from 6 pm to 10 am. This could be used to power electrolyzers, providing some 440-660 million scf H2/day, enough to fuel a fleet of 3.5 - 5.3 million fuel cell cars. The price of off-peak power would be 4-4.5 cents/kWh for small commercial customers (50-500 kW) (Tom Burhenn, So. California Edison, private communications 1995), and 3 cents/kWh for large customers (>500 kW). Electrolyzers producing 0.1-2.0 million scf H2/day would be in the 400-8000 kW range.

Hydrogen from landfill gas

It has been estimated that about 1300 kg (0.52 million scf) of hydrogen per day could be produced for about 20 years at a single landfill site in the LA area (Glenn Rambach, LLNL, private communication 1995). This would be enough to refuel about 40 PEMFC buses/day. The economics would be competitive with other sources of hydrogen. The total resource has not been quantified, but this suggests the possibility of fuels production at landfills.

Summary: total hydrogen available from near term sources

Hydrogen could be produced either in a centralized plant or at the refueling station from natural gas. To produce hydrogen to fuel one million FCVs would require less than 2% of the current natural gas flow in the utility system.

Onsite electrolysis is another potentially large resource. If all the available off-peak power in the LA area were devoted to electrolytic hydrogen production, a fleet of 3-5 million FCVs could be fueled.

Hydrogen from landfill gas is another possibility which might be exploited in the near term.

In Figure 17, we compare the projected hydrogen demand for vehicles in the LA Basin from 1998-2010 to the amount of hydrogen which could be supplied from various existing and near term supplies. Hydrogen from existing industrial and refinery sources in the LA area could fuel a fleet of perhaps 30,000-100,000 fuel cell cars or 700-2000 Ballard buses/day. Beyond this level, there is sufficient natural gas to fuel a fleet of 3-6 million FCVs (assuming that 5-10% of the current natural gas flow is used for hydrogen production), and sufficient off-peak power to produce electrolytic hydrogen for 3-4 million FCVs.

Economics of Hydrogen Production and Delivery

We now estimate the delivered cost of hydrogen transportation fuel in Southern California for various options.

Energy prices for Southern California are summarized in Table 7, based on data obtained from Southern California Gas Company and Southern California Edison. The delivered cost of hydrogen transportation fuel is then estimated, using data developed in our earlier studies of hydrogen transportation fuel supply options (Ogden et.al 1995). A range of refueling station sizes from 0.1 to 2.0 million scf/day is considered (e.g.about 80-1600 fuel cell cars/day or 8-160 fuel cell buses/day).

The delivered cost of hydrogen for Southern California conditions is shown in Figure 18 for a variety of station sizes and supply options. The cost contributions of various factors are shown for each technology over a range of station sizes.

Although all the supply options are roughly competitive, it appears that onsite electrolysis would be somewhat more expensive in than other options, because of the relatively high cost of off-peak power in the LA area. (If the cost of off-peak power were reduced from 3 cents/kWh to 1-1.5 cents/kWh, hydrogen costs would be much more competitive.)

Truck delivered liquid hydrogen gives a delivered hydrogen cost of $20-30/GJ, depending on the station size. This alternative would be attractive for the first demo projects, as the

capital requirements for the refueling station would be relatively small (Ogden et.al. 1995), and no pipeline infrastructure would be required.

Costs are shown for onsite reforming of natural gas based on conventional small steam reformer systems. With conventional reformer technology, hydrogen is expensive at small station sizes, but is attractive at larger station sizes. As discussed above, with improvements in small scale reformer technology, it is possible that delivered hydrogen costs could be sigificantly lower at small station size. From Figures 10 and 11b, we see that the reformer capital cost might be reduced by about 2/3 for station capacities of 0.1-1.0 million scf/day. This would make onsite reforming competitive with liquid truck delivery over the whole range of station sizes considered. Onsite production has the advantage that no hydrogen distribution system is required.

Under certain conditions, pipeline hydrogen could offer low delivered costs. The capital cost of building a small (3" diameter) hydrogen pipeline would be about $1 million per mile in the heavily populated LA area (Lenci 1995). Figure 19 shows the cost of hydrogen pipeline delivery in a 3" diameter pipeline as a function of the pipeline flow rate and the distance. The levelized cost of pipeline delivery in LA is about

Ppipeline($/GJ) = $1.2/GJ x distance (in km)/flow rate (in million scf H2/day).

Centrally produced hydrogen ranges in cost from $3/GJ (for refinery excess) to $5-9/GJ for large scale steam reforming to $8-10/GJ for hydrogen from biomass, coal or MSW). If the cost of hydrogen producition is low, higher pipeline costs could be tolerated. Still, for pipeline hydrogen to be competitive wth truck delivery or onsite reforming, pipeline costs can be no more than a few $/GJ. For a small scale hydrogen pipeline system to be economically competitive a large, fairly localized demand would be required. Alternatively, a small demand might be served by a nearby, low cost supply of hydrogen.

Lifecycle Cost of Owning and Operating a Hydrogen Fuel Cell Car or Bus Compared to Alternatives

As we have shown in earlier work, the cost of owning and operating a hydrogen fuel cell automobile would be comparable to that of gasoline and other alternatives, assuming mass production cost goals for PEM fuel cells are reached (Ogden, Larson and Delucchi 1994). Performance and cost assumptions for alternative fueled vehicles are outlined in Table 8, comparing fuel cell automobiles to gasoline automobiles and fuel cell buses to Diesel buses (se also Larson, Worrell and Chen 1996). Using the data in Figure 18 for the delivered cost of hydrogen transportation, fuel, the lifecycle cost of transportation can be estimated. This is shown for a PEMFC bus in Figure 20. The capital cost of the vehicles is higher, but the efficiency is higher, so that the overall cost of transportation could be similar to that of today's vehicles.

Possible scenarios for developing a Hydrogen Refueling Infrastructure in the Los Angeles Basin

Introduction of PEMFC Buses

There are a number of reasons why PEM fuel cell buses might be the first users of hydrogen as a transportation fuel.

* Ballard will be demonstrating hydrogen fueled PEMFC buses in several cities starting this year, with commercialization planned for 1998.

* Refueling with hydrogen or any alternative fuel is easier at centralized fleet locations such as bus garages.

* The daily demand for hydrogen for a bus depot would be large enough to bring the delivered cost of hydrogen down somewhat because of economies of scale, especially for stations based on small scale reformers.

* Fuel cells might be economically competitive first in bus markets, where cost goals are not as stringent as for automobiles.

To understand the potential for fuel cell buses in the Los Angeles area, we gathered data on the bus system (Chaiboonma 1996). A total of about 3000 Diesel buses operate in the LA area. Typically, buses are driven 50,000 miles/year, and have a fuel economy of about 3.5 miles per gallon of Diesel, and a range of 350 miles. The lifetime of a typical Diesel bus is about 10 years (500,000 miles). Buses are refueled overnight where they are garaged (at depots). Typical sizes for bus depots in LA are about 60-200 buses.

Major bus depots are shown in Figure 21. It is interesting to note that all the urban transit bus depots in the LA area are within an hour or so of the Praxair liquid hydrogen plant. Several depots are located in the Long Beach area, possibly within pipeline distance of refineries or the Air Products plant.

Assuming a replacement rate for Diesel buses of 10% per year, about 300 new buses would be needed in LA every year. If fuel cell buses made up 10% of the new buses about 30 new fuel cell buses per year would be required. Existing industrial hydrogen sources would be sufficient to supply several hundred buses.Hydrogen could be trucked in as a liquid or piped short distances to bus depots near the Long Beach refinery area. Alternatively, onsite production of hydrogen from natural gas might be used. A fleet of about 8 PEMFC buses could be refueled daily using a small scale reformer producing 100,000 scf H2/day. Rapid developments in small scale reformer technology are making this an increasingly attractive supply option.

Introduction of PEMFC automobiles in Southern California

Several major automobile manufacturers are conducting R&D on PEM fuel cell cars (including GM, Ford, Chrysler, Daimler-Benz, Mazda, Toyota, and Honda). A PEMFC mini-van using compressed hydrogen gas storage was demonstrated in May 1996 by Daimler-Benz, and it is likely that the first mid-size PEMFC automobiles may be demonstrated before the year 2000. The first mass-produced commercial models might be available a few years later in the 2004-2010 time frame.

If PEMFC cars capture a significant fraction of the mandated ZEV market, the demand for hydrogen could grow rapidly (Figure 15), and new hydrogen production capacity and delivery infrastructure would be needed. In near term (1998-2010) liquid hydrogen truck delivery or onsite production of hydrogen from natural gas would probably give the lowest delivered transportation fuel costs to the consumer. Because of the high cost of building small scale gaseous pipelines, development of new, large scale, centralized production capacity with pipeline distribution would require a fairly large, localized hydrogen demand. This might not develop until a larger fraction of the automotive population were hydrogen-fueled. (Exceptions might be found, where gaseous distribution was more attractive, e.g.a

cluster of fleet cars in an industrial area.) Onsite electrolysis appears less economically attractive than steam reforming in the LA area, because of the relatively high cost of off-peak power (3 cents/kWh). (If lower cost electricity supplies were available this alternative would be more competitive.)

Natural gas supplies would probably be sufficient to supply feedstock for hydrogen production for up to several million PEMFC cars, for several decades. In the longer term, other hydrogen supplies might be phased such as gasification of municipal solid waste (a potential resource capable of serving several million FCV cars) or biomass, or solar (a potentially huge resource, which could meet foreseeable demands, even for a 100% ZEV transportation system). Hydrogen might also be produced from fossil fuels (natural gas or coal) or biomass with sequestering of the byproduct CO_2 in gas fields or aquifers, and piped via large scale, long distance hydrogen pipelines to users (Williams 1996).

Conclusions

If hydrogen fuel cell vehicles captured a significant fraction of the projected ZEV market, a large demand for hydrogen could develop over the next 15 years. If PEMFC cars accounted for half the mandated ZEV population, there would be about 350,000 cars on the road in the LA Basin by 2010, requiring 55 million scf of hydrogen per day.

We found that a considerable amount of hydrogen, perhaps 5-15 million scf/day, would be available in the LA Basin from existing industrial gas supplies and from refinery excess hydrogen. Fleets of perhaps 30,000 to 100,000 fuel cell cars or 700-2000 PEM fuel cell buses might be fueled without building new hydrogen production capacity. New hydrogen distribution and refueling station capacity would be needed to bring the available hydrogen to consumers.

The cost of hydrogen from existing sources might be $20-30/GJ for truck delivered liquid hydrogen. Costs for gaseous hydrogen delievered by small pipeline would depend on the level of demand and the pipeline length. This might be attractive even for small demands located near an inexpensive hydrogen source (such as refinery excess or the Air Products plant in Wilmington.) The delivered cost of hydrogen from onsite steam reforming of natural gas may rival that of existing sources, although the capital costs would be higher than for liquid hydrogen refueling stations.

Once demand for hydrogen exceeded existing production capacity (perhaps 5-15 million scf/day), new production capacity would be needed. Natural gas supplies would probably be sufficient to supply feedstock for hydrogen production for up to several million PEMFC cars, for several decades. In the longer term, other hydrogen supplies might be phased such as gasification of municipal solid waste or biomass, or solar.

For energy prices and conditions in the LA area, it appears that in the near term, truck delivery of liquid hydrogen and onsite production via small scale steam reforming offer the lowest costs and would allow the addition of hydrogen production capacity in small increments, without building a new hydrogen pipeline distrubution system. Improvements in small scale reformer technology might make this option even more attractive.

Hydrogen produced via small scale electrolysis was somewhat more expensive, largely because of the relatively high cost of off-peak power in the LA area.

In the longer term, for large, geographically concentrated demands, pipeline distribution might ultimately yield the lowest delivered fuel cost. Pipeline delivery might also be

prefered for a smaller demand very close to an existing low cost source of hydrogen (e.g. refinery excess).

The first hydrogen vehicles in the LA Basin are likely to be PEM fuel cell buses, which could be commercialized as early as 1998. Early bus demos might be fueled from existing sources (trucked in liquid hydrogen, or piped in hydrogen for depots near the LA refinery area). Or they might use small scale reformer systems now being commercialized for stand-alone hydrogen production.

Once fuel cell cars were introduced, hydrogen production from natural gas would offer the lowests costs for the near term. In the longer term, other supplies might be phased in such as hydrogen from wastes, biomass or solar.

3.3 Assessment of potential markets for hydrogen in Southern California

We are conducting a case study of how hydrogen markets might develop in Southern California over the next five years. It is likely that fleets of hydrogen vehicles will be introduced in California in the early part of the next century, in response to the zero emissions vehicle (ZEV) mandate. Other possible uses of hydrogen energy in this time frame include co-firing and fuel cells. In this task we are estimating the size of these potential hydrogen markets. This work is being carried out with input from Southern California Gas Company, SCAQMD, and industrial hydrogen suppliers.

3.4 Assessment of the role of hydrogen as a fuel for fuel cell vehicles

In this task, we are comparing hydrogen to other fuels for fuel cell vehicles, such as methanol and hydrocarbon fuels derived from crude oil.

We are interacting with fuel cell manufacturers and with automotive companies (including Ford, Chrysler and GM and their subcontractors) which are considering fuel cell vehicle demonstrations as part of the DOE/OTT and PNGV programs. We also interact with groups at Los Alamos National Laboratory, and Argonne National Laboratory who are studying fuel cell vehicle systems, as well as other academic groups (UC Davis, U of Michigan, Georgetown U.).

This year we are evaluating the projected performance, cost and emissions characteristics of alternative fuel cell vehicles with:

(a) compressed gas hydrogen storage
(b) onboard reforming of methanol
(c) onboard partial oxidation of hydrocarbon fuels derived from crude oil

This subtask draws on existing vehicle modelling work ongoing as part of the DOE/OTT and PNGV programs on fuel cell vehicles, as well as studies by other academic groups (UC Davis, U of Michigan, Georgetown U.). Although a considerable amount of modelling work has been done on hydrogen and methanol fuel cell vehicles, there is little published data on vehicles where hydrogen is produced onboard via partial oxidation of

hydrocarbon fuels derived from crude oil. We are concentrating on understanding the issues for this alternative.

4. Plans for Future Work

Assessments of the role of hydrogen as a fuel for fuel cell vehicles

We plan to continue our studies of the role of hydrogen as a fuel for fuel cell vehicles, as compared to onboard steam reforming of methanol or partial oxidation of hydrocarbon fuels. In the future, we plan to:

*Evaulate the refueling infrastructure requirements for each alternative.

* Determine the delivered fuel cost for the various fuels including hydrogen from natural gas, coal, biomass, municipal solid waste (MSW), solar, wind or nuclear; methanol from natural gas, biomass, MSW or coal; and hydrocarbon fuels such as gasoline or Diesel from crude oil.

* Calculate the lifecycle cost of transportation for each alternative.

* Evaluate the potential resources for fuel production for each alternative.

* Evaulate the fuel cycle emissions of pollutants and greenhouse gases for fuels derived from various primary sources listed above.

Assessment of strategies for introducing hydrogen transportation fuel made from municipal solid waste in the New York City area

Costs for landfilling are high in many urban areas of the United States, and environmental concerns are constraining the use of incineration to dispose of waste. Even if extensive recycling programs are sucessfully implemented, MSW will continue to be a substantial disposal problem.

Preliminary calculations by Eric Larson at Princeton (Larson, Chen and Worrell 1995) suggested that hydrogen from MSW might be attractive as fuel for fuel cell vehicles in the New York City area. The economics are potentially attractive, because of the high tipping fees in the New York area. Research engineers at the New York City Department of Sanitation and the New York Power Authority have expressed interest in these preliminary findings. (The city's landfill is near capacity, and incinerators are unlikely to be permitted.) They indicated willingness to provide the data we would need to extend the initial study by Larson et.al. to a more detailed case study and implementation strategy for fuels from MSW in the New York City area.

We would like to pursue the following areas of research.

* Better understand the MSW resource in the New York City area, for example, what is the composition of the waste, and where is it available.

* Model the cost and performance of demonstration size and full size MSW gasifier plants in a variety of configurations, and estimate the production cost of hydrogen.

* We would look at the potential demand for hydrogen transportation fuel in New York City, and examine fuel distribution infrastructure issues for using hydrogen as a fuel for fuel cell vehicles.

* We would compare the projected economics of fuel cell vehicles used MSW-derived fuels with alternative vehicles using gasoline, Diesel, and electric batteries.

* Sketch possible strategies for introducing hydrogen from MSW as a fuel for fuel cell vehicles in New York City.

5. Status Of Economic Evaluation/Systems Analysis

Technical and economic assessment and systems analysis are the main foci of our work and are explicitly included in all our studies.

6. Projected Goals/Basis For Goals

The goal of our work is to illuminate possible pathways leading from present hydrogen markets and technologies toward wide scale use of hydrogen as an energy carrier, highlighting important technologies for RD&D.

7. Major Barriers To Meeting Goals

Not surprisingly , it is sometimes difficult to obtain the very latest data for near commercial technologies such as fuel cells, reformers, etc. Still, we have received extremely helpful assistance and advice from a wide range of industrial and government sources.

Because many of our studies address near term issues for hydrogen energy, interactions with industry are an important component of our work. In our studies of the past few years we have developed contacts at gas utilities (Southern California Gas Company), reformer manufacturers (Howe-Baker Engineering, Hydrochem, Haldor Topsoe, Hydrogen Burner Corp., KTI), industrial gas suppliers (Praxair, Air Products, British Oxygen Company), manufacturers of hydrogen compressors and storage systems (RIX compressors, Christy Park Industries), and fuel cell manufacturers (Energy Partners, H-Power, Ballard Power Systems, International Fuel Cells). We have received useful comments and advice from researchers at the Institute of Gas Technology and the National Hydrogen Association. For our study of Southern California hydrogen markets, data were obtained from the South Coast Air Quality Management District, the California Air Resources Board and the LA Metropolitan Transit Authority. We have had discussions with researchers at oil companies (Exxon, Mobil) and automotive companies (Chrysler, Mazda, Daimler-Benz, Ford, GM) and their subcontractors (Directed Technologies, Inc) involved with fuel cell vehicles as part of the Clinton Administration's Partnership for a New Generation for Vehicles (PNGV) program. We have also contacted researchers at national laboratories (ORNL, LLNL, Sandia, LANL) and academia (UC Davis, Texas A&M).

Acknowledgments

For useful conversations, the authors would like to thank Archana Agrawal (California Air Resources Board), Richard Bellows (Exxon), Jeff Bentley (AD Little), Tom Burhenn (Southern California Edison), Eck Chaiboonma (Los Angeles Metropolitan Transit Authority), David Crain (David Crain Associates), Ernst Ecker (UOP), Michael Furgeson (Southern California Gas Company), Ranji George (South Coast Air Quality Management District), Mr. Green (Southern California Edison), Michael Kerr (Praxair), Nathaniel Kong (California Air Resources Board), Paul Kydd (BOC), Christian Lenci (Praxair), Paul Lancaster (Ballard Power Systems), Jon Leonard (SCAQMD), Robert Miller (Air Products and Chemicals, Inc.), Robert Moore (Air Products and Chemicals, Inc.), David Nahmias (consultant), Michael Payne (ARCO), James Provenzano (Xerox), Venki Raman (Air Products and Chemicals, Inc.), Glenn Rambach (LLNL), Mr. Soriano (LA Department of Water and Power), Margaret Steinbugler (Princeton University), Wayne Tanaka (Southern California Gas Company), Sandy Thomas (Directed Technologies, Inc.), Mr. Thomas (Southern California Gas Company), Robert Williams (Princeton University), Gary Youngman (ARCO), Ed Yotter (CARB), and Robert Zweig (Clean Air Now).

References

Arthur D. Little. 1994. "Multi-Fuel Reformers for Fuel Cells Used in Transportation, Assessment of Hydrogen Storage Technologies, Phase I Final Report," USDOE Office of Transportation Technologies, Contract No. DE-AC02-92-CE50343.

Buswell, R. July 4, 1978. "Multi-tube Catalytic Reaction Apparatus," US Patent No. 4,098,588.

Buswell, R. et.al. November 1, 1994. "Hydrocarbon Fueled Solid Polymer Fuel Cell Electric Power Generation System," US Patent No. 5,360,679.

Buswell, R. et.al. January 16, 1996. "Catalytic Hydrocarbon Reformer with Enhanced Heat Transfer Mechanism," US Patent No. 5,484,577.

Delucchi, M.A.. 1992. "Hydrogen Fuel Cell Vehicles," UCD-ITS-RR-92-14, Institute of Transportation Studies, University of California, Davis.

Dennis, E.B. May 1994. "Design and Feasibility of a Gaseous Hydrogen Refueling Station Based on Small Scale Steam Reforming of Natural Gas," Princeton University senior thesis, Department of Chemical Engineering.

Ecker, Ernst, UOP, private communications 1996.

Farris, P. International Fuel Cells, private communications 1996.

George, Ranji, South Coast Air Quality Management District, private communcations, 1995, 1996.

Haldor-Topsoe. 1988."Endurance Testing of a High-Efficiency Steam Reformer for Fuel Cell Power Plants", EPRI Report No. AP-6071.

Haldor-Topsoe. 1993."Heat Exchange Reformer", company brochure.

Han C. and D. Harrison. 1994. "Simultaneous Shift Reaction and Carbon Dioxide Separation for the Direct Production of Hydrogen," Chemical Engineering Science, v. 49, No. 24B, pp. 5875-5883.

Kerr, Michael, Praxair Inc., private communications 1995, 1996.

Larson, E.D., R.H. Williams, R.E. Katofsky and J. Chen. July 1995. ""Methanol and Hydrogen from Biomass for Transportation with Comparisons to Methanol and Hydrogen from Natural Gas and Coal," Princeton University Center for Energy and Environmental Studies Report No. 292.

Larson, E.D., E. Worrell and J. Chen. January 1996. Princeton University Center for Energy and Environmental Studies Report No. 293.

Lyon, R., Energy and Environmental Research Corp., private communications 1996.

Mitchell, W., et.al., 1995. "Development of a Catalytic Partial Oxidation Ethanol Reformer for Fuel Cell Applications," Proceedings of SAE Alternative Fuels Conference, SAE Paper No. 95261.

Muradov, N. 1996. "Production of Hydrogen by Thermocatalytic Cracking of Natural Gas," presented at the USDOE Hydrogen R&D Program Review Meeting.

Ogden, J.M. and R.H. Williams. October 1989. Solar Hydrogen : Moving Beyond Fossil Fuels, World Resources Institute, Washington DC.

Ogden, J.M. and R.H. Williams. 1990. "Electrolytic Hydrogen from Thin Film Solar Cells," International Journal of Hydrogen Energy, v. 15, p.155.

Ogden, J.M. 1991."Cost and Performance Sensitivity Studies for Solar Photovoltaic/Electrolytic Hydrogen Systems," Solar Cells, v. 30, No. 1-4, p. 515.

Ogden, J.M. and J. Nitsch. 1993. "Solar Hydrogen," Chapter 22 in T. Johansson, H. Kelly, A.K.N. Reddy and R.H. Williams, Renewable Energy: Fuels and Electricity from Renewable Sources, Island Press, Washington, DC.

Ogden, J.M. June 24, 1993. "Renewable Hydrogen Energy Systems Studies," final report for NREL Contract No. XR-2-11265-1.

Ogden, J.M. and M.A. DeLuchi. 1993. "Solar Hydrogen Transportation Fuels," Chapter 8, in D. Greene and D. Santini, eds., Proceedings of the Conference on Transportation and Global Climate Change, American Council for an Energy Efficient Economy, Washington, DC.

Ogden, J.M., E.D. Larson and M.A. Delucchi. May 27, 1994. "An Assessment of Renewable Transportation Fuels and Technologies," report to the US Congress Office of Technology Assessment.

Ogden, J.M., J.W. Strohbehn and E. Dennis. April 19, 1994. "Hydrogen Energy Systems Studies," Proceedings of the USDOE Hydrogen Program Review Meeting.

Ogden, J.M, E. Dennis and J.W. Strohbehn, "A Technical and Economic Assessment of the Role of Natural Gas in a Transition to Hydrogen Transportation Fuel," presented at the 10th World Hydrogen Energy Conference, Cocoa Beach, FL, June 21-24, 1994.

Ogden, J.M., E. Dennis, M. Steinbugler and J. Strohbehn. Jan. 18, 1995. "Hydrogen Energy Systems Studies," final report to USDOE for Contract No. XR-11265-2.

Ogden, J.M., E. Dennis and K. Montemayor. March 1995. "Development of Refueling Infrastructure for Hydrogen Vehicles," Proceedings of the 6th National Hydrogen Association Meeting, p. 237.

Ohsaki, K. et.al. April 6, 1993. "Apparatuts for Catalytic Reaction," US Patent No. 5,199,961.

Rostrup-Nielsen, J.R. 1984. Catalytic Steam Reforming, Springer-Verlag, New York, NY.

Sederquist, R.A. Jan. 31, 1978. "Steam Reforming Process and Apparatus Therefor," US Patent No. 4,1071,330.

Sederquist, Nov. 28, 1995. "Fuel Cell Power Plant Reformer Burner Gas Flow Control System," US Patent No. 5,470,360.

Sircar, S. , M. Anand, B. Carvill, J. Hufton, S. Mayorga, and B. Miller. 1996. "Sorption Enhanced Reaction Process (SERP) for Production of Hydrogen," presented at the USDOE Hydrogen R&D Program Review Meeting.

Stahl, H. et.al. May 16, 1989. "Reactor for the Catalytic Reforming of Hydrocarbons," US Patent No. 4,830,843.

Twigg, M.V.,ed. 1989. Catalyst Handbook, Wolfe Publishing, Ltd., Frome, England.

Williams, R.H. January 1996. "Fuel Decarbonization for Fuel Cell Applications and Srquestering of the Separated CO_2," Princeton University Center for Energy and Environmental Studies Report No. 296.

Table 0. Conversion Factors and Economic Assumptions

1 GJ (Gigajoule) = 10^9 Joules = 0.95 Million BTU
1 EJ (Exajoule) = 10^{18} Joules = 0.95 Quadrillion (10^{15}) BTUs

1 million standard cubic feet (scf) = 28,300 Normal cubic meters (m_N^3) = 362 GJ (HHV)
1 million scf/day = 2.80 tons/day = 4.19 MW H_2 (based on the HHV of hydrogen)

1 scf H_2 = 362 kJ (HHV) = 344 BTU (HHV)
1 lb H_2 = 64.4 MJ (HHV) = 61.4 kBTU (HHV) = 178.5 scf

1 m_N^3 = 12.8 MJ (HHV)
1 kg H_2 =141.9 MJ (HHV) = 393 scf

1 gallon gasoline = 130.8 MJ (HHV)
$1/gallon gasoline = $7.67/GJ (HHV)

All costs are given in constant $1993.

Capital recovery factor for hydrogen production systems, distribution systems and refueling stations = 15%

Passenger car owners' real discount rate is assumed to be 3.8%
The real discount rate is taken to be 10% for urban buses.

Table 1. Characteristics Of Small-Scale Methane Reformers

Company	Capacity H2 out (scf/day)	Feed Pressure	Feed Purification	Reformer Temp	Shift reactor	Hydrogen Purification	Efficiency	Dynamic response	Physical Size and Cost
CATALYTIC STEAM REFORMERS									
Haldor-Topsoe	67,000-3.3 million	Supply pressure	Zinc-oxide	1525°F	high and low temp.	99.999% w/PSA	80%	Cold start in 3 hours, 25-100% load in 30 seconds	$500/kW, 30' high, 8' diameter
Howe-Baker Engineers	1-5 million	300 psig	Zinc-oxide	1550-1600°F	High temp (675-800°F)	99.999% w/PSA	80%	Cold start in several hours	$3 million for 1 million scf/day
Hydro-chem	120,000-5 million	275 psig	Zinc-oxide		High temp	99.99% pure w/PSA		Cold start in 2-4 hours, 100% to 30% load in 1 hr	40' high, 40x80' area, $1 million for 120,000 scf/day
KTI/Air Products and Chemicals, Inc.	0.1-3 million	Supply pressure				99.99% pure w/PSA	80%		$3 million for 1 million scf/day
International Fuel Cells/ONSI	48,000-140,000	Supply pressure		Steam Reforming Fuel Processor Unit in Fuel Cell Cogeneration Package	High temp.	Less than 75% pure H2, product contains H2, CO, CO2	84%	Cold start in less than 3 hours, Idle to 100% load in 1 second	10' high, 4' diameter, $500/kWe for refomerBeing developed as part of a PAFC cogen package
Ballard Power Systems	6000 120,000	Supply pressure				99.99% pure (for use with PEM fuel cell)	80% eff.		Being devel. as part of a fuel cell package est. $500/kWe
Chiyoda (JAPAN)				Stea, Reformer used with 100-200 kW Phosphoric Acid Fuel Cells					
PARTIAL OXIDATION SYSTEMS									
Arthur D. Little	12,500		Zinc oxide	1600-1800°C (catalytic POX)	high and low temp.	Pref. oxidation	80% eff	Fast	R&D only, not commercial yet
Hydrogen Burner Technology	12,000 96,000			2500°F (POX)	High and low temp	Palladium membrane 99.999% pure	75-80%	Fast	less than $200,000 for 96,000 scf/day unit with production of a few systems
AUTOTHERMAL REFORMERS									
Rolls-Royce/ Johnson-Mathey	7-25 kW H_2 (1700-6200 scf H_2/day)	ambient pressure		Exeprimental Autothermal Reformer Unit			>90%	Fast	60 liters
International Fuel Cells/ONSI	1.5-20 kW			Autothermal Reformer under development				Fast	

Table 2.
Fuel Cell Steam Methane Reformers

Haldor-Topsoe:	Heat Exchange Reformer for PAFC applications. 0.85 million scf/day unit built (corresp. to 1.25 MWe FC)
IFC:	Reformers for Phosphoric Acid Fuel Cell cogeneration systems PC25 series for 200 kWe FC Joint venture w/ Praxair for H2 production system based on PC-25 fuel cell reformer
BALLARD:	10 kWe FC reformer for PEM Size: 52" x 48" x 86" 250 kWe FC multi-tube reformer for PEM Size: 27,600 lb, 1200 cu.ft., 8' x 8' x 18' operational mid-1996; 50 units by 1998
OSAKA GAS:	Built Haldor-Topsoe type multi-cylinder single tube reformer for FC. Has plans to build multi-tube, more compact unit [10.5 m x 8 m x 3.6 m (ht)]

Table 3.
Comparison Of Small Scale (0.1-2 Million Scf/Day)
Steam Methane Reformers For Chemical And Fuel Cell Applications

	SMR for Chemical Applications[a]	Fuel Cell SMR for PEM system
Reformer Operating temp °C	845-870°C	745°C [b]
Reformer Operating Pressure (psig)	225-375	70-85 [b]
Reformer tube material	Nickel chrome alloy steels	Stainless steel
Heat Transfer	Radiative	Convective
Tube length (ft)	30	6-8
Energy conversion efficiency CH_4-> H_2	85%	81.4% (reformer) [b] 70.7% (fuel proc. system incl. aux)
Purification Technology	PSA	Selective catalytic oxidation to convert CO-> CO_2
Outlet Gas Composition (% volume) H_2 CH_4 N_2 CO_2 H_2O	99.999%	68.8% [b] 3.9% 0.7% 17.2% 9.3%
Outlet Gas Pressure (psig)	200 (from PSA)	65 (from PROX)
Capital Cost	$\$3 \times 10^6$ x (capacity in million scf/day)$^{0.3}$	\$500/kWe (mass produced)
120,000 scf H_2/day	$\$1.6 \times 10^6$	\$100,000
Lifetime (yr)	20	>15

a. From Howe-Baker
b. From Ballard Power Systems U.S. Patent No. 5,360,679 Nov. 1, 1994

Table 4. Zero Emission Vehicle Mandate

Year	Original ZEV Mandate	1996 Revised ZEV Mandate
1998	2%	0%
1999	2%	0%
2000	2%	0%
2001	5%	0%
2002	5%	0%
2003	10%	10%

Table 5. Assumed Characteristics Of Fuel Cell Vehicles

	PEM FC Bus	PEM FC Car
Fuel economy	52 scf H2/mile = 6.9 mpg Diesel equivalent [a]	71.4 mpg gasoline equiv.[b]
Miles/yr	50,000[c]	11,140[d]
Fuel Storage	H2 gas @3600 psi	H2 gas @5000 psi
Hydrogen stored onboard (scf)	13,000[a]	1200
Range (mi)	250[a]	250
Energy use per year (GJ/yr)[e]	976	20
Hydrogen use per year (million scf/yr)[f]	2.60	0.056

a. Based on the efficiency of the Ballard Phase II PEMFC bus (Larson, Worrell, and Chen 1996). The mile per gallon gasoline equivalent efficiency for a fuel cell vehicle is estimated assuming that 1 gallon of gasoline contains 0.1308 GJ (HHV) and that 1 scf of hydrogen contains 362 kJ (HHV).

b. Based on estimates by Delucchi for a PEMFC automobile (Ogden, Larson and Delucchi 1994).

c. Typical annual mileage for a bus in the LA Basin (E. Chaiboonma, LA Metropolitan Transit Authority, private communications 1995, 1996).

d. Typical annual mileage for a passenger car in the LA Basin. (R. George, SCAQMD, private communications 1995, 1996).

e. Energy use was estimated assuming that the HHV of gasoline is 0.1308 GJ/gallon.

f. Hydrogen use was estimated based on the HHV of hydrogen,
362 GJ = 1 million scf

Table 6. Fuel Cell Vehicles And Hydrogen Use

Hydrogen Use	FCVs refueled/day	Total Fleet Fueled
1 million scf H2/day	800 FCV cars/day	Total fleet of 6500 FCV cars
	80 FC Buses/day	Total fleet of 140 FCV Buses

Table 7. Assumed Energy Prices in Southern California

Application	Annual Average Electricity Cost ($/kWh)
Onsite Reforming Station Pipeline Hydrogen Station LH2 Station	7.2 cents/kWh
Onsite Electrolysis Station Continuous Operation Off-peak Operation	 4.8 cents/kWh 3.0 cents/kWh

Source: Southern California Edison

Natural Gas Price	$2.8/GJ

This is the price of natural gas delivered to a CNG vehicle station.
Source: Southern California Gas Company

Water Price	$0.0035/gallon

Source: Los Angeles Department of Water and Power

Table 8. Comparison of Projected Vehicle Performance and Lifecycle Cost

	Urban Buses		Mid-size automobiles	
	PEM FC Bus	Diesel Bus	PEM FC Car	Gasoline ICEV
Efficiency	6.9 mpg Diesel equiv.[a] = 52 scf/mile	3.5 mpg Diesel[c]	71.4 mpg gasoline equiv.[b]	26 mpg[b]
Miles/yr	50,000[c]	50,000[c]	11,140[d]	11,140[d]
Fuel Storage	H2 gas @3600 psi	Diesel Fuel	H2 gas @5000 psi	Gasoline
Range (mi)	250	250	250	400
Vehicle lifetime (years)	15	10	13.4[b]	10.7[b]
Purchase price ($)	325,000	237,000	24,550[b]	17,976[b]
Annual Maintenance Costs ($/year)	7438[e]	7438[e]	372[b]	396[b]

a. Based on the efficiency of the Ballard Phase II PEMFC bus (Ballard Power Systems, private communications 1995, 1996). The mile per gallon equivalent efficiency for a fuel cell vehicle is estimated assuming that 1 gallon of gasoline or Diesel contains 0.1308 GJ (HHV) and that 1 scf of hydrogen contains 362 kJ (HHV).

b. Based on estimates by Delucchi for mid-size (Ford Taurus) PEM fuel cell and gasoline automobiles (Ogden, Larson and Delucchi 1994).

c. Based on typical annual mileage and fuel use for a bus in the LA Basin (E. Chaiboonma, Los Angeles Metropolitan Transit Authority, private communications 1995).

d. Typical annual mileage for a passenger car in the LA Basin. (R. George, SCAQMD, private communications 1995, 1996).

e. For the Diesel bus, this includes annual maintenance plus upgrades at 3 and 8 years, and a major overhaul at 5 years. The maintenance for the PEM fuel cell bus is assumed to be the same (E. Larson et.al 1995).

Figures

Figure 1. Hydrogen production via steam reforming of natural gas.

Figure 2. "Conventional" steam methane reformer with long tubes and radiative heating.

Figure 3. Equilibrium methane conversion in steam reforming as a function of reformer operating pressure and temperature. Acheiving the same conversion of methane to hydrogen at higher pressure requires higher temperature.

Figure 4. A compact, tubular steam methane reformer developed for fuel cell applications, with convective heat transfer.

Figure 5. The installed capital cost of conventional small scale steam methane reformers vs. hydrogen production capacity.

Figure 6. Comparison capital cost of fuel cell reformers and conventional steam methane reformers vs. hydrogen production capacity.

Figure 7. Diagram of a) a conventional steam reformer for industrial applications, b) a fuel cell reformer coupled to a fuel cell, c) a fuel cell type reformer with compression and PSA clean-up for stationary hydrogen production.

Figure 8. Capital cost contributions of various components in a conventional small scale steam reforming system.

Figure 9. Capital cost of small scale pressure swing adsorption (PSA) systems as a function of PSA gas inlet flow rate.

Figure 10. Capital cost of a fuel cell reformer plus compression and PSA clean-up compared to a conventional steam methane reformer vs. hydrogen production capacity.

Figure 11. Impact of reducing the capital cost of small scale steam reformers on the delivered cost of hydrogen transportation fuel.

Figure 12. Capital cost of small scale hydrogen production systems: a) conventional small scale steam methane reforming system, b) fuel cell steam methane reformer with compression and PSA clean-up, c) POX with PSA clean-up.

Figure 13. Capital cost of PSA units for POX and SMR systems vs. hydrogen production rate.

Figure 14. Cumulative number of ZEV automobiles mandated for the LA Basin under the original and revised ZEV mandates.

Figure 15. Projected hydrogen demand for fuel cell vehicles in the LA Basin 1998-2010.

Figure 16. Map of existing and potential hydrogen supplies in the LA Basin

Figure 17. Near term hydrogen supplies and projected hydrogen demand for ZEVs in the LA Basin

Figure 18. Delivered cost of hydrogen transportation fuel in Southern California.

Figure 19. Cost of hydrogen pipeline transmission vs. pipeline length and flow rate.

Figure 20. Lifecycle cost of transportation for PEM fuel cell and Diesel buses.

Figure 21. Bus stations in the LA area and potential hydrogen supplies.

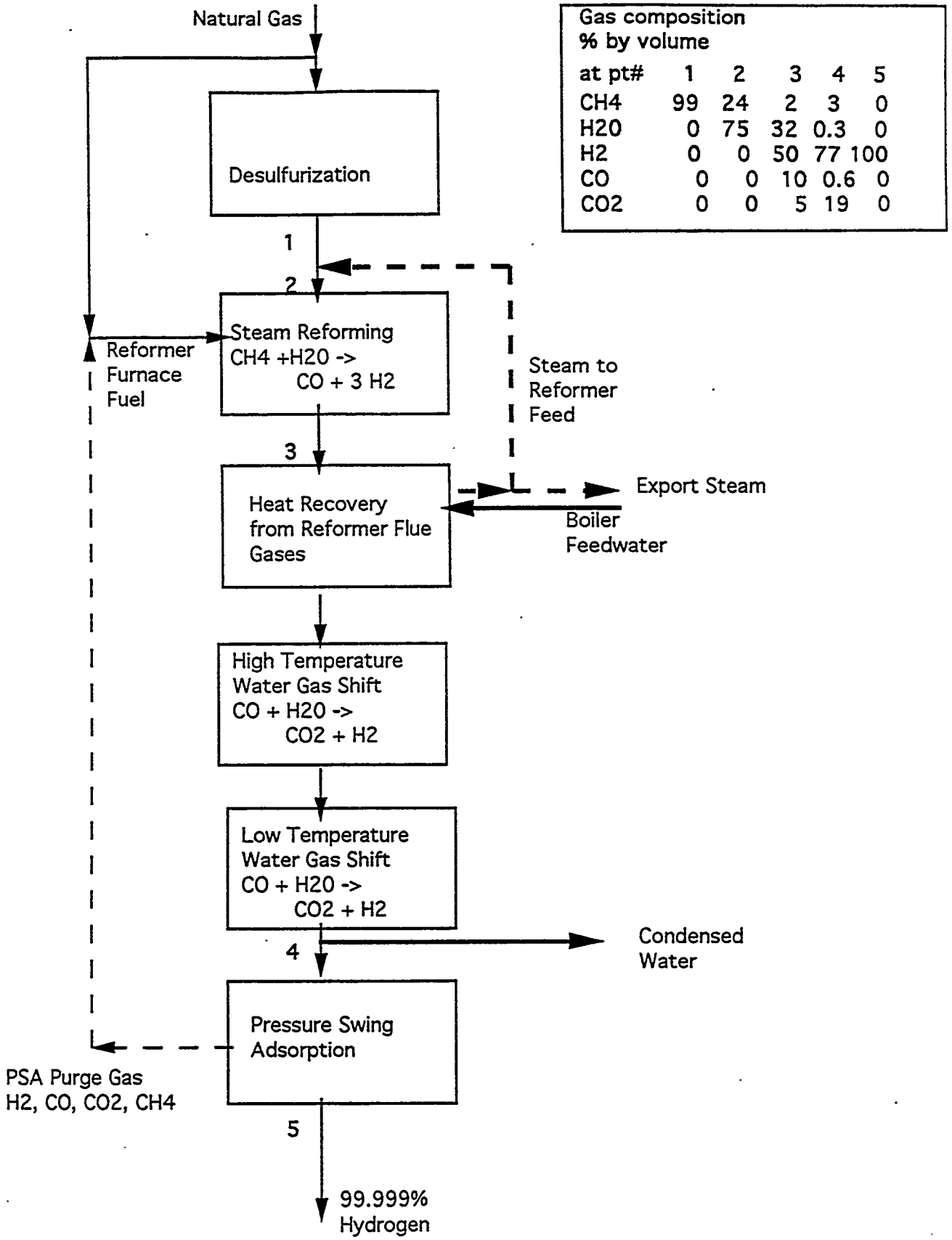
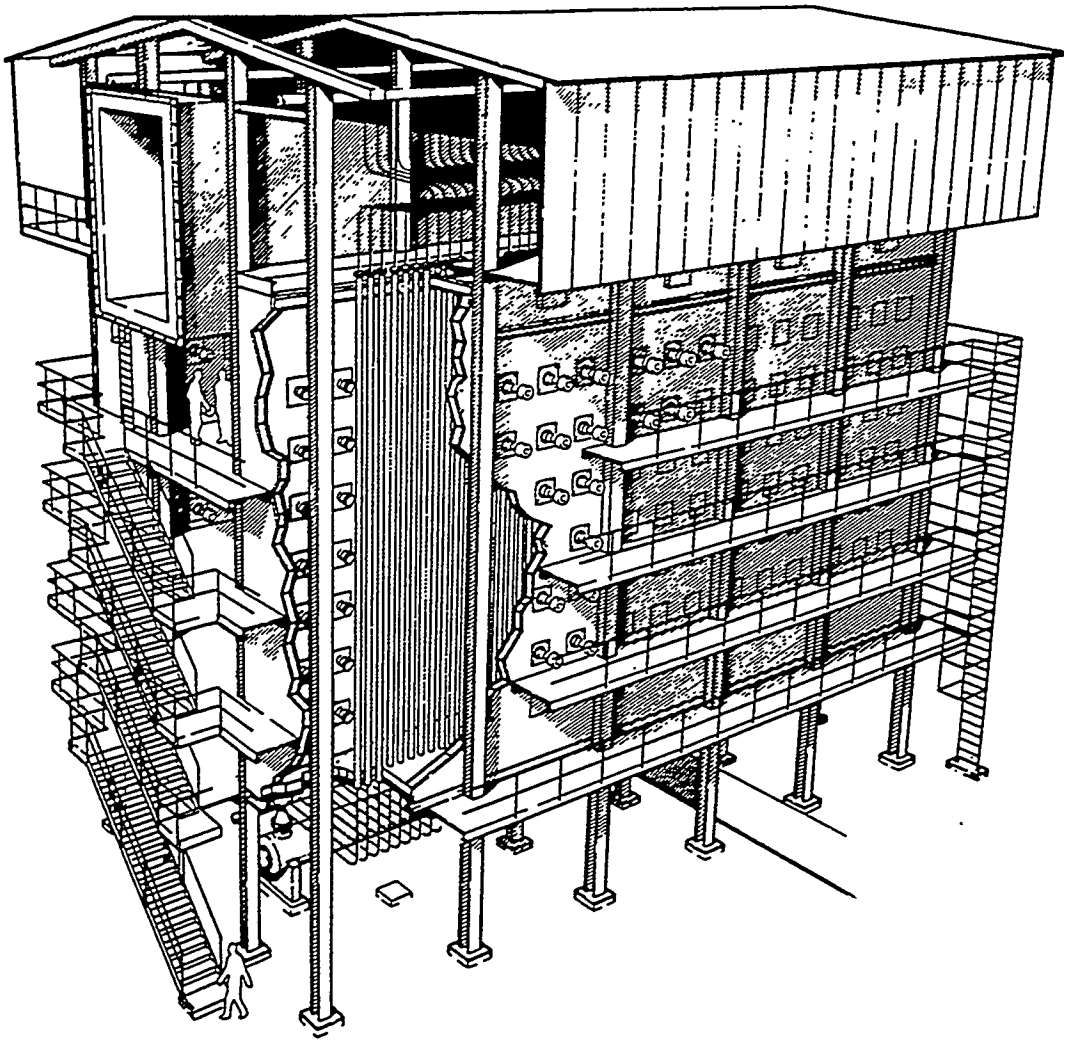


Figure 1. Process steps for production of hydrogen via steam reforming of natural gas, using PSA purification



. Reformer furnace. Tube and burner arrangement. Topsøe design. In the non-fixed end of the tubes thermal expansions of the tubes are absorbed by hairpins. The pre-heated gas (673–773 K) is distributed to the inlet hairpins (low alloy steel or stainless steel), and the exit gas (973—1173 K) passes *via* high alloy hairpins (incoloy etc.) to a bricklined collector system

Figure 2. "Conventional" steam methane reformer with long tubes and radiative heating.

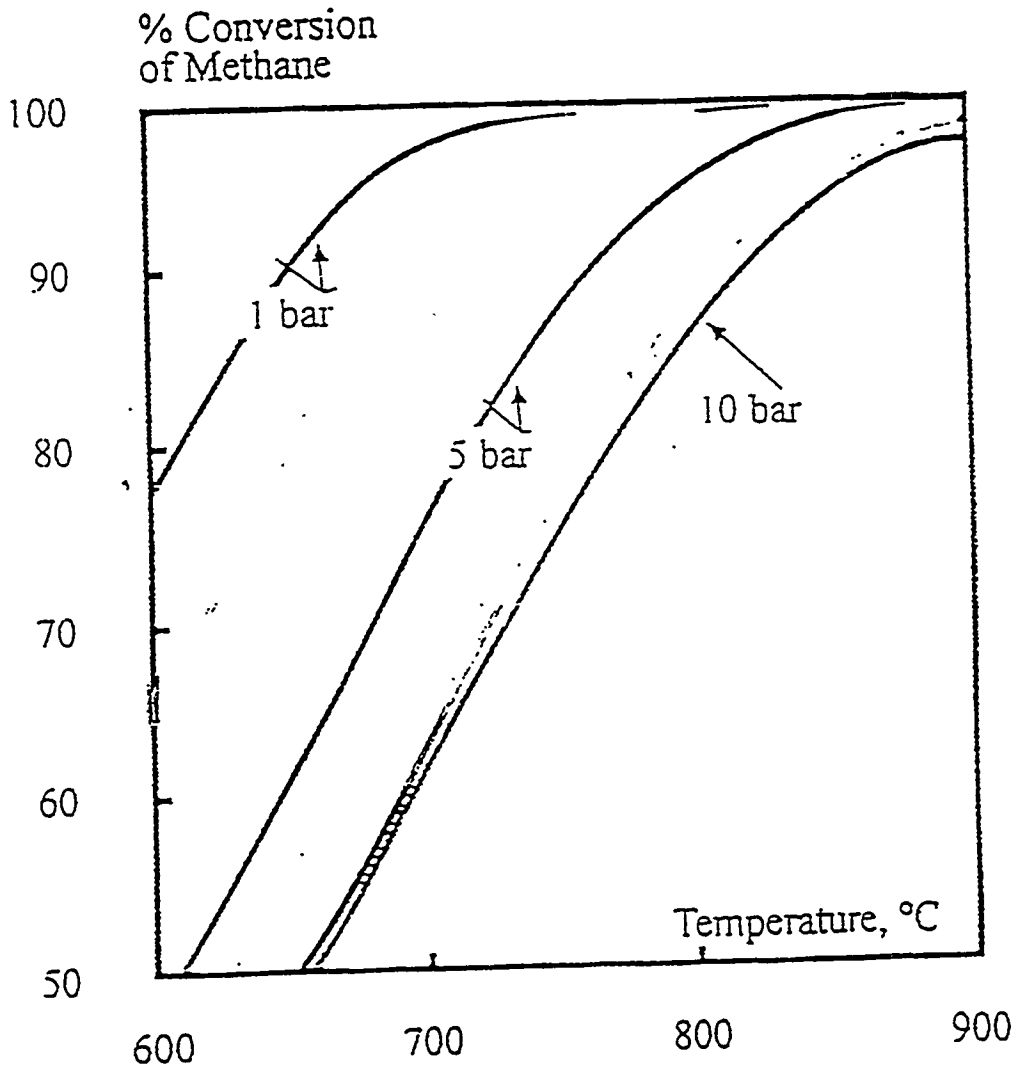


Figure 3. Equilibrium methane conversion in steam reforming as a function of reformer operating pressure and temperature. Acheiving the same conversion of methane to hydrogen at higher pressure requires higher temperature.

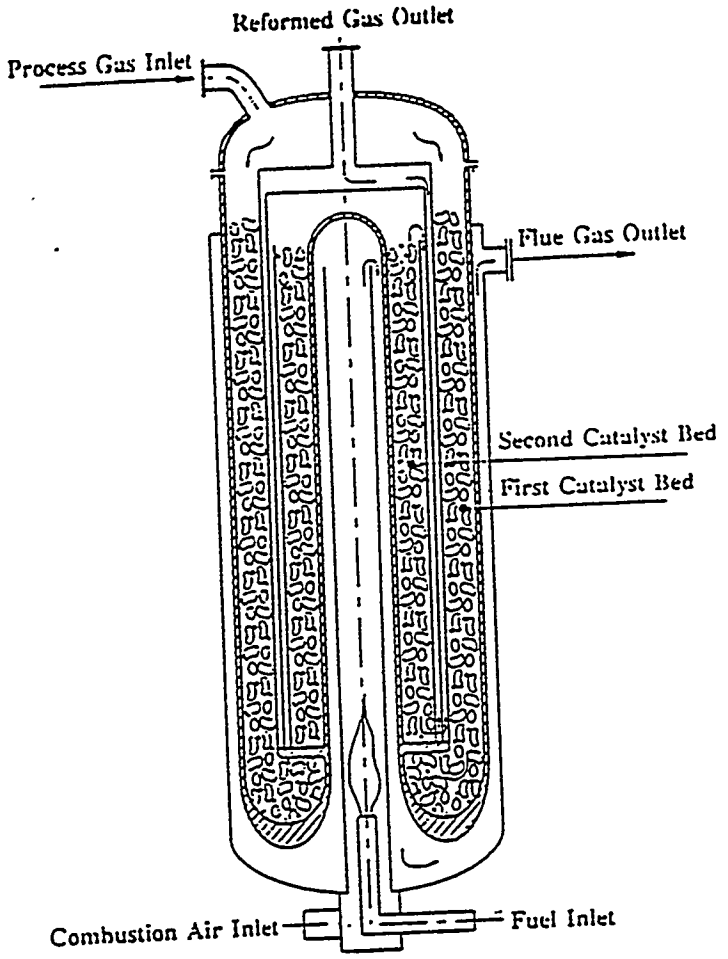


Figure 4. A compact, tubular steam methane reformer developed for fuel cell applications, with convective heat transfer.

Figure 5.
Capital Cost of Conventional Small Scale Steam Methane Reformers

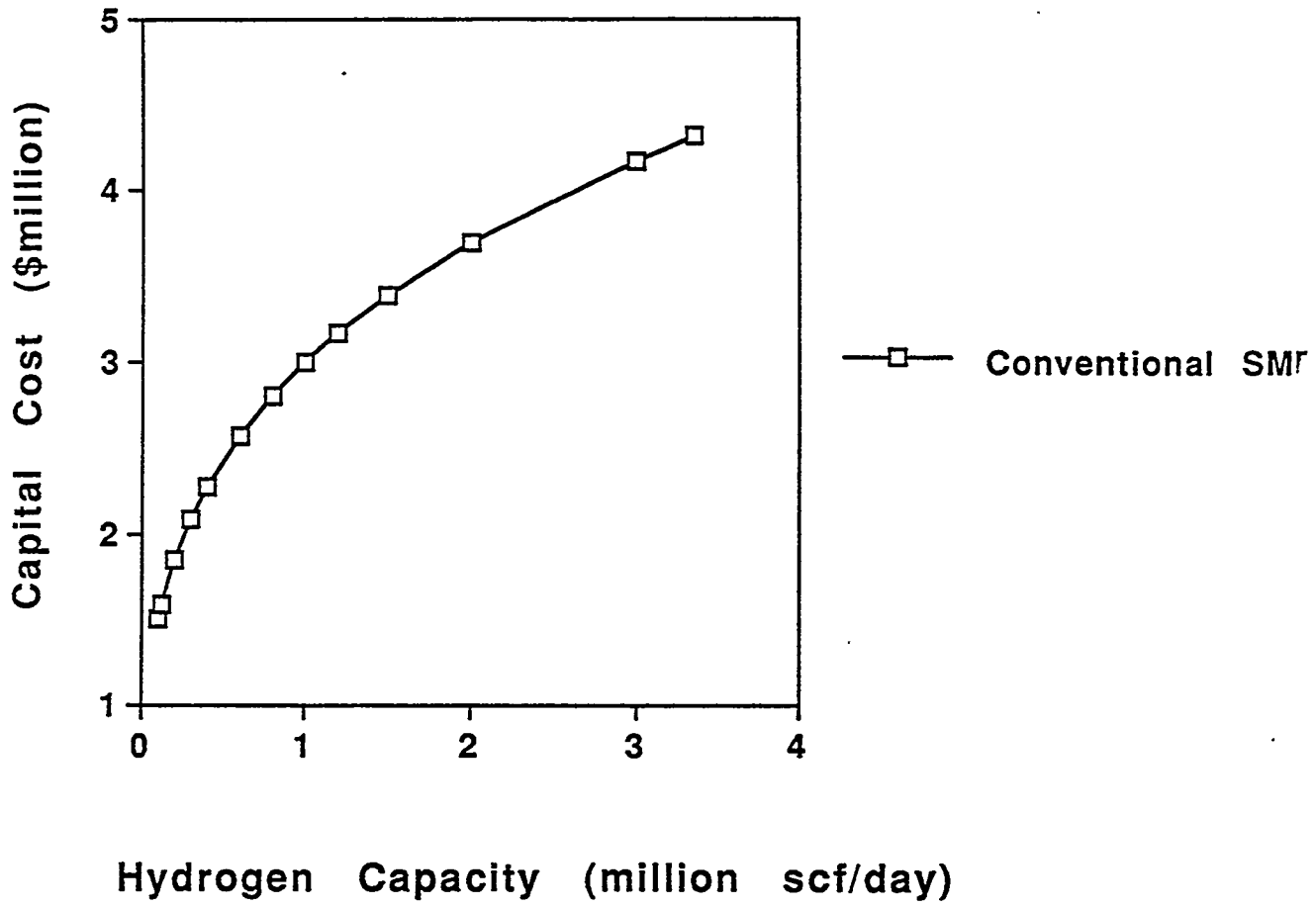


Figure 6.
Capital Cost of Small Scale Steam Methane Reformers

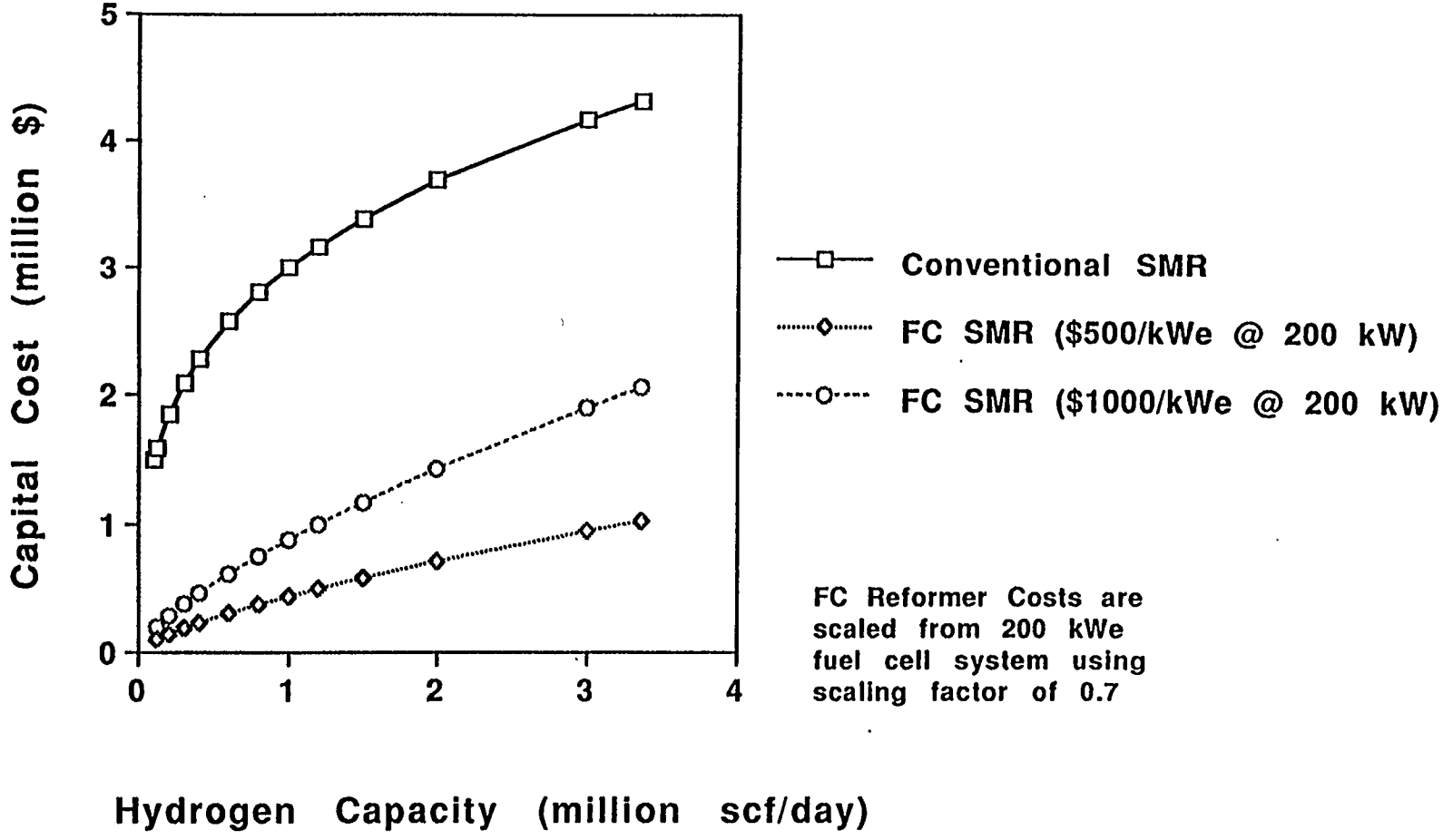
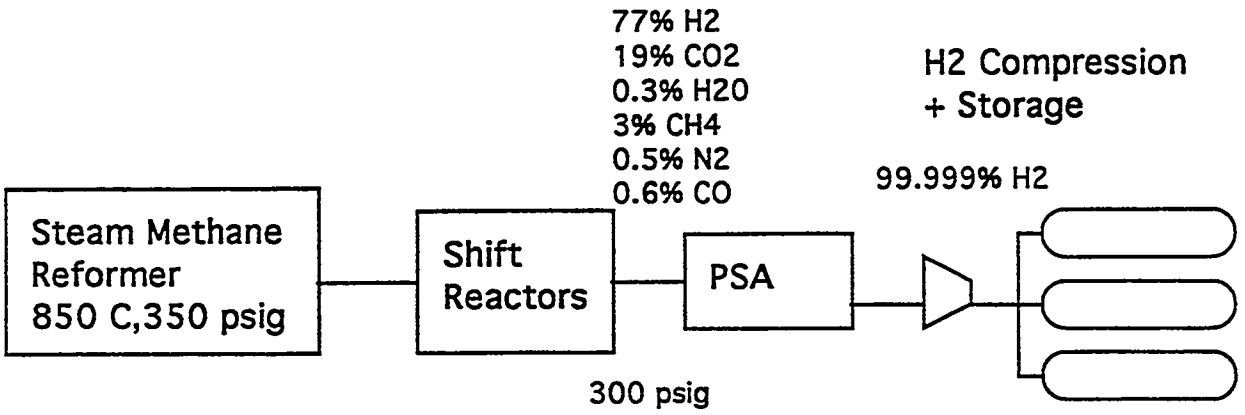
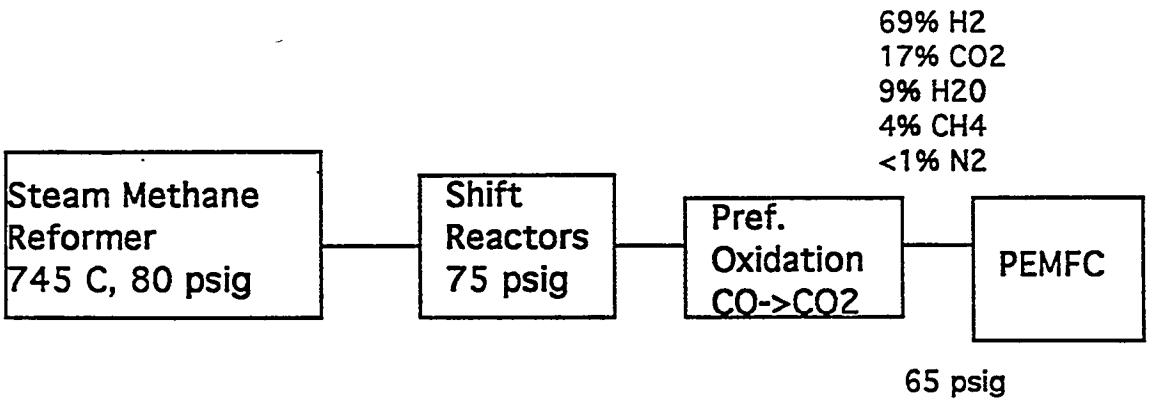


Figure 7.
STATIONARY H2 PRODUCTION FROM METHANE
WITH CONVENTIONAL AND FUEL CELL SMR

a) Conventional Small SMR



b) Fuel Cell SMR



c) Fuel cell SMR w/PSA

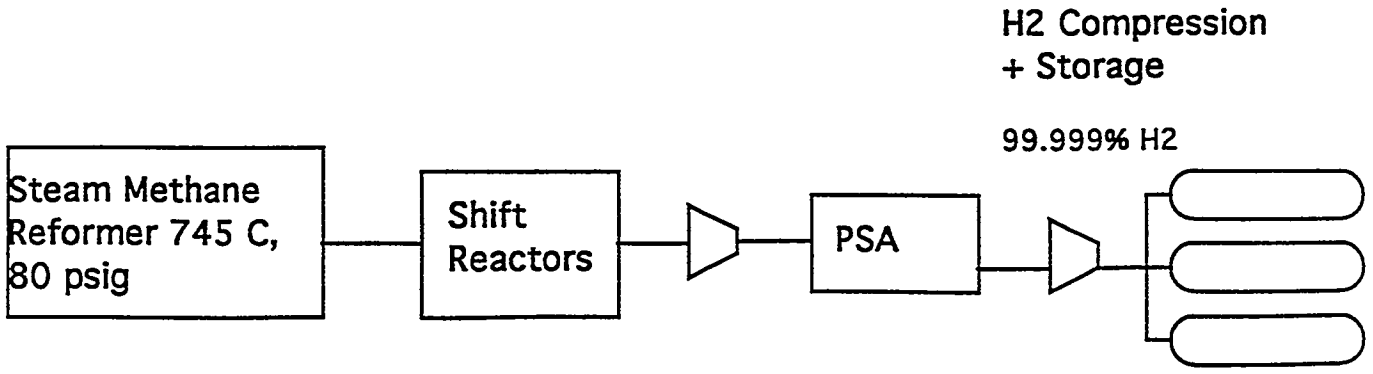
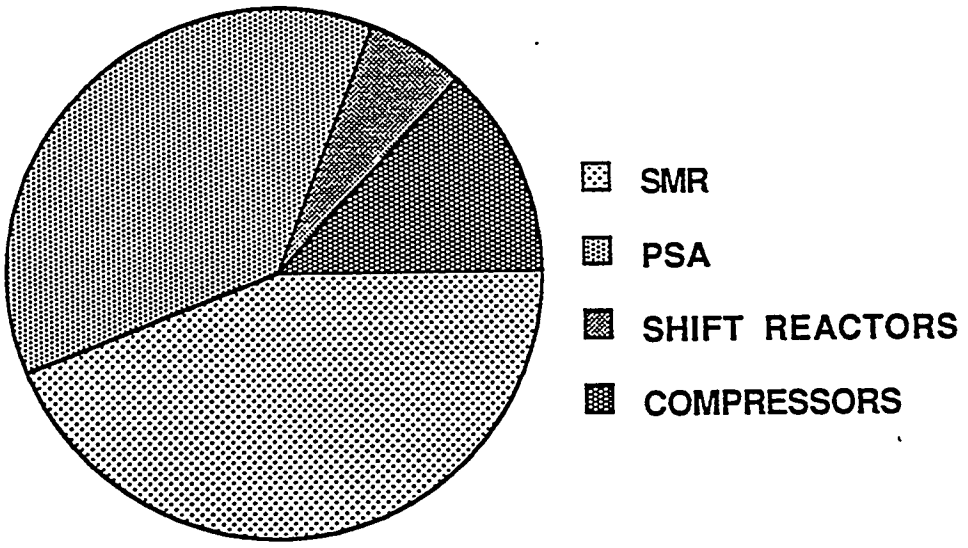


Figure 8.
CAPITAL COST COMPONENTS OF CONVENTIONAL SMALL SCALE STEAM METHANE REFORMER



Based on costs for a 1.6 million scf/day Reformer

Figure 9. Capital Cost of Small Scale PSA Units as Compared Total Hydrogen Plant Cost (Conventional SMR)

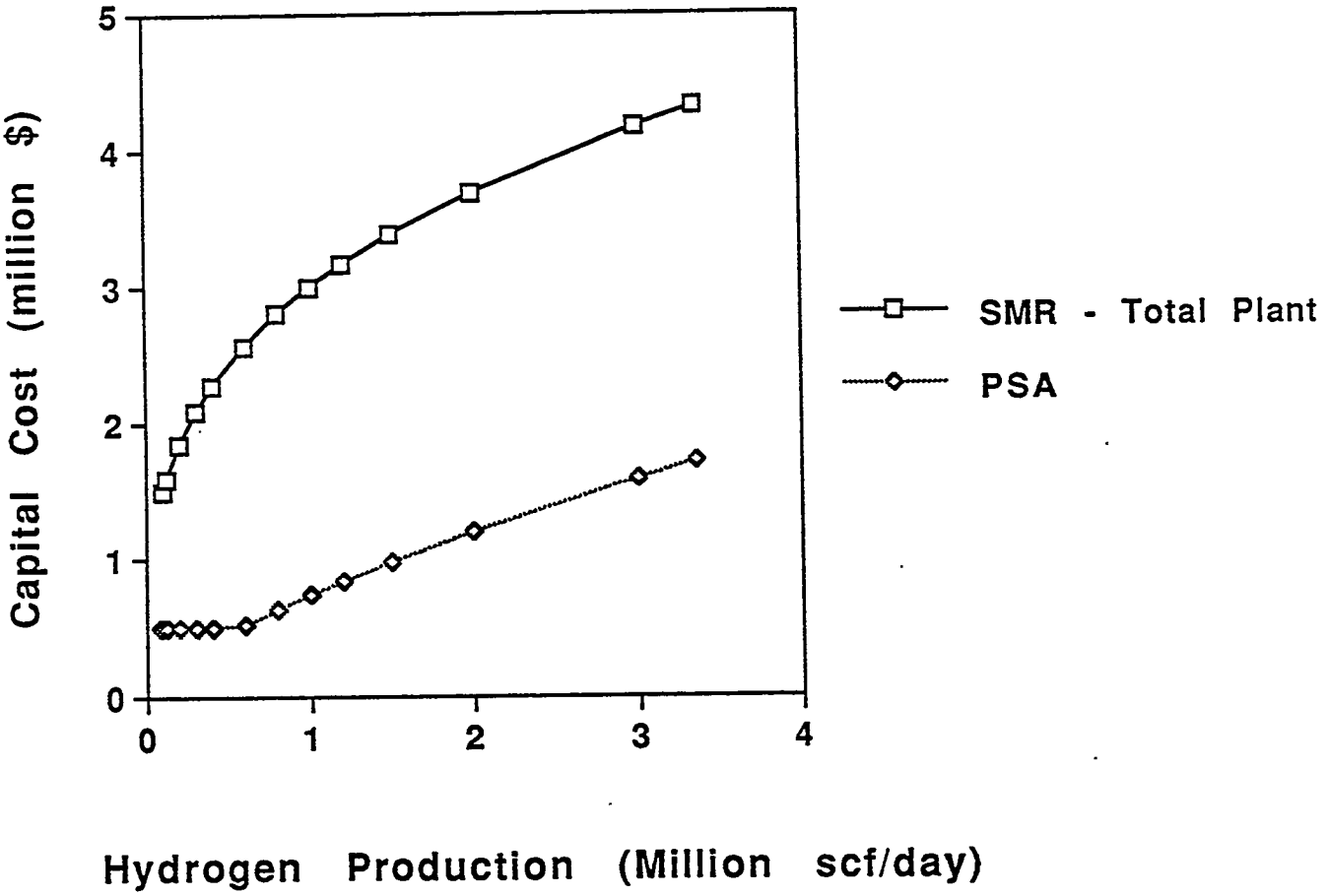


Figure 10.
Capital Cost of Small Scale Hydrogen Plants Based on Conventional and Fuel Cell Steam Reformers

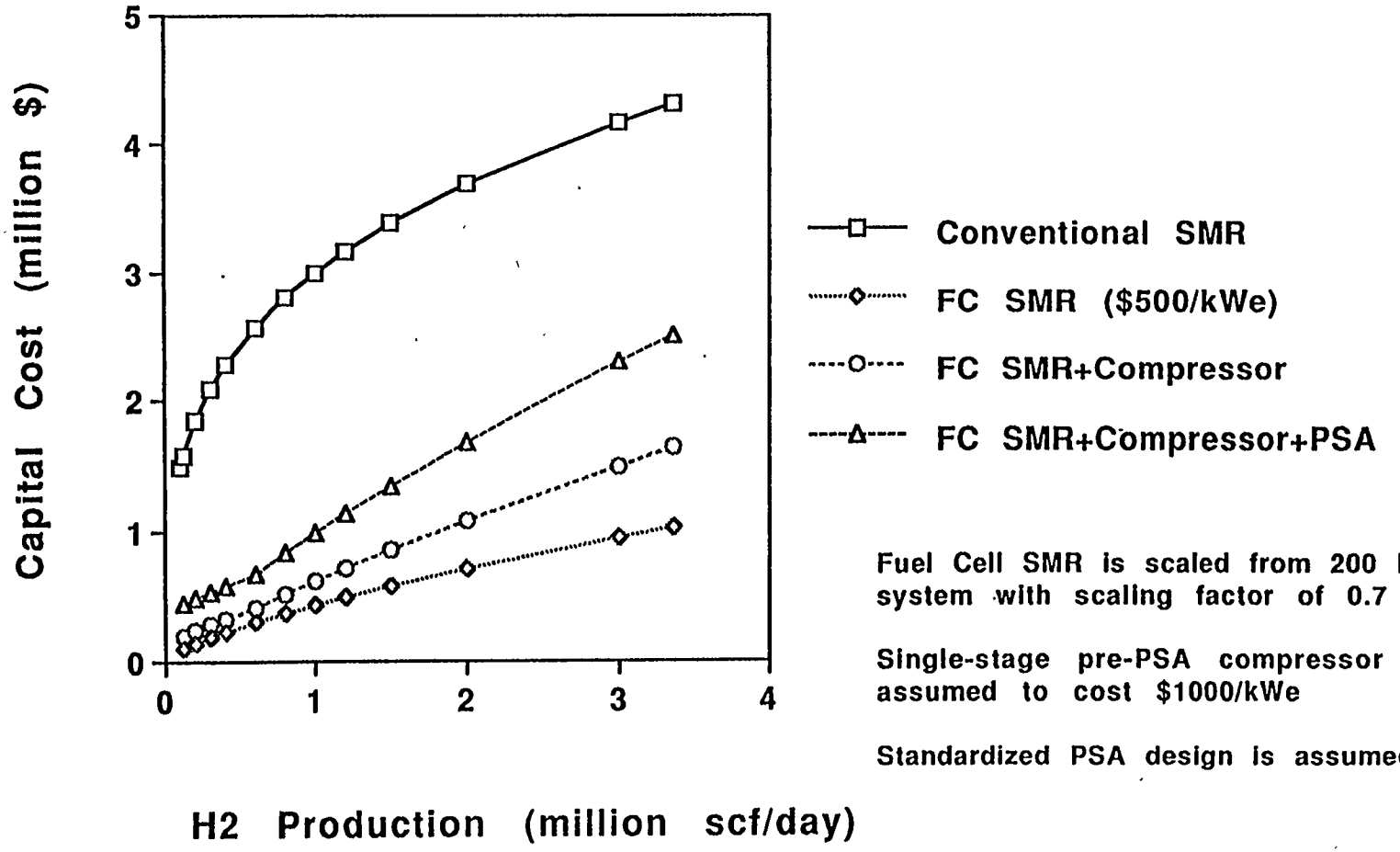


FIGURE 11a. REFUELING STATION WITH ONSITE REFORMING OF NATURAL GAS

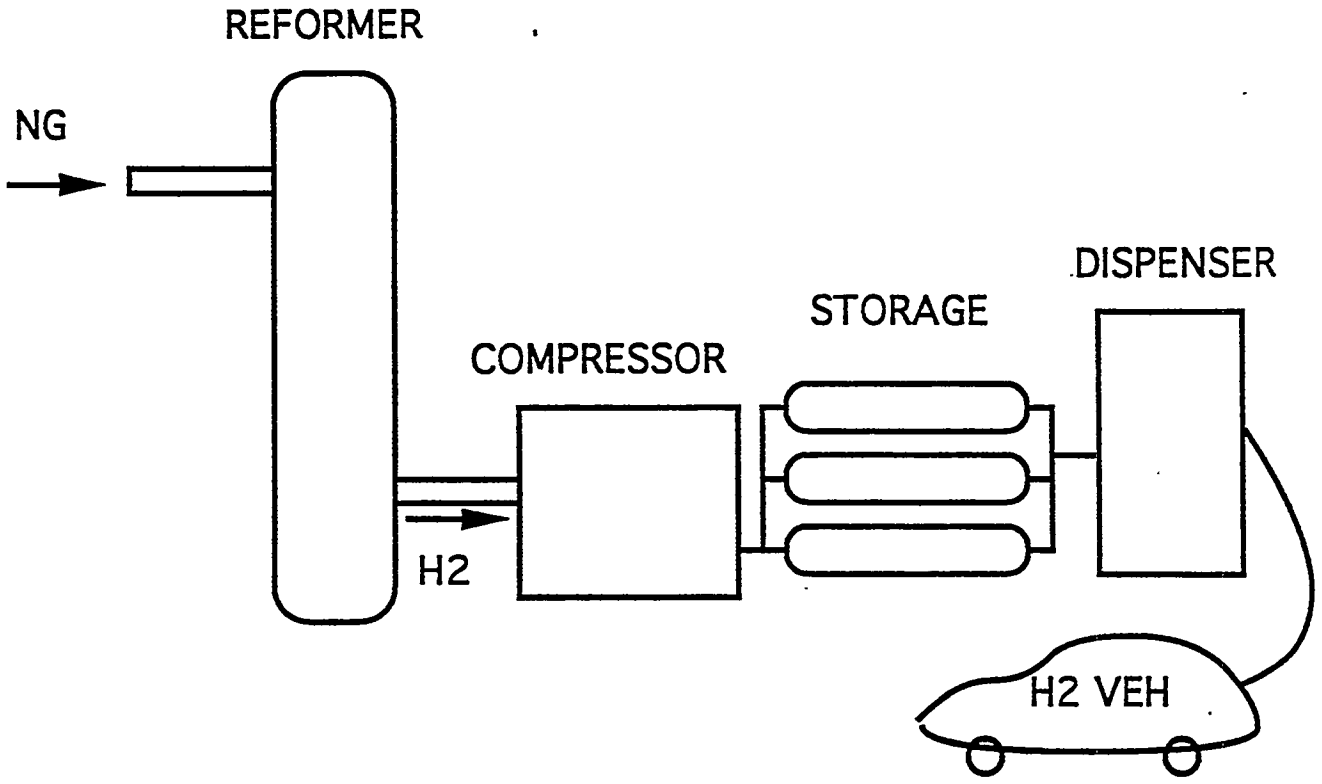


Figure 11b. Delivered Cost of Hydrogen Transportation Fuel: Onsite Reforming of Natural Gas

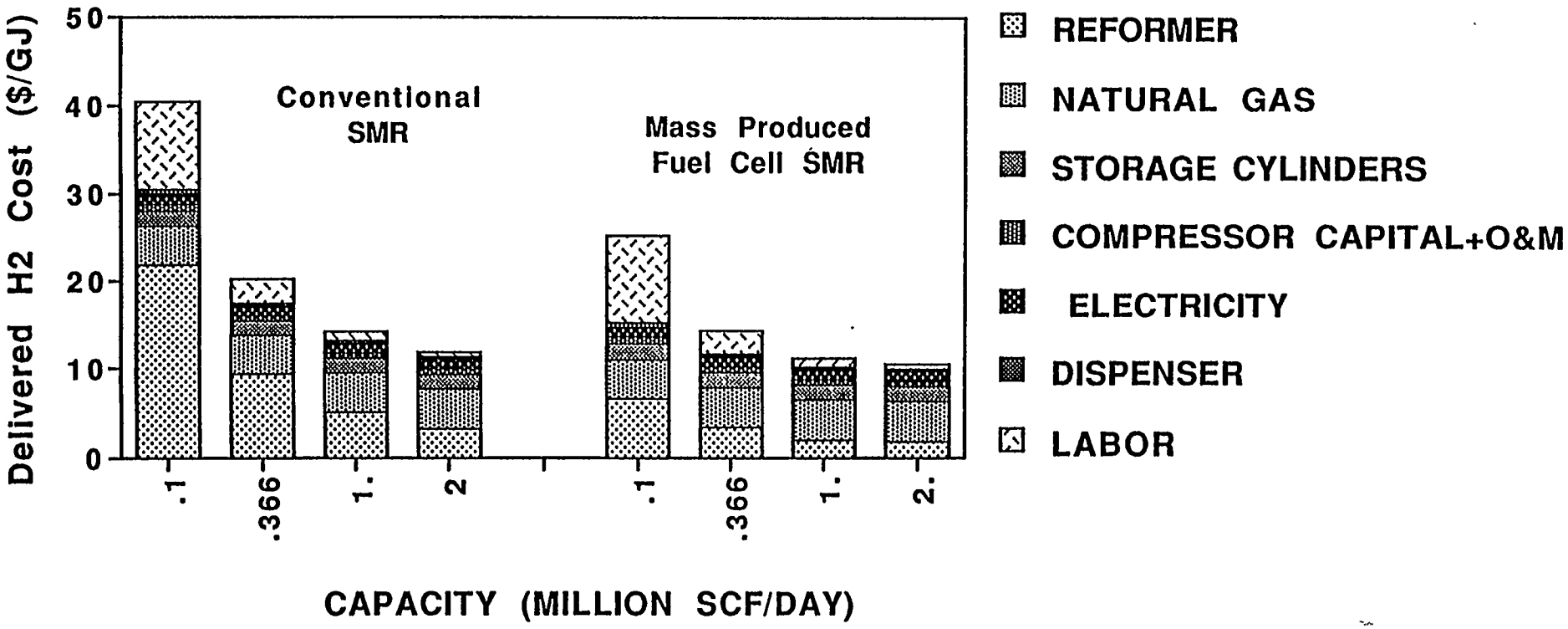


Figure 12.
Capital Cost of Small Scale Reformers

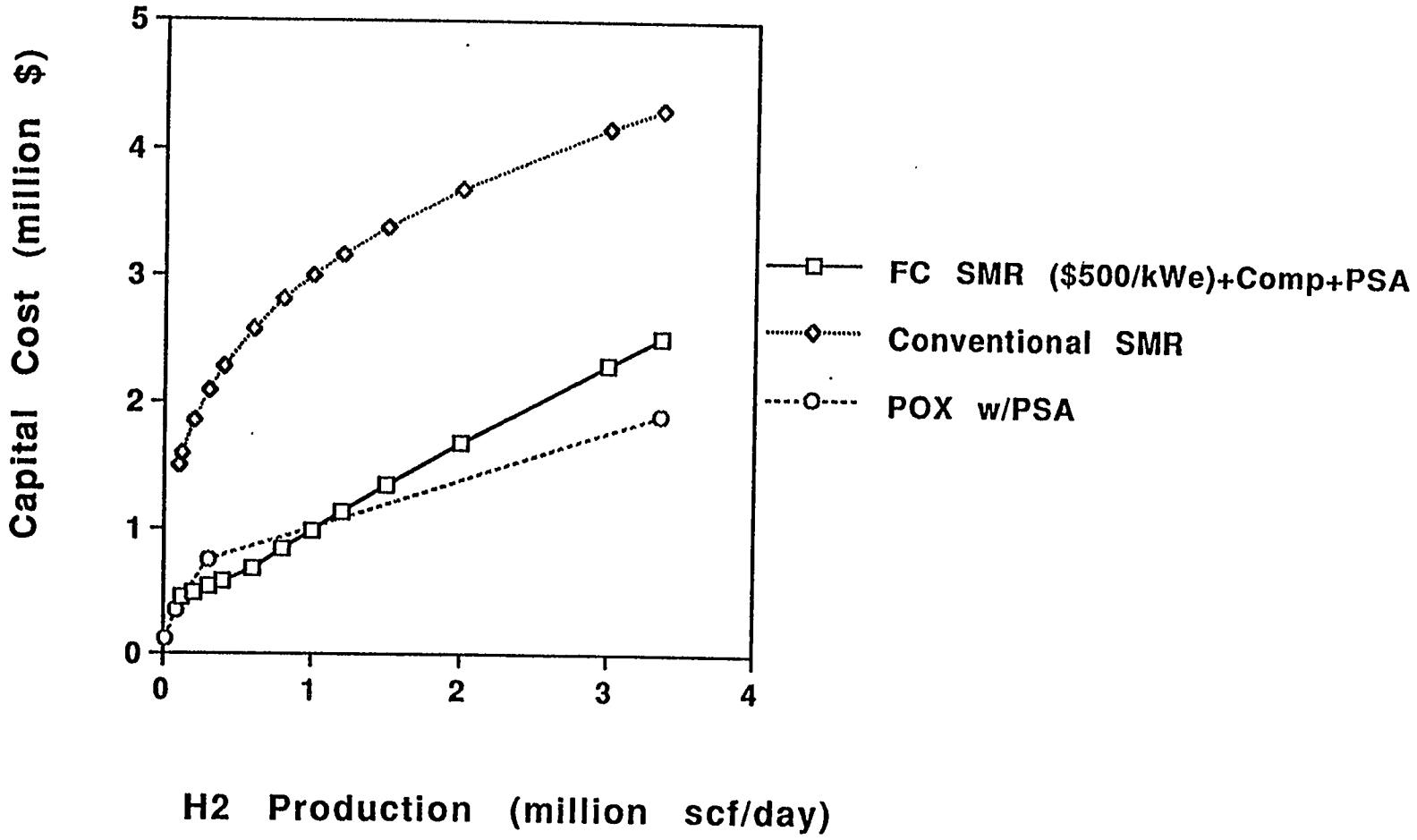
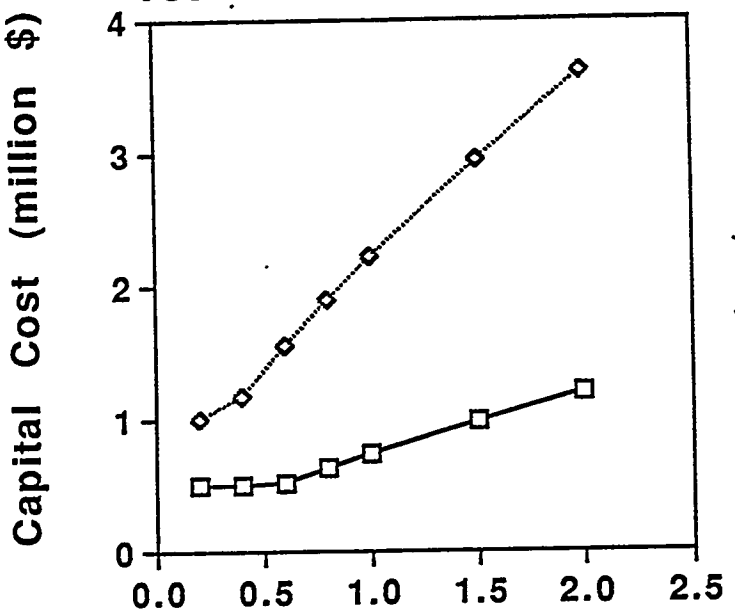


Figure 13.
Capital Cost of Small Scale PSA Units for Use with SMR and POX



For commercial one of a kind projects. Costs might be reduced 50% in mass production

Figure 14.
Projected Number of ZEV Passenger Cars in the LA Basin

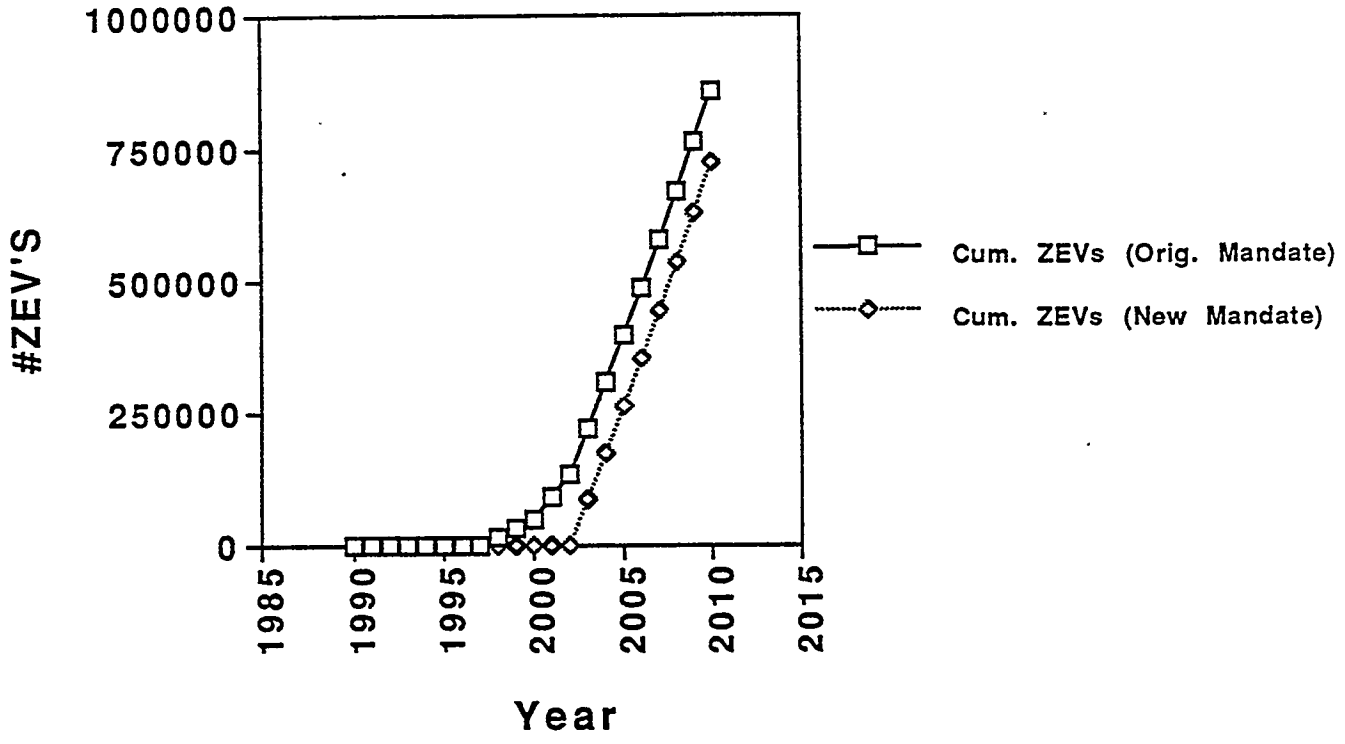
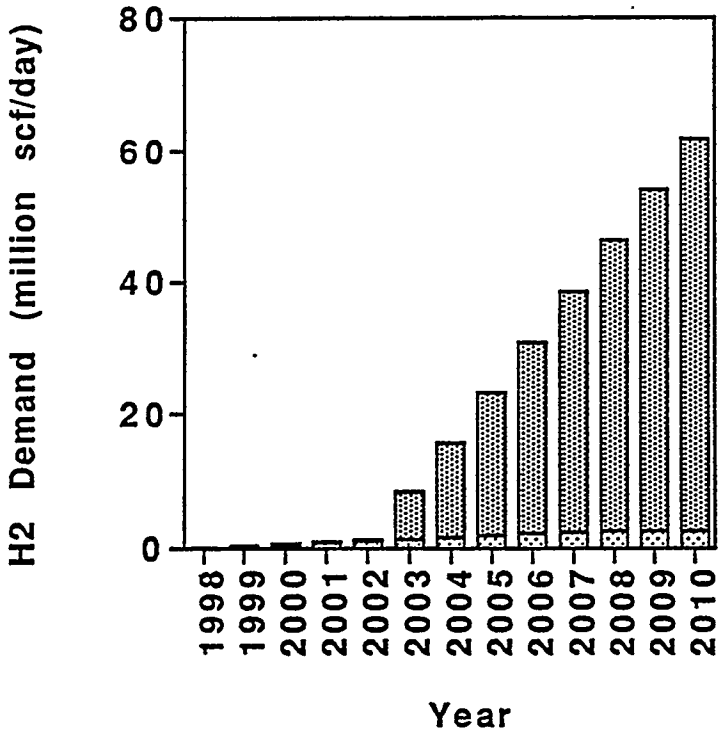


Figure 15.
Projected Hydrogen Demand for Fuel Cell Vehicles in the LA Basin



10% of New Buses = FCVs starting in 1998

5% of New Cars = FCVs starting in 2003

H2 for Buses

H2 for Cars

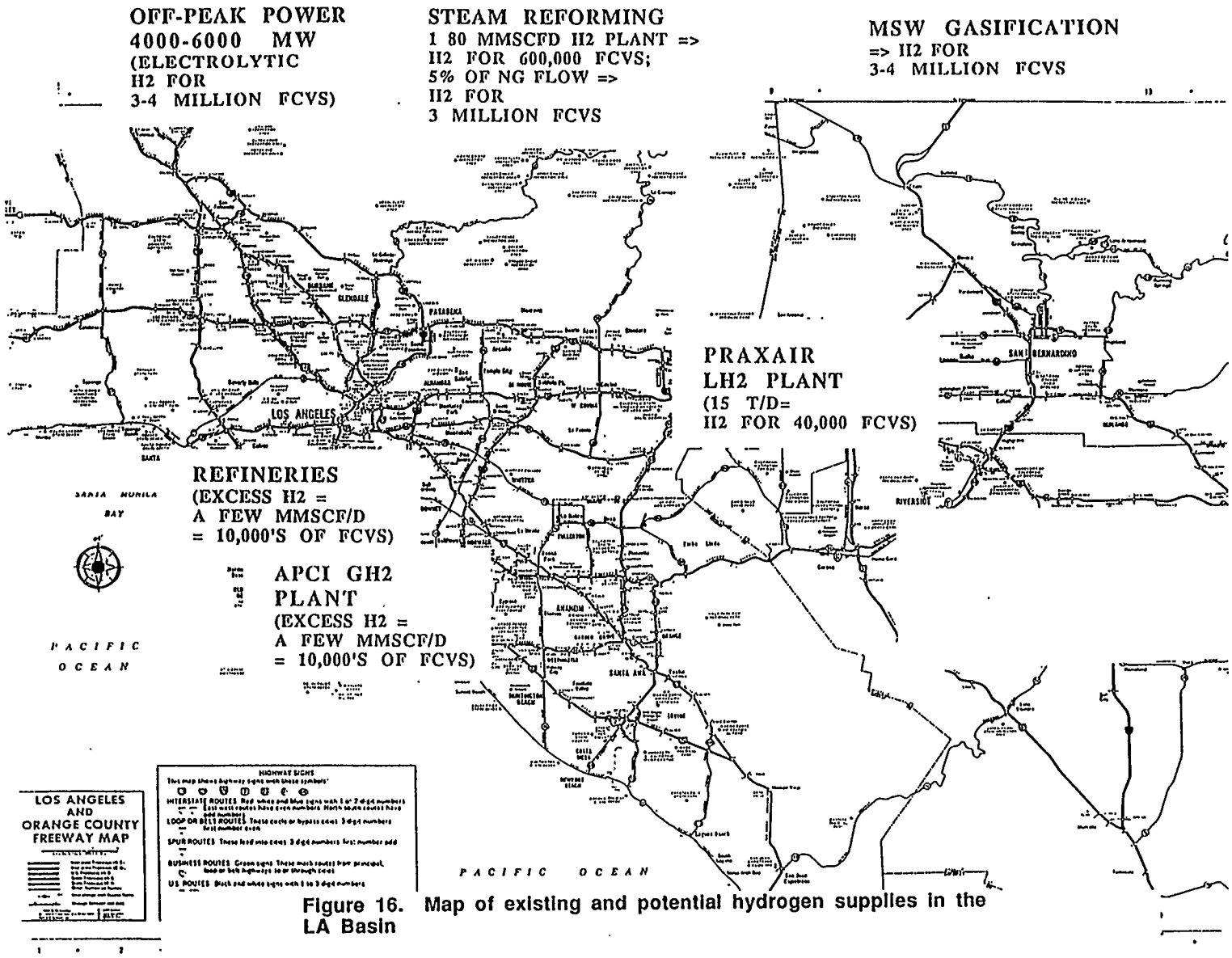


Figure 16. Map of existing and potential hydrogen supplies in the LA Basin

Figure 17.
Near Term Hydrogen Supplies and Projected
Hydrogen Demand in the LA Basin

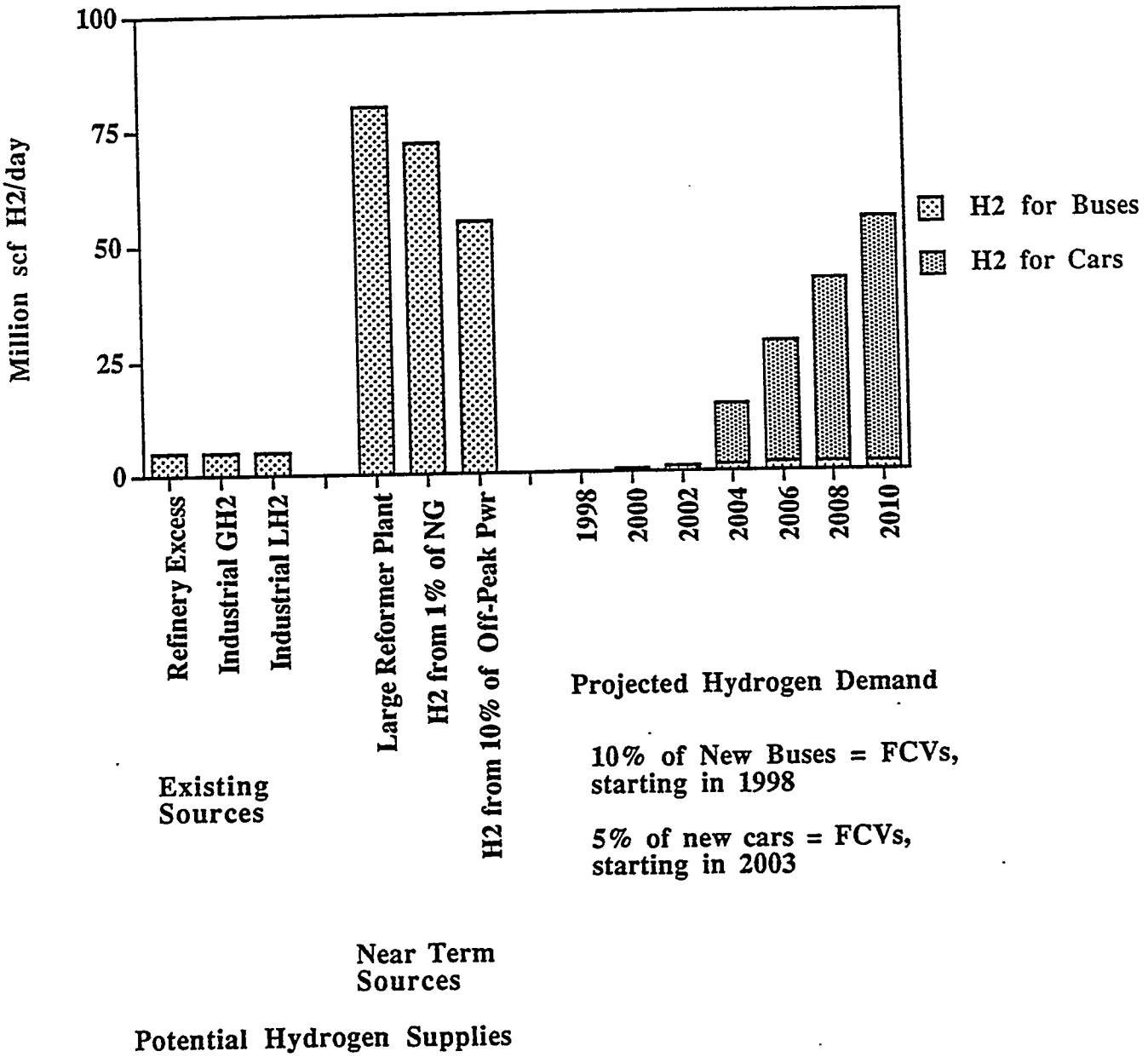


FIGURE 18. DELIVERED COST OF HYDROGEN TRANSPORTATION FUEL IN THE LA BASIN VS. STATION SIZE

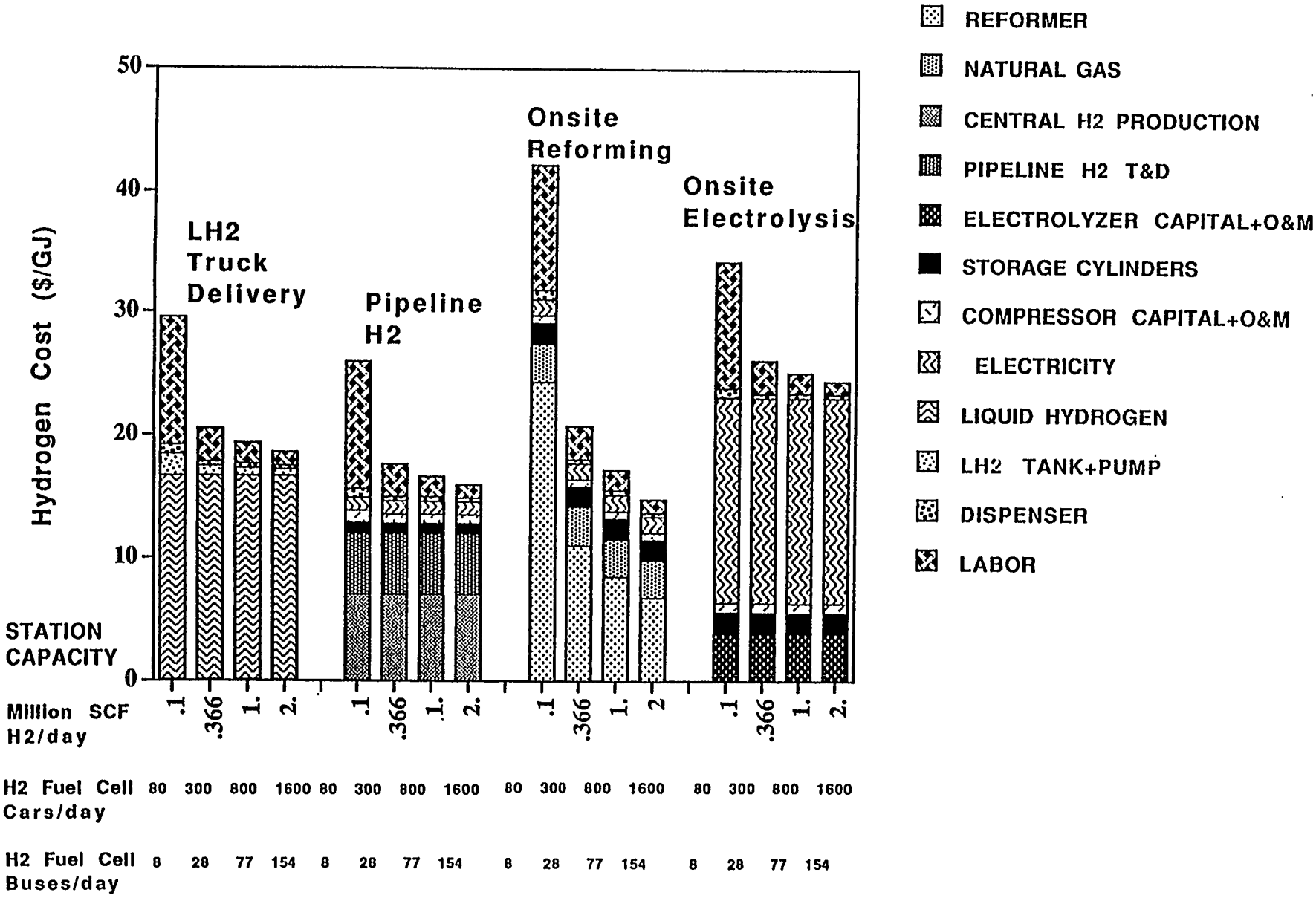
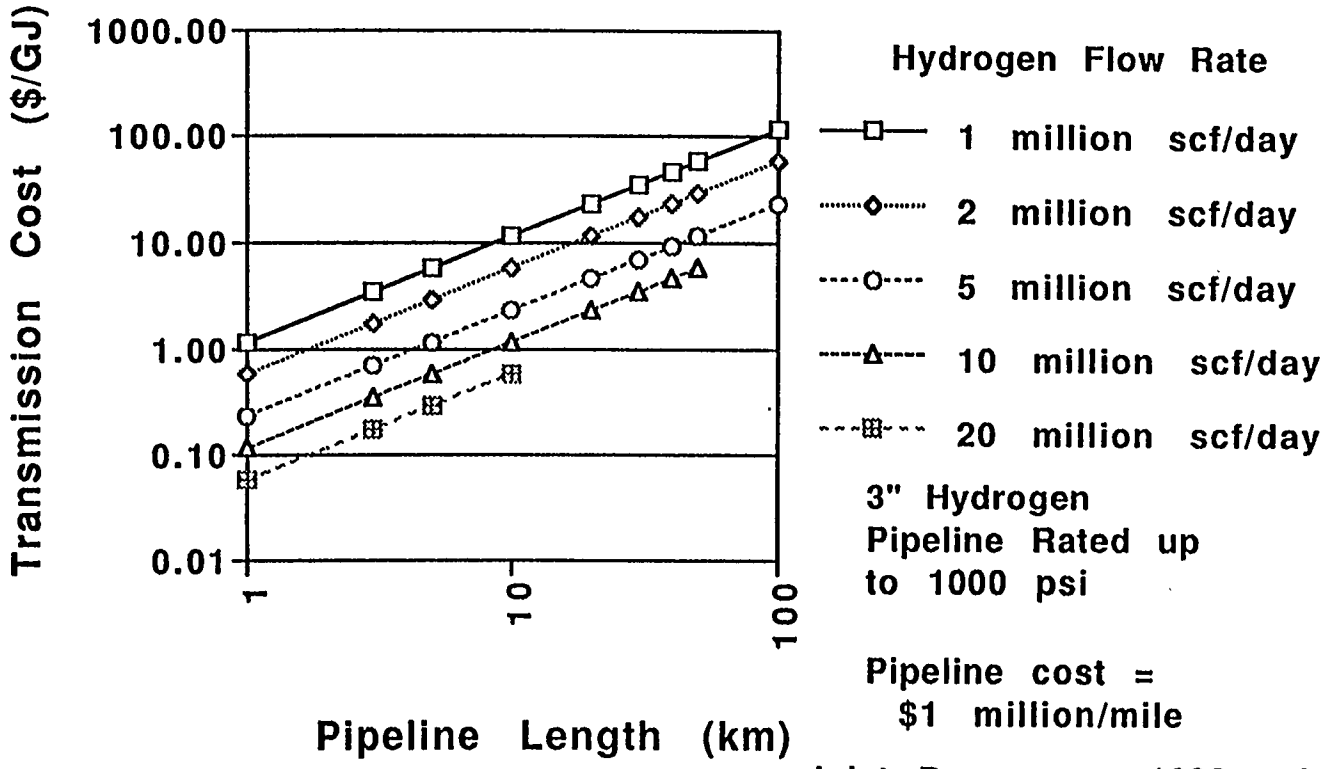


Figure 19.
Cost of Hydrogen Pipeline Transmission vs. Pipeline Length and Flow Rate



Cost of H2 Transmission
= $1.2 GJ x Length (km)/ Flow rate (million scf/day)

Figure 20.
Lifecycle Cost of Transportation
for PEMFC and Diesel Buses

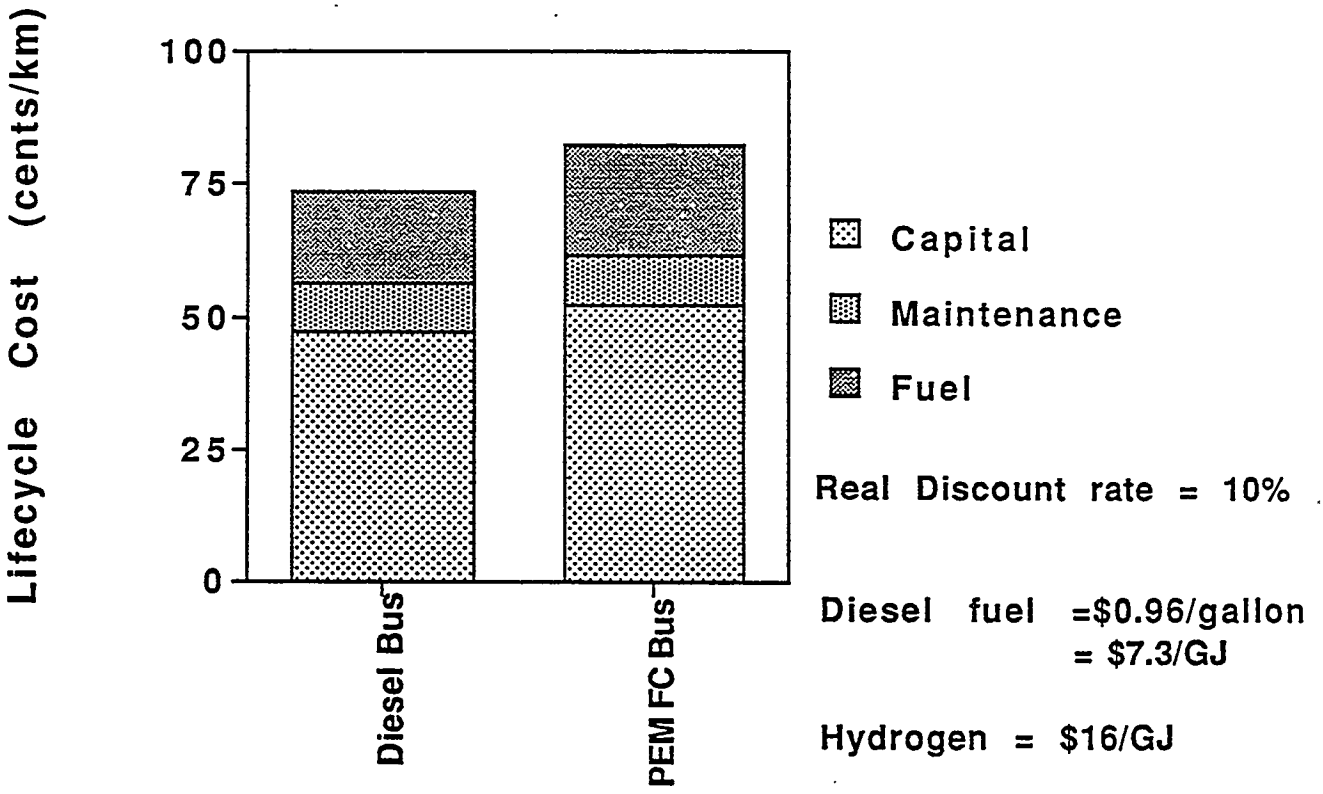
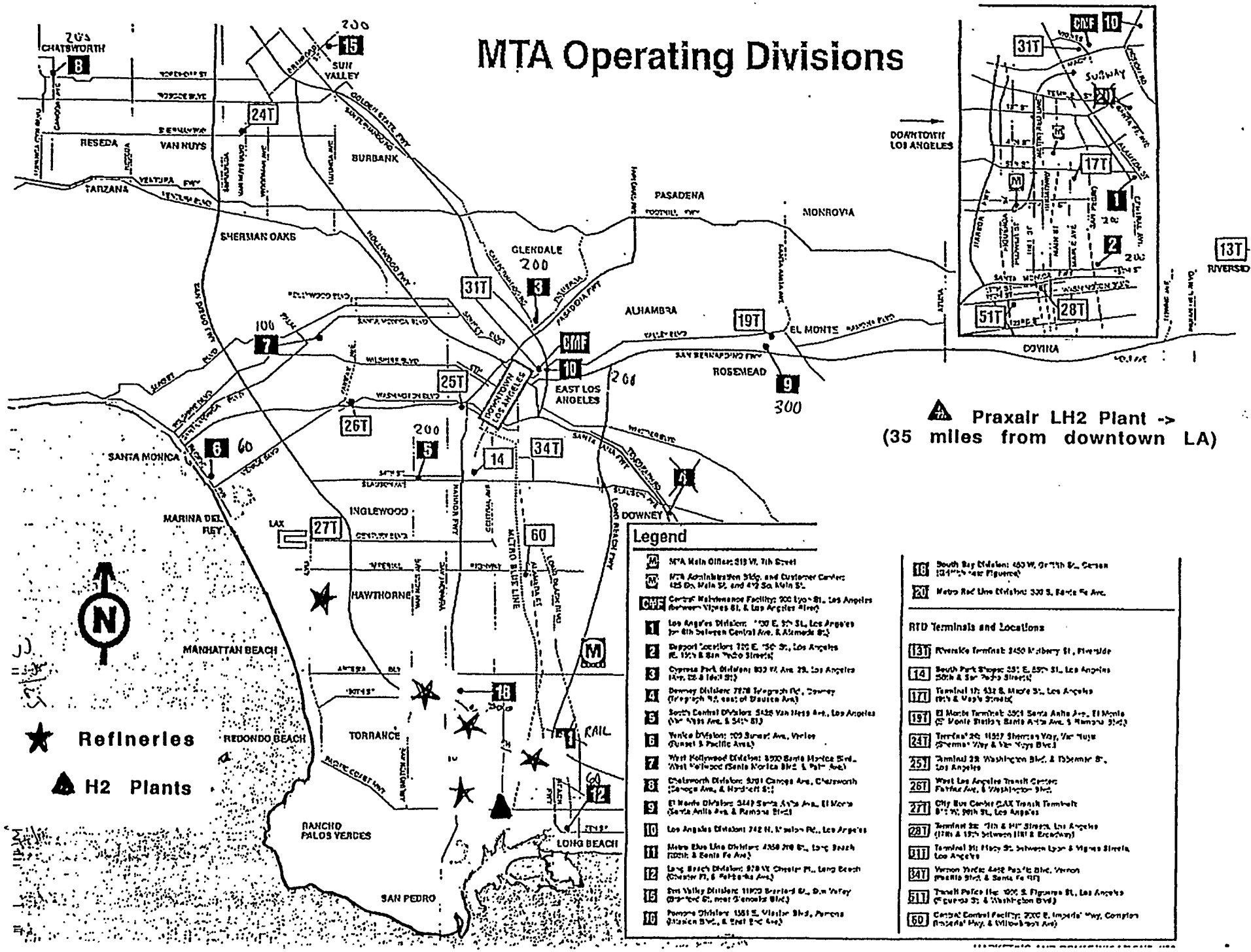


Figure 21. Los Angeles MTA Bus Depots and Potential Hydrogen Supplies



COUPLING RENEWABLES VIA HYDROGEN INTO UTILITIES: TEMPORAL AND SPATIAL ISSUES, AND TECHNOLOGY OPPORTUNITIES

Joseph J. Iannucci, Susan A. Horgan, James M. Eyer
Distributed Utility Associates
3170 Crow Canyon Place, Suite 140
San Ramon, CA 94583

Susan Schoenung
Longitude 122 West, Inc.
1010 Doyle Street, Suite 10
Menlo Park, CA 94025

Abstract

This paper discusses the technical potential for hydrogen used as an energy storage medium to couple time-dependent renewable energy into time-dependent electric utility loads. This analysis will provide estimates of regional and national opportunities for hydrogen production, storage and conversion, based on current and near-term leading renewable energy and hydrogen production and storage technologies. Appropriate renewable technologies, wind, photovoltaics and solar thermal, are matched to their most viable regional resources. The renewables are assumed to produce electricity which will be instantaneously used by the local utility to meet its loads; any excess electricity will be used to produce hydrogen electrolytically and stored for later use. Results are derived based on a range of assumptions of renewable power plant capacity and fraction of regional electric load to be met (e.g., the amount of hydrogen storage required to meet the Northwest region's top 10% of electric load).

For each renewable technology national and regional totals will be developed for maximum hydrogen production per year and ranges of hydrogen storage capacity needed in each year (hydroelectric case excluded). The sensitivity of the answers to the fraction of peak load to be served and the land area dedicated for renewable resources are investigated. These analyses can serve as a starting point for projecting the market opportunity for hydrogen storage and distribution technologies. Sensitivities will be performed for hydrogen production, conversion, and storage efficiencies representing current and near-term hydrogen technologies.

Step two is to estimate the electric resource available from renewables. For PV output vs time, we will use simple and intuitive models (e.g.)currently in use at Distributed Utility Associates for this task. We will perform simple hand analyses for hydro power.

- The amount of renewable resource must be considered differently for the four options:
- Hydroelectricity will be assumed to be nearly fully developed and site limited; thus we will assume constant electricity production at today's levels.
- Flat plate photovoltaics can use any quality of insolation and thus are theoretically feasible throughout the regions. We are likely to use an upper bound of full annual energy consumption in every region for photovoltaics. We will not include concentrating photovoltaics in the analysis.
- Solar thermal requires high levels of direct normal insolation, normally only available in the Southwest, California, and perhaps the South Central regions. We will assume that solar thermal could produce all of the load demand in those regions but none in the other regions.
- Wind is an enormous resource; several sources have estimated the high quality wind potential to be greater than the US electricity consumption nationally, but have shown regional variations; the Southeast is especially poor in wind resource. We have used regionally adjusted wind resource capacities to determine whether a region is resource or electric utility demand limited.

Develop hydrogen production from renewables estimation model

Accepted conversion rates for current hydrogen production systems will be used. A parametric conversion efficiency analysis will be performed, yielding the land area resource needed for hydrogen production to serve given annual electric utility loads.

Technology assumptions and specifications.

Summarize capabilities of current and near-term electrolysis technologies. Provide technical specifications for 1) the hydrogen production systems, 2) renewable technologies, and 3) the interfaces that control power to the grid and/or to the hydrogen system. A likely electrolytic system is the SPE approach.

Time-Dependent Load Mapping

Estimate electric load profile by geographic region. (The same geographic regions addressed earlier will be included.)

Data from specific utilities known to be interested in renewables would be ideal. Some possibilities are: Arizona Public Service, SCE Corp. PG&E, Niagara Mohawk, BPA, Georgia Power, Northern States Power.

The electric load growth in each region would be projected to the year 2010 and an assumption of a target renewables energy penetration will be used to size the renewables plants to supply that energy in each year.

Matching Renewables to Utility Load Patterns

Summarize and select technology characteristics for hydrogen storage and electricity production from hydrogen (fuel cells). Parameterize performance in terms of capacity, efficiencies, charge and discharge rates for current and near-term systems. As a starting point, we will use Office of Transportation Technologies projections for fuel cell performance.

Build or adapt a very simple model to estimate hydrogen conversion to electricity. Build a model to estimate the range of hydrogen storage required to reconcile electricity production capability to load pattern for a given geographic region and year. This will be a time-dependent model (8760 hours) that takes the full hourly transient nature of storage into account. The storage efficiency, electrolyzer efficiency, and fuel cell efficiency will be included in the energy balance

This task will bring together all the previous pieces. A parametric analysis will be used to show the size of hydrogen storage required and electrolyzer and fuel cell capacities to match power production to load for each region and renewable technology as a function of two assumptions:

- The land area of the renewable power plant,
- The percent of load assumed to be carried by renewables, from 100% of the load down to 10% (peak clipping).

For item a), we recognize the argument that the renewable resource can be either minimally sized to maximize the need for storage, or oversized so as to meet the extreme load and minimize the need for storage. The impacts on the need for storage are shown in the figure below, where S is storage size (in MBTU or MWh) and A is land area of renewables considered. Curves for each region/renewable resource combination will be created. (For hydroelectric power no such curves are required as mentioned above.)

For item b), we recognize that when renewables meet only a partial load, the size of storage is also affected, as shown in the figure below, where P is electric load. Similar storage capacity curves will be determined for each region/renewable resource combination.

Analysis, Interpretation and Documentation

From the results of the previous tasks, we will summarize and discuss trends in the findings regarding storage capacity needed by region.

5.Status of economic evaluation/systems analysis:

Tasks for follow-on economic analysis will be designed.

We are likely to find a wide range of hydrogen production capabilities among the renewables and a strong dependence on the amount of electric utility load we choose to address via hydrogen. The storage needs will vary even more dramatically since the patterns of match and mismatch will be regionally dependent as well as the absolute electric utility demand levels.

6.Projected Goal:

- Determine the technical potential for hydrogen as an energy storage medium to couple time-dependent renewable energy into time-dependent electric utility loads.
- Provide estimates of regional and national opportunities for hydrogen production
- Determine for each renewable technology national and regional totals for maximum hydrogen production per year

Determine ranges of hydrogen storage capacity needed in each year for each renewable (hydroelectric case excluded)

7. Major Barriers to Goals:

We do not fore see any barriers to completing this analysis.

References

Marion, William, and Urban, Ken. 1995. *User's Manual for TMY2s: Typical Meteorological years. Derived from the 1961-1990 National Solar Radiation Data Base.* Golden CO: National Renewable Energy Laboratory

Barnes, P.R., Van Dyke, J.W., Tesche, F.M., and Zaininger H.W. 1994. *The Integration of Renewable Energy Sources into Electric Power Distribution Systems,* ORNL-Technical Report 6775/V1 Oak Ridge, Tennessee: Oak Ridge National Laboratory

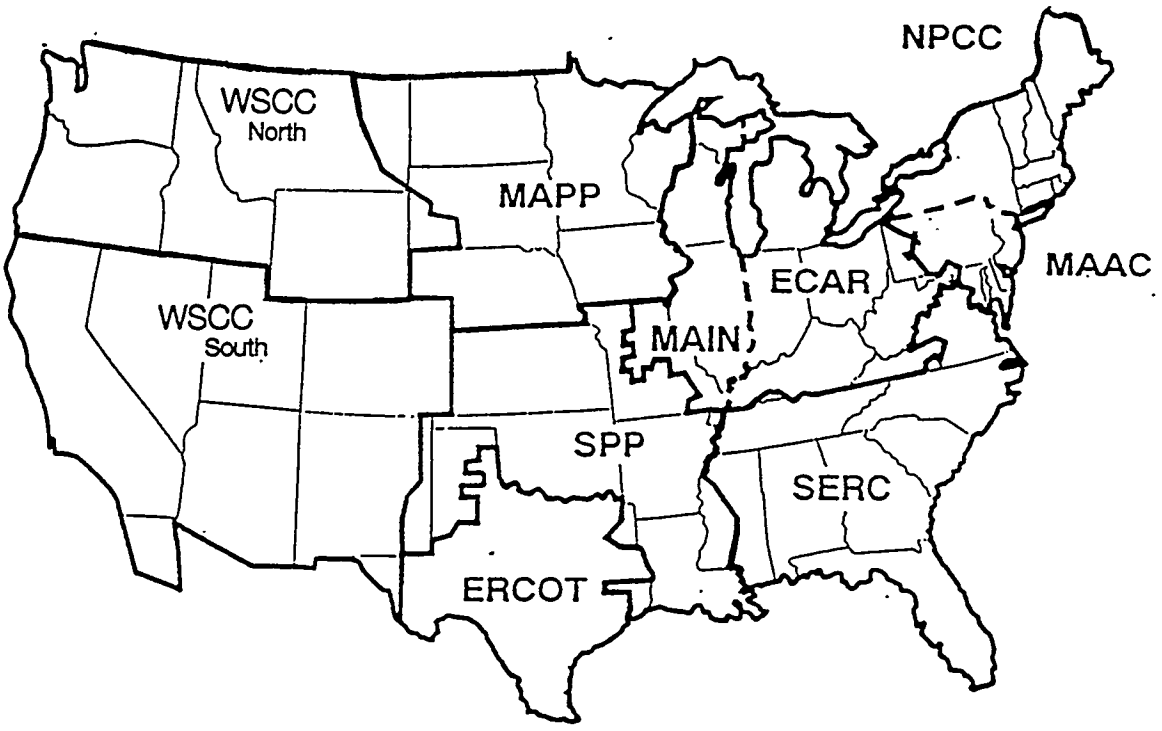
Figure Titles

Figure 1: Proposed renewable resources by region

Figure 2: Storage size required v. area of renewable resource

Figure 3: Storage size v. percent of electric load

Figure 4: Modeling elements



PV	Wind	Solar Thermal
SERC	SPP	WSCC South
ECAR / MAIN	MAPP	ERCOT
NPCC / MAAC	WSCC South	
WSCC South	ERCOT	
ERCOT	WSCC North	

Figure 1: Proposed renewable resources by region

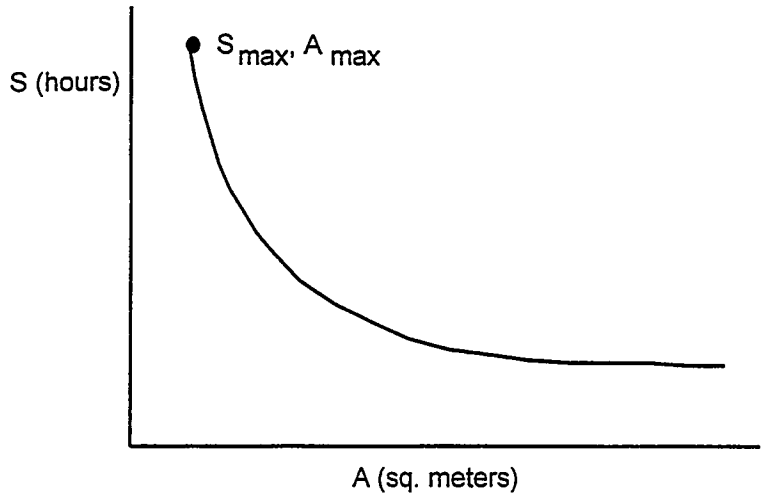


Figure 2: Storage size required v. area of renewable resource

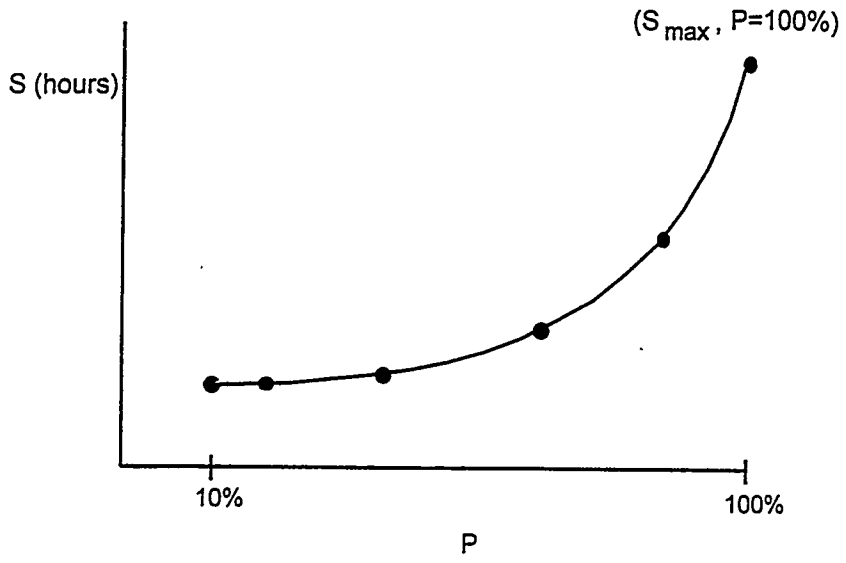


Figure 3: Storage size v. percent of electric load

Modeling Elements

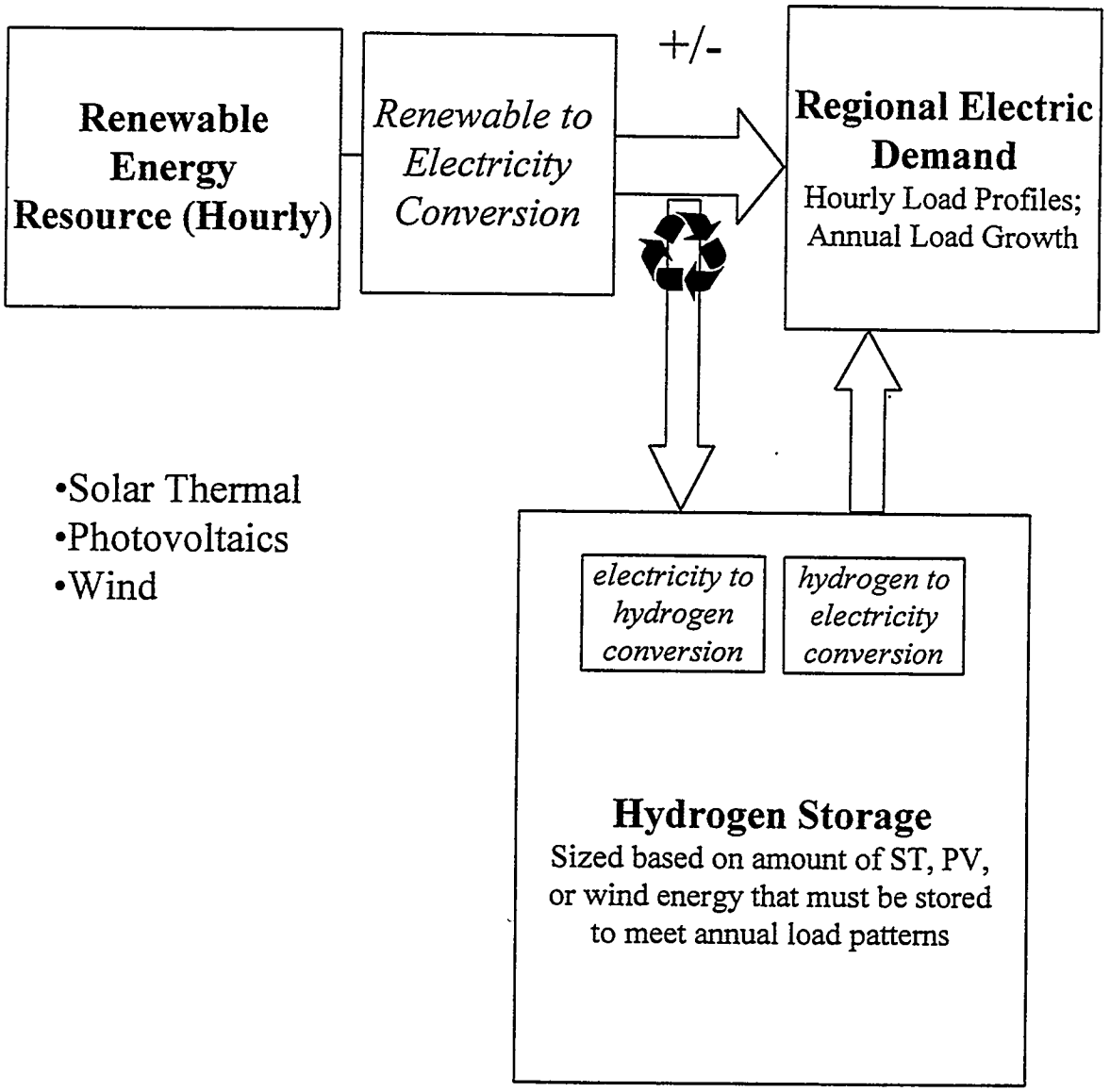


Figure 4: Modeling Elements

MODELING OF HYDROGEN PRODUCTION METHODS: SINGLE PARTICLE MODEL AND KINETICS ASSESSMENT

R.S. Miller and J. Bellan
Jet Propulsion Laboratory
California Institute of Technology
Pasadena, CA 91109-8099

Abstract

The investigation carried out by the Jet Propulsion Laboratory (JPL) is devoted to the modeling of biomass pyrolysis reactors producing an oil vapor (tar) which is a precursor to hydrogen. This is an informal collaboration with NREL whereby JPL uses the experimentally-generated NREL data both as initial and boundary conditions for the calculations, and as a benchmark for model validation. The goal of this investigation is to find drivers of biomass fast-pyrolysis in the low temperature regime. Once these drivers are found, they can be used to control and optimize the operation of each of the modeled reactors. The rationale is that experimental observations produce sparse discrete conditions for model validation, and that numerical simulations produced with a validated model are an economic way to find control parameters and an optimal operation regime, thereby circumventing costly changes in hardware and tests.

During this first year of the investigation, a detailed mathematical model has been formulated for the temporal and spatial accurate modeling of solid-fluid reactions in biomass particles. These are porous particles for which volumetric reaction rate data is known *a priori* and both the porosity and the permeability of the particle are large enough to allow for continuous gas phase flow. The methodology has been applied to the pyrolysis of spherically symmetric biomass particles by considering previously published kinetics schemes for both cellulose and wood. A parametric study has been performed in order to illustrate the effects of reactor temperature, heating rate, initial porosity, initial particle size and initial temperature on char yields and conversion times. Results from the numerical simulation show that while high temperatures and fast heating rates minimize the production of char in both reactions, practical limits exist due to endothermic reactions, heat capacity and thermal diffusion. Three pyrolysis regimes are identified: 1) initial heating, 2) primary reaction at the effective pyrolysis temperature and 3) final heating. The relative durations of

each regime are independent of the reactor temperature and are approximately 20%, 60% and 20% of the total conversion time, respectively. The results also show that models which neglect the thermal and species boundary layers exterior to the particle will generally over predict both the pyrolysis rates and experimentally obtainable tar yields. An evaluation of the simulation results through comparisons with experimental data indicates that while the cellulose kinetics is reasonably accurate, the wood pyrolysis kinetics is not accurate; particularly at high reactor temperatures. Current effort in collaboration with NREL is aimed at finding accurate wood kinetics.

Further, a mathematical model of tangentially injected biomass particles in a vortex reactor has been developed and is in the initial stages of coding. In this model, clusters of particles are followed on their trajectories as they slide on the wall. The model consists of a set of several nested and interacting models whose building block is the particle model described above. Components of this set are: (1) the cluster model, (2) the turbulent boundary layer model on the wall, and (3) heating of the particles by contact with the wall.

Introduction

Biomass fast-pyrolysis is different from conventional pyrolysis in that char yield is minimized and gaseous tar and volatiles yield resulting from the secondary reactions are maximized. In the NREL vortex reactor, particles enter tangentially, are pushed to the hot wall and their temperature rises through heat transfer from the wall. Due to heating, the biomass is thermally transformed through bond breaking and new bond formation to a new state labelled "active". This active state biomass reacts to yield tar (vaporized oil), char and gas; tar further reacts to yield a gas and/or char. Catalytic reactions may transform the vaporized oil into hydrogen and other by-products. The exact chemical composition of tar varies according to the specificity of the biomass, however, some major compounds that are hydrogen precursors will be present in all tars.

Current literature predictions of biomass pyrolysis in reactors are the result of empirical models. More fundamental descriptions have been made only for single biomass particles. As discussed in the following, even these more fundamental models lack first-principles descriptions of the flow of volatiles through the particle and of the ensuing secondary reactions in the gas surrounding the particle. For this reason, although previously published results from other investigators could sometimes duplicate experimentally measured char yield, they could not duplicate tar yield.

Modeling of single biomass particle pyrolysis is inherently difficult due to complexities associated with the multi-phase aspect. Particle porosity, two- and three-phase interactions, and ill-defined boundaries due to solid phase reaction products (e.g. char) need to be considered in a complete model. The combustion of a solid porous fuel particle can be divided into six primary physical processes:

- Solid fuel reactions at both the particle surface and the interior.
- Secondary solid/liquid phase reactions at both the particle surface and the interior.
- Gas phase reactions both internal and external to the particle.
- Gas and liquid phase diffusion ("pore diffusion") and/or convection within the particle.
- Mass transfer with the surroundings.
- Heat transfer with the surroundings.

The combination of the above processes which determines the combustion characteristics is dependent on the particular reaction of interest. The ratio of reaction to diffusion time scales is in general too small for kinetically controlled models to be effective (see e.g. Di Blasi 1996b). "Pore diffusion" can control the

rate of reaction by limiting the surrounding oxidizer delivery to the particle's interior and/or by cooling the particle's surface due to emerging interior gases. Solid phase fuels may produce additional solid and/or liquid phase products such as char which can act to thermally insulate the particle. In addition, reactions of gas phase species outside of the particle can influence both heat and mass transfer (e.g. exothermic reactions).

Significant early research in this area has been directed at incorporating the above mentioned processes into theoretical models of char combustion and gasification. Early models were limited to analyzing the external particle surface reactions coupled with gas phase transport (Caram & Amundson 1977; Mon & Amundson 1978; Sundaresan & Amundson 1980). Extensions included the addition of inner-particle diffusion, reaction and pore growth effects (Sotirchos & Amundson, 1984a; Sotirchos & Amundson 1984b). Further efforts relied on stochastic descriptions of pore distributions and overlap. This latter approach typically employs assumptions of either spherical voids (Loewenberg *et. al.* 1987), infinite cylindrical voids (Gavalas 1980; Gavalas 1981), or arbitrary void sizes and distributions (Bhatia & Perlmutter 1980; Bhatia & Perlmutter 1981). All of the above mentioned models rely on *a priori* knowledge of pore surface regression rates as a function of carbon oxidation and invoke a quasi-steady state assumption for the particle surroundings.

While the above mentioned models have shown some success for modeling char combustion, these approaches are not directly applicable to other types of solid particle reactions. Reaction rates may occur volumetrically (not only at exposed surfaces) and are more easily measured in this manner in the laboratory. Density changes due to thermal swelling and/or intermediate solid or liquid phase species may cause temporary pore shrinkage. In addition, the presence of gas phase species within the particle results in a nearly uniform diffusion time scale across the particle boundary and a quasi-steady assumption for the particle exterior cannot be justified.

One type of solid reaction which exhibits several of the above characteristics is the pyrolysis of biomass. As biomass is heated in the absence of an oxidizer it produces char, tar and volatile gases. It is now widely accepted that as the heating rate is increased, relative proportions of tar and volatile gases can be increased while producing little, if any, char (Reed *et. al.* 1980; Diebold 1980). Fast pyrolysis in the ablation regime has been investigated for wood rods in contact with a hot, spinning disc by Lede *et. al.* (1985) who found that fast pyrolysis is possible when both high heating rates and efficient removal of the reaction products are present. Possible applications of these processes involve the rapid heating of ground biomass particles (e.g. waste saw dust) in either fluidized beds (Lim *et. al.* 1995) or vortex reactors (Diebold and Power 1988) in order to maximize tar and volatile gas yields. The collected gases and tars can be further processed for use in adhesives, resins or for hydrogen fuel production whereas large char yields are desirable for charcoal production.

The large diversity of biomass feedstock has motivated analyses of the somewhat simplified case of cellulose pyrolysis. In general, biomass is composed of approximately 50% cellulose by mass (Di Blasi 1993b) and many of the kinetic and hydro/thermo- dynamic processes involved in cellulose pyrolysis may be common to the more general case of biomass. The majority of previous models for both cellulose and wood pyrolysis are based on first order kinetics schemes. These models range in complexity from one-

step global to multi-step kinetics involving both primary and secondary reactions (see Di Blasi (1993b); Antal and Varhegyi (1995) for recent reviews). Only the most recent of these models have attempted to incorporate hydrodynamic and thermodynamic effects. Kothari and Antal (1985) investigated the effects of heatup time and devolatilization time on the flash pyrolysis of cellulose. They found that time delays and endothermic reactions place practical limits on attainable particle temperatures. Simmons and Gentry (1986) studied the kinetically controlled regime of the cellulose pyrolysis of sub-millimeter sized particles. Using a mathematical model with prescribed particle surface conditions, they were able to make predictions of the range of kinetic control as a function of particle size and heating temperature. Poor comparisons with experiments were attributed to neglect of the external thermal boundary layer in the model. Di Blasi (1994) extended the kinetics scheme of Bradbury *et. al.* (1979) to include secondary reactions of volatiles to simulate the pyrolysis of cellulose slabs. The model accounts for both heat and mass transfer within the slab through an equation for internal energy and Darcy's law for the gas phase velocity, and has been extended to multi-step kinetics for wood pyrolysis (Di Blasi 1992; Di Blasi 1993a). The model is applicable only within the slab and the particle surface conditions are assumed functions of the reactor temperature. However, effects on pyrolysis due to the thermal boundary layer and chemical reactions outside of the particle can become significant and have recently been connected to the wide variation of kinetic parameters measured in experiments (Narayan and Antal 1996).

The objective of this paper is to present a model of solid particle reactions which is sufficiently robust to incorporate all of the above listed physical processes both internal and external to the particle, and which is applicable to volumetric reaction rate data. In particular, no quasi-steady assumption is made for the particle surroundings, and the particle surface conditions are allowed to evolve in a "natural" manner determined by the far field temperature and pressure. The model is then applied to example cases of spherically symmetric cellulose and wood particle pyrolysis in an initially quiescent environment of high temperature steam. The effects of reactor temperature, heating rate, initial particle size, initial porosity and initial particle temperature on both char formation and conversion times are investigated. A comparison of the simulated results with experimental data is made and is discussed in evaluating the accuracy of the assumed kinetics schemes. The paper is organized as follows: Section 2 presents the general model equations together with the kinetics schemes and properties for both cellulose and wood reactions. Numerical solutions and a parametric study are presented in Section 3 along with discussions of char yields, conversion times, spatial tar distributions and comparisons with experiments. Section 4 is devoted to conclusions and further discussions.

Theoretical Formulation

Consider a single porous solid particle having both a porosity (ratio of pore volume to total volume) and a permeability sufficiently large to allow for continuous gas flow. Assume that the particle is allowed to react and that only volumetric reactions are known. In this case, a detailed analysis of the internal pore structure is superfluous because only the bulk "effective" properties of the porous material are needed. We allow for the general case in which both liquid and gaseous reaction products may be formed; however, both convection and diffusion of the liquid are neglected. This last assumption is justified provided that

either the viscosity of the liquid is substantially larger than that of the gases or the reaction time scale of the liquid is much smaller than its convection and diffusion time scales.

Governing Equations

The governing equations for the solid particle dynamics are presented in spherically symmetric form; the extension to multi-dimensions being straight forward. A combination of two perspectives is employed to describe the particle dynamics. In the first approach, the various species and phases within the particle are viewed as a "mixture." In this case, it is the partial densities which are relevant. We denote partial densities as $\rho_{\alpha,i}$ and true densities as $\widehat{\rho}_{\alpha,i}$, where the subscripts denote both the phase [$\alpha = s$ (solid or liquid), g (gas)] and the species ($i = 1, ...N$; where N is the total number of species). Note that the above assumptions imply that solid and liquid phase species are treated identically. The mass conservation equation for the solid phase species is:

$$\frac{d\rho_{s,i}}{dt} = \dot{S}_{s,i}, \tag{1}$$

where the appropriate source/sink terms due to reactions are contained in $\dot{S}$ (subscripts as defined above) and both convection and diffusion are neglected. In similar fashion, the gas phase continuity equation is:

$$\frac{\partial \rho_g}{\partial t} + \frac{1}{r^2}\frac{\partial}{\partial r}\left(r^2 \rho_g u\right) = \dot{S}_g \tag{2}$$

where the radial coordinate is r, the radial velocity component is u, the gas phase partial density is $\rho_g = \sum^g \rho_{g,i}$ and the corresponding source term is $\dot{S}_g = \sum^g \dot{S}_{g,i}$ (the summation $\sum^\alpha$ denotes a sum over all species of phase α). So far, the porosity of the particle (ε) only appears indirectly through the relation between the partial and true densities:

$$\rho_g = \varepsilon \widehat{\rho}_g, \qquad \rho_{s,i} = (1-\varepsilon)\widehat{\rho}_{s,i}, \tag{3}$$

$$\varepsilon = 1 - \sum^s \rho_{s,i}/\widehat{\rho}_{s,i}. \tag{4}$$

In general, the true densities of the solid phase species are described through additional equations of state; however, for the purpose of the present work they are assumed to have prescribed constant values. By definition, the porosity is based only on the gas phase volume whereas the stationary medium includes both the solid and the liquid phases.

The above equations are coupled through both source terms and additional equations for species, momentum and energy conservation, along with an appropriate equation of state for the gas phase. The species conservation equations are formulated in terms of the gas phase mass fraction Y_i ($\sum^g Y_i = 1$):

$$\frac{\partial \rho_g Y_i}{\partial t} + \frac{1}{r^2}\frac{\partial}{\partial r}\left(r^2 \rho_g Y_i u - r^2 \rho_g D_{eff}^{(i)} \frac{\partial Y_i}{\partial r}\right) = \dot{S}_{g,i}\,. \tag{5}$$

The species diffusion is assumed to be Fickian with an effective molecular diffusivity $D_{eff}^{(i)}$ due to porosity effects. Following classical porous media theory and empirical measurements, the effective diffusivity is assumed to be proportional to the porosity and is modeled as $D_{eff}^{(i)} = \varepsilon D^{(i)}$ where $D^{(i)}$ is the molecular

diffusivity of species i (Bear 1972). In general, the porosity is represented by a rank two symmetric tensor to properly describe anisotropic pore distributions; however, only locally isotropic porosities and diffusivities are considered in the current work as more precise information is not available.

The conservation equation for the gas phase momentum is modeled through a "channel" description (second perspective), *i.e.* as a mixture of gases flowing through individual "channels" (pores) within the particle:

$$\frac{\partial \rho_g u}{\partial t} + \varepsilon \left[\frac{\partial}{\partial r} \left(\rho_g u^2 \right) \right] = -\frac{\partial p}{\partial r} + \frac{1}{r^2} \frac{\partial}{\partial r} \left[r^2 \mu_{eff} \left(2 \frac{\partial u}{\partial r} - \frac{2}{3} \Pi \right) \right] + \frac{4}{3} \frac{\mu_{eff} \Pi}{r} - 4 \frac{\mu_{eff} u}{r^2} \tag{6}$$

where the velocity divergence is:

$$\Pi = \frac{1}{r^2} \frac{\partial}{\partial r} \left(r^2 u \right), \tag{7}$$

the pressure is p and the effective molecular viscosity is μ_{eff}. The fully compressible form of the momentum equation is employed, as a source term in the continuity equation results in non-zero divergence of the velocity field. The effective viscosity is modeled in a similar manner as the diffusivity; however, the values of the gas species' molecular viscosities ($\mu^{(i)}$) are locally mass averaged to account for mixture effects:

$$\mu_{eff} = \varepsilon \sum^{g} Y_i \mu^{(i)}. \tag{8}$$

Although the gas diffuses according to the effective viscosity relation, additional drag forces are experienced by a flow convecting through a porous medium. These effects are due to the geometry of the voids and to viscous shear stresses along solid-gas boundaries. In order to avoid a complicated analysis of the pore geometry, these effects are lumped together and modeled by "damping" the convective terms in the momentum equation proportional to the porosity. This damping is somewhat arbitrary, yet appears to be reasonable under the previous restriction of relatively large porosity and/or permeability. The above momentum equation offers several advantages over the traditional use of Darcy's Law which states that the velocity is proportional to the product of the pressure gradient and the permeability. Equation (6) is derived theoretically and with relatively few, and known, assumptions. It is valid for both the interior and the exterior of the particle and takes full account of transient effects. Darcy's Law is completely empirical and has not been correlated for the case where gas phase sources occur within porous media, nor for flows in which transient effects are important (Bear 1972).

The temperature is obtained through a "mixture" modeled conservation equation for the internal energy. Local thermal equilibrium is assumed for all species and phases ($T = T_i$, all i). All species are assumed calorically perfect such that the partial internal energy (e_i) is proportional to the specific heat at constant volume; $e_i = \rho_i C_v^{(i)} T$. With this notation, the gas phase partial internal energy is:

$$e_g = \rho_g \left(\sum^{g} C_v^{(i)} \right) T, \tag{9}$$

and the total internal energy is:

$$e_t = e_g + \left(\sum^{s} \rho_{s,i} C^{(i)} \right) T, \tag{10}$$

where $C_v^{(i)}$ is the constant volume specific heat of gas phase species i, and $C^{(i)}$ is the specific heat of either solid or liquid phase species i. With this notation, the total internal energy is governed by:

$$\frac{\partial e_t}{\partial t} + \frac{1}{r^2}\frac{\partial}{\partial r}\left[r^2 e_g u - r^2 \lambda_{eff}\frac{\partial T}{\partial r}\right] = p\Pi + \sum \dot{S}_i \, \Delta h_i \tag{11}$$

where Fourier conduction with effective thermal conductivity λ_{eff} is assumed, only gas phase energies are allowed to convect and viscous dissipation is neglected. The last term on the right hand side (*rhs*) represents a summation over all reactions which accounts for both heat release and/or phase changes with heats of reaction Δh_i. Modeling the effective conductivity is more complex than the previous transport properties due to the fact that heat transfer occurs simultaneously through all phases and species. We choose to model the multi-phase heat transfer in terms of a *parallel conduction* model inspired by previous empirically tested models of two-species conduction in porous media (Bear 1972):

$$\lambda_{eff} = (1-\varepsilon)\left\{\frac{\sum^s \rho_i \lambda^{(i)}}{\sum^s \rho_i} + \lambda_{\text{rad}}\right\} + \varepsilon \sum^g Y_i \lambda^{(i)}, \tag{12}$$

where $\lambda^{(i)}$ is the thermal conductivity of species i. Gas phase species are assumed to be transparent to radiation while the solid and liquid phase radiation are modeled as in Chan *et. al.* (1988) with an effective conductivity: $\lambda_{\text{rad}} = \sigma T^3 d/\omega$, where $\sigma = 5.67 \times 10^{-11} kJ/m^2 s K^4$ is the Stefan-Boltzmann constant, ω is the emissivity and d represents a characteristic length scale for the pore size. The above model quantifies a "flow" of heat simultaneously (in *parallel*, implying volume averaging) through both the solid and gas phases, where individual species conductivities are mass averaged among species of the same phase. While other conduction models have been proposed (e.g. *series* and combinations of *series-parallel*), all are at best intuitive and compare similarly with experiments (Bear 1972).

The above set of governing equations is completed by an equation of state. The total pressure driving the gases is assumed to be related to the temperature and density through the perfect gas law:

$$p = \frac{\rho_g}{\varepsilon}\left(\sum^g Y_i/M_i\right)\overline{R}T, \tag{13}$$

where M_i is the molecular weight of species i and $\overline{R}$ is the universal gas constant. The presence of the porosity in the equation of state indicates that the pressure is related to the "true" gas density $\widehat{\rho}_g$. Equations (1)-(13) describe the essential physical processes of reactions in porous solid particles with multi-species/phase interactions. They are valid for both the interior and the exterior ($\varepsilon \rightarrow 1$) of the particle and provide a fully transient description of the particle behavior with relatively few assumptions.

Biomass Pyrolysis

The equations derived in Section 2.1 are applied to the pyrolysis of both cellulose and wood particles by implementing the kinetics schemes compiled by Di Blasi (1994) and Di Blasi (1993a), respectively. The two reaction schemes both employ a simplified decomposition of the primary solids to form three lumped product groups; solid char, tar vapors and low molecular weight gas (Fig.1). The cellulose is additionally considered to pass through an intermediate solid form labelled active cellulose. All of the reactions are first

order, irreversible and follow Arrhenius temperature dependencies of the form $K_i = A_i \exp[-E_i/\overline{R}T]$ where K_i is the reaction rate, A_i is the rate frequency constant, E_i is the activation energy and the subscript refers to the reacting species. The reaction rates are applied to the particle model to form source terms of the form:

$$\dot{S}_i = -\rho_i K_i, \qquad \dot{S}_j = +X_j \rho_i K_i \tag{14}$$

for the reaction of solid phase species i ($\dot{S}_i$) with corresponding production of species j ($\dot{S}_j$) and X_j is the molar fraction (note that there is no summation over repeated indices throughout the paper). Similar forms for the gas phase reactions are in terms of the partial densities. Values of the activation energies, rate constants and heats of reaction are provided in Table 1. Reaction K_2 is assumed to produce both char and gas in the respective ratios of 0.35 and 0.65 and all remaining X_j are equal to unity. All solid phase reactions, with the exception of the primary cellulose decomposition are endothermic while secondary gas reactions are exothermic. The reaction frequencies for the wood pyrolysis are consistent with the original values as calculated by Thurner and Mann (1981). The frequency constants for the primary wood reactions used in Di Blasi (1993a) appear to be larger than the originals by a factor of 3600; we were informed that this was a modification made by the author (Di Blasi 1996a) to duplicate experimental char densities. Implications of this modification will be discussed below.

Table 1: Reaction parameters.

Reaction	$A_i[1/s]$	$E_i[kJ/kmol]$	$\Delta h_i[kJ/kg]$
K_1	2.8×10^{19}	2.424×10^5	0
K_2	1.3×10^{10}	1.505×10^5	-418
K_3	3.28×10^{14}	1.965×10^5	-418
K_4	4.28×10^6	1.08×10^5	$+42$
K_5	1.43×10^4	8.86×10^4	-418
K_6	4.13×10^6	1.127×10^5	-418
K_7	7.38×10^5	1.065×10^5	-418
K_8	1.0×10^5	1.08×10^5	$+42$

The particles considered in this work are initially at equilibrium in an environment composed of inert super-heated steam. All material properties are taken from the compiled data of Di Blasi (1994) and Di Blasi (1993a) for the reacting species, while the H_2O properties are from appropriate steam tables. The wood kinetics and reactions were originally compiled from several sources and do not correspond to any specific wood type. Tables 2 and 3 contain the solid and gas phase properties, respectively. The steam data is taken at a reference pressure of $p = 100kPa$ and temperature of $T = 800K$, and unavailable gas properties are assumed to be the same as the steam. All of the true solid densities are defined in terms of the initial porosity of the material. There are two advantages to this approach. First, experimental measurements of the true density are very difficult, whereas the apparent, or partial, density is relatively simple to measure. Second, with the density definition employed here, the initial porosity may be varied in order to study its influence without altering the total mass of the particle. The true density of char is

assumed to be the same as the corresponding primary reactant. The emissivity is taken to be $\omega = 1$ and the radiation length scale is $d = 4.0 \times 10^{-5} m$ taken from Chan *et. al.* (1988).

Table 2: Property values for the solid phase species. The superscript * indicates assumed values.

Species	$(1-\varepsilon_0)\widehat{\rho}\,[kg/m^3]$	$C\ [kJ/kgK]$	$\lambda\ [\frac{kJ}{m \cdot s \cdot K}]$
cellulose	420	2.3	2.426×10^{-4}
active	420	2.3	2.426×10^{-4}
char	$(420, 650)^*$	1.1	1.046×10^{-4}
wood	650	2.3	1.046×10^{-4}

Table 3: Property values for the gas phase species. The steam values are given for $T_R = 800K$ and $p = 100kPa$, and the superscript * indicates assumed values.

Species	$M_i\ [\frac{kg}{kg \cdot mole}]$	$C_v\ [kJ/kgK]$	$\mu\ [\frac{kg}{m \cdot s}]$	$\lambda\ [\frac{kJ}{m \cdot s \cdot K}]$	$D\ [m^2/s]$
H_2O	18.016	2.20	2.9×10^{-5}	7.8×10^{-5}	1.1×10^{-4}
gas	18.016*	1.1	3.0×10^{-5}	2.577×10^{-5}	$1.1 \times 10^{-4*}$
tar	18.016*	2.5	3.0×10^{-5}	2.577×10^{-5}	$1.1 \times 10^{-4*}$

Turbulence Considerations

The equations presented above do not include a turbulence model. Although the particles are assumed to be initially located in a quiescent environment, significant gas phase velocities can result in turbulent diffusion around the particle. This could result in three primary alterations to the particle surroundings: 1) Increased temperature gradients near the boundary can increase the total heat flux to the particle. 2) Enhanced mixing of gas phase reactants can significantly increase the rate of chemical conversion near the particle for diffusion flames. 3) Turbulent diffusion of the gases can change the spatial distributions of exothermic reactions and therefore indirectly affect the particle heating rate. Neglect of a turbulence model for the present biomass pyrolysis is considered to be justified in regard to 2) and 3) because only first order reactions are considered (non-diffusion limited) and only mildly exothermic heats of combustion are involved. In regard to issue 1), the present study treats the thermal radius, and therefore the heating rate, as a free parameter. These considerations combined with *a posteriori* analysis of the simulation results indicate that the neglect of a turbulence model is justified for the present biomass particle pyrolysis.

Initial Conditions, Boundary Conditions and the Thermal Radius

A particle of initial radius $R_{p,0}$ and uniform temperature $T_{p,0}$ is exposed at time $t = 0$ to a quiescent envi-

ronment composed of super-heated steam. Numerical solutions are obtained for the spherically symmetric domain within the interval $[0, R_R]$ where the outer domain radius, R_R (referred to as the reactor radius), corresponds to the reactor conditions. Symmetry conditions are employed at the inner domain boundary; i.e. $u = 0$ and $\partial/\partial r = 0$ for all remaining variables. We model the exterior boundary in a manner similar to the "sphere of influence" (SOI) approach of Bellan and Cuffel (1983) which was originally proposed to account for thermodynamic interactions among liquid droplets in sprays (clusters). The SOI represents a characteristic length scale for these interactions and corresponds to the radius of a fictitious sphere located at the droplet center. This radius, R_R, is equal to one half the mean droplet center separation. The proper boundary conditions at $r = R_R$ are obtained by matching the temperature and pressure (and therefore the density) to the local reactor conditions while assuming that $\partial/\partial r = 0$ for all remaining variables. R_R is a function of both the local number density and the three dimensional packing factor. We extend the original SOI concept to introduce a "thermal radius" $R_T \leq R_R$ which is defined such that the temperature is held constant and equal to the local reactor conditions, i.e. $T = T_R$, for all $r \geq R_T$. In this manner, the effective heat flux received by the particle can be altered independently of the reactor temperature while resolving gas phase reactions exterior to the particle. The results presented in the following section are obtained for a single particle and a fixed normalized reactor radius $R_R = 10R_{p,0}$ with constant reactor pressure $p = 100kPa$. In addition to other quantities, both the reactor temperature and the thermal radius are varied in order to independently study the effects of the heating temperature and the heating rate, respectively.

Solution Procedure

The modeled equations are solved numerically utilizing a procedure based on finite difference approximations for both spatial and temporal derivatives. All convective and first order derivatives are approximated via upstream differences in order to maintain proper ellipticity of the equation set, while diffusion second derivatives are second order central. Acoustic waves are filtered through use of a semi-implicit iterative pressure solver. The basic method is as follows: The solid phase density, gas mass fraction and internal energy equations are integrated one time step (from time level n to $n+1$) using an explicit forward time difference. These values give an approximation for the gas phase density and all necessary properties at time level $n+1$. A predictor value of the velocity is then calculated from the gas phase continuity equation. Next, the pressure is obtained by solving a Poisson equation obtained by taking the divergence of the momentum equation. The pressure is then used to correct the gas density and the process is repeated until convergence is achieved. All simulations are performed with a compressed and staggered 64 grid point spatial resolution of the radial coordinate with compression increasing towards the origin such that 21 grid points are within the initial particle boundary. Sixty eight simulations were performed on a Cray-YMP supercomputer requiring a total central processor time of approximately 50 hours.

Results

Before proceeding with a parametric study it is informative to illustrate the particle evolution through a "baseline case" simulation for both cellulose and wood and to compare their behavior. The baseline case

conditions are: $T_{p,0} = 500K$, $T_R = 900K$, $R_T = 5R_{p,0}$, $R_{p,0} = 5mm$ and $\varepsilon_0 = 0.7$. The simulation is terminated at a final time t_c (the conversion time) at which the remaining solid mass, minus the char, has reached 0.1% of the initial particle mass. The conversion times for the cellulose and wood simulations are $t_c = 253.7s$ and $t_c = 347.8s$, respectively.

Figure 2 depicts the temporal evolution of the partial char density for both cellulose and wood. In both cases, no char exists initially. The small amount of char forming outside of the radial position $R_{p,0}$ is due to the necessary smoothing of the initial particle gradients for numerical resolution across the outer boundary of the particle. As the particles are exposed to the high temperature steam environment, heat diffusion into the particle results in a pyrolysis wave having a thickness $\sim 1mm$ which travels radially inward producing solid char residue. Approximately six times more char by mass is formed by the wood reaction than by the cellulose. The final porosity values are nearly uniform within each of the particles; however, the average values differ and are $\varepsilon(t = t_c) \approx 0.98$ and $\varepsilon(t = t_c) \approx 0.91$ for cellulose and wood, respectively. The smaller final char densities near the origin are due to biomass remaining at the termination of the simulations.

As the pyrolysis wave travels through the particle, both tar vapors and gas are produced from the reacting solids and, due to pressure gradients, are ejected from the particle. The production of both tar and gas drives the inert steam out of the pores and away from the particle. Figure 3 indicates that the maximum tar mass fractions are located within the particle. In this region, the tar fraction maintains a nearly uniform value due to near uniform temperatures and reaction rates within the particle (discussed below). In addition, the slightly larger tar mass fractions observed for the cellulose particle indicate that the effective production rate of tar is larger for cellulose than for wood. As tar is ejected, it encounters the hot environment resulting in increased conversion rates to gas. In fact, for both cellulose and wood, nearly all of the tar is converted to gas within the range $r \leq 5R_{p,0}$. This range therefore represents the effective range for which exterior gas phase reactions may influence the pyrolysis evolution due to exothermicity. The rapid tar decomposition near the particle has consequences for experimentally obtainable pyrolysis product measurements and is discussed in more detail below.

The temporal evolution of the temperature profiles can provide insight into the importance of the outer particle regions in affecting the pyrolysis process. Figure 4 illustrates this effect for both cellulose and wood. The high temperature environment maintains relatively large temperature gradients at the particle surface, whereas endothermic reactions smooth the internal thermal gradients. These competing processes result in a relatively thin reaction zone located at the particle surface. The final core temperature for the wood particle is larger than that corresponding to the cellulose particle despite the larger mass (with the same endothermic heat of reaction) of the wood particle. This is a result of the smaller reaction rate of the wood particle as can be deduced from the above listed conversion times. The slower wood reactions absorb heat endothermically at a lesser rate than the cellulose; thus allowing for thermal diffusion to heat the particle to larger temperatures. Examination of Fig.4 reveals that the actual particle surface temperature never reaches the reactor temperature T_R. In fact, during the majority of the conversion, the particle surface temperatures are $\sim 200K$ less than T_R. Analysis of the surface temperature indicates that its rate of increase with time cannot accurately be modeled as a linear function . These results suggest that pyrolysis models which neglect the outer particle thermal boundary layer may substantially over predict

the reaction rates.

Pressure gradients resulting from the conversion of solid to vapor produce maximum gas phase velocities at the location of the pyrolysis front (Fig.5). Convection carries endothermically cooled interior tar and gas out of the particle and thus aids in maintaining a relatively low particle surface temperature. The magnitudes and relative profiles of the interior velocities are in general agreement with the cellulose pyrolysis simulations based on Darcy's Law by Di Blasi (1994). Outside of the particle there are no gas phase mass sources and the velocities decay roughly as r^{-2}. The cellulose actually yields a larger maximum velocity than the wood although it produces substantially less gas phase species by mass. This is because the velocity is related to the reaction rate which is larger for cellulose. Analysis of these results along with others not shown here indicates that an outer computational radius of $10R_{p,0}$ is sufficient to capture the pertinent physics of the particle pyrolysis without significant artificial boundary effects. In addition, due to the complete conversion of tar to gas within the computational domain, further discussions are primarily limited to char yields with the caveat that the remaining products are converted entirely to the gas species within the particle's near field surroundings. However, in order to provide insight into the role of the exterior gas phase reactions, a discussion of spatial tar distributions as a function of the reactor temperature is provided in Section 3.1.3.

Effects of the Reactor Temperature

In this section, the focus is on the values of the conversion times and on the final char yields. Knowledge of the final char yields is necessary in order to either maximize or minimize char formation depending on the particular application; e.g. charcoal or volatile gas production, respectively. On the other hand, conversion times dictate the types of reactors and residence times which are capable of producing the desired yields. The most obvious parameter influencing both t_c and the pyrolysis products is the reactor temperature. Thus simulations are conducted for both particle types for $600K \leq T_R \leq 1500K$ with all other parameters equal to the baseline case values ($R_T = 5R_{p,0}$, $R_{p,0} = 5mm$, $\varepsilon_0 = 0.7$ and $T_{p,0} = 500K$). The conversion times and char yields are presented in Fig.6 for both cellulose (c.) and wood (w.). For both particles, the most substantial effects of the reactor temperature occur for relatively low ambient temperatures. A "transition" value of the reactor temperature, $T_R \sim 700K$, appears to separate two regimes of pyrolysis behavior. The value $700K$ is not meant to quantify a precise transition temperature but is only listed as an apparent range for which the observed changes occur. Below this value, the conversion times increase rapidly with decreasing reactor temperatures (from minutes to hours). The char yield for the cellulose particle also shows a relatively sharply increasing trend in this region. The wood particle shows a nearly constant char yield of ≈ 0.32 for all reactor temperatures; however, the char yields decrease slightly for $T_R < 700K$. On the other hand, for $T_R > 700K$ only relatively mild variations of both the char yield and the conversion time are observed for both particles.

Kinetic Limitations

The pyrolysis trends observed in Fig.6 are best explained in terms of two competing processes; 1) reaction kinetics and 2) "thermal inertia." Kinetics dictate the limitations imposed on pyrolysis due to reaction rates, whereas thermal inertia accounts for limitations imposed on both the particle temperature and its

rate of increase due to diffusion, heat capacity and endothermic solid reactions. If the ratio of the thermal diffusion time scale to the reaction time scale $\ll 1$, then particle pyrolysis occurs in the kinetically controlled regime. The particle temperature is instantaneously raised to the reactor temperature and any variations due to exothermic/endothermic reactions are smoothed by diffusion infinitely fast. Under these conditions, it is possible to define both a kinetic char limit and a kinetic conversion time limit for the reactions, both being functions of T_R only. Table 4 lists the definitions of these limits for both cellulose and wood pyrolysis where the reaction rates (K_i) are evaluated at $T = T_R$. The conversion time is evaluated as that corresponding to a residual mass of 10^{-3} which makes the definition independent of the initial particle size or mass. The time to convert raw cellulose to the active form has been neglected as being much smaller than the remaining reaction times, and secondary char production has been included for wood pyrolysis.

Table 4: Kinetic limits for char yields and conversion times. The baseline values correspond to limits evaluated at $T_R = 900K$.

Reaction	char limit	conversion limit $[s]$
cellulose	$0.35K_2(K_2+K_3)^{-1}$	$-\log(0.001)(K_2+K_3)^{-1}$
	baseline: 6.4×10^{-3}	baseline: $5.3 \times 10^{-3}s$
wood	$\left\{K_7 + K_6\frac{A_5}{A_4+A_5}\right\}(K_5+K_6+K_7)^{-1}$	$-\log(0.001)(K_5+K_6+K_7)^{-1}$
	baseline: 0.29	baseline: $3.9s$

Figure 7 presents the kinetic limits on char yields and conversion times for both cellulose and wood pyrolysis as a function of T_R. The limiting values of the conversion times are observed to be strong functions of the reaction temperature. Complete pyrolysis at the kinetic limit can require anywhere from weeks to micro-seconds within the range of reactor temperatures in current use. For all practical ranges for which char production is to be minimized (large T_R), the wood reaction is always slower than the cellulose reaction. It is well known that commercial processes which aim at maximizing char yields generally employ long residence times with low final heating temperatures. For example, char yields as high as 50% have been reported from the pyrolysis of bagasse at $530K$ with 65 hour heating times (see e.g. Antal and Mok 1990). The kinetic char yield limit for cellulose pyrolysis is in good qualitative agreement with these observations since the yield decreases monotonically with reactor temperature. However, the wood reaction shows a peak char yield at $T_R \approx 650K$ with a relatively sharp drop in yield below this temperature. This apparent contradiction with experimental observation may indicate a flaw in the wood pyrolysis kinetics scheme.

In order to quantify the relative ratio of the kinetically controlled and the diffusion controlled pyrolysis regimes, it is convenient to define two kinetic "efficiency" factors. Both a yield efficiency and a conversion efficiency are defined as the ratio of the kinetic limit to the actual simulation value of the final char yield and the conversion time, respectively. Values of these ratios which approach unity indicate the kinetically controlled regime, whereas ratios approaching zero indicate strongly diffusion controlled pyrolysis. Both

ratios must be in agreement as a yield efficiency of unity alone is not sufficient to conclude kinetically controlled pyrolysis. Both efficiency factors are illustrated in Fig.8 as a function of T_R. It is apparent that diffusion effects are substantial throughout the entire range of temperatures considered. Only as T_R is decreased below $600K$ and conversion times become on the order of hours and larger can biomass pyrolysis truly be considered to be kinetically controlled. In the case of wood pyrolysis, kinetically controlled predictions of product yields may give reasonable results, even though the conversion times indicate that diffusion effects are strong. This is an artifact of the present kinetics scheme for wood pyrolysis which yields only mild variations in char yield with reaction temperature. The quantitative results presented thus far are valid only for the particular particles under consideration and are expected to be functions of particle size and heating rate in addition to other properties (conductivities, heats of reaction, *etc.*).

Effective Pyrolysis Temperature

A comparison of the results of Figs.6 and 7 suggests that the simulated pyrolysis of both cellulose and wood is occurring within a relatively narrow effective reaction temperature range slightly larger than $600K$. This hypothesis is confirmed by examining the mass averaged particle temperature:

$$< T_p >= \frac{\int_0^\infty 4\pi r^2 \rho_s' T \cdot dr}{\int_0^\infty 4\pi r^2 \rho_s' \cdot dr}, \tag{15}$$

where ρ_s' indicates the partial solid phase density *excluding* the char. Figure 9 depicts the mass averaged particle temperature evolution as a function of non-dimensional time for several values of the reactor temperature in the range $[700K, 1200K]$. The curves are almost identical for both cellulose and wood when time is normalized with t_c. Examination of the mean particle temperature indicates three primary phases of evolution for both cellulose and wood pyrolysis: 1) An initial rapid increase in temperature as heat diffuses into the particle from the surroundings. 2) A primary reaction regime at a nearly constant "effective pyrolysis temperature" during which endothermic reactions strongly resist any further particle heating. 3) A secondary reaction regime within which only relatively small particle mass remains and the total heat loss due to reactions is significantly smaller than heat diffusion into the particle. The majority of the pyrolysis occurs in the primary regime within which the particle temperatures for both cellulose and wood are limited to values in the range of approximately $(600K, 650K)$. Only relatively small variations of char yield and conversion time can be expected for reactor temperatures above this range. The behaviors associated with regimes 1) and 2) are in agreement with the numerical results of flash cellulose pyrolysis by Kothari and Antal (1985) obtained using a much simpler particle model. Their results indicate a larger maximum particle temperature than Fig.9 indicates; approximately $775K$ for particle diameters $\leq 0.5mm$. However, these particles may have a mass too small for the endothermic heat absorption to overcome the inward thermal diffusion. The present results indicate that the effective pyrolysis temperature is determined primarily by the magnitude of the primary reaction endothermicity, the particle mass and the reaction rate: The pyrolysis temperature is therefore not directly related to kinetic and diffusion reaction limits.

Further evidence for the three pyrolysis regimes is found in Fig.10 which depicts the particle heating rate as a function of both non-dimensional time and T_R. For the purpose of this study, the heating rate

is defined as the time derivative of $< T_p >$. This definition is appropriate for the current discussion because the endothermic reactions maintain a fairly uniform temperature profile within the solid and the spherical mass averaging of the temperature gives a larger "weighting" to the actual pyrolysis temperatures near the particle surface (the nonlinear temporal dependence of the surface temperature was discussed above). In addition, this definition eliminates any ambiguity in prescribing the location of the particle surface and also neglects contributions from residual char regions left behind the pyrolysis wave which no longer influence the temperature via endothermicity effects. Figure 10 clearly reveals the three pyrolysis regimes as distinguished by regions of; 1) relatively large positive, but decreasing, heating, 2) virtually zero heating rate when inward thermal diffusion balances endothermic absorption, and 3) positive and increasing heating rates when the particle mass has become too small for endothermic reactions to prevent the particle temperature growth. Both Figs.9 and 10 suggest that the relative durations of the pyrolysis regimes (with respect to t_c) appear to be independent of the reactor temperature and are approximately 20%, 60% and 20%, respectively. The heating rates in the normalized time frame are almost identical except for early times when large reactor temperatures result in increased heat fluxes into the particle. In general, the heating rates are always less than $10K/s$ (a factor of ten larger than reactor heating rates used in traditional TGA experiments; e.g. Bilbao *et. al.* 1992) and their functional dependence on time is highly nonlinear.

The presence of the three regimes is not always readily apparent. For example, Bilbao *et. al.* (1992) studied the effect of the reactor heating rate on the thermal decomposition of spherical pine particles in the size range $4.0cm \leq R_{p,0} \leq 11.2cm$. They presented experimentally obtained results for the temporal dependence of the particle temperature for various radial positions inside of the particle. The initial particle masses are relatively large and thus endothermic heat absorption should be substantial; however, only the particle core temperatures exhibit the primary pyrolysis regime (as observed by intervals of near constant temperature). The reason for this apparent discrepancy is twofold: First, the experimental measurements for outer radial positions do not consider that the pyrolysis front passes through these positions, leaving behind only char with no further endothermic reactions to balance thermal diffusion. Second, the experiments considered particles which began in a "cold" reactor which was slowly heated to the final reactor temperature (from $303K$ to $923K$ at rates $\leq 12K/\min$). Examination of their data shows that nearly 50% of the pyrolysis is complete before the reactor temperature reaches $700K$, even for the largest particle size and heating rate. The primary reaction regime will only be easily distinguishable when the reactor temperature is significantly larger than the effective pyrolysis temperature. This is indeed the case for the results of Figs.9 and 10 in which the reactor temperature is constant and $T_R \geq 700K$.

Tar Distributions

Important issues are the accurate measurement of tar yields and whether tar yields increase at a constant rate with increasing reactor temperature.

The general form of the tar profiles was demonstrated in Fig.3 and in the corresponding discussions. Another consequence of the rapid depletion of tar in the particle's vicinity is its influence in the experimental analysis of pyrolysis vapor yields. The typical experimental method of vapor collection is to rapidly quench the gas phase species in order to hault the reactions and to therefore achieve representative

samples of the various species yields. For example, Scott *et. al.* (1988) measure both cellulose and wood pyrolysis products using a "cryovortactor" which quenches the gas phase products via injection of a turbulent stream of cryogenic nitrogen immediately after the pyrolysis. Accurate measurements of the true product yields are only possible when the time lag between pyrolysis and quenching is much smaller than the tar conversion time scale. The results presented previously in Fig.3 suggest that the sample measurements may vary substantially from the actual exit yields due to rapid gas phase reactions occurring in the immediate vicinity of the particle.

An examination of the tar distribution within the particle surroundings provides a qualitative analysis of the limitations on gas phase pyrolysis measurements as caused by tar decomposition near the particle. Figure 11 presents both the maximum normalized radius at which the tar mass fraction has decayed to 0.05 (the "5% tar radius") and the maximum tar mass fraction for both cellulose and wood as a function of the reactor temperature ("maximum" indicates for all times). Radial values $> 10R_{p,0}$ indicate that the 5% radius is located exterior to the computational domain. All of the actual tar profiles are of the same general form as those previously shown in Fig.3. These two parameters provide a measure of how closely to the particle the tar is distributed and how much tar is produced, respectively. The 5% tar radius and the maximum tar fraction show opposite dependence on the reactor temperature. Figure 11 indicates that as the reactor temperature is increased, the tar evolves an increasingly narrower distribution adjacent to the particle surface. On the other hand, the maximum tar (at the surface and interior to the particle) increases as the reactor temperature is increased. These observations have important consequences to both experiments and commercial reactors.

Figure 11 suggests that experimental measurements may under predict the actual tar yields which exit the particle as further tar decomposition occurs both rapidly and near to the particle. This argument can be used to explain the results of Di Blasi (1996b) who used a numerical pyrolysis model, based on the same cellulose kinetics scheme as employed in this paper, to predict the tar, gas and char yields measured by Scott et. al. (1988) in the "cryovortactor." The Di Blasi model does not include reactions in the outer particle domain and the total tar yields correspond only to the total tar exiting the particle surface. The numerical model was applied for a nearly kinetically controlled particle size in an attempt to duplicate the experimental conditions. Comparisons showed good agreement for the total char yield predictions; however, with significant over prediction of the total tar yields. Further tar decomposition may have occurred outside of the particles before the cryogenic nitrogen stream could quench the reactions. In this case, it would be expected that a pyrolysis model which neglects the particle surroundings would display the above trends. That is, an over prediction of experimental tar yields, even if the kinetics scheme is accurate and the total char yield is well predicted.

The results of Fig.11 also indicate that there exists an optimal temperature for applications which aim at maximizing tar yields (e.g. biomass pyrolysis for commercial hydrogen production). Although increasing reactor temperatures produce increasing total tar yields, the relatively narrow distributions of the tar near to the particle surface limit the effective tar yields which can be harvested. Caution must be exercised in raising the reactor temperature because the quenching of the pyrolysis products may not be fast enough to capture the increased tar productions. In this case the added expense of heating the reactor to large temperatures may not only be costly, but may actually yield less tar than a lower, and less expensive,

optimal reactor temperature. The present model is capable of predicting such optimal reactor temperatures. Experimental measurements of optimal tar producing reactor temperatures as a function of both the reactor type and the biomass feedstock are needed to validate the predictions.

Effects of Additional Parameters

In order to make useful predictions of biomass pyrolysis, it is necessary to extend the results of the previous section to include the effects of R_T (heating rate), $R_{p,0}$, ε_0 and $T_{p,0}$. As the variation of each parameter is studied, the remaining parameters are kept constant and take the baseline case values; $T_R = 900K$, $R_T = 5R_p$, $R_p = 5mm$, $\varepsilon_0 = 0.7$ and $T_{p,0} = 500K$. The kinetic limits on yield and conversion time are not dependent on these parameters. As such, the efficiency factors are inversely proportional to the proceeding simulation results. Therefore, quantitative values for these factors are only discussed intermittently and when pertinent; however, the efficiency magnitudes can be calculated from the data provided in Table 4. In addition, the parameters studied in this section show significantly less influence on the tar distribution than did the reactor temperature. As such, tar distributions are no longer discussed; however, we note that with $T_R = 900K$ all of the cases considered in this section are characterized by total tar decomposition within the simulated domain.

Effects of the Thermal Radius

Heating rates are known to strongly influence biomass pyrolysis yields and evolutions (see e.g. Antal and Mok 1990). Previous numerical investigations which address this issue have been restricted to models which either model the particle surface conditions or which use steady state assumptions for the particle surroundings (see e.g. Di Blasi, 1993a). Variations in the heating rate within experimental and commercial reactors are difficult to model quantitatively. In addition to T_R, the heating rate is determined by many factors. For example, free stream velocities, turbulence intensity, contact with solid surfaces and clustering of the biomass particles within the reactor may all strongly affect the heating rate each particle experiences. Therefore, for the purpose of the present work, effects due to the heating rate are studied only in a qualitative manner by varying the thermal radius, R_T.

The final time char yields and conversion times for the biomass particles are presented in Fig.12 for thermal radii in the range $1.15 \leq R_T/R_{p,0} \leq 10$. The largest effect of the heating rate is observed in the variations of the conversion times for both cellulose and wood. In agreement with previously observed trends (Antal and Mok 1990), an increase in the heating rate decreases both the char yield and the conversion time. When the high temperature source (at $r = R_T$) is moved closer to the particle surface, t_c changes as a result of two competing processes: the increase in T_p due to the increasing heating rate, and the decrease in temperature due to endothermic reactions. The reduced conversion times imply that it is the first process which dominates in the small R_T/R_p limit. However, the char yields only show mild relative decreases for the smallest R_T values, indicating that the effective pyrolysis temperature is only raised by a relatively small amount for the present parameters. Even for the most rapid conversions, the efficiency ratios indicate that diffusion effects cannot be neglected in the accurate simulation of the particle pyrolysis considered here.

An additional interesting result suggested by Fig.12 concerns the free stream boundary placement. The variation of R_T indirectly gives a measure of the distance from the particle at which the computational boundary must be placed in order to correctly simulate particle pyrolysis within an infinite domain. Numerical simulations of liquid droplet combustion generally require external droplet resolutions greater than 25 times the initial droplet radius in order to eliminate effects due to the boundary placement (see Harstad and Bellan 1991). Figure 12 indicates that a much smaller domain can be considered in the case of solid particle pyrolysis. In fact, only very small variations in both char yield and conversion time are observed for values of $R_T > 5R_{p,0}$. The differences between pyrolysis and liquid droplet simulations are due to the nature of the processes. Liquid fuel combustion generally involves initial evaporation followed by second order reaction kinetics with rates which are mixing (diffusion) controlled. Boundary placement near the droplet will significantly increase the mixture fraction of free stream species at the droplet surface. In addition, exothermicity of liquid fuels is generally much larger than the pyrolysis gas phase reactions, resulting in substantial thermal expansion effects relatively far from the droplet. The trends observed for both cellulose and wood particles indicate that the value $R_R = 10R_{p,0}$ is sufficiently large to make boundary placement effects negligible for the final yields and conversion times.

Effects of the Particle Size

It is commercially desirable to pyrolyze large biomass particles as the grinding process necessary to reduce the particle size is overly expensive (Di Blasi 1993). Kinetic limits are not necessarily applicable for modeling biomass pyrolysis in reactors. Simmons and Gentry (1986) investigate kinetic limits for pyrolysis control as a function of both $R_{p,0}$ and the heating temperature. Using a mathematical model with prescribed particle surface conditions they estimated that a $200\mu m$ biomass particle is heat transfer limited for temperatures larger than $775K$. However, comparisons with experiments indicated limiting values well below the model predictions. This discrepancy was attributed to the neglect of the thermal boundary layer outside of the particle in the model. The current work addresses the issue of particle size on pyrolysis yields and kinetic efficiencies for relatively large initial particle sizes and accounts for all inner and outer particle effects.

Figure 13 illustrates the effect of the initial particle size on the final char yields and conversion times. The initial particle diameter is varied in the range $[0.05cm, 2.0cm]$. Both the char yield and t_c are observed to be increasing functions of $R_{p,0}$. However, only relatively small changes in char yield are found for particles larger than $R_{p,0} \approx 0.4cm$. Below this value there is insufficient particle mass for the endothermic reactions to overcome heat diffusion from the surroundings. Therefore, the particle is pyrolyzed at higher effective heating temperatures. For particles larger than this limit, endothermicity maintains an approximately constant effective heating temperature in agreement with the results of Fig.9. For the given reactor conditions, the optimal particle size for char maximization is approximately $0.4cm$. Larger particles will produce only relatively small increases in char yield, at the expense of substantially longer reactor residence times (minutes→hours). The data also reveals that only wood pyrolysis approaches the kinetic control limit within the range of parameters investigated. The conversion efficiencies for the smallest initial particles sizes are 0.004 and 0.42 for cellulose and wood, respectively.

Effects of the Initial Porosity

The initial porosity of the biomass particle can also affect the pyrolysis behavior. Porosity is directly related to the particular biomass specimen under consideration; however, it is not an intrinsic property of the substance. Values of the porosity in hard woods have been reported in the range $0.71 < \varepsilon_0 < 0.85$ by Magnaterra *et. al.* (1992) using both porosimetry and electron scanning microscopy and may be smaller for compactified biomass. Results are presented in Fig.14 for char yields and conversion times as a function of ε_0 in the range [0.4, 0.9]. This range of values is sufficient to capture the pertinent characteristics of a variety of viable pyrolysis materials, yet is sufficiently large to remain within the bounds of the assumptions used in the model derivation. The total mass of each particle remains constant due to the prescribed values for the initial partial densities of cellulose and wood (Table 2). Figure 14 reveals several interesting influences of ε_0. The char yields for both cellulose and wood remain nearly constant over the entire range of considered porosities due in part to the fixed initial particle mass. On the other hand, t_c shows an increasing trend with initial porosity for both cellulose and wood. Therefore, the effective heating rates of the particles are being decreased with increasing ε_0. This can be explained in terms of the thermal conduction model employed in the internal energy equation. The effective conductivity λ_{eff} is modeled in terms of a *parallel* conduction model corresponding to volume averaging over the respective solid and gas phase conductivities. Tables 2 and 3 show that the conductivity for the solids is in general an order of magnitude larger than that of the gases. Therefore, the *parallel* model results in relatively smaller effective heat diffusion into the particle for increasing ε_0. A mass averaged conduction model would be expected to show very little effect of ε_0 on t_c. Further experimental results are needed in order to ascertain which type of conduction model is more realistic. Experimentally derived plots of the char yield and t_c versus ε may indicate the correct modeling approach for the effective conductivity.

Effects of the Initial Particle Temperature

One method of testing the reliability of results in experiments is to pre-treat the biomass before analysis. Varhegyi and Antal (1989) employed thermal pre-treatment in addition to investigating the effects of catalysts ($NaCl$, $FeSO_4$, $ZnCl_2$) on Avicel cellulose pyrolysis. Although the presence of the catalysts altered the reaction kinetics, pre-treatment of the pure specimen at $535K$ for 1 hour did not produce significant changes in the observed evolutions. Other experiments have addressed the issue of ambient pressure and its effect on the pyrolysis. For example, Richard and Antal (1992) were able to increase char yields from 6% to 41% by raising the pressure from $0.1MPa$ to $1.0MPa$ for the pyrolysis of cellulose in a packed bed reactor. The present cellulose and wood kinetics schemes do not allow for the investigation of catalyst, thermal pre-treatment duration or pressure effects. However, the value of $T_{p,0}$ can be expected to affect t_c, and possibly the char yield. Figure 15 illustrates these effects by varying $T_{p,0}$ in the range $300K \leq T_{p,0} \leq 600K$. It is evident that $T_{p,0}$ does not significantly affect the effective pyrolysis temperature as both cellulose and wood char yields remain nearly constant. Conversion times are decreased with increasing $T_{p,0}$, as expected. However, the time required to raise the particle temperature from $300K$ to $600K$, as estimated from the difference in conversion times, is approximately $100s$. This value is significantly less than the total conversion time and gives further evidence that it is the endothermicity of the solid phase reactions which primarily governs conversion times and, therefore, the effective heating rates.

Comparison with Experiments

The simulations presented in this work have not been conducted with the intent of representing either the conditions or parameters of specific experiments. However, comparisons with past laboratory results are useful in interpreting the validity of the particle model, as well as the cellulose and the wood kinetics schemes. The minimum requirement from a model or kinetic scheme is that it should predict the total char (and therefore the vapor) yields and also the required time for complete conversion. To the author's knowledge, there are no experiments with measured yields and/or conversion times for "large" isolated cellulose or wood particle pyrolysis. This is because it is advantageous to consider very fine particle sizes (kinetically controlled pyrolysis) when measuring reaction rate parameters. Nevertheless, by comparing simulations with available data for a variety of conditions and materials, it is possible to qualitatively evaluate both the particle model and kinetics schemes. The two kinetics schemes addressed in this work place limits on the total possible char yields and conversion times (see Fig.7). Limiting the discussion to T_R in the range $[550K,\ 1100K]$ (corresponding to total pyrolysis time scales less than $\sim 10^6 s$), then the possible available char yield must be less than ≈ 0.2 for the cellulose scheme, whereas the wood scheme limits char yields to a range of approximately (0.27, 0.32). Any experimental evidence for char yields outside of these ranges would indicate an inconsistency in the modeled pyrolysis kinetics.

In Fig.16 comparisons are made for the total char yield as a function of T_R for the baseline case cellulose and wood particles with the results of seven experiments. Two different sets of measurements conducted with pure cellulose are included. Shafizadeh *et. al.* (1979) performed experiments using cellulose powder in a vacuum tube furnace at relatively low temperatures. The very fine powder sizes in addition to the low heating temperatures suggests that the pyrolysis is nearly completely kinetically controlled. In agreement with this hypothesis, the experimental data compare very well with the kinetic limits of the present model. Cellulose pyrolysis in both fluid bed and entrained flow reactors was studied for a larger temperature range and particle size ($R_{p,0} \approx 50\mu m$) by Scott et. al. (1988). As may be expected, the larger particle size shows slightly more char yield than does the vacuum pyrolyzed powder. The data reveal that the slightly larger particles employed by Scott *et. al.* still pyrolyze near the kinetic limit. The much larger particle size ($R_{p,0} = 5mm$) considered in our simulations is dominated by diffusion limitations and, as such, shows larger char yields than either experiment. However, the smallest cellulose particle considered in the current work has $R_{p,0} = 0.25mm$ and was pyrolyzed at $T_R = 900K$ (see Fig.13). In this case, the final char yield is approximately 0.02; comparable to the data of Scott et. al. (1988). Both sets of experimental cellulose char yields are consistent with the limits imposed by the model kinetics scheme (< 0.2). The cellulose kinetics scheme is thus considered to be in good agreement with experiments, and the numerical particle model shows the correct qualitative behavior for diffusion dominated pyrolysis.

Experimental data from wood pyrolysis show that the wood kinetics scheme is inadequate. Figure 16 includes four sets of experimentally obtained data for wood pyrolysis. Thurner and Mann (1981) measured char yields from the pyrolysis of Oak sawdust ($R_{p,0} \sim 1mm$), over a relatively low temperature range, using a furnace reactor at atmospheric pressure. Their results suggest a nearly constant char yield of approximately 0.3 over the temperature range $[602K,\ 665K]$. Good agreement with both the wood particle model and the kinetic limit is observed (Fig.16). This is not surprising as the primary reaction constants used in the current model were extracted from the Thurner and Mann measurements. The small over prediction as compared to their data is a result of the secondary char producing reaction (K_8) which was not originally included in their kinetics scheme. The remaining wood pyrolysis data are for Poplar

wood and Olive husk measured in a semi-batch moving bed reactor by Maschio *et. al.* (1992), and for Eastern Red Maple pyrolyzed in both a fluid bed and a transport reactor by Scott et. al. (1988). All of these experiments used relatively small particle sizes in order to remain near the kinetic control limits. Relatively good agreement is found between the experiments and the model for only the lowest temperatures considered (near kinetic control). However, all of the experiments display a much sharper reduction in char yield with increasing reactor temperatures than either the particle model or the kinetic scheme is capable of producing. Analysis of Fig.7 indicates that the wood kinetics scheme is not capable of reproducing the lower experimental data for any reactor temperature. These results reveal a major flaw in the present wood pyrolysis scheme in predicting char yields.

Although not included in the data of Fig.16, the present model results can be used to make a qualitative assessment of the modified wood kinetics scheme used in both Di Blasi (1993a) (paper I) and Di Blasi (1992) (paper II). The modified wood scheme is essentially the same as the present wood kinetics scheme except that the original primary reaction frequency constants presented in Thurner and Mann (1981) were modified by the author (apparently increased by a factor of 3600) (Di Blasi 1996a). Both papers I and II provide tabular data for char yields at a time when 10% of the original particle mass remains, and with $T_R \approx 1100K$. In both cases, nearly constant char yields are reported with very little deviations over a relatively wide range of parameters. The respective mean char yields are approximately 0.41 and 0.49 for papers I and II. The discrepancy between char yields obtained with apparently the same reaction scheme has not been explained. In addition, the final yields are even higher when the remaining particle mass is consumed. Since a comparison with Fig.16 shows that these char yields are exceedingly high, it seems that the modified scheme of Di Blasi is of questionable merit.

Quantitative comparisons with experimentally measured conversion times are difficult to make. This is particularly true since such reported data are usually in terms of particle residence times in the reactor. Even when complete pyrolysis conversion is achieved, the final times are not generally tabulated. However, some data exist which show that the present model is in approximate agreement with experiments. Figure 13 illustrates that the smallest cellulose particle ($R_{p,0} = 0.25mm$) converts completely in $1.6s$ at a reactor temperature of $T_R = 900K$. This value compares favorably to the $0.7s$ residence time for an Avicell cellulose particle of initial radius of $R_{p,0} \approx 0.3mm$ in a $973K$ reactor measured by Scott *et. al.* (1988). Oak sawdust pyrolysis at temperatures $627K \leq T_R \leq 665K$ occurs on total reaction time scales between 23 and 31 minutes according to Thurner and Mann (1981). Again, these values are similar to the present simulation results as depicted in Fig.6 for slightly larger particles ($\approx 2000s$). These comparisons suggest that the present particle model is able to reproduce experimental conversion times for both cellulose and wood particles with a reasonable degree of accuracy.

Conclusions and Future Work

A mathematical model is presented which is capable of modeling both the temporal and the spatial evolutions of porous solid particle reactions for which volumetric reaction rate kinetics are known *a priori*. The model is derived for conditions in which both the porosity and the permeability are assumed

large enough to allow for continuous gas phase flow within the particle, and is valid in both the interior and the exterior particle regions. Although the equations are relatively intensive computationally, they provide an accurate representation of particle reactions which may be used to evaluate various kinetics schemes for detailed comparisons with experiments and previous models.

The mathematical model is used to simulate the pyrolysis of spherical biomass particles in initially quiescent super-heated steam environments by considering previously published kinetics schemes for both cellulose and generic wood reactions. As many as five competing reactions are employed, including complete property variations, thermal and mass transport, and both endothermic and exothermic heats of reaction. Numerical solutions to the modeled equations are used to illustrate the effects of the reactor temperature, heating rate, porosity, initial particle size and initial particle temperature on both char yields and conversion times. Solutions for "baseline case" particles reveal that the modeled equations are capable of reproducing the qualitative evolutions of the pyrolysis process as observed in past experiments and models.

In general, the variation of any parameter which produces an increase in the effective pyrolysis temperature will reduce both the total char yields and the conversion times for both cellulose and wood particles. Such parameter changes include; 1) increasing the reactor temperature, 2) increasing the heating rate, or 3) decreasing the initial particle size. However, practical limits on maximum effective pyrolysis temperatures are imposed by the relative endothermicity of the interior pyrolysis reactions (as related to the particle mass), and also to a lesser extent by thermal diffusion and heat capacity effects. As the particle is heated from its initial value, three stages of evolution are observed. First, an initial rapid heating during which only negligible reactions occur. This is followed by a period of primary pyrolysis which occurs at relatively constant effective pyrolysis temperatures determined by the relative endothermicity. The final regime is reached when the particle mass has been reduced sufficiently to allow the inward thermal diffusion to overcome endothermic heat absorption. The remaining particle mass is then rapidly heated until pyrolysis completion occurs, generally at temperatures less than the reactor temperature. Both the mean particle temperature and the heating rate are observed to be almost identical when time is normalized by the final conversion time. In all cases considered, the three pyrolysis regimes correspond to approximately 20%, 60% and 20% of the total conversion time, respectively.

The simulated results show that models which neglect the exterior particle thermal boundary layer can substantially over predict both the pyrolysis rate and the experimentally attainable tar yields. Variations of either the initial porosity or the initial particle temperature primarily affect the conversion time, whereas only relatively minor deviations in the total char yields are observed. An increase in the conversion time with increasing porosities is attributed to the *parallel* thermal conduction model employed for the multi-phase heat transfer within the particle. This trend needs further validation through future experiments. In almost all of the particle simulations considered, the kinetically controlled assumption proved to be invalid.

A qualitative comparison with experimental results from several investigations is provided. These comparisons indicate that the cellulose kinetics scheme provides a relatively accurate prediction of char yields and conversion times over a large range of reactor temperatures. The wood pyrolysis kinetics display

fair agreement with experiments for very low reactor temperatures. However, at higher reactor temperatures the wood kinetics scheme substantially over predicts the char yields and is inconsistent with the experimental measurements. It is suggested that significant improvements be made to the wood pyrolysis kinetics scheme before any practical predictions are attempted. Although the experimental data were performed for very small particle sizes in order to exhibit kinetically controlled rates, comparisons with the present particle model have indicated a good qualitative agreement for diffusion limiting particle dynamics.

Future work includes: (1) establishing, in collaboration with NREL, a kinetic scheme capable of reproducing experimental wood pyrolysis results, and (2) expanding the model in order to portray a variety of reactor conditions, such as available at NREL, including turbulent diffusion, wall effects, and free stream convection. The building block for these reactor models is the biomass particle model presented above.

Acknowledgements

This research was conducted at the Jet Propulsion Laboratory (JPL) and sponsored by the U.S. Department of Energy (DOE), with Mr. Neil Rossmeissl (DOE Headquarters) and Mr. D. Hooker (DOE Golden Center) serving as contract monitors, under an agreement with the National Aeronautics and Space Administration. Computational resources are provided by the super computing facility at JPL. The authors wish to thank Mr. Jim Diebold and Dr. Esteban Chornet of the National Renewable Energy Laboratory for helpful discussions, and also Dr. Kenneth Harstad of JPL for advice on the numerical method.

References

Antal, M. J., and W. S. L. Mok. 1990."Review of Methods for Improving the Yield of Charcoal from Biomass. *Energy and Fuels*, 4(3):221–225.

Antal, M. J., and G. Varhegyi. 1995."Cellulose Pyrolysis Kinetics: The Current State of Knowledge." *Ind. Eng. Chem. Res.*, 34(3):703–717.

Bear, J. 1972. *Dynamics of Fluids in Porous Media*. American Elsevier, Ney York, New York.

Bellan, J., and R. Cuffel. 1983."A Theory of Nondilute Spray Evaporation Based upon Multiple Drop Interactions." *Comb. and Flame*, 51:55–67.

Bhatia, S. K., and D. D. Perlmutter. 1980. "A Random Pore Model for Fluid-Solid Reactions: I. Isothermal, Kinetic Control." *AIChE Journal*, 26(3):379–386.

Bhatia, S. K., and D. D. Perlmutter. 1981. "A Random Pore Model for Fluid-Solid Reactions: II. Diffusion and Transport Effects." *AIChE Journal*, 27(2):247–254.

Bilbao, R., A. Millera, and M. B. Murillo. 1992. "Heat Transfer and Weight Loss in the Thermal Decomposition of Large Wood Particles." In A. V. Bridgwater, editor, *Advances in Thermochemical Biomass Conversion*, volume 2, pages 833–845. Blackie Academic and Professional, New York, New York.

Di Blasi, C. 1993. "Analysis of Convection and Secondary Reaction Effects within Porous Solid Fuels Undergoing Pyrolysis." *Combust. Sci. and Tech.*, 90:315–340.

Di Blasi, C. 1993. "Modeling and Simulation of Combustion Processes of Charring and Non-Charring Solid Fuels." *Prog. Energy Combust. Sci.*, 19:71–104.

Di Blasi, C. 1994. "Numerical Simulation of Cellulose Pyrolysis." *Biomass and Bioenergy*, 7:87–98.

Di Blasi, C. 1996 "Kinetic and Heat Transfer Control in the Slow and Flash Pyrolysis of Solids." *Ind. Eng. Chem. Res.*, 35:37–46.

Bradbury, A. G., Y. Sakai, and F. Shafizadeh. 1979 "A Kinetic Model for Pyrolysis of Cellulose." *J. App. Polymer Sci.*, 23:3271–3280.

Caram, H. S., and N. R. Amundson. 1977. "Diffusion and Reaction in a Stagnant Boundary Layer about a Carbon Particle." *Ind. Dng. Chem. Fundamentals*, 16:171.

Chan, W. R., M. Kelbon, and B. Krieger-Brockett. 1988. "Correlations of Reaction Products with Process Conditions." *Ind. Eng. Chem. Res.*, 27:2261–2275.

Di Blasi, C. 1992. "Modeling of Transport Phenomena and Kinetics of Biomass Pyrolysis." In A. V. Bridgwater, editor, *Advances in Thermochemical Biomass Conversion*, 2:906–921. Blackie Academic and Professional, New York, New York.

Di Blasi, C. , Feb 1996. Personal communication.

Diebold, J. P. Oct. 1980. "Ablative Pyrolysis of Macroparticles of Biomass." In *Proc. Spec. Workshop Fast Pyrolysis of Biomass*, 237–251, Copper Mountain, Colorado. Solar Energy Research Institute.

Diebold, J. P, and A. Power. 1988. "Engineering Aspects of the Vortex Pyrolysis Reactor to Produce Primary Pyrolysis Oil Vapors for Use in Resins and Adhesives." In A. V. Bridgwater and J. L. Kuester, editors, *Research in Thermochemical Biomass Conversion*, 609–628. Elsevier Applied Science, New York, New York.

Gavalas, G. R. 1980. "A Random Capillary Model with Application to Char Gasification at Chemically Controlled Rates." *AIChE Journal*, 26(4):577–585.

Gavalas, G. R. 1981. "Analysis of Char Combustion Including the Effect of Pore Enlargement." *Comb Sci. and Technol.*, 24:197–210.

Harstad, K., and J. Bellan. 1991. "A Model of the Evaporation of Binary-Fuel Clusters of Drops." *Atom. and Sprays*, 1:367–388.

Kothari, V., and M. J. Antal. 1985. "Numerical Studies of the Flash Pyrolysis of Cellulose." *Fuel*, 64:1487–1494.

Lede, J., J. Panagopoulos, H. Z. Li, and J. Villermaux. 1985. "Fast Pyrolysis of Wood: Direct Measurement and Study of Ablation Rate." *Fuel*, 64:1514–1520.

Lim, K. S., J. X. Zhu, and J. R. Grace. 1995. "Hydrodynamics of Gas-Solid Fluidization." *Fuel*, 21(Suppl.):141–193.

Loewenberg, M., J. Bellan, and G. R. Gavalas. 1987. "A Simplified Description of Char Combustion." *Chem. Eng. Comm.*, 58:89–103.

Magnaterra, M., J. R. Fusco, J. Ochoa, and A. L. Cukierman. 1992. "Kinetic Study of the Reaction of Different Hardwood Sawdust Chars with Oxygen. Chemical and Structural Characterization of the Samples." In A. V. Bridgwater, editor, *Advances in Thermochemical Biomass Conversion*, 1:116–130. Blackie Academic and Professional, New York, New York.

Maschio, G., A. Lucchesi, and C. Koufopanos. 1992. "Study of Kinetic and Transfer Phenomena in the Pyrolysis of Biomass Particles." In A. V. Bridgwater, editor, *Advances in Thermochemical Biomass*

Conversion, 2:746–759. Blackie Academic and Professional, New York, New York.

Mon, E., and N. R. Amundson. 1978. "Diffusion and Reaction in a Stagnant Boundary Layer About a Carbon Particle 2. An extension." *Ind. Dng. Chem. Fundamentals*, 17:313.

Narayan, R., and M. J. Antal. 1996. "Thermal Lag, Fusion, and the Compensation Effect During Biomass Pyrolysis." *Ind. Eng. Chem. Res.*, submitted.

Reed, T. B., J. P. Diebold, and R. Desrosiers. Oct. 1980. "Perspectives in Heat Transfer Requirements and Mechanisms for fast Pyrolysis." In *Proc. Spec. Workshop Fast Pyrolysis of Biomass*, 7–20, Copper Mountain, Colorado. Solar Energy Research Institute.

Richard, J. P., and M. J. Antal. 1992. "Thermogravimetric Studies of Charcoal Formation from Cellulose at Elevated Pressures." In A. V. Bridgwater, editor, *Advances in Thermochemical Biomass Conversion*, 2:784–792. Blackie Academic and Professional, New York, New York.

Scott, D. S., J. Piskorz, M. A. Bergougnou, R. Graham, and R. P. Overend. 1988. "The Role of Temperature in the Fast Pyrolysis of Cellulose and Wood." *Ind. Eng. Chem. Res.*, 27:8–15.

Shafizadeh, F., R. H. Furneaux, T. G. Cochran, J. P. Scholl, and Y. Sakai. 1979. "Production of Levoglucosan and Glucose from Pyrolysis of Cellulosic Materials." *J. Appl. Polym. Sci.*, 23:3525–3539.

Simmons, G. M., and M. Gentry. 1986. "Particle Size Limitations Due to Heat Transfer in Determining Pyrolysis Kinetics of Biomass." *J. Anal. and Appl. Pyrolysis*, 10:117–127.

Sotirchos, S. V., and N. R. Amundson. 1984, "Diffusion and Reaction in a Porous Char Particle and in the Surrounding gas 2. Limiting Model." *Ind. Dng. Chem. Fundamentals*, 23:180.

Sotirchos, S. V., and N. R. Amundson. 1984. "Diffusion and Reaction in a Porous Char Particle and in the Surrounding gas. A Continuous Model." *Ind. Dng. Chem. Fundamentals*, 23:191.

Sundaresan, S., and N. R. Amundson. 1980. "Diffusion and Reaction in a Stagnant Boundary Layer about a Carbon Particle 5. Psuedosteady State Structure and Parameter Sensitivity." *Ind. Dng. Chem. Fundamentals*, 19:344.

Thurner, F., and U. Mann. 1981. "Kinetic Investigation of Wood Pyrolysis." *Ind. Eng. Chem. Process Des. Dev.*, 20:482–488.

Varhegyi, G., and M. J. Antal. 1989. "Kinetics of the Thermal Decomposition of Cellulose, Hemicellulose, and Sugar Cane Bagasse." *Energy and Fuels*, 3:329–335.

Figure Captions

Figure 1: Reaction schemes: (a) cellulose pyrolysis, (b) wood pyrolysis.

Figure 2: Temporal evolution of the partial char density for the baseline case simulations, (a) cellulose, $t = 53s$, $116s$, $187s$, $254s$, (b) wood, $t = 89s$, $181s$, $268s$, $348s$.

Figure 3: Temporal evolution of the tar mass fraction for the baseline case simulations, (a) cellulose, $t = 53s$, $116s$, $187s$, $254s$, (b) wood, $t = 89s$, $181s$, $268s$, $348s$.

Figure 4: Temporal evolution of the temperature for the baseline case simulations, (a) cellulose, $t = 0s, 53s$, $116s$, $187s$, $254s$, (b) wood, $t = 0s, 89s$, $181s$, $268s$, $348s$.

Figure 5: Temporal evolution of the gas phase velocity for the baseline case simulations, (a) cellulose, $t = 53s$, $116s$, $187s$, $254s$, (b) wood, $t = 89s$, $181s$, $268s$, $348s$.

Figure 6: Char yield and conversion time as a function of the reactor temperature for $T_{p,0} = 500K$, $R_T = 5R_{p,0}$, $R_{p,0} = 5mm$ and $\varepsilon_0 = 0.7$.

Figure 7: Kinetic limits for char yield and conversion time as a function of the reactor temperature.

Figure 8: Kinetic efficiency for char yield and conversion time as a function of the reactor temperature for $R_T = 5R_{p,0}$, $R_{p,0} = 5mm$, $\varepsilon_0 = 0.7$ and $T_{p,0} = 500K$.

Figure 9: Mass averaged particle temperature $< T_p >$ as a function of time normalized by t_c for $T_{p,0} = 500K$, $R_T = 5R_{p,0}$, $R_{p,0} = 5mm$ and $\varepsilon_0 = 0.7$; (a) cellulose, (b) wood. The reactor temperature is varied from $700K \leq T_R \leq 1200K$ in increments of $100K$.

Figure 10: Temporal derivative of the mass averaged particle temperature $< T_p >$ as a function of time normalized by t_c for $T_{p,0} = 500K$, $R_T = 5R_{p,0}$, $R_{p,0} = 5mm$ and $\varepsilon_0 = 0.7$; (a) cellulose, (b) wood. The reactor temperature is varied from $700K \leq T_R \leq 1200K$ in increments of $100K$.

Figure 11: Maximum normalized radial position at which the tar fraction has decayed to 5% and the maximum tar fraction as a function of the reactor temperature for both cellulose and wood and for $T_{p,0} = 500K$, $R_T = 5R_{p,0}$, $R_{p,0} = 5mm$ and $\varepsilon_0 = 0.7$.

Figure 12: Char yield and conversion time as a function of the normalized thermal radius for $T_R = 900K$, $R_{p,0} = 5mm$, $\varepsilon_0 = 0.7$ and $T_{p,0} = 500K$.

Figure 13: Char yield and conversion time as a function of the initial particle radius for $T_R = 900K$, $R_T = 5R_{p,0}$, $\varepsilon_0 = 0.7$ and $T_{p,0} = 500K$.

Figure 14: Char yield and conversion time as a function of the initial porosity for $T_R = 900K$, $R_T = 5R_{p,0}$, $R_{p,0} = 5mm$ and $T_{p,0} = 500K$.

Figure 15: Char yield and conversion time as a function of the initial particle temperature for $T_R = 900K$, $R_T = 5R_{p,0}$, $R_{p,0} = 5mm$ and $\varepsilon_0 = 0.7$.

Figure 16: Comparison of final char yields as a function of the reactor temperature with experiments. Both the kinetic limits and simulation results are shown ($R_T = 5R_{p,0}$, $R_{p,0} = 5mm$, $\varepsilon_0 = 0.7$ and $T_{p,0} = 500K$): Poplar wood (◯) and Olive husk (•) from Maschio et. al. (1992), Avicell cellulose (□) and Eastern red maple (■)from Scott et. al. (1988), Oak sawdust (△) from Thurner and Mann (1981) and cellulose (◇) from Shafizadeh et. al. (1979).

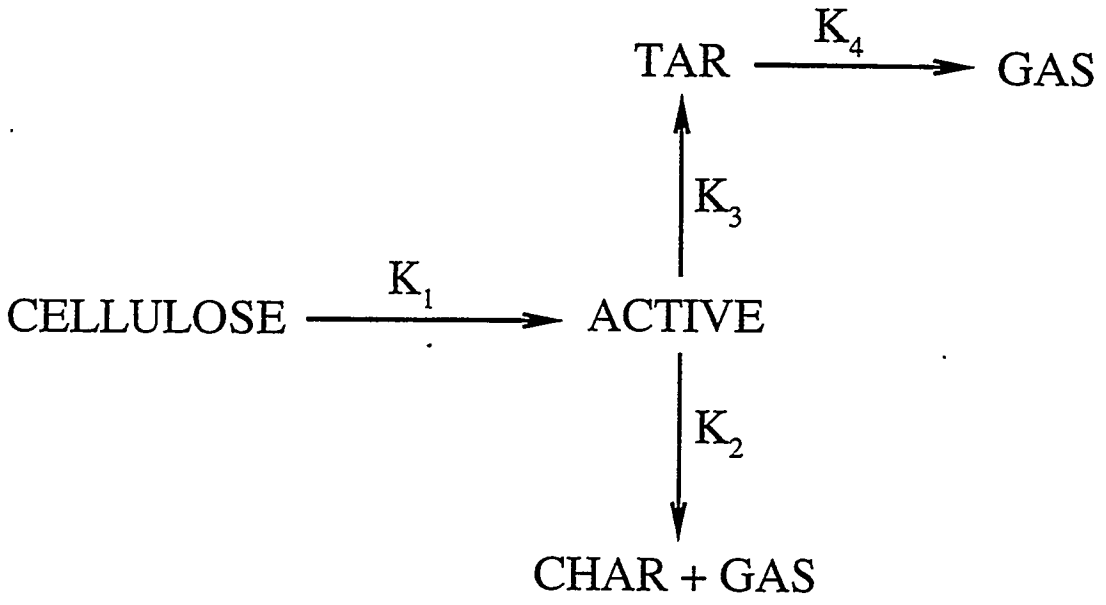


Fig. 1a

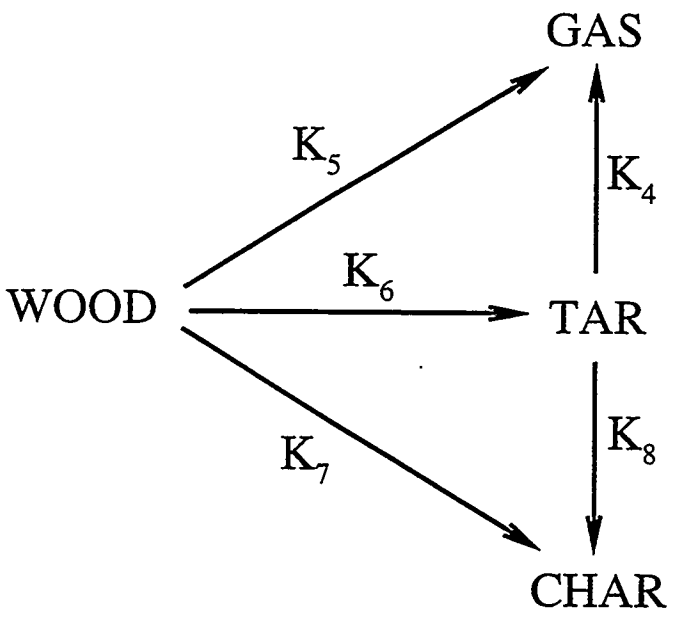


Fig. 1b

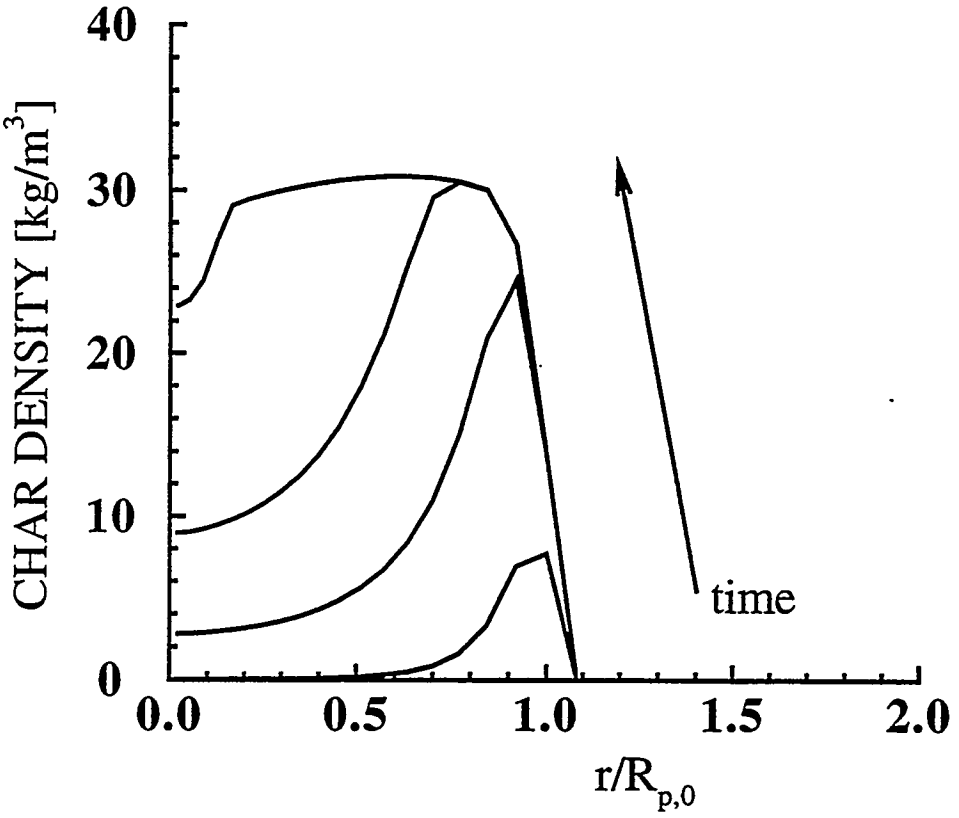


Fig. 2a

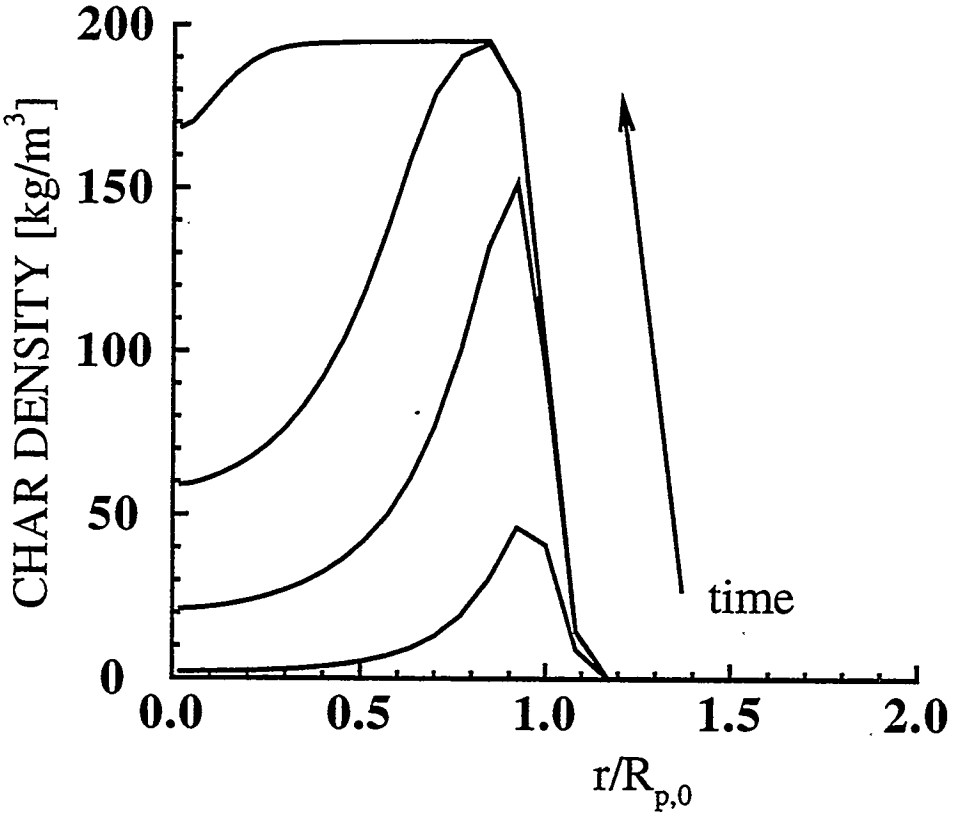


Fig. 2b

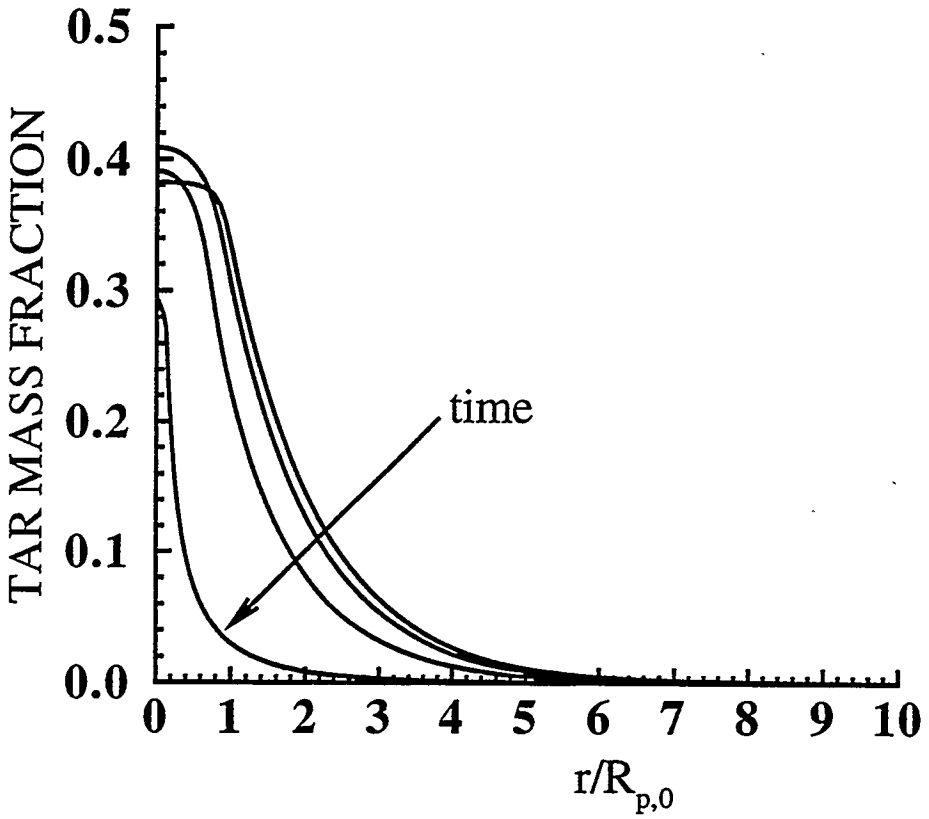


Fig. 3a

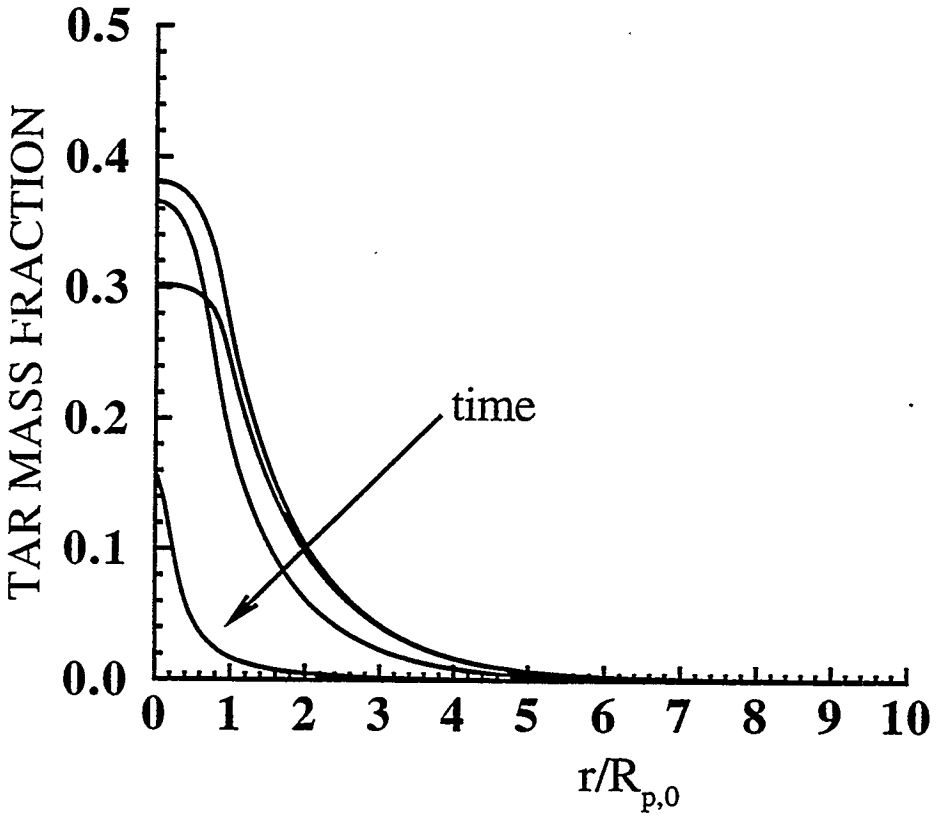


Fig. 3b

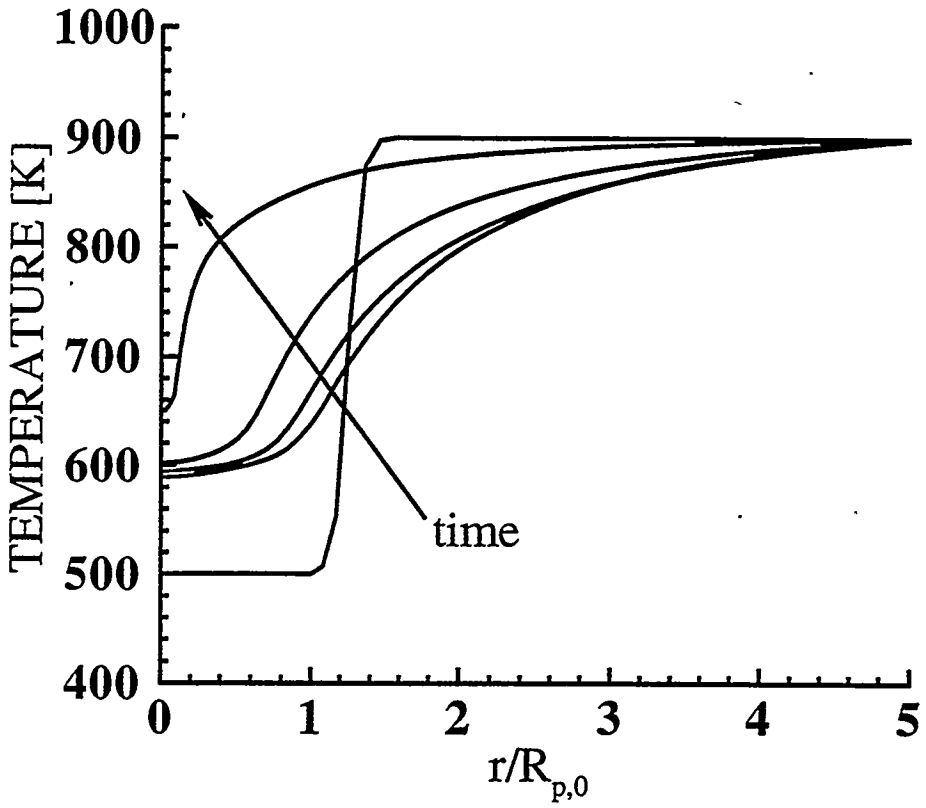


Fig. 4a

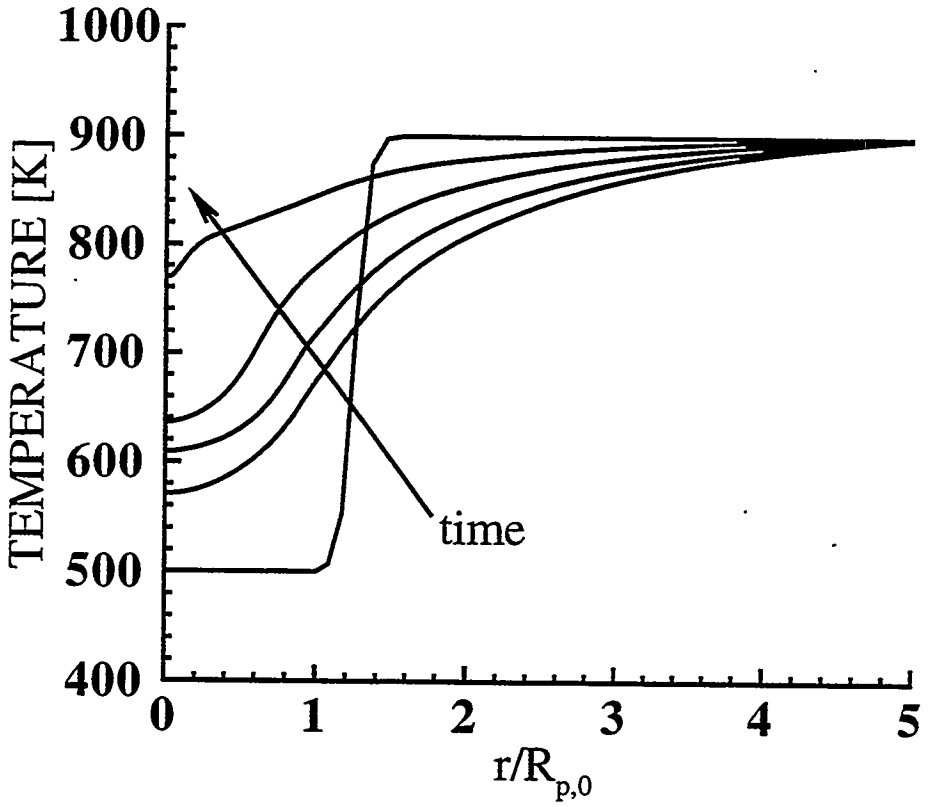


Fig. 4b

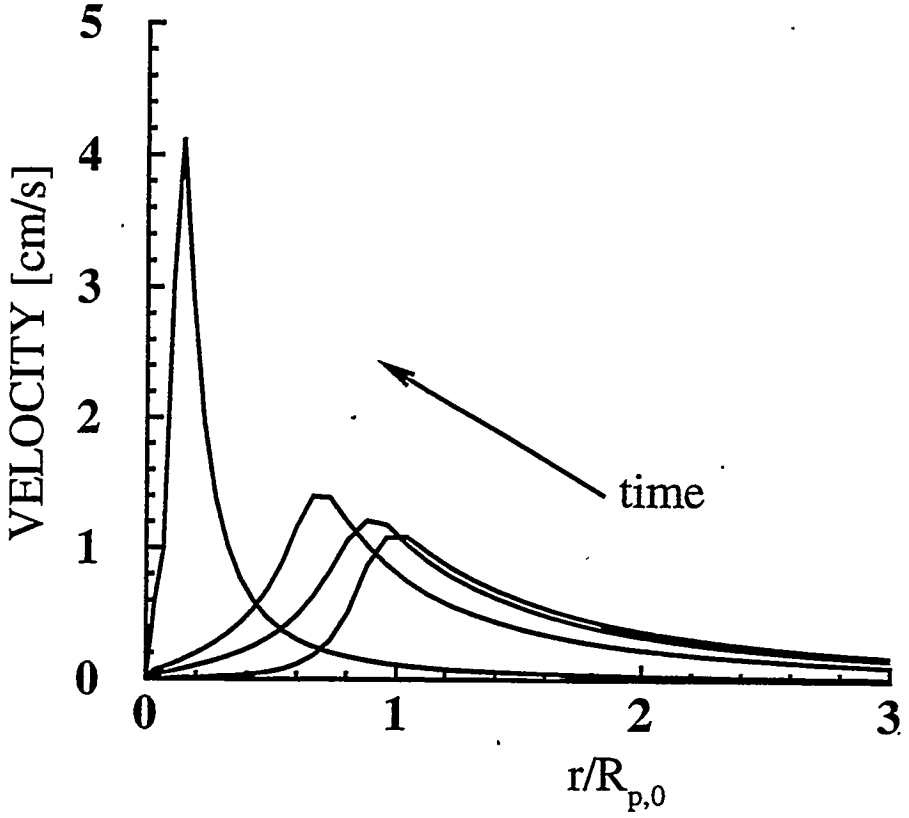


Fig. 5a

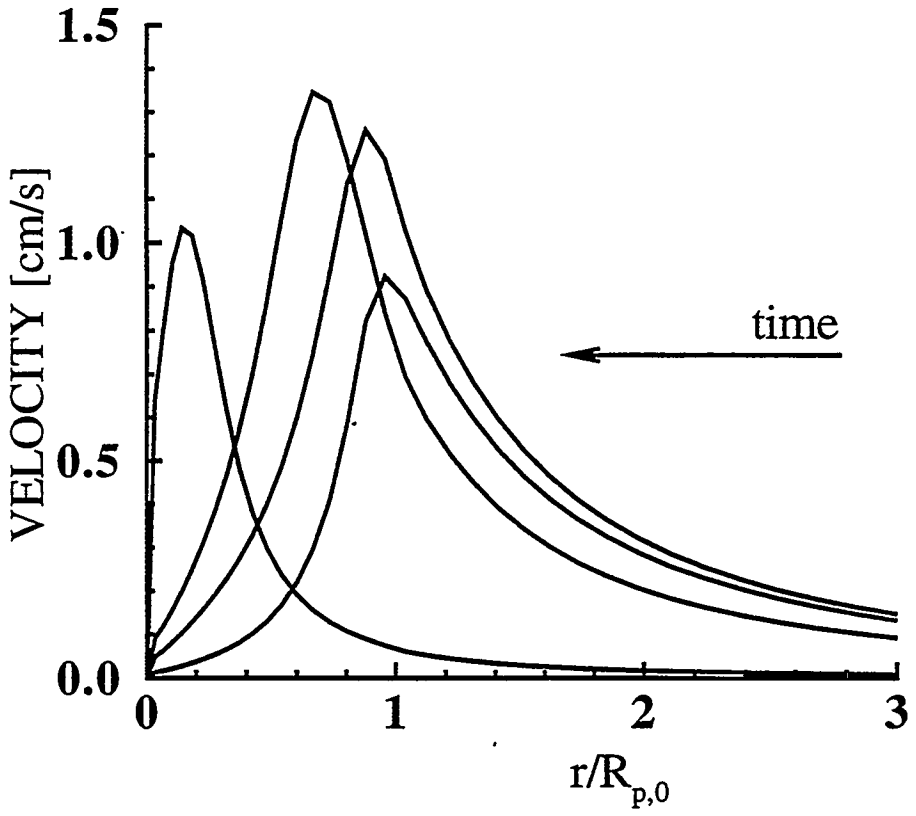


Fig. 5b

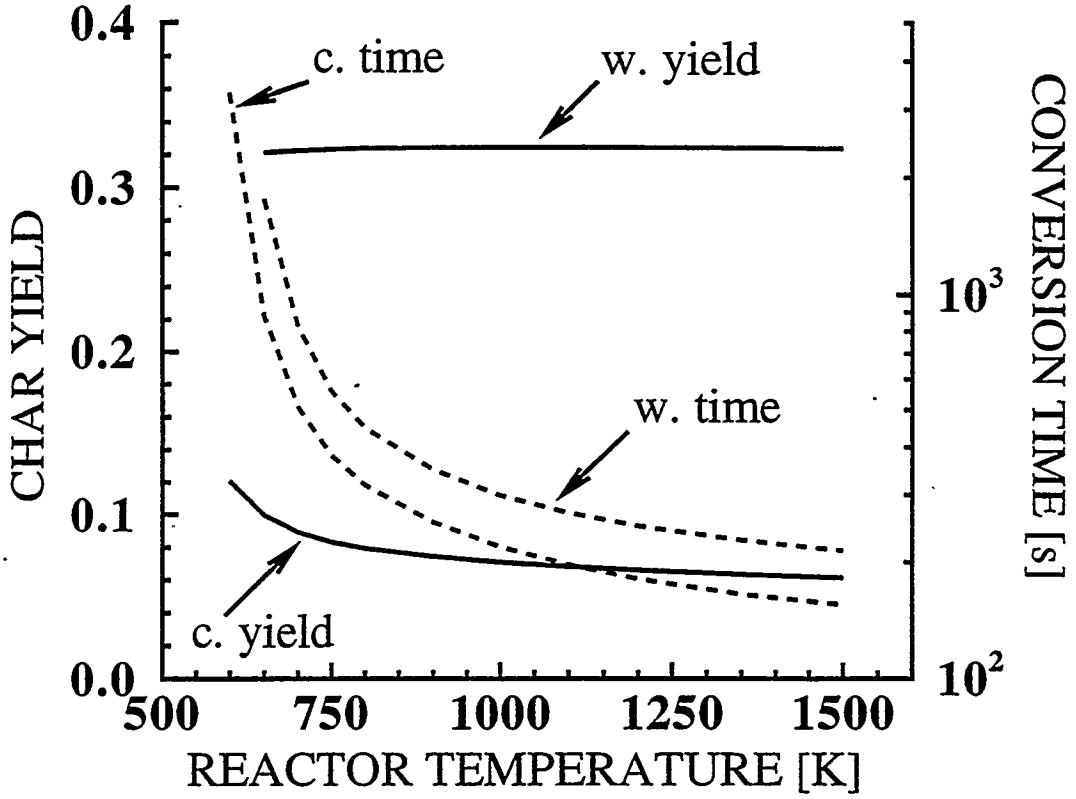

0.4
0.3
0.2
0.1
0.0
CHAR YIELD
c. time
w. yield
w. time
c. yield
10^3
10^2
CONVERSION TIME [s]
500
750
1000
1250
1500
REACTOR TEMPERATURE [K]

Fig. 6

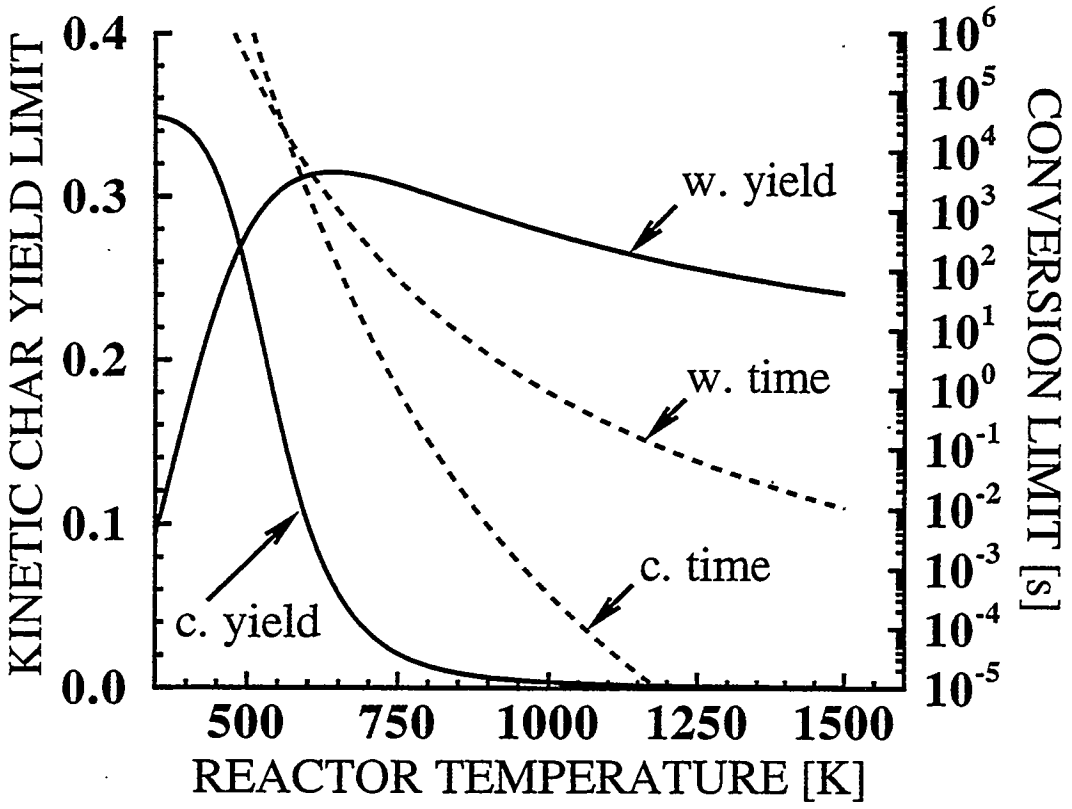

KINETIC CHAR YIELD LIMIT
0.4
0.3
0.2
0.1
0.0
w. yield
w. time
c. time
c. yield
500
750
1000
1250
1500
REACTOR TEMPERATURE [K]
CONVERSION LIMIT [s]
10^{6}
10^{5}
10^{4}
10^{3}
10^{2}
10^{1}
10^{0}
10^{-1}
10^{-2}
10^{-3}
10^{-4}
10^{-5}

Fig. 7

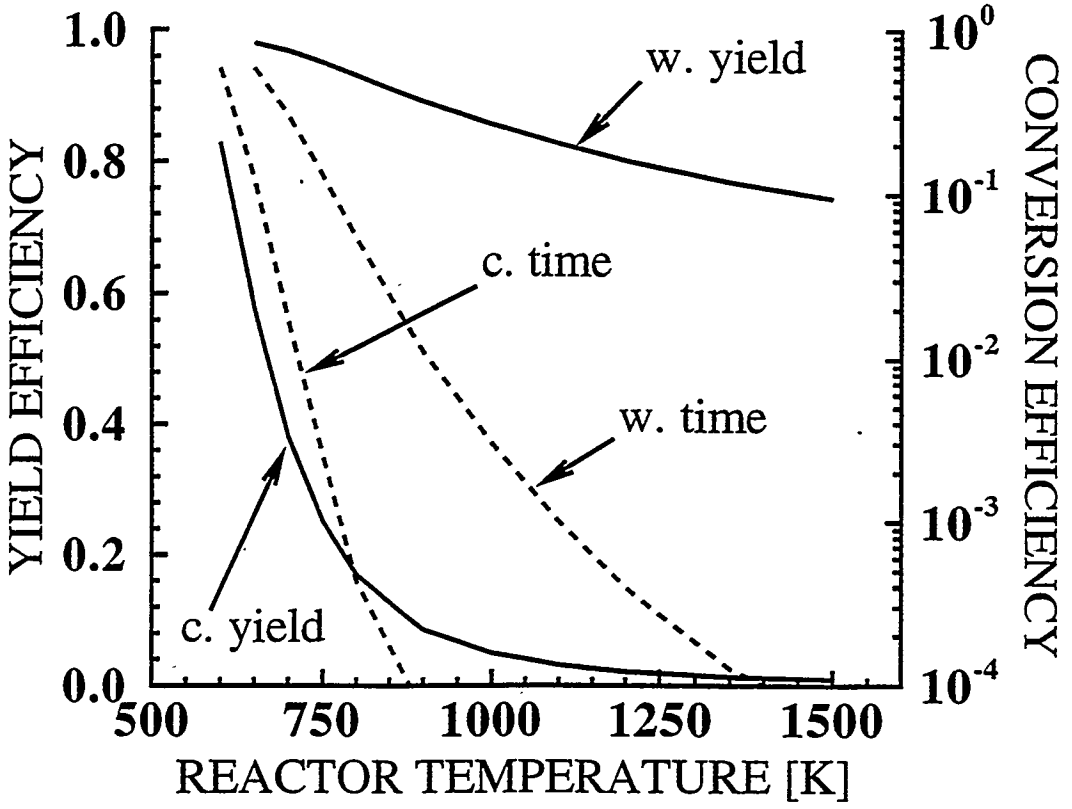

1.0
0.8
0.6
0.4
0.2
0.0
YIELD EFFICIENCY
10^{0}
10^{-1}
10^{-2}
10^{-3}
10^{-4}
CONVERSION EFFICIENCY
w. yield
c. time
w. time
c. yield
500
750
1000
1250
1500
REACTOR TEMPERATURE [K]

Fig. 8

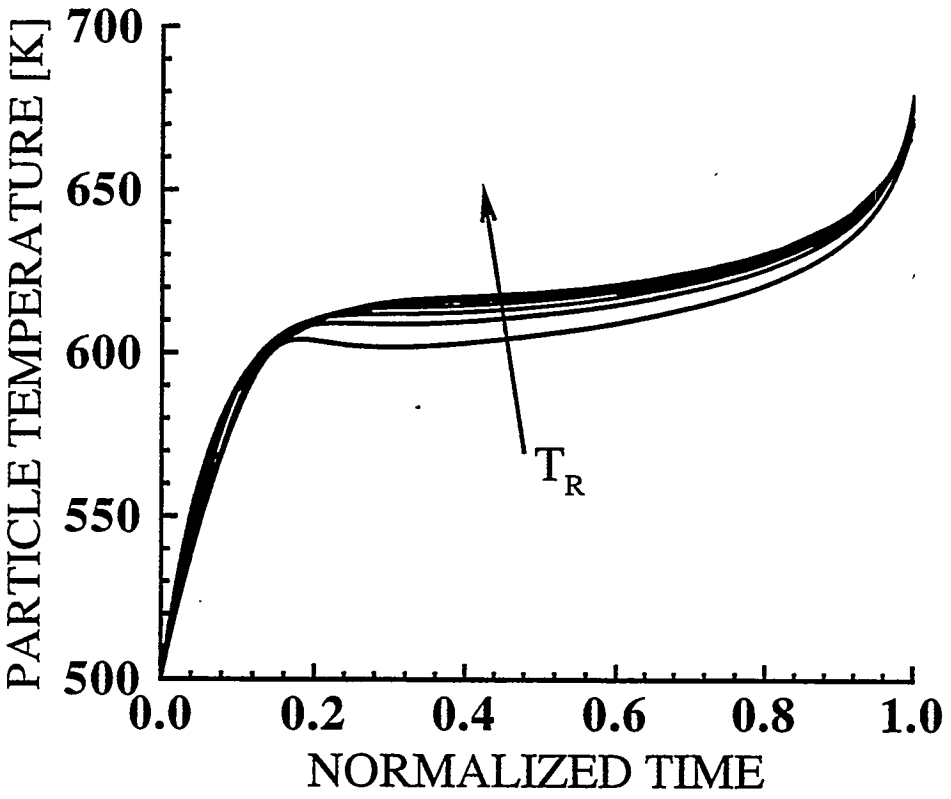

PARTICLE TEMPERATURE [K]
700
650
600
550
500
0.0
0.2
0.4
0.6
0.8
1.0
NORMALIZED TIME
T_R

Fig. 9a

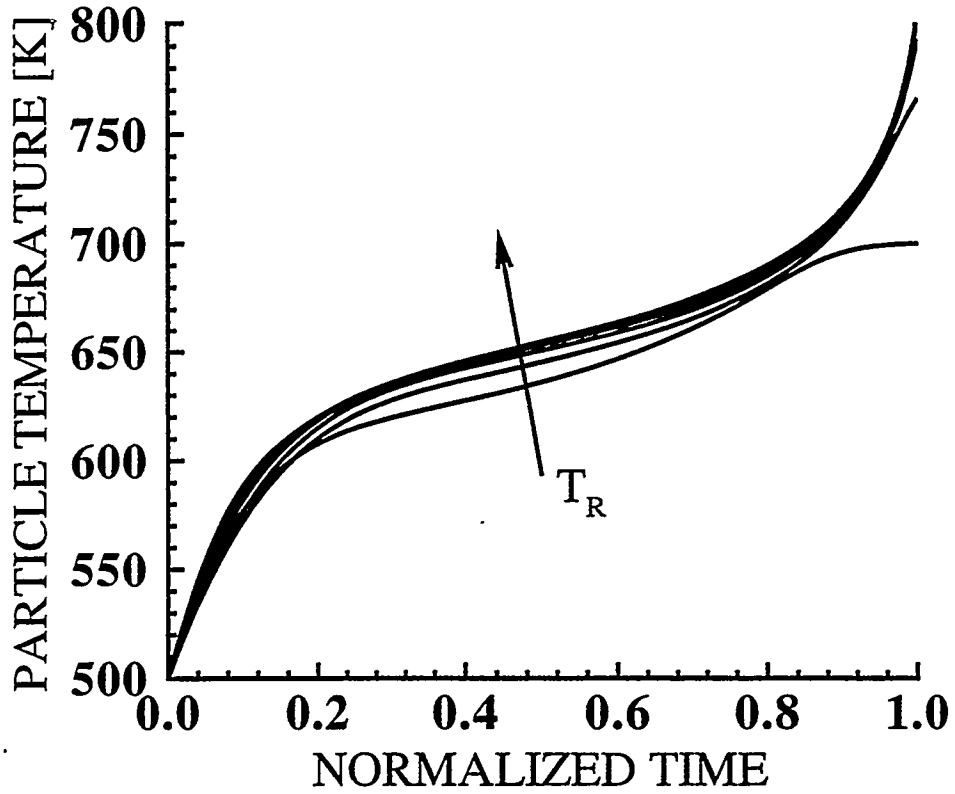

PARTICLE TEMPERATURE [K]
800
750
700
650
600
550
500
0.0
0.2
0.4
0.6
0.8
1.0
NORMALIZED TIME
T_R

Fig. 9b

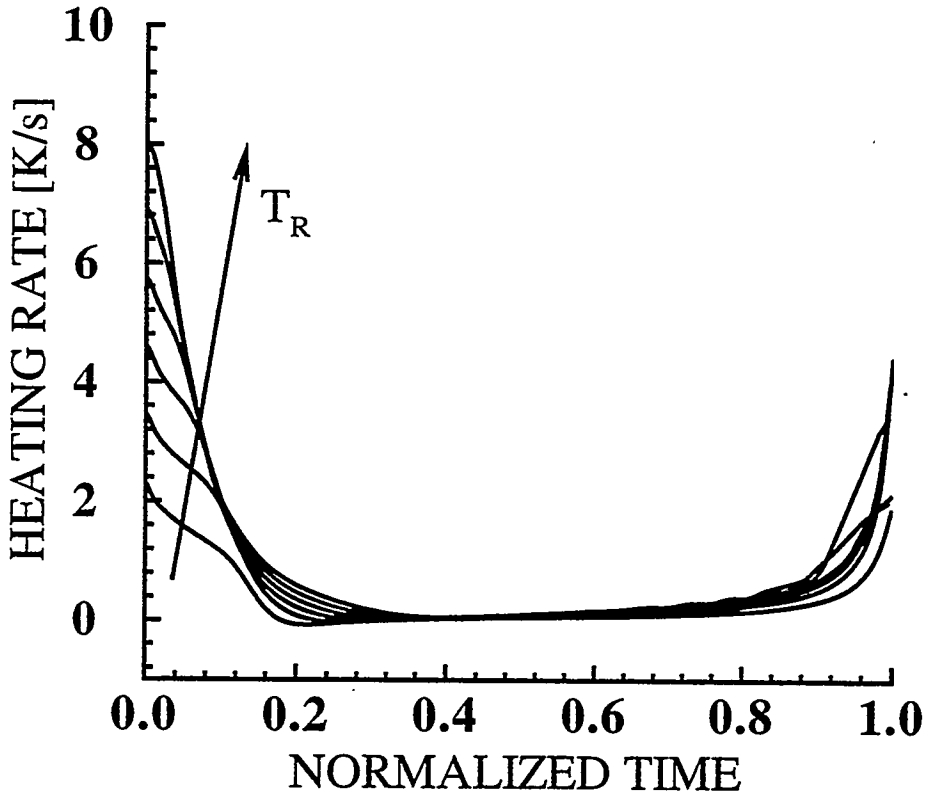


Fig. 10a

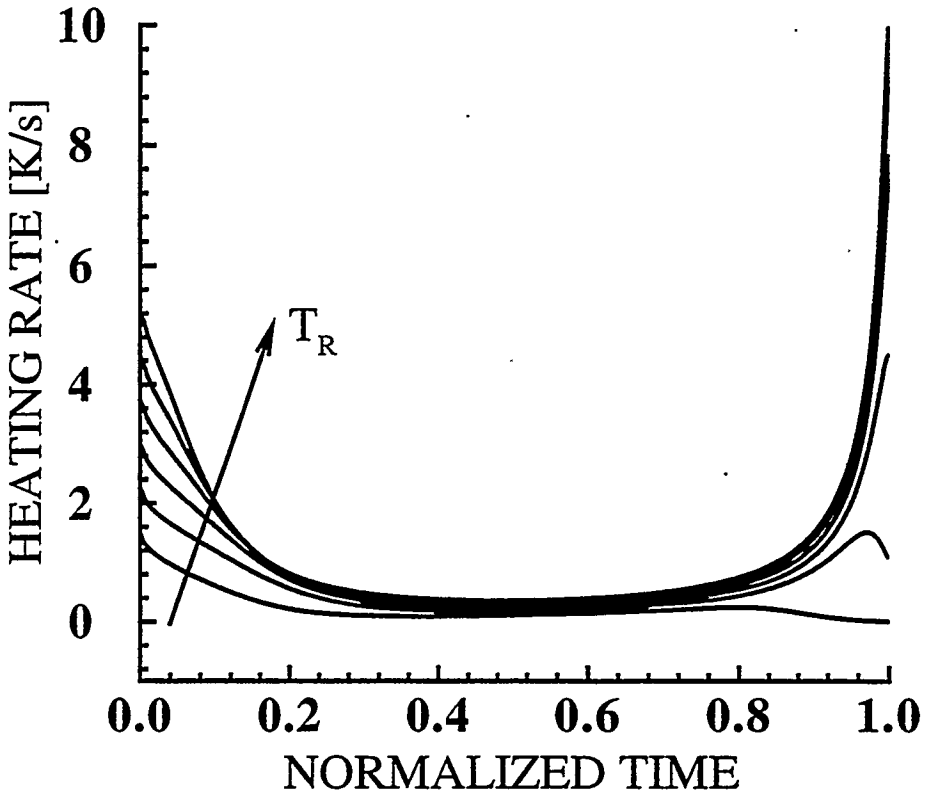


Fig. 10b

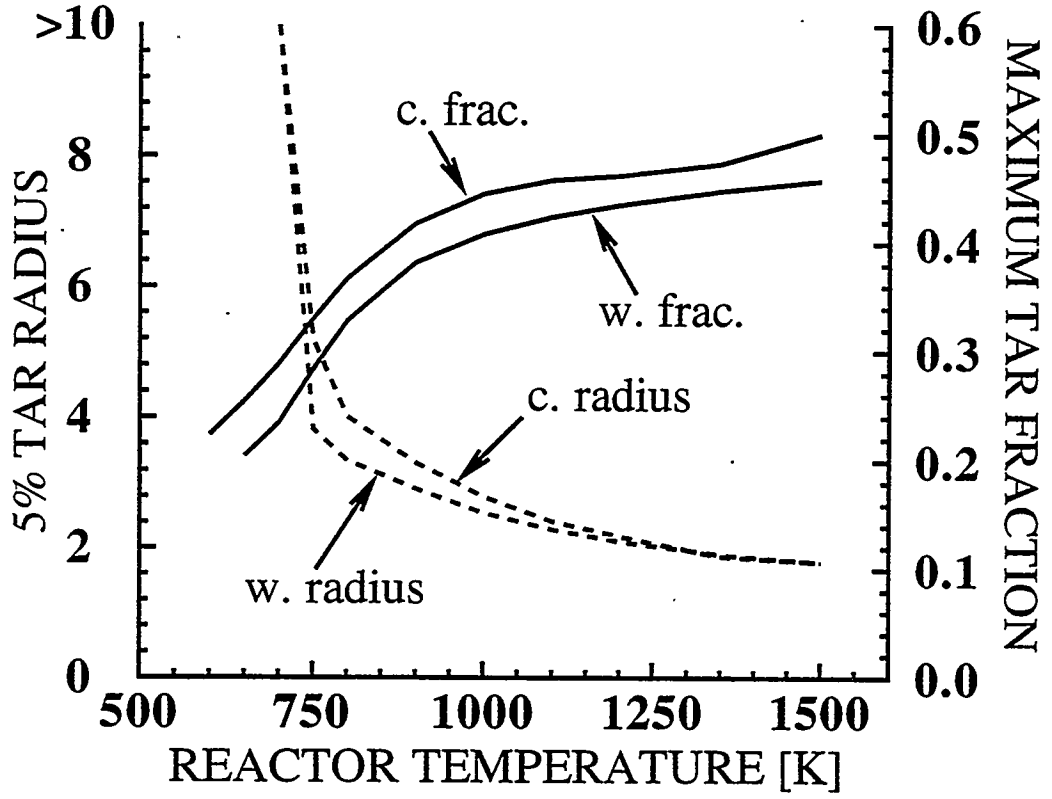

>10
8
6
4
2
0
5% TAR RADIUS
0.6
0.5
0.4
0.3
0.2
0.1
0.0
MAXIMUM TAR FRACTION
c. frac.
w. frac.
c. radius
w. radius
500
750
1000
1250
1500
REACTOR TEMPERATURE [K]

Fig. 11

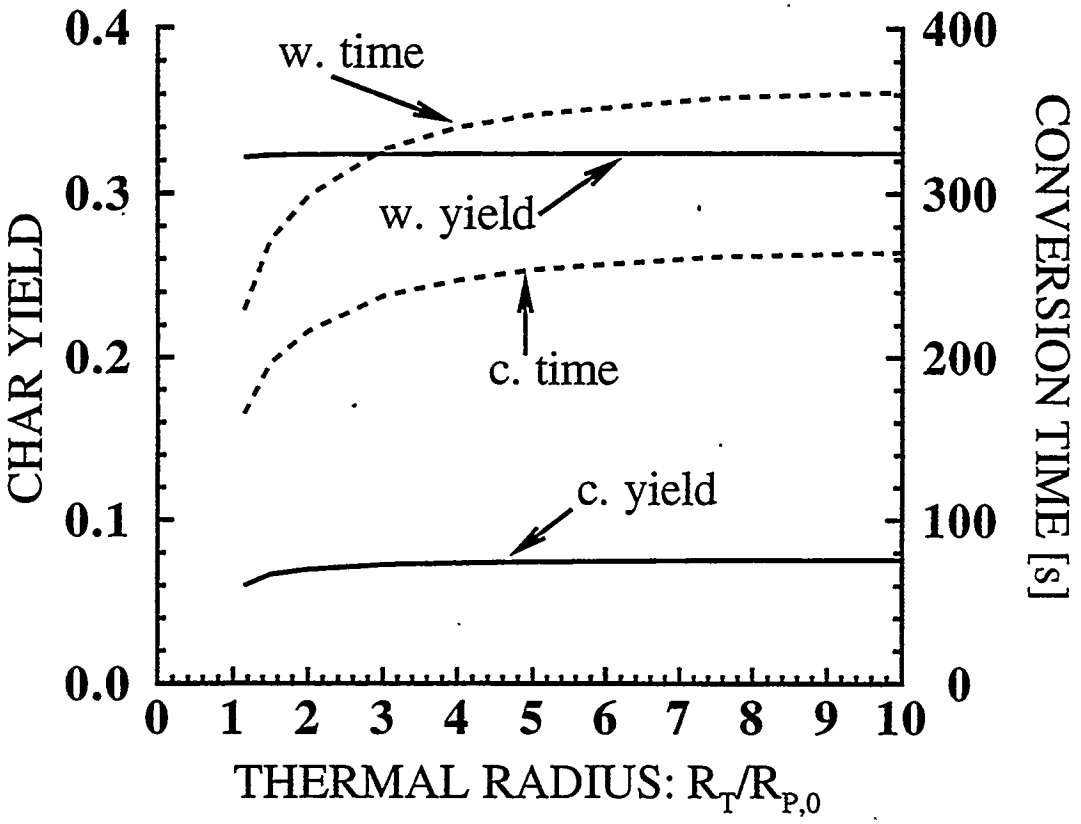

0.4
0.3
0.2
0.1
0.0
CHAR YIELD
400
300
200
100
0
CONVERSION TIME [s]
w. time
w. yield
c. time
c. yield
0 1 2 3 4 5 6 7 8 9 10
THERMAL RADIUS: $R_T/R_{P,0}$

Fig. 12

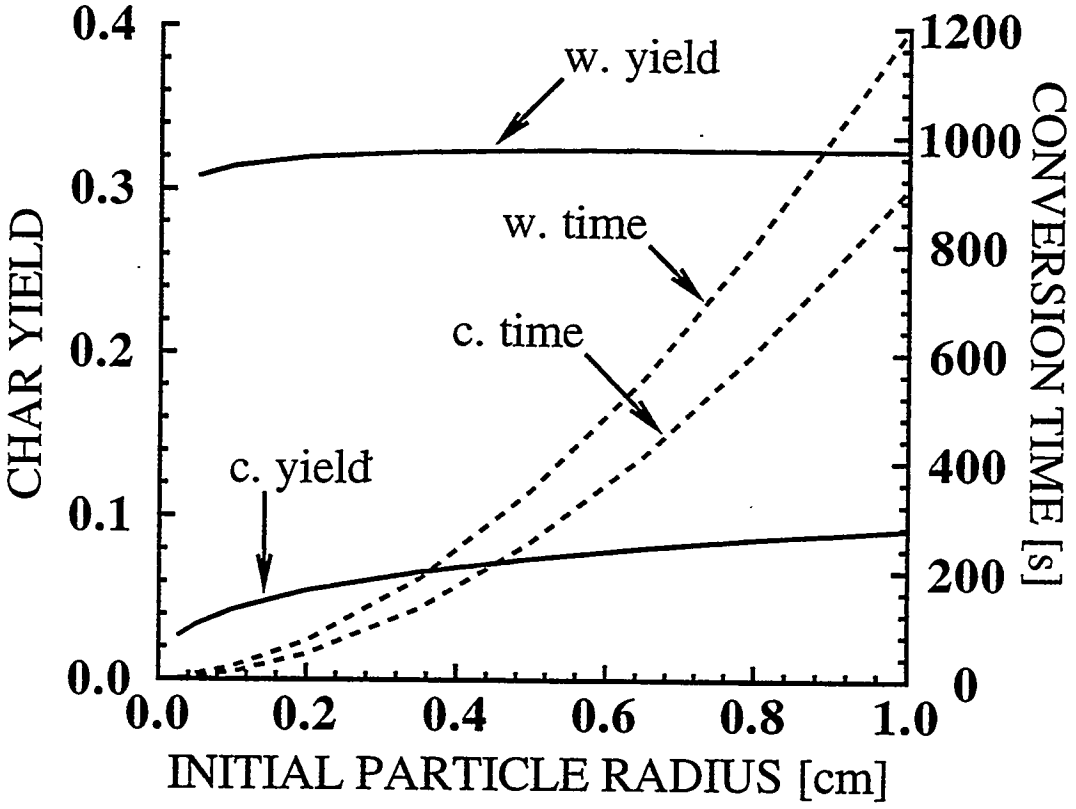

0.4
0.3
0.2
0.1
0.0
CHAR YIELD
w. yield
w. time
c. time
c. yield
1200
1000
800
600
400
200
0
CONVERSION TIME [s]
0.0
0.2
0.4
0.6
0.8
1.0
INITIAL PARTICLE RADIUS [cm]

Fig. 13

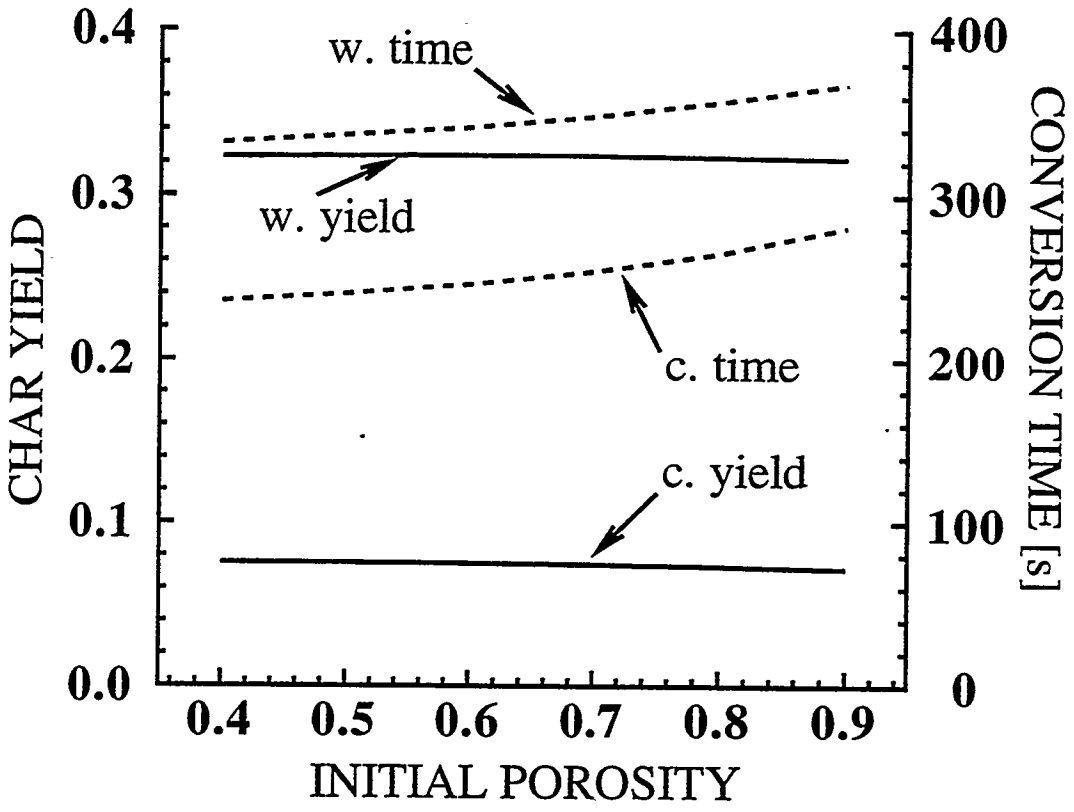

0.4
0.3
0.2
0.1
0.0
CHAR YIELD
w. time
w. yield
c. time
c. yield
400
300
200
100
0
CONVERSION TIME [s]
0.4
0.5
0.6
0.7
0.8
0.9
INITIAL POROSITY

Fig. 14

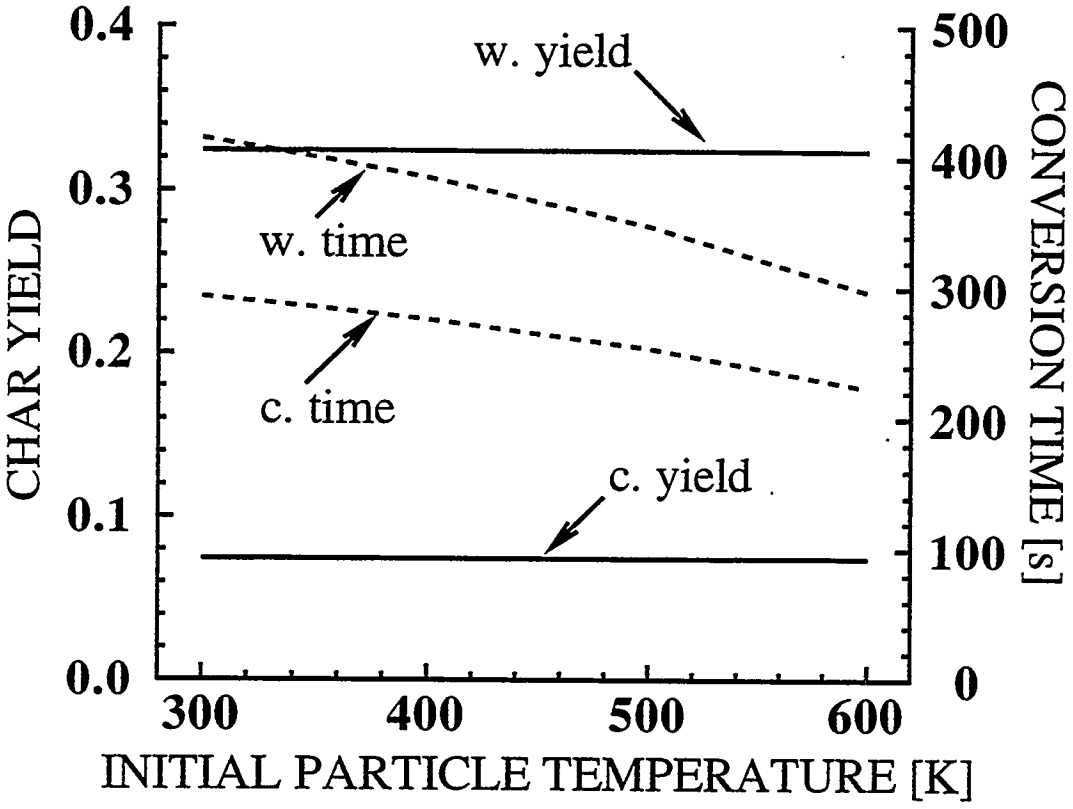

0.4
0.3
0.2
0.1
0.0
CHAR YIELD
w. yield
w. time
c. time
c. yield
500
400
300
200
100
0
CONVERSION TIME [s]
300
400
500
600
INITIAL PARTICLE TEMPERATURE [K]

Fig. 15

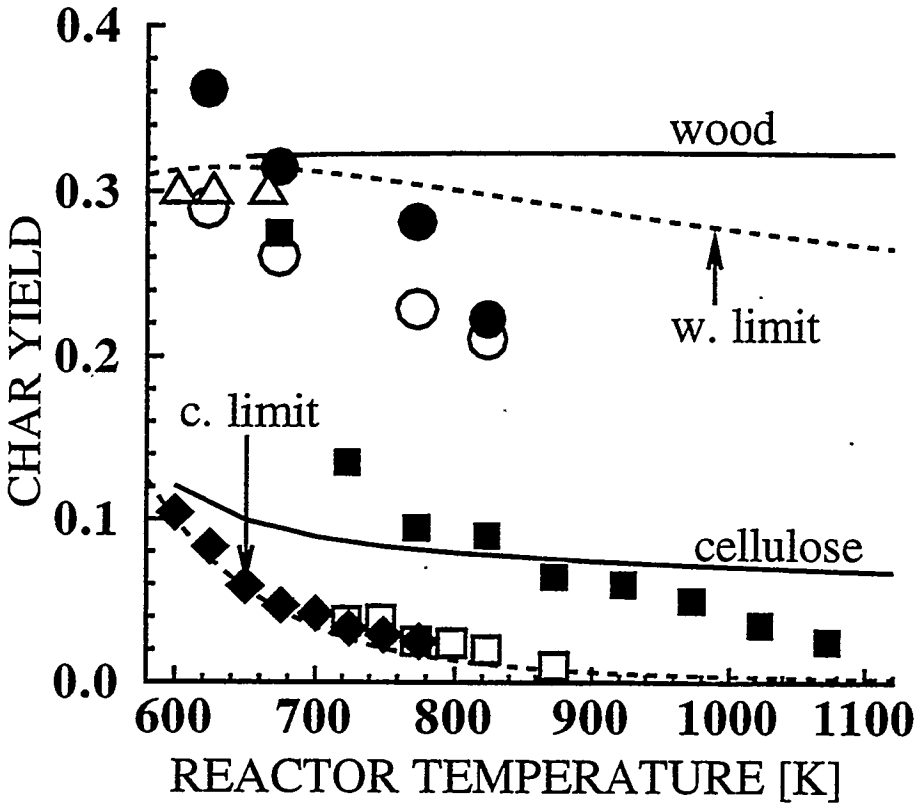

0.4
0.3
0.2
0.1
0.0
CHAR YIELD
wood
w. limit
c. limit
cellulose
600
700
800
900
1000
1100
REACTOR TEMPERATURE [K]

Fig. 16

TECHNOECONOMIC ANALYSIS OF RENEWABLE HYDROGEN PRODUCTION, STORAGE, AND DETECTION SYSTEMS

M.K. Mann, P.L. Spath, K. Kadam
National Renewable Energy Laboratory
Golden, CO 80401

Abstract

Technical and economic feasibility studies of different degrees of completeness and detail have been performed on several projects being funded by the Department of Energy's Hydrogen Program. Work this year focused on projects at the National Renewable Energy Laboratory, although analyses of projects at other institutions are underway or planned. Highly detailed analyses were completed on a fiber optic hydrogen leak detector and a process to produce hydrogen from biomass via pyrolysis followed by steam reforming of the pyrolysis oil. Less detailed economic assessments of solar and biologically-based hydrogen production processes have been performed and focused on the steps that need to be taken to improve the competitive position of these technologies. Sensitivity analyses were conducted on all analyses to reveal the degree to which the cost results are affected by market changes and technological advances. For hydrogen storage by carbon nanotubes, a survey of the competing storage technologies was made in order to set a baseline for cost goals.

A determination of the likelihood of commercialization was made for nearly all systems examined. Hydrogen from biomass via pyrolysis and steam reforming was found to have significant economic potential if a coproduct option could be co-commercialized. Photoelectrochemical hydrogen production may have economic potential, but only if low-cost cells can be modified to split water and to avoid surface oxidation. The use of bacteria to convert the carbon monoxide in biomass syngas to hydrogen was found to be slightly more expensive than the high end of currently commercial hydrogen, although there are significant opportunities to reduce costs. Finally, the cost of installing a fiber-optic chemochromic hydrogen detection system in passenger vehicles was found to be very low and competitive with alternative sensor systems.

Summary

The analyses described in this paper are on the following projects funded by the U.S. Department of Energy's Hydrogen Program: Biomass to Hydrogen via Fast Pyrolysis and Catalytic Steam Reforming; Photoelectrochemical-Based Direct Conversion Systems for Hydrogen Production; Microbes and Bioreactors for Photobiological Hydrogen; Advanced Materials for Hydrogen Storage: Carbon Nanotubes; and Low-Cost Fiber-Optic Chemochromic Hydrogen Detector. The economic feasibility of the different technologies was determined by comparing the calculated hydrogen selling price to the current market value of hydrogen. Depending on the size of the production facility and the amount of hydrogen purchased, hydrogen is valued at between$5/GJ and $14/GJ; large, steam methane reforming plants, which generate the majority of hydrogen on the market today, produce hydrogen at the low end of this range. It should be noted that the market size for hydrogen at the higher end of this price range is small, and large contributions to the hydrogen supply will come only at prices competitive with steam methane reforming.

The analysis of the production of hydrogen from biomass via fast pyrolysis and catalytic steam reforming consisted of an ASPEN Plus© model to perform material and energy balances, and a cash flow analysis to determine the necessary selling price of hydrogen for a specified rate of return. The design analyzed consists of fluid bed pyrolysis of biomass, water and ethyl acetate extraction to recover a phenolic substitute coproduct, and steam reforming to produce hydrogen. The design assumes that a number of small pyrolysis operations, using biomass where it is available and thus at lower costs, supply bio-oil to a central extraction and reforming facility. Results indicate that the necessary hydrogen selling price for the base case analysis is $7.70/GJ. A sensitivity analysis on this process was performed to determine the range of operating and feed conditions that would keep the hydrogen selling price competitive. The results of this analysis indicate that this process has significant potential to be economically feasible. A high rate of return can be obtained and the process can sustain a very high drop in coproduct selling price before the hydrogen becomes more expensive than current markets will allow. Additionally, relative to the market value of hydrogen, the process is able to sustain large changes in capital cost, hydrogen production capacity, and feedstock cost.

A cost boundary analysis was conducted on the photoelectrochemical production of hydrogen, accomplished by a device that combines photovoltaics and electrolysis into a single unit. The contribution of the semiconductor cell to the cost of hydrogen and the minimum yield necessary for economic potential were determined. Four different types of cells were examined: current tandem cells, theoretical future tandem cells, current thin films, and high efficiency thin films. The costs of the cells ranged from $150/m^2 to $55,000/m^2. Results showed that the tandem cells, even at half the price they are manufactured at today, will not produce hydrogen within the current market price range. However, the lower-cost thin films have the potential to be economically attractive hydrogen systems, although a more detailed analysis is required to determine the hydrogen selling price in an integrated system.

A detailed analysis was performed on a process that uses bacteria to shift water and the carbon monoxide in biomass syngas to hydrogen and carbon dioxide. The product gas can be fed directly into a phosphoric acid fuel cell for generation of electrical power, or can be further purified to supply pure hydrogen. The calculated hydrogen selling price for the base case design is $17/GJ, well within striking distance of the high end of current market prices. Sensitivity analyses were performed to include variations in yield, plant size, biomass cost, and capital cost. An increase in reaction rates, to those that have been demonstrated in the laboratory and those expected in a high pressure system, will have the largest impact on the effort to improve the viability of this process. Biomass costs have a large influence on the price of hydrogen, but increases in capital costs were found to have a relatively insignificant effect. If the product gas is used directly in a fuel cell, the costs associated with hydrogen purification can be eliminated; however, the measure by which this technology is then judged, is how well it competes in the electricity market. Hydrogen production

capacity has a significant impact on the hydrogen selling price, although due to hydrogen demand at these prices and limitations on biomass availability, it is unlikely that larger-size plants would be feasible.

The information necessary to define the upper cost limits for hydrogen storage by carbon nanotubes was collected. A literature search was completed to determine the costs of alternative storage technologies to determine the costs carbon nanotubes must achieve to be competitive. A wide range was found in the literature because some costs include items such as auxiliaries, taxes, labor, and other production costs. Additionally, all costs are not in the same year dollars. Nevertheless, the survey begins to define current hydrogen storage options, as well as the cost goals for this research project. Additionally, the necessary auxiliaries for each storage option were defined in an effort to ensure that complete system costs are compared.

An estimate of the cost of a fiber-optic hydrogen detection system to be installed in a passenger vehicle has been completed. Four production scenarios were examined: six and 20 sensors/vehicle at manufacturing rates of 5,000 and three million vehicles per year. Two microprocessors, with different cycling speeds, were also examined. Sensor costs ranged from $0.11/sensor to $2.34/sensor, giving installed system costs between $71/vehicle and $192/vehicle. These costs are significantly lower than the costs of existing hydrogen sensing devices. The light source is the largest cost driver in all scenarios studied, ranging from 27.4% to 49.2% of the overall hydrogen detection system cost. Additional areas which should be focused on for cost improvement are fiber polishing times and labor requirements needed to coat the fiber ends.

Approach and Rationale

The goal of this work is to provide direction, focus, and support to the development and introduction of renewable hydrogen through evaluation of the technical, economic, and environmental aspects of hydrogen production and storage technologies. The advantages of performing analyses of this type within a research environment are several fold. First, the economic competitiveness of a project can be assessed by evaluating the costs of a given process compared to the current technology. These analyses can therefore be useful in determining which projects have the highest potential for near-, mid-, and long-term success. Second, the results of a technoeconomic analysis are useful in directing research toward areas in which improvements will result in the largest cost reductions. Finally, as the economics of a process are evaluated throughout the life of the project, advancement toward the final goal of commercialization can be measured.

The level of technoeconomic analysis appropriate for a project is dictated by the maturity of the technology and the amount of data that has been gathered, as well as the purpose of the evaluation. A new initiative may require only a literature search in order to determine if process costs can be estimated from related systems or if laboratory data are needed first. Alternatively, a cost boundary analysis is appropriate for a project that has been conceptualized but has not generated a significant amount of data. This type of analysis determines the minimum yields, maximum manufacturing costs, or necessary market conditions for the technology to be economically competitive. Finally, a highly detailed analysis can be performed on processes that have been more or less fully conceptualized, and laboratory work has provided yield and operating data. This type of analysis includes a process flowsheet, material and energy balances, equipment cost estimation, and the determination of the cost of the final product over the expected life of an industrial-scale plant. The technical and economic feasibility of projects funded by the Hydrogen Program are evaluated through this task. This work serves as an integral link between laboratory research and program planning, and efforts are now underway to coordinate this work with other systems analysis activities.

When costs are determined for the various hydrogen production scenarios, they are compared to the current production cost of hydrogen today. The current selling price of hydrogen in industry is between $5/GJ and

$14/GJ, depending on the size of the production facility and the amount of hydrogen purchased. This range is for hydrogen as produced by the plant: purified, but not compressed, stored, or distributed. The rationale for using this basis is that the end-use of the hydrogen, which is not appropriately specified for these analyses, will dictate the conditions in which it is shipped from the plant.

The economic potentials of the biomass pyrolysis / steam reforming and biologically-based processes were determined using the discounted cash flow rate of return method. This method calculates the internal rate of return (IRR) that will be earned on the initial capital investment over the life of the project. Given this rate and a feedstock cost, the necessary selling price of the product can be calculated. Often, the IRR is specified as the minimum acceptable rate for an investor to finance a project. Therefore, the perceived risk of the project can be incorporated into the IRR. Because the processes studied currently carry higher risks than conventional hydrogen-generating processes, the IRR was specified to be 15% after tax, for all the analyses described in this paper. The rate for conventional processes is between 9% and 12%; the additional points are included to incorporate the perceived risk of these novel processes into the analysis. For a 37% tax rate, a 15% after-tax IRR corresponds to a pre-tax IRR of 20.4%. The economic assumptions common to these analyses are shown in Table 1.

Table 1: Major Economic Assumptions for Base Case Analyses

January, 1995 dollars	After tax internal rate of return = 15%
Equity financing	Tax rate = 37%
90% on-line factor	Current dollar analysis (i.e., zero inflation)
Two year construction period	20 year plant life
Straight-line depreciation for ten years; first and last year at 50% of other years	50% plant capacity first year of production
30% of capital investment spent first year, 70% second year	Labor rate = $27.18/hour worked (includes fringe benefits and 10% overlap) Supervisor costs = 15% of labor rate

Analysis of Hydrogen from Biomass via Pyrolysis and Steam Reforming

A detailed technoeconomic analysis has been completed on the process to produce hydrogen by catalytically steam reforming biomass pyrolysis oil. The design consists of fluid bed pyrolysis of biomass, liquid-liquid extraction of the bio-oil to recover a phenolics substitute co-product, and steam reforming of the remaining oil to produce hydrogen. A pressure swing adsorption (PSA) system is used to produce a hydrogen product pure enough to be used in a fuel cell. Steam is produced through detailed heat integration and is intended to be sold as a by-product. A schematic of the process is shown in Figure 1. The design assumes that a number of small pyrolysis operations, using biomass where it is available and thus at lower costs, supply bio-oil to a central extraction and reforming facility. The cost of the pyrolysis plant was taken from Beckman and Graham (1993), while material and energy balance results from the ASPEN Plus© model were used to determine the size and corresponding costs of major pieces of equipment in the extraction and reforming process sections. Costs were taken from various costing software packages and published literature, and brought to January 1995 dollars using equipment cost escalation ratios from Chemical Engineering Magazine.

A combination of laboratory and literature data were used to determine the mass and energy balances for the pyrolysis and extraction operations. It was assumed that the yield of oil from bone dry biomass is 66.75 wt% (Piskorz et al, 1988). The carbohydrate-derived fraction of the oil is separated from the lignin-derived fraction using water / ethyl acetate extraction. The recoverable yield of water-soluble carbohydrates from oil was assumed to be 62 wt%, decreased from the maximum yield of 68.8% because of the solubility of water in ethyl acetate. A final coproduct recovery of 31.2 wt% from oil was assumed. Because biomass pyrolysis oil is similar to petroleum crude oil in that many fuels and chemicals can be derived from it, further coproduct options will be studied. The inclusion of a coproduct option in this analysis is meant to be an example of the opportunities available from biomass pyrolysis oil once a system of coproducts is developed. Indeed, based on industrial interest, the National Renewable Energy Laboratory (NREL) is now working to commercialize the extraction process to produce the phenolic substitute for the plywood industry. In addition to the major economic assumptions shown in Table 1, those specific to this process are shown in Table 2.

Table 2: Assumptions for Base Case Analysis of Hydrogen from Bio-oil

Biomass feedstock cost = $25/T (bone dry basis)
Amount of biomass required = 930 T/d (bone dry basis)
Pyrolysis oil produced in fluid bed reactor; 15% IRR given to this process (i.e., oil is purchased rather than made in-house)
Phenolics substitute selling price = $0.44/kg
Hydrogen production capacity = 35.5 T/d (~400,000 Nm^3/d, 15 MM SCF/d)

Results indicate that the necessary hydrogen selling price for the base case analysis is $7.70/GJ. Figure 2 shows the sensitivity of this price to different parameters used in the analysis. The line down the middle of the chart gives the base case scenario. Each parameter, represented by the horizontal bars, was changed relative to the base case and independent of the other parameters, to give the resulting hydrogen selling price for that scenario. The current selling price of hydrogen is shown at the bottom for easy reference. This figure indicates quite clearly that the process to produce a phenolics substitute and hydrogen from pyrolysis via extraction and steam reforming has significant potential to be economically feasible. A high rate of return can be obtained and the process can sustain a large drop in coproduct selling price before the hydrogen becomes more expensive than current markets will allow. A previous analysis found that when no coproduct is made, but the entire bio-oil is reformed, the necessary hydrogen selling price is $11/GJ (Mann, 1995). Relative to the market value of hydrogen, this analysis found that this process remains a feasible option even with large changes in capital cost, hydrogen production capacity, and feedstock cost.

As these results demonstrate, a marketable coproduct is an important part of the economics of this process. Efforts to assess other coproduct options should continue, and the yields from the current extraction process to produce the phenolics substitute should be verified. Of primary research importance, scale-up of the current bench-scale reactor is necessary for further technical proof of the process. Additionally, to generate a complete set of laboratory data, the reforming reactor will need to be coupled to high and low temperature shift reactors. Although these units will be very similar to those used in the current process to produce hydrogen from natural gas, the full process should be tested in order to further optimize hydrogen production. For now, the analysis of this project is considered complete. However, the model that was developed will be updated as new laboratory results are obtained. Additionally, before testing new process configurations in the laboratory, the effect on hydrogen production will be tested using the ASPEN Plus model.

Analysis of Photoelectrochemical-Based Direct Conversion System

Photovoltaic systems coupled to electrolyzers represent a commercially available renewable-based hydrogen production option. However, available electrolyzers are expensive and are the major cost contributors to electrolytically produced hydrogen. Photoelectrochemical water splitting (photoelectrolysis) represents an alternative to PV/electrolysis systems, combining a semiconductor and an electrocatalyst into a single monolithic device. Researchers on this task are working to develop a stable, cost effective, semiconductor-based system that will collect solar energy and electrolyze water in one step to produce hydrogen, with sunlight as the only energy input. This system eliminates the need for an electrolyzer and additionally reduces semiconductor processing because surface contacts, interconnects and wiring are no longer necessary. Two configurations are being studied: single gap systems and multijunction systems. The theoretical efficiency of dual junction systems is 32% while single bandgap systems have an upper limit on the order of 24%. Practical systems could achieve 20% and 10% efficiencies for multijunction and single bandgap systems, respectively.

Work at NREL on photoelectrochemical direct conversion systems involves three basic areas of research: semiconducting materials, surface modification, and catalysts. Work thus far has identified gallium indium phosphide ($GaInP_2$) as a promising semiconductor, and initial work has shown it to be stable in an aqueous environment. $GaInP_2$/gallium arsenide (GaAs) has been identified as a promising tandem cell system; additionally, amorphous silicon/amorphous silicon carbide (α-Si/α-SiC) appear to be promising thin-film systems. Initial work has shown that the $GaInP_2$/GaAs system will split water with good efficiencies (10% thus far) and are relatively stable in aqueous environments. The α-Si/α-SiC system has also shown some promise, and the α-SiC has been shown to protect α-Si-based multijunction systems from surface oxidation, further enhancing the viability of using this low cost cell.

Because of manufacturing similarities, the costs of the semiconductor cells were estimated from current and predicted costs of solar cells. Based on research to date, a series of cost boundary analyses were performed, in which the necessary yield that the research should aim for was determined. Four different types of semiconductor cells were examined: current tandem cells, theoretical future tandem cells, current thin films, and high efficiency thin films. The current tandem cell cost was obtained from the inventor, J. Olson at NREL, who believes the cost to be between \$50,000 and \$60,000/m^2; \$55,000/m^2 was used in the analysis. For additional information on these cells, refer to Bertness et al (1994). To estimate the future cost of these cells, the current cost was halved to \$27,500/m^2. It is important to note, however, that researchers at NREL do not believe that the cost will decrease significantly, as these cells are currently used in the space program and at small scales. A similar tandem cell, GaAs/Ge, is reported to cost \$80,000/m^2 (Ralph, 1994), although using this cost in the analysis instead of that for the $GaInP_2$/GaAs cell does not affect the conclusions reached. Researchers in NREL's PV Program provided cost estimates of \$150/m^2 for the α-Si and α-SiC thin-film cells, and \$500/m^2 for higher efficiency thin film cells such as CdTe and CuInSe.

The first level of boundary analysis determined the contribution of the semiconductor cell to the cost of hydrogen. In this situation, no capital (other than the cell) or operating costs were included. Therefore, the likelihood that these systems will be economically feasible can first be assessed by how much this minimum hydrogen cost is below current hydrogen selling prices. If the costs are higher than the current range, it is unlikely that the system will be viable. Results of this analysis are shown in Figure 3. This figure shows that the tandem cells, even at half the price they are manufactured at today, will not produce hydrogen within the current market price range. However, the thin films have the potential to be economically attractive hydrogen systems. Note that this figure does not imply that these systems will be economic; rather, that low-cost cells have potential and that further analysis and research are warranted.

The minimum photoconversion efficiencies for the cells under consideration were determined in a second level of boundary analysis performed on this process. In effect, this analysis is the flip-side of that reported above, with the hydrogen selling price specified as $14/GJ (the high end of the current price range). The calculations were first performed using the semiconductor cell as the only cost, and secondly with estimates of other capital and operating costs included. The capital and operating costs were modified from a previous study on similar systems (Copeland, 1990). Because there is a great deal of uncertainty in these costs, the efficiency results should be considered to be preliminary and the minimum necessary. Nevertheless, an analysis of this type is useful in giving those interested in the technology an idea of the areas of research that will result in the largest cost savings. Assumptions for the case in which capital and operating costs were estimated are shown in Table 3. Other pieces of equipment included in the capital estimate but not shown in this table are pumps, electrolyte storage tank, filter, hydrogen fan, scrubber, mist eliminator, dehydrator, group island piping, electrical, instrumentation, buildings, indirect costs, contingency, land, site prep, and roads. Results of the minimum required yield calculations are shown in Table 4.

Table 3: Boundary Analysis Assumptions and Preliminary Estimates of Capital and Operating Costs

Hydrogen production capacity (million Nm^3/d)	0.26
Solar insolation including concentration by electrolyte solution (W/cm^2)	0.5
Average conversion activity (h/d)	10
Operating year (d/y)	275
Hydrogen piping costs ($/ft^2$ of facility area)	0.53
Liquid piping costs ($/ft^2$ of facility area)	3.39
Cover costs ($/m^2$)	10
Support structure costs ($/m^2$) (Ogden and Williams, 1989)	30
Cost of NaOH pellets for electrolyte solution ($/kg)	2.7
Cost of water purification by reverse osmosis ($/$m^3$ water)	0.7
Operating labor (men/shift)	2

Table 4: Minimum Required Yields

Semiconductor Cell Type	Assumed cost ($/m^2)	Calculated minimum solar conversion efficiency (HHV H_2 out / energy of sunlight in)		
		Cell is the only cost	Estimates of other costs included	Capital cost estimates reduced 10%
Current tandem cells	55,000	310%	1200%	910%
Future tandem cells	27,500	155%	600%	460%
Higher efficiency thin films (CdTe, CuInSe)	500	2.8%	17.1%	13.3%
Current thin films (α-Si, α-SiC)	150	0.9%	9.6%	7.5%

These calculated minimum yields clearly show that tandem cells cannot produce hydrogen economically, even if their cost is reduced by half. However, this cursory analysis shows that cheaper thin film cells have the potential to produce economical hydrogen if their bandgaps can be altered to split water and their surfaces modified to mitigate surface oxidation. The final column in this table indicates that the necessary efficiency is strongly affected by capital cost. Therefore, to accurately determine the feasibility of photoelectrochemical water splitting using thin film systems, better evaluations of capital costs must be made.

While the GaAs/GaInP2 tandem cells are currently very expensive, they are the only high efficiency tandem cells available. Work on these cells provides valuable information concerning the application of semiconductor cells in aqueous environments for water splitting. Issues such as spectral response, current matching, surface catalyst preparation and application, corrosion control and measurement, efficiency determination, cell and system design, and gas collection techniques, can all be studied with this system while new less expensive tandem systems are being developed. One of the promising new cells being worked on is a silicon/indium nitride tandem. Its maximum theoretical efficiency is about 30%. The NREL photoelectrochemical group is currently collaborating with a Japanese group on the study of indium nitride in aqueous solution.

The conclusion of the boundary analyses performed is clear: hydrogen production via photoelectrolysis will only have the potential to be economical with lower cost cells. However, given that the tandem cells have the appropriate bandgap and stability for water splitting, research on these cells is vital to understanding the basic science behind photoelectrochemical water splitting. If the mechanism for direct conversion of solar energy to hydrogen can be better defined, more efficient, stable cells can be fashioned. In future analyses, a better estimate of capital and operating costs will be made for the thin film-based process. Additionally, the cost of hydrogen from photovoltaic/electrolysis systems will be determined so that a baseline comparison between these two systems can be made.

Analysis of Photobiological Hydrogen Production: Reversibly Immobilized Bacteria to Effect Water-gas Shift

Researchers at NREL have found a unique type of hydrogen-producing activity in a strain of photosynthetic bacteria that functions only in darkness to shift CO (and H_2O) into H_2 (and CO_2). The product gas can be fed directly into a phosphoric acid fuel cell for generation of electrical power, or can be further purified to

supply pure hydrogen. NREL has isolated more than 400 strains of photosynthetic bacteria from local sites that perform this shift reaction in darkness but will also quantitatively assimilate CO into new cell mass in light. Many of these strains have been tested for CO shift activity and growth with crude (water-scrubbed only) syngas generated from gasified wood chips. Bacteria were immobilized on the surfaces of beads or hollow fibers. After draining away the bulk water phase, passage of gaseous CO through the interstitial zone resulted in its effective shift into hydrogen. At ambient temperature and pressure conditions and starting from 20% CO in a gas phase, less than 18 ppm of CO remained at equilibrium. Rates of 0.1-0.5 mmol H_2/min·g cells were estimated over 70 days.

The microbiology and biochemistry of this portion of the project have been largely completed. Because this project is at a relatively advanced stage of research, a full technoeconomic analysis was performed. The full process design is based on the current experimental apparatus coupled to an indirectly heated biomass gasifier similar to that developed by Battelle. Equipment and operating costs were estimated, and the final cost of hydrogen calculated. Sensitivity analyses were performed to include variations in yield, plant size, biomass cost, and capital cost.

Since the carbon source is in a gaseous state, mass transfer is of critical importance. Hence, the selection of an appropriate bioreactor and its proper design are essential to the success of the biophotolysis process. Several reactor designs have been evaluated at NREL including trickle filter, high pressure, sprinkler, bubble column, mat-forming, hollow fiber, and spiral column. The first is probably the most suitable reactor configuration based on operability, ease of scale-up, and cost. Its design is best described as a packed column with inexpensive packings for microbial growth, and is similar to that commonly used in wastewater treatment. In such operations, sloughing of cell mass is critical in order to avoid plugging. However, the growth rate is much slower in the case being considered for hydrogen production, so plugging should not be a problem.

Based on experimental results provided by NREL researchers, a design basis was formulated for a plant with a hydrogen production capacity of 35.5 T/d (400,000 Nm^3/d, 10 MM SCF/d). Syngas from the indirectly heated biomass gasifier is quenched to 40 °C, and fed to the bioreactor where the photosynthetic bacteria are immobilized on the packing material in a film approximately two cells thick. The bacteria absorb the CO and quantitatively shift it to hydrogen using water introduced at the top of the reactor. The hydrogen that is formed bubbles out of solution, but most of the CO_2 remains dissolved through pH control. The resulting product gas is about 95% hydrogen and is further purified in a pressure swing adsorption unit. The design and calculated process parameters are given in Table 5. The reactor was a trickle filter design, packed with nylon beads.

The calculated hydrogen selling price for the base case design is $17/GJ. A parametric sensitivity analysis, shown in Figure 4, reveals that the specific reaction rate and biomass cost have the greatest impact on the economics. It has been demonstrated in the laboratory that the reaction rate of 1.5 mmole H_2/min.g cell can be increased tenfold, decreasing the hydrogen selling price to $12/GJ. A further increase in reaction rate could be accomplished using a high pressure system. However, this increase will be accompanied by an increase in capital cost. Although this case is not reflected in the sensitivity analysis, the increase in capital is not expected to significantly affect the economics; a 30% rise in capital costs has a relatively small effect on hydrogen selling price. Biomass feedstock cost has a more significant effect on the price of hydrogen; a reduction in the cost from $46/T to $22/T lowers the selling price by about $4/GJ.

Table 5: Process Parameters for the Bacterial Water Gas Shift System

General Plant Data	
Overall hydrogen production capacity (million Nm^3/d)	0.40
Plant operation (d/y)	350
On-stream factor (%)	96
Gasifier	
Capacity (T/d biomass)	900
Syngas yield (m^3/lb wood)	0.324
Syngas production (m^3/d)	583,200
H_2 Reactor	
Reaction rate, k_{max} (mmol H_2/min g cells)	1.5
Microbial film thickness (mm)	0.05
Diameter of packing particles (cm)	0.1
Total surface area of packing material (m_2)	780,423
Volumetric productivity (m^3 H_2/m^3 d)	552

Other parameters that were varied in the sensitivity analysis were the use of a PSA unit, hydrogen production capacity, and IRR. If the product gas is used directly in a fuel cell, the costs associated with hydrogen purification can be eliminated. The CO levels in the product gas are <1 ppm, and the platinum electrodes in fuel cells are not poisoned by CO_2. The effects of other hydrocarbon gases present in biomass syngas on fuel cell performance, however, are unknown, although non-condensible gases should not pose a threat to the bacteria colony. If the product gas is used directly in a fuel cell, this technology must compete in the power generating market, and except in remote regions, electricity is currently very cheap. Hydrogen production capacity has a significant impact on the hydrogen selling price, although due to hydrogen demand at these prices and biomass availability, it is unlikely that larger-size plants would be feasible. Future analyses on this technology will include assessing different reactor designs including a high pressure system to take advantage of higher reaction rates. Because extensive experimental work has been completed on a hollow-fiber design, it will likely be the first reactor to be studied.

Analysis of Advanced Materials for Hydrogen Storage: Carbon Nanotubes

NREL's research into novel hydrogen storage techniques is targeted at designing carbon-based materials in the nonometer-size regime. The goals are to make this storage technology low-cost, safe, operable at ambient temperatures, with high-energy density storage capacities. The expected application is on-board storage for hydrogen passenger vehicles. The hydrogen adsorption properties of carbon nanotubes have been the initial focus of the research work due to the potential for organizing and designing the void space volume in the nanotube material. The ability to control the amount and shape of the void space will facilitate the development of systems that have higher gravimetric and volumetric energy densities than other hydrogen storage technologies.

A spark gap evaporator has been used to produce carbon nanotubes in most of the experiments performed to date. The synthesis of carbon nanotubes with this apparatus involves flowing electrical current between two closely spaced coaxial graphite rods. A plasma arc is established between the two rods and carbon atoms are evaporated from one rod and transferred to the other via a gas phase reaction. A deposit consisting of an outer shell of soots and carbon fullerenes (C_{60}, C_{70}, C_{80}, etc.), and an inner core of carbon tubules is developed on the second rod. Because production costs are largely unknown at this time, a literature search was completed to determine the costs of alternative storage technologies giving the costs carbon nanotubes must achieve to be competitive. Table 6 contains a compilation of container costs for currently tested and

potential hydrogen storage systems. Costs were not obtained for organic liquid hydrides or microspheres, although analyses of these systems will be conducted in the next year. A wide range of costs was found in the literature because some costs include items such as auxiliaries, taxes, labor, and other production costs. Additionally, all costs are not in the same year dollars. Nevertheless, this survey begins to define current hydrogen storage options, as well as the cost goals for this research project.

Table 6: Costs of Various Hydrogen Storage Systems For Passenger Vehicles

	Container Cost		
Storage System	$/GJ of hydrogen storage capacity		**Reference**
H-Power iron oxidation/reduction	130 - 500		b, i, e
Gaseous hydrogen	s-glass kevlar T-1000 carbon C-wrapped Undefined	2,300 2,700 6,700 2,000 - 7,500 3,300 - 8,500	a, b, c, e, g, h, i
Liquid hydrogen	1,000 - 3,500		a, b, e, g, h
Cryoadsorption	2,000 - 4,000		b, i
Thermocooled pressure vessel	4,000+		b
Metal hydride	$LaNi_5$ MmNi alloys FeTi alloys Mg alloys Undefined	11,000 3,900 - 4,400 1,400 - 12,000 640 - 13,000 10,000	a, b, d, e, f, g, h

References:

a: Carpetis (1994)
b: DeLuchi (1992)
c: DeLuchi, et al (1991)
d: Huston (1984)
e: Maceda and Wills (1992)
f: McLanagen (1992)
g: Schwarz (1993)
h: Schwarz and Amankwah (1993)
i: Traissi and Sadhu (1994)

When considering the many options for storing hydrogen on-board a passenger vehicle, the total fuel system costs need to be taken into account as well as the amount of usable hydrogen available from the system; all of the hydrogen contained in each storage system will not be readily recoverable as fuel. For instance, liquid hydrogen systems will loose some hydrogen to boil off, compressed hydrogen systems, including glass microspheres, can only use the gas that is at or above the pressure of the fuel cell system, and only the equilibrium amount of hydrogen can be dehydrogenated from cryoadsorption systems, nanotubes, and metal hydrides. Additionally, microspheres and the H-power system must be regenerated outside of the vehicle fuel tank; the costs associated with removal, replacement, and external regeneration of the system must also be taken into account. For operational on-board vehicle use, some of the hydrogen storage systems require auxiliaries. In most cases, most of these are not taken into account in the container costs obtained from the literature. Table 7 lists the required auxiliaries for various on-board vehicle hydrogen storage systems.

Table 7: Auxiliary Equipment Required for Different Hydrogen Storage Technologies

Storage system	Auxiliaries required
H-power iron oxidation/reduction	Metal tubes, steam and water lines, fuel lines, pumps (possibly), separators, preheaters (possibly)
Compressed gaseous hydrogen	Pressure regulator or a fuel pump
Liquid hydrogen	Pump, heat exchanger
Cryoadsorption	Kevlar-wrapped tanks need cooling system
Thermocooled pressure vessel	Pressure regulator, pre-heater, gas accumulator
FeTi metal hydride	Heat exchanger, pressure regulators
Organic liquid hydride	MCH & toluene tanks, reformer, heat exchanger, vaporizer pumps, air-cooled condenser, gas-liquid separator
Carbon nanotubes	Heating coils for releasing stored hydrogen, compressor

Future research will test the use of NREL's 10 kW High-Flux Solar Furnace and laser vaporization. These devices are anticipated to reduce the operating costs and increase the yield of carbon nanotubes, currently at 0.02 wt% of the carbon source. Overall, work will be focused on increasing the hydrogen storage capacity at ambient temperatures, increasing the yield of carbon nanotubes, utilizing a cheaper carbon source and a cheaper catalyst or no catalyst, moving from a batch process to a continuous process, decreasing the operating costs, and finally, reducing costs through scale-up. Future analysis will determine if the combination of these process improvements will result in an economical hydrogen storage option for passenger vehicles. Such an analysis will involve analyzing the cost of carbon nanotube production with the solar furnace and the laser vaporization apparatus. Preliminary costs for carbon nanotube production will be calculated from the capital and operating costs of these units using predicted and yields.

Analysis of a Fiber-Optic Chemochromic Hydrogen Detection System

This work involves the development of a reversible, thin-film, chemochromic hydrogen sensor. The sensor is being designed for use in hydrogen fueled passenger vehicles. Currently available hydrogen sensors require electrical wiring which, in the case of an electrical fault, could lead to the combustion of any hydrogen present. The NREL sensor consists of a thin-film reflector at the end of a low-cost, multi-mode, polymer optical fiber, thus eliminating electrical wiring. A prototype is being developed that will demonstrate the technical feasibility of the fiber-optic hydrogen detection system. A light beam will be transmitted along the fiber to the end of the sensor, then reflected back to a light detector. Hydrogen will cause a decrease in the reflected light signal, indicating the presence and concentration of hydrogen in the vicinity of the sensor head. Chemochromic films have been prepared by thermal evaporation of various materials including tungsten oxide, silver, and platinum onto glass and polymer substrates. Work with these substrates has focused on optimizing the response time and hydrogen selectivity in the presence of hydrocarbon gases. In the final design, the optimized coating will be applied to the ends of polymer optical fibers. The design will provide a reference signal that traverses the length of the optical fiber, but is unaffected by any hydrogen at the sensor head. The ratio of the hydrogen signal and the reference signal will be used to provide an indication of the presence of hydrogen. The appropriate response will be determined by the concentration of the hydrogen present.

An estimate of the cost of the fiber-optic hydrogen detection system has been completed. The system design, shown in the attached figure, is based on the initial prototype that is currently being constructed at NREL. Four production scenarios were examined: six and 20 sensors/vehicle at manufacturing rates of 5,000 and three million vehicles per year. The actual number of sensors required per vehicle will depend on the size of the vehicle and the layout of the hydrogen fuel system. Two microprocessors, with different cycling speeds, were also examined; it is anticipated that the low cost microprocessor, with response times on the order of milliseconds, will be adequate for monitoring the system for hydrogen leaks. Tables 8 and 9 summarize the overall hydrogen detection system cost for each scenario and a breakdown of the component costs. Note that these costs include component and system assembly costs, without profit for the manufacturer.

Table 8: Hydrogen Detector System Costs for Different Manufacturing Scenarios

Sensors/vehicle	Microprocessor type	Manufacturing capacities (vehicles per year)	
		5,000	3,000,000
6	low cost (slower response)	$17.84/sensor $107.04/vehicle	$11.77/sensor $70.62/vehicle
	high cost (faster response)	$19.34/sensor $116.04/vehicle	$13.02/sensor $78.12/vehicle
20	low cost (slower response)	$9.11/sensor $182.20/vehicle	$5.86/sensor $117.20/vehicle
	high cost (faster response)	$9.61/sensor $192.20/vehicle	$6.21/sensor $124.20/vehicle

Table 9: Breakdown of Hydrogen Detection System Component Costs

Component	Cost
Halogen light source (includes housing, reflector array, and regulating circuitry) and bundle connector	$35- $45
1 x 2 splitter (2 per sensor)	$0.50 each
Connectors (1 at the end of each sensor)	$0.20
Silicon photodiodes (2 per sensor)	$0.40 - 0.75/ two
Multiplex and support circuitry (for a set of 2 photodiodes)	$0.60 - 1.00
Module housing and module printed circuit board (cost includes soldering)	$2.00 - 4.00
Polymer optical fiber (average of 10 feet of fiber in three pieces/sensor)	$0.90 - 1.50/ three pieces
Microprocessor	$1.00 - 2.00 (slow response) $8.00 - 13.00 (fast response)
Cost of coating the sensor head	$0.11 - 2.34/ sensor

The equipment required for coating the fiber ends includes a polisher to create a flat edge on the top and angles on the side of the optical fiber, and a thermal evaporator to coat this polished fiber with thin films. The films consist of a thin layer of gold, followed by a layer of transparent, amorphous tungsten oxide covered by a very thin reflective layer of palladium. Cost estimates were made using these three metals and the following coating thicknesses: gold, tungsten oxide, and palladium at 50 nm, 10 nm, and 1 nm, respectively. It should be noted that these thickness have not been optimized and it is possible that palladium may not be required or that a different protective coating will be used.

In regards to mass production of these hydrogen sensors, it will be necessary to reduce polishing times and reduce labor requirements. For this analysis, it was assumed that one polisher could polish 10 fibers at a time at a rate of 10 fibers per 30 minutes. Currently available polishers typically polish one fiber at a time with a maximum of up to 12 at a time, in a manually intensive process. Additionally, the fibers have to be placed into the connection(s) on the polisher by a worker, and the current devices that polish up to 12 fibers at a time need to be adapted to polishing bare fibers rather than fibers in connectors. The thermal evaporator used in this analysis is the Temescal BJD-1800 Vacuum Deposition System. An electron beam will sequentially evaporate the metals and the condensing vapors will be deposited on the ends of the polymer optical fibers. It is anticipated that this unit will be able to coat 2,700 fibers at a time at a one hour per cycle rate. The parts and accessories required for the thermal evaporator include a vacuum chamber (18" diameter), instrumentation, a standard mechanical pump, a cryopump and controls, an electron beam sweep controller, an electron beam power supply, a film deposition controller, an electron beam source (triple crucible for coating three materials consecutively), and two fiber optic holders each holding a minimum of 2,700 fibers; of which one holder is a spare. Table 10 contains the assumptions used to derive the cost of coating the fiber ends.

Table 10: Fiber Coating Cost Information

Thermal evaporator	$250,000/unit	
fiber polisher	$1000/unit	
metals: gold tungsten oxide palladium	 $13/g $1/g $18/g	film thickness/fiber: 50 nm 10 nm 1 nm
operating costs	-water (3 gallons per minute minimum) -compressed air (5 cubic feet per minute) -nitrogen (for venting the machine and purging cryopump) -electricity -maintenance	
labor	-operators to run thermal evaporator(s) and polisher(s) at a salary = $27.18/hr/operator	

Figure 6 show the cost breakdown for each of the components as a percentage of the overall hydrogen detection system cost for each of the 4 production scenarios (six sensors per vehicle and 20 sensors per vehicle for production rates of 5,000 and three million vehicles per year). The light source is the largest cost driver in all scenarios studied, ranging from 27.4% to 49.2% of the overall hydrogen detection system cost. The issue of determining the most economical light source within the required light wavelength will be addressed with future experimentation after the prototype has been completed. The cost of coating the sensor head is the next highest component cost for the two low production rate cases (the six and 20 sensors/vehicle case at a production rate of 5,000 vehicles per year). Coating the fibers is a very labor intensive process,

contributing 90-98% of the total cost of coating the end of the fiber. However, each sensor still costs only $0.11 - $2.34, a cost significantly lower than the costs of existing hydrogen sensing devices. The next largest cost components in the overall hydrogen detection system for all scenarios studied are the fibers, splitters, multiplex and support circuitry, and photodiodes, respectively. These costs are higher than the microprocessor and its associated parts because they are associated with each individual sensor instead of being distributed among the total number of sensors produced. Table 11 contains data for currently available hydrogen sensing devices. The sensor costs range from $27 - $3,900, and do not include the additional costs required for an integrated hydrogen detection system. For a hydrogen passenger vehicle application, it will be necessary for a hydrogen sensor to be able to quickly detect dangerous levels of hydrogen. Although the hydrogen detection limit of these sensing devices is probably adequate for passenger vehicles, the response time is too long.

Future economic analysis will focus on updating the current analysis after the prototype is tested. Design specifications still needing to be finalized include light source criteria, chemochromic film coating requirements, reference signal ratio design, operating temperature range. Additionally, examination of the fiber polisher will determine the extent to which the process can be automated, how many fibers can be polished at one time, and at what speed the fibers can be polished. Additionally, the anticipated life and replacement costs of the various components over the life of a hydrogen vehicle must also be taken into account in the analysis. This is especially true for the light source and the sensor head, the two components with the shortest life span.

Table 11: Commercial Hydrogen Sensing Devices

Company	Type of hydrogen sensor/Model no.	Sensor cost	Hydrogen detection range	Operating temperature range (if published)	Response time	Average sensor life
Figaro Engineering Inc	semiconductor (SnO_2) TGS821	$53.50 (1-9) $40.00 (10-99) $31.00 (100-999) $26.50 (> 999)	50-1,000 ppm			
	solid-electrolytic sensor (solid state sensor)	$550-$1,600 (replacement cell cost = $165-$275)	0-100 ppm		15-60 sec	5-10 years
	electrochemical sensor	$1,000-$3,000 (replacement cell cost = $175-$300)	0.02-15 ppm		30 sec	18-36 months
Aerojet		$200/chip				
ATI		$1,150	0-40,000 ppm			
Bacharach	- Gas Sentinel Area Monitor - Vehicular Gas Detection		0-2,000 ppm 0-40,000 ppm	-20 to 55 C -40 to 125 C	<30 sec	1-2 years
DCH Technology			1-1,000,000 ppm	-100 to 140 C	<2 sec	> 3 years
Drager	6808885	$1,020	0-2,000 ppm	-20 to 40 C	<40 sec	3 years
ENMET			0-2,000 ppm	-10 to 40 C		< 2 years
General Monitors	S104/S106		0-40,000 ppm	-40 to 60 C	<10 sec	3-5 years
MST	EMK 9002	$1,200	0-1,000 ppm	-40 to 40 C	<10 sec	> 1 year
Sensidyne	Refillable Disposable		0-40,000 ppm 0-1,000 ppm	0 to 40 C 0 to 40 C	<18 sec <60 sec	3 years 1 year
Sierra Monitor	Sentry 5000	$3,920	9-2,000 ppm	-5 to 40 C	<65 sec	1-3 years
Telosense			100-400,000 ppm		<2 sec	

Conclusions

Technical and economic feasibility studies have been performed on several projects being by the U.S. Department of Energy's Hydrogen Program. The necessary selling price of hydrogen to obtain a specified internal rate of return was determined for five projects in the areas of hydrogen production from thermochemical conversion of biomass, biological water splitting and carbon monoxide conversion, and photoelectrochemical conversion of sunlight. Additionally, a search of the available literature on hydrogen storage technologies was conducted in order to set a baseline for carbon nanotube research.

The necessary hydrogen selling price for the conversion of biomass via fast pyrolysis and catalytic steam reforming was found to be $7.70/GJ. A sensitivity analysis on this process indicated that this process has significant potential to be economically feasible even if market forces cause a significant drop in coproduct selling price. Also, by themselves, large changes in capital cost, hydrogen production capacity, and feedstock cost do not cause this process to be more expensive than the range of currrent hydrogen technologies.

A cost boundary analysis showed that hydrogen production via photoelectrolysis will only have the potential to be economical with lower cost cells. The contribution of the semiconductor cell to the cost of hydrogen and the minimum photoconversion efficiency necessary for the system to have potential were determined. Results showed that the tandem cells will not produce hydrogen within the current market price range. The lower-cost thin films have the potential to be economically attractive hydrogen systems, although they are not currently appropriate for water splitting. Work on the high efficiency tandem cells provides information needed to further advance this technology, and other cells, such as the silicon/indium nitride tandem, may prove to be the link between higher efficiency and lower cost. A more detailed analysis is required to determine the hydrogen selling price in an integrated system.

The process to use photosynthetic bacteria to shift the carbon dioxide in biomass syngas was found to be economically promising with a calculated hydrogen selling price of $17/GJ. An increase in reaction rates, to those that have been demonstrated in the laboratory and those expected in a high pressure system, will have the largest impact on improving the viability of this process. Biomass costs have a large influence on the price of hydrogen, but increases in capital costs were found to have a relatively insignificant effect. If the product gas is used directly in a fuel cell, the costs associated with hydrogen purification can be eliminated. However, unless it can be located in remote regions, it is not likely that this process will be economic if the product is electricity.

With production costs largely unknown at this time, a literature search was completed to define the upper cost limits for hydrogen storage by carbon nanotubes. The total fuel system costs, including all auxiliaries and the actual amount of hydrogen available from the system should be included when comparing different storage options. The necessary auxiliaries and literature-derived costs of several storage technologies were listed. Future analyses will involve analyzing the cost of carbon nanotube production with the solar furnace and the laser vaporization apparatus. Preliminary costs for carbon nanotube production will be calculated from the capital and operating costs of these units, plus predicted yields and those obtained in laboratory experiments.

Detection of the presence of hydrogen leaks in a passenger vehicle by means of a chemochromic fiber-optic system was found to be very cost effective. The cost of such a system was determined for four production scenarios. Fiber-optic sensors are projected to cost between $0.11/sensor to $2.34/sensor, giving installed system costs between $71/vehicle and $192/vehicle. Currently available hydrogen sensors, which are not

appropriate to passenger vehicles, cost between $27 and $3,900; further, these costs do not include the additional costs required for an integrated system. The light source is the largest cost driver in all scenarios studied, ranging from 27.4% to 49.2% of the overall hydrogen detection system cost. Additional areas which should be focused on for cost improvement are fiber polishing times and labor requirements needed to coat the fiber ends.

Acknowledgments

Our thanks to the following researchers at the National Renewable Energy Laboratory for their contributions to the information in this paper: Ms Catherine Gregoire Padró (Hydrogen Program Manager), Dr. Esteban Chornet, Dr. John Turner, Dr. Mike Seibert, Dr. Maria Ghirardi, Dr. Paul Weaver, Dr. Mike Heben, and Mr. David Benson.

For further information on any of the research projects analyzed for this work, consult the respective papers in this publication, or contact the above-named principal investigators.

References

Beckman, D., R. Graham. 1993. "Economic Assessment of a Wood Fast Pyrolysis Plant." In *Advances in Thermochemical Biomass Conversion*, 1314 - 1324. A.V. Bridgwater, editor. Blackie Academic and Professional.

Bertness, K.A., Kurtz, S.R. Friedman, D.J., and Kibbler, A.E. 1994. "29.5%-Efficient GaInP/GaAs Tandem Solar Cells." Appl. Phys. Lett. 65 (8): 989-991.

Copeland, R.J. November, 1990. "Solar Photochemical Production of Hydrogen." Final report prepared for the Solar Energy Research Institute, Subcontract HB-0-19143-1.

Mann, M.K. 1995. "Technical and Economic Analyses of Hydrogen Production via Indirectly Heated Gasification and Pyrolysis." In *Proceedings of the 1995 U.S. DOE Hydrogen Program Review, Volume 1.* Coral Gables, FL: National Renewable Energy Laboratory. NREL/CP-430-20036.

Ogden, J. M., Williams, R.H. October, 1989. *Solar Hydrogen: Moving Beyond Fossil Fuels.* World Resources Institute.

Piskorz, J., Scott, D.S., Radlein, D. 1988. "Composition of Oils Obtained by Fast Pyrolysis of Different Woods." In *Pyrolysis Oils from Biomass.* E.J. Soltes, T.A. Milne, editors. American Chemical Society Symposium Series 376: 167-178.

Renewable Resource Data Center, http://rredc.nrel.gov/solar, National Renewable Energy Laboratory, U.S. Department of Energy Resource Assessment Program, Monthly Solar Radiation File, March 1996.

Ralph, E.L. December 1994. "High Efficiency Solar Cell Arrays System Trade-Offs." In *1994 First World Conference on Photovoltaic Energy Conversion, Proceedings of the 24th IEEE Photovoltaics Specialists Conference*: 1998-2001.

Figure 1: Production of Phenolics Substitute and Hydrogen from Extraction and Steam Reforming

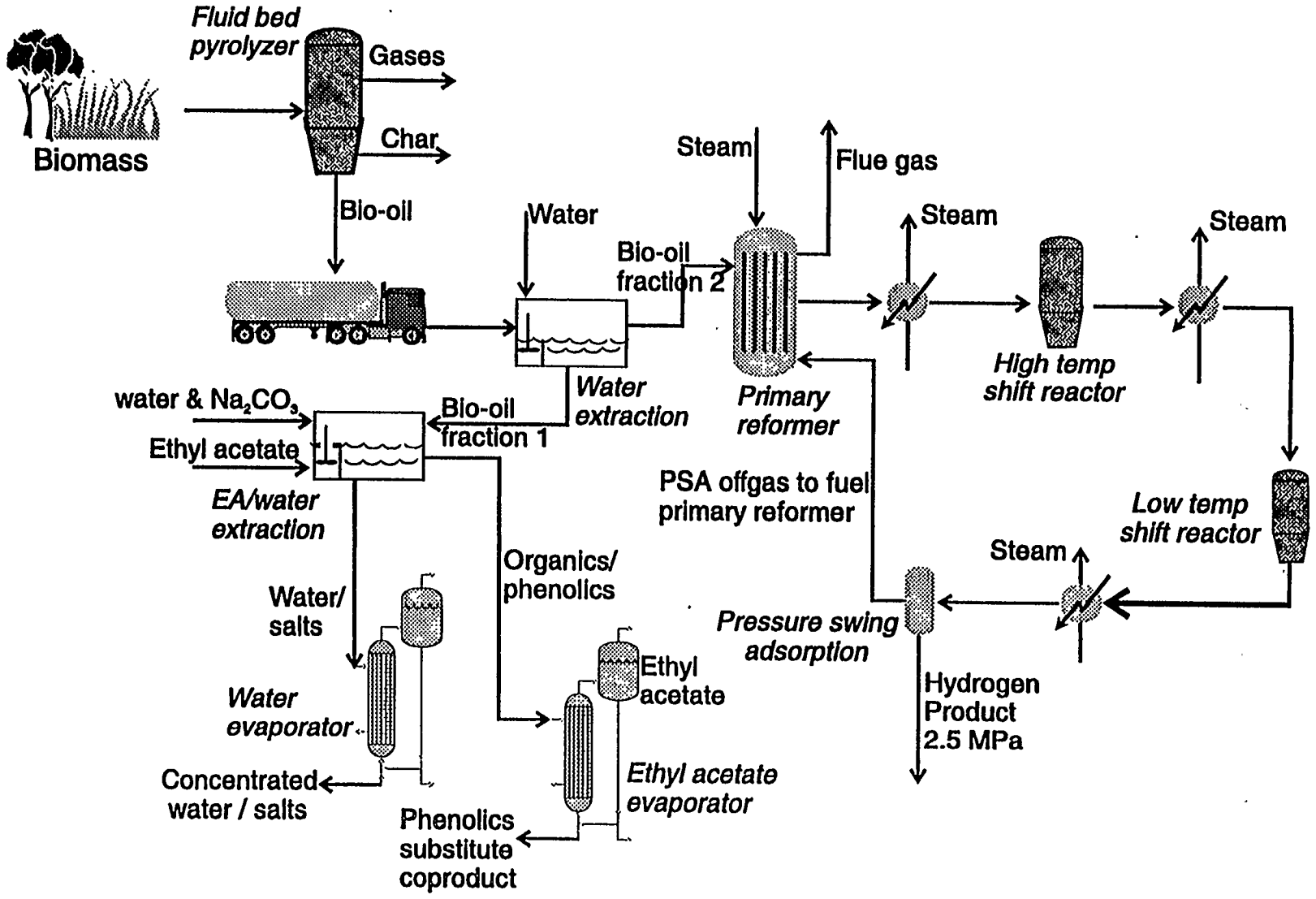


Figure 2: Parametric Sensitivity of the Calculated Selling Price of HydrogenFrom Biomass via Fast Pyrolysis and Steam Reforming

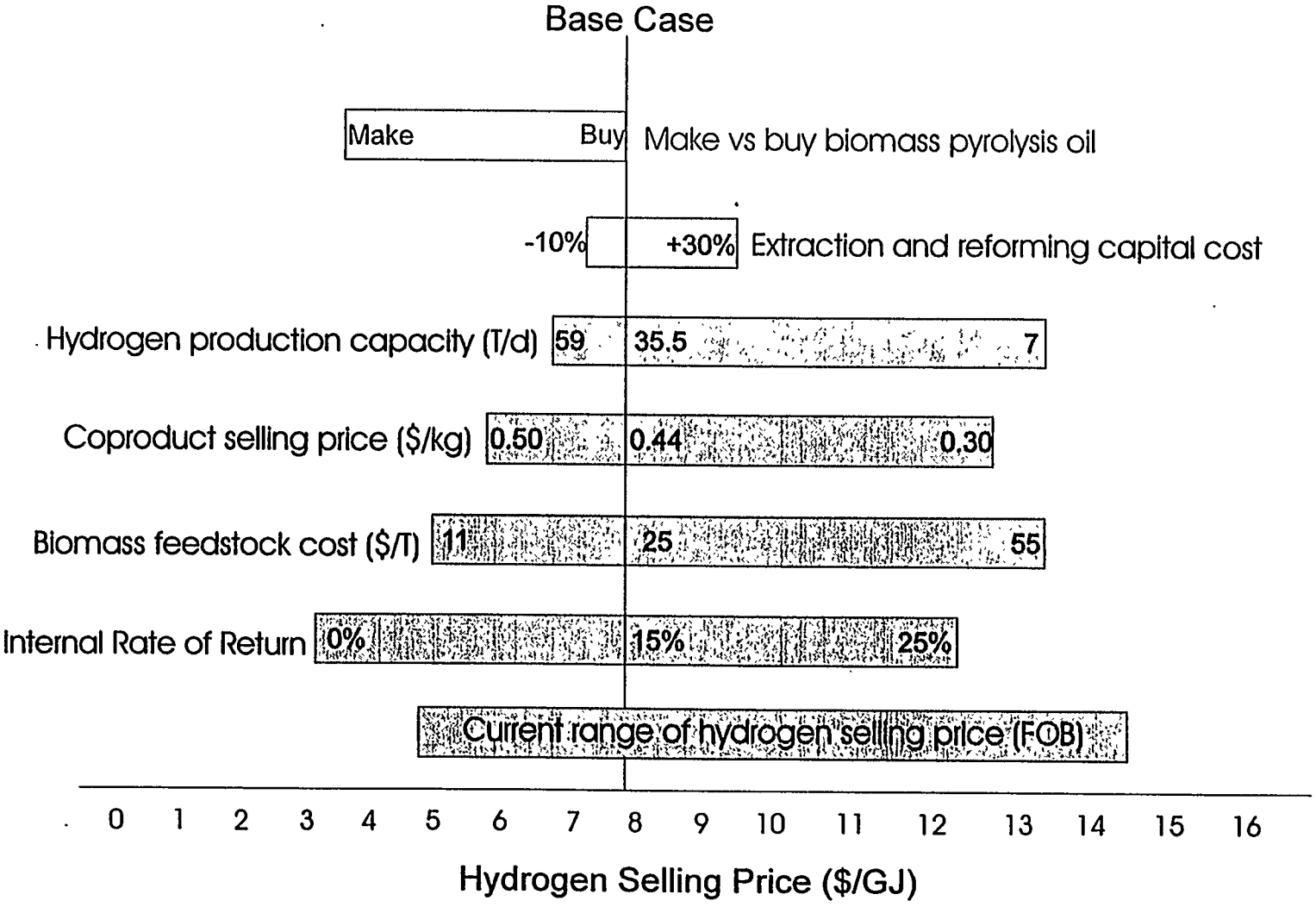


Figure 3: Cost Boundary Analysis of Photoelectrochemical Production of Hydrogen From Sunlight

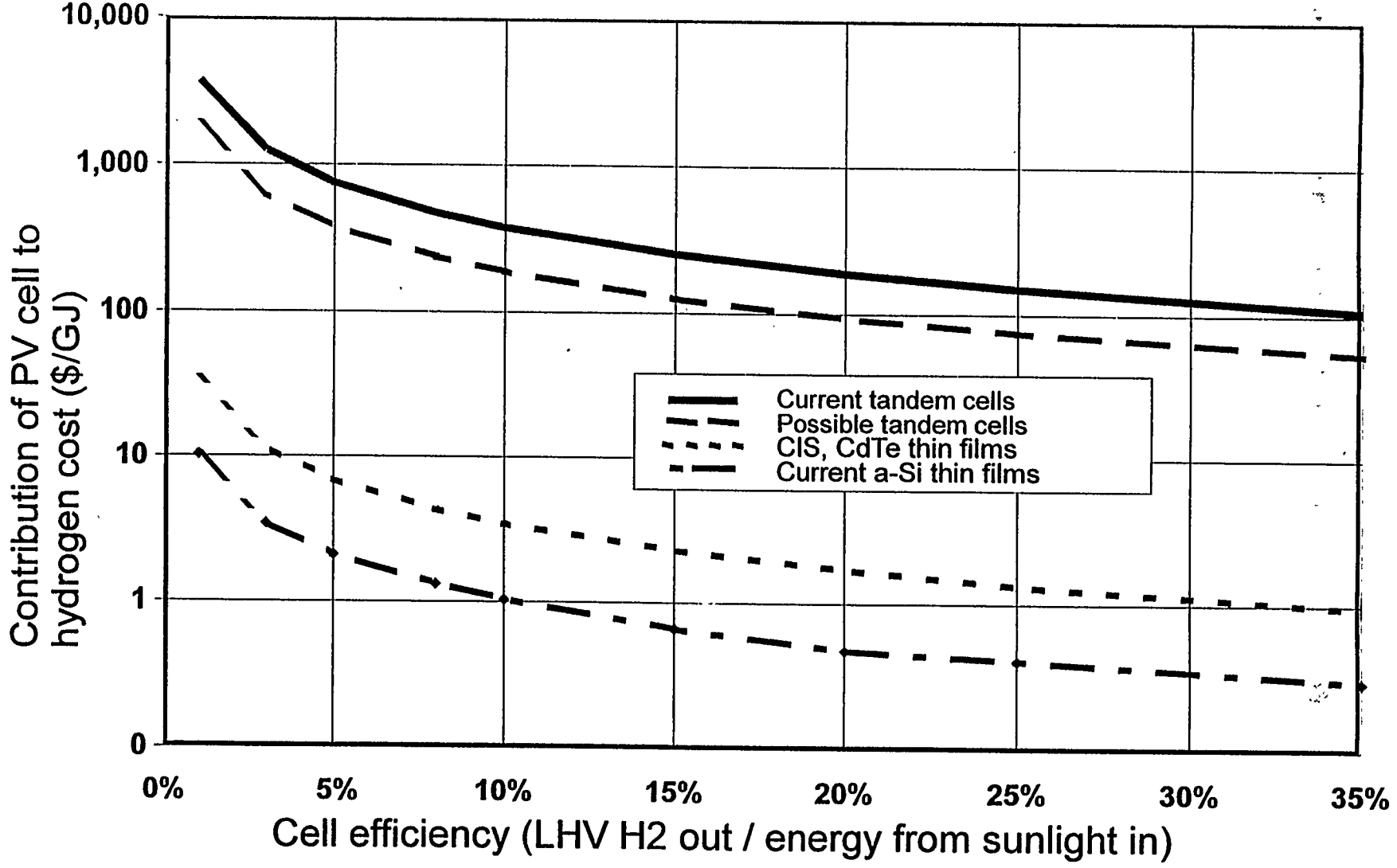
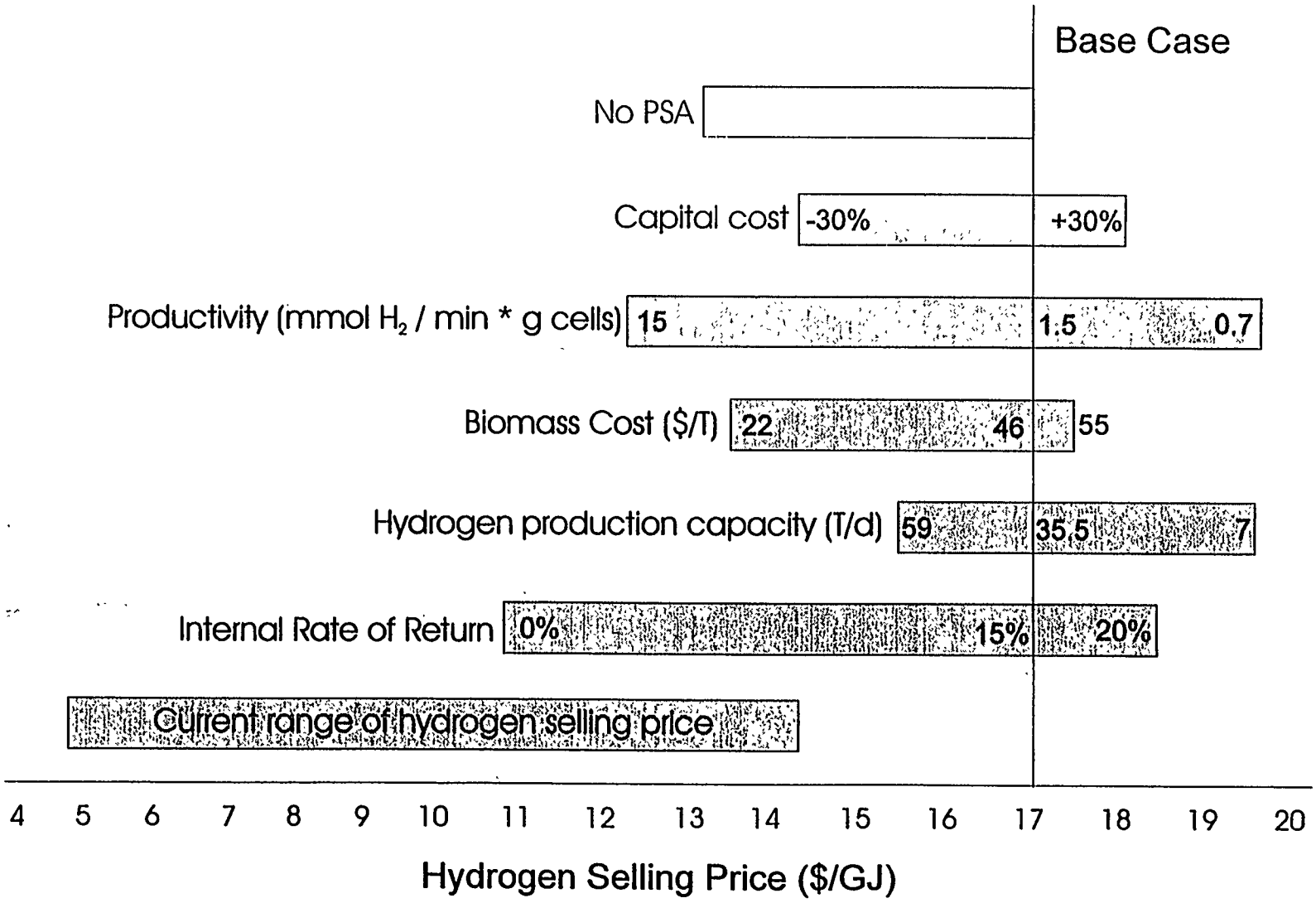


Figure 4: Parametric Sensitivity of the Calculated Selling Price of Hydrogen From Bacterial Water-Gas Shift



Prototype Fiber-Optic Hydrogen Gas Detector

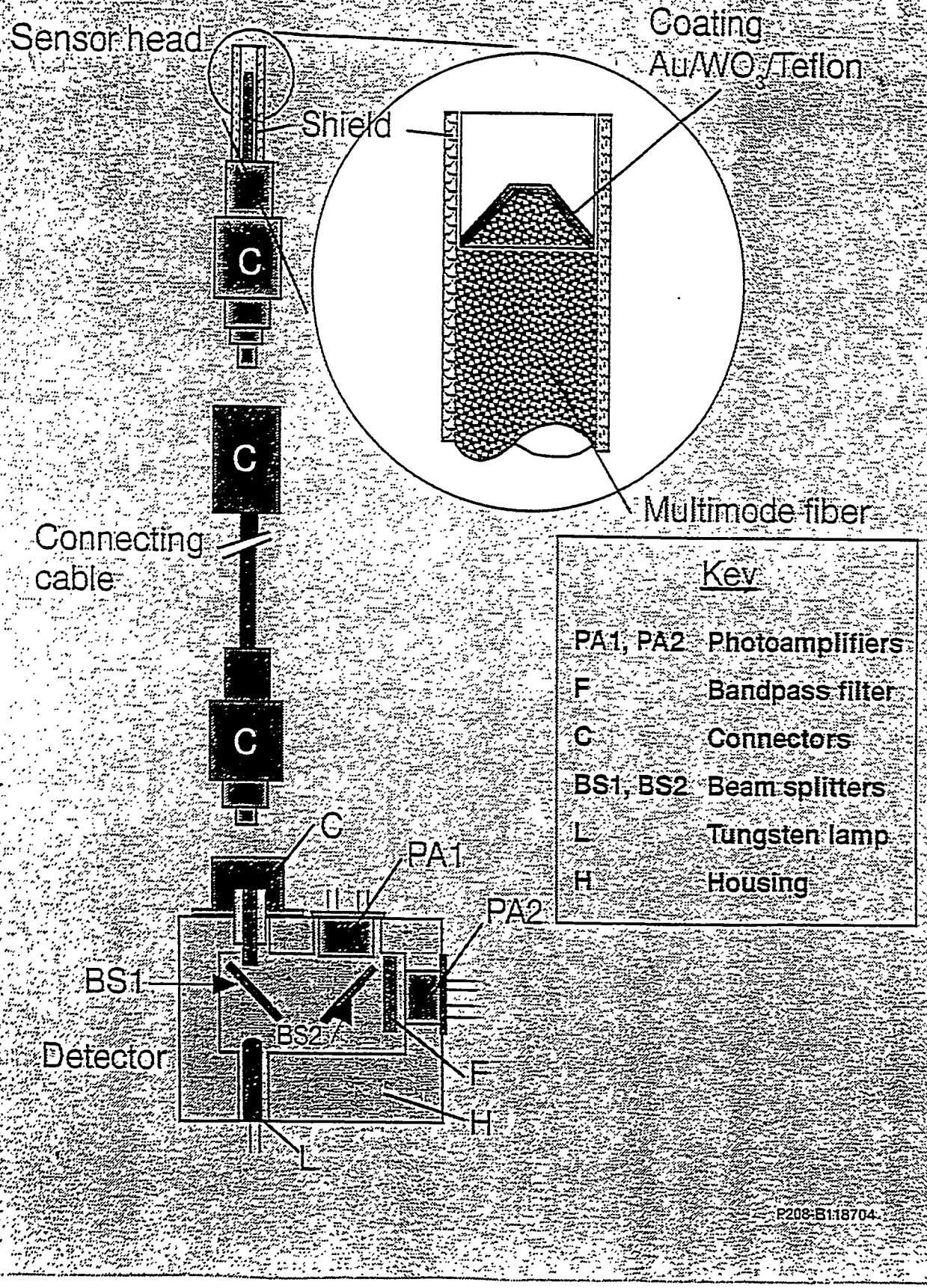
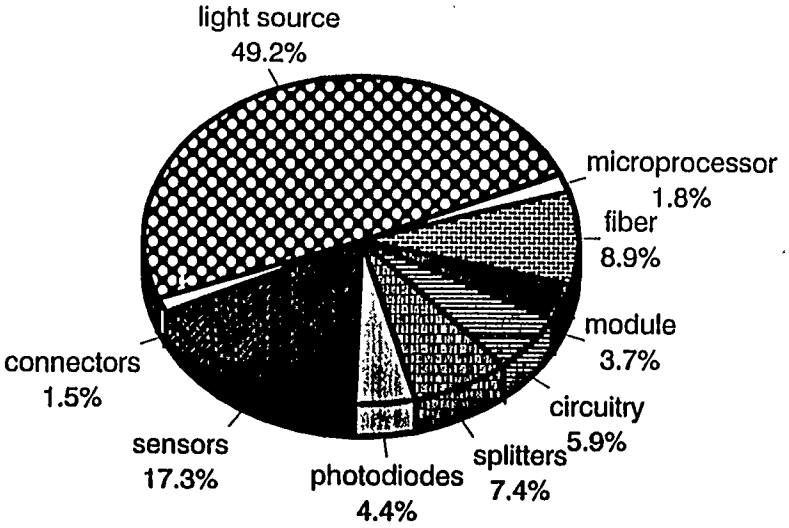
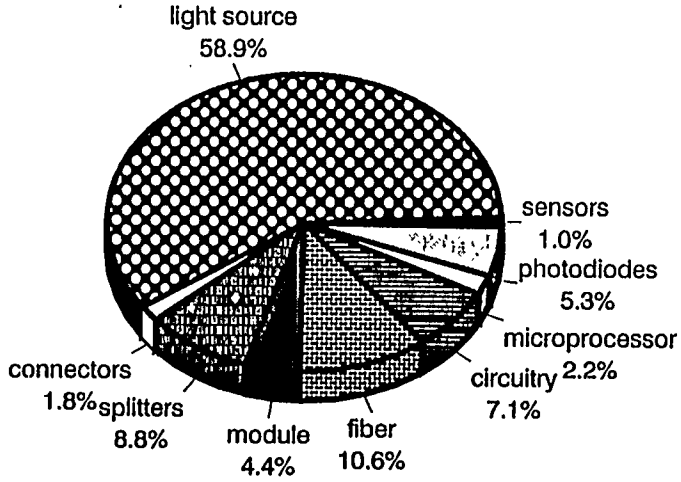


Figure 6: Breakdown of Detector System Costs

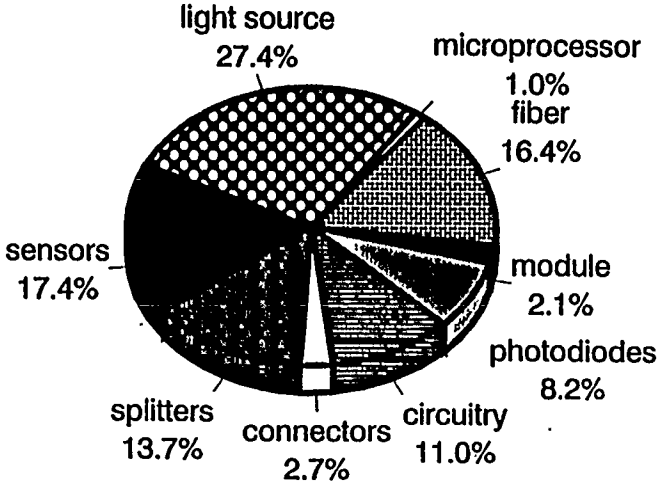
for 6 sensors/vehicle @ 5000 vehicles/year



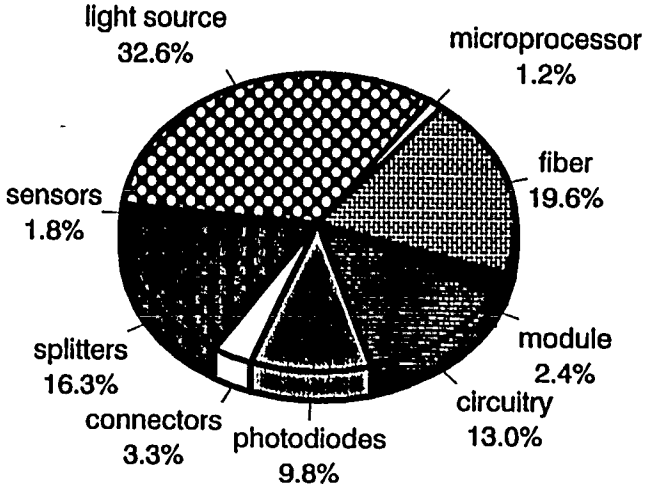
for 6 sensors/vehicle @ 3MM vehicles/year



for 20 sensors/vehicle @ 5000 vehicles/year



for 20 sensors/vehicle @ 3MM vehicles/year



HYDROGEN STORAGE AND DELIVERY SYSTEM DEVELOPMENT: ANALYSIS

J. L. Handrock
Sandia National Laboratories
Livermore, CA 94550

Abstract

Hydrogen storage and delivery is an important element in effective hydrogen utilization for energy applications and is an important part of the FY1994-1998 Hydrogen Program Implementation Plan. This project is part of the Field Work Proposal entitled Hydrogen Utilization in Internal Combustion Engines (ICE). The goal of the Hydrogen Storage and Delivery System Development Project is to expand the state-of-the-art of hydrogen storage and delivery system design and development. At the foundation of this activity is the development of both analytical and experimental evaluation platforms. These tools provide the basis for an integrated approach for coupling hydrogen storage and delivery technology to the operating characteristics of potential hydrogen energy use applications. Results of the analytical model development portion of this project will be discussed.

Analytical models have been developed for internal combustion engine (ICE) hybrid and fuel cell driven vehicles. The dependence of hydride storage system weight and energy use efficiency on engine brake efficiency and exhaust temperature for ICE hybrid vehicle applications is examined. Results show that while storage system weight decreases with increasing engine brake efficiency energy use efficiency remains relatively unchanged.

The development, capability, and use of a recently developed fuel cell vehicle storage system model will also be discussed. As an example of model use, power distribution and control for a simulated driving cycle is presented. Model calibration results of fuel cell fluid inlet and exit temperatures at various fuel cell idle speeds, assumed fuel cell heat capacities, and ambient temperatures are presented. The model predicts general increases in temperature with fuel cell power and differences between inlet and exit temperatures, but under predicts absolute temperature values, especially at higher power levels.

Introduction

Project Approach/Rationale

Hydrogen storage and delivery is an important element in effective hydrogen utilization for energy applications and is an important part of the FY1994-1998 Hydrogen Program Implementation Plan. This project is part of the Field Work Proposal entitled Hydrogen Utilization in Internal Combustion Engines (ICE). (See related DOE Hydrogen Program Review papers for additional programmatic activity discussions.) The goal of the Hydrogen Storage and Delivery System Development Project is to expand the state-of-the-art of hydrogen storage and delivery system design and development. The four parts of the Hydrogen Storage and Delivery System Development project are:

1. Analytical Evaluation Platform
2. Experimental Evaluation Platform
3. Fuel Cell Vehicle Delivery System
4. Internal Combustion Engine Vehicle Delivery System

These four separate, but related, goals provide the basis for an integrated approach for coupling hydrogen storage and delivery technology to the operating characteristics of potential hydrogen energy use applications. The development of both analytical and experimental evaluation platforms provide the basis for hydrogen storage and delivery systems development activities for two specific applications. In the first, low temperature hydride delivery systems are being developed for fuel cell vehicles as part of the Renewable Hydrogen Transportation System Program (Palm Desert). The Palm Desert program consists of a consortium headed by the Schatz Energy Research Center (SERC) whose goal is to develop a clean and sustainable transportation system for the city of Palm Desert. In the second application a light weight hydride delivery system is being developed for the Hydrogen Utilization in ICE's program. In this program hydrogen powered ICE's are integrated into a hybrid vehicle.

An essential part of the above program, and that which will be discussed in this report, is the development of an analytical evaluation platform. In the previous programmatic year a steady state model was developed which integrated ICE and storage material characteristics into the design of light weight hydride storage and delivery systems (Handrock 1995). This activity was pursued in parallel with the light weight hydride material development work being conducted as part of the ICE Hydrogen Utilization program (Thomas 1995). An investigation was completed regarding future hydride material property improvements necessary to make light weight hydride utilization feasible in high efficiency lean-burn ICE's.

In the current year ICE modeling activities were continued and modeling of fuel cell vehicle systems was initiated. ICE modeling of the dependence of hydride storage system weight and energy use efficiency on engine brake efficiency and exhaust temperature for hybrid vehicle applications was examined. Fuel cell vehicle system modeling was initiated to support the Palm Desert project. The development, capability, and use of a recently developed fuel cell vehicle hydride storage system model will also be discussed. Power distribution and control for a simulated driving cycle is presented, as well as initial model calibration results.

Discussion of Results

During the current program year the following key activities were completed.

1. ICE/hydride storage system parametric study.
2. Development of a fuel cell vehicle analytical model (vehicle simulation).
3. Evaluation of fuel cell temperatures at low loads.
4. Presentation of modeling results at the National Hydrogen Association (NHA) meeting and World Hydrogen Energy Conference (WHEC).

Hydrides have the potential for storing hydrogen in a safe, efficient, and economical manner for a variety of applications (Robinson 1994). The most commonly used hydrides are those which operate at or near room temperature (DeLuchi 1989). These materials have a relatively low heat of formation. Chemical bond characteristics of stable light weight hydrides (> 3 wt % hydrogen) are typically accompanied by elevated operating temperatures and large heats of reaction. These energy needs are in conflict with traditional operating characteristics of proposed high efficiency engines, requiring some form of supplemental heating (Hoffman 1976).

In the previous programmatic year a steady state model was developed which integrated engine and storage material characteristics in the design of light weight hydride (> 3 wt % hydrogen) storage and delivery systems (Handrock 1995). A schematic of the model is shown in Figure 1. The model includes individual modules representing the engine, startup and primary hydride beds, heat exchangers, and a burner. Energy and hydrogen mass flow balance were used as the means by which individual components in the model were linked together analytically. Modeling of the hydride material includes representation of such items as hydrogen/hydride weight fraction, reaction enthalpy, operating temperature, pressure-composition-temperature (PCT) hydrogen availability, packing density and specific heat. Material properties of the hydride container were also included to allow modeling of the hydride bed as an integral unit. In the current year this model was used to expand upon previously completed work regarding the effects of hydride operating temperature and heat of formation on system weight and energy use efficiency.

ICE Hybrid Vehicle Storage Studies

Hydrogen storage system weight and energy use efficiency were investigated for an internal combustion engine hybrid vehicle. The performance of several different hydride materials were examined over a range of engine brake efficiencies for two different engine exhaust temperatures. In each case the hybrid vehicle design performance consisted of 10k W average power and a 483 km (300 mile) range. In Figure 2 system weight is seen to decrease with increasing engine efficiency and exhaust temperature. For light weight hydrides (e.g., Mg based) the hydrogen storage system weight has the potential to be significantly less than that of low temperature hydride systems (e.g., FeTi). A 10% system weight reduction is exhibited by an increase in exhaust temperature from 300 C to 400 C. A further 20% reduction in system weight results from an increase in brake efficiency from 32% to 42. (Engine operation of about 40% brake efficiency has been demonstrated (Van Blarigan 1996).)

Energy use efficiency is the ratio of hydrogen delivered to the engine versus total hydrogen energy availability. (Typically some hydrogen is needed for supplemental bed heating and is therefore lost.) As indicated in Figure 3 energy use efficiency is relatively insensitive to engine brake efficiency. As engine efficiency increases there is less waste heat available to drive hydrogen off the hydride bed, thereby increasing parasitic hydrogen use requirements. However, as engine efficiency increases there is also a reduction in overall hydrogen demand, thereby decreasing heat of formation energy requirements. These two factors tend to be self-compensating. From an engineering design viewpoint this means that once a hydride alloy is selected hydrogen energy use efficiency will be relatively unaffected by changes in engine brake efficiency. This knowledge eases storage system sizing in the early stages of the design process. Figure 3 also shows that as exhaust temperature increases and hydride heat of formation decreases the hydrogen energy use efficiency increases. At an exhaust temperature of 400 C a system developed with Alloy SNL has a hydrogen energy use efficiency of unity over an engine brake efficiency range of 32% to 40%. (Alloy SNL is a Mg based Sandia developed alloy with a heat of formation and operating temperature less than that of traditional Mg2Ni (Handrock 1995, Thomas 1995).) Under these conditions available waste heat is sufficient to operate the hydride bed, eliminating the need for supplemental heating.

Fuel Cell Vehicle Storage System Models

The ICE hydride storage and delivery system model was expanded to provide a more generalized evaluation capability. Program coding was moved from a spreadsheet based platform to a compilable subroutine structure. This modification simplified the linking of modules and improved physical modeling capability, code documentation, and results presentation. Model components were represented via individual modules, which were linked together based upon energy/mass balance relationships. Upon assembling the necessary modules to form a desired system representation the user specifies drive power requirements as a function of time and component design characteristics (efficiencies, etc.). The model then calculates component and system operating characteristics, such as power distribution, fluid temperatures and mass flow rates, and operating duration.

The first application of this expanded modeling capability was a fuel cell vehicle model for the Palm Desert program. Figure 4 provides a schematic of the pressurized gas version of the model. Primary components include fuel cell, hydrogen pressure vessel, recirculation tank, circulation pump, heat exchangers, air blower, battery, parasitic loads, and power logic controller. These modules allow performance characteristics of the vehicle to be evaluated under a variety of operating conditions. For example, the power logic controller module controls the distribution of power between the fuel cell and battery based upon drive and parasitic power requirements. Figure 5 represents fuel cell and battery power response to a simulated vehicle drive cycle. Initially the fuel cell is able to meet total power requirements (drive power plus parasitic power (300 W) requirements). When the total power requirement exceeds the 4000 W capability of the fuel cell the battery acts a supplemental power supply. When the total power requirement drops below the fuel cell capability the fuel cell remains a full power until the battery has been recharged. Upon completion of battery recharging the fuel cell power output drops to that level necessary to meet current total power requirements.

This model was completed in collaboration with the Schatz Energy Research Center (SERC). SERC has provided Sandia with fuel cell heat generation data from both dynamometer and road test simulations for pressurized gas operation. This information is being used for initial model calibration. A sample of preliminary calibration results are given in Figure 6. Shown are fuel cell fluid (water) inlet and exit temperatures at various fuel cell idle speeds, assumed fuel cell heat capacities, and ambient temperatures. As expected, fuel cell temperatures increase with fuel cell power, ambient temperature and decrease in fuel cell specific heat. Under the prescribed conditions the model predicts the general increases in temperature with fuel cell power and

differences between inlet and exit temperatures, but under predicts absolute temperature values, especially at higher power levels. These results indicate further refinement is needed in the fuel cell heating and/or heat exchanger portions of the model. Sandia is working in collaboration with SERC to establish what additional test data are required to allow necessary refinement of individual model components. Development of a calibrated pressurized gas model will allow performance predictions of a fuel cell vehicle - hydride storage system to be made in support of the Palm Desert program. Figure 7 shows a schematic of the fuel cell vehicle - hydride storage system model. The pressurized gas vessel has been replaced with a hydride bed. An additional heat exchanger has been placed in the recirculation loop to allow maintenance of bed temperatures during gas delivery.

Plans for Future Work

Effort in the near term will be focused on the following areas:

1. Calibration of fuel cell/pressurized gas analytical model. (Complete in collaboration with SERC.)

2. Incorporation of hydride bed modules into model. Calibration with experimental data.

3. Support fuel cell vehicle storage system design and development activities.

4. Modeling of other storage and delivery system technologies.

Calibration of the fuel cell pressurized gas delivery system analytical model will be completed. Sandia is working in collaboration with SERC to establish what additional test data are required to allow necessary refinement of individual model components. Development of a calibrated pressurized gas model will allow performance predictions of a fuel cell vehicle - hydride storage system to be made. (The additional modules necessary for this model have already been developed.) These predictions will be used to assist in hardware design and development for the Palm Desert program.

The current modeling effort will be expanded to allow the performance characteristics of hydride storage systems to be compared against those of other storage systems (activated carbon, liquid, etc.). The structure of the current model was developed in a manner to support this more generalized modeling activity.

References

DeLuchi, M. A. 1989. "Hydrogen Vehicles: An Evaluation of Fuel Storage, Performance, Safety, Environmental Impacts, and Cost." *Int. J. of Hydrogen*, Vol. 14, No. 2, pp. 81-130.

Handrock, J. L., Wally, K. and Raber, T. N. 1995. "Hydrogen Storage and Delivery System Development," In *Proceedings of DOE Hydrogen Program Review,* 477-491, Coral Gables, FL: Sandia National Laboratories.

Hoffman, K. C., Reilly, J. J., Salzano, F. J., Waide, C. H., Wiswall, R. H., and Winsche, W. E. 1976. "Metal Hydride Storage for Mobile and Stationary Applications," In *Proceedings of the Society of Automotive Engineers, Fuels and Lubricants Meeting*, 760569. St. Louis, MO: Brookhaven National Laboratory.

Robinson, S. L. and Handrock, J. L. 1994. *Hydrogen Storage for Vehicular Applications: Technology Status and Key Development Areas*, Sandia Report SAND94-8229, Livermore, CA: Sandia National Laboratories.

Thomas, G. J. and Guthrie, S. E. 1995. "Lightweight Hydride Storage Materials," In *Proceedings of DOE Hydrogen Program Review,* 543-550, Coral Gables, FL: Sandia National Laboratories.

Van Blarigan, P. 1996. "Hydrogen Engine Development: Experimental Program," To Be Published In *Proceedings of DOE Hydrogen Program Review,* Miami, FL: Sandia National Laboratories.

Figure Captions

Figure 1. ICE Hydride storage model schematic.

Figure 2. ICE hydride storage system weight versus engine brake efficiency.

Figure 3. ICE hydrogen use efficiency versus engine brake efficiency.

Figure 4. Fuel cell vehicle - pressurized gas storage model schematic.

Figure 5. Fuel cell vehicle driving cycle simulation.

Figure 6. Steady state fuel cell temperatures at low loads.

Figure 7. Fuel cell vehicle - hydride storage model schematic.

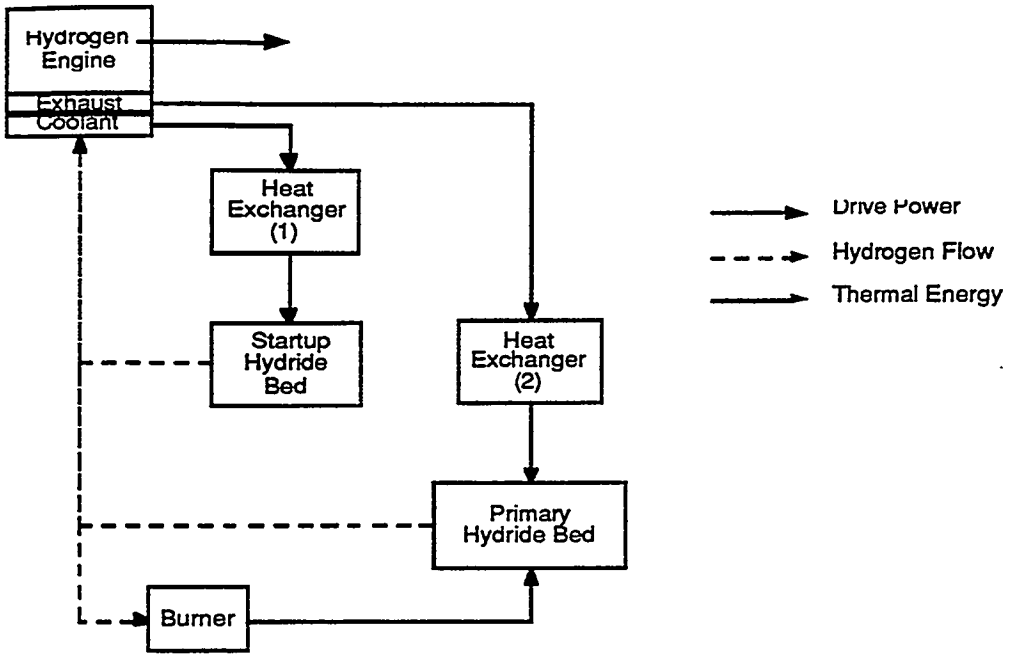


Figure 1. ICE Hydride storage model schematic.

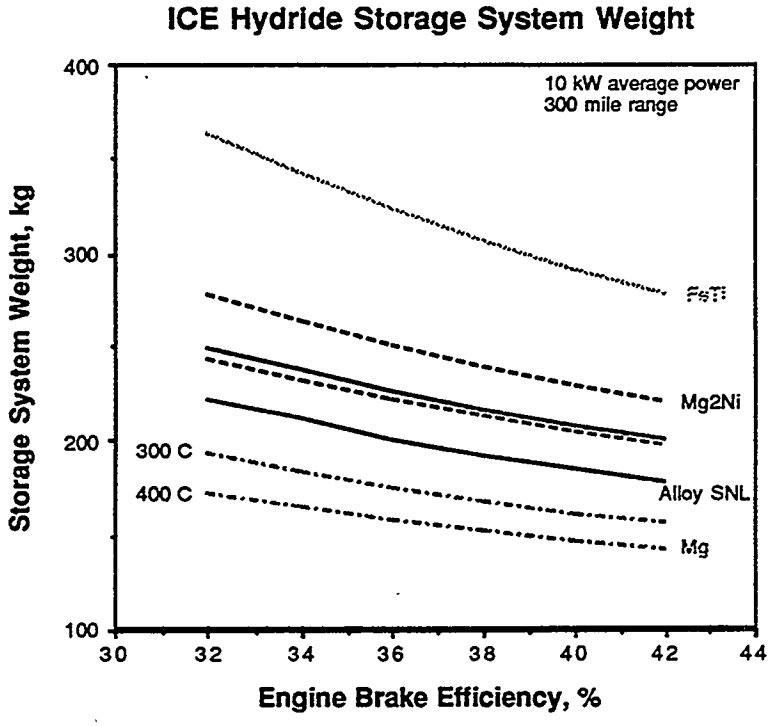


Figure 2. ICE hydride storage system weight versus engine brake efficiency.

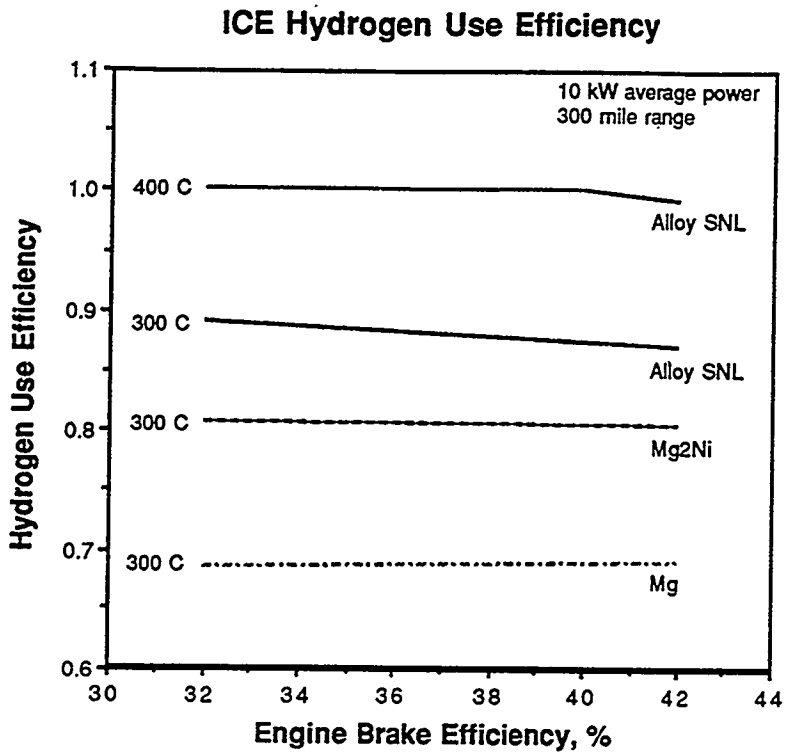


Figure 3. ICE hydrogen use efficiency versus engine brake efficiency.

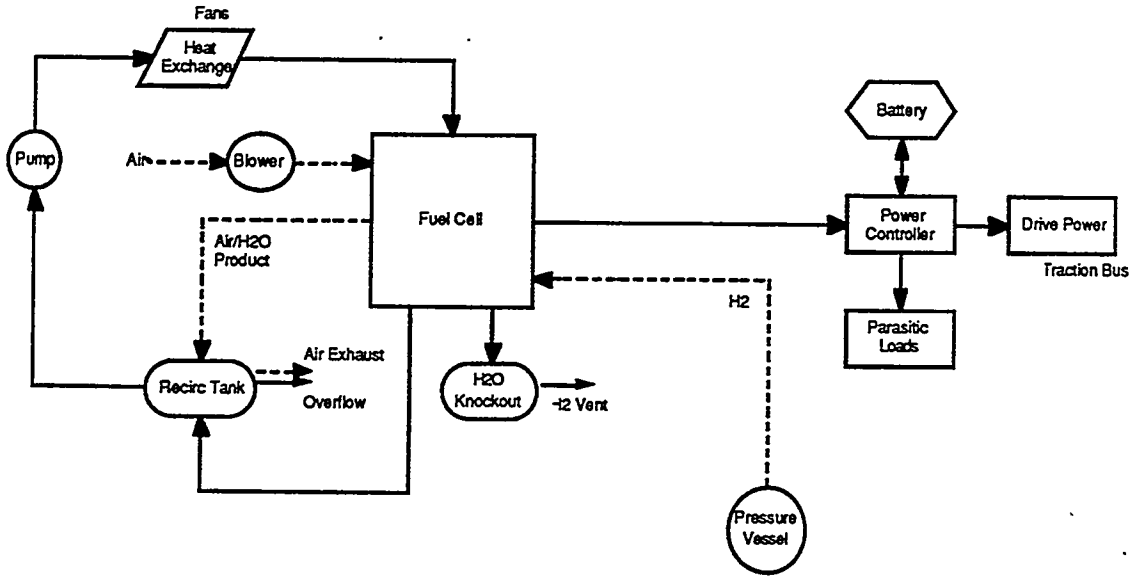


Figure 4. Fuel cell vehicle - pressurized gas storage model schematic.

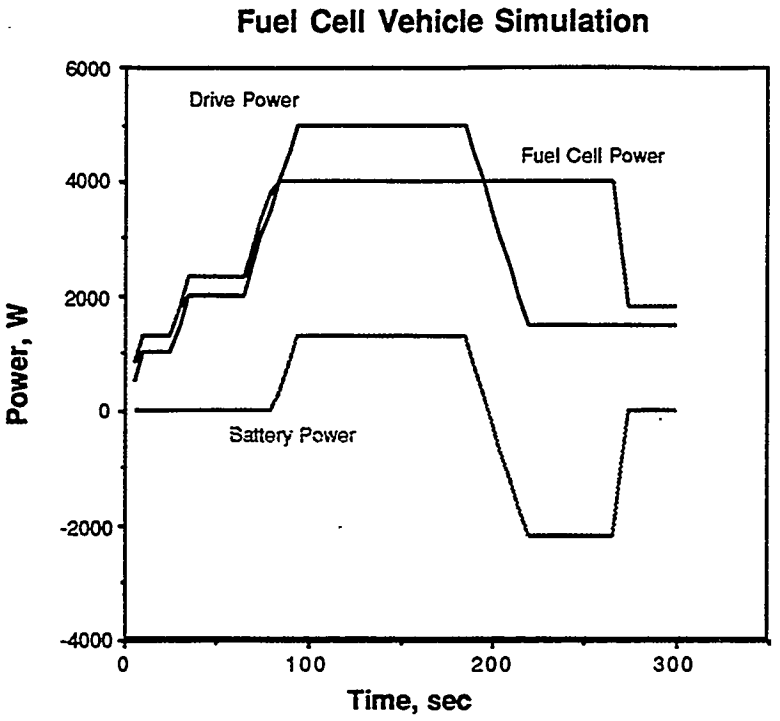


Figure 5. Fuel cell vehicle driving cycle simulation.

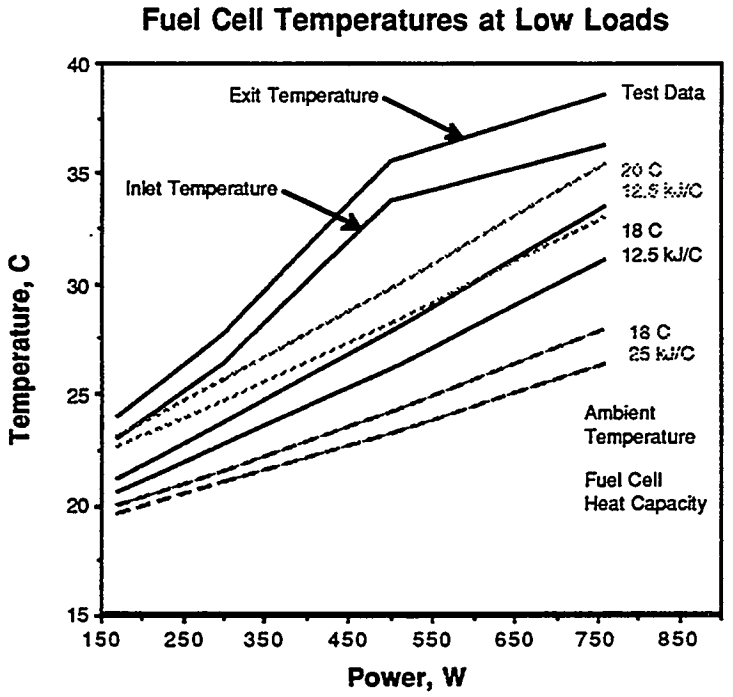


Figure 6. Steady state fuel cell temperatures at low loads.

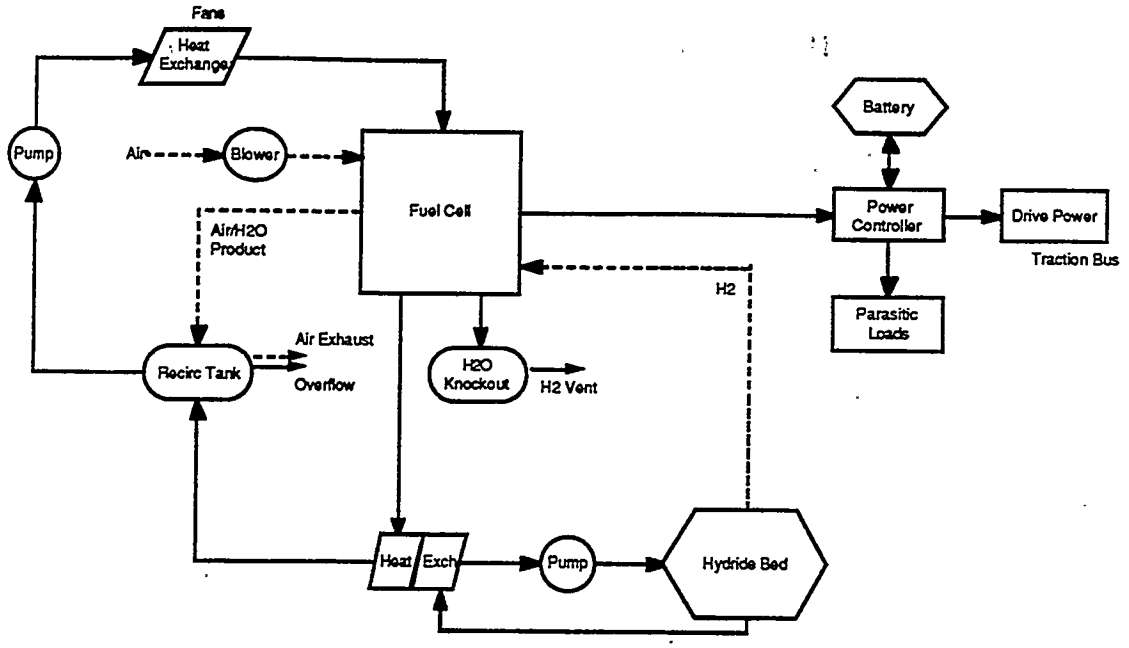


Figure 7. Fuel cell vehicle - hydride storage model schematic.

DEVELOPMENT OF AN EFFICIENT ALGAL H_2-PRODUCING SYSTEM

Maria L. Ghirardi, Sergei Markov, and Michael Seibert
National Renewable Energy Laboratory, Golden, CO 80401

Abstract

Green algae have the potential to efficiently photoevolve H_2 from water using the photosynthetic O_2-evolving apparatus and the reversible hydrogenase enzyme when CO_2 is not present. Unfortunately, algal hydrogenases are very sensitive to inactivation by O_2, the by-product of the water-splitting process. This problem has been one of the major practical factors limiting the commercial utilization of green algae for H_2 production. The other major limitation, saturation of H_2 production by algae at light intensities much lower than normal solar levels, is being addressed by ORNL. The objectives of our project are to generate O_2-tolerant, H_2-producing mutants of the green alga *Chlamydomonas reinhardtii*; to test them in a laboratory-scale system for continuous production of H_2 under aerobic conditions; and to collaborate with ORNL to improve the overall efficiency of H_2 production in intact and cell-free systems. The ultimate goal of the work is to configure a photobiological water-splitting process that will lead to a H_2-producing system that is cost effective, scalable, non-polluting, and renewable.

Our approach to obtain O_2-tolerant mutants of *Chlamydomonas* involves two types of selection techniques. The first depends on the survival of cells under photoreductive conditions, where H_2 utilization is required, and the second requires the survival of the organisms under H_2-producing conditions. In both cases, increasing O_2 stress is placed on the organisms to select for O_2-tolerant strains.

Our work this past year established optimal conditions for the H_2-production selection technique in both the wild-type (WT) and the cell-wall-less (cw15) strain of *Chlamydomonas*. We confirmed the efficacy of the selection technique by demonstrating that variants selected from WT and cw15 cell populations show an increase in up to 2.3 times the I_{50} for O_2, with no decrease in initial H_2-production rate. We also examined the effects of pre-induction of the hydrogenase, electron acceptors, changes in light intensity, and increases in O_2 concentration on the number of survivors.

Two types of photobioreactors were tested for H_2 production with a mutant of *Anabaena variabilis* that lacks uptake hydrogenase activity. This mutant was used as a working model for future improved O_2-tolerant *Chlamydomonas* strains being developed as described above. The unique aspect of this study was the use of light energy to produce H_2 from water under ambient conditions in the presence of O_2 for

long periods of time. We observed continuous H_2 production at low light levels for 9 months at 2 $ml \cdot m^{-2} \cdot h^{-1}$ with a hollow-fiber photobioreactor, and for up to 2 months at 18-19 $ml \cdot m^{-2} \cdot h^{-1}$ using a PVC tubular photobioreactor. Furthermore, we found that increases in CO_2 concentration of the gas phase (from 1.3% to 30%) resulted in increases in the rate of H_2 production in the hollow-fiber photobioreactor. The efficiency of incident light energy conversion to H_2 in the tubular bioreactor was 1-2%.

As part of our collaboration, we have independently confirmed that two of the *Chlamydomonas* mutants lacking photosystem I used by ORNL do in fact produce O_2 in the light and also evolve H_2. Not unexpectedly, they do the latter with the same O_2-sensitivity as our WT cells. This observation is crucial for the credibility of the important ORNL work, since it confirms the potential for doubling the quantum efficiency for H_2 production in these mutants.

Introduction

Project Rationale

There are three major classes of organisms that photoproduce H_2: photosynthetic bacteria, cyanobacteria, and green algae. Photosynthetic bacteria utilize reductants other than water to produce H_2, in a reaction catalyzed by the enzyme nitrogenase. While this reaction is energy intensive, requiring at least 4 ATP/H_2 produced, it is also quite functional when waste reductant is available (1). Cyanobacteria also produce H_2 via a nitrogenase enzyme system. In this case the source of reductant is H_2O, but the reaction involves the formation of a metabolic intermediate. As a result, the quantum yield of H_2 production is rather low, in the order of one H_2/9-10 quanta (2). Green algae do not synthesize nitrogenase; rather, H_2 production in these organisms is catalyzed by the hydrogenase enzyme. Algal H_2 production does not require ATP input nor the generation of metabolic intermediates. Consequently, a higher theoretical quantum yield of one H_2/4 quanta is possible (2). Recent work with mutants of *Chlamydomonas reinhardtii* lacking Photosystem I suggests that an even higher quantum yield of one H_2/2 quanta may be attainable with green algae (3).

The desired characteristics of a photobiological H_2-production system are: (a) use of water as the source of reductant, (b) solar-driven, (c) high efficiency of solar energy conversion, (d) durable and self-replicating, (e) H_2 production at high equilibrium pressure, and (f) cost-competitiveness (4). By these criteria, the use of green algae appears to be a promising and attractive alternative. On the other hand, the current practical limitations of green algae in a photobiological H_2-evolving system include (a) the sensitivity of its hydrogenase to O_2, (b) the occurrence of a dark back reaction between O_2 and H_2 (i.e., the oxy-hydrogen reaction), (c) competition between the CO_2-fixation and the H_2-production pathways for electrons from H_2O, (d) the low equilibrium pressure of H_2 release, and (e) saturation of H_2 production capacity at low light intensity.

Background

A biological approach to address the hydrogenase O_2-sensitivity issue in green algae was developed about 20 years ago by McBride et al. (5). The approach used a positive selection technique based on the reversible H_2 uptake reaction catalyzed by algal hydrogenases. Mutants were selected under this photoreductive pressure and increasing concentrations of O_2. These conditions require algal cells to utilize H_2 as a source of reducing equivalents to fix CO_2 in the presence of DCMU, an inhibitor of electron flow from photosystem II and hence from water. Consequently, cells with hydrogenase sensitive to low oxygen concentration starve to death, while cells with an O_2-tolerant hydrogenase grow. Oxygen-tolerant mutants of *Chlamydomonas reinhardtii* obtained by this technique could produce H_2 in the presence of up to 8% O_2. Unfortunately, the mutants exhibited high levels of the oxy-hydrogen back reaction (5) and were not maintained in culture for further study.

Approach

(a) Generation and Selection of Mutants

It is clear that novel approaches will be required to obtain algal hydrogenases that are stable in the

presence of O_2. We have addressed this problem by developing and examining a new technique based on the application of selective pressure under H_2-producing, rather than H_2-utilizing conditions. One of the potential advantages of this approach may be in elimination of the high rates of the oxy-hydrogen reaction observed in the old experiments.

The hydrogen-production selective pressure that we have employed in this work is based on the toxic effect of metronidazole (MNZ) on photosynthetic organisms. Metronidazole is a heterocyclic compound with a low redox potential (E_m= -325 mV at pH 6.9; ref. 6) that is normally used to treat infections caused by protozoa and anaerobic bacteria (7). In these organisms, MNZ is a strong oxidizer of ferredoxin, in a reaction catalysed by the reversible hydrogenase (7). Its toxic effect is due to one of its reduced intermediate states. The site of action of MNZ in photosynthetic organisms is restricted to chloroplasts, where it oxidizes light-reduced ferredoxin (6). Schmidt et al. (6) have proposed that the subsequent reoxidation of reduced MNZ by molecular O_2 yields a superoxide radical (8) which then disproportionates into H_2O_2 (9). Consequently, the toxicity of MNZ was attributed to the generation of H_2O_2. Long exposure (up to 24 h) to MNZ has been used to select for *Chlamydomonas* mutants defective in photosynthetic electron transport function (6). Ferredoxin (Fd) is a key electron carrier, located on the reducing side of photosystem I, and it provides the reducing equivalents to a variety of pathways. The most prevalent pathway, of course, is through $NADP^+$, which in turn is coupled to CO_2 fixation. Among the other Fd-dependent pathways is hydrogenase-catalyzed H_2 production. This pathway, of course, is inoperative during phototrophic growth due to inactivation of the enzyme by O_2 produced during the water-splitting process. We reasoned that, since MNZ toxicity depends on the accumulation of reduced Fd, an organism with an active hydrogenase will be less sensitive to MNZ toxicity in the absence of CO_2 because an alternative pathway for electrons from Fd is available.

(b) Development of a laboratory-scale photobioreactor

The main challenge here is to design simple, efficient bioreactors that consume as little energy as possible. In recent years several groups have studied the efficacy of tubular bioreactors for cultivation of photosynthetic organisms (10-12). In comparison to open ponds or tank reactors, these tubular bioreactors have the following advantages: (a) a high surface area to culture volume ratio, allowing photosynthetic microorganisms to absorb light energy more effectively, (b) better gas mass transfer rates into liquid media, and (c) low mixing energy requirements.

Hollow fibers have been used successfully in several biotechnology applications (13). Immobilization and cultivation of microorganisms on hollow fibers of semipermeable polymeric membranes have potential advantages over other types of bioreactors. As in the case of tubular reactors, one of the important advantages of hollow fiber photobioreactors is the very large surface area to volume ratio, which enhances mass transport of gases and nutrients to microorganisms immobilized at high concentrations on the outer surface of the fibers. This characteristic allows for the design of more compact bioreactor systems. In addition, cell metabolism is stabilized by the immobilization process, increasing the time that the bioreactor can operate before the microorganisms must be replaced.

In the present study, we analyzed both a tubular and a hollow fiber photobioreactor for H_2 production by a cyanobacterial mutant of *Anabaena variabilis* (PK84) obtained from Prof. S.V. Shestakov (Moscow State University). This organism lacks uptake hydrogenase activity (14) and was chosen as a model system for the O_2-tolerant green alga being developed by our group. In both photobioreactors, hydrogen was photoevolved from water and released from solution at atmospheric pressure, under conditions where the organisms were exposed to atmospheric levels of O_2. The experiments demonstrated the capability of the

organism to produce H_2 for long periods of time. Furthermore, the ability to use water as a substrate under ambient conditions could lead to a less complex and potentially more cost effective way to produce H_2 in photobioreactors than those requiring either a partial vacuum (15) or inert purge gases (16) to "harvest" H_2.

(c) Collaboration with ORNL

The objective of Dr. Greenbaum's work at ORNL has been to increase the efficiency of H_2 production in *Chlamydomonas* by manipulating the antenna size of the photosystems, or by using a PSI-deficient mutant that produces hydrogen with double the quantum efficiency of WT organisms (3). Our ultimate goal is to combine the characteristics of his high-efficiency mutant with an organism containing an O_2-tolerant hydrogenase in order to generate a double mutant with high-efficiency, H_2-producing capability under aerobic conditions.

Results and Discussion

(a) Generation and Selection of Mutants

H_2-Production Selective Pressure

We designed an innovative treatment to select for potential O_2-tolerant, H_2-producing organisms. Cells were first incubated in the presence of MNZ at different concentrations of O_2 for a short period of time in the light and then grown on minimal agar medium to determine survival rates. We examined the effect of the following treatment parameters on the rate of survival: MNZ concentration, light intensity (which limits the rate of accumulation of reduced Fd), pre-induction of the hydrogenase enzyme, and O_2 concentration in the selection medium. We tested both WT and a cell wall-less strain (cw15) of *Chlamydomonas reinhardtii*, taking into consideration that future work may require the use of genetic transformation, if we succeed in isolating a mutant containing an O_2-tolerant hydrogenase. The choice of the cw15 strain was based on the observation that the absence of the cell wall increases the efficiency of genetic transformation (17).

Figure 1 shows the effect of increasing concentrations of MNZ and light intensity on the number of cw15 *Chlamydomonas* cells surviving the selective treatment. The light intensities examined were 17.5, 50 (Fig. 1A, first experiment), 200, and 400 (Fig 1B, second experiment) W/m^2. The selective pressure was applied to anaerobically-treated cells (containing an initially active hydrogenase), and O_2 was added at 2.8%. Oxygen inhibits most of the hydrogenase activity in both WT and cw15 cells at this concentration (see Fig. 4). The maximum concentration of MNZ used in the treatment (58 mM) was determined by the solubility of MNZ in aqueous medium. It is clear from Fig. 1 that MNZ toxicity is a function of the light intensity, consistent with the theory that the extent of killing depends on the rate of electron transport. It is interesting that the curves in Fig. 1 do not fit an exponential function, which suggests that factors other than MNZ concentration are limiting the rate of killing (see the hydrogenase induction experiment below). Figure 1 also shows the degree of variability of the results obtained from different experiments. The data obtained by exposure of cells to 50 W/m^2 in the first experiment (Fig. 1A) is very similar to the data obtained with 200 W/m^2 in the second experiment (Fig. 1B). It is possible that the phase of growth at which cells were harvested for each experiment is responsible for the variability. Treatment done in the presence of light intensities above 200 W/m^2 (Fig. 1B) caused an increase in temperature that may have

affected the number of survivors detected even in control samples not exposed to MNZ.

The third parameter that we checked was the effect of hydrogenase induction on the number of survivors. The experiment was done with pre-induced and uninduced cw15 *Chlamydomonas* cells subsequently treated with different concentrations of MNZ in the presence of 2.8% O_2 and illuminated for 20 min at 200 W/m^2. Figure 2 shows that MNZ killing in the absence of a pre-induced hydrogenase is exponential. However, pre-induction of the hydrogenase causes a loss of exponential killing, consistent with the results in Fig.1. This demonstrates that the effect of MNZ is limited in cells that have an active hydrogenase, confirming our hypothesis that hydrogenase-catalyzed H_2 production provides enough of an alternative sink for electrons from reduced Fd to mitigate the effects of MNZ.

Thus far we have found that our proposed selection technique depends on the concentration of MNZ, on the amount of accumulated reduced Fd (and thus on the electron transport rate), and on the presence of an active hydrogenase. We next examined the effect of O_2 concentration on the rate of survival. Oxygen is expected to inactivate the hydrogenase in a concentration-dependent manner, thus increasing the toxicity of MNZ. Figure 3 shows the result of adding 10% O_2 to the gas phase of the selection medium on the degree of survival of cw15 *Chlamydomonas* cells treated with MNZ and exposed to 200 W/m^2 light. While the increase in O_2 concentration in gas phase appears to increase the sensitivity of MNZ-dependent killing, the magnitude of increase is not so pronounced as might be expected. One likely possibility is that internally generated photosynthetic O_2 production is affecting the MNZ treatment in part, and the impact of externally-set O_2 is superimposed on it.

Finally, confirmation of the validity of our proposed technique to select for O_2-tolerant, H_2-producing organisms comes from measurement of the O_2-sensitivity of H_2-production by some of the surviving isolates from two different selection experiments, compared to their parental strains. In order to establish baseline values, we initially determined the O_2 sensitivity of H_2 production by WT and cw15 cells. Initial rates of H_2 evolution were measured as a function of the initial concentrations of O_2 in the assay medium. Given the variability of measuring rates of H_2 evolution from day to day, the data from each experiment (from 5 to 10 points) were fitted to a single exponential decay equation from which we estimated V_0, the rate of H_2 evolution in the absence of O_2, and I_{50}, the initial O_2 concentration that causes a 50% decrease in the initial rate of H_2 evolution compared to V_0. The V_0s estimated from each experiment were then used to normalize the data obtained from all the experiments. The data in Figure 4 show that as the initial concentration of O_2 increases, the rate of H_2 evolution by cw15 (Fig. 4A) or WT cells (Fig. 4B) decreases exponentially. The normalized V_o values for the cw15 and WT strains were, respectively, 22 and 27 μmoles $H_2 \cdot$mg Chl$^{-1} \cdot h^{-1}$, and the estimated I_{50}s were 0.300%± 0.028% and 0.394%± 0.068% O_2.

Due to the variability in rates measured on different days, we always determined the O_2 sensitivity of H_2 production for survivors from different MNZ experiments and their respective parental strains on the same day. The results from two selection experiments are reported on Table I. Experiment I was done with pre-induced cw15 and WT cells treated with 58 mM MNZ in the presence of 2.8% O_2. There were 6 cw15 survivors, of which we tested 2; both showed increases in the I_{50} for O_2 compared to their parental strains. One particular survivor, identified as D5, had an estimated I_{50} 2.3 times higher than its parental strain. The other survivor, despite a higher I_{50}, had a decreased V_0 rate of H_2 evolution, perhaps indicating lower rates of electron transport. MNZ treatment of WT cells in experiment I yielded 5 survivors. Two of them showed increases in I_{50} in the order of 50% compared to their parental strain. The rate of H_2 evolution by one of the survivors was very low, but the other had a rate comparable to that of its parental strain. Experiment II was done only with WT cells following pre-induction of the hydrogenase and MNZ treatment in the presence of 5% O_2. All of the four tested survivors out of a total of 6 had low rates of H_2

evolution. Two of them had I_{50}s in the order of their parental strain, while the other two exhibited small increases in their I_{50}s.

The results using the selection technique described in this paper indicate that it is possible to select for *Chlamydomonas* isolates that exhibit H_2-production capability that is less sensitive to O_2 than the WT population. However, MNZ treatment can also select for mutants impaired in electron transport, as observed previously (6). Although H_2-production selective pressure is a valid option for reaching our long term goal, we conclude that we need to improve the screening procedure to deselect for electron transport mutants. Furthermore, our assay for O_2 sensitivity, based on measuring the I_{50} of H_2 production in the presence of O_2, is time-consuming and subject to variability. Once this is done, H_2-production selection in combination with mutagenesis could lead to the identification of mutants that are tolerant to even higher concentrations of O_2.

TABLE I. H_2-production results from two selection experiments done with cw15 and WT *Chlamydomonas reinhardtii cells*. The cells were pre-induced and subsequently treated with 58 mM MNZ for 20 min under 200 W/m^2 illumination in the presence of either 2.8% O_2 or 5% O_2. Survivors from the two experiments were plated, and selected clones were transferred to liquid medium and grown photoautotrophically for 3 days. Pre-induced cells were used in measurements of H_2-evolution rates in the presence of different initial O_2 concentrations as in Fig. 4. Estimated V_0 and I_{50} values for H_2 production obtained for each survivor were compared to values determined with control parental WT and cw15 cells on the same day.

Experiment	Organism	I_{50} for O_2, % of control	V_0, % of control
Experiment I (2.8% O_2)	cw15 (D5)	233	100
	cw15	153	20
	WT	152	100
	WT	163	12
Experiment II (5% O_2)	WT	100	23
	WT	138	44
	WT	168	21
	WT	100	5

Photoreductive Selection

Our attempts to optimize photoreductive pressure conditions to select for O_2-tolerant H_2-utilizing variants of *Chlamydomonas* are still under initial investigation. We have determined that the cells have to be pre-incubated in the dark under aerobic conditions for a few days prior to submission to the selective pressure, in order to allow the break-down of stored metabolites. If this pre-incubation is not done, WT cells will survive the selective pressure in the presence of O_2 by respiring the accumulated starch.

Surface area (m^2)

(b) Photobioreactor Development

Two types of bioreactors were designed and constructed. The first (Fig. 5) was a 2 liter (total volume), 0.4 m-high PVC tubular system, vertically spiraled to facilitate continuous H_2 production. The bioreactor consisted of (a) a transparent PVC (Nalgene, USA) 7.9 mm internal diameter tube, which was wound helically on a vertical transparent cylindrical supporting structure; (b) a H_2 measurement port, where H_2 and air are vented from the cyanobacterial suspension (gas flow rate 46 $ml \cdot min^{-1}$); (c) a CO_2 gas cylinder; (d) an air input line; (e) a gas proportioning rotameter (Omega, USA), which was used to measure and mix CO_2 and air; (f) a peristaltic pump (Masterflex, Cole-Palmer Instrument Co., USA) for circulating the cyanobacterial suspension (35 $ml \cdot min^{-1}$); and (g) a 33 W cool white fluorescent lamp. The bioreactor suspension was bubbled with a mixture of CO_2 (5%) and air through a needle/septum connection at the base of the photobioreactor to supply the cells with a carbon source and remove H_2. The inner cylindrical surface of the bioreactor (0.22 m^2) was illuminated continuously with fluorescent light (average irradiance 3.0 $W \cdot m^{-2}$), measured with a radiometer (Model 65A, Yellow Spring Instruments Co., USA) at different points on the inner surface of the reactor.

The second was a hollow-fiber reactor consisting of sixty hydrophilic hollow fibers from an AM-40M-5D cartridge cut into 110 mm lengths and sealed together at one end. The fibers were packed into a water-jacketed glass column (length, 110 mm; volume, 15 ml), as shown in Fig. 6. The cyanobacterial cells became immobilized on the outer surface of the fibers. The design and operation of this reactor were described previously (15,18). Its operation requires the growth medium to flow from the outside of the fibers to the inner lumen space. In contrast with the system described by Markov et al. (15), H_2 was collected directly from the gas phase of the medium reservoir. The photobioreactor was maintained at 28-29°C, illuminated continuously with low levels of cool white fluorescent light, and run on air/CO_2 for up to 9 months.

Hydrogen production rates in both photobioreactors were measured with a Varian Model 3700 gas chromatograph equipped with a molecular sieve 5A column and a thermal conductivity detector. Argon was used as the carrier gas. Light energy conversion efficiencies to H_2 were calculated as follows:

$$Efficiency\ (\%) = \frac{H_2\ production\ rate \times H_2\ energy\ content}{Incident\ Light\ Irradiance} \times 100\%$$

The heat of H_2O formation, 241,000 $J \cdot mol^{-1}$ was used as the energy content of the H_2 produced.

The results obtained with both reactors are shown in Table II. The average rate of H_2 production by cyanobacteria in the tubular reactor was 18.9 $ml \cdot m^{-2} \cdot h^{-1}$ over a 30-day run, which is equal to $6.29 \cdot 10^{-4}$ $mol \cdot m^{-2} \cdot h^{-1}$, yielding an average efficiency of 1.4%. The average hydrogen production rate in the hollow-fiber reactor was 2 $ml \cdot m^{-2} \cdot h^{-1}$, or 9.1 $ml \cdot g\ cdw^{-1} \cdot h^{-1}$. Finally, both types of reactors were operated continuously for either 1 or 9 months, demonstrating the possibility or using light energy to produce H_2 from water under ambient conditions for long periods of time.

---

of WT organisms. We have also demonstrated that the O_2 sensitivity of H_2-production capacity is the same in all three organisms.

Conclusion

Definition of Success

ACKNOWLEDGEMENTS

This work was funded by the U.S. Department of Energy Hydrogen Program. We thank Steve Toon for technical assistance.

REFERENCES

1. Weaver, P.F., Lien, S., and Seibert, M. (1979), in *Proceedings of the Fifth Joint US/USSR Conference of the Microbial Enzyme Reactions Project*, Jurmala, Latvia, USSR, pp. 461-479.
2. Benemann, J.R. (1994), in *Proceedings of the 10th World Hydrogen Energy Conference*, Cocoa Beach, Florida.
3. Greenbaum, E., Lee, J.W., Tevault, C.V., Blankinship, S.L., and Mets, L.J. (1995), *Nature* **376**, 438-441.
4. Weaver, P.F., Lien, S., and Seibert, M. (1980), *Solar Energy* **24**, 3-45.
5. McBride, A.C., Lien, S., Togasaki, R.K., and San Pietro, A. (1977), in *Biological Solar Energy Conversion* (A. Mitsui, S. Miyachi, A. San Pietro, and S. Tamura, eds.), Academic Press, New York.
6. Schmidt, G.W., Matlin, K.S., and Chua, N.-H. (1977) *Proc. Natl. Acad. Sci. USA* **74**, 610-614.
7. Church, D.L., and Laishley, E.J. (1995), *Anaerobe* **1**, 81-92.
8. Wardman, P., and Clarke, E.D. (1976), *Biochem. Biophys. Res. Comm.* **69**, 942-949.
9. Fridovich, I. (1974), in *Advances in Enzymology*, vol. 41, Meister, A., ed., Wiley interscience, New York, pp 35-97.
10. Lee, E.T.-Y., and Bazin, M.J. (1990) *New Phytol.* **116**, 331-335.
11. Tredici, M., and Materassi, R. (1992) *J. Appl. Phycol.* **4**, 221-231.
12. Watanabe, Y., de la Noe, J., and Hall, D.O. (1995) *Biotechnol. Bioeng.* **47**, 261-269.
13. Bunch, A.W. (1988) *J. Microbiol. Methods* **8**, 103-119.
14. Mikheeva, L.E., Schmitz, O., Shestakov, S.V., and Bothe, H. (1995) *Z. Natruforschung* **50**, 505-510.
15. Markov, S.A., Bazin, M.J., and Hall, D.O. (1995) *Enzyme and Microbial Technology* **17**, 306-310.
16. Benemann, J.R., and Weare, N.M. (1974) *Science* **184**, 174-175.
17. Kindle, K.L. (1990), *Proc Natl Acad Sci USA* **87**, 1228-1232.
18. Markov, S.A., Weaver, P., and Seibert, M. in *Proceedings of the 11th World Hydrogen Energy Conference*, Stuttgart, Germany, in press.
19. Markov, S.A., Thomas, A., and Bazin, M.J. (1994) in *Abstracts of the VIII International Symposium on Phototrophic Prokaryotes*, Urbino, Italy, p. 106.

FIGURE LEGENDS

FIGURE 1. Effect of MNZ concentration and light intensity on the number of survivors from two selection experiments. **A.** Selection was done using cw15 cells in the presence of varying concentrations of MNZ and 2.8% O_2, at either 17.5 or 50 W/m^2. **B.** Selection was done as above, under either 200 or 400 W/m^2.

FIGURE 2. Effect of anaerobic pre-induction of hydrogenase on the number of cw15 survivors. Cells submitted to the MNZ selective treatment were either pre-induced by anaerobic incubation or not induced. The treatment was done in the presence of 2.8% O_2 and 200 W/m^2.

FIGURE 3. Effect of O_2 concentration in the gas phase of the selective treatment vial on the number of survivors. MNZ incubation was done for 20 min using cw15 cells, either under completely anaerobic conditions, or in the presence of 10% added O_2 in the gas phase of the selection medium. The light intensity was 200 W/m^2.

FIGURE 4. Normalized rates of H_2 evolution measured with pre-induced (**A**) cw 15 or (**B**) WT cells injected to an assay medium pre-set to the indicated initial concentrations of O_2. H_2 concentration in the assay medium was measured immediately, and the procedure included a 2-min interval prior to illumination to allow the cells to acclimate. No H_2 production was observed during this 2-min time.

FIGURE 5. Schematic diagram of a helical PVC tubular photobioreactor for H_2 production by *Anabaena variabilis* lacking uptake hydrogenase activity. See the text for a description of a-g.

FIGURE 6. Schematic diagram of a hollow-fiber photobioreactor using a cyanobacterial mutant to produce hydrogen from water under atmospheric conditions.

FIGURE 1

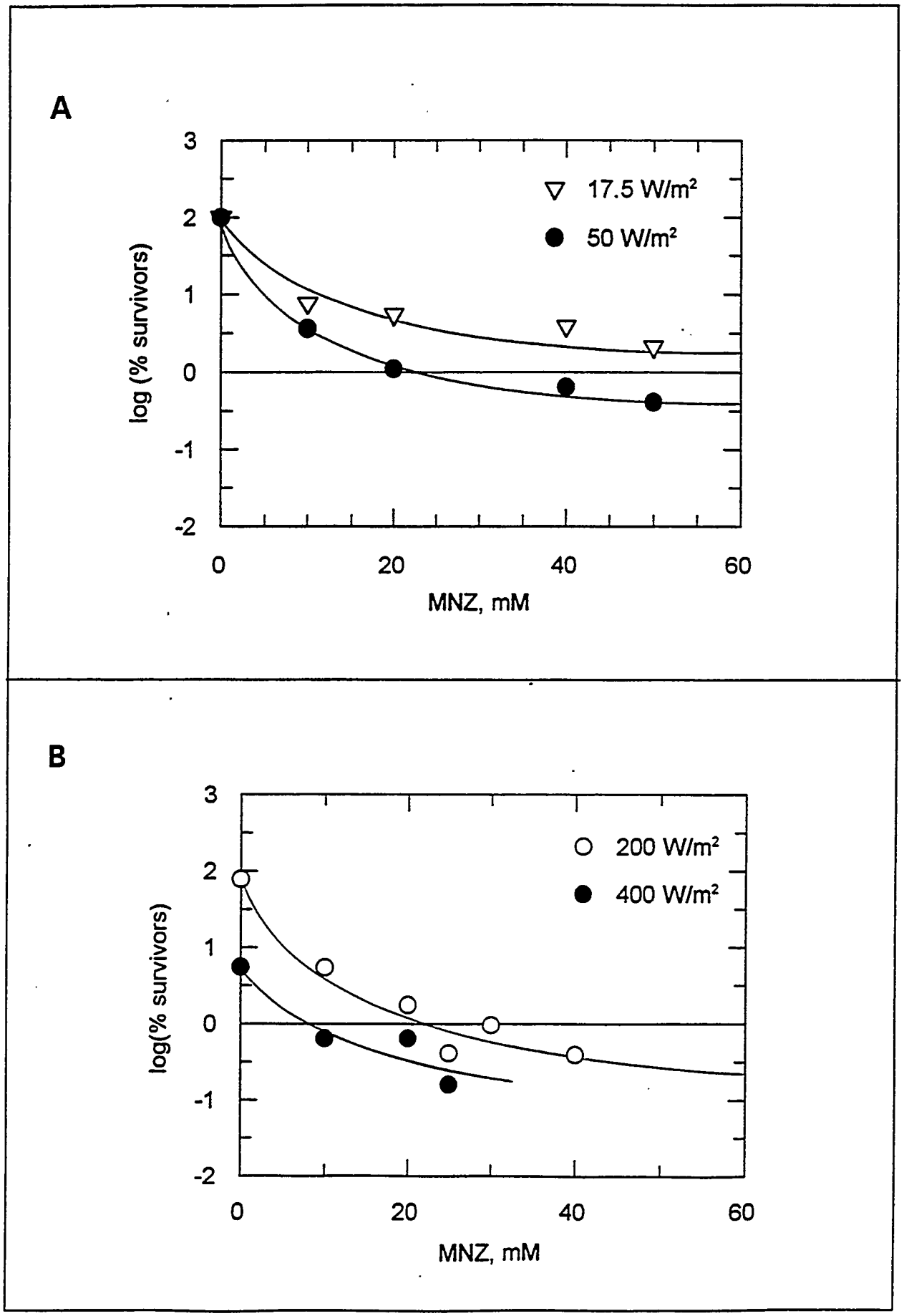

A
log (% survivors)
3
2
1
0
-1
-2
0
20
40
60
MNZ, mM
17.5 W/m²
50 W/m²
B
log(% survivors)
3
2
1
0
-1
-2
0
20
40
60
MNZ, mM
200 W/m²
400 W/m²

FIGURE 2

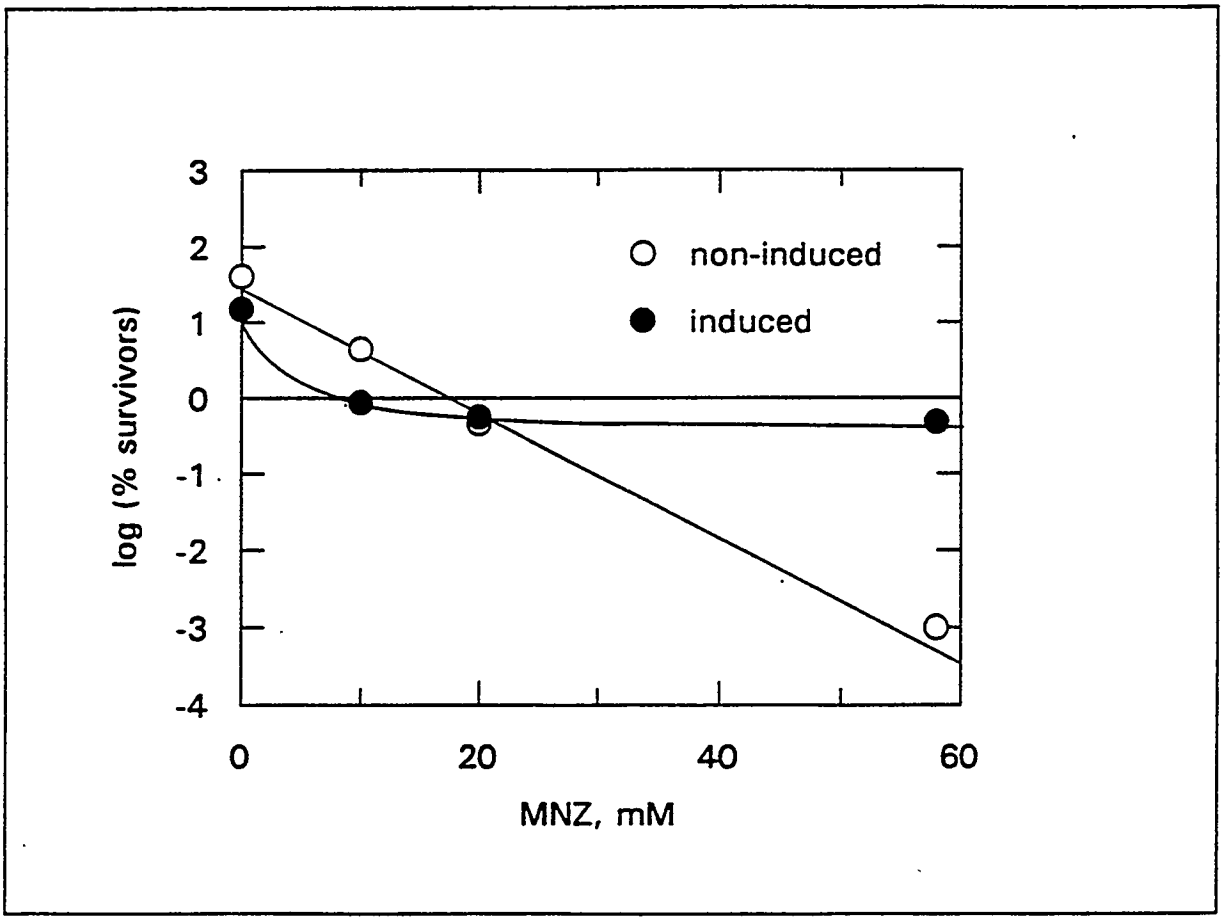


FIGURE 3

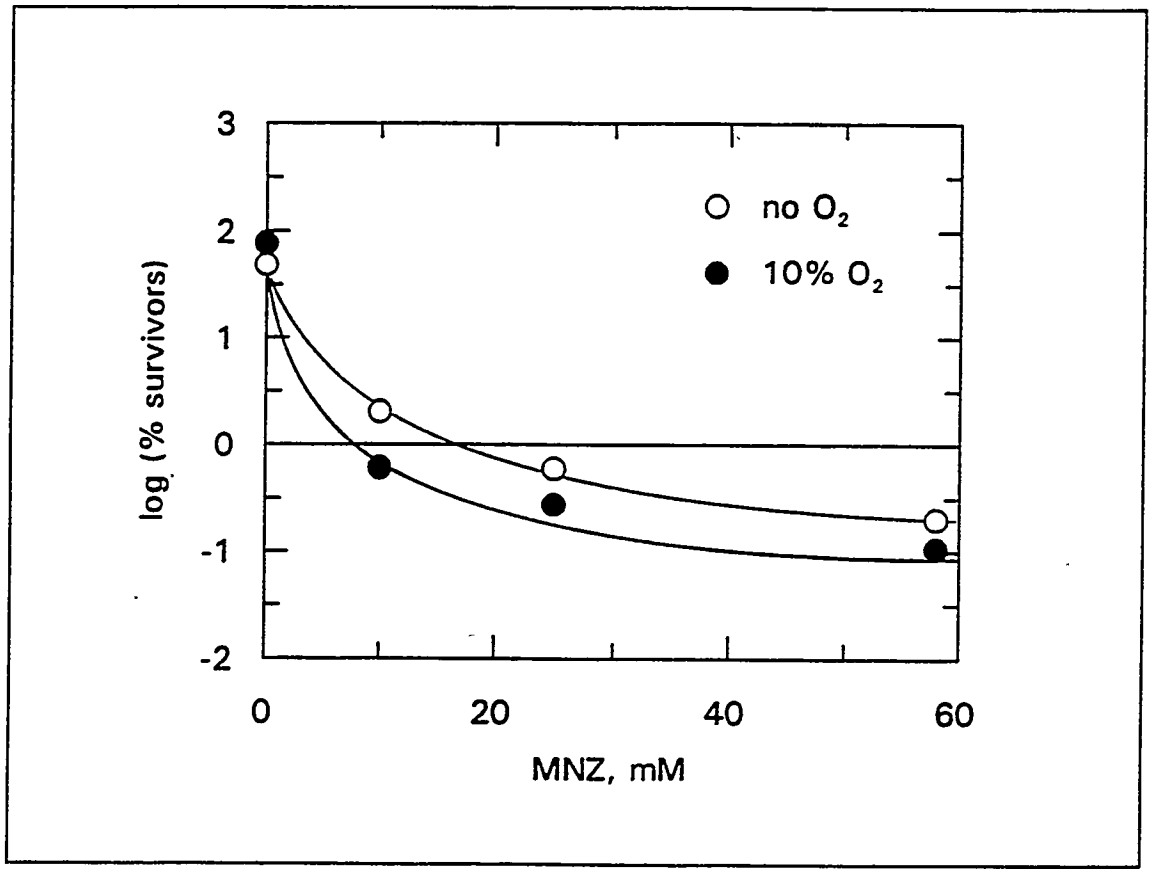


FIGURE 4

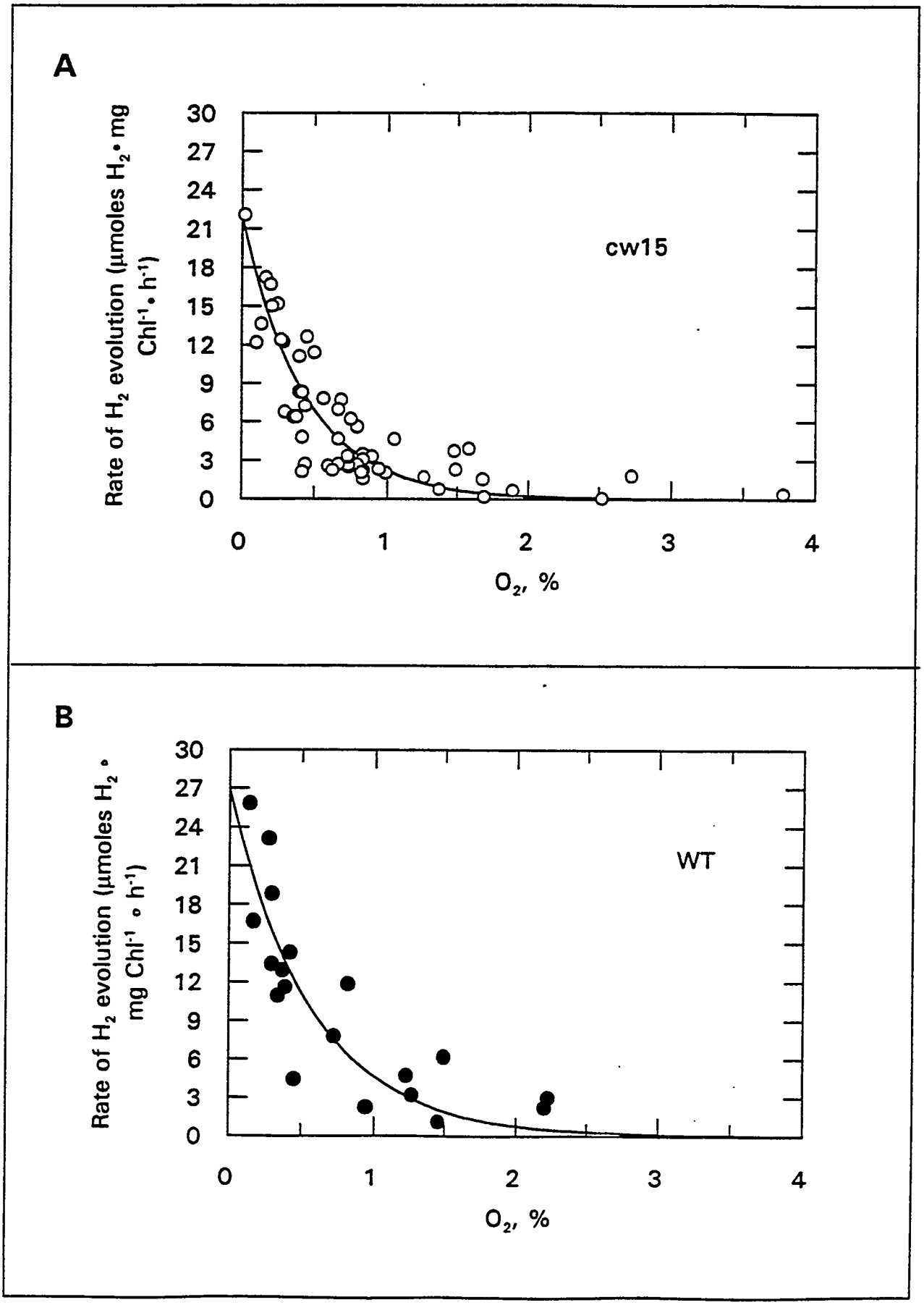

A
Rate of H_2 evolution (µmoles H_2 • mg Chl^{-1} • h^{-1})
30
27
24
21
18
15
12
9
6
3
0
cw15
0
1
2
3
4
O_2, %
B
Rate of H_2 evolution (µmoles H_2 • mg Chl^{-1} • h^{-1})
30
27
24
21
18
15
12
9
6
3
0
WT
0
1
2
3
4
O_2, %

FIGURE 5

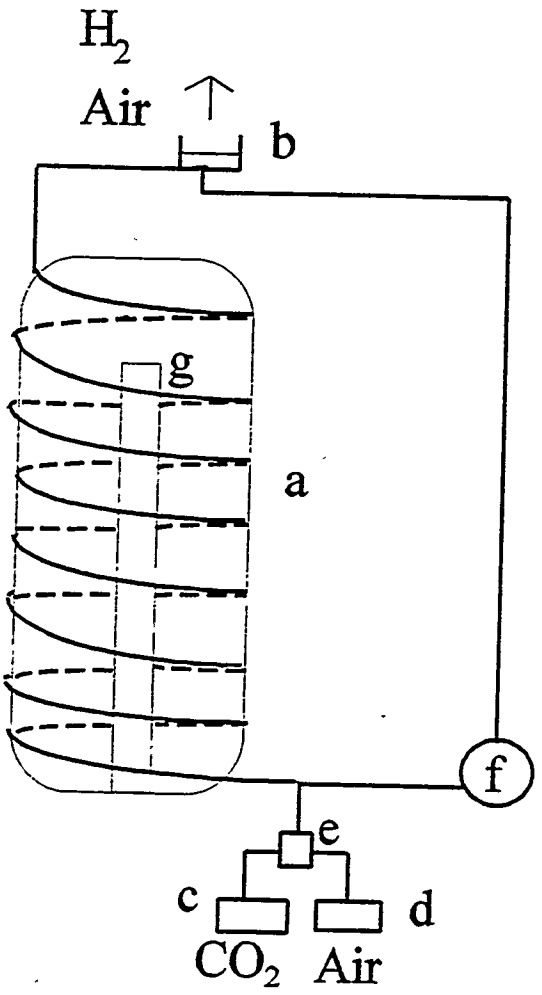
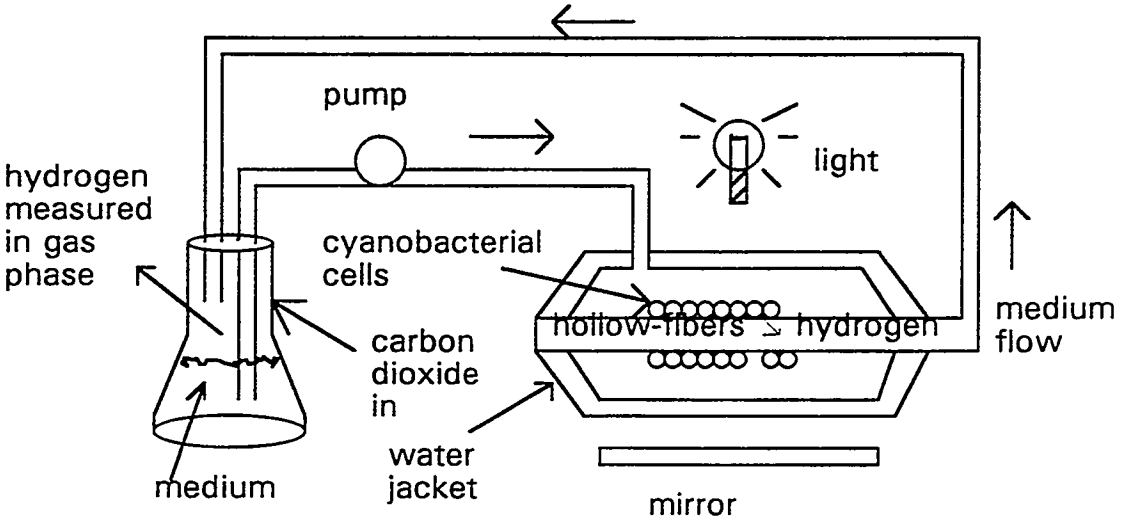


FIGURE 6


pump
light
hydrogen measured in gas phase
cyanobacterial cells
medium flow
hollow-fibers
hydrogen
carbon dioxide in
water jacket
medium
mirror

HYDROGEN PRODUCTION BY PHOTOSYNTHETIC WATER SPLITTING

E. Greenbaum, J. W. Lee, and C. V. Tevault
Chemical Technology Division
Oak Ridge National Laboratory[1]
P.O. Box 2008
Oak Ridge, TN 37831-6194

ABSTRACT

Contrary to the prediction of the "Z-scheme" model of photosynthesis, experiments demonstrated that mutants of *Chlamydomonas* containing Photosystem II (PSII) but lacking Photosystem I (PSI), can grow photoautotrophically with O_2 evolution and using atmospheric CO_2 as the sole carbon source. Autotrophic photosynthesis by PSI-deficient mutants was stable both under anaerobic conditions and in air (21% O_2) at an actinic intensity of 200 $\mu E \cdot m^{-2} \cdot s^{-1}$. This "PSII photosynthesis," sufficient to support cell development and mobility, may also occur in wild-type green algae and higher plants. The mutants can survive under 2000 $\mu E \cdot m^{-2} \cdot s^{-1}$ with air, although they have less resistance to photoinhibition.

INTRODUCTION

In the current and prevailing concept of photosynthesis, the Z-scheme, first proposed by Hill and Bendall (Hill and Bendall, 1960) PSII can split water, but is not thought to be able to perform one of PSI's assigned functions—the reduction of ferredoxin/$NADP^+$ essential for CO_2 assimilation. The Z-scheme therefore requires both PSII and PSI working in sequence for complete photosynthesis using water as the source of electrons and CO_2 as the terminal electron acceptor. Despite

[1]Managed by Lockheed Martin Energy Research Corporation for the U.S. Department Energy under contract DE-AC05-84OR21400.

disagreement from several investigators (Arnon et al., 1965; Pirt et al., 1980; Osborne and Geider, 1987; Arnon and Barber, 1990), the Z-scheme has become the textbook model of photosynthesis (Stryer, 1995; Salisbury and Ross, 1985). Recently, we have demonstrated that sustained photoassimilation of CO_2 and evolution of H_2 and O_2 in minimal medium can be achieved by the PSII light reaction without involvement of PSI in a PSI-deficient mutant of *Chlamydomonas* grown photoheterotrophically using an organic nutrient (acetate) (Greenbaum et al., 1995). In this paper, we report a more exciting discovery that PSI-deficient mutants of *Chlamydomonas* were capable of growing photoautotrophically. Since the Z-scheme requires both PSI and PSII working together in series for complete photosynthesis, it predicts that PSI-deficient mutants of green algae will not grow photoautotrophically. The discovery of photoautotrophic growth of PSI-deficient green algae without any organic nutrients, therefore, provides clear and solid evidence for the existence of a new type of photosynthesis—"PSII photosynthesis" that is an alternative to the Z-scheme. Our discovery may also provide an explanation for many "anomalous" quantum requirements that have been reported over the last 50 years, but failed to be explained by the Z-scheme.

RESULTS

Photoautotrophic growth of several PSI-deficient mutants of *Chlamydomonas* such as F8 and B4 was first observed when photoheterotrophically-grown aliquots were inoculated into 75 ml of minimal medium (Sueoka, 1960) in sterilized Erlenmeyer flasks and incubated under continuous actinic illumination [photosynthetically active radiation (PAR), 20 $\mu E \cdot m^{-2} \cdot s^{-1}$] provided by daylight fluorescent lamps. The minimal medium contained only water and mineral elements. The flasks that contained the liquid culture were capped with phenolic screw caps that allowed air (CO_2) exchange. Constant shaking of the culture flasks with a gyratory shaker at a speed of 140 rpm facilitated air exchange for CO_2 supply. Under these conditions, the algal cultures grew for months. The initial population immediately after inoculation was about 5.0×10^4 cells/ml for all cultures. Based on population growth monitored by counting algal cell density in the media using a microscopic hemacytometer, the algal cell doubling time at their logarithmic growth phase was 10, 10, and 6.7 days for F8, B4, and wild-type 137c, respectively, at the relatively low light intensity of 20 $\mu E \cdot m^{-2} \cdot s^{-1}$. The logarithmic phase lasted about 40–60 days, followed by a nearly linear growth phase. After about 100 days of incubation, the cell populations rose to more than 50 times the initial population.

Using the above photoautotrophically grown cultures as inocula, photoautotrophic growth was further demonstrated at moderate actinic intensity (PAR, 200 $\mu E \cdot m^{-2} \cdot s^{-1}$), where the growth was much faster. In these further experiments, photoautotrophic growth was studied using vertical glass growth tubes that were specially designed for algal growth and simultaneous measurement of CO_2 photoassimilation and O_2 and H_2 evolution, using an in-line CO_2 analyzer (LI-6252, Li-Cor Instruments, Inc.) with a flow-detection system described previously (Lee et al., 1995). Day and night cycles were mimicked by 12 hr of darkness and 12 hr of illumination (200 $\mu E \cdot m^{-2} \cdot s^{-1}$) provided by daylight fluorescent lamps that were controlled by an electronic timer. The liquid culture in each tube (38 cm long and 3 cm in diameter) was continuously bubbled with 700 ppm CO_2 in helium or air at a rate of 50 ml/min to supply CO_2 and to agitate the algal suspension. Algal growth was measured by cell population and chlorophyll (chl) content. As illustrated in Fig. 1, both the chl content and cell population rose quickly with time. With the supply of 700 ppm CO_2 in air and

200 $\mu E \cdot m^{-2} \cdot s^{-1}$ illumination, the chlorophyll doubling time was 1.0, 1.1, and 0.60 days for F8, B4, and 137c, respectively, which lasted for 2-3 days. Initial exponential growth followed by linear growth as self-shading and nutrient depletion set in is the normal pattern for photoautotrophically grown algae.

The data (Fig. 1) also demonstrated that the mutants were able to grow not only in air but also in anaerobiosis when CO_2 was supplied in a pure helium atmosphere. The pattern of photoautotrophic growth for CO_2 in helium was similar to that for CO_2 in air. This is important since it indicated that neither aerobic processes such as mitochondrial respiration or chlororespiration (Kow et al., 1982; Bennoun, 1994) nor anaerobic hydrogenase activity (Bemberger et al., 1982) is a requirement for cell growth. Although the absence of atmospheric O_2 slowed the growth of the wild type by about 7%, it did not significantly affect the growth rate for F8 and B4, which was supported solely by PSII photosynthesis.

The evidence that the carbon and electrons for cell growth are acquired from CO_2 fixation and water splitting was obtained by simultaneously measuring CO_2, O_2, and H_2 in the carrier gas effluent after bubbling through the growth tubes described above. The data clearly demonstrated that both CO_2 uptake and O_2 evolution were light dependent (Fig. 2). Photoassimilation of CO_2 by the PSI-deficient mutants was stable in both aerobic (Fig. 2A) and anaerobic conditions (Fig. 2B). At steady-state photosynthesis, about 40% of the CO_2 supplied by the carrier gas was taken up by the algae, corresponding to a maximal photosynthesis rate of about 100 $\mu mol\ CO_2 \cdot hr^{-1} \cdot mg\ chl^{-1}$. Under aerobic conditions, as expected, hydrogenase activity (H_2 production) was completely inactivated (Fig. 2A). However, the pattern and rates of CO_2 photoassimilation under aerobic conditions were rather similar to those under anaerobic conditions (Fig. 2B). These results indicated that neither hydrogenase activity nor any respiratory process (such as mitochondrial respiration or chlororespiration) is required by PSII photosynthesis. Even under anaerobic conditions where hydrogenase is activated, photoevolution of H_2 occurred only upon the initial onset of actinic illumination when the Calvin cycle for CO_2 reduction had not been fully activated. At steady state, H_2 evolution approached zero and reduction of CO_2 by the Calvin cycle became the exclusive sink for reductant generated by photosynthetic water splitting.

The simultaneous measurements of CO_2 uptake and O_2 evolution (Fig. 2B) also revealed that the photosynthetic quotient (CO_2 uptake/O_2 evolved) can be less than unity. After the first light cycle, the quotient (CO_2/O_2) during steady-state photosynthesis was as low as 0.90 in both the PSI-deficient algae and the wild type. The observed photosynthetic quotient is expected if CO_2 is reduced not only to the level of sugars, which would correspond to a quotient of unity, but also to the level of lipids and proteins, both of which are necessary for cell growth and correspond to photosynthetic quotients of <1 (Bell, 1985). The measured photosynthesis therefore is consistent with the observed cell growth.

Mutant F8 was obtained from mutagenesis by UV treatment and characterized as a stringent mutant that completely lacks CPI (the core of PSI) and two low-molecular-weight (20- and 21-kilodalton) polypeptides (Girard et al., 1980). Mutant B4 was obtained following metronidazole enrichment (Roitgrund and Mets, 1990). Before and after our growth experiments, PSI content of these mutant algae was examined and complete absence of PSI was confirmed. Figure 3 presents a typical set of

measurements for PSI reaction center (P700) photochemical activity by absorbance spectroscopy in thylakoid membranes that were isolated from these photoautotrophically grown algal cells. No P700 activity was detected in either F8 or B4, while the P700 signal was easily seen in the wild type. Based on signal-to-noise ratio, the chl:P700 ratio was larger than 30,000:1 in F8 and B4, whereas it was 943 (± 40):1 in 137c. Clearly, these PSI-deficient mutants grow photoautotrophically without PSI. PSII alone is sufficient to drive photosynthetic electron transport from water to the terminal acceptor CO_2 in living cells. As previously discussed (Greenbaum et al., 1995), per-photon energy captured by PSII photochemistry at 680 nm (1.8 eV) is energetically sufficient to drive water splitting and the reduction of CO_2, with a maximum energy efficiency of about 68%. Therefore, although our findings are surprising because they contradict the long-held belief that PSI is essential for oxygenic photosynthesis and for photoautotrophic growth with water as electron donor, they still obey the laws of thermodynamics.

The role of PSI in photosynthesis could therefore be rather accessory, but apparently beneficial for natural survival. As shown in Fig. 1, the presence of PSI enhanced the rate of photoautotrophic growth by about 30–40% in 137c, compared with the PSI-deficient mutants (F8 and B4). Furthermore, the presence of PSI also confers resistance to photoinhibition. As demonstrated by a photoautotrophic growth experiment under high light intensity (PAR, 2000 $\mu E \cdot m^{-2} \cdot s^{-1}$, equivalent to full sunlight intensity in summer) with air, the mutants grew from an initial population of 6.5×10^4 cells/ml to a final culture density about 8.5×10^5 cells/ml in 12 day-and-night cycles and 46.6% of the cells became colorless (photobleached), while the wild type reached a culture density of 1.72×10^6 cells/ml with only 7.8% of the cells photodamaged. These results indicate that PSI-deficient mutants can grow photoautotrophically even under high light intensity with air, although they have less resistance to photoinhibition than the wild-type.

In addition to F8 and B4, similar photoautotrophic growth was observed in initial experiments using several other nuclear PSI-deficient mutants such as ac9 (CC-521), ac80 (CC-544), and F23 (CC-1062) and a chloroplast PSI-deficient mutant, 10-3C (CC-2046), that were provided by the Duke University *Chlamydomonas* Genetic Center. Therefore, this common growth ability suggests that the observed PSII photosynthesis is likely quite prevalent, rather than a chance observation unique to a particular mutant.

DISCUSSION

Over the last 50 years, there has been a heated debate over whether the quantum requirement for photosynthesis is less than or greater than 8 photons (hν) per molecule of O_2 evolved. By analyzing measurements that have been made since 1950, Pirt (1986) and Osborne and Geider (1987) have concluded that the minimal quantum requirement is 5 to 6 $h\nu/O_2$ in wild-type green algae (Pirt, 1986; Osborne and Geider, 1987). Such values, if correct, cannot be explained by the Z-scheme since it predicts a quantum requirement of at least 8 $h\nu/O_2$. These previously reported quantum requirements may, however, be consistent with the PSII photosynthesis we demonstrated in many PSI-deficient mutants of green algae such as F8, B4, ac9, and 10-3C. The minimal quantum requirement for PSII photosynthesis should be 4 $h\nu/O_2$, since PSII photosynthesis uses a single light reaction (PSII) instead of two (PSI and PSII). Pathway studies with the chemical inhibitors, DCMU, DBMIB, NQNO, and FCCP indicated that in PSII photosynthesis, electron flow from PSII to ferredoxin/$NADP^+$ reduction

is through the plastoquinone pool and cytochrome b/f complex (Lee and Greenbaum, 1996). With consideration of both practical energy loss such as a loss of about 15% excitations in PSII antenna and involvement of PSI activity such as PSI cyclic photophosphorylation, a quantum requirement (4 $h\nu/O_2$) for PSII photosynthesis can explain the reported values of 5 to 6 $h\nu/O_2$ in wild-type green algae (Pirt, 1986; Osborne and Geider, 1987). The previously reported quantum requirement (5 to 6 $h\nu/O_2$) therefore indicates that the PSII photosynthesis that we demonstrated in mutant algae may occur even in wild-type algae under the right conditions.

Finally, the latest measurements for many C_3 higher plants by Osborne (1994) also showed a quantum requirement of < 8 $h\nu/O_2$, such as 7.67 ± 0.10 $h\nu/O_2$ for *Atriplex littoralis* and 7.69 ± 0.16 $h\nu/O_2$ for *Vicia faba* (Osborne, 1994). This finding, again, cannot be explained by the Z-scheme. Based on high energy consumption in the multiple-cell tissue, Myers (1980) and Bell (1985) have estimated that the minimal quantum requirement for Z-scheme photosynthesis would be at least about 10 $h\nu/O_2$ in C_3 higher plants (Bell, 1985; Myers, 1980). Since PSII photosynthesis can have twice the energy efficiency of the Z-scheme, the observed quantum requirement in these higher plants can, in principle, be explained by the occurrence of PSII photosynthesis. Therefore, PSII photosynthesis may occur not only in green algae but also in higher plants, and the Z-scheme may not be the only mode of oxygenic photosynthesis. The obligatory series concept embedded in the Z-scheme of photosynthetic electron transport must now be reevaluated. We can now also conceive of significantly higher photosynthetic productivity for food, biomass, and H_2 production by application of the discovery.

Acknowledgments

The authors thank T. G. Owens for contributing the data of Fig. 3. We also thank E. Harris of the Duke University *Chlamydomonas* Genetic Center for providing many PSI-deficient mutants used in this research; L. Mets of the University of Chicago for his helpful discussion and mutant B4; C. S. MacDougall, S. M. Hayes, and S. J. Bobrowski for scanning electron microscope imaging of the algal cells.

References

Arnon, D. I., and J. Barber, *Proc. Natl. Acad. Sci. USA* **87**, 5930 (1990).

Arnon, D. I., H. Y. Tsujimoto, B. D. McSwain, *Nature* **207**, 1367 (1965).

Bamberger E. S., D. King, D. L. Erbes, M. Gibbs, *Plant Physiol.* **69**, 1268 (1982).

Bell, L. N., *Energetics of the Photosynthesizing Plant Cell* (Harwood Academic Publishers, London, 1985), chaps. 6, 7, and 9.

Bennoun, P., *Biochim. Biophys. Acta* **1186**, 59 (1994).

Greenbaum, E., J. W. Lee, C. V. Tevault, S. L. Blankinship, L. J. Mets, *Nature*, **376**, 438 (1995).

Girard J., N. H. Chua, P. Bennoun, G. Schmidt, M. Delosme, *Curr. Genet.* **2**, 215 (1980).

Hill, R., and F. Bendall, *Nature* **186**, 136 (1960).

Kow, Y. W., D. L. Erbes, M. Gibbs, *Plant Physiol.* **69**, 442 (1982).

Lee, J. W., S. L. Blankinship, E. Greenbaum, *Appl. Biochem. Biotechnol.* **51/52**, 379 (1995).

Lee, J. W., and E. Greenbaum, in preparation (1996).

Myers, J., *Primary Productivity in the Sea*, W. Ruhland, Ed. (Springer-Verlag, Berlin, 1980), pp. 1-16.

Osborne, B. A., *Plant Cell Environ.* **17**, 143 (1994)

Osborne, B. A., and R. J. Geider, *New Phytol.* **106**, 631 (1987).

Osborne, B. A., and R. J. Geider, *Plant Cell Environ.* **10**, 141 (1987).

Pirt, S. J., *New Phytol.* **102**, 3 (1986).

Pirt, S. J., Y. K. Lee, A. Richmond, M. W. Pirt, *J. Chem. Tech. Biotechnol.* **30**, 25 (1980).

Roitgrund, C., and L. J. Mets, *Curr. Genet.* **17**, 147 (1990).

Salisbury, F. B., and C. W. Ross, *Plant Physiology* (Wadsworth Publishing Company, Belmont, CA, ed. 3, 1985), pp. 191–194.

Stryer, L., *Biochemistry* (W. H. Freeman and Company, New York, ed. 4, 1995), pp. 658–664.

The composition of the minimal medium was essentially the same as that of N. Sueoka, *Proc. Natl. Acad. Sci. USA*, **46**, 83 (1960), except that the concentration of NH_4Cl, $CaCl_2$, and $MgSO_4$ in our minimal medium was 7.5, 0.35, and 0.41 mM, respectively.

Figures

Fig. 1 Photoautotrophic growth curves of PSI-deficient mutants F8 (diamonds), B4 (squares), and wild-type 137c (circles) using 700 ppm CO_2 in either air (open symbols) or helium (filled symbols) with cycles of 12 hr of darkness and 12 hr of light (PAR, 200 $\mu E \cdot m^{-2} \cdot s^{-1}$). The population growth was measured by both chl content (**A**) and cell density (**B**) of the cultures in the minimal medium. The preculture was prepared on a rotary shaker using overhead room lights and atmospheric CO_2 as the sole carbon source. The growth experiment utilized a specially designed flow system with CO_2 in the carrier gas and bank of fluorescence lamps for illumination.

Fig. 2 Photoassimilation of CO_2 and zero-rate production of H_2 by F8 and 137c with 700 ppm CO_2 in air (**A**); photoassimilation of CO_2 and evolution of O_2 and H_2 by F8 with 700 ppm CO_2 in helium (**B**). In each case, the initial algal population in the minimal medium (140 ml) was such that the chl concentration was about 0.4 µg/ml. The actinic illumination (PAR, 200 $\mu E \cdot m^{-2} \cdot s^{-1}$) was provided by daylight fluorescent lamps. The upward and downward arrows mark the on- and off-phases, respectively, of the actinic illumination.

Fig. 3 A typical set of reversible P700 photooxidation data obtained from thylakoids that were isolated from photoautotrophically grown cells of F8 (dots), B4 (circles), and 137c (line). The thylakoids were treated with cyanide (CN^-) to inhibit plastocyanin, which otherwise may interfere with P700 measurement by donating its electrons to the PSI reaction centers. The chl concentration was 47 µM for all samples (thylakoids). Before the measurements, the samples were dark adapted in the presence of ascorbate so that the PSI reaction centers were all kept in their reduced state (P700). The photoconversion of P700 to $P700^+$ was measured as the absorbance change at 697 nm. The downward arrow marks the onset of actinic illumination.

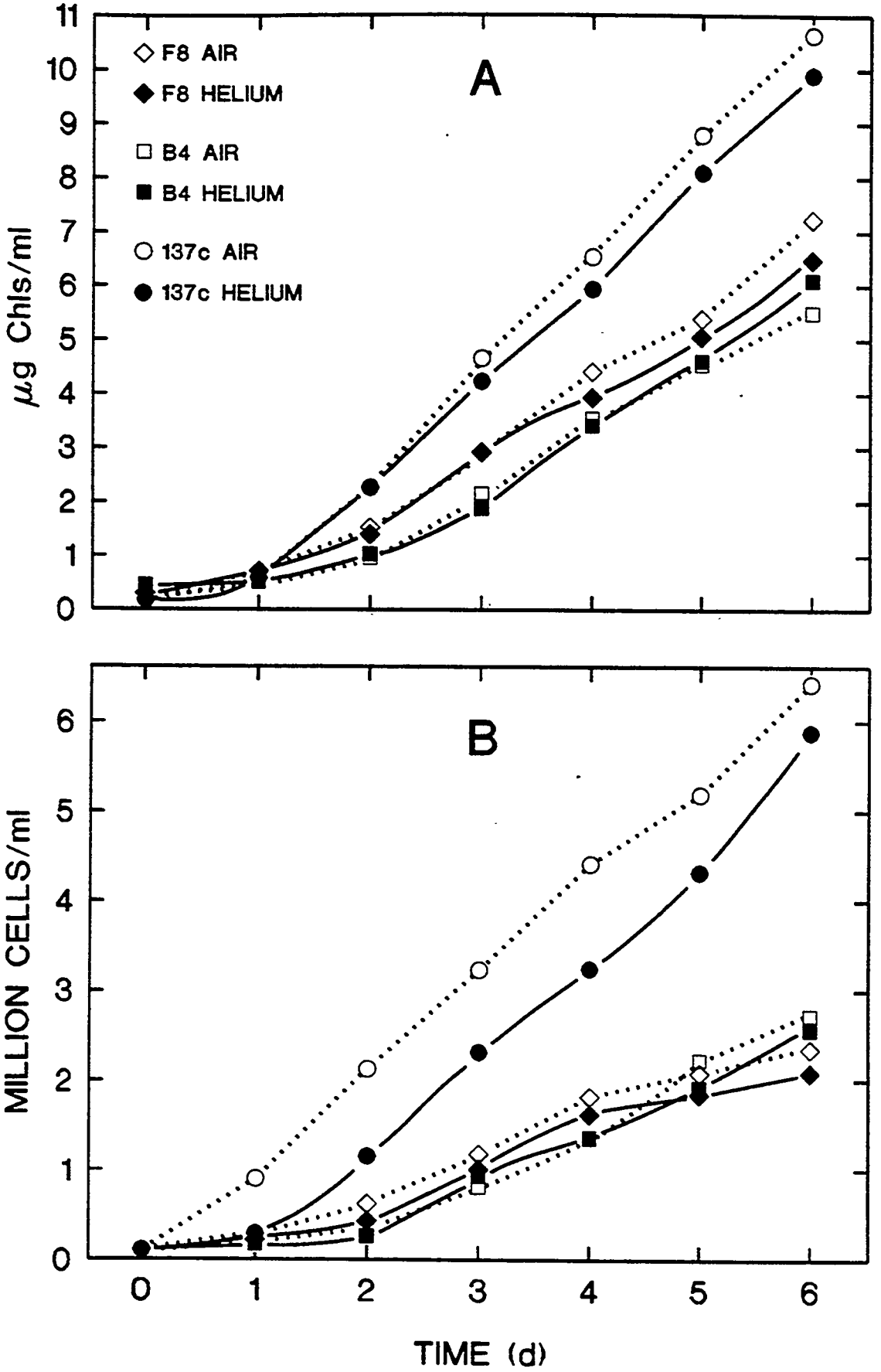


Fig. 2
J. Lee et al.

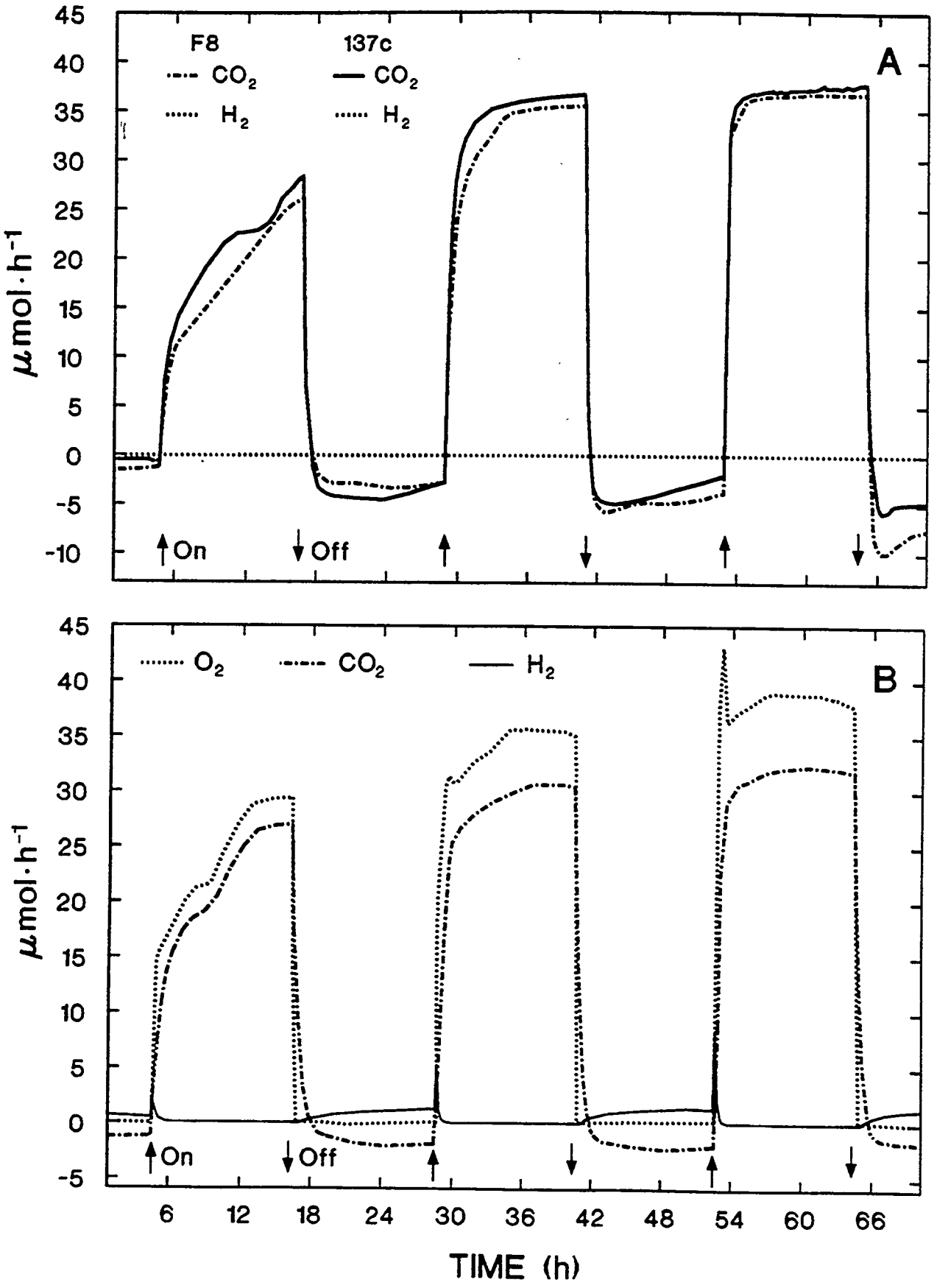


Fig. 3
J. Lee et al.

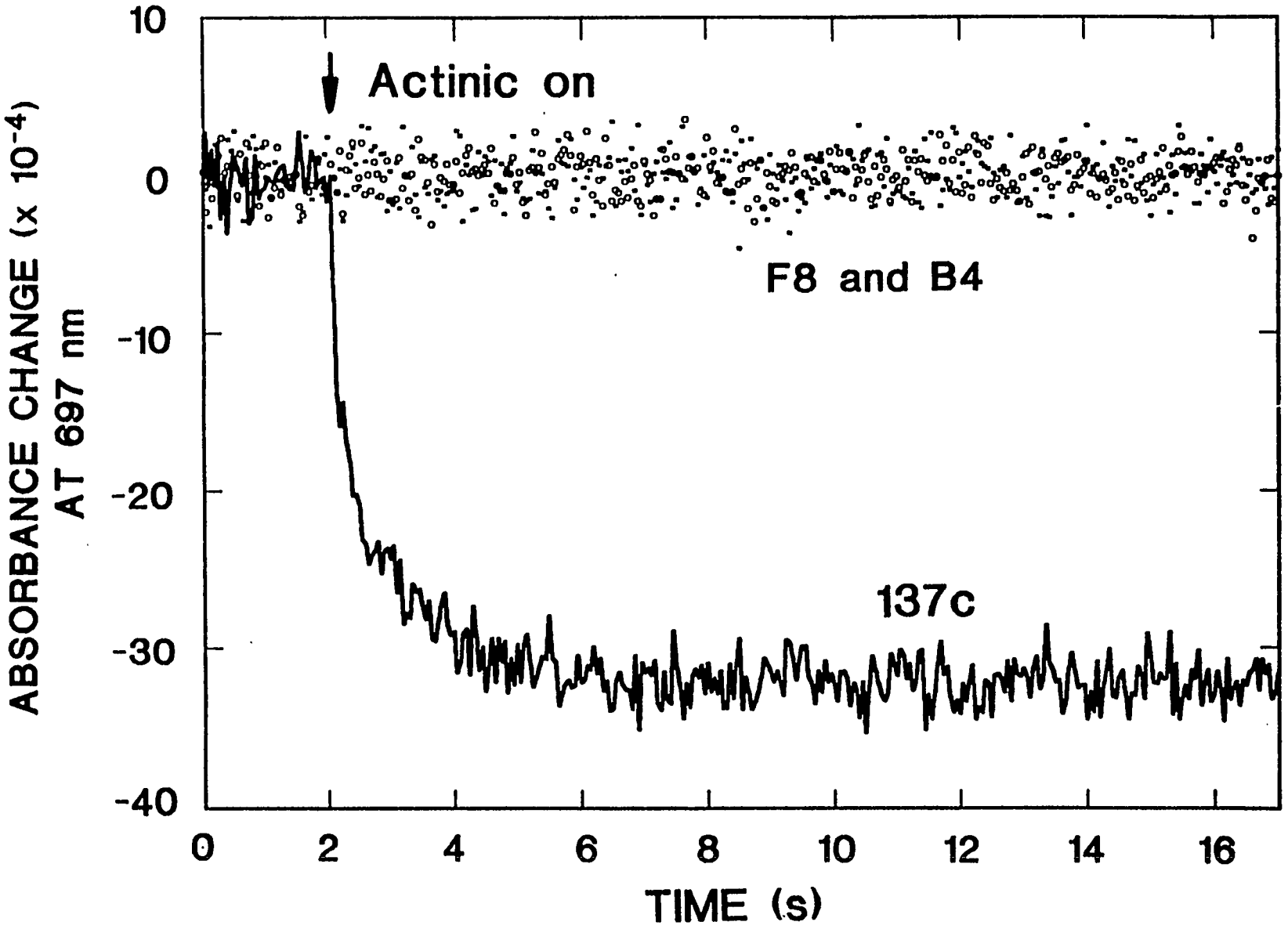


Fig. 5
J. Lee et al.

In Vitro Hydrogen Production by Glucose Dehydrogenase and Hydrogenase

Jonathan Woodward
Chemical Technology Division
Oak Ridge National Laboratory[2]
Oak Ridge, Tennessee 37831-6194

Abstract

A new *in vitro* enzymatic pathway for the generation of molecular hydrogen from glucose has been demonstrated. The reaction is based upon the oxidation of glucose by *Thermoplasma acidophilum* glucose dehydrogenase with the concomitant oxidation of NADPH by *Pyrococcus furiosus* hydrogenase. Stoichiometric yields of hydrogen were produced from glucose with continuous cofactor recycle. This simple system may provide a method for the biological production of hydrogen from renewable sources. In addition, the other product of this reaction, gluconic acid, is a high-value commodity chemical.

The future use of hydrogen as a renewable fuel is receiving wide attention in both political and technical circles (Lepkowski, 1995; Lawler, 1995; Lee and Greenbaum, 1995). Gasification, pyrolysis and fermentation of biomass have been and are being considered as potential routes to hydrogen production (Kitani and Hall, 1989), but little consideration has been given to an *in vitro* enzymatic method for the conversion of biomass-derived glucose to hydrogen that would require relatively mild conditions and generate hydrogen without the immediate formation of waste gases such as CO_2 and CO.

Glucose dehydrogenase (GDH) obtained from animal and bacterial sources catalyzes the oxidation of glucose to glucono-δ-lactone, which hydrolyzes to gluconic acid (Harrison, 1931). The cofactor is either NAD^+ or

---

[1]To whom correspondence should be addressed

[2] Managed by Lockheed Martin Energy Research Corporation for the U.S. Department of Energy under contract DE-AC05-96-OR22464

$NADP^+$, is reduced. Although most hydrogenases from microbial sources do not interact with physiological electron carriers such as NADPH because of its insufficient low-potential (Greenbaum, 1980), two hydrogenases-one from the aerobic bacterium *Alcaligenes eutrophus* and the other from the anaerobic archaeon *Pyrococcus furiosus*-have been shown to use NADPH as an electron donor (Egerer et al., 1982). The possibility existed, therefore, that a combination of GDH and hydrogenase could be used to generate molecular hydrogen from glucose which in turn could be derived from sources such as cellulose, starch and lactose, all of which are abundant and renewable (Fig. 1). Continuous regeneration and recycle of $NADP^+$, as well as enzyme stability, would be essential for prolonged hydrogen generation.

GDH and hydrogenase have been purified from *T. acidophilum and P. furiosus,* which are thermophilic Archaea (formerly Archaebacteria) that grow optimally at 59°C and 100°C respectively (Bright et al., 1993). In the study reported here, the combination of *T. acidophilum* GDH and *P. furiosus* hydrogenase was, as shown in Fig. 2, capable of hydrogen production from glucose. The data are significant in that, 1) electron flow occurred from GDH to hydrogenase via $NADP^+$ with the concomitant evolution of molecular hydrogen, 2) maximum stoichiometric yields of hydrogen were obtained, 3) the cofactor $NADP^+$ was recycled at least 20 times and 4) a new pathway has been found for obtaining hydrogen from renewable sources of glucose without the formation of waste gases.

Experimental Protocol
Materials, Enzymes, Preparation and Assay

The gene for *T. acidophilum* glucose dehydrogenase was cloned , sequenced and expressed in *Escherichia coli* from which the enzyme was purified and assayed as described previously (Smith et al., 1989; Bright et al., 1993). The enzyme possessed a specific activity of 420 units/mg protein where 1 unit is defined as the amount of enzyme required to produce 1 µmol NADPH/min at 55°C and pH 7.0. Hydrogenase from *P. furiosus* was purified as described previously and assayed by measuring hydrogen evolution from reduced methyl viologen in 50 mM Tris, pH 8.0 containing 1 mM sodium dithionite at 80°C (Bryant and Adams, 1989). It possessed an activity of 1,005 units/ml. β-$NADP^+$ was purchased from Sigma Chemical Company, St. Louis, MO. β-D-Glucose was purchased from Calbiochem, San Diego, CA. Cellulase (Novozyme 342-an alkaline cellulase produced by *Humicola insolens*) was obtained from Novo Nordisk, Franklinton, NC. Prior to its use it was subjected to gel filtration and the filtered enzyme was determined to have a protein concentration of 20 mg/ml.

Experimental Apparatus for the Measurement of Hydrogen

A continuous flow system was constructed to measure the production of hydrogen as shown in Fig. 2. This system, described in detail by Greenbaum (Greenbaum, 1984), was continuously purged with helium and calibrated with an inline electrolysis cell and Faraday's law of electrochemical equivalence connected in tandem with the hydrogen detection system. The latter consisted of a combustible gas analyzer (Bio-Gas Detector Corporation, Okemos, MI) consisting of a Figaro semiconductor tin oxide gas sensor. A voltage increase occurs across the sensor when a combustible gas comes into contact with the sensor surface due to a decrease in the sensor resistance and this was measured by a Keithley Model 2000 multimeter. Current was measured with a Keithley Model 485 picoammeter. Data was analyzed using ASYST™ Technologies, Inc., 4.0 Analysis Software.

Results and Discussion

The data in Fig. 3 indicate that the integrated yield of hydrogen (10 µmol) generated from glucose represented the maximum stoichiometric yield possible and that the rate of hydrogen production reached a maximum (7.5 µmol/h) within minutes following initiation of the experiment by the addition of $NADP^+$. Hydrogen evolution reached zero after 3 h; however, when another 10 µmol of glucose was added to the reaction mixture several

hours later, immediate evolution of hydrogen occurred and maximum yield of hydrogen was obtained again. The rate limiting step in this pathway was the glucose concentration since the concentration of $NADP^+$ used in this experiment was 0.5 mM, about 5 times the reported K_m value for this GDH (Smith et al., 1989). Results also showed that the presence of 10 mM gluconic acid in the reaction mixture did not affect the rate or yield of hydrogen production; therefore, gluconic acid does not appear to be an inhibitor of this enzyme-coupled process under these experimental conditions. Also noteworthy, was the stability of $NADP^+$ at 50°C for at least 20 h. In the second experiment, 100 µmol of glucose (50 mM) was used to determine whether sustained evolution of molecular hydrogen could be achieved. The data shown in Fig. 4 indicate that this was indeed the case; at the cessation of the experiment approximately 64 µmol of hydrogen had been generated, although it was clear that the maximum yield of hydrogen had not been reached. At this concentration of glucose there was an initial burst of hydrogen evolution during the first few minutes of the reaction followed by a gradual rise to a maximum rate of 6.5 µmol/h at 6 h. After this time the rate started to decline due, presumably, to the reduction in glucose concentration since in another experiment conducted with an initial 10 µmol of glucose, the maximum rate of hydrogen evolution was approximately 1.7 µmol/h. The lower maximum rate of hydrogen evolution as compared with that observed in Fig. 3 was due to the lower reaction temperature (40°C) used. It is also noteworthy that $NADP^+$ could be reduced and re-oxidized at least 64 times without apparent loss in its ability to shuttle electrons from glucose to hydrogenase. Although the pH of the reaction mixture had dropped from pH 7.0 to pH 5.85 after 16 h, both enzymes retained significant activity. At 40°C there is little difference between the activity of hydrogenase at pH 5.5 and pH 7.0 (Adams, unpublished). The optimum temperature for this enzyme has been determined to be 85°C with NADPH as the substrate (Ma et al., 1994). The activity of GDH at pH 6.0 was determined to be about 50% of its optimal activity at pH 7.0. The loss of enzyme stability under these conditions, however, cannot be discounted. GDH and hydrogenase are composed of four identical and four non-identical subunits respectively (Pedroni et al., 1995). In the case of GDH from *T. acidophilum*, the enzyme is stable at room temperature in 50% methanol, acetone or ethanol and in 4M urea for 6 h (Smith et al., 1989). Such stability could suggest that the oligomeric structure would be unlikely to dissociate under the experimental conditions described above, especially since this enzyme naturally functions under extreme environmental conditions (Danson, 1993). This would be in contrast to *Bacillus megatarium* GDH that dissociates below pH 5.0 and above pH 7.0 under mild conditions; however, its oligomeric structure is stabilized by the cofactor NAD^+ (Pauly and Pfleiderer, 1977). Hydrogenase is remarkably stable even at 80°C with a half-life at 100 °C of 2 h *in vitro* (Bryant and Adams, 1989). Although higher reaction temperatures are possible with these enzymes because of their inherent stability, the use of such temperatures in our experimental apparatus resulted in evaporation of the reaction mixture.

The rationale behind these experiments was to determine whether a mild enzymatic procedure for the generation of molecular hydrogen from renewable resources could be developed. Examples of renewable resources include cellulose, starch (corn syrup) and lactose all of which are abundant and readily available. Cellulose is the most abundant source of glucose and can be hydrolyzed to glucose by the action of cellulases (Walker and Wilson, 1991). The data in Fig. 5 show that cellulose was converted to hydrogen when cellulase was present in the reaction mixture. Under the experimental conditions, the maximum rate of hydrogen evolution was approximately 325 nmol/h, and after 22 h the stoichiometric yield of hydrogen was approximately 2.6%. The rate limiting step in this reaction was the rate of glucose formation from cellulose since addition of another 400 µg of cellulase to the reaction mixture caused an immediate increase in the rate of hydrogen evolution (Woodward and Mattingly, unpublished).

The only other product of this reaction is gluconic acid, an important industrial chemical used by major industries for sequestration and chelation (Sodium Gluconate Handbook, 1994). This compound can also be considered to be a valuable commodity, and its current market price of $1.20/lb ($2.65/kg) could have a significant impact on the overall economics on the enzymatic production of hydrogen from renewable resources, especially if the source of glucose was corn syrup (which sells for around 8 cents/lb or 17.6 cents/kg). The cost of producing glucose from cellulose using cellulase is similar to that of corn syrup (7 cents/lb) but this could be reduced to 1.5

cents/lb if cellulase was produced on site rather than purchasing it commercially. Although an economic analysis of this process is beyond the work described here, the higher cost of gluconic acid compared to the substrate used, could contribute to the commercial feasibility of this process. It is clear, however, that the gluconic acid generated by this process could greatly exceed current demand which, undoubtedly, would affect gluconic acid prices. Other sources of hydrogen include starch and lactose, both of which can easily be degraded to their monomeric sugar units by amylase/amyloglucosidase and lactase, respectively. The GDH used in this work has approximately 70% of its maximum activity when acting on galactose (Smith et al., 1989) so, theoretically, 2.0 mol H_2/mol lactose could be obtained since both glucose and galactose could be oxidized simultaneously.

Cellulosic waste represents a vast untapped source of hydrogen. For example, current annually available waste newspaper in the United States comprises 16 billion lbs (7.26 million tons) of cellulose (Woodward et al., 1994) which, theoretically, could yield 37.5 billion standard cu ft (1.06 trillion dm^3) of hydrogen or 12.2 trillion btu (assuming standard gas conditions at 60 °F and 14.696 psi (15.6 °C and 1.033 kg cm^2) where 1 lb-mol or 1 g-mol hydrogen is equivalent to 379.495 cu ft or 23.7 dm^3 respectively). This volume of hydrogen could serve 37 cities whose gas demand is equivalent to that of Oak Ridge, a city of population approximately 27,000, and a natural gas consumption of 1.08 billion cu ft or 30.6 billion dm^3 for the fiscal year ending April 1995 (Data provided by the Oak Ridge Utility District, Oak Ridge, TN).

In conclusion, a new enzymatic pathway for the conversion of glucose to molecular hydrogen has been demonstrated and current studies are aimed at optimizing the reaction with respect to pH, temperature and enzyme ratio. It should be possible to use cellulose, starch or lactose as sources of glucose and to use immobilized forms of GDH and hydrogenase in a bioprocess for continuous and long term hydrogen production. The utilization of enzymes from the Archaea would be advantageous because of their ability to withstand extreme environments such as high temperature. Further studies of this nature would be of interest in the context of hydrogen production from renewable resources.

Acknowledgments

The authors thank M.E. Reeves, J.W. Lee and E. Greenbaum for comments and criticism, S.L. Blankinship for technical assistance and L. Cross for secretarial assistance. This work was supported by the Office of Utility Technologies, Advanced Utility Concepts Division, U.S. Department of Energy under contract DE-AC05-96OR22464 with Lockheed Martin Energy Research Corporation.

References

Bright, J.R., Byrom, D., Danson, M.J., Hough, D.W. and Towner, P. 1993. Cloning, Sequencing and Expression of the Gene Encoding Glucose Dehydrogenase from the Thermophilic Archaeon *Thermoplasma acidophilum.* Eur. J. Biochem. **211:** 549-554.

Bryant F.O. and Adams, M.W.W. 1989. Characterization of Hydrogenase from the Hyperthermophilic Archaebacterium, *Pyrococcus furiosus*. J. Biol. Chem. **264:** 5070-5079.

Danson, M.J. 1993. Central Metabolism of the Archaea, p. 1-24. *In*: The Biochemistry of Archaea (Archaebacteria). Kates, M., Kushner, D.J. Matheson, A.T. Eds. Elsevier, Amsterdam.

Egerer, P., Günther, H. And Simon, H. 1982. On the Hydrogen-Deuterium Exchange Reaction Catalyzed by the Soluble Hydrogenase from *Alcaligenes eutrophus* H16 in the Free and Immobilized State. Biochim. Biophys. Acta **703:** 149-157.

Greenbaum, E. 1980. Simultaneous Photoproduction of Hydrogen and Oxygen by Photosynthesis. Biotechnol. Bioeng. Symp. **10:** 1-14.

Greenbaum, E. 1984. Biophotolysis of Water: The Light Saturation Curves. Photobiochem. Photobiophys. **8:**323-332.

Harrison, D.C. 1931. Glucose Dehydrogenase: A New Oxidizing Enzyme from Animal Tissues. Biochem. J. **26:**1016-1027.

John, J., Crennell, S.J., Hough, D.W., Danson, M.J. and Taylor, G.L. 1994. The Crystal Structure of Glucose Dehydrogenase from *Thermoplasma acidophilum*. Structure **2:** 385393.

Kitani, O. and Hall, C.W. 1989. Biomass Handbook. Gordon and Breach Science Publishers, New York, NY.

Lawler, A. 1995. Walker Bill to Boost Hydrogen sparks Democratic grumbling. Science **267:** 613.

Lee, J.W. and Greenbaum, E. 1995. Bioelectronics and Biometallocatalysis for Production of Fuels and Chemicals by Photosynthetic Water Splitting. Appl. Biochem. Biotechnol. **51/52:** 295-305.

Lepkowski, W. 1995. The Politics of Hydrogen. Chem.& Eng. News **73(20):**26-49.

Ma, K., Zhou, Z.H. and Adams, M.W.W. 1994. Hydrogen Production from Pyruvate by Enzymes purified from the Hyperthermophilic Archaeon, *Pyrococcus furiosus*: A key role for NADPH. FEMS Microbiol. Lett. **122:** 245-250.

Pauly, H.E. and Pfleiderer, G. 1977. Conformational and Functional aspects of the Reversible Dissociation and Denaturation of Glucose Dehydrogenase. Biochemistry. **16:**4599-4604.

Pedroni, P., Volpe, A.D., Galli, G., Mura, G.M., Pratesi, C. And Grandi, G. 1995. Characterization of the Locus Encoding the [Ni-Fe] Sulfhydrogenase from the Archaeon *Pyrococcus furiosus*: Evidence for a relationship to bacterial sulfite reductases. Microbiol. **141:** 449-458.

Sodium Gluconate Handbook. 1994. PMP Fermentation Products, Inc., Chicago, ILL.

Smith, L.D., Budgen, N., Bungard, S.J., Danson, M.J. and Hough, D.W. 1989. Purification and Characterization of Glucose Dehydrogenase from the Thermoacidophilic Archaebacterium *Thermoplasma acidophilum*. Biochem. J. **261:**973-977.

Taguchi, F., Mizukami, N., Yamada, K., Hasegawa, K. and Saito-Taki, T. 1995. Direct Conversion of Cellulosic Materials to Hydrogen by *Clostridium* sp. Strain no. 2. Enzyme Microb. Technol. **17:**147-150.

Tranulis, M.A., Christopherson, B. and Borrebaek, B. 1994. Glucose Dehydrogenase in beef (*Bos taurus*) and Rainbow Trout (*Oncorhynchus mykiss)* liver: a Comparative Study. Comp. Biochem. Physiol. **109B:** 427-435.

Walker L.P. and Wilson, D.B., Eds. 1991. Enzymatic Hydrolysis of Cellulose. Elsevier Applied Science, London and New York.

Woodward, J., Stephan, L.M., Koran, L.J., Jr., Wong. K.K.Y., Saddler, J.N. 1994 Enzymatic Separation of High-Quality Uninked Pulp Fibers from Recycled Newspaper. Bio/Technology **12:**905-908.

Legend to Figures

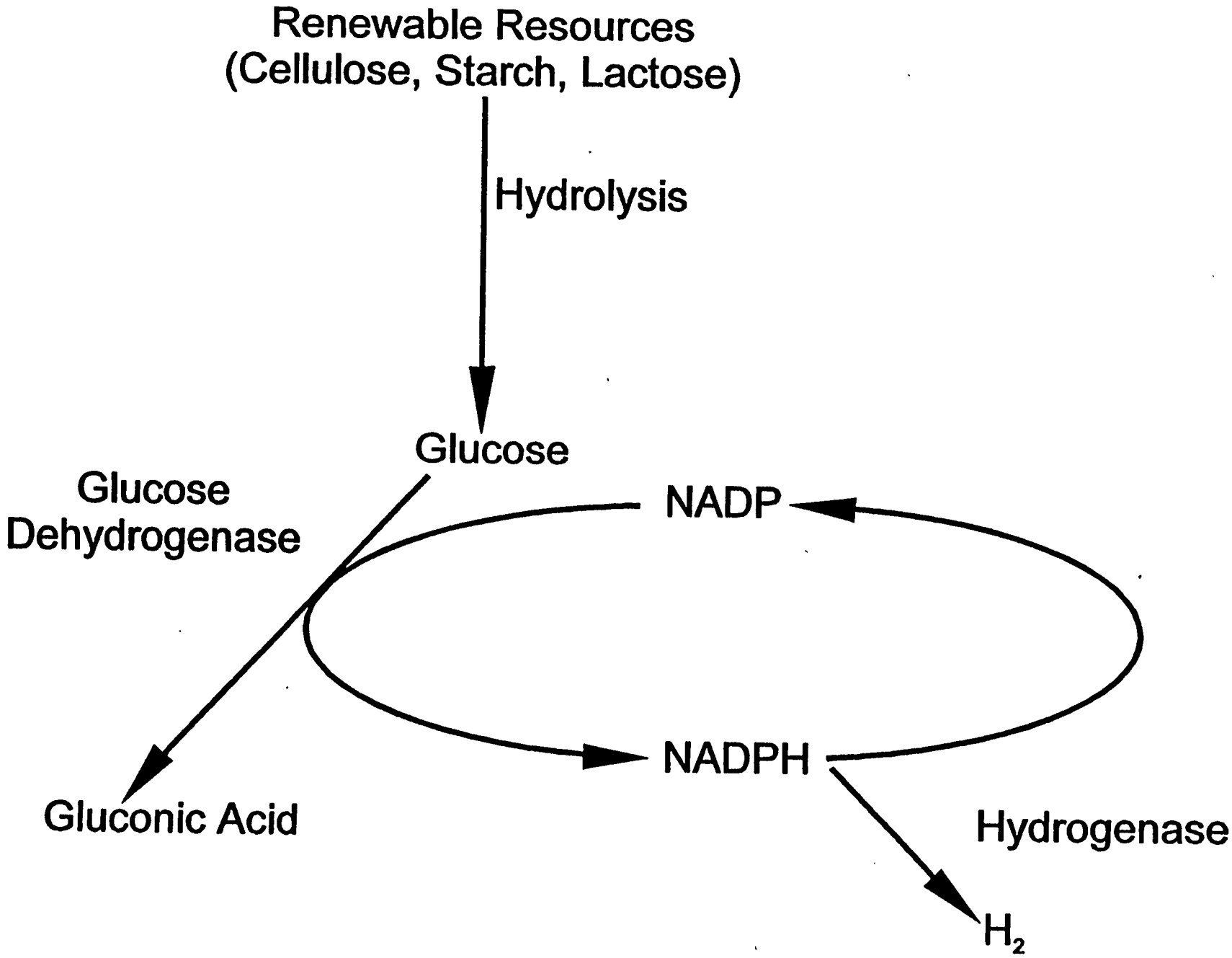
Figure 1. Enzymatic pathway for the conversion of renewable resources to hydrogen.

Figure 2. Schematic illustration of the apparatus used to measure hydrogen production.

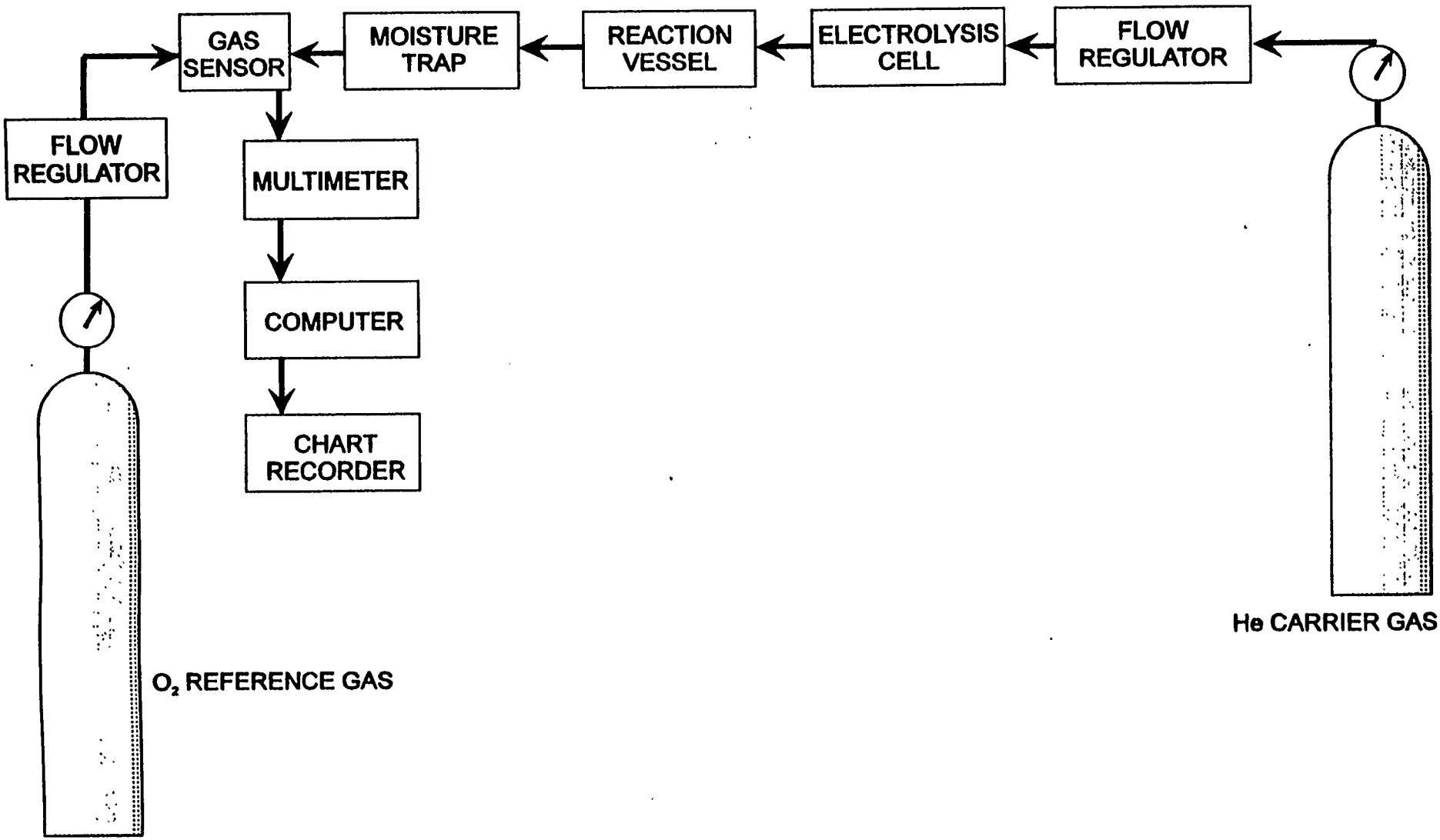
Figure 3. Hydrogen production from glucose using *T. acidophilum* glucose dehydrogenase and *P. furiosus* hydrogenase. The reaction mixture consisted of 2.0 ml 50 mM sodium phosphate buffer, pH 7.0, containing 10 μmol glucose, 26 units of hydrogenase, 12.6 units of GDH and 1 μmol of $NADP^+$ at 50°C. The reaction was started by the addition of $NADP^+$. After 18 h another 10 μmol of glucose was added to the reaction mixture.

Figure 4. Continuous hydrogen production from glucose at 40°C. The reaction mixture was as described in the legend to Fig. 1 except that it contained 100 μmol of glucose and 20.7 units of hydrogenase.

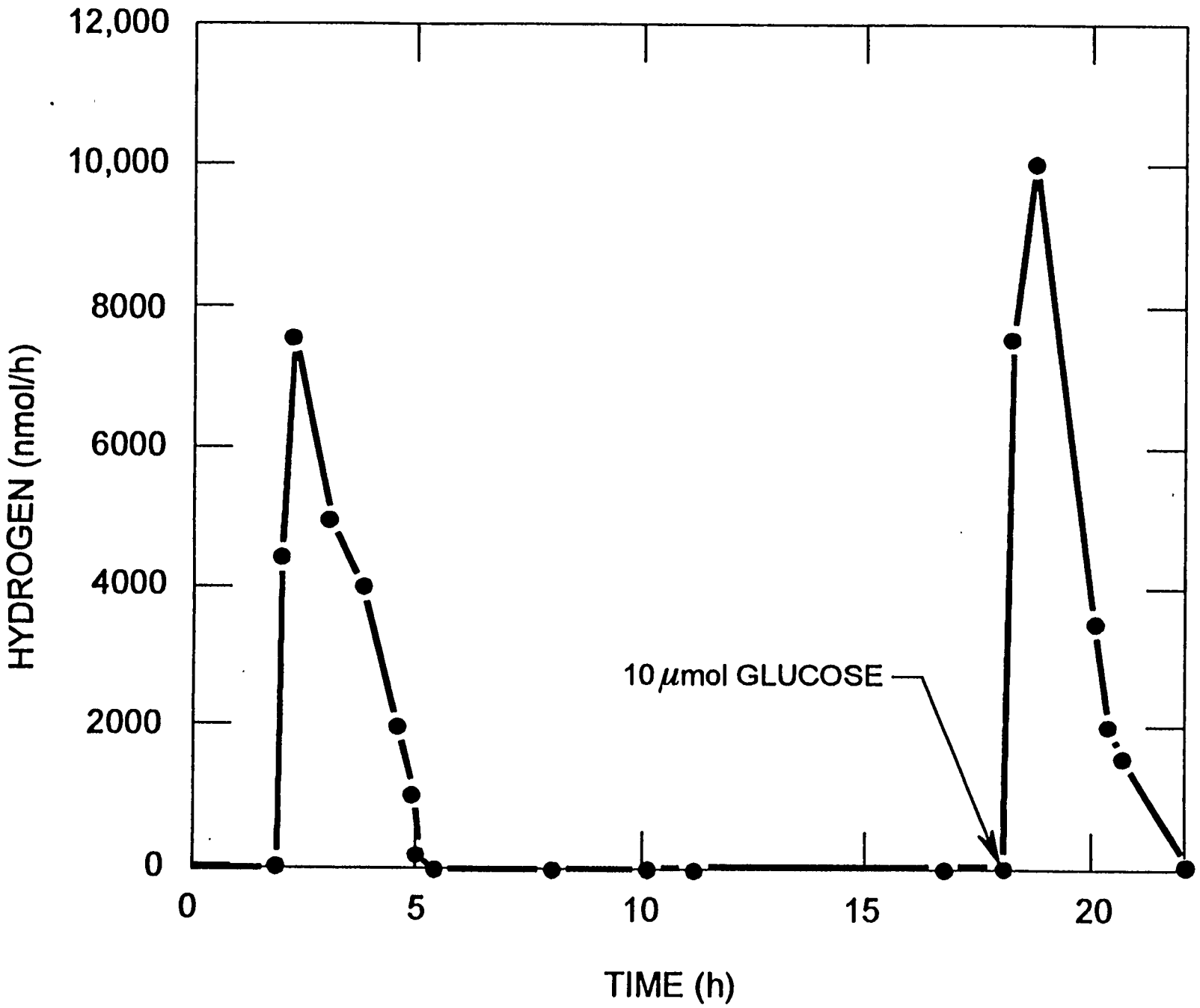
Figure 5. Hydrogen production from microcrystalline cellulose. As for Fig. 1 except that the reaction mixture contained 40 mg of microcrystalline cellulose (Avicel) and no glucose and 0.4 mg of cellulase protein.


Renewable Resources
(Cellulose, Starch, Lactose)
Hydrolysis
Glucose
Glucose
Dehydrogenase
NADP
NADPH
Gluconic Acid
Hydrogenase
H_2

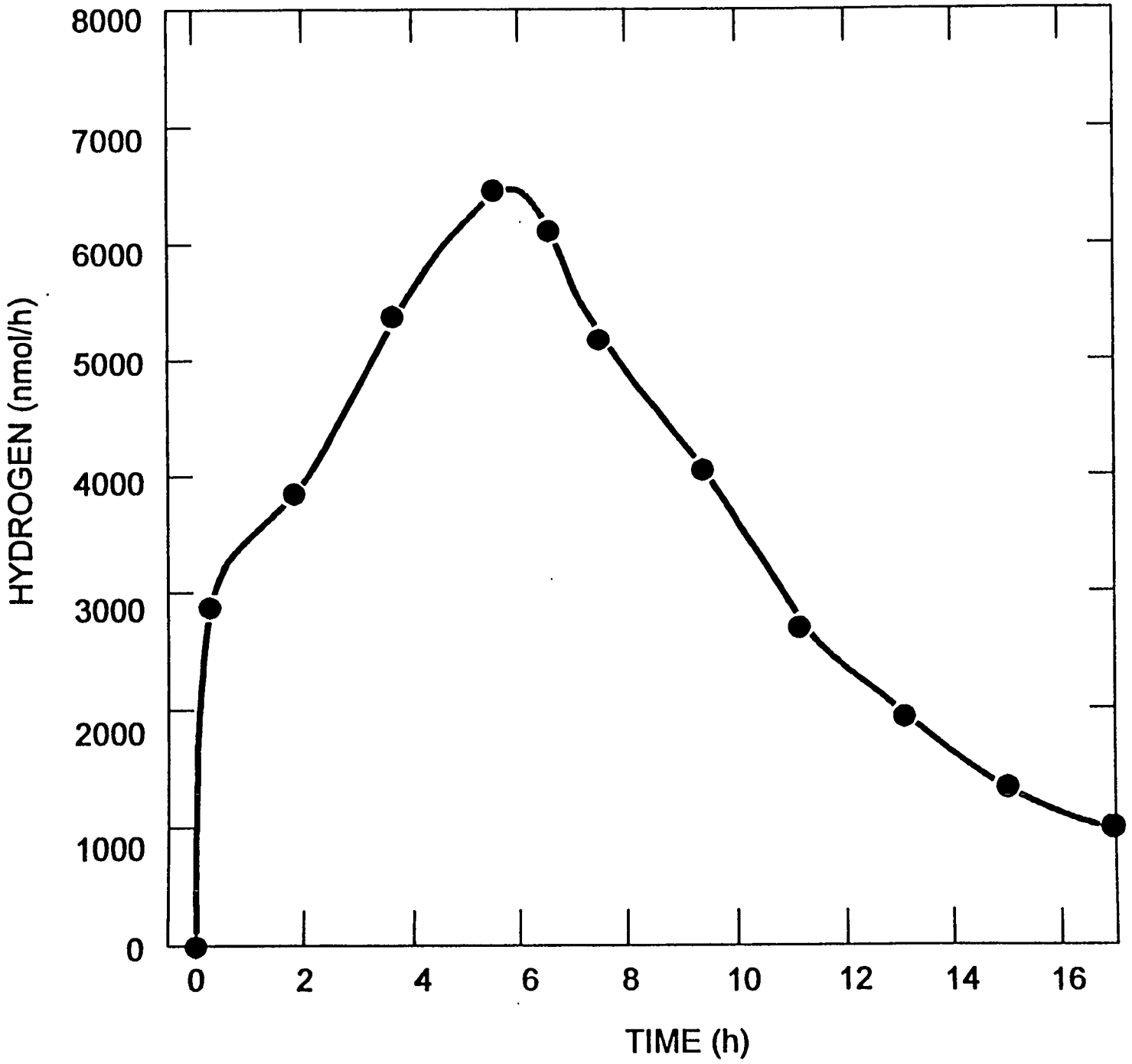
ORNL DWG 95C-894

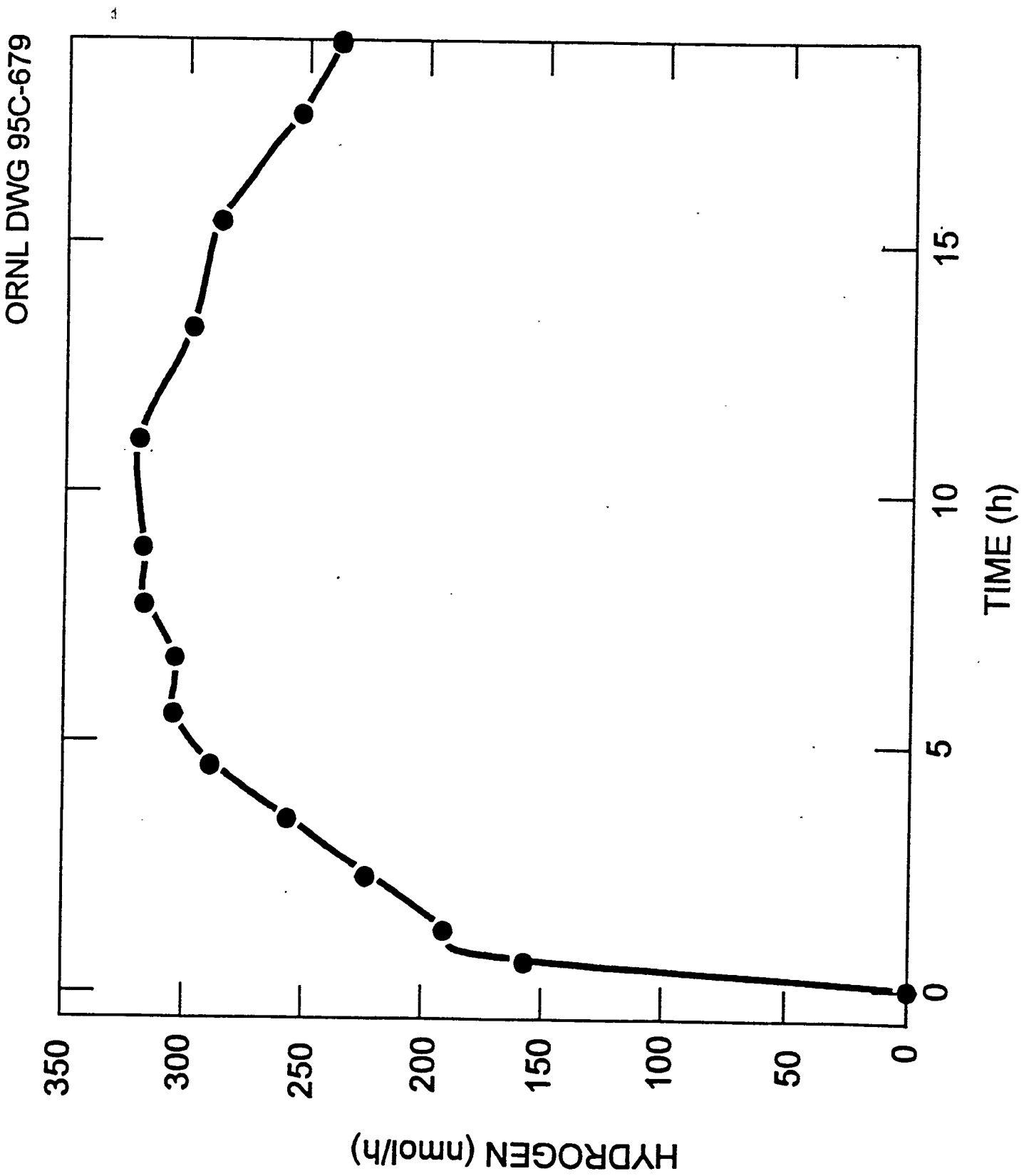


ORNL DWG 95C-677



ORNL DWG 95C-678




ORNL DWG 95C-679
HYDROGEN (nmol/h)
350
300
250
200
150
100
50
0
0
5
10
15
TIME (h)

Biological H_2 from Syngas and from H_2O

P. Weaver, P.-C. Maness, S. Markov, and S. Martin
National Renewable Energy Laboratory
Golden, Colorado 80401

Summary

The two stand-alone objectives of the research are to economically produce neat H_2 in the near term from biomass (thermally gasified to syngas) and in the mid term from H_2O using cyanobacteria or algae with an oxygen-tolerant bacterial hydrogenase.

Photosynthetic bacteria have four different terminal enzymes that mediate their H_2 metabolisms—nitrogenase, uptake hydrogenase, fermentative hydrogenase, and carbon monoxide-linked hydrogenase. Each has been microbiologically and biochemically examined for their potential to specifically generate H_2 in large-scale processes. Based on measurements of maximal activities, stabilities, energy requirements, equilibria, and partial pressures of the H_2 producing reactions, the CO-linked hydrogenase is easily the most suited for practical applications. The enzyme mediates H_2 production from CO at rates up to 1.5 mmol·min^{-1}·g cell dry weight^{-1} at near ambient temperature and pressure. Hydrogen can be produced and evolved at linear rates up to at least 2 atmospheres of partial pressure (100% CO). The rate-limiting step with high cell density suspensions is the mass transfer of CO into the aqueous phase. Bioreactor designs have been examined which enhance the mass transfer. Hollow-fiber bioreactors with bacterial cells immobilized on the fiber surfaces evolve H_2 at ambient pressure at rates of about 0.3-0.7 mmol·min^{-1} g cdw^{-1}. One such reactor has been producing H_2 from CO continuously for 9 months with only occasional changes of liquid medium. A trickle-filter reactor with bacteria immobilized on beads removed from a bulk water phase and a pumped-bubble coil reactor with bacteria in suspension are also being examined.

By sampling natural sites, bacterial strains were isolated that perform the shift reaction to H_2 even in the presence of air. In order to survive the selection process, the bacteria must possess an O_2-tolerant, H_2-producing mechanism. The membrane-bound, CO-linked hydrogenase has been extracted and purified from one such strain (and mutants derived from it which exhibit further O_2 tolerance). Spectral analysis indicates it is probably a non-heme iron protein of about 58,000 molecular weight. The extracted protein is tolerant to the 20% O_2 in full air for at least 5 hours. Experiments are underway to determine whether it remains physiologically active during O_2 exposure as well (i.e., is the enzyme O_2-insensitive as well as O_2-tolerant?). We are also examining whether the hydrogenase will spontaneously partition back into depleted bacterial or cyanobacterial membranes once it has been solubilized and purified. Favorable answers to these questions will allow us to begin efforts to genetically transfer the hydrogenase DNA into an algal or cyanobacterial host.

Introduction: An economic process for producing hydrogen, whether biologically or chemically based, would ideally be (1) H_2O derived, (2) solar driven, (3) highly efficient, (4) durable, (5) insensitive to hydrogen partial pressure, and (6) inexpensive to build and operate. A complete system fulfilling all of these goals is not currently available. Of the biological options, systems employing intact cells of photosynthetic bacteria are the most advanced. Unlike cyanobacteria or algae, however, photosynthetic bacteria do not oxidize water and therefore do not directly fulfill criterion (1). They do, however, evolve H_2 from biomass (previously photosynthetically generated from H_2O and CO_2). These bacteria employ several different enzymatic mechanisms that may have commercial potential for possible near term applications of H_2 production from biomass. One mechanism that incorporates thermal and biological processes appears particularly promising.

The desired criterion for sustained hydrogen production based on the direct photooxidation of water is the most difficult to achieve. Oxygen production is inherent in the oxidation of water, and the hydrogen-evolving enzymes of cyanobacteria and algae are usually rapidly inactivated by oxygen. A number of newly isolated photosynthetic bacterial strains contain an O_2-resistant, evolving hydrogenase enzyme. This hydrogenase has been partially purified from two strains of bacteria, where it is found tightly bound to membrane fractions. The enzymes require an additional electron mediator for H_2 production. Genetic transfer and expression of the oxygen-resistant, bacterial hydrogenase enzyme and cofactor in a cyanobacterial or algal host could provide a method for the linkage of photoreduced ferredoxin to an evolving hydrogenase, even in the simultaneous presence of photoevolved oxygen. This type of genetic construct could grow naturally when CO_2 was present, but would concomitantly photoevolve H_2 and O_2 from water in the absence of CO_2. Creation of a recombinant microbe to fulfill all of the ideal criteria listed above is considered an early mid-term goal.

Approach: The two stand-alone objectives of the research are to economically produce neat H_2 in the near term from biomass (thermally gasified to syngas) using ambient temperature bacteria as catalysts and in the mid term from H_2O using cyanobacteria or algae with an oxygen-tolerant bacterial hydrogenase.

Past Results: Photosynthetic bacteria have four different terminal enzymes that mediate their H_2 metabolisms—nitrogenase, uptake hydrogenase, fermentative hydrogenase, and carbon monoxide-linked hydrogenase. Each has been microbiologically and biochemically examined for their potential to specifically generate H_2 in large-scale processes.

Of the intact cell metabolisms of phototrophs that evolve hydrogen, the nitrogenase-mediated reactions have been the most studied. Nearly all isolates of photosynthetic bacteria have a nitrogenase enzyme complex (Weaver et al. 1975), which, in the absence of ammonium ion or dinitrogen gas and in the presence of oxidizable organic materials, functions to reduce protons and evolve hydrogen. A large variety of soluble organic acids, alcohols, and sugars can be nearly totally photoconverted into H_2 and CO_2 by this metabolism. Rates of 131 μmol H_2 evolved/min·g cell dry weight have been obtained in saturating light. Hydrogen evolution is largely light dependent (Schultz et al. 1985) and strongly exergonic. The hydrolysis of about 4 ATP (largely synthesized in light) is required to generate each H_2 and can drive the gas production to equilibrium pressures in excess of 100 atmospheres. Radiant energy conversion efficiencies (ignoring the chemical energy of the organic

substrate) are about 5.3% for the most active strains of photosynthetic bacteria. The best outdoor, solar-driven efficiency is 3.4%. Cultures grown on glutamate as the nitrogen source produced H_2 at linear rates for 7-10 days before *nif*$^-$ strains began to dominate the cultures. Experiments with weekly feedings of N_2 maintained the *nif*$^+$ wild-type genotype dominant and active H_2 production could be observed for more than 30 days. Even with the assumption that the best strains and conditions could be maintained, the maximum solar conversion efficiencies that could be expected are probably less than 10%, however, due to the large energy expenditure of the bacteria in performing this H_2-evolving metabolism. Non-sterile, solar-driven cultures (200-300 liter scale) were susceptible to contamination by sulfate-reducing and methanogenic bacteria growing on the evolved H_2 plus CO_2. Limiting the available fixed nitrogen, including that present in sedimented photosynthetic bacteria, is necessary to limit H_2S and CH_4 evolution by the contaminants. Algal growth is similarly inhibited by this method and also by the strongly reducing conditions. An in-house cost analysis of the process has been performed (Herlevich and Karpuk). First year costs for H_2 production, clean-up, and compression are estimated at \$24.40 per 10^6 Btu at 5% solar energy conversion and \$15.70 per 10^6 Btu at 10% conversion efficiency.

Many strains of photosynthetic bacteria also produce hydrogen from organic substrates by way of a fermentative hydrogenase enzyme when grown in intermittent or low, continuous light (Schultz and Weaver 1982). High, continuous light represses synthesis of the enzyme. The enzyme does not require ATP. It can mediate hydrogen production at rates more than 3-fold those of nitrogenase, or about 440 µmol H_2/min·g cells. However, it equilibrates at low partial pressures of about 0.1 atmospheres of H_2. The active rates of hydrogen production can thus only be maintained by sparging with inert gas, by vacuuming, or by scavenging with a hydrogen-consuming process. Sparging or vacuuming are considered prohibitively expensive, although closed-loop, sparged systems connected to fuel cells may be effective. Methanogenic bacteria strongly contaminate non-sterile cultures. In fact, methanogenic bacteria naturally scavenge the H_2 to such low levels that they are extremely effective in maintaining the H_2 partial pressure considerably below the equilibrium pressure, which functions to "pull" the conversion of organic materials into H_2 and CO_2 and then into CH_4. This apparently natural process is the basis for an NREL patent on solar-enhanced anaerobic digestion (Weaver, 1990).

A unique type of hydrogen producing activity was found in a strain of photosynthetic bacteria by Uffen (1976) that functioned only in darkness to shift CO (and H_2O) into H_2 (and CO_2). We have isolated more than 400 strains of photosynthetic bacteria from local sites that perform this shift reaction in darkness, as does the Uffen strain, but will also quantitatively assimilate CO into new cell mass in light, unlike the Uffen strain, which makes them easy to grow. We have tested many of our strains for CO shift activity and growth with crude (water-scrubbed only) synthesis gas (primarily CO and H_2) generated from thermally gasified wood chips. In light, the novel photosynthetic bacteria assimilate the CO and H_2 components and a portion of the trace gases. In darkness, all of the isolates respond similarly by shifting the CO component of synthesis gas into additional H_2, thereby leaving a product gas highly enriched in H_2 (with CO_2 and trace pyrolysis gases). No inhibitory effects of synthesis gas on long-term photosynthetic growth were noted. At ambient temperature and pressure conditions and starting from 200,000 ppm of CO in the gas phase, less than 18 ppm of CO remained at equilibrium. The product gas could be fed directly into a phosphoric acid fuel cell with generation of electrical power. No harmful effects to the fuel cell were noted.

Bacterial catalyzed rates as high as 1.5 mmol H_2 produced from CO per min per g cell dry weight were obtained from vigorously agitated cultures at low cell density. Less actively stirred cells at more normal cell densities (2-6 g cells per liter) exhibit H_2 production rates of 10-100 µmol per min per g cells, reflecting a limiting mass transfer of CO into solution. Gas pressures (10% CO) of more than 12 atmospheres strongly increased shift rates but were still limiting.

Current Results: Bacterial cultures grown in light with 20% CO in the gas phase are probably not maximally induced for CO shift activity. The specific activity for CO shift activity increased by a factor of six when light-grown cultures were incubated in darkness in a Paar cell at seven atmospheres of 20% CO gas pressure. This indicates that increased availability of CO to the cells causes a further derepression of shift activity enzymes. Cultures can be adapted easily to two atmospheres of 100% CO, but do not adapt to seven atmospheres of 100% CO. Inert gas at similar pressures had no effect. The capability of running syngas shift reactors at a few atmospheres of pressures is being incorporated into new reactor designs.

A variety of bioreactor designs that show enhanced mass transport of CO (at near ambient pressure) were built and tested. Hollow-fiber reactors (0.5 m^2 surface area) with bacterial cells immobilized on the outer fiber surfaces evolved H_2 at rates of about 0.3-0.7 mmol·min^{-1}·g cdw^{-1}. One such reactor produced H_2 from CO (10% in N_2) continuously over a 9 month period with only occasional changes of medium. No detectable levels of CO remained in the effluent gas stream. FTIR analysis of an equilibrated gas sample indicated that remaining CO was less than 0.1 ppm. This is easily clean enough to be directly injected into phosphoric acid or PEM fuel cells which maximally tolerate 10 ppm or 1 ppm CO, respectively. In fact, the effluent gas of one reactor has been directly injected into small mW fuel cells of both types and shown capable of generating electricity to power small motors and lamps. No effect on the fuel cells could be noted.

A bubble-train bioreactor was constructed of PVC tubing helically coiled around a vertical column. A bacterial suspension was pumped through the coil. When bubbles of 20% CO were injected at the base of the coil, CO was shifted into H_2 at rates of about 0.5 mmol·min^{-1}·g cdw^{-1}. The activity was stable for at least 10 days. Bubble-tower and sprinklered bioreactor designs using suspended bacteria proved less active.

A trickle-filter bioreactor was constructed by adsorbing bacterial cells to 3 mm nylon beads and placing them in a 1" x 12" stainless steel column. A sump reservoir at the column base held 40 ml of basal salt medium, which was slowly pumped externally to the top of the column and trickled over the beads and back to the sump. A synthetic syngas (10% CO) flowed through the column and contacted the microbes at relatively high rates in the absence of a bulk water phase. Counter-current flow proved better than co-current flow. Rates of CO shift are estimated to be about 0.8 mmol·min^{-1}·g cdw^{-1}. The CO_2 product of the shift reaction is largely trapped as bicarbonate ion in the sump, where it can be stripped by sparging with N_2. The column effluent gas is much reduced in CO_2 and devoid of CO. This bioreactor is constructed to withstand 10 atmospheres of gas pressure and will soon be run in a pressurized mode.

While CO_2 buildup in the aqueous phase tends to lower the pH, it is also likely that dark fermentation of endogenous sugars into organic acids generates acidic conditions with time. This problem is being examined.

The photosynthetic bacterial strains that perform the water-gas shift reaction were normally isolated under strictly anaerobic conditions since hydrogen is an essential intermediate in their growth, and evolving hydrogenase enzymes are normally rapidly inactivated by oxygen. By intentionally adding oxygen to the enrichment cultures, however, conditions are established that positively select only bacterial strains from nature that have an oxygen-resistant hydrogenase. As a result, far fewer bacterial isolates occur in enrichment cultures under aerobic conditions, but about 12 strains have been isolated by this method. Subsequent testing of these isolates showed relatively small losses in evolving hydrogenase activity over a one or two hour exposure to full air. If the O_2-tolerant hydrogenase enzymes from bacteria could be genetically transferred into cyanobacteria or algae, expressed, integrated into their membranes, and linked to photoreduced ferredoxin in the absence or limitation of CO_2, then a new whole-cell method for the photoproduction of H_2 from H_2O becomes feasible.

Further rounds of O_2-tolerance selection on isolated strains have resulted in mutants or variants within the general strain population that are able to tolerate even higher concentrations of O_2. The CBS-2 variant responds by synthesizing 160% of the carbon monoxide dehydrogenase (CODH) activity and 340% of the hydrogenase activity of its parent.

CHAPS detergent was effective at extracting the CODH and hydrogenase proteins from membranes. Ion exchange and gel exclusion chromatography were used to separate and purify the proteins from each other and from any traces of remaining bacteriochlorophyll and membranes. The hydrogenase was purified 86-fold from other membrane proteins. The purified evolving hydrogenase stirred in full air exhibited a half-life of 17 hours. This compares extremely favorably to an evolving formate-linked hydrogenase from a similar organism that shows a half-life of only 2 minutes in air. The O_2-tolerant hydrogenase exhibits no oxy-hydrogenase activity in the presence of H_2 and O_2.

Before attempting genetic exchange of the O_2-resistant hydrogenase, it is first necessary to determine whether the hydrogenase will couple to photoreductants generated from H_2O photolysis. Adding the bacterial hydrogenase to a thylakoid preparation from a spinach extraction produced very little coupling until methyl viologen, a redox mediator, was also added. Purified samples of two of the four known ferredoxins from photosynthetic bacteria would not replace the methyl viologen. Nevertheless, these data indicate that water-splitting linked to O_2-resistant H_2 production is possible with an appropriate native cofactor. Hydrogen production ceases when oxidized $NADP^+$ is added to the mixed cell-free extracts, thereby implying that normal electron transfer in the phototroph would dominate when CO_2 was present, but H_2 production would commence when CO_2 becomes limiting.

Since the purified CODH and hydrogenase enzymes do not link in extracts, it is evident that one or more electron transfer proteins are necessary to mediate electron flow between the enzymes. We have so far been unable to reconstitute CO shift activity in depleted membranes with the purified enzymes. Supplemental NAD^+, $NADP^+$, FAD, FMN, pteridines, or ferredoxins did not promote linkage. However, a new spectral assay based on metronidazole reduction by CO has been

developed. Metronidazole reduction by CO is not observed with purified CODH, but an additional protein fraction promotes the linkage. The physical nature and properties of this additional fraction are being pursued for its essential nature in the shift reaction. Presumably it also will be necessary in a genetically transformed, oxygenic host.

Future Work: Further mutant selections should result in significantly increased specific activities in the CO shift reaction. Thermophiles will also be selected. Strains with a lower K_s for CO will be sought. The hollow fiber reactor design will be scaled up about 40-fold. The bubble-train bioreactor will be enlarged sufficiently to effect syngas conditioning in a single pass. The trickle-filter bioreactor will be operated at 2 to 5 atmospheres of gas pressure. The Outdoor Photobiology Test Area will be expanded to accommodate the new bioreactors. Necessary cofactors for the O_2-tolerant hydrogenases will be further explored and characterized. A review article on biological hydrogen production schemes and bioreactors will be written.

Economic Evaluation/Systems Analysis: Analyses are being performed on a separate task in the Hydrogen Program. The bacterial shift reaction is being examined as a possible low cost, single-step gas conditioning process for crude syngas. The projected cost of hydrogen is $17/GJ using a base case of purchased biomass at $46/ton and thermal gasification with biological shift (15% ROI). If biomass is purchased at $22/ton, the price of pure H_2 drops to $13.5/GJ, well within current market prices. A 10-fold increase in specific shift activity (from 1.5 $mmol \cdot min^{-1} \cdot g\ cdw^{-1}$) will decrease the cost by $4.70/GJ. If further gas purification is not needed to remove the CO_2 produced, the selling price is further reduced another $3.80/GJ. For many gas uses, such as in PEM or phosphoric acid fuel cells, it is only necessary that the gas stream be free of CO and H_2S, while not necessarily free of CO_2. In these applications the cost of gas purification can probably be discounted.

Projected Goals: The equilibrium constant of the CO shift reaction at room temperature is sufficiently large to generate a bacterially conditioned syngas stream with sub-ppm concentrations of CO remaining. Assuming there is no appreciable sulfide present as well, the gas stream is clean enough (with or without CO_2 diminishment) to be directly injected into phosphoric acid or PEM fuel cells. This would effectively eliminate the costs (see Economics) for pressure-swing absorption (or similar gas clean-up process) to yield neat H_2 for fuel cell use. Our near-term goal will be for this type of fuel cell application.

A genetic construct containing an O_2-tolerant hydrogenase would create an inexpensive photobiological catalyst that would switch in the absence of CO_2 from a growth mode to a H_2-producing mode at nearly maximal solar conversion efficiency. The successful construction and testing of such an oxygenic phototroph is our mid-term goal to photobiologically produce H_2 from H_2O in a single-stage bioreactor.

Major Barriers: The long-term effects on bacteria of trace components in syngas have not bee examined and may necessitate more frequent change-out of bacteria. Mass transfer of CO to the bacteria remains rate limiting and needs to be enhanced. Genetic enhancement can easily match any large increase in mass transfer rates. There are a few more unknowns in the photobiological process to produce H_2 from H_2O. The O_2-tolerant hydrogenase must be genetically transferred and expressed

in a biophotolytic host and shown to be active in linking to photoreductants. This has been demonstrated in mixed extracts, however.

References:

Herlevich, A., and M. Karpuk. 1982. SERI/TP-235-1548, 12 pp.

Schultz, J.E., and P.F. Weaver. 1982. *J. Bacteriol.*, 149:181-190.

Schultz, J.E., J.W. Gotto, P.F. Weaver, and D.C. Yoch. 1985. *J. Bacteriol.*, 162:1322-1324.

Uffen, R.L. 1976. *Proc. Nat. Acad. Sci.*, 73:3298-3302.

Weaver, P.F. U.S. Patent #4,919,813, issued April 24, 1990.

Weaver, P.F., J.D. Wall, and H. Gest. 1975. *Arch. Microbiol.*, 105:207-216.

PHOTOELECTROCHEMICAL BASED DIRECT CONVERSION SYSTEMS FOR HYDROGEN PRODUCTION

Shyam Kocha, Mark Peterson, Doug Arent, Heather Scott, Art Frank, and John A. Turner
National Renewable Energy Laboratory
Golden, CO 80401-3393

Abstract

Photon driven, direct conversion systems consist of a light absorber and a water splitting catalyst as a monolithic system; water is split directly upon illumination. This one-step process eliminates the need to generate electricity externally and subsequently feed it to an electrolyzer. These configurations require only the piping necessary for transport of hydrogen to an external storage system or gas pipeline. This work is focused on multiphoton photoelectrochemical devices for production of hydrogen directly using sunlight and water. Two types of multijunction cells, one consisting of a-Si triple junctions and the other $GaInP_2$/GaAs homojunctions, were studied for the photoelectrochemical decomposition of water into hydrogen and oxygen from an aqueous electrolyte solution. To catalyze the water decomposition process, the illuminated surface of the device was modified either by addition of platinum colloids or by coating with ruthenium dioxide. These colloids have been characterized by gel electrophoresis.

Introduction

Photovoltaic systems coupled to electrolysers represent a commercially available, renewable based, hydrogen production system. However, commercial electrolysers suffer from high capital costs, and are a major contributor to the cost of electrolytically produced hydrogen. Photoelectrochemical water splitting, also known as photoelectrolysis, represents an advanced alternative to a PV/electrolysis combination. The photoelectrolysis direct conversion system combines a photovoltaic material and an electrolyzer into a single monolithic device. This monolithic system eliminates the cost of an electrolyzer and additionally reduces semiconductor processing since surface contacts, interconnects, and wiring are no longer necessary, only the piping necessary for the transport of hydrogen to an external storage system or gas pipeline is required.

The goal of this research then is to develop a stable, cost effective, photoelectrochemical based system that will split water directly upon illumination, producing hydrogen and oxygen. Our focus for the light harvesting system involves the use of multijunction and tandem cell technology. Tandem cell technology connects photovoltaic layers (pn junctions) with different semiconductor bandgaps in series, one behind the other, in a single monolithic cascade device. This configuration offers a greater utilization of the solar spectrum, providing the highest theoretical conversion efficiency for any photoconversion system. The monolithic structure also minimizes the amount of active area needed for specific power applications. This work is directed at designing, testing, and optimizing multijunction cell technology for water splitting, and integrating it into a photoelectrolysis system. In summary, we hope to accomplish our objective by; (1) choice of semiconductor material and solid state structure; (2) surface modification to improve the energetics and stability and, (3) development of transparent and highly active catalysts.

Discussion

Technical Approach

For a direct conversion process to be viable, the light harvesting system must generate enough voltage to decompose water, and the system must be stable in a water environment. Our approach is to use the best semiconductor materials and structures that are available, consistent with the energy requirements for a water splitting system and stability in an aqueous environment. Our efforts are directed at two promising semiconductor multijunction systems; III-V semiconducting materials (materials are made with various combinations of gallium, indium, arsenic and phosphorous), and amorphous silicon based systems. The III-V tandem cell structures are the semiconductors that solid state research groups are focusing on as the next generation of high efficiency solar cells. We are working with NREL's Photovoltaic and Basic Sciences Centers to provide us the state of the art III-V materials and structures.

Amorphorous silicon multijunction devices consist of multiple layers of a-Si cells. These multi-layer cells provide higher efficiency than single junction cells at low cost and reduce the amount of photodegradation that is common to all a-Si devices. The combination of lower system cost and higher efficiency, represent an important area of research for hydrogen production systems. Further, manufacturing capability for a-Si systems is high, with current production capability of these type of devices at over 20 megawatts per year in the US alone. Our approach here is to work with an industrial collaborator to develop optimized a-Si systems designed specifically for water splitting.

To address the issue of the stability of the semiconductor/electrolyte interface, we have separate approaches depending on the cell material. For the III-V semiconducting materials, indium is an important constituent. In aqueous solution indium forms an oxide layer that stabilizes the interface. We are also investigating nitridation techniques to attempt to form gallium and/or indium nitrides at the surface. Recent work in our laboratory and others, has shown that these nitrides are very stable in aqueous environments. For the amorphous silicon systems, amorphous silicon carbide has been chosen as a promising protective surface layer. We are also working on the possibility of using transparent conducting oxides such as indium tin oxide and zinc oxide as surface coatings. These oxides are currently used in the commercial a-Si devices to provide electrical contact. Catalysts are also deposited onto the surface to decrease the overvoltage for the oxygen and hydrogen evolution reactions.

The nature, coverage and stability of the catalyst are critical for an optimized direct-water splitting system. Catalyst coverage must be sufficient to both protect the semiconductor from undesirable side reactions (corrosion) and provide adequate catalytic activity to handle the current flux. The catalyst must also not introduce surface states that would lead to surface recombination and efficiency losses. Transparency of the catalyst is important to minimize light loses. The catalysts must be stable and remain active over the lifetime of the device. Since colloids are used in our photoelectrolysis studies, knowledge of the net charge and size distribution, is necessary to maximize the efficiency of our water splitting devices.

Colloidal Catalysts

Gel electrophoresis was used as a qualitative tool to characterize the charge and relative size distribution of the following metal colloid particles: Gold (Au), Platinum (Pt), palladium (Pd), and ruthenium dioxide (RuO_2). All colloid samples were produced in-house. A 10^{-3} M gold colloid was prepared by reducing $HAuCl_4$ with $NaBH_4$. The particles were stabilized using a trisodium citrate solution. Electron diffraction patterns revealed that the particles were crystalline. Similarly, a 1.5 x 10^{-4} M palladium colloid was prepared from $PdCl_3$. The 10^{-5} M platinum colloid was prepared by reducing H_2PtCl_6 with sodium citrate. The particles are likely to be amorphous in nature. Another platinum colloid was prepared using methanol as the reducing agent. Ruthenium dioxide colloids are made by taking 15 mls of a 6.66 x 10^{-4} solution of ruthenium tetroxide and adding 50 µl of a 30% hydrogen peroxide solution. The solution is stirred rapidly for 2 minutes and passed through a 0.5 µm filter.

Gel electrophoresis was performed on the colloid samples using the Gibco BRL Horizon® 58 Horizontal Gel Electrophoresis Apparatus (Life Technologies) with the Gibco BRL Model 200 Power Supply. The electrophoresis buffer was prepared from a 10X Tris borate-EDTA (TBE) stock solution The final pH was approximately 8.3 (Life Technologies).

Results

All colloid samples, with the exception of the ruthenium dioxide (RuO_2) colloid, traveled toward the anode, indicating a net negative charge on the particles. Smaller RuO_2 particles exhibited both positive and negative charge, while larger particles exhibited only positive charge. As expected, the migration rates increased with increasing applied voltage. Likewise, they showed a general downward trend with increasing gel concentrations. Comparison of the leading and trailing edge migration rates for each colloid also gives an indication of the relative size distribution.

An attempt was made to quantify the charge and size of the colloid particles by comparison with the electrophoretic movement of a known ion exchange resin. However, the particles of the smallest

available resin were on the order of 10 microns and would not exit the well into the gel. Drawing from the results of the gold colloid movement, the resin particles must be on the order of 10 Å or less for successful electrophoretic migration to occur.

The colloids were also tested with two additional buffers (Hydrion phosphate buffers of pH 7 and pH 8) at 100 V with 1.2% gel concentration. All colloids behaved similar to the previous runs, exhibiting the same net charge as before. However, the colloids moved faster in these buffers than in the TBE electrophoresis buffer. Also, the bands of the smaller ruthenium dioxide colloid were uniform, not pointed toward the anode and broad toward the cathode.

All particles studied, with the exception of RuO_2, exhibited negative charge. Smaller RuO_2 particles exhibited both positive and negative charge, while larger particles exhibited only positive charge. Relative size distributions were deduced from the quality of movement of the band through the gel. The relative size distribution was in agreement with our TEM micrograph data. Au and RuO_2 spanned a large size range, while Pt, and Pd occupied smaller ranges.

Single Gap Systems

Previously, we have worked on both single gap systems and tandem cell devices. With the results of the last proposal review, we have directed our efforts primarily at the tandem cell devices. We have, however, continued some single gap work to look at promising materials and to complete past work for publication.

In our search for promising semiconductor materials that could split water as single gap electrodes, we have identified crystalline beta silicon as a possible candidate for photoelectrolysis device. This is one of the various forms of crystalline silicon carbide and is obtainable from commercial sources. Its bandgap is 2.2 eV which is sufficient for water splitting. An n-type (nitrogen doped) sample was obtained from Cree Research. It was characterized and the energetic position of its band edges determined with respect to the Standard Hydrogen Electrode. Since the samples as received, did not have any ohmic contacts, the back surface was ground/etched and contacts were made using In wire and silver paste. The Mott-Schottky plots were found to linear in various electrolytes of different pHs following a Nernstein relationship of about 60mV/pH. The bandedges are located such that they straddle the oxygen and hydrogen evolution reactions (figure 1). However, instead of the expected oxygen evolution reaction, illumination of the material apparently caused corrosion of the material, forming porous SiC and CO_2. Although p-type material is not commercially available, we expect it to be a more promising material since the surface would be under reducing conditions, generating hydrogen and not subject to oxidation. Possible sources for p-type include Howard University and the Jet Propulsion Laboratory.

Gallium and indium nitrides are semiconducting materials of interest to us as possible water splitting systems, since they have bandgap energies ranging from 1.9 to 3.4 eV, withstand string oxidants and are expected to have better energetics than GaAs, InP, or $GaInP_2$. At the last program review, we identified indium nitride with a bandgap of 2.2eV as an ideal candidate for a single gap water splitting system. At that time we had initiated correspondence with Prof. Akio Yamamoto at Fukui University in Japan to obtain some of his samples. We have finally received the samples of indium nitride from Prof. Yamamoto. While these initial samples were of poor semiconductor quality, our experiments have shown that the bandedges are perfectly positioned energetically for water splitting (figure 2). That coupled with the ideal bandgap of 2.2 eV is very encouraging. We hope to obtain some better materials soon.

We have also initiated a study on converting the surface of some of our semiconductor samples to nitrides. The objective would be to generate a more stable surface layer and possibily shift the band edges to more favorable positions. Initial thermal treatments of InP electrodes with ammonia produced a surface layer of InN and a 100 mV shift in the valence band edge (figure 3). To our knowledge, this is the first ever conversion of the surface of InP to InN.

Multijunction Cells

We have grown and tested an new design of the $GaInP_2$ /GaAs tandem cell. This sample was grown with a 0.1um layer of high doped p-$GaInP_2$ on top of the n-$GaInP_2$ surface emitter layer (figure 4). The results were very encouraging. The cell split water from both electrodes (rather than just from the illuminated surface) and the gas evolution stopped when the second electrode was disconnected (in contrast to some of our previous separated water splitting samples. There were two reasons we wanted to look at this sample. The first is that our electrochemical impedance spectroscopy results indicated a barrier at the interface similar to a n-type sample. At the semiconductor electrolyte interface, this barrier would oppose the flow of electrons towards the surface. A barrier of this type is clearly what one would expect, and we have always known that this barrier existed. Our assumption in the past has been that since this n-layer is fairly thin and highly doped, it would have very little effect on the cell characteristics. However, the EIS results indicate that this barrier might be larger than expected. A p-layer at the interface would have exactly the reverse effect. The other reason is that we put colloidal metal catalysts down on the surface. A degenerative doped surface layer may provide a more ohmic-like contact for the metal colloids.

We tested our new design of the $GaInP_2$ /GaAs tandem cell in the solar simulator, illumination was direct normal, AM1.5. Figure 5 shows the current voltage curve. The HHV efficiency, measured at short circuit current was 5.5%. Note: in contrast to the way efficiencies are measured in standard photovoltaic cells, the maximum efficiency for the water splitting cell is measured at short circuit current. We plan to try a number of different thicknesses and doping levels to optimize this new design.

A subcontract to Energy Conversion Devices to manufacture test multi-junction a-Si cells specifically for water splitting has been awarded. Because we want hydrogen to be evolved from the illuminated surface, this contract is to grow samples specifically for water splitting. This involves growing the a-Si layers in reverse order as compaired to standard solar cells. Instead of growing the layers in the order n-i-p, for our use they are grown p-i-n. Since this is not something that is usually done, we expect the initial samples to be of lower quality that the standard samples. However, we have been told by ECD that once they have optimized the growth parameters, the efficiency of these samples should be commensurate with the standard cells. At the time of the program review, we had received two sets of samples. The first set were characterized by low voltages and low fill factors, however the second set showed excellent characteristics. We plan to test the samples and have a full report for the '97 program review.

Plans for Future Work:

In general, our future work will involve: the identification and growth of promising multi-junction systems including designing unique multi-junction systems focused specifically on water splitting; establishment of cooperative efforts to obtain samples or development of in-house growth capabilities; and lifetime testing and efficiency measurements for working systems. The study of the interaction of colloidal catalysts with the various tandem cell surfaces is also a very important area for future work. More specifically, we will focus on continued investigation of the III-V material system concentrating on tailoring the tandem cell structure specifically for an aqueous environment and the energetics of the water splitting reaction. We will be evaluating various surface treatments to enhance stability and

energetics. We will initially focus on nitridation as a surface treatment. We will also be working with our industrial collaborators to optimize the α-Si multi-junction systems for water splitting.

A novel concept that has been an interest of ours for some time now involves the designing, growing and testing of mixed PV/PEC systems. These structures consist of a buried homojunction capped by a Schottky type photoelectrochemical junction and represent a new concept in photoelectrochemistry. Theoretically, these devices could have an efficiency higher than that of a similar PV device.

Major Barriers

In general, the major problems that must be addressed in order to produce a viable system are: stability of the semiconductor/electrolyte interface, and system energetics. Materials and catalysts must be found that protect the semiconductor surface, but allow electrons to pass through unimpeded. While we lack full understanding of the fundamental characteristics of the semiconductor/electrolyte interface, considerable progress has been made. For the a-Si multi-junction cells the design of the water-splitting cells must be optimized for maximum efficiency. For the III-V systems, to maximize their efficiency, materials and designs must be identified for lower voltage, higher current applications.

Figure Captions

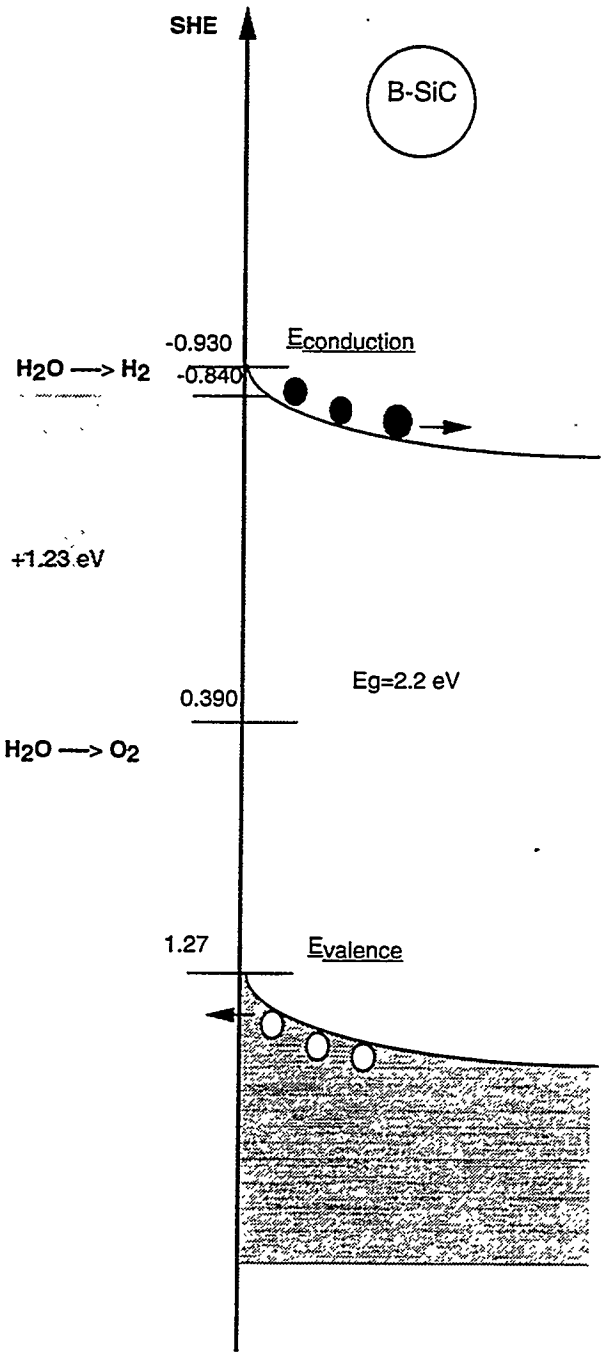
Figure 1 Bandedge positions for n-type beta-silicon carbide, showing near ideal energetics for water splitting.

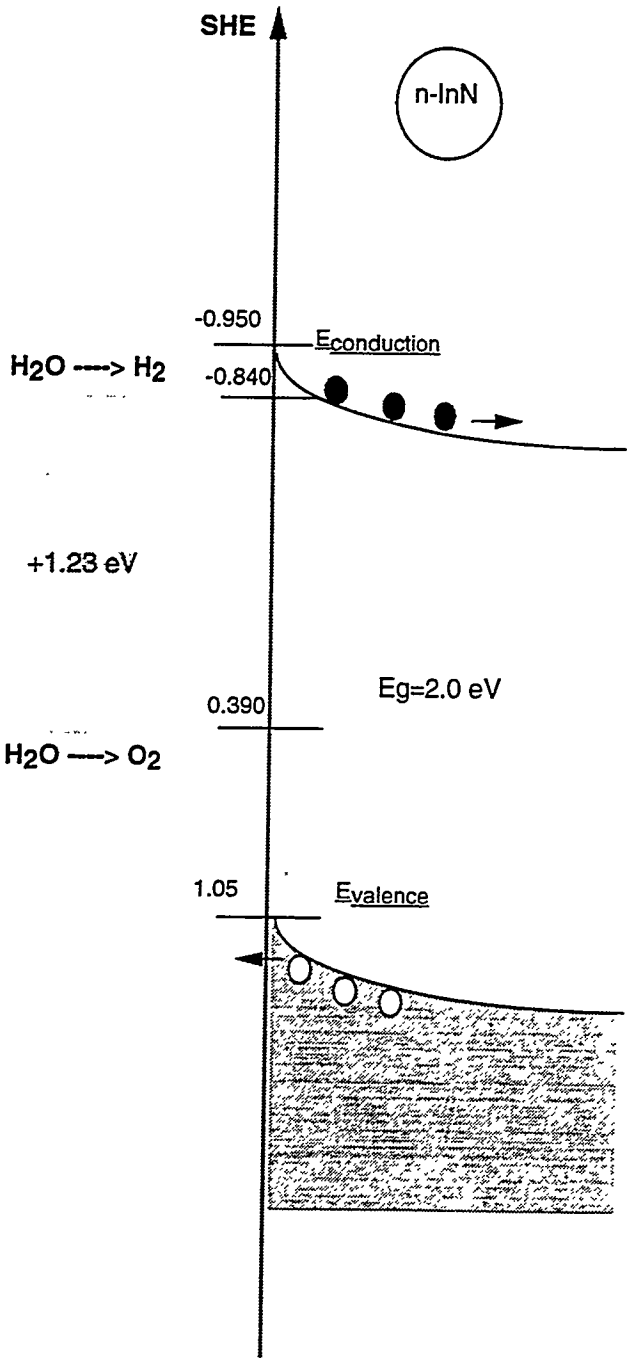
Figure 2 Energetic position of the bandedges for n-type indium nitride. This material also shows near ideal energetics for water splitting.

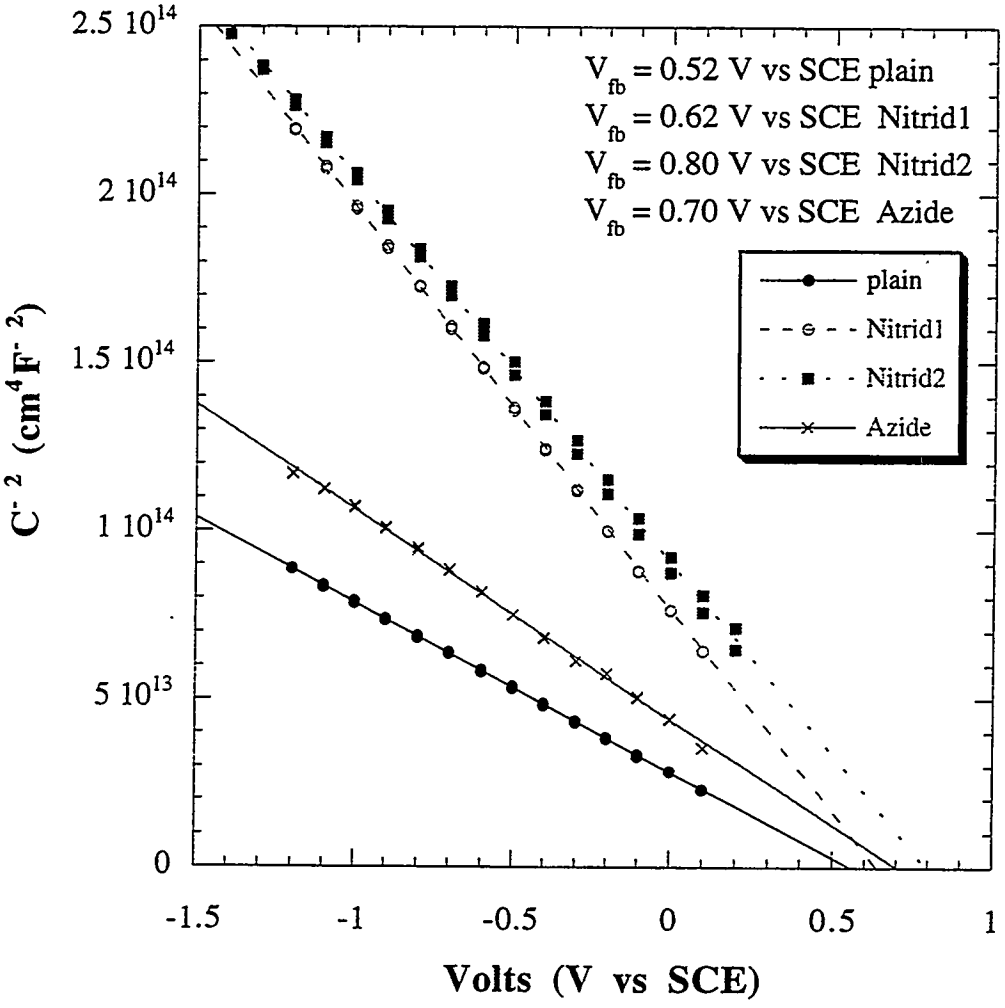
Figure 3 Mott-Schottky plots of p-InP nitrided samples (using nitrogen and azide) in pH 2 electrolyte at 10kHz.

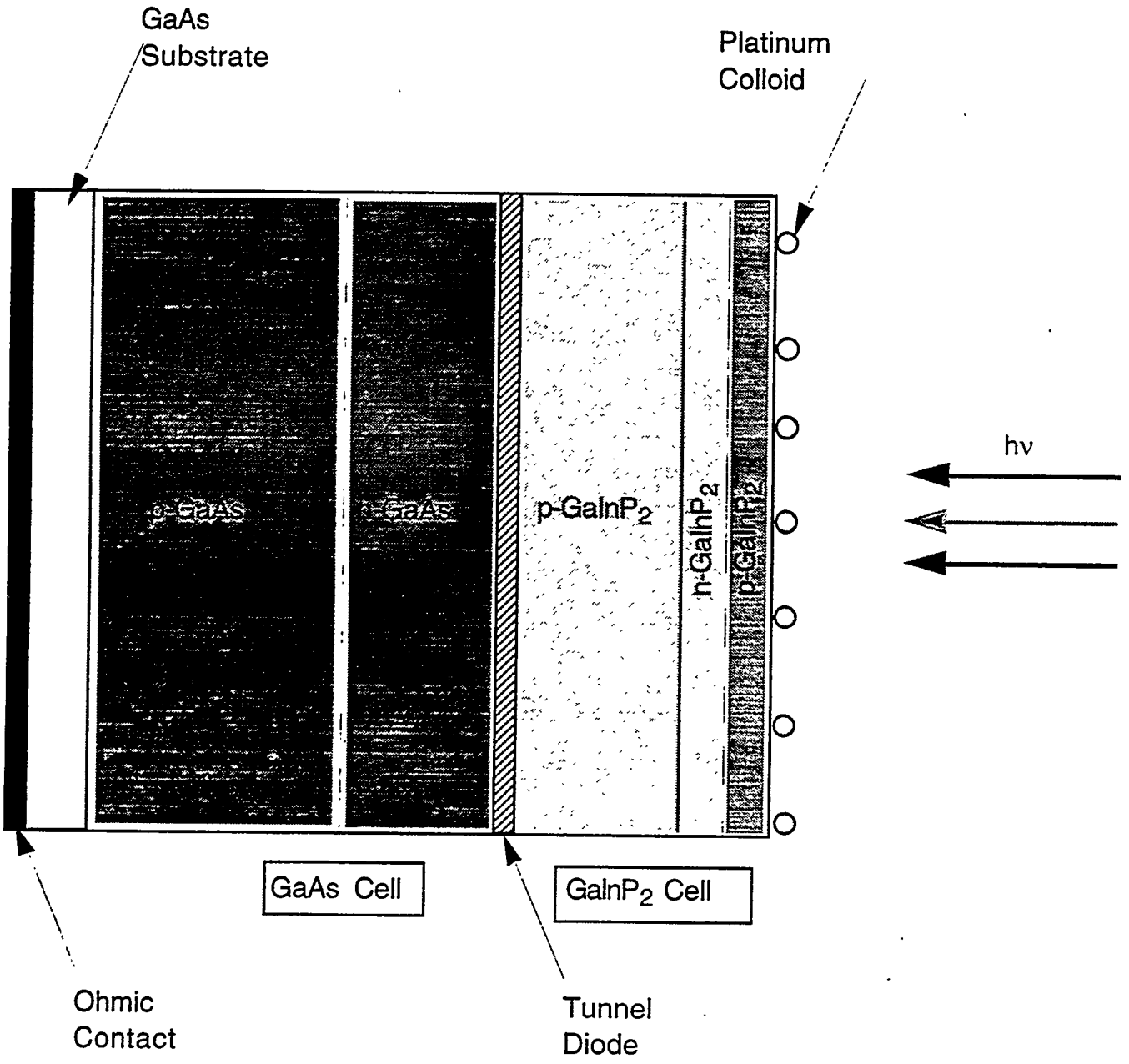
Figure 4 Modified tandem cell design. Cell now has a high doped p-layer at the interface.

Figure 5 Water splitting efficiency measurement for modified cell design. Solar simulator AM1.5 light used.


SHE
B-SiC
-0.930
Econduction
H2O —> H2
-0.840
+1.23 eV
Eg=2.2 eV
0.390
H2O —> O2
1.27
Evalence


SHE
n-InN
-0.950
Econduction
H2O ----> H2
-0.840
+1.23 eV
Eg=2.0 eV
0.390
H2O ----> O2
1.05
Evalence


2.5 10^14
2 10^14
1.5 10^14
1 10^14
5 10^13
0
C^-2 (cm^4F^-2)
-1.5
-1
-0.5
0
0.5
1
Volts (V vs SCE)
V_fb = 0.52 V vs SCE plain
V_fb = 0.62 V vs SCE Nitrid1
V_fb = 0.80 V vs SCE Nitrid2
V_fb = 0.70 V vs SCE Azide
plain
Nitrid1
Nitrid2
Azide


GaAs
Substrate
Platinum
Colloid
p-GaAs
n-GaAs
p-GaInP2
n-GaInP2
p-GaInP2
hν
GaAs Cell
GaInP2 Cell
Ohmic
Contact
Tunnel
Diode

PHOTOELECTROCHEMICAL HYDROGEN PRODUCTION

Richard E. Rocheleau, Eric Miller, and Anupam Misra
Hawaii Natural Energy Institute
School of Ocean and Earth Science and Technology
University of Hawaii
Honolulu, HI 96822

Abstract

The large-scale production of hydrogen utilizing energy provided by a renewable source to split water is one of the most ambitious long-term goals of the U.S. Department of Energy's Hydrogen Program. One promising option to meet this goal is direct photoelectrolysis in which light absorbed by semiconductor-based photoelectrodes produces electrical power internally to split water into hydrogen and oxygen. Under this program, direct solar-to-chemical conversion efficiencies as high as 7.8 % have been demonstrated using low-cost, amorphous-silicon-based photoelectrodes. Detailed loss analysis models indicate that solar-to-chemical conversion greater than 10% can be achieved with amorphous-silicon-based structures optimized for hydrogen production. In this report, we describe the continuing progress in the development of thin-film catalytic/protective coatings, results of outdoor testing, and efforts to develop high efficiency, stable prototype systems.

Introduction

In 1972, Fujishima and Honda reported that n-TiO_2 photoanodes immersed in electrolyte and exposed to sunlight could provide a significant fraction of the energy needed to split water. Following their report, a serious search was undertaken by the scientific community to identify semiconductor/electrolyte systems which would split water into H_2 and O_2 with sunlight as the only energy source. Although high solar conversion efficiencies could be achieved when reversible redox couples were used (e.g., Heller et al. 1981; Rosenbluth and Lewis 1986), the effort to develop of an efficient system for production of hydrogen from an aqueous electrolyte without assistance from an external energy source was hampered by the high voltage required to dissociate water and the corrosive nature of the aqueous electrolytes. The only single photon processes demonstrated to split water without external bias employed very wide bandgap materials such as $SrTiO_3$ and $KTaO_3$ (Wrighton et al. 1977; Kraeutler and Bard 1978). Unfortunately, these materials utilize only the high energy part of the solar spectrum, resulting in low current densities and very low solar-to-chemical efficiencies.

In 1986, the development of high efficiency photoelectrochemical systems able to split water into H_2 and O_2 with sunlight as the only energy source became one of the major milestones of the Department of Energy's Hydrogen Program. Much of the effort has focused on developing "classic" photoelectrochemical cells, that is, systems in which the junction (and electric field) is produced by placing a semiconductor in direct contact with the aqueous electrolyte. Although many different semiconductors and surface treatments were explored, appropriate combinations of materials yielding both high efficiency and stability were not found.

The lack of progress in resolving these issues led to a new but somewhat controversial approach in which the higher voltage required for direct water splitting is provided by monolithically-integrated series-connected solid state solar cells in contact with the electrolyte, usually through a protective/catalytic barrier. Such systems, which operate at higher voltages than single junction devices, can utilize absorber layers of different bandgap allowing a large fraction of the solar spectrum to be used. Because the electrical fields in such systems are generated by junctions within the solid state, the requirement for intimate contact between the semiconductor and electrolyte is eliminated. This results in greater flexibility in the photoelectrode design and a wider choice of semiconductor materials and protective coatings that may be used. Concerns that the use of multiple photons to generate a single usable electron would limit the efficiency of such systems have been addressed (Rocheleau et. al. 1994), and, in fact, given reasonable projections for catalyst performance, the multiphoton systems are expected to be more efficient than the single junction, single photon systems.

The feasibility of using multijunction systems to produce hydrogen directly from water has been demonstrated in several laboratories using photoelectrodes fabricated from multijunction amorphous-silicon (Lin et al. 1989; Matsumura et al. 1986; Rocheleau et al. 1994), hybrid crystalline-amorphous silicon (Sakai et al. 1988), and crystalline III-V multijunction devices (Kocha et. al. 1994). However, program goals require that these processes operate at high efficiency, and be applicable over large areas at relatively low-cost, milestones that have not, to date, been fully met. Achieving these goals requires parallel efforts along several fronts including: (1) development of reliable models to identify optimal system and photoelectrode designs, (2) development of stable electrode/electrolyte interfaces, and (3) development and demonstration of high-efficiency, stable photoelectrochemical systems operating under realistic conditions in low cost electrolyte.

In this report, we summarize the status of engineering models developed to allow comparison of alternate technologies and design of high efficiency photoelectrode structures optimized specifically for H_2 production; describe further progress in the development of sputter-deposited, thin-film metal oxide and intermetallic catalysts for the oxygen and hydrogen evolution reactions; and report significant advances in the development of high-efficiency, amorphous silicon photoelectrodes. Notable accomplishments during the past year, include demonstration of solar-to-hydrogen conversion efficiencies of 7.8 % (based on the LHV of H_2 produced/incident sunlight) under outdoor testing, and development of low overpotential thin film catalysts which exhibit a high degree of stability in 1N KOH. Research needs for future improvements in photoelectrode efficiency and stability, and plans for development of a prototype system are also discussed.

Scope/Technical Approach

Quantitative loss analyses based on widely accepted models for photocells have been combined with models of the electrolysis reactions to determine the hydrogen production rates (the solar-to chemical conversion efficiency) of a variety of single, tandem, and triple junction structures. Semiconductor systems evaluated included low-cost amorphous silicon tandem and triple junction cells; crystalline/amorphous silicon hybrid structures; and high-cost, high-performance crystalline III-V materials. Multijunction amorphous silicon and amorphous silicon/crystalline silicon hybrid devices clearly have the greatest potential for achieving high direct solar-to-hydrogen production efficiencies at reasonable cost.

Specific materials and system design issues differ significantly depending on the choice of cell structure and electrolyte even when the choice is restricted to amorphous silicon (a-Si) or crystalline/a-Si hybrid structures. We have selected to focus on the development of prototype systems using a-Si and hybrid silicon photoelectrodes in which the light enters the semiconductor structure through the p-layer. All commercial development of amorphous silicon today utilize similar structures (light through the p-layer) to take advantage of the higher current collection and electrical efficiencies which can be achieved compared to structures which have light entering through the n-layer. Use of cells with p-type window layers thus also provides access to readily available laboratory and even commercial product for testing and will, in the long-term, result in the highest solar-to-hydrogen conversion efficiencies. We have, for the current work, further restricted ourselves to the use of alkaline electrolyte due, primarily, to the lack of adequate choices for a low overpotential, chemically stable, low cost oxygen evolution catalyst for acid medium.

Research efforts are focused on solving the critical materials issues required to develop stable, high-efficiency photoelectrodes. Activities include synthesis of high activity, stable thin-film catalytic coatings, development of semiconductor/catalyst interfaces which exhibit long-term stability in alkaline electrolyte, and demonstration of high efficiency under realistic operating conditions. Materials and interfaces are performance tested using potentiodynamic and potentiostatic measurements. Surface analysis techniques are used to examine chemical and structural characteristics of the materials, identify failure modes, and identify new materials options. Complete photoelectrodes and photoelectrochemical systems are tested outdoors.

Results

Loss Analysis

A significant finding of our early loss analysis (Rocheleau et al. 1994) was that single-junction photoelectrodes, whether based on solid-state or electrochemical junctions, require semiconductor bandgaps greater than 2.0 eV and have hydrogen production rates only about half that of the best multiphoton devices when realistic oxygen and hydrogen evolution kinetics (operating voltages of 1.5 to 1.7 volts) are considered. Below 2.0 eV, insufficient voltage is generated to operate in the high current regime required for significant hydrogen production rates. Above 2.0 eV, the maximum current is limited by the absorption spectra of the semiconductor. While photoelectrodes based on III-V crystalline materials were predicted to perform best, their exceedingly high cost makes them untenable for photoelectrolysis in which solar concentration will be limited to modest factors by mass transfer limitations at the electrolyte interface. Triple-junction amorphous silicon with high-quality, thin-film catalysts are expected to produce hydrogen at up to 50% of the maximum hydrogen production rate of the III-Vs at much lower cost, while crystalline/a-Si hybrid cells could achieve as much as 75% of the maximum. With further reduction of overpotentials, a-Si tandem cells with higher current densities (higher hydrogen production rates and efficiencies) become feasible as well.

Although providing a reasonable means for comparison of alternate materials systems, the early loss analysis models did not include optical losses or collection losses due to carrier transport properties and

so could not be used to provide engineering specifications for optimal multijunction cell designs (e.g. specification of bandgap and thickness of individual layers). A detailed phenomenological model for the a-Si devices, which accounted for these losses was developed (Rocheleau and Vierthaler 1994). Unfortunately, the early versions of this model required significant CPU time on the University workstations and were somewhat difficult to operate. During the current phase, we have modified the phenomenological model to include a more accurate optical model, have rewritten the algorithms for solution of the circuit equations significantly reducing computation time, and have integrated the model with a graphical user interface (GUI) to allow easier evaluation of alternate designs and optimization of design and operating parameters. The latest version allows quantitative analysis of the JV characteristics of solar cells and photoelectrodes to characterize critical materials properties or can be used to specify optimal designs based on the quality of the semiconductors and catalysts available (or expected). A PC-based version operating in the Windows 3.1 environment is operating in our laboratory and will be available for distribution to interested parties for use later this year.

Catalyst Development

Conventional electrochemical catalysts derive a significant activity enhancement by having high effective surface area in a porous structure, often synthesized through a high temperature sintering process. Unfortunately, these catalysts and processes may not be applicable to semiconductor photoelectrodes due to additional requirements for optical transparency, restrictions on processing temperature imposed by the semiconductor devices, and compatibility of the process itself with the semiconductor materials. Due to the critical need for improved coatings to serve as both catalysts and protective coatings, a large fraction of our efforts have been focused on developing stable high-activity catalysts with properties optimized specifically for application to photoelectrodes. To address DOE's cost goals, high cost materials such as Pt and Ir are not being considered for use.

Multijunction amorphous silicon cells are available commercially in two different configurations. Solarex Thin Film Division (and others) fabricates multijunction cells on a transparent substrate coated with a transparent conducting oxide (TCO). Solarex uses a glass/TCO/pin-pin-pin/metal configuration although some cells are also available on TCO coated plastic. In contrast, ECD fabricates their cells on stainless steel substrates yielding a SS/nip-nip-nip/CTO structure. As noted earlier, the incident light enters through the p-layer in both configurations.

The cathodic (hydrogen) catalyst which is deposited on the n-side of the devices must be stable and exhibit low overpotentials but is not, in either configuration, required to be transparent. In previous years, we reported the successful development of both electrodeposited and reactive sputter deposited Co-Mo films with very low overpotentials. The sputtered Co-Mo films which exhibited excellent uniformity, adherence, and stability have been used again this year as the counterelectrodes for testing anodic catalysts still under development and for outdoor testing of photoelectrodes.

Requirements for the anodic (oxygen) catalysts include long term electrochemical stability, low overpotential for the oxygen evolution reaction, and processing compatible with the underlying structure but requirements for transparency vary depending on the specific cell structure used. Systems using the glass/pin/pin/pin/metal configuration are likely to depend on area separation of the anodic and cathodic surfaces (See Figure 1) and hence do not rely on transmission of light through the catalyst to enter the active semiconductor layers. Systems based on the SS/nip/nip/nip/CTO cells will require a highly transparent anodic catalyst and stabilized SiC/catalyst interface.

Last year we reported significant progress in the development of transparent NiO_X anodic catalysts. During the present phase, we have achieved additional reductions in overpotential by the introduction of transition metals into the sputtered films (e.g. Fe) and have conducted detailed characterization of both the NiO_X and $NiFeO_X$ in order to understand factors controlling the optical and electrochemical properties of the films. Key results are summarized below. The detailed characterization of these materials is the subject of a Ph.D. dissertation to be published in late June and of two papers which will be submitted to the J. Electrochem. Soc. later this summer.

We previously reported that testing of the stability of the catalyst films was limited to approximately 30 hours due to degradation of the epoxy packaging used to define the electrode area. Films (and

photoelectrodes) are now characterized in test cells, shown schematically in Figure 2, which use external Teflon sealing instead of epoxy encapsulation. The new test cells allow simultaneous gas collection and measurement of half-cell potentials. The well defined geometry of the Plexiglas cells also allows characterization of resistive losses.

Figure 3 shows the current density as a function of overpotential for the sputtered $NiFe_yO_x$ films of different Fe contents. Overpotentials include all interfacial ohmic losses but not the resistive losses in the electrolyte which were subtracted from the raw current voltage measurements based on the ionic conductivity of the 1N KOH. The films were grown by reactive sputtering from metal targets in a 20% O_2/argon mixture at 10 mtorr background pressure using the apparatus previously described (Rocheleau et. al. 1995). Films with an iron content of 2% (total metals basis) exhibited the lowest overpotentials in the current range of interest for photoelectrolytic applications.

Figure 4 shows the half-cell and full-cell voltages (including electrolyte resistances) for a cell operating with a $NiFe_{.02}O_x$ anode and a sputter deposited CoMo cathode in 1N KOH made from deionized water. There is no observable degradation of the either the half-cell or full-cell voltage consistent with our last year's hypothesis that degradation was due to problems with packaging. A number of our catalyst films have been subjected to repeated 100 hour tests at fixed current without degradation. Figure 5 shows the half cell voltammetry curve for the $NiFe_{.02}O_x$ catalyst at the start and end of continuous operation for 1 month at 20mA/cm^2, again in 1N KOH from deionized water. Some small changes in overpotential are observed. In the range of current densities of interest for photoelectrolytic applications the overpotential has increased slightly while at lower current densities, the overpotentials are actually slightly lower in the final state than in the initial test. Longer term testing to confirm and characterize these changes is planned.

Of practical importance for low cost hydrogen production is stability of the electrodes in aqueous electrolytes made from more conventional water sources. Studies to characterize stability of the thin-film catalysts in 1N KOH made from less pure water sources was initiated during this report period. Efforts to operate at fixed current density using unfiltered tap water were unsuccessful. Overpotentials increased significantly in a matter of minutes due, we believe, to electrodeposition of various metals and minerals from the water.

Figure 6 shows the results of a 144 hour test using a commercial drinking water. This water, supplied by Menehune Water Company, Aiea Hawaii is well water which has been purified using a 5 micron filter and a reverse osmosis treatment. Water is then sterilized by UV light and Ozone conditioning. Fig 6 shows that both oxygen and hydrogen photoelectrodes were extremely stable during the 144 hour test. The stability of photoelectrodes in low cost purified water was one of the major achievements of this project.

Amorphous Silicon Photoelectrodes

Photoelectrodes have been fabricated using high-efficiency, triple-junction, amorphous silicon solar cells provided by the Solarex Thin Film Division. The Solarex glass/CTO/pin-pin-pin cells were approximately 10.3% efficient in the solid state under 1 sun conditions with an open-circuit voltage of 2.4 V, a short-circuit current of 6.1 mA/cm^2, and fill factor of 70. The test cells were provided as an array of 16 square devices, each 0.27 cm^2 in area. Photoelectrodes were fabricated from individual cells cut from the array with a border of several mm allowing access to the underlying CTO. The cathodic (exposed) surface was protected with a thin Ni foil catalyzed with approximately one micron of sputter-deposited Co-Mo. An electrical lead was attached to the CTO for connection to an independent anodic counterelectrode and saturated calomel reference electrode for half-cell characterization.

Last year we reported 7% solar-to-hydrogen conversion efficiency in 1N KOH from DI water. In these tests, the counterelectrode consisted of a thin Ni foil coated with sputter deposited microcrystalline NiO_x. The photoelectrodes were stable for the first 5 hours of test, degraded slowly beyond that time and exhibited a sudden failure usually around 30 hours of operation. As described under our catalyst development, the failure of the device was attributed to the failure of epoxy used in sealing the edges of the photoelectrode. During the course of the year, we also become concerned about the spectral

sensitivity of the multijunction cells used for photoelectrodes and the mismatch of our inexpensive ELH lamp with the real solar spectrum. Key goals for the most recent phase therefore included elimination of the epoxy packaging and initiation of outdoor testing of photoelectrodes to improve the accuracy of our efficiency estimates.

The cell developed for outdoor testing of the photoelectrodes is the same as that use for stability testing of the catalyst films (Figure 2). During outdoor testing, total current and evolved gas is measured. A small area, crystalline silicon solar cell is mounted to the test apparatus, close to and in the same plane as the photoelectrode to monitor insolation as a function of time. The silicon cell, calibrated at the Institute of Energy Conversion , University of Delaware, has a a short circuit current density of 24.25 mA/cm^2 at 100 mW/cm^2 of incident radiation The outdoor test apparatus is connected via low-impedance connections to a Keithley Model 236 source-measurement unit interfaced to a Macintosh LC computer running Labview software. Data are acquired every 15 seconds. Outdoor tests were conducted on both clear and partly cloudy days.

Fig. 7 shows the result of a two hour outdoor test performed between 1:00 PM and 3:00 PM on a partly cloudy day. The line shows the insolation (right ordinate) as a function of time assuming linear response of our crystalline silicon standard cell. The symbols (circles) show the measured current density between the anodic and cathodic surfaces of the photoelectrodes. The inset at the top of the figure shows the net conversion efficiency of the photoelectrode as a function of time. A conversion efficiency of 7.5% was maintained even though the combination of clouds and reflection from nearby building resulted rapid changes in insolation ranging from 32 to 128 mW/cm^2 during the test. Subsequent testing of other photoelectrodes on a clear day has yielded net solar-to-hydrogen conversion efficiencies of 7.8% during midday testing. Efficiency is lower during the late afternoon hours because of the spectral mismatch of the triple junction cells with the afternoon solar spectrum which has a reduced blue content. Detailed characterization of this effect is planned.

To date, photoelectrodes for outdoor testing have been fabricated using the glass/pinpinpin/metal cells provided by Solarex Thin Film. However, the reduced sheet resistance of the SS substrate in ECD's SS/nipnipnip cells compared to the TCO of the glass based cells does offer some potential efficiency and design advantages. Simple deposition of materials to catalyze and protect the surface of already completed cells has met with only limited success. Development of integrated p-Si/catalyst and ip/catalyst structures which are stable in the electrolyte and which are fully compatible with ECD's processing would allow incorporation of these materials into the manufacturing process. Amorphous SiC and p-type a-SiC, appropriate materials for the outer layers, have exhibited excellent corrosion resistance in both acidic and alkaline electrolytes in our initial stability tests. These materials are being grown in our Plasma Enhanced Chemical Vapor Deposition system using silane, methane, diborane, and hydrogen mixtures to allow complete electrochemical characterization of the a-SiC:H/catalyst interface. Carbon content, bandgap, and electrical properties of the a-SiC:H can be modified by changing the gas mix and process parameters to optimize chemical stability. The ability to deposit pinhole-free films will be critical as pinholes can lead to corrosion of the underlying unalloyed silicon films. A procedure to characterize the electrochemical corrosion using a scanning vibrating electrode apparatus which allows area specific characterization of the corrosion has been developed by Dr. Lloyd Hihara of the Department of Mechanical Engineering. A study of the corrosion of the a-SiC films using this technique in collaboration with Dr. Hihara has been initiated.

Summary and Plans

Direct hydrogen production with a solar-to-chemical conversion efficiency as high as 7.8% under natural sunlight has been demonstrated using photoelectrodes fabricated from triple junction amorphous silicon solar cells. There has been no observable degradation during repeated 2 hour outdoor testing. It is our intent to design, build, and operate a prototype reactor (Figure 1) which uses fully integrated photoelectrodes with no external contacts, and incorporates flowing electrolyte and larger area photoelectrodes than tested to date. The hydrogen and oxygen gas will be carried out by the flowing electrolytes and collected in separate chambers. The flowing electrolyte is also expected to improve the ionic conduction in the electrolyte and gas collection efficiency. A tentative design of such a reactor for both cell configurations is shown in Figure 1.

Increased solar to conversion efficiency requires further reduction of the overpotentials. Efforts will be focused on achieving critical catalyst properties which would allow the use of dual junction a-Si in place of the triple junction cells used in efficiency testing. The potentially higher currents of the tandem cells compared to the triple junction could lead to significant efficiency increases. We will use the coupled photovoltaic/electrolysis phenomenological models to identify catalyst and cell specifications. We will work closely with Solarex to obtain prototypes of these cells.

In the future we expect to conduct a more in-depth study of the effect of electrolyte on cell performance. The effect of electrolyte composition and concentration on efficiency and stability will be examined. Long term stability studies of catalyst and photoelectrodes in low cost electrolytes will be conducted.

The effort to develop stable a-SiC:H/catalyst structure for incorporation into the SS/nipnipnip designs will be accelerated. Portions of this work will be conducted in collaboration with John Turner (NREL) and Jan Augustynski (University of Geneve, Switzerland) under auspices of the IEA, Annex X activities.

Acknowledgments

We wish to thank the U.S. Department of Energy under Cooperative Agreement No. DE-FG04-94AL85804. We also wish to thank Dr. Liu Yang and Dr. Robert Oswald of the Solarex Thin Film Division and Dr. Xunming Deng of Energy Conversion Devices for the amorphous silicon samples used in this work. I also wish to thank Dr. Steven Hegedus at the Institute of Energy Conversion of the University of Delaware for many useful discussion during development of our models.

References

Fujishima, A., and K. Honda. 1972. *Nature*, 238:37.

Heller, A., B. Miller, and F. Thiel. 1981. *Appl. Phys. Lett.*, 38 :232

Kocha, S., M. Peterson, H. HJilal, D. Arent, and J. Turner. 1994. *Proceedings of the 1994 U.S. Department of Energy/National Renewable Energy Laboratory Hydrogen Program Review*, 301. Livermore, CA: U.S. Department of Energy and National Renewable Energy Laboratory.

Kraeutler, B. and A.J. Bard. 1978. *Journal of the American Chemical Society*, 100:4317.

Lin, G.H., M. Kapur, R.C. Kainthla, and J. O'M. Bockris. 1989. *Applied Physics Letter*, 55(4):386.

Matsumura, A.J., Y. Sakai, S. Sugahara, Y. Nakato, and H. Tsubomura. 1986. *Solar Energy Materials*, 12:57.

Rocheleau, R.E. , Z. Zhang, E. Miller, and Q. Gao. 1994. *Proceedings of the 1994 U.S. Department of Energy/National Renewable Energy Laboratory Hydrogen Program Review*, 335. Livermore, CA: U.S. Department of Energy and National Renewable Energy Laboratory.

Rocheleau, R.E., Z. Zhang, E. Miller, and M. Vierthaler. 1994. "Photoelectrochemical Production of Hydrogen: Engineering Loss Analysis." *Hydrogen Energy Progress X*, 2:737-746, D.L. Block and T. Veziroglu (eds.) Pergammon Press.

Rocheleau, R.E., and M. Vierthaler. 1994. "Optimization of Multijunction a-Si:H Solar Cells Using an Integrated Optical/Electrical Model." *Proceedings of the 21st World Conference on Photovoltaic Energy Conversion* (in press). New York: IEEE.

Rocheleau, R.E. , E. Miller, and Z. Zhang. 1995. *Proceedings of the 1995 U.S. Department of Energy Hydrogen Program Review*, 605. Coral Gables FL: National Renewable Energy Laboratory.

Rosenbluth, M., and N.S. Lewis. 1986. *Journal of the American Chemical Society*, 108:4689.

Sakai, Y., S. Sugahara, M. Matsumura, Y. Nakato, and H. Tsubomura. 1988. *Canadian Journal of Chemistry*, 66:1853.

Wrighton, M.S., P.T. Wolczanski, and A.B. Ellis. 1977. *Journal of Solid State Chemistry*, 22:17.

Figures

Figure 1. Schematic of a H2 photoelectrolysis cell using multijunction amorphous silicon photoelectodes. Schematic shows fully integrated anodic and cathodic surfaces with flowing electrolyte.

Figure 2. Teflon sealed reactors used for catalyst characterization and outdoor testing of photoelectrodes.

Figure 3. Half-cell overpotentials of sputter-deposited $NiFe_yOx$ in 1N KOH with up to 5.6% Fe (metals basis)

Figure 4. Stability test of sputter deposited $NiFe_{.02}O_x$ anodes and CoMo cathodes in 1N KOH at a constant current density of 20 mA/cm^2.

Figure 5. Half-Cell overpotential of a $NiFe_{.02}O_x$ anode as-deposited and following one month of continuous operation at a current density of $20mA/cm^2$

Figure 6. Comparison of the half-cell and full-cell potentials required to maintain constant current density of $20ma/cm^2$ with sputter deposited $NiFe_{.02}O_x$ anodes and CoMo cathodes in 1N KOH from DI water and from purified drinking water.

Figure 7. Solar to hydrogen conversion efficiency of a photoelectrolysis cell using a multijunction amorphous silicon photoelectrode based on photoelectrode current density (circles) during a two hour outdoor test on a partly cloudy day (insolation shown by line. Inset at top shows solar-to-hydrogen conversion efficiency based on measured current density and LHV of hydrogen.

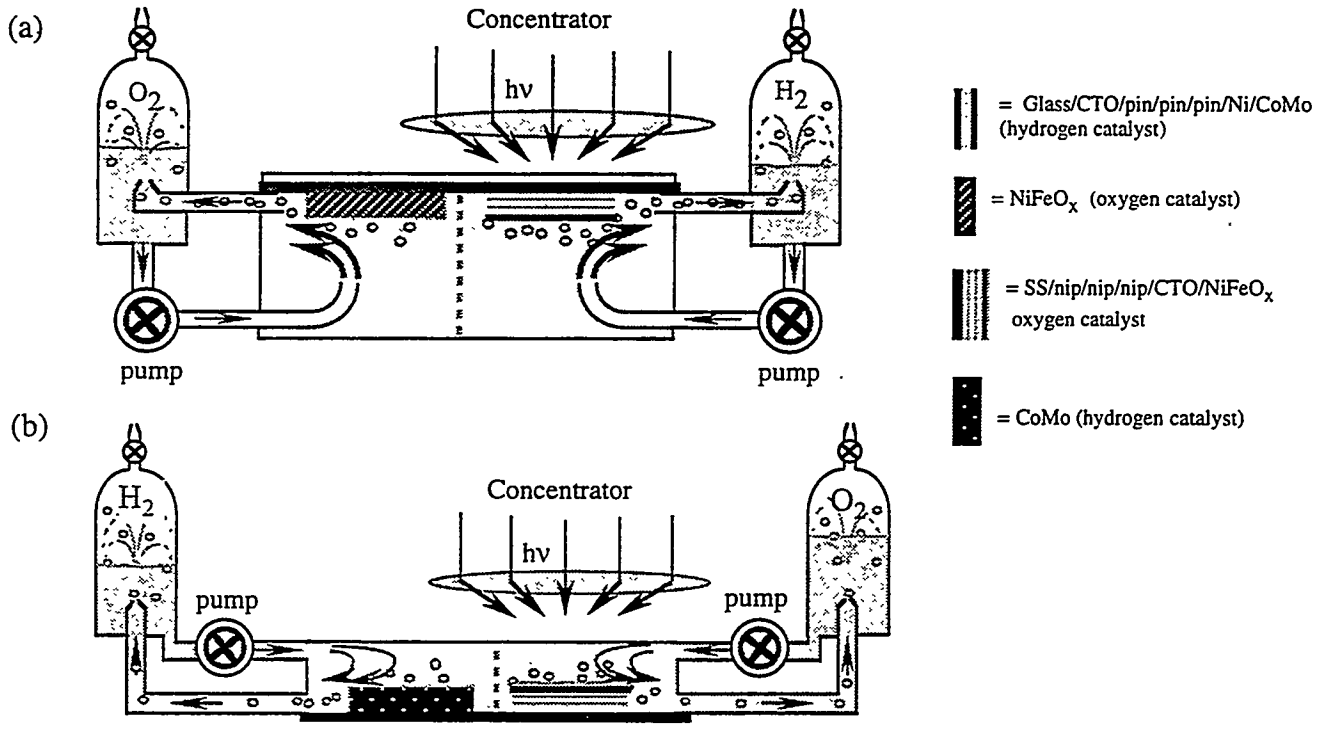

(a)
Concentrator
hν
O_2
H_2
pump
pump
= Glass/CTO/pin/pin/pin/Ni/CoMo (hydrogen catalyst)
= $NiFeO_x$ (oxygen catalyst)
= SS/nip/nip/nip/CTO/$NiFeO_x$ oxygen catalyst
= CoMo (hydrogen catalyst)
(b)
H_2
Concentrator
hν
O_2
pump
pump

Fig. 1

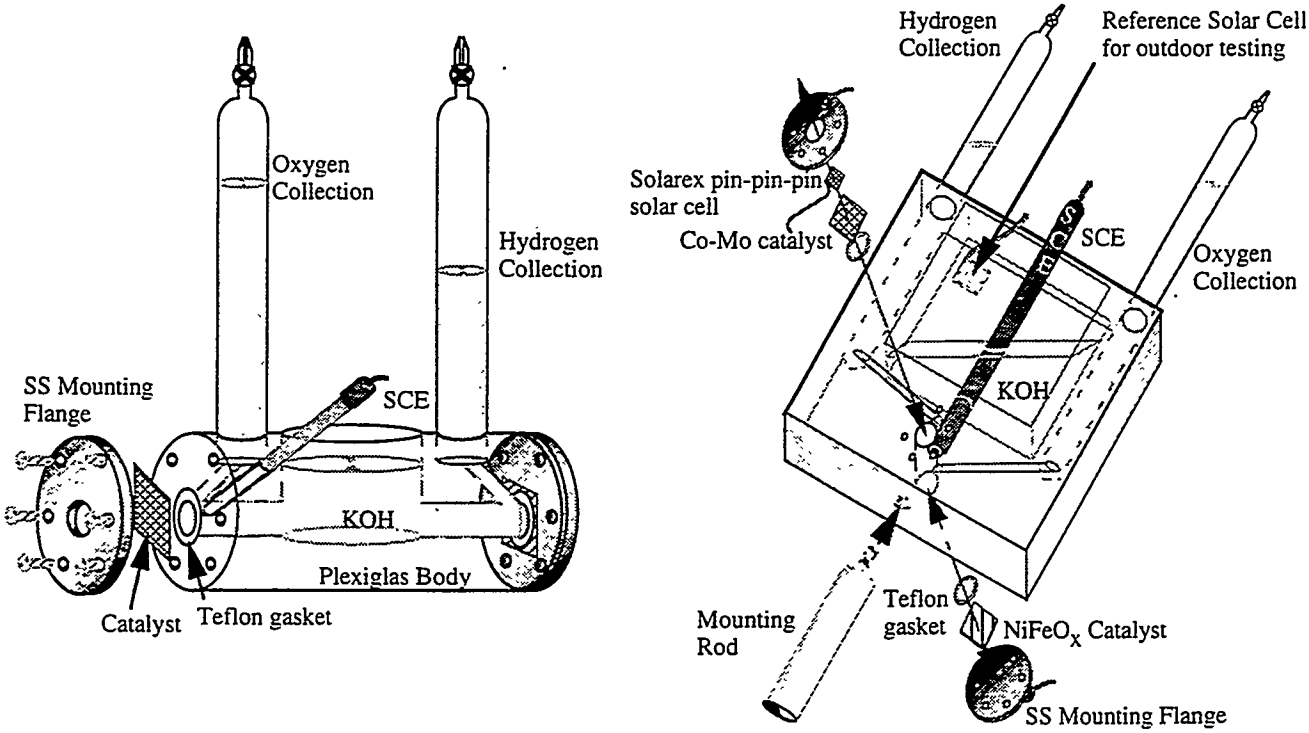

Oxygen Collection
Hydrogen Collection
SS Mounting Flange
SCE
KOH
Plexiglas Body
Catalyst
Teflon gasket
Hydrogen Collection
Reference Solar Cell for outdoor testing
Solarex pin-pin-pin solar cell
Co-Mo catalyst
SCE
Oxygen Collection
KOH
Mounting Rod
Teflon gasket
$NiFeO_x$ Catalyst
SS Mounting Flange

Fig. 2

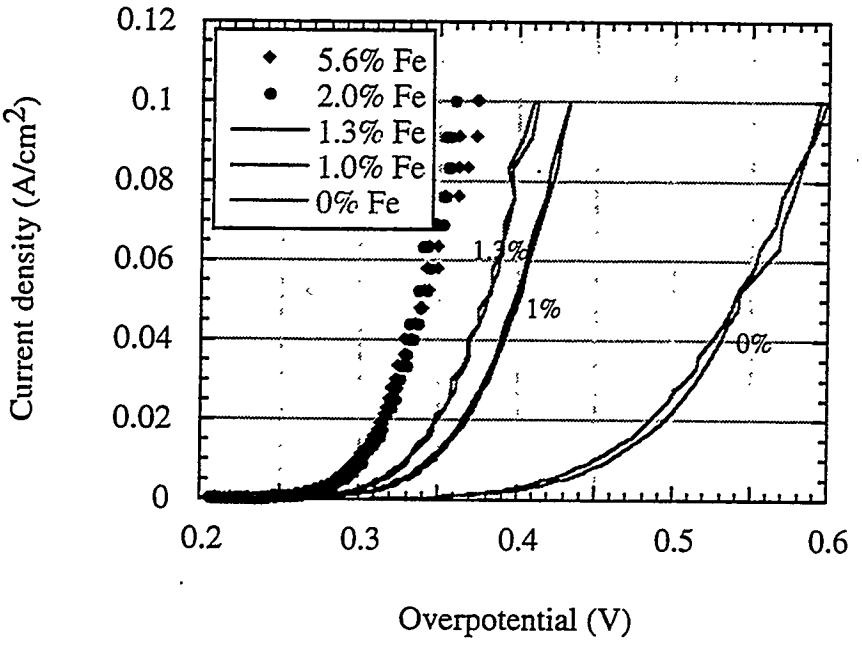

0.12
0.1
0.08
0.06
0.04
0.02
0
Current density (A/cm2)
5.6% Fe
2.0% Fe
1.3% Fe
1.0% Fe
0% Fe
1.3%
1%
0%
0.2
0.3
0.4
0.5
0.6
Overpotential (V)

Fig. 3

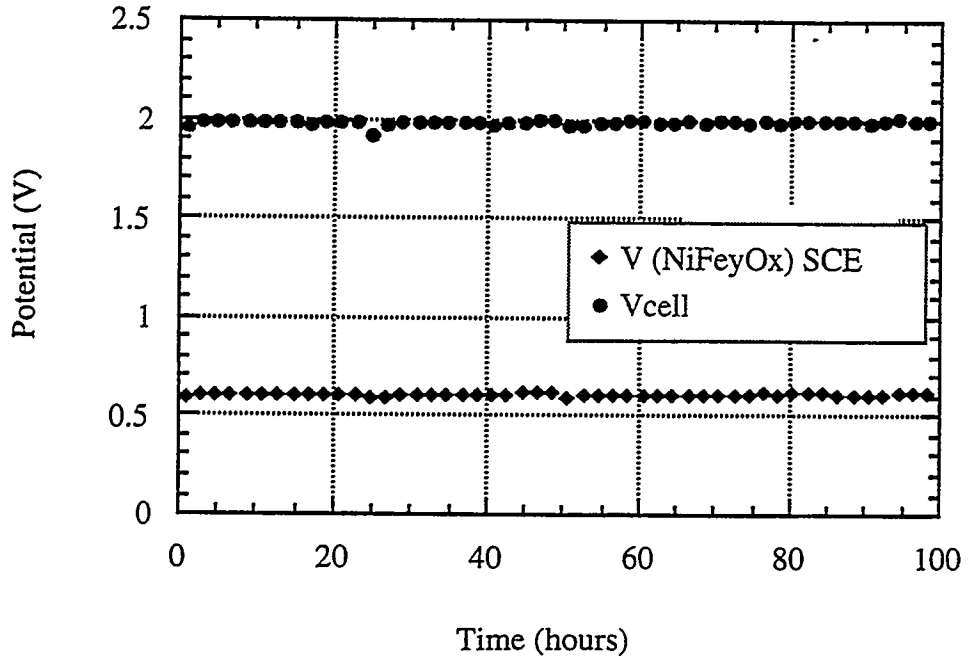

2.5
2
1.5
1
0.5
0
Potential (V)
V (NiFeyOx) SCE
Vcell
0
20
40
60
80
100
Time (hours)

Fig. 4

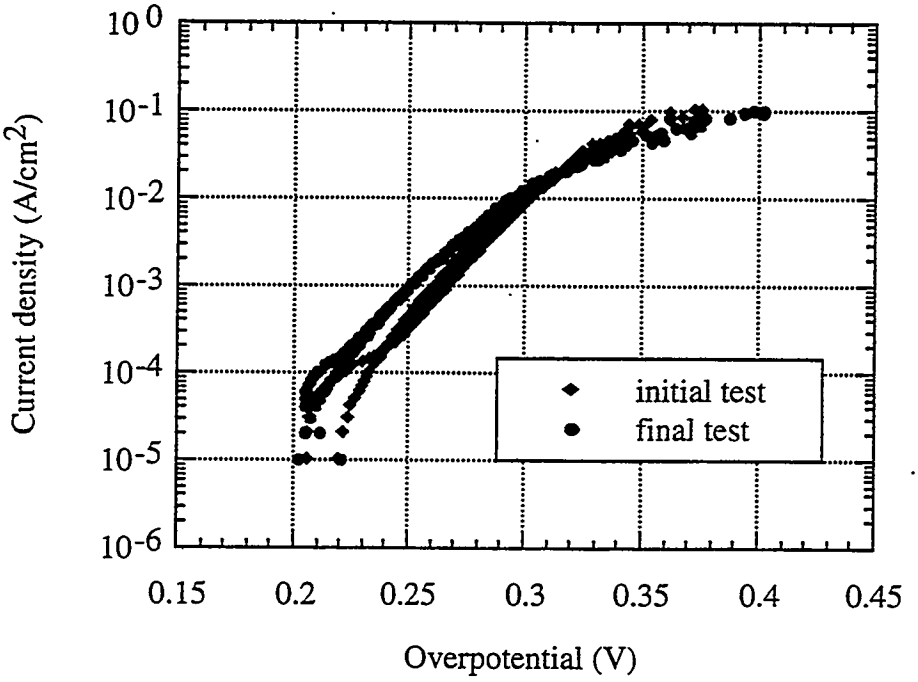

Current density (A/cm2)
10 0
10-1
10-2
10-3
10-4
10-5
10-6
0.15
0.2
0.25
0.3
0.35
0.4
0.45
Overpotential (V)
initial test
final test

Fig. 5

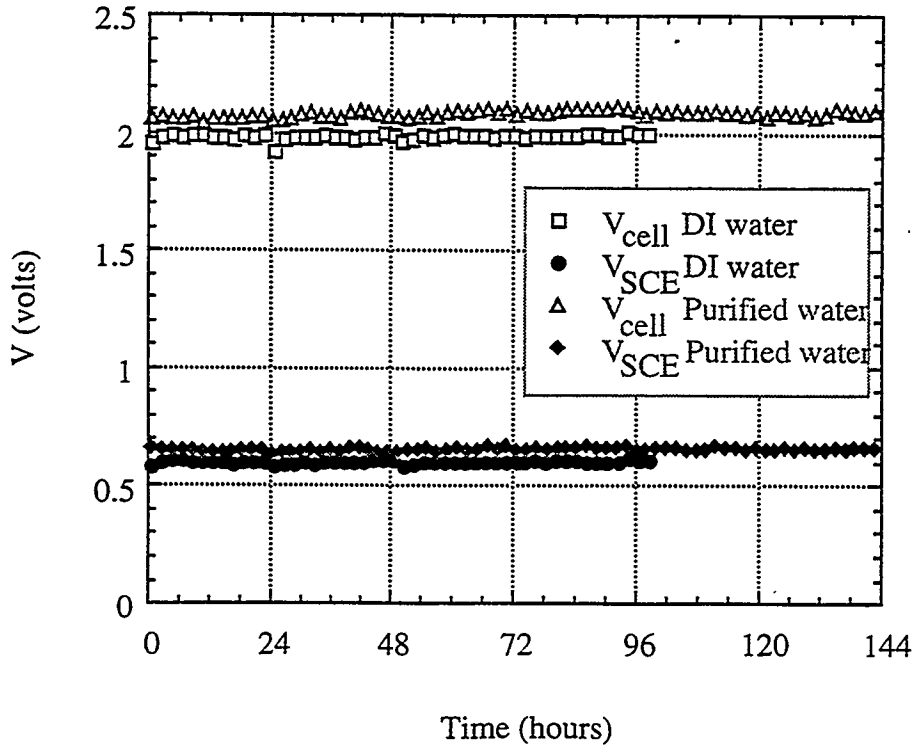

V (volts)
2.5
2
1.5
1
0.5
0
0
24
48
72
96
120
144
Time (hours)
Vcell DI water
VSCE DI water
Vcell Purified water
VSCE Purified water

Fig. 6

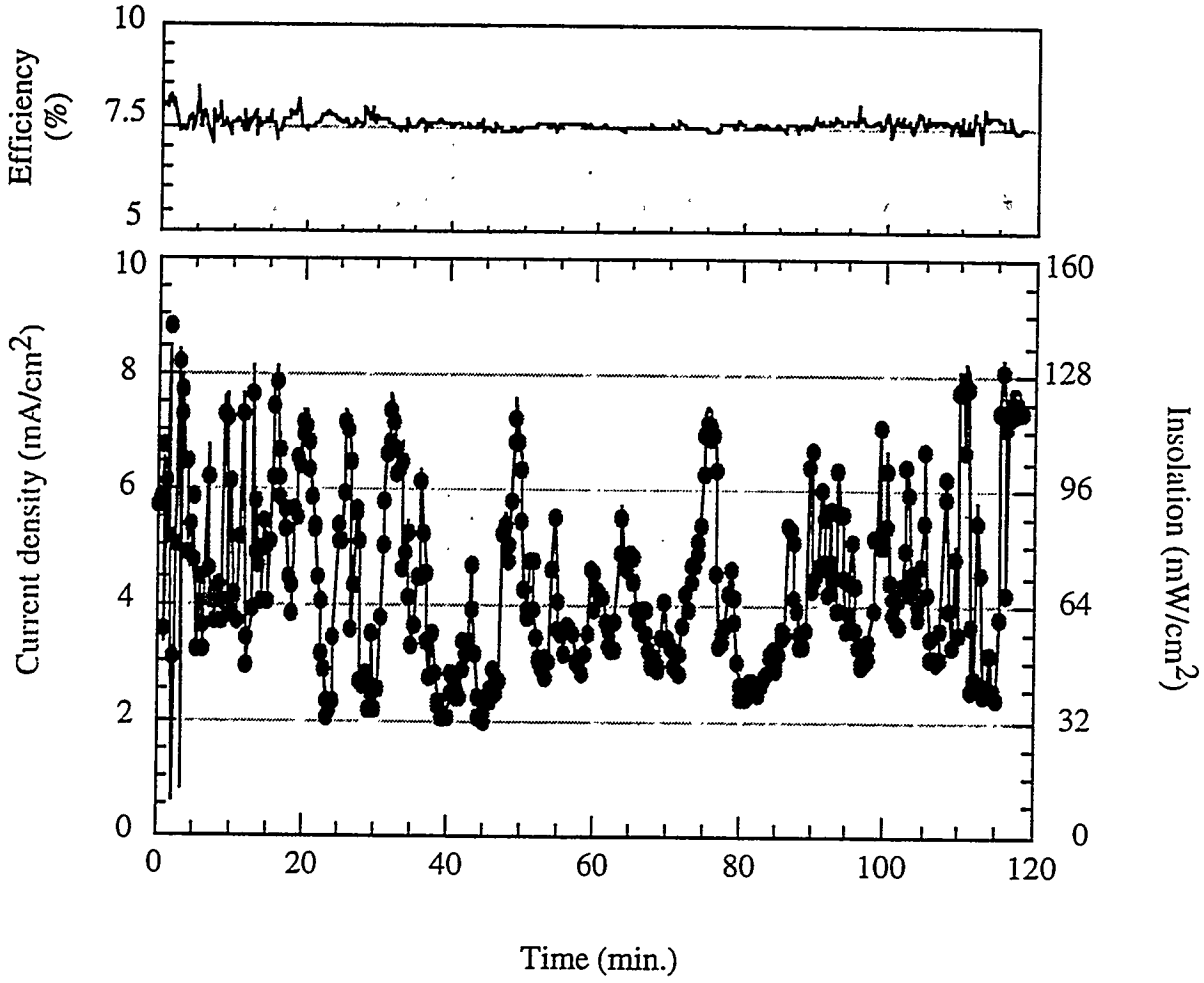

Efficiency (%)
10
7.5
5
Current density (mA/cm2)
10
8
6
4
2
0
Insolation (mW/cm2)
160
128
96
64
32
0
0
20
40
60
80
100
120
Time (min.)

Fig 7

PHOTOVOLTAIC HYDROGEN PRODUCTION

H. W. Hiser, S. B. Memory, T. N. Veziroğlu and J. Padin
University of Miami
Coral Gables, FL 33124, U.S.A.

ABSTRACT

This is a new project, which started in June 1995, and involves photovoltaic hydrogen production as a fuel production method for the future. In order to increase the hydrogen yield, it was decided to use hybrid solar collectors to generate D.C. electricity, as well as high temperature steam for input to the electrolyzer. In this way, some of the energy needed to dissociate the water is supplied in the form of heat (or low grade energy), to generate steam, which results in a reduction of electrical energy (or high grade energy) needed. As a result, solar to hydrogen conversion efficiency is increased.

In the above stated system, the collector location, the collector tracking sub-system (i.e., orientation/rotation), and the steam temperature have been taken as variables. Five locations selected - in order to consider a variety of latitudes, altitudes, cloud coverage and atmospheric conditions - are Atlanta, Denver, Miami, Phoenix and Salt Lake City. Plain PV and hybrid solar collectors for a stationary south facing system and five different collector rotation systems have been analyzed. Steam temperatures have been varied between 200°C and 1200°C.

During the first year, solar to hydrogen conversion efficiencies have been considered. The results show that higher steam temperatures, 2 dimensional tracking system, higher elevations and dryer climates causes higher conversion efficiencies. Cost effectiveness of the sub-systems and of the overall system will be analyzed during the second year. Also, initial studies will be made of an advanced high efficiency hybrid solar hydrogen production system.

INTRODUCTION

There are two important global issues facing mankind: Depletion of fossil fuels and environmental problems caused by the combustion of fossil fuels. Fossil fuels today meet about 80% of our energy requirement. However, they are being depleted fast. According to the best estimates, petroleum production and natural gas production will peak early 2000s, and will then start to decline. Coal

deposits will last longer. It is possible to manufacture synthetic gasoline and synthetic natural gas from coal. However, we may not be able to use all the coal resources because of the environmental complications.

Combustion products of fossil fuels produce pollution, acid rains, global warming and ozone layer depletion. According to our studies at the University of Miami's Clean Energy Research Institute, the worldwide environmental damage caused by fossil fuels will be $ 2,600 billion for this year alone, which is about 14% of the Gross World Product. This is a very large figure. Conversion to clean energy sources and carriers would enable the world to save this enormous sum, and perhaps use it to improve the quality of life throughout the planet Earth - not only for humans, but also for its flora and fauna, as well.

Because of the foregoing, there is a need for new and environmentally compatible primary energy sources and energy carriers. Studies show that this condition is best met by hydrogen, a clean and efficient energy carrier, produced using solar energy, an environmentally compatible and renewable primary energy source. A solar hydrogen energy system could meet the energy requirements of the world, as well as that of the United States, forever or at least as long as the sun exists.

In the solar hydrogen energy system, it is important that hydrogen must be produced as efficiently as possible, and as economically as possible. The first year's study concentrates on obtaining the best efficiency, and the second year's study will concentrate on cost optimization.

APPROACH AND RATIONALE

In the electrolysis of water, it is well known that as the water temperature increases, electrical energy required to electrolyze the water decreases. If high temperature steam is used instead of high temperature water, the electrical energy needed for electrolysis further decreases. Low grade thermal energy is used in order to reduce the amount of high grade electrical energy.

In a PV collector only electricity (d.c. electricity) is produced. However, using a hybrid solar collector, one could produce both electricity and heat, thereby increasing the overall conversion efficiency. Hence, it becomes quite convenient to match a solar hybrid collector with a high temperature steam electrolyser in order to increase the solar to hydrogen conversion efficiencies. It has therefore been decided to investigate a hybrid collector/high temperature electrolyser system for solar hydrogen production, in order to come up with an efficient, clean and sustainable energy system.

SOLAR HYDROGEN PRODUCTION SYSTEM

Fig. 1 is a schematic of the solar hydrogen production system investigated. It consists of a solar hybrid collector, electricity storage sub-system, power regulator, high temperature steam storage sub-system and a high temperature steam electrolyser. As raw material, water is supplied to the system, and the products are hydrogen, oxygen and high temperature steam.

Fig. 2 is a schematic of a possible solar hybrid collector. Relatively high temperature PV cells, such as GaAs, are to be wrapped around the water/steam tubes located along the focal axis of each parabola (Sharan et al 1987). The tubes could be single flow or possibly counter flow to produce a more uniform temperature for the PV cells mounted on them (Sopian et al 1995). A cover over the collector can be used to reduce losses from the water/steam tubes. Also, it may be possible to use a transparent thin film PV membrane on the upper surface of this cover in order to increase the overall electrical production (Seidenfaden 1995).

In a hybrid collector, solar radiation of certain wavelengths can be converted to D.C. electricity with efficiencies of 5 to 30%, depending on the photovoltaic material and temperature. The remainder of the solar radiation (viz., 70 to 95%) can be converted to heat with higher efficiencies (e.g., 50%), and this heat can be used to produce high temperature steam in parabolic through type collectors.

In this system study, five different collector rotation systems have been selected as suitable for use with two dimensional hybrid parabolic collectors. Four systems rotate around a single axis, and the fifth system rotates around two axes, so that the collector is always facing the sun (See Fig. 3).

The electrical storage sub-system, in order to provide for a 24 hour operation, could use batteries, hydro, fly wheel, compressed air, etc. The high temperature storage sub-system should be well insulated.

In order to see the effect of location (latitude, elevation, humidity, wind speed and cloud coverage), five locations have been selected. They are: Atlanta, Georgia; Denver, Colorado; Miami, Florida; Phoenix, Arizona; and Salt Lake City, Utah. The steam temperatures have been varied between 200°C and 1200°C.

ANALYSIS

Solar Insolation:

In order to make comparisons of collector mounting axes and rotation as they affect incident annual solar energy and production

efficiencies of hydrogen, oxygen and excess heat, it is necessary to define collector orientation angles. Fig. 4 presents the collector orientation angle definitions relative to a horizontal surface tangent to the earth at the collector location. Note that for a sun-tracking collector, the collector angle would equal the solar elevation angle. Also, the collector azimuth angle γ would equal the solar azimuth angle γ_s.

Insolation Equations:

In this sub-section, the equations defining the insolation impinging on the collector area are presented. The total annual solar energy impinging on the receiver or collector (E_s) is made up of a direct component (I_{dr}), a diffuse component (I_{df}) and a ground reflected component (I_{re}), i.e.,

$$E_s = A_c \sum_{N=1}^{365} \int_{tr}^{ts} m_i (I_{dr} + I_{df} + I_{re}) dt \qquad (1)$$

where A_c is the collector area, n is the day, i is the augmentation factor due to ith-type tracking system, I_{dr} and I_{re} are the components of solar radiation, t_s and t_r are the sunset and sunrise hours, and t the time.

Direct component of solar radiation is given by

$$I_{dr} = I_b R_b \qquad (2)$$

where R_b is the geometric factor, and I_b is the beam radiation on a horizontal surface.

Diffuse radiation, I_{df}, has three components: isotropic diffuse sky dome radiation, circumsolar diffuse radiation and horizon diffuse radiation (Duffie and Beckman 1991), and can be expressed as

$$I_{df} = I_{df,sd} + I_{df,cr} + I_{df,hd} \qquad (3)$$

where radiation from sky dome,

$$I_{df,sd} = I_d(1-F_1)\ (1+\mathrm{Cos}(\beta))/2 \qquad (4)$$

circumsolar radiation,

$$I_{df,cr} = I_d F_1 a/b \quad (5)$$

horizon diffuse radiation,

$$I_{df,\,hd} = I_d F_2 \mathrm{Sin}(\beta) \quad (6)$$

Also, I_d is the radiation on a horizontal surface; ß is the surface elevation angle depending on tracking system; F_1 and F_2 are the circumsolar and horizon brightness coefficients; and a and b are the angles of incidence parameters for the cone of circumsolar radiation.

Ground reflected component of solar radiation is given by,

$$I_{re} = I\rho(1 - \mathrm{Cos}(\beta))/2 \quad (7)$$

where ρ is the ground reflectivity and I is the total insolation on a horizontal surface. Fig. 5 presents a schematic of the solar radiation components given above, which are impinging on a solar collector.

Hybrid Collector Energy Conversion:

In the hybrid collector, solar radiation is converted both to electrical and thermal energies. Annual electricity production is given by,

$$E_{ce} = \eta_{ce} A_c E_s \quad (8)$$

where η_{ce} is the electrical energy conversion efficiency for the collector.

Annual thermal energy production is given by,

$$E_{ct} = \eta_{ct} A_c E_s \quad (9)$$

where η_{ct} is the thermal energy conversion efficiency. Then, the total annual energy conversion rate for the collector becomes,

$$E_c = (\eta_{ct} + \eta_{ce}) A_c E_s \quad (10)$$

Energy Entering Electrolyser:

Electrical and thermal energies produced in the collector follow two paths on the way to the electrolyser. Electricity goes either directly to the power regulator or to the electrical storage to be used during the periods of insufficient (or no) PV electricity generation. From the power regulator electricity is supplied to the high temperature electrolyser.

Annual electrical energy entering the electrolyser is given by,

$$E_{ee} = \eta_{se}\eta_{re}E_{ce} \qquad (11)$$

where η_{se} is the electrical energy storage efficiency, and η_{re} is the electrical power regulator efficiency.

High temperature steam produced in the collector enters the thermal storage sub-system, where water is used to regulate the steam temperature. Steam at the desired temperature and quantity then enters the electrolyser. Because of the discrepancies between the electrical and thermal conversion efficiencies of the solar collector, and the electrical and thermal requirements of the electrolyser, there is always more steam produced than the amount which can be electrolysed. Excess steam then becomes available for various residential, commercial and/or industrial applications.

Annual thermal energy (steam energy) entering the electrolyser becomes,

$$E_{et} = \eta_{st}\eta_{rt}\,(e_{et}/e_{ee})\,E_{ce} \qquad (12)$$

where η_{st} is the thermal energy storage efficiency, η_{rt} is the thermal energy regulating efficiency, e_{et} is the thermal energy requirement of the electrolyser per unit mass of steam and e_{ee} is the electrical energy requirement of the electrolyser per unit mass of steam.

Total energy supplied to the electrolyser per year becomes,

$$E_e = (\eta_{se}\eta_{re} + \eta_{st}\eta_{rt}\,(e_{et}/e_{ee}))E_{ce} \qquad (13)$$

Then the excess thermal energy available per year is given by,

$$E_h = \eta_{st}\,(E_{ct} - E_{et}) \qquad (14)$$

High Temperature Electrolyser Characteristics:

Fig. 6 presents the electrical energy (high grade energy) and the thermal energy (low grade energy) requirements of a steam electrolyser as a function of steam temperature. It can be seen that as the steam temperature rises thermal energy requirement increases and electrical energy requirement decreases. The pertinent relationships are presented here below.

The electrical energy (high grade energy) requirement per unit mass of steam is defined as,

$$e_{ee} = e_{ee,373} + S_e(T_e - 373) \ldots (= \Delta G) \quad (15)$$

The thermal energy (low grade energy) requirement per unit mass of steam is defined as,

$$e_{et} = e_{et,373} + S_t(T_e - 373) \ldots (= T\Delta S) \quad (16)$$

The total energy requirement of electrolyser is given as,

$$e_e = e_{ee,373} + e_{et,373} + (S_e + S_t)(T_e - 373) \ldots (= \Delta G + T\Delta S) \quad (17)$$

where S_e is the change in electrical energy requirement of the electcrolyser per unit mass of steam per unit temperature difference (de_{ee}/dT), ΔG is the free energy change, T is the absolute temperature, S_t is the change in thermal energy requirement of the electrolyser per unit mass of steam per unit temperature difference (de_{ct}/dT), ΔS is the entropy change.

Fig. 7 shows the mismatch between the electrical and thermal energies produced at the hybrid collector in one hand, and those required at the electrolyser in the other hand for an electrolyser temperature of 1000 °C. It can be seen that whereas the E_{therm}/E_{elect} ratio at the collector is 1.80, it is 0.45 for the electrolyser. Hence, there is always some excess heat produced, which increases with the energy generation.

Hydrogen, Oxygen and Excess Heat Production Rates:

At the electrolyser, annual hydrogen and oxygen production are given by,

$$\dot{m}_{H2} = \eta_e E_e/9e_e \quad (18)$$

and

$$\dot{m}_{02} = \eta_e 8E_e/9e_e \quad (19)$$

where η_e is the electrolyser efficiency, and $\dot{m}$ is the annual amount (mass) produced.

At the thermal storage, the annual amount of excess heat (in terms of energy) available is given by,

$$E_h = \eta_{st} (E_{ct} - E_{et}) \quad (20)$$

where η_{st} is the thermal energy storage efficiency, E_{ct} is the thermal energy production per year in the hybrid collector, and E_{et} is the thermal energy entering the electrolyser per year.

EVALUATION AND DISCUSSION

In calculating the annual hydrogen, oxygen and excess heat production rates, various conversion efficiencies included in the above equations are needed. It should be pointed out that the calculations are to be made for the early 2000s. The conversion efficiencies selected for such a time are presented in Table I. They are considered to be quite reasonable.

The augmentation factors m_i have been calculated using the formula presented in (Duffie and Beckman 1991) for various collector rotations. The atmospheric data needed, i.e., insolation, wind speed and direction, dew point temperature, dry bulb temperature, ambient temperature and snow depth, for the five cities selected have been obtained from the TMY2 files, down loaded from the National Renewable Energy Laboratory's data bank.

Using the above stated data together with the equations (1) through (20), annual insolation, hydrogen, oxygen and excess heat production rates for the five tracking systems and the five cities selected, and for various steam temperature levels, together with the pertinent efficiencies have been calculated. The results are presented in Tables II through VI.

Table II presents the insolation results for the five tracking systems plus the stationary system, for Miami. It can be seen that the annual insolation received per square meter of collector area ranges from a minimum of 2014 kW.hr for the stationary system to a

maximum of 2910 kW.hr for the 2D tracking system. The second best tracking system is the 1D system with the axis of rotation parallel to the Earth's north-south axis, followed by the 1D system with a horizontal axis parallel to the local north-south direction. The last two columns of Table III presents the difference in insolation and the percent improvements with respect to the insolation for the stationary collector. It can be seen that the 2D system is 45% more efficient, followed by the 1D north-south axis system with 36% more efficiency.

The percentage improvements for the other cities (for any location for that matter) would be the same, although actual insolation would differ from location to location.

Table III presents the annual hydrogen, oxygen and excess heat production rates for plain PV and hybrid collectors, and six tracking systems for Miami. The collector area is 1 m^2 and the electrolyser temperature 1000°C. It can be seen that the hydrogen production rates (and for that matter the oxygen production rates) follow the insolation rates, i.e., 2D tracking system gives the highest rates, followed by 1D system with the axis parallel to the north-south axis of Earth. The stationary system gives the lowest rates, as expected.

When plain PV and hybrid collectors are compared regarding hydrogen and oxygen production rates, hybrid collectors are about 57% more efficient.

Excess heat produced by the hybrid collectors follow the same trend as the hydrogen/oxygen production rates, i.e., 2D tracking system giving the best result, followed by the 1D system with axis parallel to the north-south axis of Earth.

Local efficiencies have been calculated for "hydrogen" and for "hydrogen + excess heat" based on the local insolation. For plain PV collectors, they are 17%, as there is no heat generation. For hybrid collectors, hydrogen production efficiency is 27% (58% higher than the plain PV case), and the total energy (hydrogen + excess heat) production efficiency is 50%. The last column in Table III, gives the efficiencies based on the 2D tracking system. In this case the efficiencies follow the insolation rates, the best being those for 2D system.

Table IV presents the annual averages for the meteorological conditions (i.e., temperature, wind, humidity, clearness and insolation) for the five locations considered. Table V presents hydrogen, oxygen and excess heat production rates for the plain PV and hybrid collectors, for the same locations. The tracking system is the 2D system, collector area 1 m^2 and the electrolyser temperature 1000°C. It can be seen that the location with higher insolation, higher clearness index, lower humidity and lower wind

speed (i.e., Phoenix) gives the best production rates. Hence, in the last column of Table V, the locations selected have been compared with Phoenix. It can be seen that the second best location is Salt Lake City, followed by Atlanta and Denver tying for third place. Although Miami is the most southerly location, higher humidity and higher wind speed (i.e., higher collector losses) make it a close fourth.

Table VI presents the production rates as a function of the steam temperature. The location is Miami, collector area 1 m^2 and the tracking system 2D. It can be seen that the hydrogen and oxygen production rates increase with increasing steam (or electrolyser) temperatures. The excess heat production rate decreases with increase in temperatures, as more of the heat produced is outlined in the electrolyser.

CONCLUSIONS

As a result of this investigation the following conclusions are reached:

1. Hydrogen (and oxygen) production rates are greater for hybrid collectors than those for plain PV collectors. In the case studied, hybrid collectors are 59% more efficient.

2. Hybrid collectors also produce excess (useful) heat. In the case studied, excess heat generation ranged from 16% of the insolation for a stationary collector to 23% for a 2D tracking system.

3. When the tracking systems are compared, 2D system is the best, followed by the 1D system with the axis parallel to the north-south axis of Earth. For the system studied, in comparing hydrogen production, only the 2D system was 42% more efficient than the stationary system. The ratio was the same for the excess heat generation.

4. Locations with higher insolation, higher clearness index, lower humidity, lower wind velocity and higher ambient temperature are better suited for increased hydrogen/excess heat production.

WORK PROPOSED FOR NEXT YEAR

The work proposed for the next year is divided into two parts: (A) cost studies for the hybrid collector/high temperature hydrogen production system, and (B) Initial studies for a super efficiency solar hydrogen production system.

A. **Costing of Present System:** This will cover the following studies.

1. Types of hybrid collectors - related costs,

2. Types of electricity storage sub-systems - related costs,

3. Types of thermal storage sub-systems - related costs,

4. Types of electrolysers - related costs,

5. Overall systems and related costs,

6. Comparisons (environmental and economic).

B. Initial Studies for Super Efficient System:

Fig. 8 presents the proposed super efficient solar hydrogen system. In this system, part of the excess heat is used for D.C. electricity generation through a heat engine/generator combination, and the rest is used as the high temperature steam for additional hydrogen production.

The study will cover the following items:

1. Efficiency studies for sub-systems,

2. Efficiency for overall system.

BIBLIOGRAPHY AND REFERENCES

Books:

Duffie J.A. and Beckman W.A. 1991. Solar Engineering Of Thermal Processes. John Wiley & Sons Inc.

Fraas P.A. and Ozisik N.M. 1965. Heat Exchange Design. John Wiley and Sons.

Hornbeck W.R. 1975. Numerical Methods. Prentice-Hall, Inc.

Incropera P.F. and Witt D.P. 1990. Fundamentals of Heat and Mass Transfer. John Wiley and Sons.

Jet Propulsion Laboratory. 1976. Solar Cell Array Design Handbook. California Institute Of Technology, Pasadena, California. Vol. 2.

Justi E.W. 1987. A solar-Hydrogen Energy System. Plenum Press.

Kakac S. 1991. Boilers, Evaporators and Condensers. John Wiley and Sons.

Kakac S. and Yener Y. 1993. Heat Conduction. Taylor and Francis.

Kays M.W. and Crawford M.E. 1993. Convective Heat Transfer., McGraw-Hill.

Kraus A.D. and Avram B.C. 1995. Design and Analysis Of Heat Sinks. Wiley & Sons.

Luke Y.L. 1962. Integral Of Bessel Functions. McGraw-Hill.

Mills A.F. 1992. Heat Transfer. Irwin.

Moran M.J. 1990. Availability Analysis. ASME.

Shapiro H.N. and Moran M.J. 1988. Fundamentals of Thermodynamics. John Wiley and Sons.

Stull R.B. 1988. An Introduction To Boundary Layer Meteorology. Kluwer Academic Publishers.

Young D.M. and Gregory R.T. 1988. A Survey of Numerical Mathematics - Volume 1. Dover Publications, Inc.

Young D.M. and Gregory R.T. 1988. A survey of Numerical Mathematics - Volume 2. Dover Publications, Inc.

Journal Articles:

Abdul F. and Hamad W. 1988. "The Performance of a Cylindrical Parabolic Solar Concentrator". Energy Conversion Management, Vol. 28, No. 3 pp. 251-256.

Alkan C. Sekerci M. and Kunc S. 1995. "Production of Hydrogen Using Fresnel Lens-Solar Electrochemical Cell". Int. J. Hydrogen Energy, Vol. 20, No 1, pp. 17-20.

Anis R.W. and Nour A.S. 1995. "Energy Losses In Photovoltaic Systems". Energy Conversion Management, Vol. 36, No. 11, pp. 1107-1113.

Barra L. and Coiante D. 1993. "Energy Cost Analysis For Hydrogen-Photovoltaic Stand-Alone Power Stations". Int. J. Hydrogen Energy, Vol. 18, No. 8, pp. 685-693.

Barra L. and Coiante D. 1993. "Hydrogen-Photovoltaic Stand-Alone Power Stations: A Sizing Method". Int. J. Hydrogen Energy, Vol. 18, No. 4, pp. 337-344.

Bertness K.A., Sarah K.R., Friedman D.J. and Kibbler E.A. 1995. "29.5%-efficient GaInP/GaAs Tandem Solar Cells". Applied Physics Letter, Vol. 65, No. 8, pp. 989-991.

Carlson D.E. 1995. "Recent Advances In Photovoltaics". IECEP Paper No. RE-414, ASME.

Chiu D.M. 1995. "Thermopower Of Amorphous Chalcogenides Under Photoexciation". IECEC Paper No. RE-238, ASME.

Clark D.R., Klein S.A., and Beckman W.A. 1983. "Algorithm For Evaluating The Hourly Radiation Utilizability Function". J. of Solar Energy, Vol. 105, pp. 281-287.

Contreras M.A. , Gabor A.M., Tennant A.L., Asher S., Tuttle J., and Noufi R. 1994. "16.4% Total-area Conversion Efficiency Thin-film Polycrystalline MgF_2/ZnO/CdS/Cu(In, Ga) Se_2/Mo Solar Cell". Progress in Photovoltaics: Research and Applications, Vol. 2, pp. 287-292.

Eljrushi G.S. and Zubia J.N. 1994. Solar Hydrogen: "The Great Sahara Project". Int. J. Hydrogen Energy, Vol. 19, No., 3 pp. 215-218.

Evans D.L. 1981. "Simplified Method For Predicting Photovoltaic Array Output". Solar Energy, Vol. 27, No. 6 pp. 555-560.

Evans D.L. and Florschuetz L.W. 1977. "Cost Studies On Terrestrial Photovoltaic Power Systems With Sunlight Concentration". Solar Energy, Vol. 19, pp. 255-262.

Garg. et. al. 1995. "Indian Institute of Technology Hybrid Collector". Energy Conversion and Management, Vol. 36, No. 2, pp. 87-99.

Hassmann K. and Kuhne H.M. 1993. "Primary Energy Sources For Hydrogen Production". Int. J. Hydrogen Energy, Vol. 18, No. 8, pp. 635-640.

Hollenberg J.W., Chen E.N., Lakeram K. and Modroukas D. 1995. "Development Of A Photovoltaic Energy Conversion System With Hydrogen Energy Storage". Int. J. Hydrogen Energy, Vol. 20, No. 3, pp. 239-243.

Kauranen P.S., Lund P.D., and Vanhanen J.P. 1993. "Control of Battery Backed Photovoltaic Hydrogen Production". Int. J. Hydrogen Energy, Vol. 18, No. 5, pp. 238-390.

Klein S.A. 1978. "Calculation Of Flat-Plate Collector Utilizability". Solar Energy, Vol. 21, pp. 393-402.

Kurtz S.R., Olson J.M., Bertness K.A., and Kibbler A.E. 1995. "High-Efficient, Radiation-Hard GaInP/GaAs Solar Cells". Solar Engineering, Vol. 2.

Lufti N. and Veziroğlu T.N. 1991. "A Clean And Permanent Energy Infrastructure For Pakistan: Solar-Hydrogen Energy System". Int. J. Hydrogen Energy, Vol. 16, No. 3 pp. 169-200.

Mathur S.S., Kandpal C.T., and Negi B.S. 1991. "Optical Design and Concentration Characteristics of Linear Fresnel Reflector Solar Concentrators-I. Mirror Elements of Varying Width". Energy Conversion Management, Vol. 31, No. 3, pp. 205-219.

Mathur S.S. Kandpal, C.T., and Negi B.S. 1991. "Optical Design and Concentration Characteristics of Linear Fresnel Reflector Solar Concentrators-II. Mirror Elements of Equal Width". Energy Conversion Management, Vol. 31, No. 3, pp. 221-232.

Menicucci D.V. 1986. "Photovoltaic Array Performance Simulation Models". Solar Cells, Vol. 18, pp. 383-392.

Muehl W.W. 1995. "Photovoltaic Power Without Batteries For Continuous Cathodic Protection And An Alternate Photovoltaic/Ultracpacitor Combined Power Source". IECEC Paper No. RE-76, ASME.

Perez R., Seals R., Ineichen P., Stewart R., and Menicucci D. 1987. "A New Simplified Version Of The Perez Diffuse Irradiance Model For Tilted Surfaces". Solar Energy, Vol. 39, No. 3, pp. 221-231.

Raghruraman P. 1981. "Lincoln Laboratory, MITC Air and Water Hybrid Collectors Design". Journal of Solar Energy Engineering. Vol. 103, pp. 291-298.

Seidenfaden U. 1995. "Power Stations in a Window of Glass". The German Research Service, Vol. 11, No. 12, December.

Sharan S.M. Mathur S.S. and Kandpal T.C. 1987. "Analysis of a Combined Photovoltaic-Thermal System Consisting of a Linear Solar Concentrator and a Tubular Absorber". Energy Conversion Management, Vol. 27, No. 1, pp. 55-59.

Sigel M.D., Klein S.A., and Beckman W.A. 1981. " A Simplified Method For Estimating The Monthly-Average Performance Of Photovoltaic System". Solar Energy, Vol. 26, pp. 443-418.

Sopian, et. al. 1995. "Double Pass Hybrid Collector", ASME Winter Conference, San Francisco.

Steeb H., Seeger W., and Aba Oud H. 1994. "Hysolar: An Overview On The German-Saudi Arabian Programme On Solar Hydrogen". Int. J. Hydrogen Energy, Vol. 19, No. 8, pp. 683-686.

Szyska A. 1994. "Neunburg Vorm Wald - Test Center For Solar Hydrogen Technology". Int. J. Hydrogen Energy, Vol.19, No. 10, pp. 823-841.

Thomas S., and Basso T.S. 1995. "Progress Under The Photovoltaic Module And System Performance And Engineering Project". IECEC Paper No. RE-308, ASME.

Tiris M.T.C., and Ture E.I. 1995. "Effects Of Fin Design On Collector Efficiency". Energy, Vol. 20, No. 10, pp. 1021-1026.

Technical Reports:

Almaram G.H., Ventre G.G., Maytrott C.W. and Dunlop J.P.: "Long-Term Performance And Reliability Assessment Of Crystalline Silicon Photovoltaic Modules". Florida Solar Energy Center, 300 State Road 401, Cape Canaveral, Fl 32920 USA.

Bertness K.A., Sarah K.R., Friedman D.J. Kibbler E.A., Kramer C., and Olson J.M. 1994. "19.6% Electron-Irradiated GaInP/GaAs Cells". National Renewable Energy Laboratory, 1617 Cole Blvd., Golden, CO 80401-3339 USA.

Bertness K.A., Sarah K.R., Friedman D.J. Kibbler E.A., Kramer C., and Olson J.M. 1994. "High-Efficiency GaInP/GaAs Tandem Solar Cells For Space and Terrestrial Applications". National Renewable Energy Laboratory, 1617 Cole Blvd., Golden, CO 80401 USA.

Clark, R.H. and Brook R.R. 1979. "The Kooring Expedition - Atmospheric Boundary Layer Data Over Tropical Savannah Land". Department of Science and the Environment, Bureau of Meteorology, January.

"Converting Humidity Expressions with Computers and Calculators". Cooperative Extension, University of California Division of Agriculture and Natural Resources.

Hug W., Bussman H., and Brinner A. "Intermittent Operation And Operation Modelling Of An Alkaline Electrolyzer". German Aerospace Research Establishment, DLR, Institute for Technical Thermodynamics Pfaffenwalding 38-40, 7000 Stuttgart 80, Germany.

Lamb H., Stefanakos E., Arbogast T. and Smith T. "Comparative Studies Of Direct Photovoltaic And AC Rectified Power Supplies For Battery Charging". Clean Energy and Vehicle Research Center, University of South Florida, 4202 E. Fowler Ave., ENG 118 Tampa, FL 33620-5350 USA.

Morner S.O. Beckman W.A., and Klein S.A. "Comparison Of Simulations Of A Photovoltaic-Hydrogen System With Measurements From The Schatz Solar-Hydrogen Project". Department of Heating and Ventilation, University of Trondheim, 7034 Trondheim, Norway. Solar Energy Laboratory, University of Wisconsin, 1500 Johnson Dr., Madison, WI 53706-1687 USA.

Sopian K. 1989. "Solar Radiation Estimates". M.S. Thesis, University of Pittsburgh.

Vanhanen J.P., Kauranen P.S., and Lund P.D. "Operation Experiences Of A Phosphoric Acid Fuel Cell In Solar Hydrogen Energy Systems". Helsinki University of Technology, Department of Technical Physics, FIN-02150, ESOP, Finland.

Table I. EFFICIENCIES USED IN ANALYSIS

1. Collector Electrical Efficiency, $\eta_{ce} = 0.25$
2. Collector Thermal Efficiency, $\eta_{ct} = 0.38$
3. Electrical Storage Efficiency, $\eta_{se} = 0.80$
4. Thermal Storage Efficiency, $\eta_{re} = 0.80$
5. Electrical Regulator Efficiency, $\eta_{st} = 0.95$
6. Thermal Regulator Efficiency, $\eta_{rt} = 0.95$
7. Electrolyser Efficiency, $\eta_{e} = 0.90$

Table II. ANNUAL SOLAR ENERGY INCIDENT ON A 1 m^2 COLLECTOR AREA VERSUS COLLECTOR MOVEMENT (MIAMI)

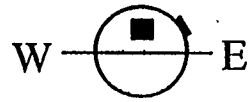
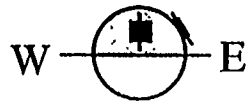
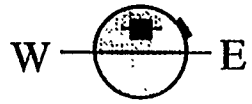
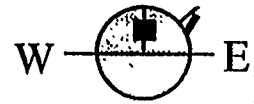
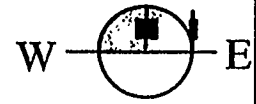
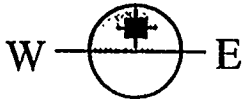
Collector Movement Mode	Annual Solar Energy Incidence E_s (kWhr)	Difference $E_{si} - E_{sf}$ (kWhr)	Percent Improvement
1. Stationary 	2014	0	0
2. 1-D North-South Axis Continuous Adjustment 	2633	619	31
3. 1-D East-West Axis Continuous Adjustment 	2154	140	7
4. 1-D Rotation About Vertical Axis, Fixed-Slope Continuous Adjustment 	2415	401	20
5. 1-D Parallel-to-Earth Axis Continuous Adjustment 	2733	719	36
6. 2-D Axis Continuous Adjustment 	2910	897	45

Table III. ANNUAL HYBRID SOLAR HYDROGEN, OXYGEN AND EXCESS HEAT PRODUCTION VERSUS COLLECTOR MOVEMENT

(Location: Miami; Collector Area: 1 m^2; Hybrid System Electrolyser Temp.: 1000C)

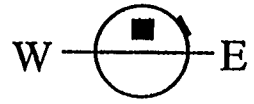
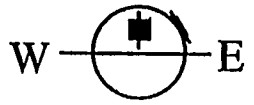
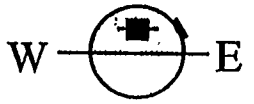
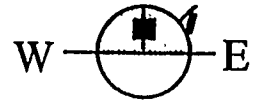
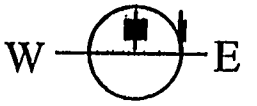
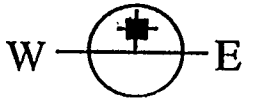
Collector Movement Mode	Type	Hydrogen		Oxygen	Excess Heat	Local Efficiency		2-D Efficiency	
		kg	kWhr	kg	kWhr	Hydrogen	Hydrogen + Heat	Hydrogen	Hydrogen + Heat
1. Stationary 	Plain	8.6	341	68.8	0	17	17	12	12
	Hybrid	13.6	536	108.8	468	27	50	19	35
2. 1-D North-South Axis Continuous Adjustment 	Plain	11.4	447	91.2	0	17	17	15	15
	Hybrid	17.8	700	142.4	612	27	50	24	45
3. 1-D East-West Axis Continuous Adjustment 	Plain	9.3	365	74.4	0	17	17	13	13
	Hybrid	14.5	573	116.0	500	27	50	20	37
4. 1-D Rotation About Vertical Axis, Fixed-Slope Continuous Adjustment 	Plain	11.3	442	90.4	0	17	17	15	15
	Hybrid	17.6	693	140.8	606	27	50	24	45
5. 1-D Parallel-to-Earth Axis Continuous Adjustment 	Plain	11.8	463	94.4	0	17	17	16	16
	Hybrid	18.5	727	148.0	635	27	50	25	47
6. 2-D Axis Continuous Adjustment 	Plain	12.5	493	100.0	0	17	17	17	17
	Hybrid	19.6	774	156.8	676	27	50	27	50

Table IV. ANNUAL MEAN METEOROLOGICAL CONDITIONS FOR DIFFERENT LOCATIONS

Location (Latitude, Elevation)	Mean Temp. (C)	Mean Wind Speed (m/s)	Mean Humidity (%)	Mean Clearness Index	Mean Insolation (MJ/m^2)
Atlanta (33.7 deg./315 m)	16.0	4.0	68.3	0.50	0.70
Denver (40.0 deg./1634 m)	10.0	3.6	51.9	0.63	0.69
Miami (25.8 deg./2 m)	24.3	4.3	72.5	0.51	0.74
Phoenix (33.4 deg./339 m)	22.5	3.0	36.3	0.68	0.87
Salt Lake City (40.8 deg./1288 m)	11.3	4.0	53.9	0.63	0.70

Table V. ANNUAL HYBRID SOLAR HYDROGEN, OXYGEN AND EXCESS HEAT PRODUCTION FOR DIFFERENT LOCATIONS

(2-D Tracking System; Collector Area: 1 m^2; Hybrid System Electrolyser Temp.: 1000 C)

Location (Latitude, Elevation)	Type	Hydrogen		Oxygen	Excess Heat	local Efficiency		Phoenix Efficiency	
		kg	kWhr	kg	kWhr	Hydrogen	Hydrogen + Heat	Hydrogen	Hydrogen + Heat
Atlanta (33.7 deg./315 m)	Plain	13.1	519	104.8	0	17	17	14	14
	Hybrid	20.8	815	166.4	712	27	50	22	40
Denver (40.0 deg./1634 m)	Plain	13.0	515	104.0	0	17	17	14	14
	Hybrid	20.5	808	164.0	706	27	50	22	40
Miami (25.8 deg./2 m)	Plain	12.5	493	100.0	0	17	17	13	13
	Hybrid	19.6	774	156.8	676	27	50	21	38
Phoenix (33.4 deg./339 m)	Plain	16.3	643	130.4	0	17	17	17	17
	Hybrid	25.6	1010	204.8	882	27	50	27	50
Salt Lake City (40.8 deg./1288 m)	Plain	13.6	538	108.8	0	17	17	14	14
	Hybrid	21.5	845	172.0	738	27	50	23	42

Table VI. ANNUAL HYBRID SOLAR HYDROGEN, OXYGEN AND EXCESS HEAT PRODUCTION VERSUS STEAM TEMPERATURE (Location: Miami; Collector Area: 1 m^2; 2-D Tracking System)

Electrolyser Temperature (C)	Type	Hydrogen		Oxygen	Excess Heat	Local Efficiency	
		Kg	KWhr	Kg	KWhr	Hydrogen	Hydrogen + Heat
Room	Plain	13.1	515	104.8	0	17	17
200	Hybrid	16.4	644	131.2	852	21	50
400	Hybrid	16.5	679	132.0	821	22	50
600	Hybrid	18.3	717	146.4	787	24	50
800	Hybrid	19.3	760	154.4	749	25	50
1000	Hybrid	19.8	774	158.4	676	27	50
1200	Hybrid	21.9	863	175.2	657	28	50

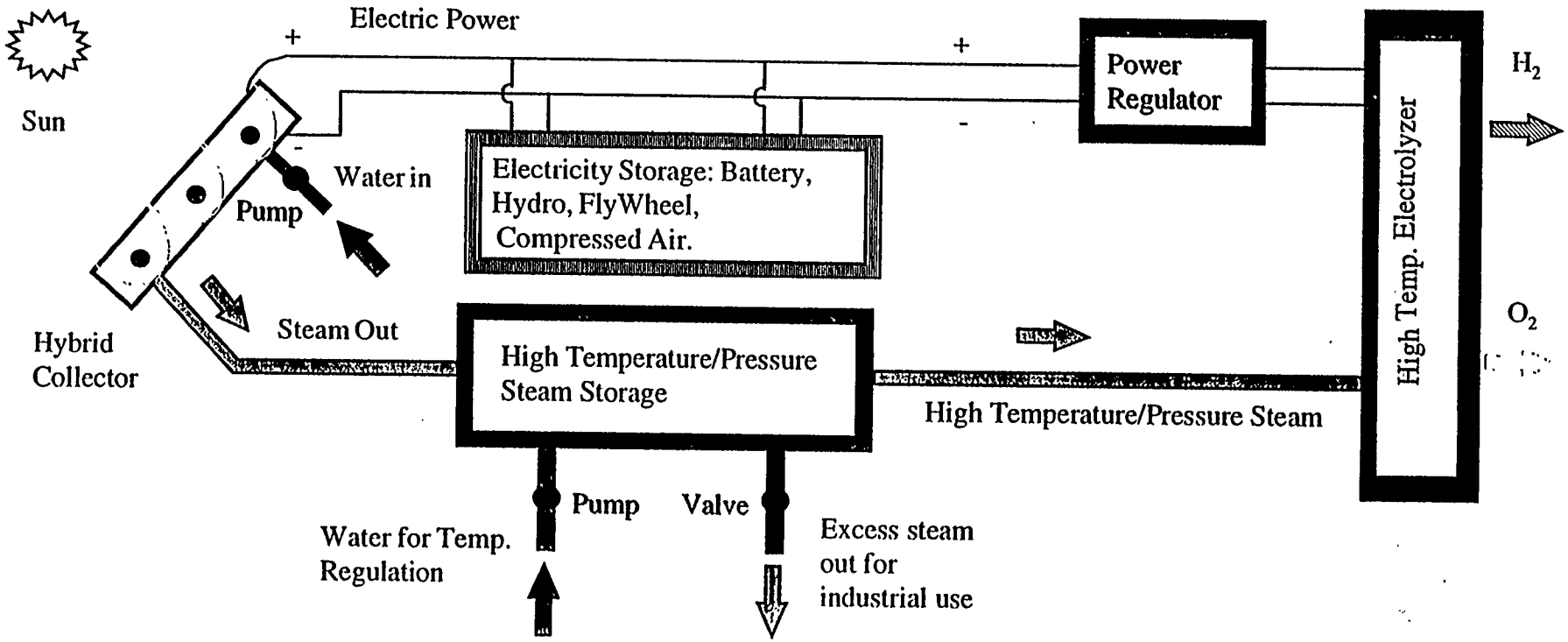


Fig. 1. Schematic of Solar Hydrogen Production System

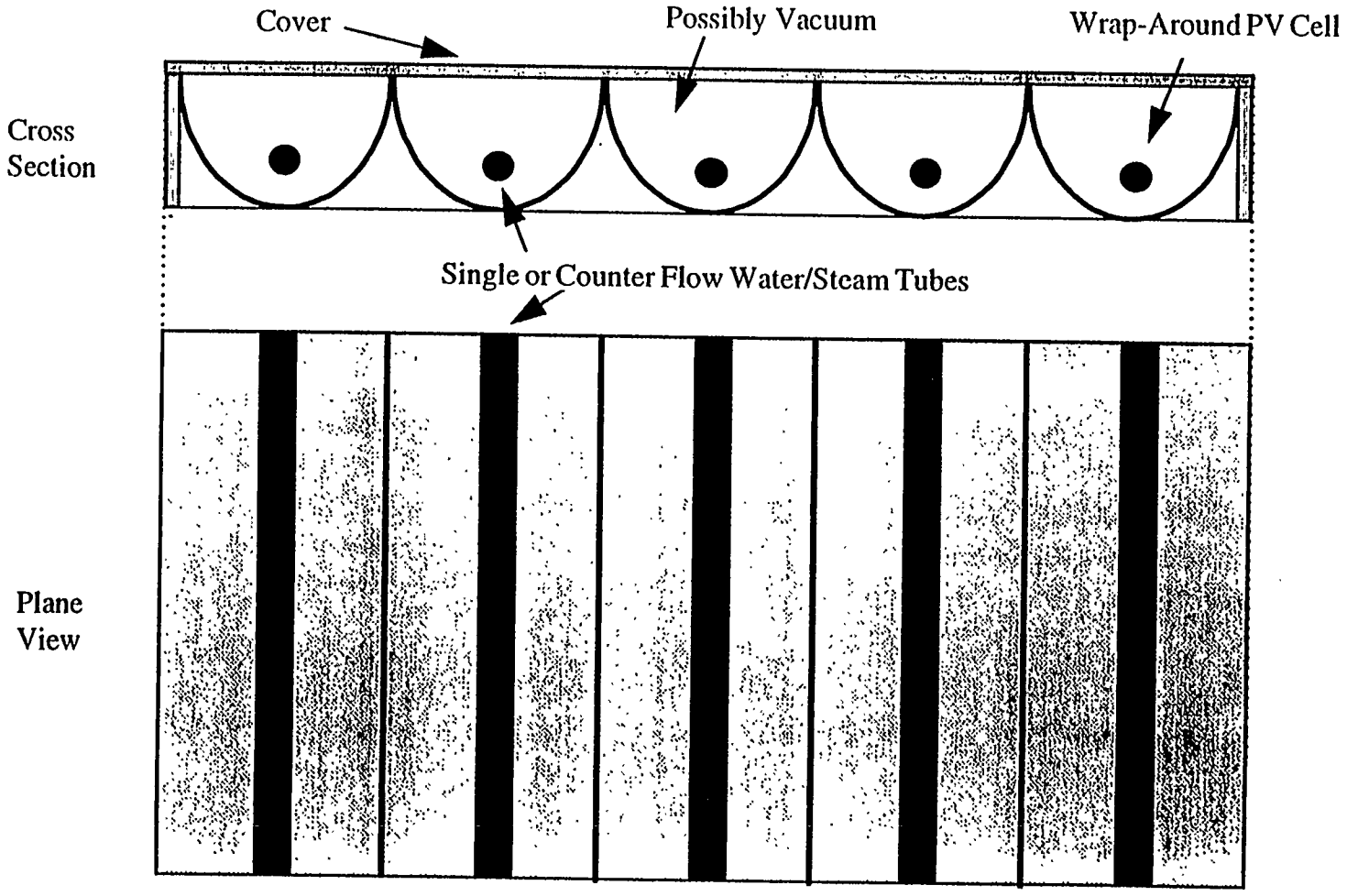


Fig. 2. Schematic Diagram of Hybrid Collector

A. Rotation About East-West Axis

B. Rotation About North-South Axis

C. Rotation About Vertical Axis

D. Rotation About Axis Normal To Equatorial Plane

E. Movement About Two Axes

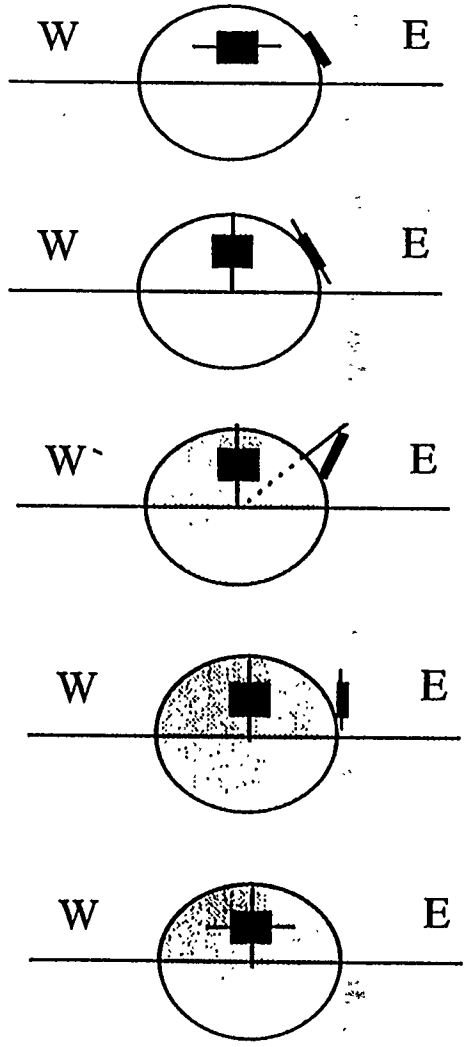


Fig. 3. Collector Tracking Systems

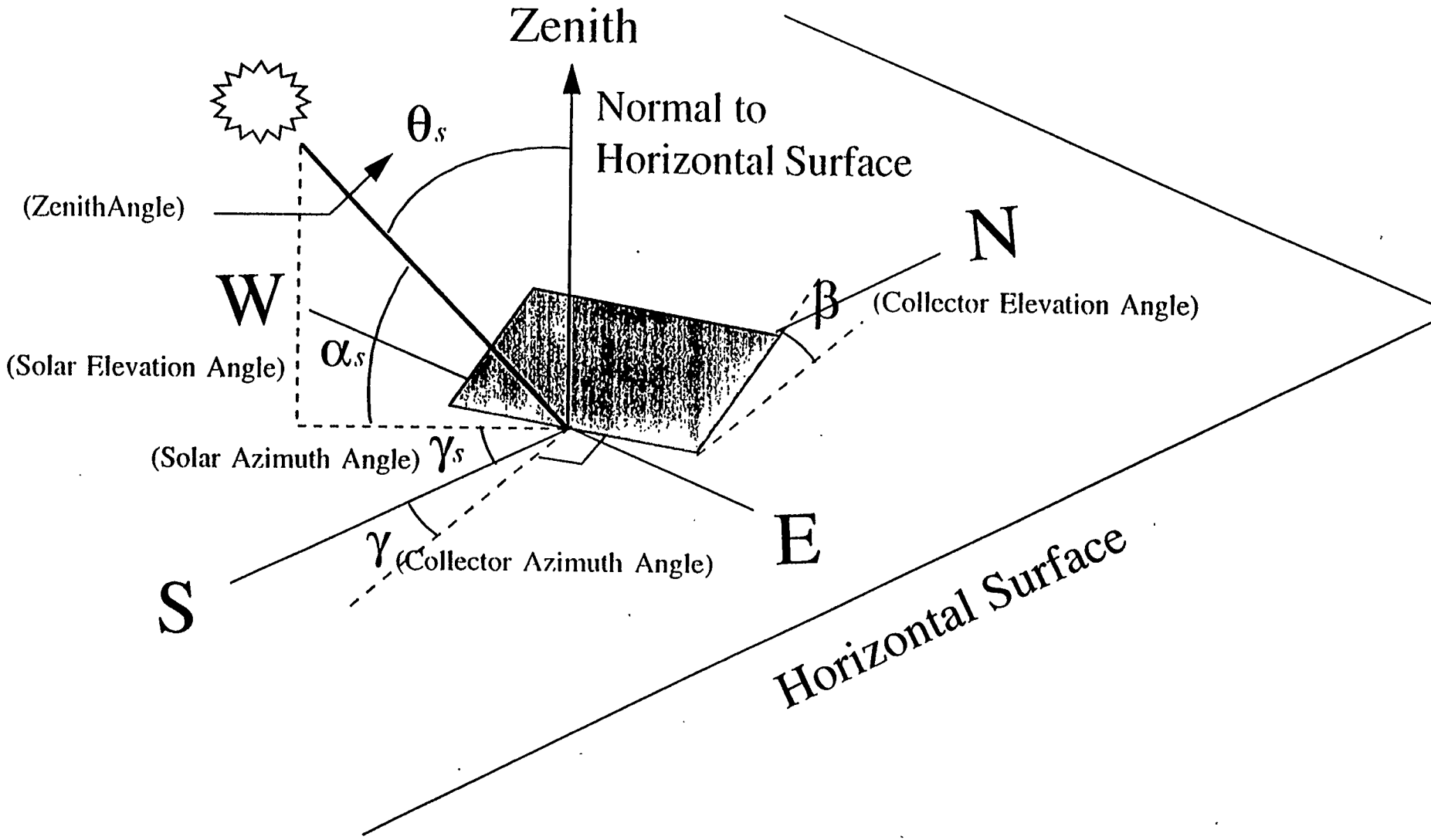


Fig. 4. Collector Orientation and Angle Definitions

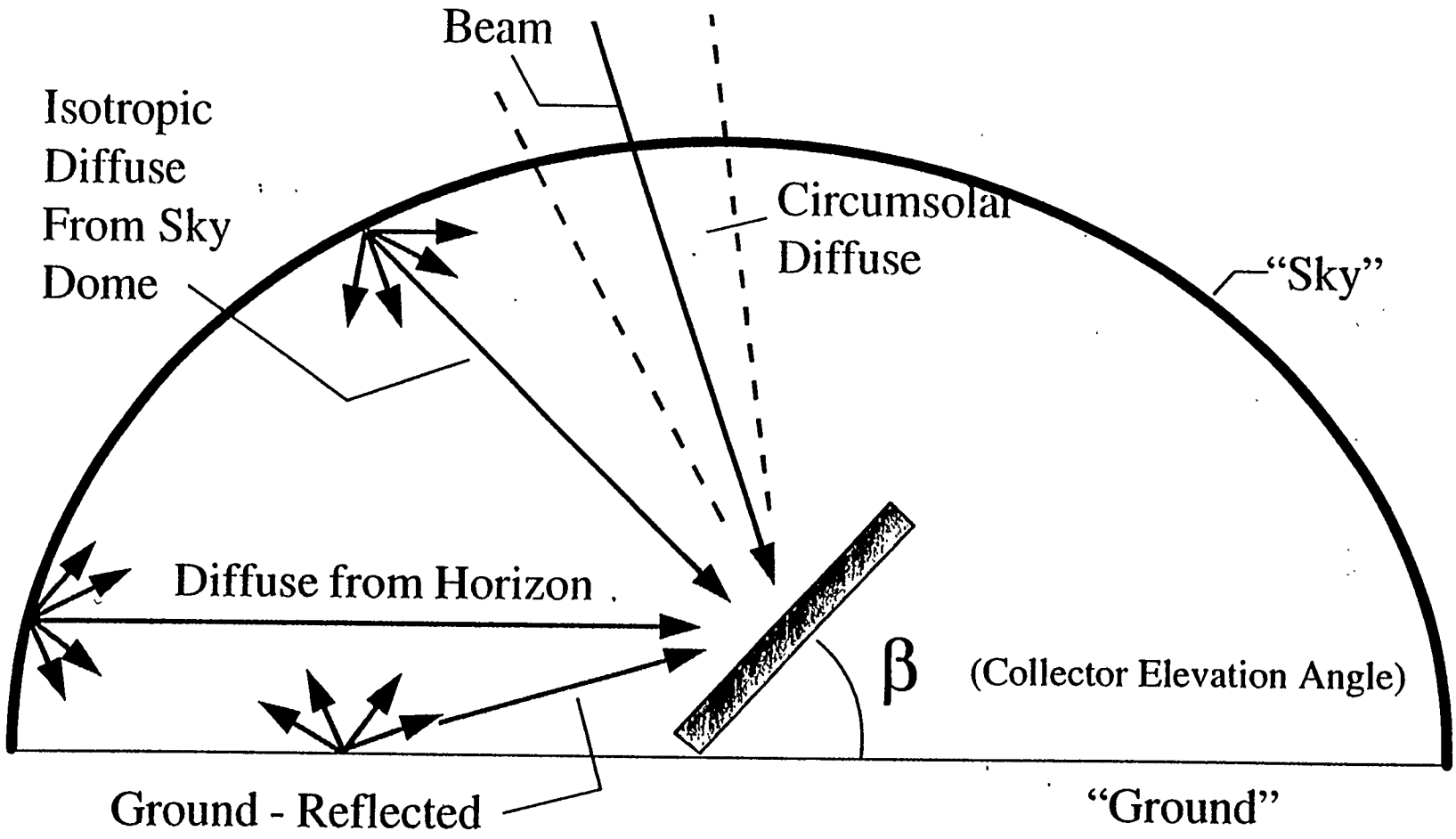


Fig. 5. Solar Radiation Components

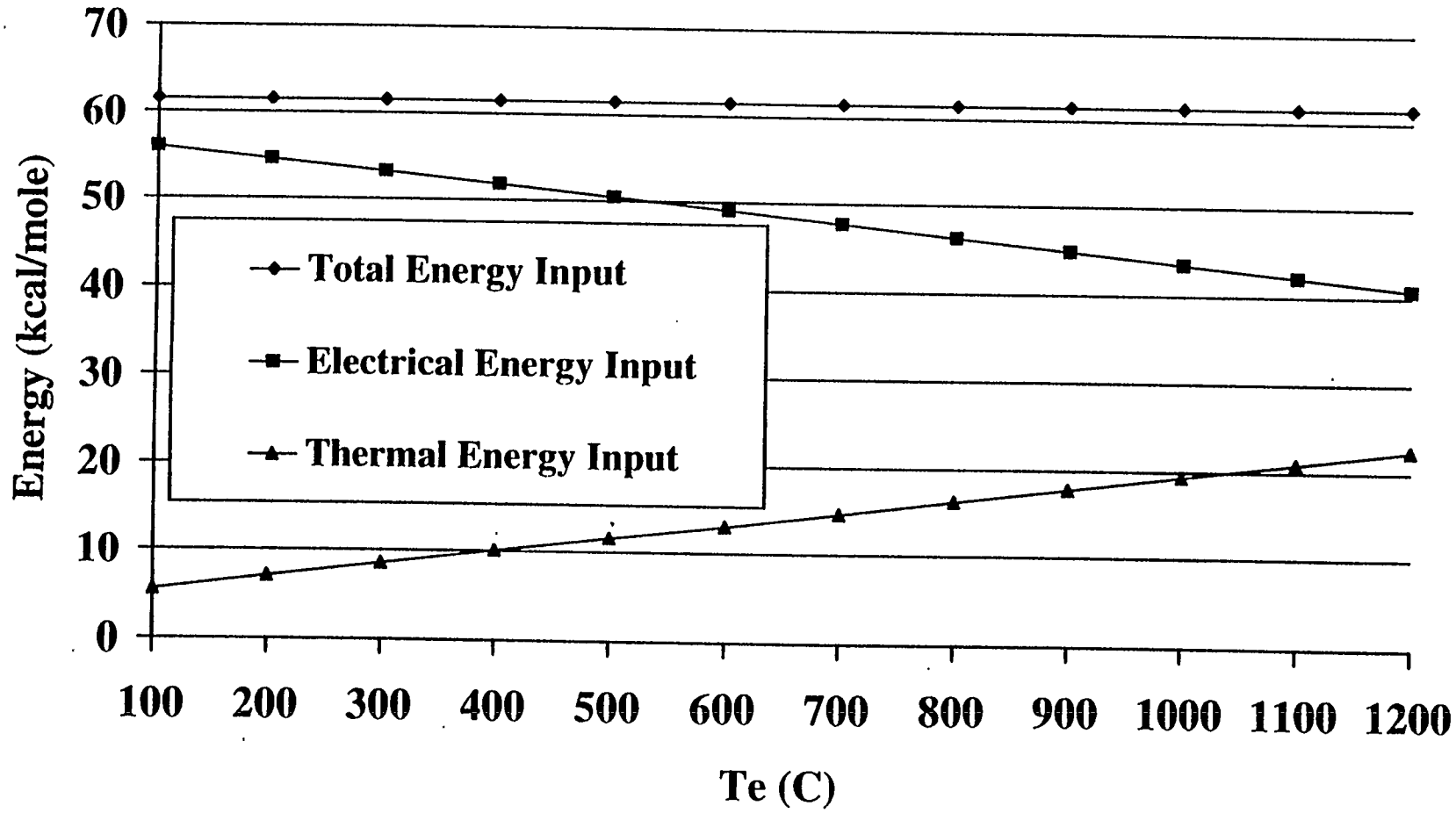


Fig. 6. Energy Relationships for Steam Electrolysis

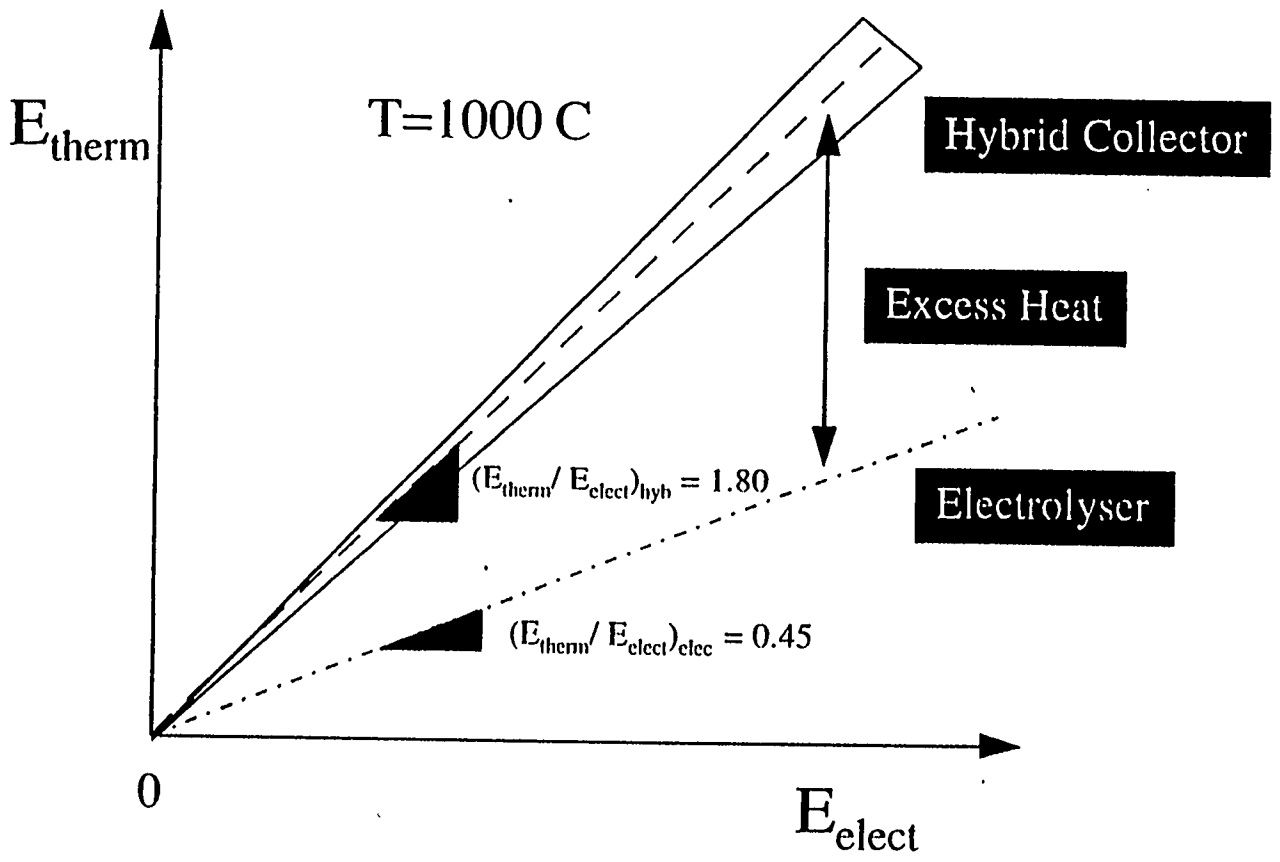


Fig. 7. Energy Production and Use Mismatch

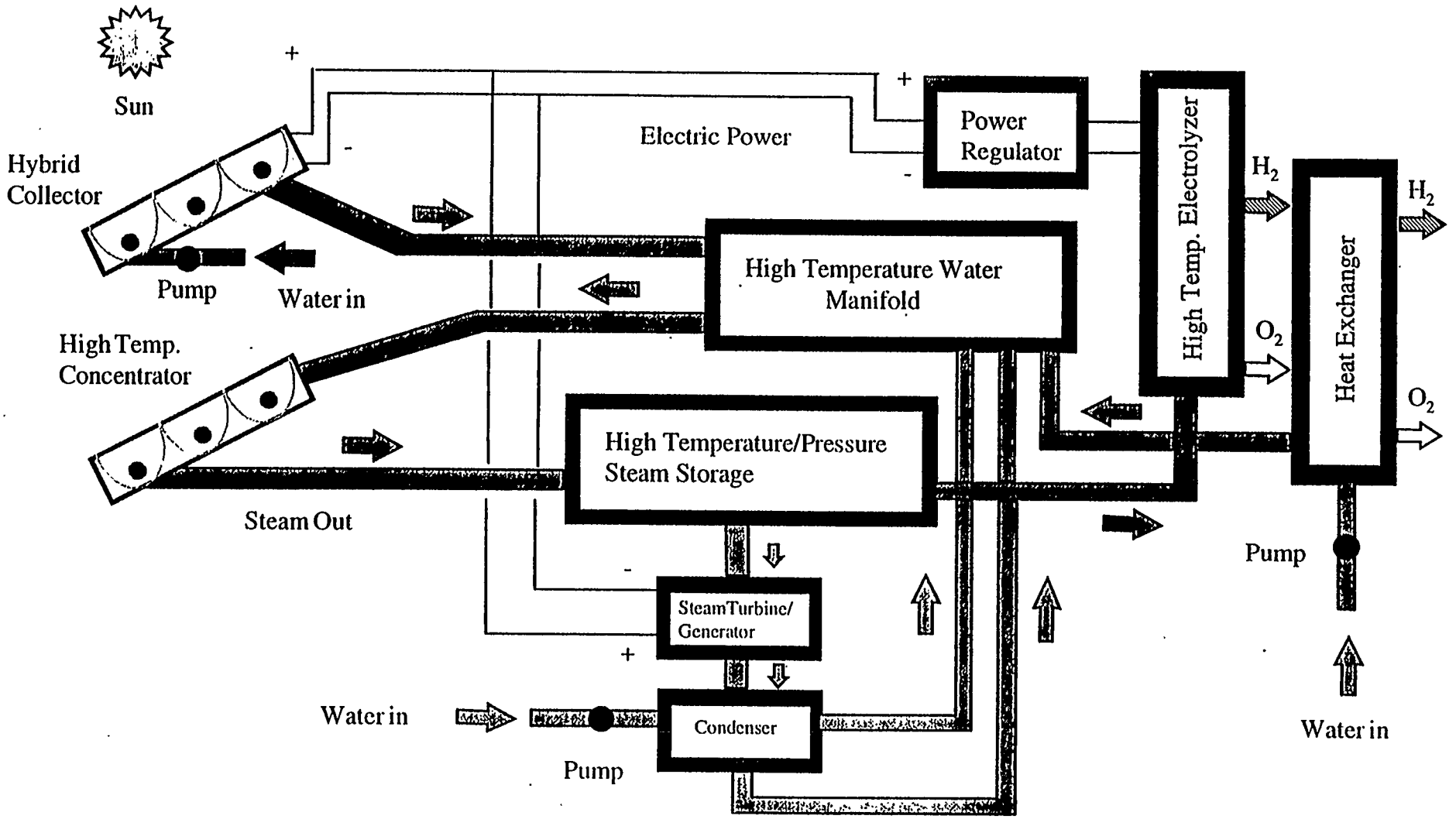


Fig. 8. Schematic of High Efficiency Solar Hydrogen Generating System

SOLAR PHOTOCATALYTIC H_2 PRODUCTION FROM WATER USING A DUAL BED PHOTOSYSTEM

Clovis A. Linkous
Florida Solar Energy Center
1679 Clearlake Road
Cocoa, FL 32922-5703

Abstract

We are developing a dual stage, direct photoconversion scheme for water splitting. The overall system consists of an aqueous solution circulated through two modules, or beds, each of which contains a photochemically active surface layer below the solution. The idea is to divide the energy requirement for water decomposition between the two photosystems, so that more abundant, lower energy photons in the solar spectrum can be utilized, and that the H_2 and O_2 products can be evolved separately from each other. Catalyst-modified semiconductor powders, immobilized within a polymer binder, are currently being employed as the photoactive layers. TiO_2 and platinized-InP have been employed for the O_2 and H_2 evolution tasks, respectively. A major effort over the last year was identification of a suitable redox mediator that is responsible for transferring electron equivalents from one unit to the other. After testing more than dozen candidates, spanning a wide range of electropotentials, under a variety of conditions, it was found that the bromide/bromate (Br^-/BrO_3^-) and iodide/iodate (I^-/IO_3^-) redox systems could function in both modules, necessary for closed cycle operation.

Introduction

Photoelectrochemical production of H_2 from water has been under consideration for over 25 years, yet several major obstacles remain to be surmounted before the technology can make a significant impact in the overall energy economy. One of these regards the chemical stability of the semiconductor electrodes that are employed. Those whose absorption well matches the solar spectrum, such as Si, Ge, etc, are susceptible to corrosion in aqueous solutions, especially under bandgap irradiation. Another involves the cost of manufacturing the module. Much of the inherent cost is related to fabrication of the semiconductor photoelectrode, which involved much the same process technology as is utilized for photovoltaic cell manufacture. With the incident radiant power of sunlight only in the 1.0 kW/m^2 range, and practical efficiencies lying in the 10-30% range, the module cost of the photoconversion system, regardless of the technology, must lie in the \$100/m^2 range or less.

Thus our objective in this work is to develop an efficient, affordable, direct photoconversion scheme for generating H_2 from water using sunlight. We have sought to find an alternative to photoelectrochemical cell

configuration, where wafers of single crystal or polycrystalline semiconductors are cut to fashion electrodes. Since the essential feature of photoelectrochemical energy conversion was development of a barrier voltage at the semiconductor/electrolyte interface, it was realized that this could just as well be accomplished with the semiconductor in powder form. Our approach then has been to use semiconductor powders in a dual bed configuration, breaking down the energy requirement for water splitting into a 2-photon process, and enabling separate production of H_2 and O_2.

Much of our work has been geared toward understanding how photoparticle systems operate, and how a large scale reactor system might be configured. We have found that fixed bed arrays of particulates make the most economic use of the solar energy-converting material. Furthermore, the loss in conversion efficiency compared to loose colloidal systems is compensated by the technical advantages of having a flow system that moves the dissolved products of reaction out the photoreactor, lessening the extent of back reaction.

This scheme is depicted in Figure 1. An aqueous solution is circulated through the two modules connected in series, the first evolving H_2, the second O_2, although the order could just as well be reversed, since the electronic structure of the semiconductor determines whether oxdation or reduction will occur. A redox mediator, or species capable of reversible electron transfer, is dissolved in the working fluid. The band characteristics of the photocatalysts will limit what redox agents could possibly serve as mediator in the dual particle bed system. The positive limit of redox potential is determined by the valence band edge of the H_2-evolving photocatalyst, while the negative limit is determined by the conduction band edge of the O_2-evolving photocatalyst.

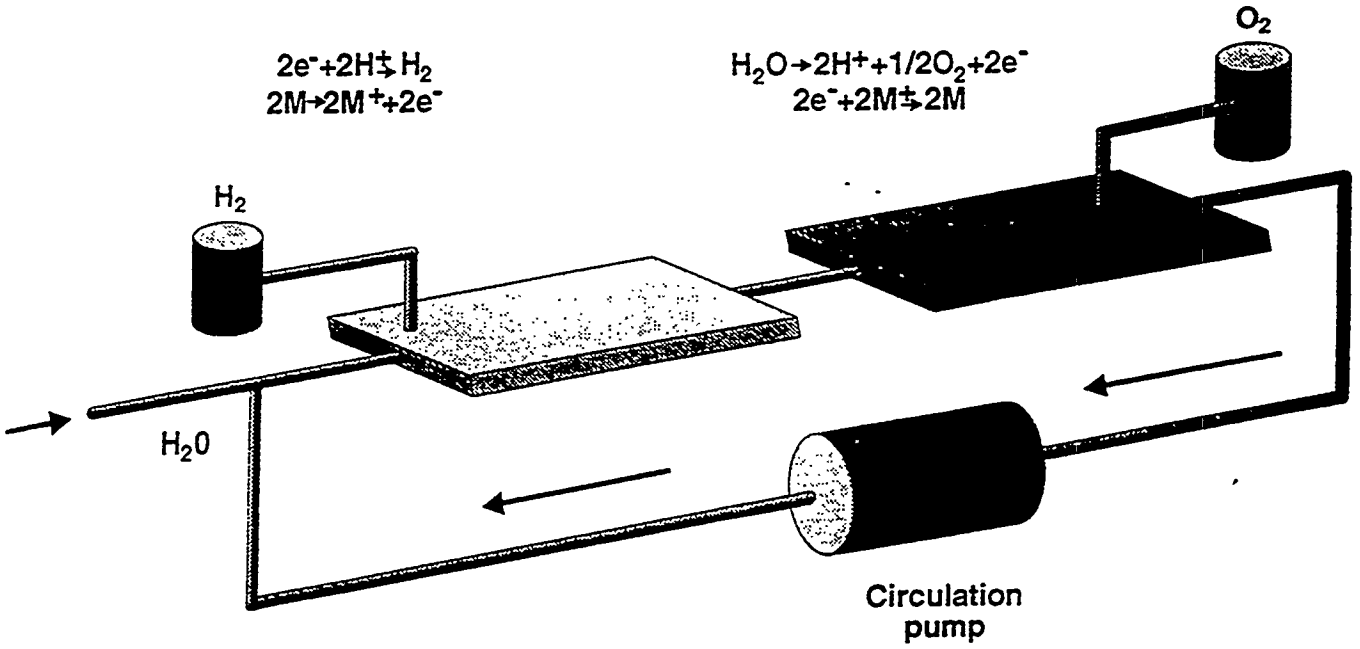


Figure 1. Schematic of Dual Bed Photoparticle Scheme for Water Splitting

The general chemical mechanism for a dual bed concept photosystem would be as follows:

Photoreactor 1, PC-R: $4H_2O + 4M^\circ \rightarrow 2H_2 + 4OH^- + 4M^+$

Photoreactor 2, PC-O: $\underline{4OH^- + 4M^+ \rightarrow O_2 + 2H_2O + 4M^\circ}$

net: $2H_2O \rightarrow 2H_2 + O_2$

where PC-R = photocatalyst for the reductive stage of the process
PC-O = photocatalyst for the oxidative stage of the process, and
M = redox mediator

Each photoreactor maintains an internal charge balance, so that external electrical connection between the modules is not necessary. The redox mediator terms cancel when the two module reactions are summed, so that the net reaction is simple water decomposition. The mechanism as written reflects an alkaline medium, but acidic environments can be considered as well. The stoichiometry of the acid or base equivalents in each stage may also differ from the above due to their involvement in the redox mediator chemistry, but would nevertheless cancel out when the module reactions are added together.

Experimental

Our experimental approach has been to look at each of the photosystems separately, first identifying materials and condition that were satisfactory for either H_2 or O_2 evolution, and then comparing the results to identify any overlap. The first task was to identify the semiconductor materials that could be used for either H_2 or O_2 evolution, and devise ways to immobilize them on a surface. We decided to use TiO_2 as PC-O and InP as PC-R. Much of the work done over the years in photoelectrochemistry suggested that these were most successful as photoanodes and photocathodes, respectively, so they represented functional materials that required the least amount of developmental work. Even though a narrower band gap material than TiO_2 and a more chemically stable material than InP would be desirable, we nevertheless wanted to get to proof-of-concept stage in the near term, so as to validate this approach to water splitting.

Instead, we have concentrated our effort on identification of a redox equivalent transfer agent or mediator that is needed to provide the anodic half-cell reaction in the H_2-evolving reactor and the cathodic half-cell back reaction in the O_2-evolving reactor. The following redox couples were examined: Sn^{4+}/Sn^{2+}; Anthraquinone-2,6-disulfonate; IO_3^-/I^-; $[Fe(CN)_6]^{3-}/[Fe(CN)_6]^{4-}$; 1,4-Napthoquinone-2-sulfonate; Toluidine Blue; I_2/I^-; Thionine/Leucothionine; BrO_3^-/Br^-; Fe^{3+}/Fe^{2+} (SO_4^{2-}); 1,4-Benzoquinone/Hydroquinone; NO_3^-/NO_2^-; VO_2^+/VO^{2+}; Br_2/Br^-; Cl_2/Cl^-; and H_5IO_6. Their standard redox potentials are listed below in the Results section .

The experimental set-up was as follows. A 50 ml solution of the redox mediator was placed in a 1" diameter test tube. It was desirable for the mediator to be as concentrated as possible, so as to increase the probability of hole or electron injection. For the inorganic salts, this was typically in the 0.1-1.0 M range. The organics were usually kept in the millimolar range, however, due to either solubility limitations or the light attenuation effects for those which were intensely colored. To each solution 200 mg of either TiO_2 or InP powder was added. Light from a 1000 Watt Xe arc lamp was passed through a water filter with 4 inch pathlength to remove most of the infrared and then focused with a quartz convex lens onto the test tube. The test vessel contained a stir bar so that the semiconductor powder suspension could be maintained throughout the experiment. The vessel had a side armature near the top, opening into the head space over the redox solution. This was connected to a gas measurement apparatus consisting of a hose leading into an inverted graduated cylinder. A septum cap on the test tube also enabled syringe sampling of any gas that percolated up into the head space for gas chromatographic analysis. A schematic of the experimental apparatus is shown in Figure 2.

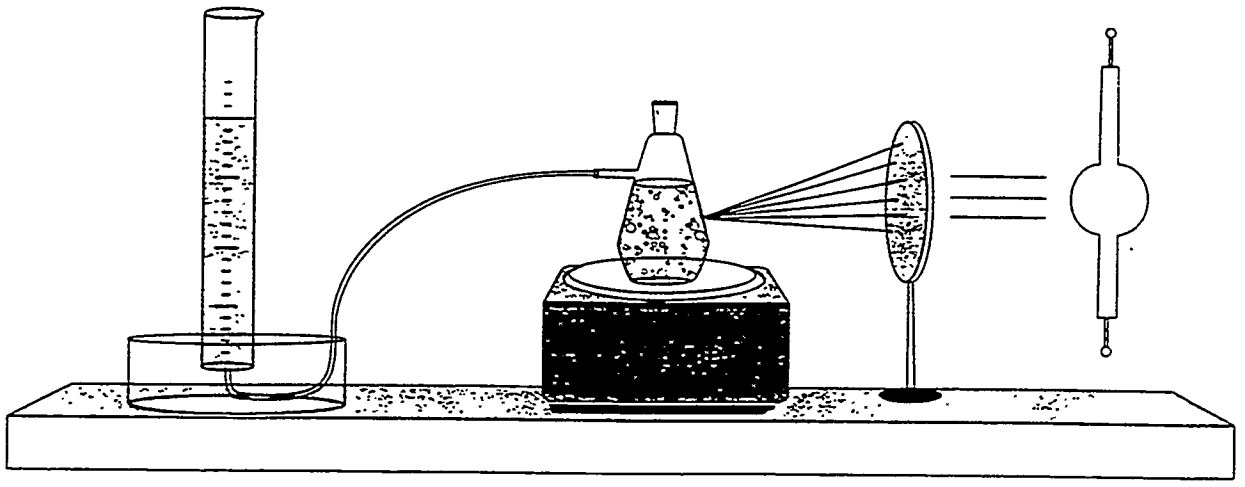


Figure 2. Experimental Apparatus for Photolytic Gas Evolution Measurements

To measure O_2-evolution, TiO_2, sometimes catalyst modified with either Pt or Ir, would be placed into a solution containing the "Ox" or oxidized form of the redox couple of interest. For H_2-evolution, InP, which was invariably platinized once control experiments showed that plain InP was poorly catalytic for the H_2 reaction, would be added to a solution contained the "Red" or reduced form of the redox couple.

Results

We first needed to confirm that our prognostications on the photochemical behavior of our photosystems were correct, i.e., the electronic structure of the photocatalysts dictated whether H_2 or O_2 is evolved. In almost every case, gas of some sort was evolved. While the gas volume measurement apparatus gave reliable results for the most active systems, there were problems with the less active ones, where the gas evolution rate was only a few milliliters per hour or less. Irradiation with the Xe lamp caused heating of the test suspension from ambient to 60-80° C; this in turn caused expansion of the gas over it. Typically we would measure 8 ml of volume expansion in our apparatus whether there was effervescence in the test suspension or not. This was in good agreement with ideal gas PV expansion calculations based on the temperature gain and initial dead volume determinations.

One could still expect to circumvent this problem with prolonged irradiation times, but it was difficult to measure a steady gas evolution rate for any appreciable length of time. As shown in Figure 3 for Pt-InP in alkaline iodide solution, the total gas volume reaches a steady state in about an hour of illumination. This was interpreted as analogous to a "photostationary state", where a photochemical reaction generates products and depletes reactants until the reverse reaction rate equals the forward one.

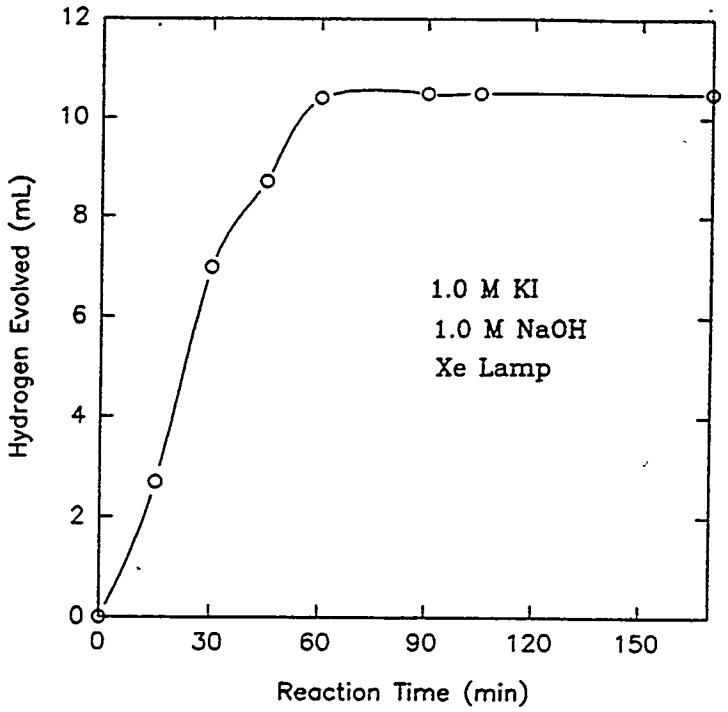


Figure 3. Gas Volume versus Time for H_2 Evolution on Pt-InP

Ultimately, gas chromatography was used to determine whether the gas evolved was H_2, O_2, or something else. Using injection standards, retention times for H_2 and O_2 were determined. In numerous cases with InP, the lone peak in the gas chromatogram was H_2. In comparatively fewer cases as will be seen below, with TiO_2, chromatograms were also obtained where the only peak was that of O_2. While some adventitious O_2 would sometimes be observed in the InP chromatograms, there never was a stoichiometric 2:1 H_2:O_2 relationship that would imply net water decomposition. In other cases, especially with the organic redox agents, photolysis would produce effervescence, but neither H_2 nor O_2 would be detected.

The series of redox reagents were irradiated with a Xe lamp in aqueous slurries of photocatalytic powders to probe the limits of energy storage that each semiconductor is capable of. For example, if the voltage generation requirement is shared equally between the two photoreactors, the redox mediator will have a standard redox potential of 0.6 V (acidic standard state). The further the mediator's redox potential departs from that value, the more uneven the energy storage load becomes. Realistically, about 1 volt of electrochemical potential should be generated in each module, so as to overcome unavoidable overpotential requirements.

In Table 1 below, evolution results are given for two-hour irradiation of TiO_2 and Pt-InP suspensions in the presence of various redox reagents. It was expected that those with the highest redox potentials would perform best for O_2-evolution, while those with low redox potential would perform best for H_2- evolution.

As it turned out, only a few clear cut cases for O_2-evolution were found. One of these was H_5IO_6, periodic acid, the reagent with the highest redox potential. O_2 evolution with H_5IO_6 does not clearly represent energy storage at all, since its redox potential is positive of water oxidation--the TiO_2 is acting as a photocatalyst, but not as an energy transducer. The only other examples of O_2-evolution came from IO_3^-, VO_2^+, and BrO_3^-.

Many representatives from the series of redox agents were tested as electron donors in the photocatalytic evolution of H_2 using InP. As can be seen in the Table 1 results, many of the redox reagents gave a positive result. When HCl solution itself gave a positive result, our suspicions were raised, since the valence band edge

of InP was thought to be negative of the redox potential necessary for Cl_2-evolution. After some prolonged photolysis testing, it was confirmed gravimetrically that the InP itself was being consumed and supplying electron equivalents to the H_2.

Table 1. O_2 and H_2 Evolution Results for Various Redox Mediators

Mediator	E° (V vs NHE)	O_2 evolution from TiO_2	H_2 evolution from InP
Sn^{4+}/Sn^{2+}	0.139	-	✓
Anthraquinone-2,6-disulfonate	0.228	×	-
$K_3[Fe(CN)_6]/K_4[Fe(CN)_6]$	0.46 (NaOH)		✓
1,4-Napthoquinone-2-sulfonate	0.47	×	×
Toluidine Blue	0.534	×	-
KI/I_2, IO_3^-	0.535	✓	✓
thionine/leucothionine	0.563	×	-
$FeSO_4$	0.68	-	✓
1,4-benzoquinone	0.699	-	×
NO_3^-	0.84	×	-
V_2O_5 (VO_2^+)/$VOSO_4$	1	✓	×
KBr/Br_2, BrO_3^-	1.087	✓	✓
HCl	1.358	-	✓
H_5IO_6	1.7	✓	-

✓ = positive result; the desired gas was detected.
× = negative result; any gas evolution did not correspond to the substance of interest.
- = reaction not attempted.

Comparing the H_2- and O_2-evolution results, it is shown that respective Ox and Red species from the IO_3^-/I^- and BrO_3^-/Br^- redox couples enabled both types of gas evolution. Therefore, one could conceive of constructing a dual bed system based on TiO_2 and Pt-InP with either of these couples as redox mediators.

Conclusion

The possibility of performing photocatalytic H_2O-splitting using two separate photoparticle arrays has been described. Experimentation has attempted to identify suitable O_2-evolving and H_2-evolving photocatalysts,

as well as a common redox mediator. Although many possible redox mediator candidates were identified in the H_2-evolution module, only a few positive results were obtained in the O_2-evolution module. Either the TiO_2 needs to be made more active through doping or catalyst modification, or alternatives need to be found; ultimately, new chromophore/photoconductor systems for O_2 and H_2 evolution must be developed.

Acknowledgement

The author wishes to thank Darlene Slattery, Marty Megregian, and Anthony Ouelette for their technical assistance on this project. Funding from the U.S. Department of Energy, Office of Solar Thermal, Biomass Power, and Hydrogen Technologies, is gratefully acknowledged.

INTERNATIONAL MARINE BIOTECHNOLOGY CULTURE COLLECTION (IMBCC)

Oskar R. Zaborsky, Ph.D. and Kathleen Baker, Ph.D.
University of Hawaii at Manoa
Hawaii Natural Energy Institute
Marine Biotechnology Center
2540 Dole Street, Holmes 246
Honolulu, HI 96822

Abstract

The objective of this project is to establish a premier culture collection of tropical marine microorganisms able to generate hydrogen from water or organic substances. Both eukaryotic and prokaryotic microorganisms will serve as the biological reservoir or "library" for other DOE Hydrogen Program contractors, the biohydrogen research community and industry. This project consists of several tasks: (a) transfer of the Mitsui-Miami strains to Hawaii's International Marine Biotechnology Culture Collection (IMBCC) housed at the Hawaii Natural Energy Institute (HNEI); (b) maintain and distribute Mitsui-Miami strains; (c) characterize key strains by traditional and advanced biotechnological techniques; (d) expand Hawaii's IMBCC; and (e) establish and operate an information resource (database). The project was initiated only late in the summer of 1995 but progress has been made on all tasks. Of the 161 cyanobacterial strains imported, 147 survived storage and importation and 145 are viable, with most exhibiting growth. Of the 406 strains of other photosynthetic bacteria imported, 392 survived storage and importation and 353 are viable, with many exhibiting growth. This project is linked to cooperative efforts being supported by the Japanese Ministry of International Trade and Industry (MITI) through its Marine Biotechnology Institute (MBI) and Research Institute of Innovative Technology for the Earth (RITE).

Introduction

Over the past twenty years, advances have been made in the elucidation of the complex physiological, biochemical, and genetic processes underlying the hydrogen evolution capabilities of microalgae and bacteria (San Pietro 1994). The key to commercialization, like in other biotechnology processes such as the production of antibiotics by bacteria, is the quality and characteristics of the particular organisms in question. Thus, while interesting microbes have been described in the literature from time to time, there is still a need for better and more effective hydgrogen producers.

One research activity dedicated to finding better microbes that generate hydrogen was initiated by the late Professor Akira Mitsui at the University of Miami in 1975, then funded by the National Science Foundation (NSF) and later assumed by the U.S. Department of Energy (DOE). The Mitsui-Miami strains (cyanobacteria and other photosynthetic bacteria) were collected in mangrove communities, grass flats, mud flats, rocky areas, coral reefs, estuarine waters, open ocean water, and other habitats around Florida and the Caribbean. Such a variety of habitats ensures a diverse array of species that represent a variety of environmental conditions that differ in concentrations of ammonia, nitrate, phosphate, organic compounds, dissolved oxygen, hydrogen sulfide, salinity, and pH. Many of the species collected were in close association with dead and decaying organic matter (Mitsui 1975).

At the time of his untimely death, the collection consisted of 928 pure strains of cyanobacteria and other photosynthetic bacteria. In addition, there were 1992 enrichment cultures of cyanobacteria that have yet to be identified. It was also recognized that this collection has value and that it should be preserved. A decision was ultimately made to transfer this collection (or at least the most valuable strains) to Hawaii, specifically to the Hawaii Natural Energy Institute (HNEI) of the University of Hawaii at Manoa. The former Mitsui-Miami culture collection is now part of HNEI's International Marine Biotechnology Culture Collection (IMBCC).

Summary of Approach/Rationale

The objective of this project is to establish a premier culture collection of tropical marine microorganisms able to generate hydrogen from water or organic substances. Both eukaryotic and prokaryotic microorganisms will serve as the biological reservoir or "library" for other DOE Hydrogen Program contractors, the biohydrogen research community and industry. Without the availability of effective hydrogen-producing strains through DOE leadership and support, industry will not be able to develop commercial processes. This project consists of several tasks:

- transfer of the Mitsui-Miami strains to Hawaii's International Marine Biotechnology Culture Collection (IMBCC) housed at the Hawaii Natural Energy Institute (HNEI);

- maintain and distribute the Mitsui-Miami strains;

- characterize key strains by traditional and advanced biotechnological techniques (especially morphological and genetic characterization);

- expand Hawaii's IMBCC, specifically through the gathering of indigenous marine microbes from the Hawaiian archipelago followed by their identification and characterization; and

- establish the operation of an information resource (database) of tropical marine microbes having the ability to produce hydrogen and other products.

Hawaii's approach is to have both a service and research activity that benefits DOE and others. During the past year, the service activity has been dominant as the Mitsui-Miami strains were transferred and maintained for viability and growth. During the coming year, however, the research activity must be enhanced to impart value to these cultures for benefit to DOE, the scientific community and industry. In subsequent years, the research activity will continue to be dominant but a small service activity will still be essential because strains of interest must be maintained and distributed to others. Hawaii's approach is to establish a science-based culture collection with effective management (including database management) that ultimately will be linked to other world-class culture collections, especially those in the United States and Japan.

Importantly, this DOE project is linked to cooperative efforts being supported by the Japanese Ministry of International Trade and Industry (MITI) through its Marine Biotechnology Institute (MBI) and Research Institute of Innovative Technology for the Earth (RITE).

Past Results

This project on the Mitsui-Miami culture collection was initiated in the summer of 1995 with funding being received in October, 1995. The work described represents only Current Year Results.

Current Year Results

Importation

The genera of cyanobacteria in pure culture include: *Anabaena, Aphanothece, Calothrix, Chroococcus, Gloeothece, Hapalosiphon, Lyngbya, Nostoc, Oscillatoria, Rivularia, Scytonema, Synechococcus, and Synechocystis.* The other photosynthetic bacteria include purple nonsulfur bacteria (*Rhodopseudomonas, Rhodospirillum,* and *Rhodomicrobium*), purple sulfur bacteria (*Chromatium, Ectothiorhodospira, Thiocystis, Thiodictyon, and Thiospirillum*), and green sulfur bacteria (*Chlorobium and Prosthecochloris*). This collection of microorganisms, the former Mitsui collection, is being temporarily housed in Larry Brand's laboratory at the University of Miami.

The first task that needed to be performed within the overall IMBCC effort was to secure the proper authorization from the State of Hawaii to import strains of the Mitsui collection. The unique environmental characteristics of Hawaii that make it ideal for tropical biological cultivation and experimentation also makes it particularly vulnerable to threats of harmful foreign species. The nature of this threat is evidenced by the vast majority of native Hawaiian species that are either extinct or endangered -- victims of the uncontrolled spread of foreign species or diseases against which they had no defenses. In order to protect Hawaii's delicate and vulnerable ecology against even more destruction, the State of Hawaii enacted the United States' most restrictive and comprehensive plant and animal importation laws and regulations.

With respect to microorganisms, Hawaii's policy is that the importation of any microorganism is prohibited unless explicitly permitted. Operationally, this is done through a series of Hawaii state government established lists that identify genera of microorganisms as: (a) "conditionally approved," (b) "restricted" for scientific or industrial purposes, or (c) "prohibited." All genera not on the approved or restricted lists are treated as "prohibited." There is, however, a statutory exception which permits the issuance of special permits for unlisted species for the purpose of conducting medical research or remediating environmental or ecological disasters.

In Hawaii, importation is the administrative responsibility of the State's Department of Agriculture, Plant Quarantine Branch (PQB). Importation can be legally approved only through securing a permit from PQB. The time and effort required to secure importation permits depends on the category in which the microorganism in question falls. Approval can require anywhere from two months to two years.

Under Hawaii regulations, the Mitsui collection fell into two categories and accordingly two separate applications had to be made to import the desired strains. The first consisted of an application to import those strains that appear on the State's "restricted" lists. This application, made on February 22, 1995, was approved by the Board of Agriculture on May 18, 1995. Strains associated with the ten genera of cyanobacteria and two genera of photosynthetic bacteria approved in that application were imported to Hawaii in August 1995.

The second application was to cover the request to import strains that do not currently appear on a Hawaii State list. They are treated as "prohibited" unless they are formally added to the "restricted" list. The process of "listing" is a time-consuming process involving approvals from departmental staff, the Microorganisms Advisory Subcommittee, the Plants and Animals Advisory Subcommittee, the Board of Agriculture, the Attorney General, public hearings, and the Office of the Governor. Depending upon internal workload within these organizations, degree of controversy, and degree of perceived importance, the process can take anywhere from between two months and two years. The IMBCC "listing application" for the 11 unlisted genera has been approved by the Department of Agriculture.

Despite the laudable purpose of Hawaii's quarantine policy and system, it is obvious that the administrative and temporal burdens imposed by the various organizations involved restrict or inhibit the development of a vital, accessible international culture collection. HNEI has been working with

Table 2. Cyanobacteria - Record of Strains

Genus	List. Quar. Appl.	Listed Not Imported	Imported	Imported Visibly Viable	Imported Not Visibly Viable	Transfer. Visibly Viable	Transfer. Not Visibly Viable
Anabaena	17	0	17	16	1	16	0
Calothrix	25	0	25	25	0	24	1
Gloeothece	2	0	2	2	0	2	0
Hapalosiphon	1	1	0	0	0	0	0
Lyngbya	4	3	1	1	0	1	0
Nostoc	54	0	54	48	6	48	0
Oscillatoria	35	2	33	29	4	29	0
Scytonema	6	0	6	6	0	6	0
Synechococcus	21	0	21	18	3	17	1
Synechocystis	2	0	2	2	0	2	0
Totals	**167**	**6**	**161**	**147**	**14**	**145**	**2**

Table 3. Purple Nonsulfur Bacteria - Record of Strains

Genus	List. Quar. Appl.	Listed Not Imported	Imported	Imported Visibly Viable	Imported Not Visibly Viable	Transfer. Visibly Viable	Transfer. Not Visibly Viable
Rhodopseudo-monas	458	53	405	391	14	352	53
Rhodospirillum	3	2	1	1	0	1	0
Totals	**461**	**55**	**406**	**392**	**14**	**353**	**53**

Plans for Future Work

Status of Economic Evaluation/System Analysis

While it is premature to conduct an economic evaluation or systems analysis, the Mitsui-Miami cultures represent multi-million dollar investments from DOE and NSF over a 20-year time span. The IMBCC represents a valuable resource to DOE, research scientists, and industry because it already contains the largest number of tropical marine microbes able to generate hydrogen. A key to commercialization is the availability of the "right" microbes to be used by industry.

Projected Goals/ Basis for Goals

Success in the near term will be: completing the transfer of remaining strains of potential value in the Mitsui-Miami collection; maintaining the viability of cultures already transferred; characterizing presently available strains; expanding the IMBCC with indigenous marine microbes; and completing the formulation of the information resource (database). Success in the long term will be: serving the role of the prime U.S. repository for tropical marine microbes capable of producing hydrogen and other valuable products; providing strains to other scientists for research; serving as the "core" for an international bioinformatics network on these microbes; and ultimately providing superior strains to industry for use in commercial operations.

Major Barriers to Meeting Goals

Major barriers include: restrictions on importing mixed cultures of the Mitsui-Miami collection into Hawaii; timely upgrading of the facility now housing the IMBCC (with backup systems for storage and maintenance of valuable cultures); timely application of digital image analysis; and the development of effective bioinformatics data storage and distribution systems.

Special Features of Project

This project, being funded by DOE, is part of a general U.S.-Japan understanding that fosters binational cooperative research in biological hydrogen production. DOE is providing funding for the transfer of the Mitsui collection, the establishment of a scientific base of the IMBCC collection, and for the dissemination of the Mitsui strains to other qualified researchers at national laboratories and industry. Funding from Japan is being used in two ways. Funding from the Research Institute of Innovative Technology for the Earth (RITE) is being used to evaluate photosynthetic bacteria in Mitsui's collection for active hydrogen production. Funding from MBI is being used for systematics and database improvements.

Relationship to Hawaii's Biohydrogen Program

This project is part of Hawaii's (HNEI) overall research effort on biological hydrogen production. It is, however, the basis for future research on other aspects, in particular the proposed project on bioprocess engineering and system design that will employ a two-stage single cyanobacteria (*Spirulina*) for producing hydrogen.

Acknowledgment

The authors thank the other senior research members of the Hawaii's Biohydrogen team: Dulal Barthakur and Brian Nakamura. We also acknowledge the technical support of Brenda Yass and

ABSTRACT

We maintain a culture collection of over 2,500 cyanobacteria and photosynthetic bacteria and 2,000 eukaryotic algae for research on H_2 biophotoproduction as well as other projects. A high H_2-producing strain Synechococcus sp. Miami BG 043511 from the collection has been used to examine H_2 production in relation to water photolysis and substance degradation, high O_2-tolerance characterization of nitrogenase, and interactive effects of light intensity and cell density on H_2 production and its stable isotope fractionation. When cellular carbohydrate is depleted, no H_2 production occurs. However, when pyruvate or glucose is added, H_2 production begins. On the other hand, when glucose and DCMU are added to cellular carbohydrate-depleted cells from synchronous cultures, H_2 production is inhibited compared with that with glucose addition alone. These results indicate that water photolysis alone cannot directly induce H_2 production, but it acts together with cellular glucose degradation to enhance H_2 production. The cyanobacteria strain, unlike unicellular green algae, shows no significant difference in H_2 evolution with or without O_2 removal reagent (Fieser's solution: sodium dithionite/sodium anthraquinon-ß-sulfonate/KOH water solution) treated. When 10-hr cells are incubated in the dark with injected O_2, H_2 evolution is induced, accompanied by O_2 consumption. When zero-hr cells of synchronous cultures are incubated with 5% CO_2, the carbon is assimilated under light and O_2 accumulates. Even when cells are under aerobic conditions with 25 μmol O_2/mg dry wt., H_2 production is still induced, comparable with that under anaerobic conditions. The H_2-light curve has a pattern similar to CO_2-light curves, the light saturation point increasing, and the magnitude of H_2 accumulation decreasing, with increasing cell density. Fractionation factor, α_{H_2} values, varied from 0.30 to 0.41 in light intensities ranging from 10 to 150 μmol $\cdot$ m^{-2} $\cdot$ s^{-1}. At a given cell density, however, deuterium in H_2 is enriched, instead of the expected depletion, linearly with light-induced increase in H_2 production.

INTRODUCTION

Cyanobacteria is one of three groups of photosynthetic microorganisms (Senger, 1996) that have been investigated for H_2 photoproduction. The other two groups are aquatic green algae and photosynthetic bacteria. In terms of electron source, there are two types of H_2-photoproducing biosystems. Aquatic green algae and cyanobacteria use water as an electron source and photosynthetic bacteria use organic or inorganic compounds such as CO (Weaver, et al. 1993) as electron sources for conversion from protons to H_2.

Since the 1970's, both marine cyanobacteria and photosynthetic bacteria have been used in the lab as materials for H_2 photoproduction. These isolates plus Brand's prokaryote and eukaryote collections have provided a valuable resource pool for research on H_2 biophotoproduction and other purposes. These collections are maintained for the needs of all other laboratories for further development.

Since the 1980's, some unicellular cyanobacterial strains, Synechococcus sp. Strain Miami BG 043511 and 043522 with certain advantageous characteristics, have been used as the primary materials for H_2 photoproduction. These studies have attracted other researcher's attention worldwide (Rao and Hall 1996) and been recommended for further examination.

In recent years, we have focused on those aspects that are closely associated to the practical application of H_2 biological hydrogen production, specifically, the characteristics of the currently used strains in the rate of H_2 photoproduction, O_2-tolerance or O_2-resistance, and the responses to some nutrients.

In the past year, we made more efforts on the following aspects: maintenance of the isolates, and experiments with Synechococcus 043511, which include H_2 production in relation to water photolysis and substance degradation, high O_2-tolerance of nitrogenase, and the interaction of light intensities and cell density on H_2 production.

MATERIALS AND METHODS

1. Organism, cultures and cultural conditions

Synechococcus sp. strain Miami BG. 043511 (Mitsui et al. 1986, 1987) was used as a material for batch and synchronous cultures.

1) Batch culture

The strain was inoculated and grown as described previously (Luo and Mitsui 1994) in a 2.5 liter culture flask containing 1.5 liter of a combined nitrogen-free artificial seawater medium, A-N, with a salt condition of 3% (18 gram of NaCl per liter) and with a pH value of 8.5 (adjusted by 2 N of NaOH). Culture was maintained at 27±1°C under continuous illumination of 150 $\mu E \cdot m^{-2} \cdot s$ from one side and was constantly aerated by bubbling air from the bottom.

2) Synchronous cultures

The strain was grown in a combined nitrogen-free and $NaHCO_3$-enriched (2.5 g/liter) artificial seawater medium, A-N, at 30°C and aerated with 4% CO_2-enriched air, as described previously (Leon, Kumazawa and Mitsui1986; Mitsui and Cao, 1988). The growth under a continuous illumination with white fluorescent light of an intensity of 150 $\mu E \cdot m^{-2} \cdot s^{-1}$ was for 72 hr before the cultures were treated with synchronous growth with a period of 16 hr in dark and 16 hr in light. After the treatment, the synchronous growth began under continuous light. Base on the needs of experiments, zero-hr cells (harvested at the end of synchronous cultures) or 10-hr cells (harvested at the 10 hr after the end of synchronous culture), or both were used in the studies.

2. Preparation of incubation medium and organic substances

Composition of incubation medium was the same as that of batch culture medium except with 10 mM HEPES buffer and final pH = 7.6.

Organic compounds, glucose and pyruvate salt were dissolved in the incubation medium. When the pH of the organic compound solution deviated more than ±0.1, it was adjusted to 7.6 with 4N NaOH or HCl solution. 2 M stock solutions were prepared from each of the organic compounds.

3. Incubation conditions

The cultures were harvested by centrifugation, and washed once and resuspended with A-N medium (pH = 7.6) with buffer HEPES (20 mM). The NaCl concentration of A-N medium for washing and suspending the synchronous cells was 18 g/liter. Aliquot of 5 ml cell suspensions were put into 25 ml micro-Fernbach flasks and sealed with butyl rubber stoppers. The gas phase of the flasks was changed to argon gas by repeatedly evacuating and flushing. The flasks were

incubated in an shaker illuminated underneath water bath by white light intensity (150 μE • m-2 • s-1) at 30° C. For light controlled experiments, light scheme was made by setting different layers of screen on the bottom of water bath and light intensities were varied from 10 to 150 μE/m2/s. Incubation period was varied with experiments.

4. Determination of H_2 and O_2 production

The amounts of H_2 and O_2 evolved were determined by taking a small aliquot (100 μl) of sample with needle from incubation vessel and then measuring at a gas chromatography (GC-8A, Shimadzu) (Kumazawa and Mitsui 1981).

5. Measurements of cellular glycogen (glucose)

Cells were harvested by centrifugation, washed twice with incubation medium and suspended in distilled water. Cellular glycogen (glucose) was then determined by the method of Dubois et al. (1956).

6. O_2 removal

Five ml of Synchronously cultural cells were distributed into 25-ml incubation vessel around a 1.5 ml volume of little vial that was set the center of vessel. Varied content of Fieser's solution: sodium dithionite/sodium anthraquinon-ß-sulfonate/KOH water solution was added on a piece of paper filter that was inserted into the vial. O_2 photo-evolution from the cells are removed from the gas phase into the vial by reaction of the Fieser's solution with O_2.

7. Dry weight and chlorophyll measurement

Twenty five ml of cell suspension was collected on a preweighted glass micro-fiber filter (Whatman, 934AH) and washed twice with distilled water. Cellular dry weight was measured after the filter was dried at 90°C for 24 hr.
In some cases, the dry weight of the cell suspension was estimated from its chlorophyll concentrations using a standard curve correlating dry weight and chlorophyll concentrations. Chlorophyll was determined by the method of Holm-Hansen and Riemann (1978).

8. H_2 isolation from gas phase for stable isotope analysis

Flasks with the produced gases were connected to a vacuum system and gases passed through two liquid nitrogen traps, one with glass beads to remove water and another with silica gel (about 10 grams, mesh size 8~20, Davison Chemical Baltimore, Maryland USA) to remove argon, oxygen and all other condenscible trace gases. Hydrogen gas (between 100 to 160 μmols) was collected with a Toepler pump for a period of one and a half hour and analyzed for D/H ratios. Medium with cell suspension in flasks was frozen and hydrogen gas pumped two to three times so that gases dissolved in water would also be collected. This process effectively separated hydrogen gas from other contaminants without fractionation, as described by Luo et al (1991).

9. Stable isotope expression

Hydrogen isotopic ratios are expressed here as δD values, where

$$\delta D\ (‰) = [(D/H)_{sample}/(D/H)_{SMOW} - 1] \times 10^3 \qquad (1),$$

where subscription SMOW is an abbreviation for standard mean ocean water. δD values of photoproduced hydrogen increase linearly with increasing concentration of deuterium in medium water (Luo et al. 1991) and agreed with a linear relation described by the equation:

$$\delta D_{H_2} = \alpha_{H_2} \bullet \delta D_w + (\alpha_{H_2} - 1)\ 10^3 \qquad (2),$$

or

$$\alpha_{H_2} = (\delta D_{H_2} + 10^3) / (\delta D_w + 10^3) \qquad (3),$$

where α_{H_2} is fractionation factor for the production of hydrogen gas and equal to $(D/H)_{H_2}/(D/H)_w$, the ratio of deuterium to hydrogen in H_2 relative to deuterium content in H_2O in which the cyanobacteria was incubated. Subscript w means water from which H_2 is derived. The values of α_{H_2} are thus varied between zero, e.g., no deuterium in a gas sample (an extreme situation) and one, e.g., D/H ratio is equivalent between gas and water (another extreme case). Therefore, the larger the value of α_{H_2}, the enriched the deuterium content in hydrogen gas.

I. MAINTENANCE OF COLLECTIONS

Our culture collection consists of approximately 200 pure cyanobacterial cultures, 750 pure cultures of photosynthetic bacteria that have been identified, approximately 1,700 cyanobacterial cultures that have not yet been identified and approximately 2,000 cultures of eukaryotic algae. We maintained 3 sets of each culture in 3 different temperature controlled culture rooms to insure that the cultures are not lost.

Culture media include both artificial sea water (Mitsui and Cao, 1988) and natural seawater autoclaved in teflon bottles with various nutrients added. We have several tons of this seawater collected from the Northeast Providence Channel of the Bahamas. This seawater is used because it is much cleaner than coastal water or artificial seawater. The cyanobacterial cultures are maintained in the culture media shown in Table I-1, except that nitrate and ammonia are left out of the media for nitrogen fixers. Details on the procedures we use for maintaining our cultures are given in Brand (1990). To maintain some of the cultures in the conditions that they are presently in, some of the media have their salinity altered to 9, 18, and 45 ppt and pH altered to 6.5, 7.5 and 9.5. The lower salinity are achieved by adding 18 megaohm deionized water and the higher salinity is achieved by evaporation. The lower pHs are achieved by adding HCl and the higher pH is achieved by adding NaOH.

We maintain these cultures and provide them to researchers interested in their hydrogen production capabilities as well as other biochemical capabilities.

II. WATER PHOTOLYSIS AND SUBSTANCE DEGRADATION

for H_2 production by Synechococcus sp. 043511

Hydrogen biologically derived from water photolysis is the target of the biosolar energy conversion project that has been long pursued. However, the rate of H_2 driven only by water splitting never reaches a level equivalent to one tenth of general photoconversion efficiency.

The rate of H_2 photoproduction is controlled by multiple factors. Even if the effects of environmental factors is not taken into account, the characteristics of a species itself, e.g. enzyme catalyzing activities, coupling mechanism between electron sources and protons, and O_2 tolerance, photoconversion efficiency, etc., all affect the rate of H_2 production. In other words, photoconversion efficiency is not the sole factor that determines hydrogen conversion from protons. Bothe (1983) indicated that if H_2 is derived from water only, a rate of 20 μmoles H_2/mg Chl • hr means that all the electrons flowing to nitrogenase must reduce proton. Only cells devoid of any regulatory mechanism to switch off the energy consuming reaction would sustain such high production over a longer period.

However, our previous work has shown that the rates of H_2 production with Synechococcus 043511 and Oscillatoria BG 7 are 10 times higher than that Bothe estimated. We hypothesize that the enhancement in H_2 production by the

cyanobacteria is because hydrogen evolution is driven by electrons from both water photolysis and degradation of cellular substance that has been accumulated through photosynthesis in early stage. In this study, we examined the dependence of H_2 production by Synechococcus 043511 on substance and the dependence of enhancing H_2 production on incident light intensity.

Results

H_2 evolution in relation to cellular carbohydrate

In batch culture, H_2 photoproduction activity last longer in young cells than old cells. As shown in Fig. II-1A, under the same incubation conditions, 2-day old cells can continue H_2 evolution for 7 days to reach the maximum level of H_2 accumulation. With cell aging, the time of maintaining a H_2 evolution activity decreases. As a result, the maximum H_2 accumulation from each age of cells reduced rapidly from about 30 μmol per vessel by the 2-day old cells to less than 2 μmol per vessel by the 9-day old cells, although chlorophyll a concentration in the same volume of incubation vessels increased with cell age of batch cultures.

There is a close correlation between H_2 evolution activities or the maximum H_2 accumulation in each age of cells and the relative glycogen content in the corresponding age of cells (Fig. II-1B). The correlation line might be separated into two age stages on the basis of H_2 production activity. H_2 evolution seems to have a stronger dependence on cellular glucose in the stage one, 2 to 4 days cells, than the second stage, 5 to 9 days old cells. The cellular glucose content corresponding to the two age stages are above and below 30%, respectively. When cellular glucose content is below 5%, for example, shown in 9 day old cells, H_2 photoproduction tends to be trace.

2. H_2 evolution in relation to substrate added

Batch cultures

Subsequently, we used 9-day old cells of batch cultures from a fermenter cultivation facility for a new observation. Results are shown in Fig. II-2. H_2 evolution is soon activated for suspensions that were incubated with addition of pyruvate. A constant rate is maintained for about 5 days for the suspension samples with 5 mM of pyruvate added (Fig. II-2A) and about two weeks for the samples with 25 mM of pyruvate added (Fig. II-2B). In contrast, suspensions without addition of pyruvate had no H_2 photoproduction detectable when the cells

were incubated under the same condition as described above. However, after the "death"-like cells were incubated for 8 days, H_2 photoproduction activity can be reactivated by pyruvate addition (solid cycles in Fig. II-2A,B).

Synchronous cultures

Cells from synchronous cultures were harvested at two times: the end of the last dark period, noted as zero-hr cells (cellular carbohydrate-depleted cells), and the 10-hr after light on, noted as 10-hr cells (cellular carbohydrate-enriched cells). When zero-hr cell suspension was continuously incubated for 24 hr, almost no H_2 photoprouduction was assayed (Fig. II-3A). If glucose is added, H_2 evolution is induced after incubation for more than 10 hr (Fig. II-3B). In contrast to zero-hr cells, 10-hr cells have a strong H_2 photoproduction activity and showed a rapid H_2 accumulation when they are once incubated (Fig. II-3C).

3. Aerobic H_2 evolution in the dark

Since the above measurements indicate a dependence of H_2 evolution on the substrate in cells, it has been assumed that H_2 evolution could be driven by the reducing power via oxidative phosphorylation process. We divided 10-hr cells into two groups, one was incubated under light and anaerobic conditions and another was incubated under aerobic (with 20% of O_2) and dark conditions. The results (Fig. II-4.) show that H_2 evolution indeed occurs in the dark with an accompanied decline in O_2 in the vessel (solid cycles in Fig. II-4B), but the H_2 accumulation is one third of H_2 obtained under light and anaerobic conditions (Fig. II-4A). H_2 evolution curves also indicate that the difference in H_2 evolution by light-anaerobic and dark-aerobic cells appears at the early beginning of incubation.

4. Enhancement effect of light-driven H_2 evolution

The above assay indicates that H_2 production by 10-hr cells was much higher in light than in the dark. In order to demonstrate whether light-driven H_2 evolution has caused the enhancement effect, we divided zero-hr cells with glucose addition into two groups, one was control and another was injected with 15 μM of DCMU. Both were incubated under the same light and temperature conditions for 24 hr. The results show that H_2 evolution is induced at the second period (10 - 20 hr) in both control and DCMU treatments, but in the latter, H_2 production is remarkably inhibited (solid cycles in Fig. II-5A). Interestingly, the

DCMU inhibition to H_2 evolution is partially relief by increasing the concentration of glucose added (Fig. II-5B, C).

Discussion

Results obtained through these experiments with both batch cultures (Fig. II-1 and 2) and synchronous cultures (Fig. II-3 and 4) indicate that carbohydrate degradation is essential for induction of H_2 evolution activity. There are two possibilities that may explain the dependence of H_2 evolution induction on carbohydrate substance. One is that carbohydrate may play a mediating role by increasing C/N ratio that further induces synthesis of nitrogenase. Another is that carbohydrate may be as an electron source (Singh, Chen and Gibbs, 1992).

In batch culture, nitrogenase activity reaches a peak at 2-3 days growth stage, thereafter the activity rapidly decline (Luo and Mitsui, 1994). This observation is consistent with that by Yakunin et al. (1995) with Anabaena sp. Nitrogenase activity has been found to have a good relationship to C/N ratio (Hoover and Ludden, 1984; Yakunin et al. 1995). However, in some other observations (Ernst and Bopger 1985; Nagata and Watanabe, 1990) showed that the C/N ratios in the phototrophic cultures of cyanobacteria growing both under natural and laboratory conditions varies insignificantly in response to environmental changes. Therefore, the C/N ratio in cyanobacteria has been commented not to be a regulating factor for the synthesis of nitrogenase (Ernst and Bopger 1985). Therefore, the mechanism is not clear.

We believe that using molecular biological technology could ultimately understand the mechanism of C/N ratio in mediating nitrogenase activity. Since the mRNA of nitrogenase has been found to exhibit a periodical change that coincides with the appearance and disappearance of nitrogenase activity (Campbell, Takiyama and Mitsui 1994). If C/N ratio determines nitrogenase synthesis, it should be detected by nitrogenase activity after addition of substrate.

Carbohydrate as an electron source for H_2 photoproduction may extensively exist in microorganisms. Thus far, cyanobacteria (Mitsui et al. 1986, 1987; Kumazawa and Mitsui 1992; Luo and Mitsui 1994) and aquatic green algae (Senger 1980; Strecher and Senger 1981) investigated usually use both water (direct) and photosynthate (indirect use of water) rather than water alone as electron sources for synthesis of H_2. Electrons derived from the accompanied dehydrogen process during substrate degradation may support H_2 formation.

III. HIGH O_2-TOLERANT CHARACTERISTICS

Synechococcus sp. 043511 has been demonstrated to have a rate of H_2 production much higher than others. However, the strain like most of other cyanobacteria is a nitrogenase-catalyzing biosystem. Indeed, compared with hydrogenase, nitrogenase needs extra energy to overcome the activation energy barrier. The energy-consuming process has been thought to reduce light use efficiency. However, the process bring two advantages which so far any other H_2 producers lack. First, N_2-fixing cyanobacteria will be self-enriched in nitrogen nutrition that may increase solar conversion efficiency by reducing photoinhibition and the culture would be cheapest. Second, the process makes the H_2 production reaction unidirectional to 100 atm of H_2 (Weaver et al. 1993).

These facts imply that the interest that the high efficiency brings to H_2 production may be offset by the defects in enzyme activity or O_2-resistance, or other factors. We agree with the suggestion by Rao and Hall (1996), at this stage one should not attach too much importance to quantitative photosynthetic efficiency when the solar radiation is free.

In the water-based H_2-producing systems, both hydrogenase and nitrogenase are inevitable to be inhibited by O_2 evolved accompanying H_2 production from water splitting. This has been a main problem to impede the enhancement of H_2 photoproduction in the rate and yield in both micro-green algae and cyanobacteria. However, our previous observations have shown that Synechococcus sp. 043511 has a O_2-tolerant capacity higher than others (Nemoto 1995) that have been investigated.

In order to further examine the characteristics of Synechococcus sp. 043511 in O_2 resistance or tolerance during nitrogenase activity stage, we performed the experiments: the effect of O_2 removal on H_2 photoproduction, the effects of O_2 injected (outer O_2) on H_2 photoproduction, and the effect of O_2 accumulated (inner or cellular O_2) during photosynthesis stage on H_2 photoproduction.

Results

1. Effect of deoxygen agent on H_2 and O_2 evolution

In incubation vessel, oxygen evolved from cell suspension under light was trapped by deoxygen agent. There are no significant alterations in H_2 accumulation between control and deoxygen-agent treated samples (Fig. III-1A), although the concentration of oxygen in gas phase of vessels decrease with increasing the concentration of deoxygen agent (Fig. III-1B). Since H_2 accumulation has no statistical difference, the change in oxygen is expressed here by O_2/H_2 ratio. When cell suspension was incubated without deoxygen agent, the ratio is around 0.5 on average at the end of 24-hr incubation, although there was a big deviation between two periods (0 - 12 hr and 12 - 24 hr). In the same time period, the ratio was decreased to about 0.25, 0.1 and almost zero, respectively, when 0.05 ml, 0.1 and 0.2 ml of deoxygen agent solution were added into the vials in the incubation vessels.

2. H_2 productions in aerobic/dark and in anaerobic/light conditions

Ten-hr cells (carbohydrate-enriched cells) of synchronous culture has a active H_2 evolution when they are incubated under anaerobic and light conditions (Fig. III-2A). In the dark, when the culture is incubated with various O_2 concentration, H_2 evolution also is induced (Fig. III-2B, C). The activity of H_2 evolution was increased with increasing O_2 concentration up to 40% in incubation vessel (Fig. III-2C). Correspondingly, oxygen is being consumed with incubation time. Interestingly, during the 12-hr incubation, the relationship is non-linear between the maximum H_2 accumulation and the amount of O_2 consumption (Fig. III-3).

3. Effect of inner O_2 evolved from photosynthesis on H_2 production

In light, when zero-hr cells (carbohydrate-depleted cells) were incubated with various concentration of CO_2 injected, O_2 evolution rapidly accumulated in the incubation vessel accompanying CO_2 assimilation during photosynthesis stage (Fig. III-4). The suspension could fix whole CO_2 injected within 3 hrs in 1.5% and 5% CO_2 treatments but it might take more than 10 hrs in 20% CO_2 treatment. After 10 hr incubation, the half of these incubation vessels were subjected to re-flushing with Ar and then continued to be incubated, H_2 evolution was induced during the next 10 hr, nitrogenase activity stage. In contrast, another half of incubation vessels that were not reflushed with Ar seemed to evolve H_2 earlier than Ar-reflushed treatments. For example, 5% CO_2 injected vessels contained 25 μmol O_2 /mg dry wt., H_2 accumulation reached 6.5 μmol/mg dry

wt. by the end of the experiment, whereas it reached about 8 μmol H_2/mg dry wt. in the Ar-reflushed samples.

Discussion

Although 0.1 ml of deoxygen agent solution treated suspension had the highest H_2 accumulation, the deviation (n = 5) shows no significant differences among the treatments and control. Therefore, Synechococcus sp. 043511, unlike unicellular green algae (Krasna, 1977), is insensitive to O_2 removal.

The efficiency of dark H_2 conversion from carbohydrate degradation seems to be much low as compared with those in anaerobic and light conditions, but it implies a high O_2-tolerance of nitrogenase in the strain. In addition, the maximum H_2 accumulation has an exponent relation to the dark consumption of O_2, probably indicating dependence of the efficiency on the O_2 pressure in incubation vessels.

When zero-hr cells from synchronous cultures were incubated in light with 5% CO_2, the carbon was absorbed rapidly and simultaneously O_2 (25μmol/mg dry wt.) evolved. Under the O_2 concentration, the strain does maintain H_2 production, comparable with that under anaerobic condition. The interactive effects of light and O_2 conditions on H_2 production need to further studied.

IV. INTERACTION OF LIGHT INTENSITIES-CELL DENSITIES

Previous work has shown that H_2 photo-produced by both unicellular strain, Synechococcus sp. 043511, and heterocystous filamentous strain, Anabaena sp. TU 37-1 is extremely depleted in deuterium relative to water from which the gas is derived (Luo et al. 1991). We compared them with deuterium content in gaseous hydrogen formed from electrolysis of water, and found that biologically photo-produced H_2 is always enriched in deuterium as compared with electrolytically produced H_2.

As dynamic effect determines stable isotope fractionation, deuterium would be more depleted in gaseous hydrogen, if it is faster converted from protons and electrons into H_2. This explains the difference in hydrogen isotope fractionation between biologically photo-produced H_2 and electrolytically produced H_2,

because H_2 formation reaction experiences more steps in biological pathway relative to water electrolysis process (Krasna, 1977). If this explanation is correct, then an enhancement in the rate of H_2 photoproduction should induce a relative depletion in deuterium in H_2.

In order to demonstrate whether deuterium depletion in H_2 is associated to an increase in the rate of H_2 formation in cells, we used synchronous cultures of strain 043511 for H_2 biophotoproduction and controlled the rate of H_2 production by altering light intensities and the concentration of chlorophyll a for incubations. Correspondingly, stable isotope composition of H_2 evolved by the cultures were analyzed.

Results

1. H_2 production responses to low light intensities

Assays were made with two different synchronous cultures for measurements of H_2 production. H_2 productions by the suspensions with various cell densities are plotted against light intensities (Fig. IV-1A,B), showing the same pattern in H_2 production-light intensities curves in the two independent measurements. Light intensities varied from 10 to 150 $\mu E \cdot m^{-2} \cdot s^{-1}$ within this range of light intensity, H_2 production tended to cease if Chl a below 80 μg/ml suspension.

2. H_2 production by suspensions with different cell densities

When H_2 productions are plotted against the concentration of Chl a, there are the same pattern in H_2 production-cell densities curves in the two independent measurements. The both measurements (Fig. IV-2A,B) showed that when cell densities were low, the differences in H_2 production that were caused by the various light intensities were small. However, when cell density was high, the difference increased.

3. Effects of light intensities on Chl a in incubated cells

During 24-hr incubation, to certain extent, all incubated suspensions were changed in green color. After the incubation, the suspensions were taken for the measurements of Chlorophyll a again. The results showed that there were a significant deviation in the concentration of Chl a before and after incubation.

As shown in Fig. IV-3A and B, Chl a ratio, that is, the concentration of Chl a in the suspension after incubation over before incubation, is generally below or close to one, then increased with increasing light intensity. When light intensity was elevated to more than 40 μE • m^{-2} • s^{-1}, the ratio declined.

4. Stable isotope fractionation of photoproduced H_2

Stable hydrogen isotope fractionation is expressed here as α_{H_2} value (see the Method section for the definition). The α_{H_2} values have a close linear correlation with H_2 photoproduction (μmol H_2 • mg Chl.$^{-1}$) at a given cell density (Fig. IV-4A,B). Under a given light intensity, concentration of Chl a, and 25-hr period of incubation, each point represents a independent measurement for H_2 production and for α_{H_2} value of the corresponding hydrogen. Points at the lower part of lines indicate the rate of H_2 production and α_{H_2} values under low light intensities, whereas points around upper part of lines show the results under higher light intensities.

Furthermore, if extrapolating down each linear line in Fig, 3 A and B, all these lines would reach the same point at α_{H_2} axis, around 0.25, that is, the value of α_{H_2} in electrolytically produced H_2.

When the concentration of Chl a is low, the rate of H_2 production is relatively high. Thus, the slope of the linear relationship between α_{H_2} and H_2 photoproduction (α_{H_2}/H_2 • mg Chl a) is the index of compartmentation effect of hydrogen stable isotope. It roughly has a linear change with the concentration of Chl a in suspension (Fig. IV-5).

Discussion

Although the H_2-light curves describe a H_2 producing process and CO_2-light curves describe an CO_2-assimilating process, probably equivalent in energy consumption, they are similar in the following three points: (1) the hyperbola pattern of the curves; (2) the light saturation point that increases with increasing cell density; (3) the magnitude of H_2 accumulation that decreases with increasing cell density. For example, when Chl a was increased from 24 μg to 49 μg per 5 ml of suspension, H_2 accumulation increased one time. When Chl a was doubled on the basis of 49 μg, H_2 increased about only one third of H_2 derived from suspension sample with 49 μg of Chl a.

Since the triple measurements (two results are shown here in Fig. IV-3A and B) are similar, these differences in the concentration of Chl a between before and after incubation do not seem to be caused by the error in the experiments. In addition, since the concentration of Chl a was also declined in the suspension that was incubated under low light, the change in Chl a does not seem either to be caused by photobleach. However, at a given cell density, the light intensity under which Chl a was the highest is the same where H_2 production was also the highest. It implies that the changes in Chl a in suspension after incubation could be associated with the H_2 production, but not directly with the light intensity itself. The cause of the changes in the concentration of Chl a after incubation is not totally clear.

Value α_{H_2} represents a relative ratio of deuterium content in gaseous hydrogen to that in water from which the gas is derived. In this present study, when light intensities are varied from around 10 to 150 μmol • m^{-2} • s^{-1}, the α_{H_2} values of H_2 produced by Synechococcus sp. 043511 are ranging from 0.30 to 0.41 (Fig. IV-4A,B). Thus, we have demonstrated that isotope fractionation of bio-photo-produced H_2 would change with light intensities and the concentration of Chl a. However, the trend of the alterations in hydrogen isotope fractionation with the rate of H_2 photoproduction opposites to that we expected. In the other words, the dynamic isotope effect fails to directly describe the alterations in hydrogen isotope fractionation in the H_2 biophotoproduction process.

Cell compartmentation may be a mechanism that can explain the fractionation of deuteron/proton ratio. Because in the process of electrolysis of water into gaseous hydrogen, water pool and the corresponding hydrogen ion pool is much larger, a constant and quick mixture of water near electrode with surrounding water makes it less possible that deuterium enriched water left around electrode could be established. In contrast, in a tiny compartment space, the water pool for H_2 bioproduction in cell protoplasm is limited and may be rapidly enriched in deuterium with constant H_2 photoproduction. In this case, both protons and deuterons are therefore used for H_2 formation, leading to an increase in α_{H_2} value with an increase in H_2 photoproduction.

In fact, compartmentation is a quite common adjusting mechanism for organisms from cells, tissues, organs, till ecosystems. A particular compound gradient across membrane or cell wall may be established within short time. For example, hydrogen ion gradient can be built up between two sides of thylakoid membrane soon after a green organism exposed under light (Rottenberg, 1977).

REFERENCES

Baldwin, E.1970. An introduction to comparative biochemistry. Cambridge University Press. Pp. 88-119.

Bothe, H. 1982. Hydrogen production by algae. In: New trends in research and utilization of solar energy through biological systems. EXS 43. Mislin, H and Bachofen, R. (Ed.), Birkhauser Verlag, Basel. Pp. 65-72.

Brand, L.E. 1990. The isolation and culture of microalgae for biotechnological applications. pp. 81-115, In: Isolation of Biotechnological Organisms from Nature, Ed. by D. P. Labeda, McGraw-Hill.

Cooper, T.G., Filmer, D., Wishnick, M, Lane, M.D. 1969. The active species of 'CO_2' utilized by ribulose diphosphate carboxylase. J. Biol. Chem. 244: 1081-1083.

Dubois, M., Gilles, K. A., Hamilton, J. K., Rebers, P. A., Smith, F. 1956. Colorimetric method for determination of sugars and related substances. Anal. Chem. 28: 350-356.

Ernst, A. And Boger, P.1985. Glycogen accumulation and the induction of nitrogenase activity in the heterocyst-forming cyanobacterium Anabaena variabilis. J. Gen. Microb. 131(12): 3147-3153.

Holm-Hansen, O., Riemann, B. 1978. Chlorophyll a determination: improvements in methodology. OIKOS 30: 438-447.

Hoover, T. And Ludden, P. 1984. Derepression of nitrogenase by addition of malate to cultures of Rhodospirillum rubrum growth with glutamate as the carbon and nitrogen source. J. Bacteriol. 159(1): 400-403.

Krasna, A. I. 1977. Catilatic and structural properties of the enzymes and its role in biophotolysis of water. In Biol. Solar Energy Conversion, Mitsui, A., Miyachi, S., San Pietro, A. And Rtamura, S. (Eds.). Academic Press, New York. Pp. 53-60.

Kumazawa, S., Mitsui, A. 1981. Characterization and optimization of hydrogen photoproduction by a saltwater blue-green alga, Oscillatoria sp. Miami BG 7. I. Enhancement through limiting the supply of nitrogen nutrients. Int J. Hydrogen Energy 6: 339-348.

Kumazawa, S., Mitsui, A. 1992. Photosynthetic activities of a synchronously grown aerobic N_2-fixing unicellular cyanobacterium, Synechococcus sp. Miami BG 043511. J. Gen. Microbiol. 138: 467-472.

Kumazawa, S., and Mitsui, A. 1994. Efficient hydrogen photoproduction by Synchronous grown cells of a marine cyanobacterium, Synechococcus sp. Miami BG 043511, under high cell density conditions. Biotechnol. and Bioengine. 44: 854-858.

Lucas, W.J. And Berry, J.A. 1984. Inorganic carbon uptake by aquatic

photosynthetic organisms. American Society of Plant Physiologists.
Luo, Y-H., L. Sternberg, S. Suda, S. Kumazawa, and A. Mitsui. 1991. Extremely low D/H ratios of photoproduced hydrogen by cyanobacteria. Plant Cell Physiol. 34(6): 897-900
Luo, Y-H. and Mitsui, A. 1994. Hydrogen production from organic substrates in an aerobic nitrogen-fixing marine unicellular cyanobacterium Synechococcus sp. strain Miami BG 043511. J. Biotech. Bioengin. 44: 1255-1260.
Mitsui, A., Cao, S. 1988. Isolation and culture of marine nitrogen-fixing unicellular cyanobacterium, Synechococcus. Methods Enzymol. 167: 105-113.
Mitsui, A., Cao, S. Takahashi, A., Arai, T. 1987. Growth synchrony and cellular parameters of the unicellular nitrogen-fixing marine cyanobacterium, Synechococcus sp. strain Miami BG 043511 under continuous illumination. Physiol. Plant 69:1-8.
Mitsui, A., Kumazawa, S., Takahashi, A., Ikemoto, H., Cao, S, Arai, T. 1986. Strategy by which nitrogen-fixing unicellular cyanobacteria grow photo-autotrophically. Nature 323: 720-722.
Nemoto, Y., Blackwelder, P., Mitsui, A. 1994. Ultrastructural changes during synchronous growth of aerobic nitrogen-fixing marine unicellular cyanobacterium Synechococcus sp. strain miami BG 043511. J. Mar. Biotechnol. 1: 177-183.
Nagata, T. And Watanabe,Y. 1990. Carbon- and nitrogen-to- volume ratios of bacterioplankton grown under different nutritional conditions. Appl. Envirn. Microbiol. 56(5): 1303-1309.
Nemoto, Y. 1995. Biological hydrogen photoproduction. Proceedings of the 1995 U.S. DOE Hydrogen Program Review, Vol. II. April 18-21, 1995. Coral Gables, Florida.NREL. Pp. 617-674.
Rottenberg, H. 1977. Proton and ion transport across the thylakoid membranes. In Photosynthesis I. Photosynthetic electron transport and photophosphorylation. Edited by Trebst, A. And Avron, M. Springer-Verlag, Berlin. Pp. 338-349.
Schmitz, O., Kentemich, T., Zimmer, W., Hundeshagen, B., Bothe, H. 1993. Identification of the nifJ gene coding for pyruvate:ferredoxin oxidoreductase in dinitrogen-fixing cyanobacteria. Arch Microbiol. 160: 62-67.
Senger, H. 1980. Is water the source of photohydrogen? In: Biological applications of solar energy (Snanam, A. et al. eds.). MacMillan Co. of India, Ltd., 1980, Madras, pp. 196- 198.
Senger, H. 1996. Preface to special issue: Biological hydrogen production. J. Mar. Biotechnol. 4: 9.

Singh, K. K., Chen, C. and Gibbs, M. 1992. Characterization of an electron transport pathway associated with glucose and fructos respiration in the intact chloroplast of Chlamydomonas reinhardtii and Spinach. Plant Physiol. 100: 327-333.

Strecher, U. and Senger, H. 1981. Photohydrogen evolution, photoproduction of CO_2 and hydrogenase activity during the cell cycl of Scenedesmus obliquue: Photosynthesis VI Photosynthesis and roductivity, photosynthesis and environmental Sciences Service, Philadelphia, pp. 681-688.

Suda, S., Kumazawa, S., Mitsui, A. 1992. Change in the H_2 photoproduction capability in a synchronously grown aerobic nitrogen-fixing cyanobacterium, Synechococcus sp. Miami BG 043511. Arch Microbiol. 158: 1-4.

Weaver, P., Maness, P.C., Frank, A. Lange, M, and Blaho, J. 1993. Photobiological hydrogen production using whole-cell or cell-free system. In Proceedings of the 1993 DOE/NREL programm review (May 4-6, 1993. Cocoa Beach, Florida. Pp. 7-12.

Yakunin, A. F., Troshina, O.Yu, and Gogotov, I. N. 1995. Relationship between nitrogenase synthesis and the C/N ratio in the nitrogen-fixing cyanobacterium Anabaena variabilis. Microbiology 64(1): 5-6.

Table 1. Basic culture media in natural seawater

Compounds	Concentration
$NaNO_3$	10^{-4} M
NH_4Cl	10^{-5} M
NaH_2PO_4	10^{-5} M
Na_4EDTA	10^{-6} M
FeEDTA	10^{-6} M
$MnCl_2$	10^{-7} M
$ZnCl_2$	10^{-8} M
$CoCl_2$	10^{-9} M
$CuSO_4$	10^{-9} M
$NiSO_4$	10^{-9} M
H_2SeO_3	10^{-9} M
Thiamine	10^{-7} M
Vit B_{12}	10^{-8} M
Biotin	10^{-8} M

CAPTION

Fig. II-1. Hydrogen production by batch culture of Synechococcus 043511 incubated under 150 $\mu E \cdot m^{-2} \cdot s^{-1}$ and 30°C. [A] Time course of H_2 accumulation (μmol H_2/vessel) of various aged cells (some are shown here). [B] The correlation of the maximum H_2 accumulation per mg cell dry weight (μmol/mg dry wt.) to the content of cellular glucose (% of cell dry weight). When cellular glucose content is below 5%, for example, shown in 9 day old cells, H_2 photoproduction tends to be trace.

Fig. II-2. Hydrogen production of 9-day old batch culture. Time course of hydrogen production incubated under light (150 $\mu E \cdot m^{-2} \cdot s^{-1}$) with and without addition of glucose and at the beginning and at the middle (arrows) of incubation in the addition of glucose, and time course of the corresponding O/H ratios. [A] 5mM pyruvate added and [B] 25mM pyruvate added.

Fig. II-3. Time course of H_2 and O_2 evolutions by zero-hr cells (carbohydrate-depleted cells) ([A], control) and ([B], glucose added), and 10-hr cells (carbohydrate-enriched cells) of synchronous cultures incubated under light and anaerobic conditions.

Fig. II-4. Time courses of hydrogen production [A] and oxygen evolution or consumption (μmol/mg dry wt.) [B] by the 10-hr cells of synchronous culture of Synechococcus 043511 incubated under light (150 $\mu E \cdot m^{-2} \cdot s^{-1}$) and in the dark.

Fig. II-5. Time courses of hydrogen production (μmol/mg dry wt.) by the zero-hr cells of synchronous culture incubated with addition of glucose under light (150 $\mu E \cdot m^{-2} \cdot s^{-1}$) with and without DCMU addition.

Fig. III-1. Time courses of O_2/H_2 ratio and H_2 photoproduction during 24-hr incubation of 10-hr cells (carbohydrate-abundant cells) from synchronous culture. A. The changes in O_2/H_2 ratios with time indicate that O2 concentrations in the gas phase were reduced with increasing concentrations of deoxygen agent (Fieser's solution: sodium dithionite/sodium anthraquinon-ß-sulfonate/KOH water solution). B. There were not significant differences in statistics in H_2 photoproduction among O_2 removal treatments and control. Each points represents a mean value of

5-sample measurements.

Fig. III-2. Time courses of H_2 and O_2 production in the anaerobic (gas phase replaced with Ar) and light conditions (150 $\mu E \cdot m^{-2} \cdot s^{-1}$) (A) and O_2 consumption in the aerobic (Ar gas phase injected with O_2) and the dark conditions (B and C) during 12-hr incubation of 10-hr cells (carbohydrate-abundant cells) from synchronous culture. Both the dark and light incubations were maintained at 30°C. Each point is a mean value of triplicates.

Fig. III-3. The maximum H_2 accumulation (μmol H_2/mg Dry Wt.) at each oxygen treatments during 12.5-hr incubation is plotted against the corresponding amount of consumed O_2. Each point represents a mean value of triplicates and the numbers nearby the points indicate the initial O_2 concentration (%) in the gas phase in incubation vessels.

Fig. III-4. Time courses of H_2 and O_2 evolutions or consumptions by zero-hr cells (carbohydrate-depleted cells) of synchronous culture, which were incubated in vessels under light (150 $\mu E \cdot m^{-2} \cdot s^{-1}$) and anaerobic conditions but with injection of gaseous CO_2: 1.5% (A and B), 5% (C and D), and 20% (E and F). After the first period (at 10 hr), one half of vessels were subjected to be in anaerobic conditions by being reflushed with gaseous Ar (A, C and E), whereas another half were retained (B, D and F) for the rest time of the incubation. Note the differences in scale between CO_2 treatments.

Fig. IV-1. Fractionation factor of H_2 produced by Synechococcus sp. 043511, α_{H_2} value, as a function of light intensity(μmol $\cdot$ $m^{-2} \cdot s^{-1}$). The alterations in α_{H_2} value is associated with the concentration of Chl a in the suspensions for incubation. See context for details.

Fig. IV-2. Fractionation factor of H_2 produced by Synechococcus sp. 043511, α_{H_2} value, as a function of the concentration of Chl a (μg/5 ml) in suspension of synchronous cultures. [A] The results in higher light intensities; [B] The results in lower light intensities. See context for details.

Fig. IV-3. Fractionation factor H_2 produced by Synechococcus sp. 043511., α_{H_2} value, as a function of H_2 photoproduction (μmol/μg Chl.a) during 25-hr

incubation. Each point represents an independent incubating sample for H_2 production.

Fig. IV-4. Index of compartmentation effect of hydrogen stable isotope, α_{H_2}/H_2, is plotted against the concentration of Chl a, indicating that in light intensities ranging from 5 to 150 μmol • m^{-2} • s^{-1}, the compartmentation would induce a enrichment of deuterium in H_2 with an increase in the concentration of Chl a in incubation.

Figure 5. Compartmentation model to explain its effect on biological fractionation of stable isotope in bio-produced H_2 and in bio-fixed CO_2 in photosynthesis.

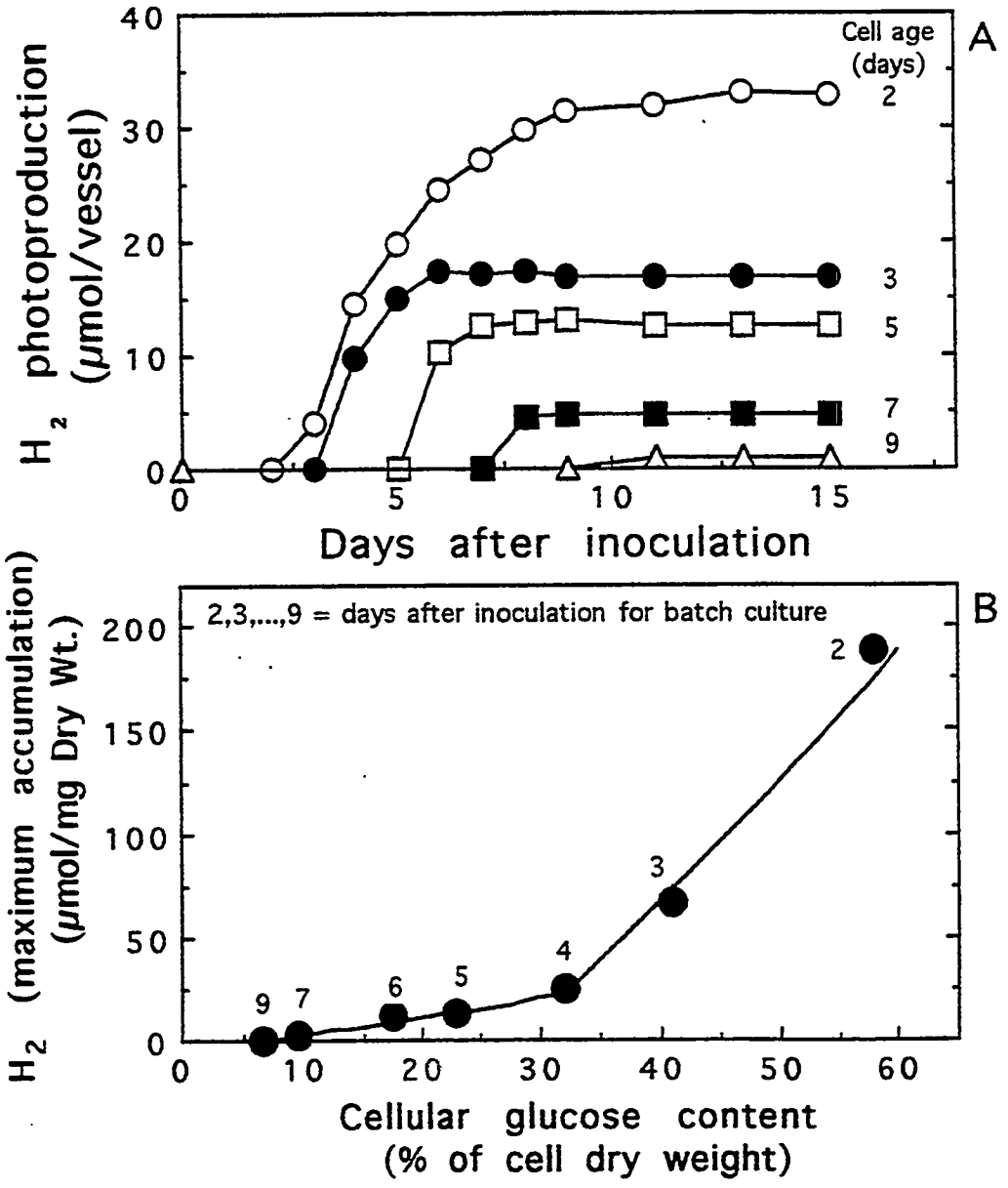

A
Cell age (days)
2
3
5
7
9
H_2 photoproduction (μmol/vessel)
Days after inoculation
B
2,3,...,9 = days after inoculation for batch culture
H_2 (maximum accumulation) (μmol/mg Dry Wt.)
Cellular glucose content (% of cell dry weight)

Figure II-1

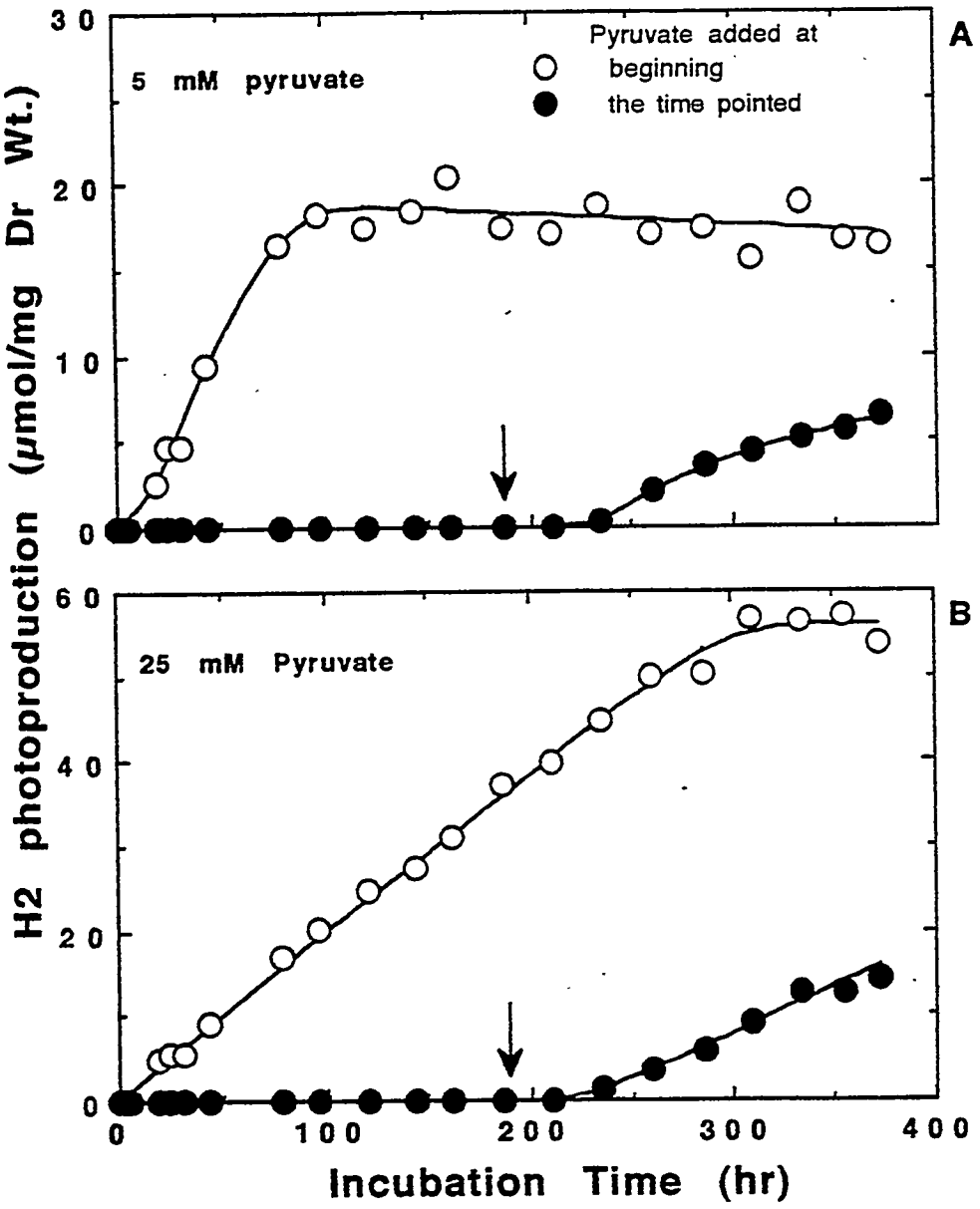

A
5 mM pyruvate
Pyruvate added at
beginning
the time pointed
B
25 mM Pyruvate
H2 photoproduction (μmol/mg Dr Wt.)
Incubation Time (hr)
0
10
20
30
40
60
100
200
300
400

Figure II-2

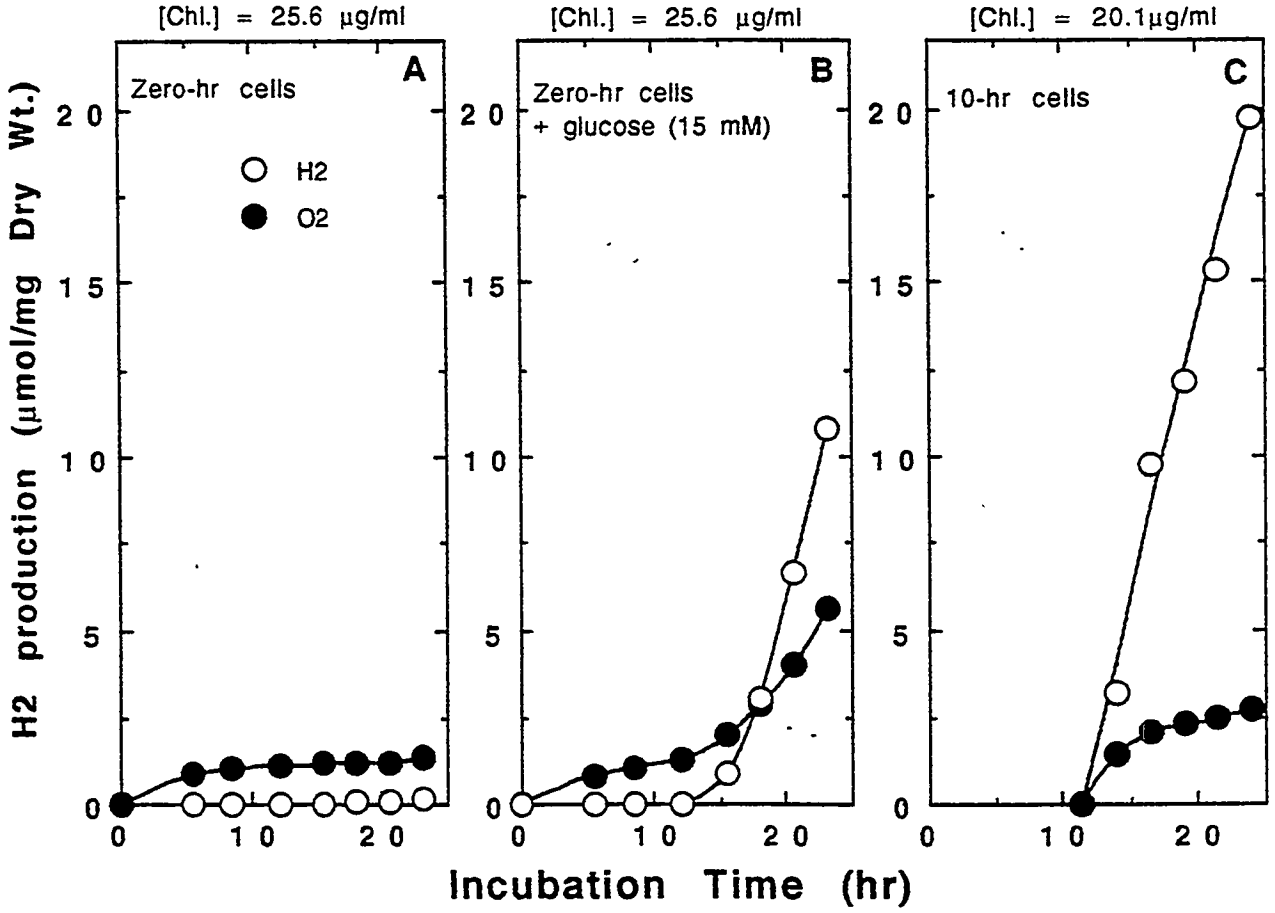

[Chl.] = 25.6 µg/ml
Zero-hr cells
A
H2
O2
[Chl.] = 25.6 µg/ml
Zero-hr cells
+ glucose (15 mM)
B
[Chl.] = 20.1µg/ml
10-hr cells
C
H2 production (µmol/mg Dry Wt.)
0
5
10
15
20
0
10
20
Incubation Time (hr)

Figure II-3

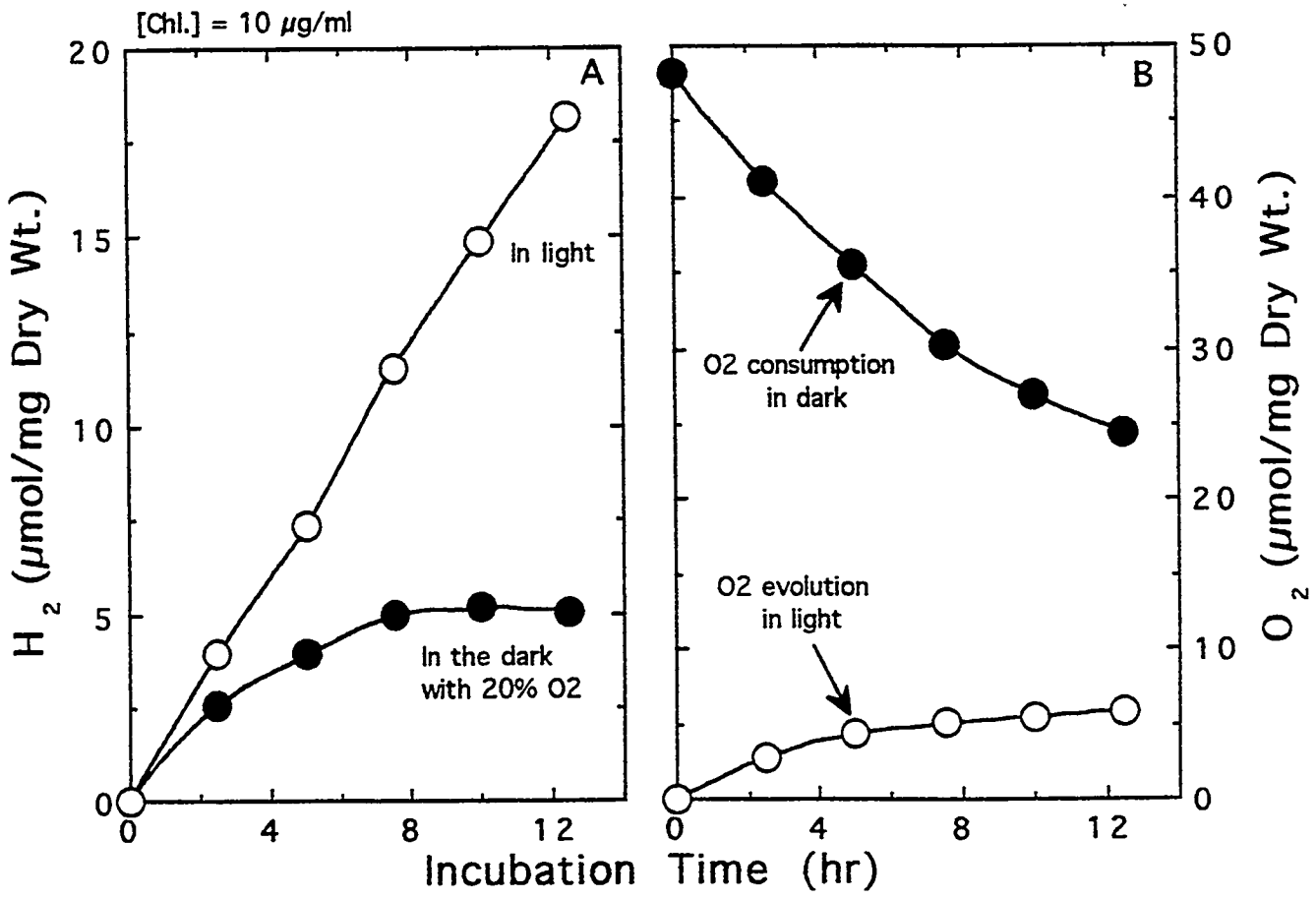

[Chl.] = 10 μg/ml
A
B
In light
In the dark
with 20% O2
O2 consumption
in dark
O2 evolution
in light
H2 (μmol/mg Dry Wt.)
O2 (μmol/mg Dry Wt.)
Incubation Time (hr)
0
4
8
12
0
5
10
15
20
0
10
20
30
40
50

Figure II-4

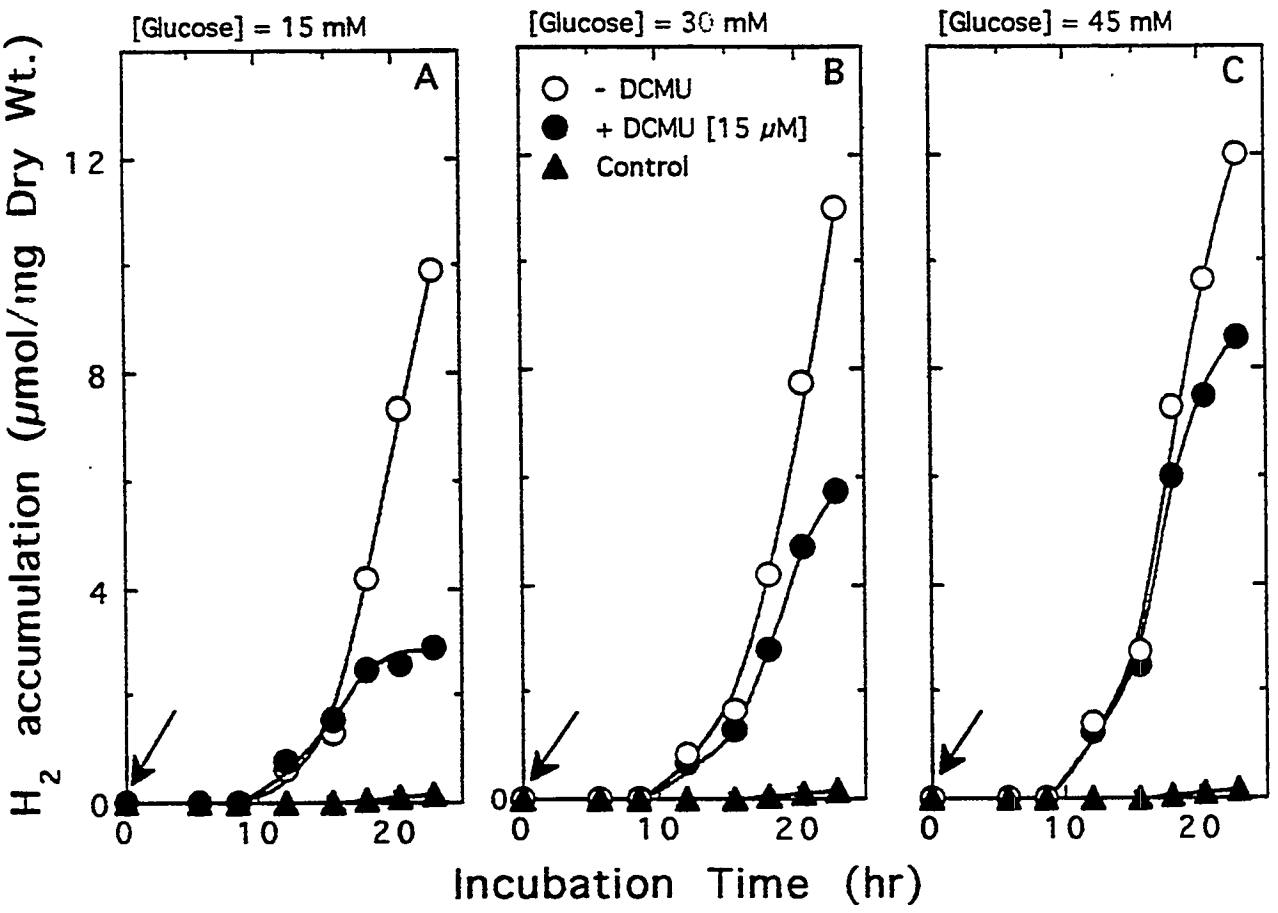

[Glucose] = 15 mM
[Glucose] = 30 mM
[Glucose] = 45 mM
A
B
C
- DCMU
+ DCMU [15 μM]
Control
H2 accumulation (μmol/mg Dry Wt.)
0
4
8
12
0
10
20
Incubation Time (hr)

Figure II-5

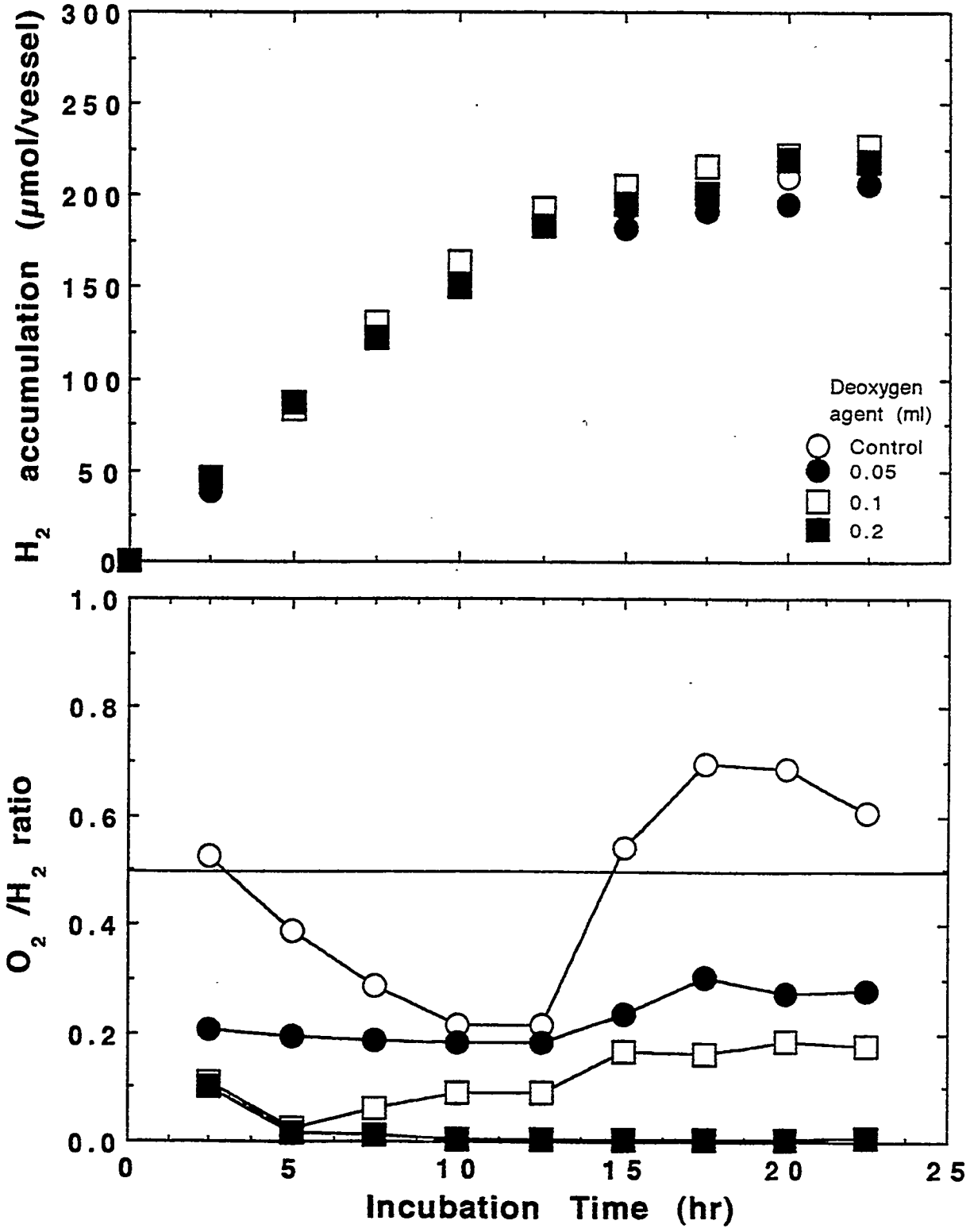

H2 accumulation (μmol/vessel)
300
250
200
150
100
50
0
Deoxygen agent (ml)
Control
0.05
0.1
0.2
O2 /H2 ratio
1.0
0.8
0.6
0.4
0.2
0.0
0
5
10
15
20
25
Incubation Time (hr)

Figure III-1

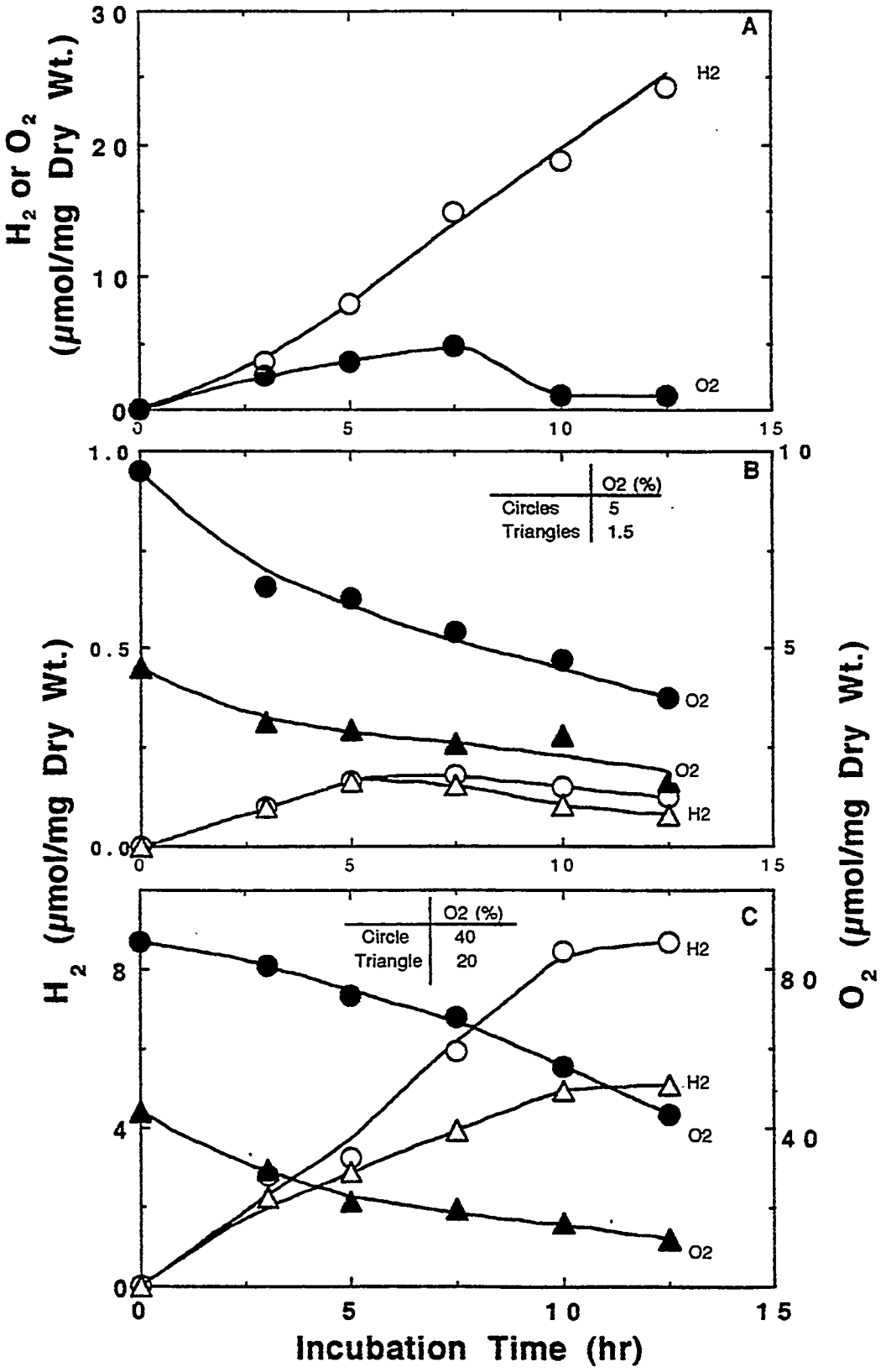

A
B
C
H2
O2
O2 (%)
Circles 5
Triangles 1.5
Circle 40
Triangle 20
H2 or O2 (μmol/mg Dry Wt.)
H2 (μmol/mg Dry Wt.)
O2 (μmol/mg Dry Wt.)
Incubation Time (hr)

Figure III-2

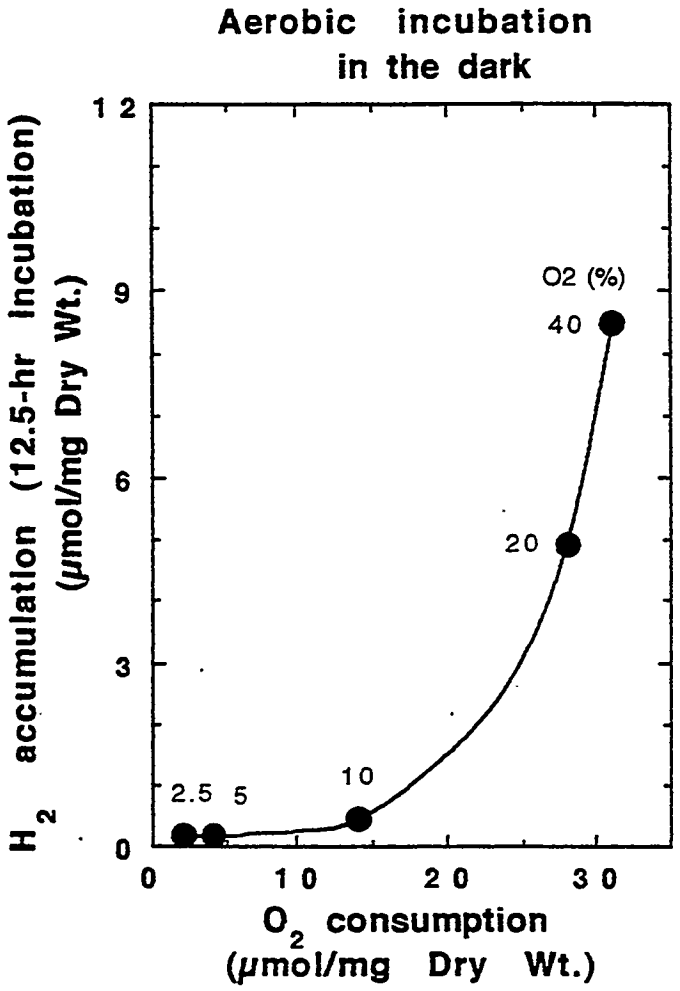

Aerobic incubation
in the dark
H2 accumulation (12.5-hr Incubation)
(μmol/mg Dry Wt.)
12
9
6
3
0
O2 (%)
40
20
10
2.5
5
0
10
20
30
O2 consumption
(μmol/mg Dry Wt.)

Figure III-3

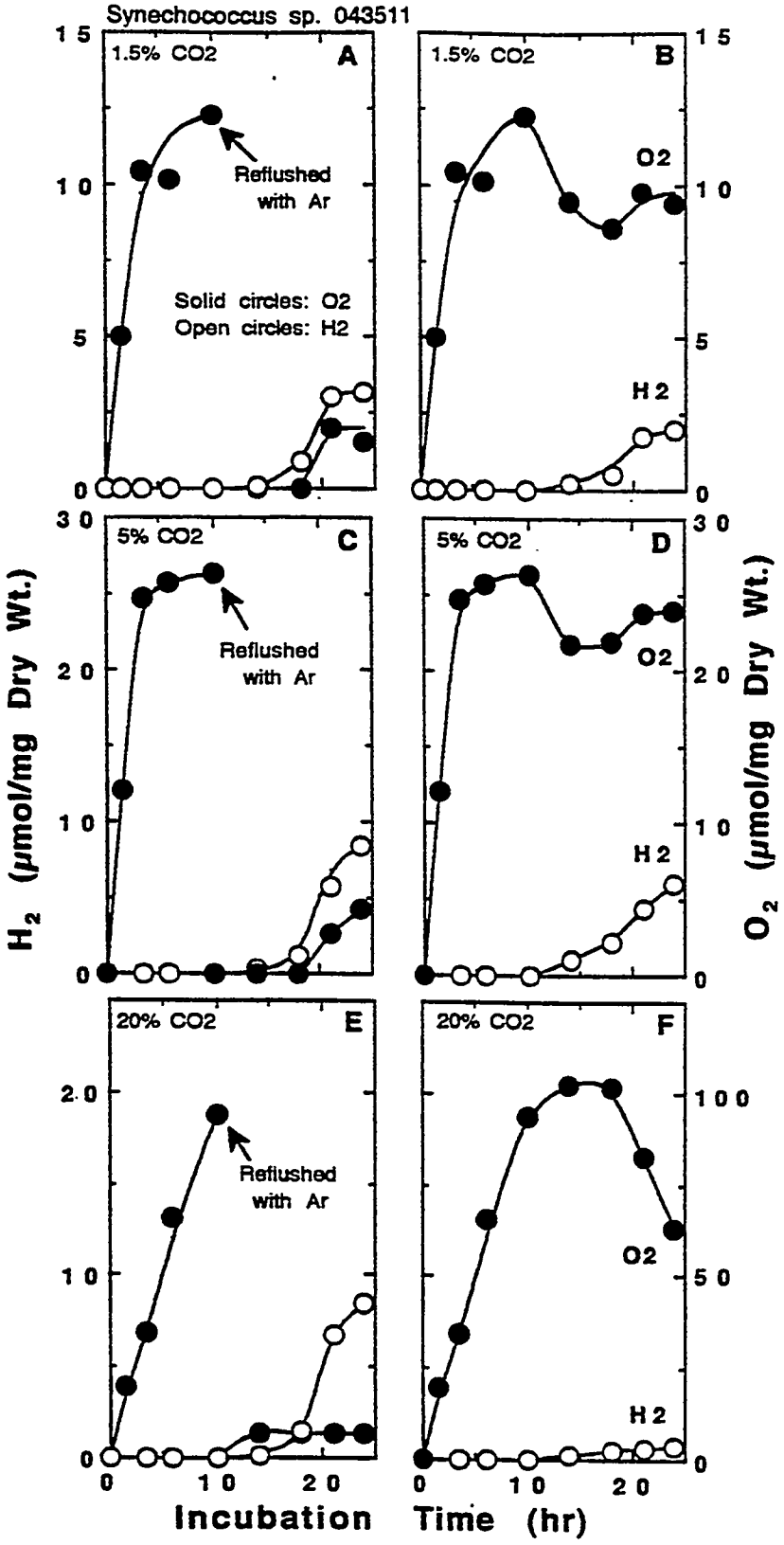

Synechococcus sp. 043511
1.5% CO2
A
Reflushed with Ar
Solid circles: O2
Open circles: H2
1.5% CO2
B
O2
H2
5% CO2
C
Reflushed with Ar
5% CO2
D
O2
H2
20% CO2
E
Reflushed with Ar
20% CO2
F
O2
H2
H2 (μmol/mg Dry Wt.)
O2 (μmol/mg Dry Wt.)
Incubation Time (hr)

Figure III-4

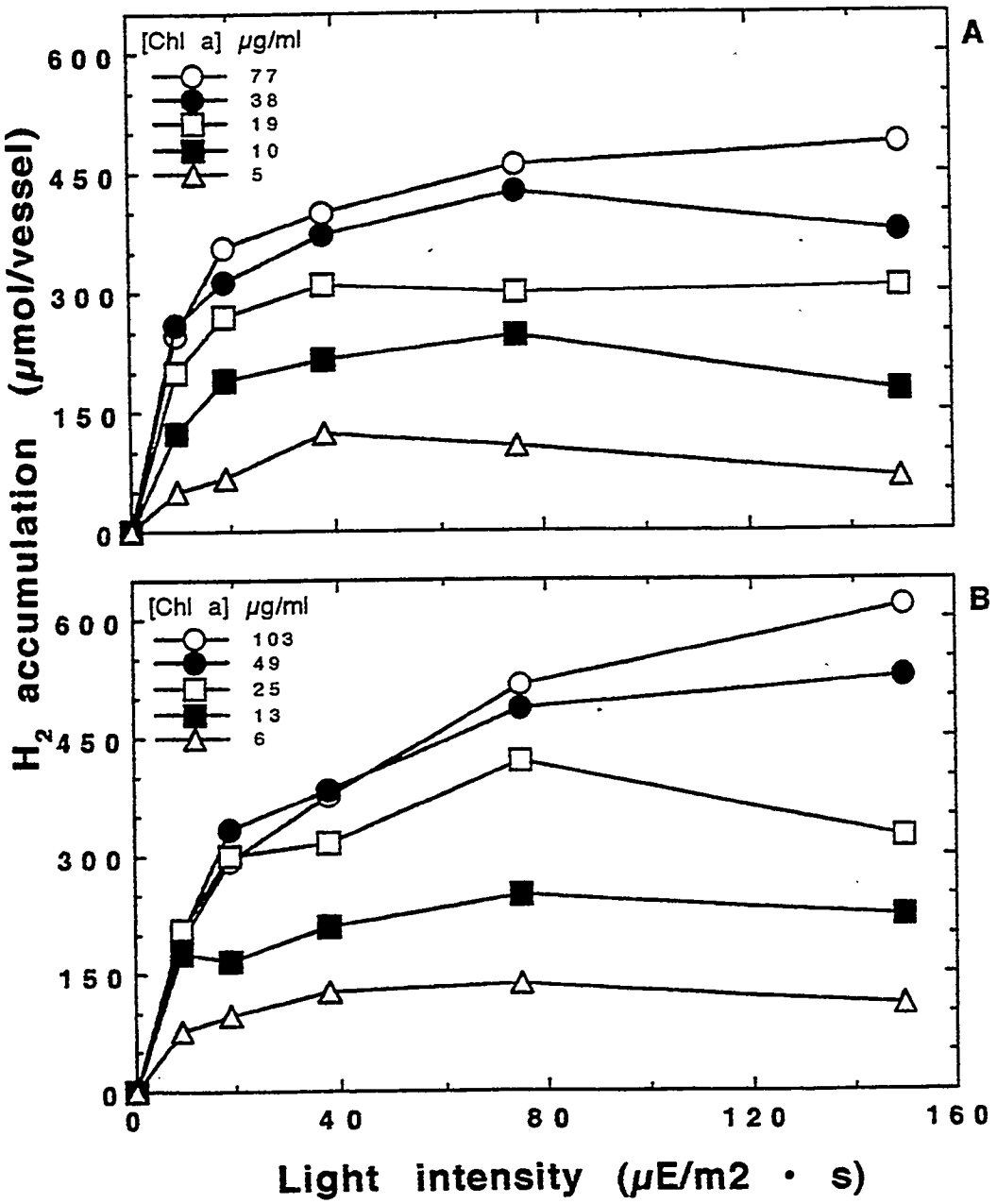

A
[Chl a] μg/ml
77
38
19
10
5
600
450
300
150
0
B
[Chl a] μg/ml
103
49
25
13
6
600
450
300
150
0
0
40
80
120
160
H2 accumulation (μmol/vessel)
Light intensity (μE/m2 • s)

Figure IV-1

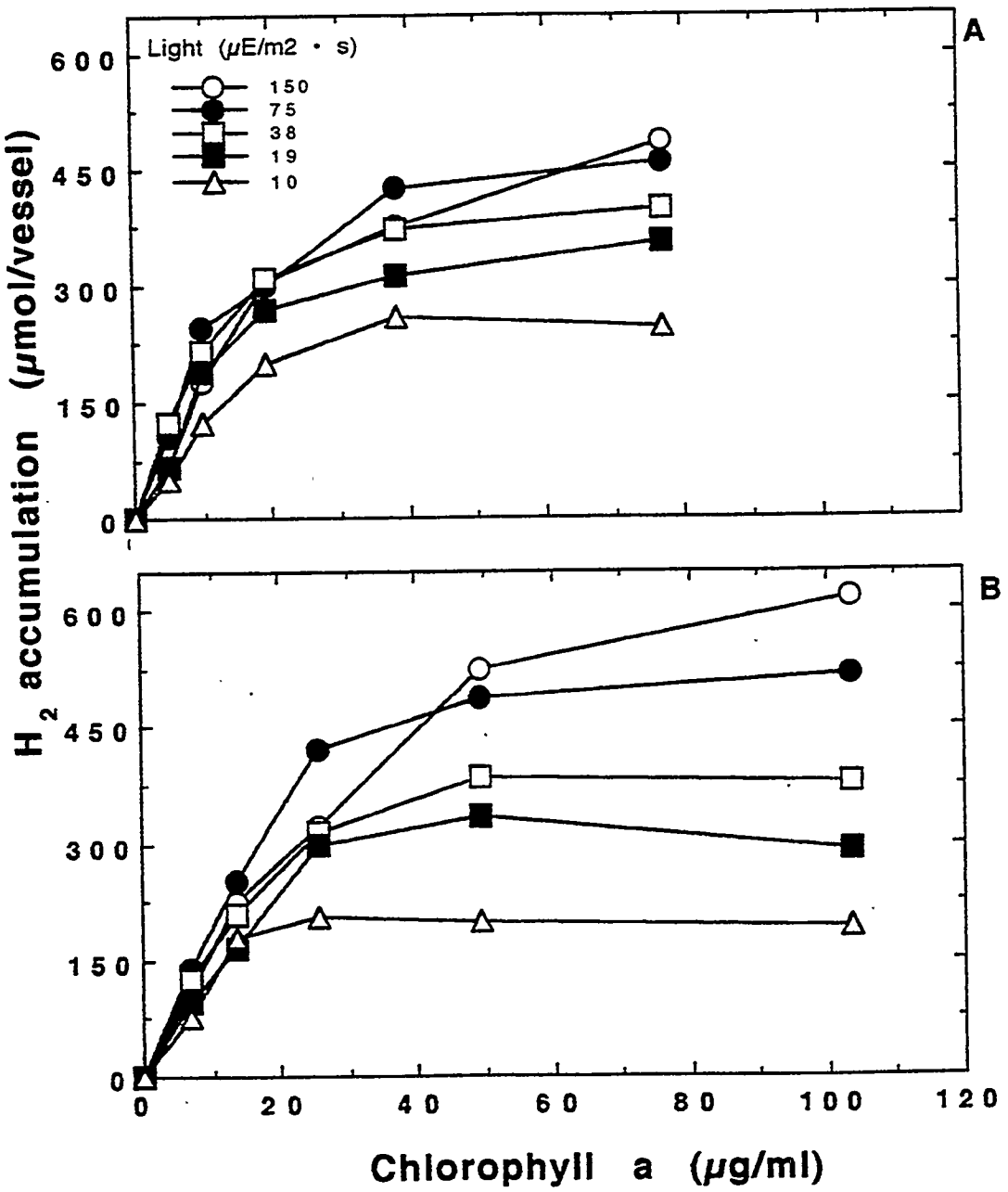

A
B
Light (μE/m2 • s)
150
75
38
19
10
600
450
300
150
0
H2 accumulation (μmol/vessel)
0
20
40
60
80
100
120
Chlorophyll a (μg/ml)

Figure IV-2

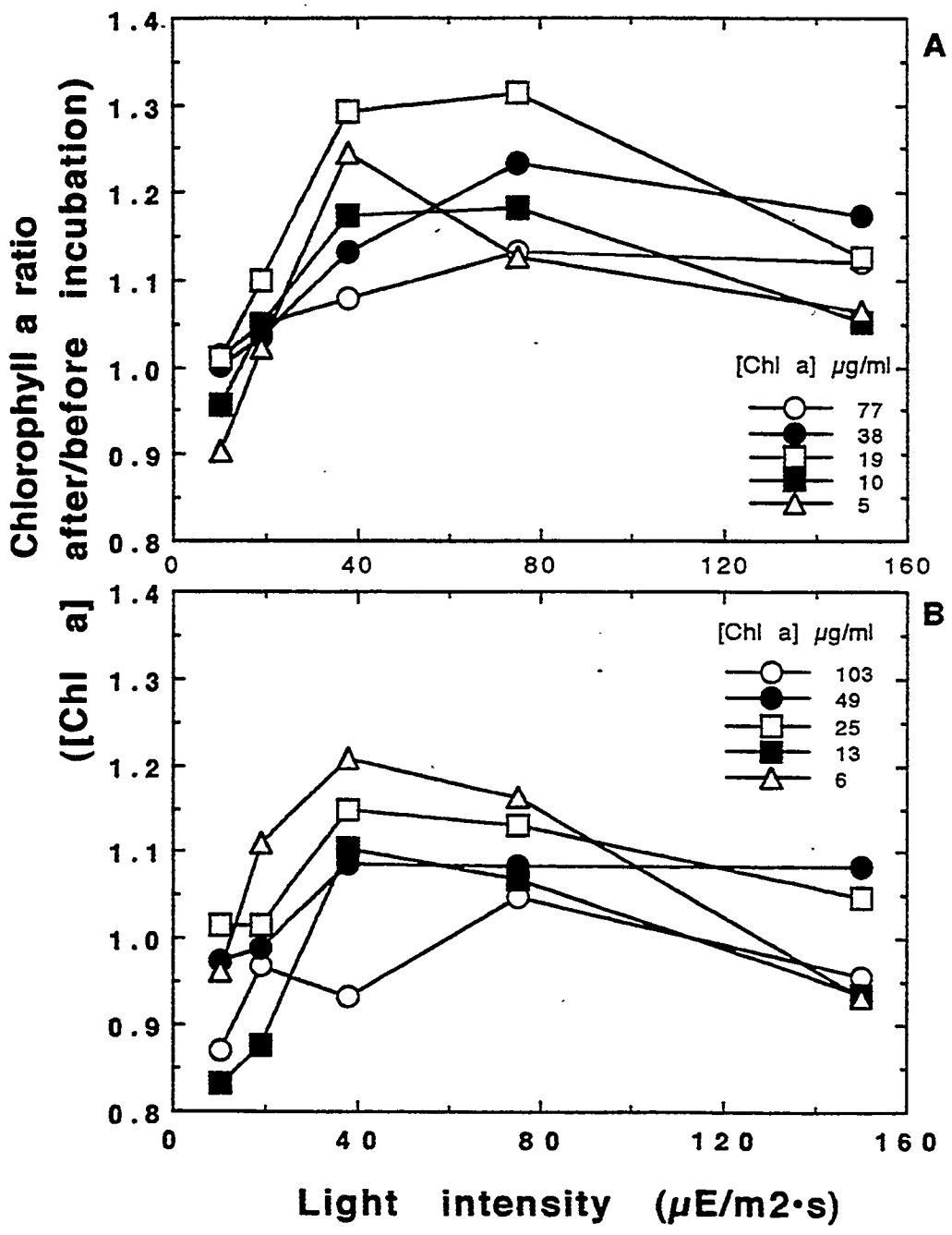

Chlorophyll a ratio
([Chl a] after/before incubation)
A
B
[Chl a] μg/ml
77
38
19
10
5
[Chl a] μg/ml
103
49
25
13
6
1.4
1.3
1.2
1.1
1.0
0.9
0.8
0
40
80
120
160
Light intensity (μE/m2·s)

Figure IV-3

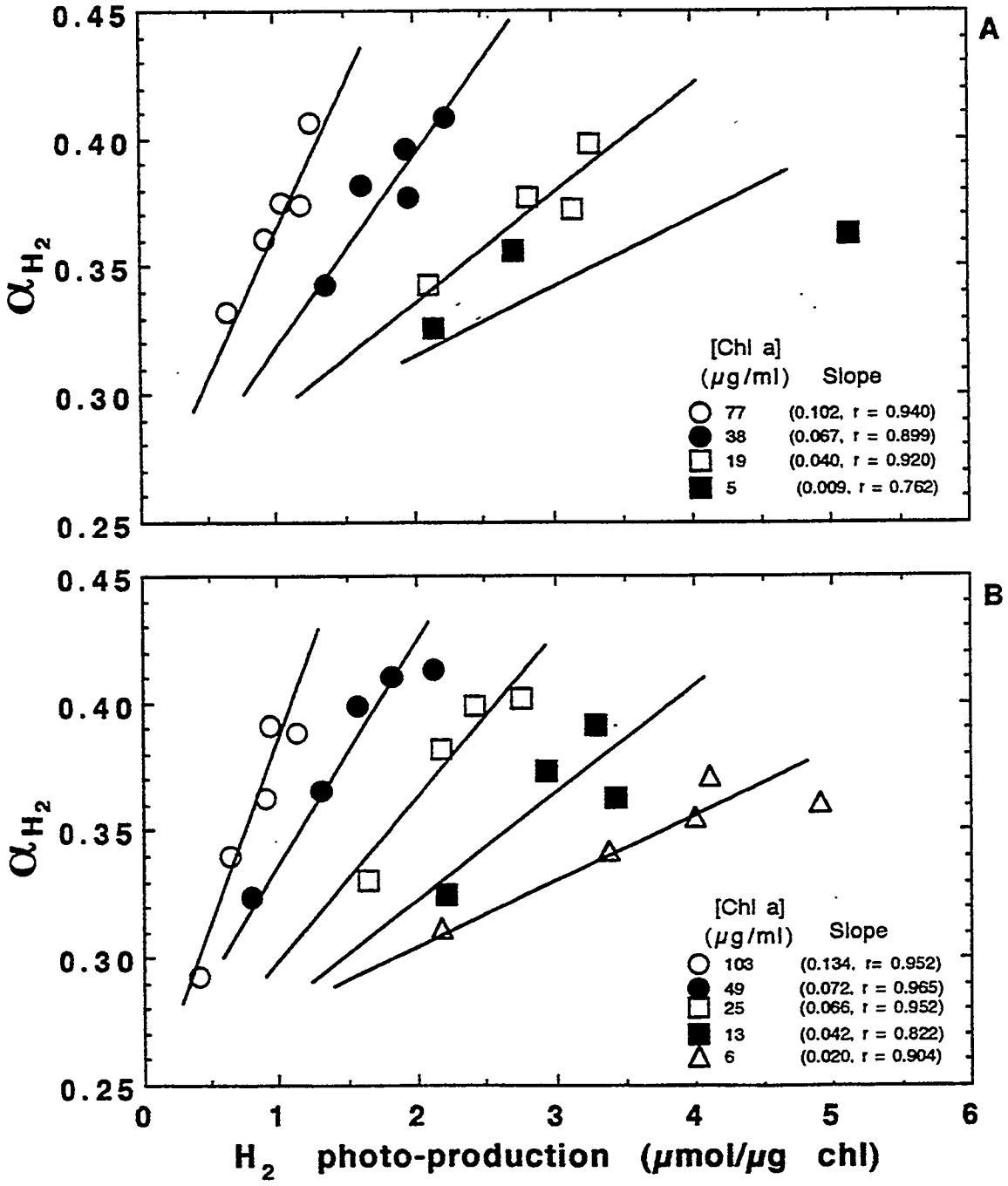

A
B
α_{H_2}
0.45
0.40
0.35
0.30
0.25
[Chl a] (μg/ml) Slope
77 (0.102, r = 0.940)
38 (0.067, r = 0.899)
19 (0.040, r = 0.920)
5 (0.009, r = 0.762)
[Chl a] (μg/ml) Slope
103 (0.134, r= 0.952)
49 (0.072, r = 0.965)
25 (0.066, r = 0.952)
13 (0.042, r = 0.822)
6 (0.020, r = 0.904)
0
1
2
3
4
5
6
H_2 photo-production (μmol/μg chl)

Figure IV-4

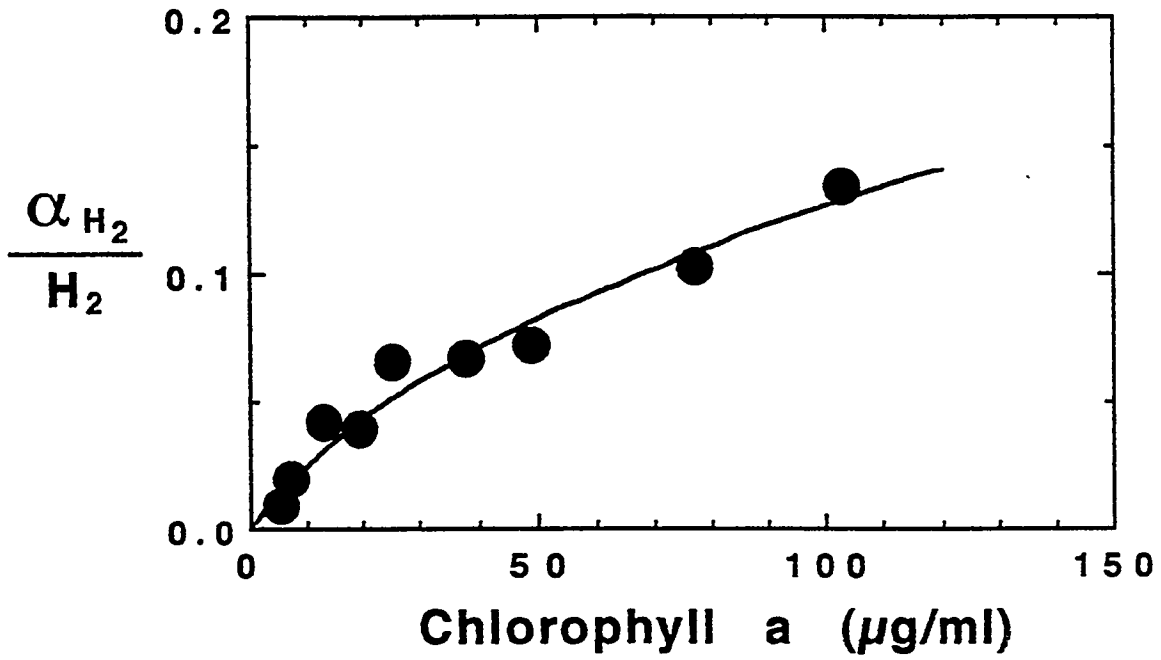


Figure IV-5

DEVELOPMENT OF SOLID ELECTROLYTES FOR WATER ELECTROLYSIS AT HIGHER TEMPERATURE

Clovis A. Linkous
Florida Solar Energy Center
1679 Clearlake Road
Cocoa, FL 32922-5703

Abstract

This report describes our efforts in developing new solid polymer electrolytes that will enable operation of proton exchange membrane electrolyzers at higher temperatures than are currently possible. Several ionomers have been prepared from polyetheretherketone (PEEK), polyethersulfone (PES), and polyphenylquinoxaline (PPQ) by employing various sulfonation procedures. By controlling the extent of sulfonation, a range of proton conductivities could be achieved, whose upper limit actually exceeded that of commercially available perfluoralkyl sulfonates. Thermoconductimetric analysis of samples at various degrees of sulfonation showed an inverse relationship between conductivity and maximum operating temperature. This was attributed to the dual effect of adding sulfonate groups to the polymer: more acid groups produce more protons for increased conductivity, but they also increase water uptake, which mechanically weakens the membrane. This situation was exacerbated by the limited acidity of the aromatic sulfonic acids ($pK_A \approx 2$-3). The possibility of using partial fluorination to raise the acid dissociation constant is discussed.

Introduction

The objective of this research is to reduce the cost of electrolytic H_2 by making better use of its energy inputs. The main energy input is, of course, the electrical voltage applied to the cell. It is also possible, however, for the endothermic water splitting reaction to extract heat from the surroundings. This is shown in Figure 1, where the various thermodynamic functions associated with water decomposition are shown as a function of temperature. It is seen that as temperature rises, an ever increasing energy component consists of heat uptake from the surroundings. This increase is complemented by a drop in free energy, which corresponds to the applied voltage to the electrolyzer.

Therefore, as long as thermal or process heat-derived energy costs less than electrical energy, it behooves us to try and substitute heat for electricity. This means operating the electrolyzer at higher temperature. For example, let us consider a state-of-the-art PEM electrolyzer that operates with acceptable current density at 1.75 V,

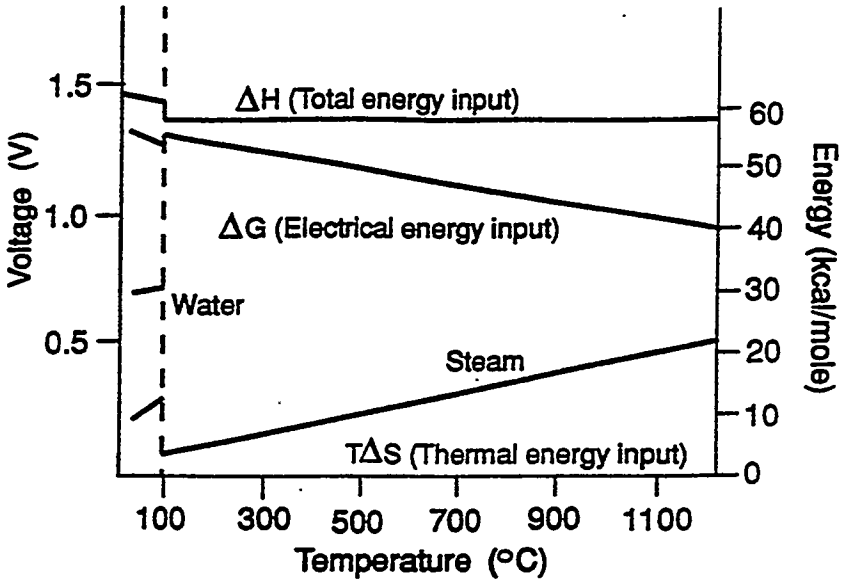


Figure 1. Energy Relationships in Water Electrolysis

indicating an overpotential of 520 mV. Typical operating temperature is 80° C. If temperature could be raised to 327° C, and overpotential could be reduced to 100 mV, then with a conventional fossil fuel electrical power plant efficiency of 35%, a 29.7% energy savings based on the primary thermal energy source could be realized.

As device temperature rises, thermohydrolytic stress is put upon all of the cell components: anode, cathode, electrolyte, and current collectors. Frequently, it is the electrolyte that is the first component to fail. Therefore, our approach to higher temperature electrolysis is to develop new solid polymer electrolytes that exhibit exceptional thermohydrolytic stability. This has involved converting known, thermohydrolytically stable high temperature polymers into ionomers, i.e., polymers containing covalently bonded ionic groups.

In Figure 2, molecular structures for 5 candidate high temperature polymers are shown, along with that of Nafion™, the leading PEM material made by Du Pont: polyetheretherketone (PEEK), polyethersulfone (PES), polyphenylquinoxaline (PPQ), polyimide (PI), and polybenzimidazole (PBI). There are 2 main differences between the candidate polymers and the commercial material: 1) the high temperature polymers consist mostly of phenyl rings connected together by a repeating series of oxo, keto, and sulfonyl groups, while the commercial material is a singly bonded chain; 2) the Nafion is perfluorinated, i.e., every available hydrogen atom has been replaced with fluorine, while the polymers under study are unfluorinated. It is believed that fluorination raises the cost of the ionomer considerably.

Experimental

Conversion of the polymer to an ionomer was done via sulfonation, or synthesis of sulfonic acid derivative polymers. Understanding how to sulfonate the polymers is an ongoing effort. There are a number of

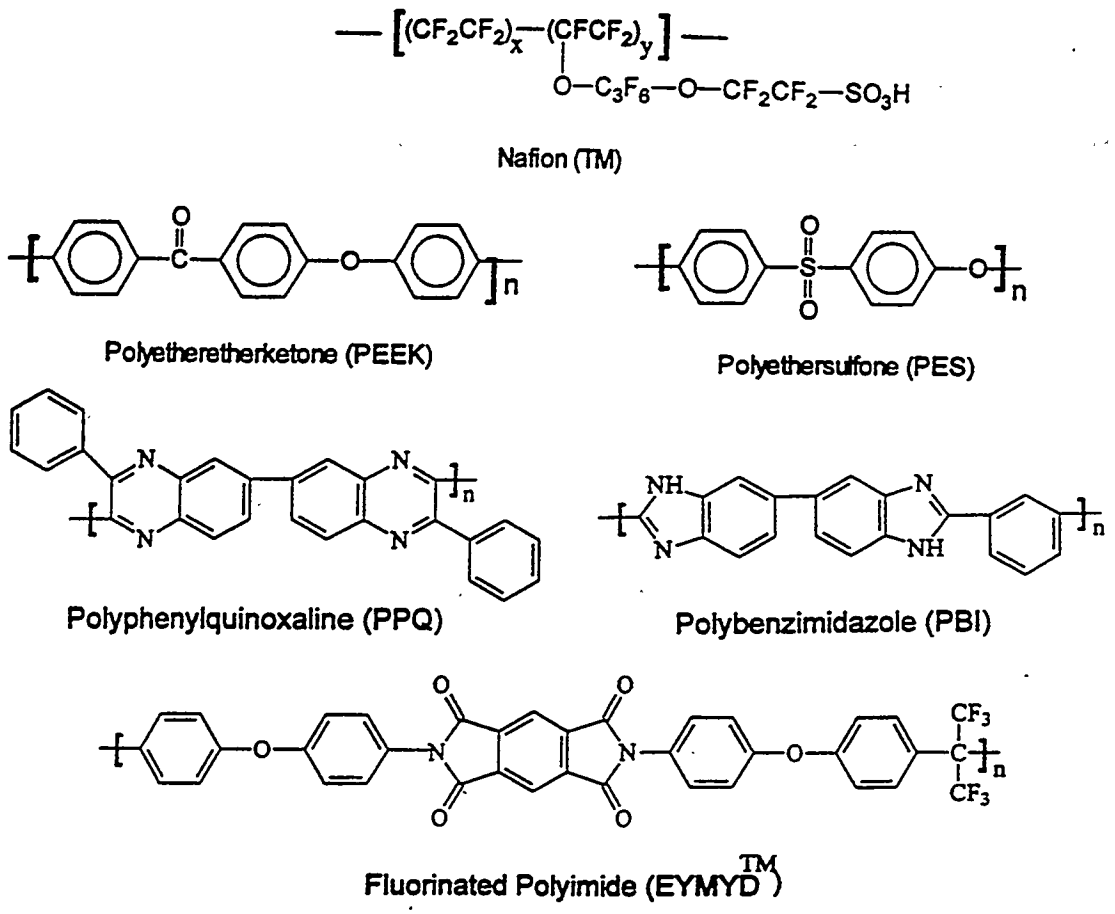


Figure 2. Molecular Structures of Candidate High Temperature Polymers

sulfonation methods available. For some of the polymers, this can be as simple as dissolution in H_2SO_4. This was the method employed for PEEK. A majority of the polymers, however, were impervious to the action of sulfuric acid, either dissolving and reprecipitating without reaction or not interacting at all. More forcing conditions could be applied with sulfur trioxide, SO_3. Polyethersulfone was sulfonated either by dissolution in oleum (30% SO_3 in H_2SO_4), or by reaction with the solvated complex SO_3:triethyl phosphate. Dissolving SO_3 in a compatible organic solvent such as dichloromethane was also effective for PES.

PPQ was sulfonated by the "soak and bake" method, where a moderately concentrated solution of H_2SO_4 is swelled up into the solid polymer, which is then subjected to a rapid heat treatment at 300+°C (< 1 minute). The acid apparently decomposes to SO_3 and water, provided an effective way to introduce SO_3 into the solid polymer.

Another synthetic method for PBI is still being worked out, although it supposedly is amenable to the soak and bake method described above. Sulfonation of PI is also in progress. Insolubility at this point is the greatest problem. Another approach under consideration for PI is sulfonation of one of the precursor monomers. Either a bisphenol, or a mono- or diaminobenzene, or the aromatic dianhydride could possibly be sulfonated and then polymerized with its co-monomers to form the polyimide.

Once the polymer is sulfonated, it is characterized with respect to water uptake, acid group density (milliequivalents/g), and proton conductivity as a function of temperature. The thermoconductimetric test was

routinely run as high as data could be collected before failure of the membrane occurred. Thus a maximum operating temperature, or T_{max}, was derived.

Results

Except for the PPQ, which was cast as a membrane before sulfonation, the sulfonated polymers must be fabricated into membranes for testing in electrolysis cells, etc. The polymers were dissolved as a 10% solution in an organic solvent, typically a high boiling polar solvent such as N,N'-dimethylformamide, DMF, or dimethylsulfoxide, DMSO. Membranes were fabricated by casting these solutions onto glass plates followed by evaporation of the solvent. The membranes had to be vac-oven heated overnight, or in some cases for several days, to drive off all the solvent.

These membranes for subjected to a variety of characterization procedures. One of them was a thermoconductimetric analysis, in which the polymer film was mounted in a conductivity cell and then immersed into an autoclave. Conductivity at 1000 Hz was measured as a function of temperature under steam-saturating conditions. An exponential rise in conductivity was typically observed until T_{max} was reached, afterwhich the membrane failed and σ dropped quickly. A plot of $\log(\sigma)$ versus $1/T$ gave a straight line from whose slope the activation energy for proton transfer could be derived.

Performance data for S-PEEK, S-PES, and S-PPQ are shown in Table 1, along with that of Nafion. Note that while the density of acid groups present for the three polymers well exceeds that of Nafion, proton conductivity of the commercial product is clearly higher, by nearly an order of magnitude. This difference in ease of proton transport is also manifested in the differing activation energies. It would appear that sulfonic acid groups attached to a perfluorinated aliphatic chain are better able to conduct protons than those attached to hydrocarbon aromatic rings.

Table 1. Performance Data for Ionomer Membranes

Sample	% SO_3H	n(meq/g)	T_{max}(°C)	E_{act}(kcal/mole)	$\sigma_{H^+}(\Omega\text{-cm})^{-1}$ *
Nafion	13	0.83	150	0.9	0.18
SPEEK	20	0.66	112	4.5	0.020
SPES	29	1.14	127	12.5	0.028
SPPQ	107	1.87	153	3.9	0.005

* conductivities were measured at 1000 Hz and 100° C

Proton conductivity correlated directly with temperature and degree of sulfonation of the polymer, as shown in Figure 3. The 65% degree of sulfonation conductivity curve actually exceeded that of the Nafion. Unfortunately, increasing density of sulfonic acid groups also contributed to a lowering of T_{max}. For example, T_{max} for S-PEEK dropped from 112° C at 20% sulfonation nearly to 80° and 65% sulfonation. Post mortem analysis suggested that mechanical failure of the membrane was the problem, i.e., water uptake and swelling under saturating steam pressure caused the membrane to sag and tear under its own weight. Thus high degrees of sulfonation as a means of compensating for low conductivity suffers due to lower operating temperature.

Instead, one must make better use of the acid groups that are available. In order for the sulfonic acid to contribute to protonic conductivity, it must be dissociated. For weak acids, most of the labile protons are attached to their binding sites. It is preferable then to have a strong acid that is mostly dissociated. The

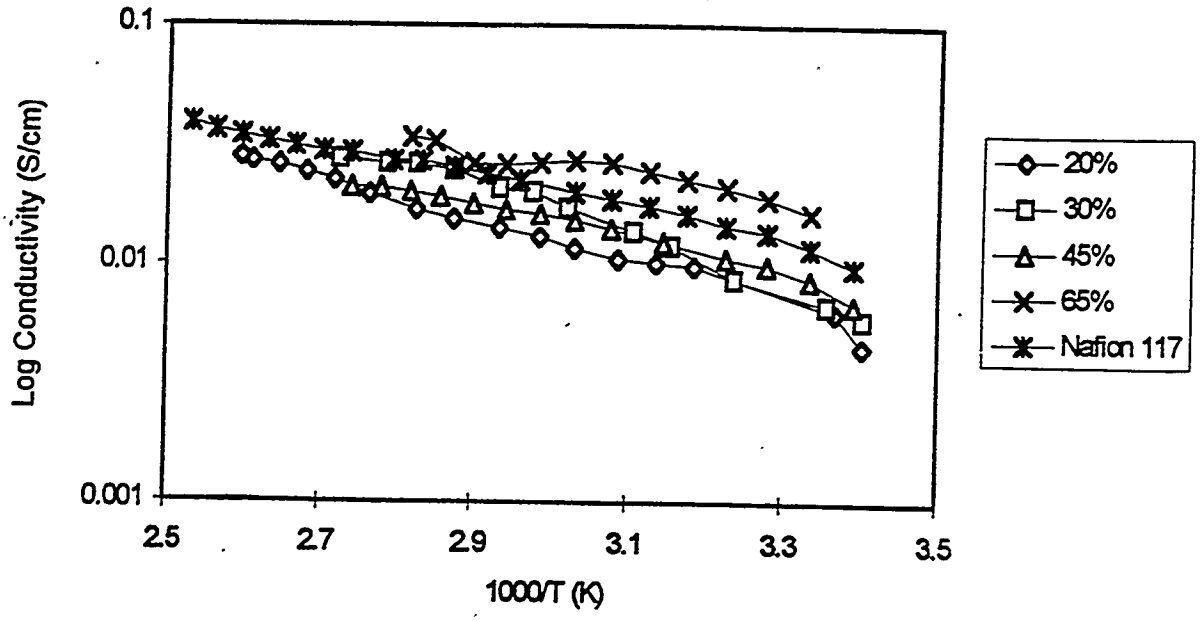


Figure 3. S-PEEK Conductivity as a Function of Temperature for Different Degrees of Sulfonation

acidity of aromatic sulfonic acids in general lie in the pK_A = 0.5-3.5 range, which means that the percent of dissociated acid groups can vary from 41 to only a couple percent. The pK_A acidities of S-PEEK and S-PES were found to be 2.8 and 2.25, respectively. Thus only about 5% of the S-PEEK protons are dissociated at any moment. Nafion, on the other hand, is a fluorosulfonic acid. These compounds are known as super acids, whose acidity is so great that it must be measured relative to other acids instead of water. The extent of dissociation in water is essentially 100%. Thus for equal sulfonic acid density, Nafion would be expected to be 20 times more conductive than S-PEEK.

It was decided then to make fluorosulfonic acids of PEEK and the other polymer candidates. But to obtain high acidity, it was thought that only the carbon atoms immediately adjacent the sulfur atom need to be fluorinated. Perfluorination could replace every hydrogen atom on the polymer with a fluorine, but it was not obvious that fluoroaromatics were more stable than their respective hydrocarbons. If anything, literature references suggested that a slight weakening may occur.

Thus it was decided to perform a partial fluorination, where only the carbons closest to the sulfonic acid are fluorinated. A synthetic scheme was devised as shown in Figure 4. Sodium dithionite, $Na_2S_2O_4$, dissociates in polar organic solvent to yield the monothionite ion, SO_2^-. Monothionite reduces a di-iodoperfluoroalkane to generate the corresponding mono-iodoperfluorocarbon radical. The radical attaches to an aromatic ring, displacing a hydrogen atom. Additional dithionite equivalents remove the remaining iodine atom from the fluoroalkyl aromatic, and then add to the radical to make a sulfinate species. Oxidation with H_2O_2 and acidification gives the sulfonic acid.

To date, the monoiodide of perfluorobutane has been attached to aniline. Unfortunately, this had to be performed in acetonitrile solvent, which is incompatible with the polymers of interest. Work with PBI has

shown that either the polymer or the perfluorobutyl iodide will dissolve in DMF, but not together. The lack of comiscibility could be a fundamental problem with this type of approach. It may be necessary to sulfonate the monomer first and then polymerize.

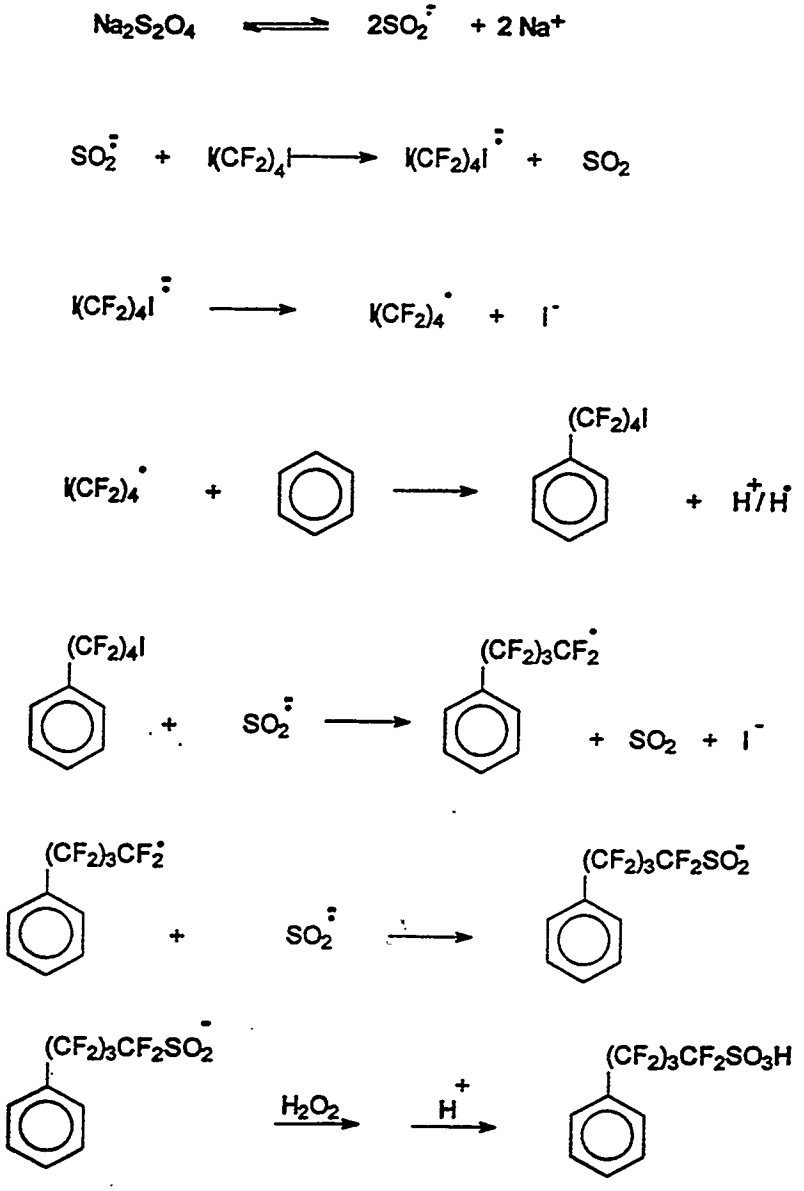


Figure 4. Synthetic Scheme for Aromatic Fluorosulfonic Acids

Acknowledgement

The author wishes to thank Bob Kopitzke, Dan Wagner, and Randy Anderson for their technical assistance on this project. Funding from the U.S. Department of Energy, Office of Solar Thermal, Biomass Power, and Hydrogen Technologies, is gratefully acknowledged.

SOLAR PHOTOCHEMICAL PRODUCTION OF HBr FOR OFF-PEAK ELECTROLYTIC HYDROGEN PRODUCTION

Harley Heaton
Solar Reactor Technologies Inc.
Miami, FL 33133

Abstract

Progress is reported on the development of a unique and innovative hydrogen production concept utilizing renewable (Solar) energy and incorporating energy storage. The concept is based on a solar-electrolytic system for production of hydrogen and oxygen. It employs water, bromine, solar energy and supplemental electrical power. The process consumes only water, sunlight and off-peak electricity, and produces only hydrogen, oxygen, and peaking electrical power. No pollutants are emitted, and fossil fuels are not consumed. The concept is being developed by Solar Reactor Technologies, Inc., (SRT) under the auspices of a Cooperative Agreement with the U.S. Department of Energy (DoE).

Summary of the Approach

The SRT concept entails (i) absorption of concentrated solar radiation by bromine vapor $Br_{2(g)}$ in a high-temperature reactor, (ii) reaction of $Br_{2(g)}$ with water yielding hydrogen bromide (HBr) and oxygen, and (iii) electrolysis of the stored hydrogen bromide for production of $H_{2(g)}$ and recovery of $Br_{2(l)}$ for recycling back into the process. Incorporation of solar radiation in the primary photochemical step (i) reduces by 50 - 75% the electrical power required to split water. The absorption spectrum of bromine is well matched to the solar emission spectrum as it is received on the earth's surface. The SRT concept is very attractive from an economic viewpoint. A reversible electrolytic fuel cell employed in the SRT process is capitalized via its use in load leveling by the user. This reversible or regenerative fuel cell has been developed by others up through the demonstration stage and the technology is available. Thus the price of SRT-produced hydrogen reflects only the cost of the solar hardware components and off-peak electrical power. Independent analysis (R. K. Sen/Energetics Inc. November 1995) suggests that the cost

to produce hydrogen via this process is $9.00/MMBtu, exceeding DoE goals of $10.00/MMBtu. Figures 1 and 2 show the integrated process as it is presently envisioned.

Results

Past Results

The Phase I project was started in December 1994. The first review was performed in April 1995. At that time a 1 kW bromine/steam solar reactor had been designed and constructed. It was felt that the electrolyzer/fuel cell development work should not commence until the reactor concept was proven. Advanced chemical thermodynamic calculations for the bromine/steam reaction were also performed during the same period. The thermodynamic calculations confirmed preliminary calculations that indicated the reaction was feasible and promising in terms of economic potential.

Current Year Results

1 kW Solar Reactor

The 1 kW reactor was employed in taking survey data of the reaction between bromine and steam at temperatures between 900 and 1300 °K during the first half of the year. This reaction was run both under purely thermal conditions (in the absence of solar photons) and utilizing solar energy. The difference in bromine conversion with and without solar photons under identical operating conditions was determined. Significant differences between the two were not found as shown in Fig. 3.

Results in terms of bromine conversion obtained however were very encouraging. At reactor set point temperatures of 950°C, up to 40% of the bromine was converted to HBr in a single pass (Goal was up to 50%, this point is not shown in Figure 3). These conversions were within 50 to 70% of the values predicted by thermodynamics. HBr concentrations of 3 M were attained in the solar reaction studies at bromine mole fractions of 0.25. Higher bromine mole fractions will yield correspondingly higher HBr concentrations, in the 5 - 8 M range, which is optimal for the reversible fuel cell. Thermodynamic predictions which were verified were:

- Bromine to HBr conversion rate
  - increases with temperature,
  - increases with decreasing Br_2/H_2O mole fraction,

- HBr Concentration in products
  - increases with increasing Br_2/H_2O mole fraction,
  - increases with longer residence time.

10 kW Solar Reactor

The success of the 1 kW reactor lead to initiation of the Phase II effort where the objective was to scale up to a 10 kW (solar input) level and then add the electrochemical cell. The effort was expanded to include contributions to the project from other laboratories:

- The National Renewable Energy Laboratory (NREL)- Golden Colorado, which is providing a test bed (it's 10 kW solar furnace facility) for the 10 kW reactor, has helped with reactor design assistance and is providing reaction diagnostics (Molecular Beam Mass Spectrometer, MBMS) for real-time, *in-situ* chemical species measurement,
- Sandia National Labs (SNL)- Livermore California, which is providing design and analysis support in the form of chemically reacting flow models . These models will be used to predict the behavior and economics of the process as data becomes available,
- The Florida Solar Energy Laboratory (FSEC)- Cocoa Florida, providing assistance in the design of product separation processes and electrochemistry,
- R. K. Sen and Energetics Inc.- Maryland, providing independent cost and economic analysis models.

At the time of this writing the 10 kW reactor and associated gas delivery and analysis systems have been designed, built, installed and tested at the NREL solar furnace facility. NREL supported and documented the testing with personnel, equipment, and diagnostic instrumentation. Additional assistance in FTIR measurement of reactor temperatures and HBr concentrations was obtained from Advanced Fuel Research (East Hartford, CT). Analysis of the data is in progress but some early conclusions can be drawn. These are:

- Addition of Br_2 vapor to the solar reactor gas mixture resulted in gas temperature increase, presumably due to increased absorption of the solar spectrum (Fig. 4). In most cases the temperature of the gas exceeded that of the reactor walls by more than 200°C,
- Corrosion of wetted metal (monel, hastalloy C), polymeric (Teflon, PFA, Kynar) and glass (Pyrex,quartz) parts exposed to bromine and or HBr was not observed during testing.
- Bromine and bromine/HBr/water mixtures were easy to handle as liquids using normal glass labware and procedures at room temperatures and pressures,
- The reactor, while designed for 10 kW, required only 2.0 - 2.5 kW to operate. This indicates that the reactor volume could be increased by a factor of 4 - 5 for 10 kW , which would result in increased residence time and increased light absorption volume.

The integrated unit (again, without the electrochemical cell) was tested using as variables bromine and steam flow rates, solar power levels and temperatures.

10 kW Reactor Kinetic Modeling (Sandia)

Sandia assembled a model of the solar reactor for data analysis and design use. Included in the model were; a kinetics model of the H-O-Br system at high temperatures developed initially by Lawrence Livermore National Labs (LLNL), a model of photochemically induced Br_2 disassociation, and a reactor flow model. The three models were modified and integrated so that the behavior of the solar reactor could be better understood. The integrated model was verified using data collected from the 1 kW experiments, and will be further exercised by comparison of model predictions to the 10 kW data. The model has provided the following insights:

- HBr yield is a strong function of temperature and residence time,
- Photodissociation of Br_2 may increase HBr yields in the reactor over thermochemical yields by shifting the equilibrium value (superequilibrium),
- High induced yields can be realized in the product stream by quenching the outlet of the reactor to lower temperatures quickly.

Reactor Product Separation Studies (FSEC)

FSEC has performed theoretical and experimental work on simulated solar reactor product streams to determine how best to separate the HBr from unreacted bromine and water, so that the latter two could be recycled to the reactor. Initial indications were that bromine liquid would separate from HBr/water solutions by gravity but experiment showed that only about 20% of the unreacted bromine could be recovered in this fashion. Additional experiments showed that the rest of the bromine and HBr could be recovered by distillation. A trade study to determine the economics of concentrating the reactor products by distillation/condensation as opposed to utilizing it directly in the electrolyzer will be performed.

Plans For Future Work

Plans for future work include redesign of the 10 kW reactor to improve thermal management and optimize HBr production, and the development and application of the reversible HBr electrolyzer/fuel cell. SRT has solicited and received a number of bids from qualified vendors to provide the electrochemical equipment and technology. Once the electrochemistry is in place another round of testing at the 10 kW level will follow to verify complete system performance/economics. After this testing takes place the process will be scaled up to the 100 kW level and a demonstration plant will be built in Palm Desert, California. A site for the plant has been chosen and discussions with local authorities has commenced.

Status of Economic Evaluation

Energetics Inc. has constructed an independent economic and cost model on the SRT process for the DoE. The model utilizes inputs generated by the team members and industry groups to determine the economic potential for the process. Utilizing data from the 1 kW solar reactor experiments and estimates of electrochemical performance from vendors, Energetics has estimated that the process (at the 10 MW size) can produce hydrogen at a cost of $9.00/MMBtu and peaking electricity at 8.2 cents/kWh. Energetics has also examined the markets existing for hydrogen and electricity and has determined that plants as small as 1 MW would generate a positive return on investment. The economic and cost models are constantly undergoing revision and updating as new data is generated or economic conditions change. SRT, in cooperation with Dawnbreaker Inc. (Rochester, NY) is also developing a business/commercialization plan for the process.

Projected Goals

Near term (6 months)

- Integrate electrochemical technology
- Obtain strategic partner for commercialization

Mid term (18 months)

- Conduct Demonstration at Palm Desert

Far term (2 years)

- Commercialization, at least 1 full size plant in operation

Major Barriers to Meeting Goals

Technical challenges:

- Low single pass yields of HBr in the solar reactor will need to be augmented to meet economic goals. Methods to improve yields will include:
  - Improving thermal management for the system,
  - Optimizing solar energy absorption volume in the reactor,
  - HBr/ oxygen separation from product stream,
  - Unreacted product recycle,
  - Addition of catalysts for improved production rates and/or lower temperatures,
- Corrosion studies will need to be focused on the longer term.

Economic:

- Market acceptance (new technology), Funding shortfalls.

Acknowledgments

The author would like to thank the following contributors for their collaboration in the project: Mark Stoy, Ralph Schlief and Robert Hanrahan of Solar Reactor Technologies, Inc.; Allan Lewandowski, Greg Glatzmaier, Kent Scholl and Carl Bingham of the National Renewable Energy Laboratory, Golden, Colorado; Steve Vosen and Jay Keller of Sandia National Laboratory, Livermore, California; and Clovis Linkous, Florida Solar Energy Center, Cocoa, Florida.

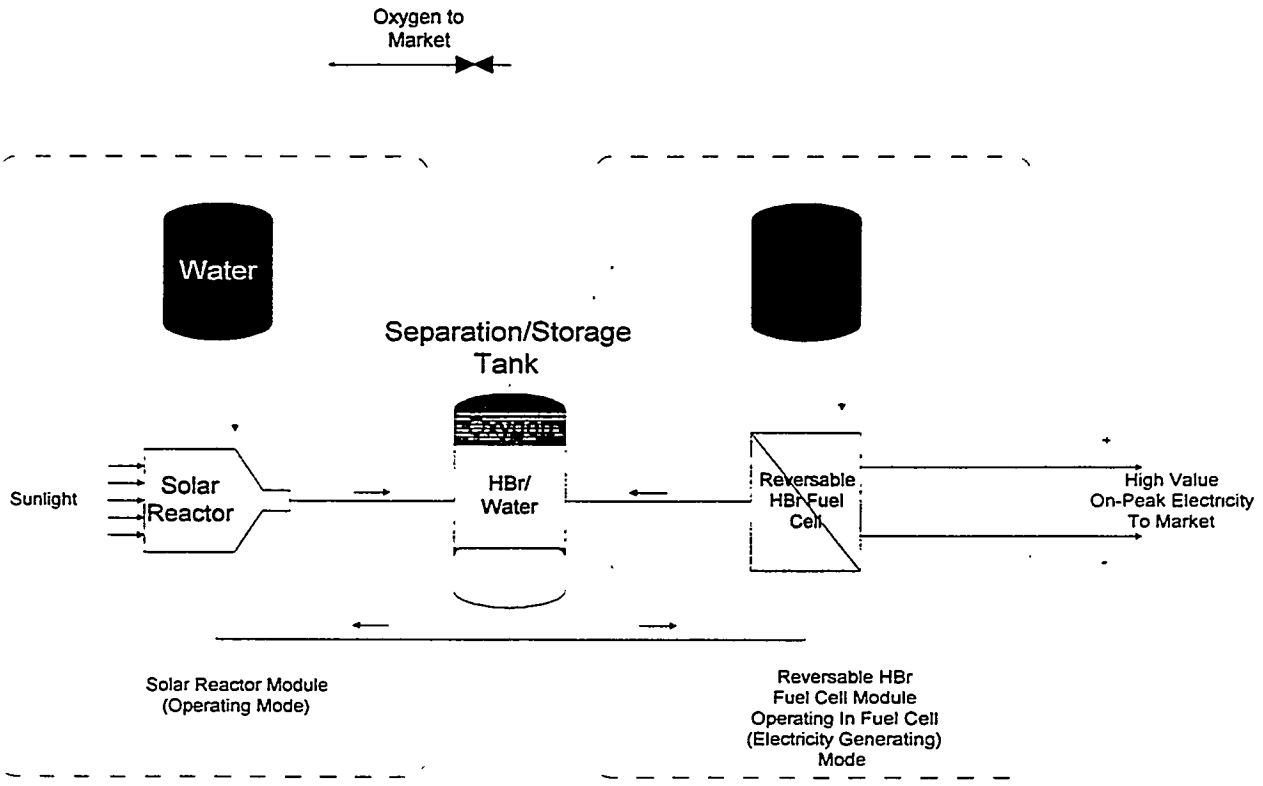


Figure 1. The SRT system operating during the day. Note that both the solar reactor and the electrochemical cell generate HBr and consume Br_2 in this mode. Electricity and oxygen are produced for market at this time.

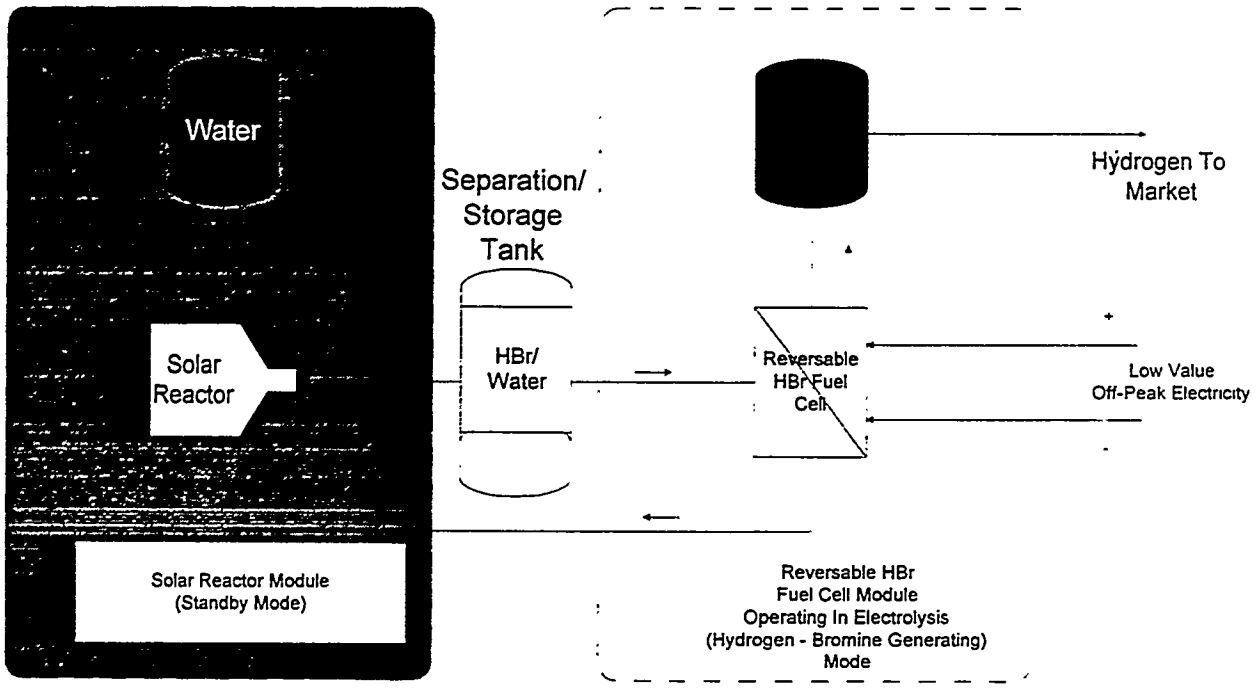


Figure 2. The SRT system at night. The solar reactor is in standby mode. The electrochemical cell consumes HBr and off-peak electricity and generates hydrogen and Br_2. After producing enough hydrogen and Br_2 for the next day's electricity production the HBr produced by the solar reactor during the day is electrolyzed, resulting in excess hydrogen for market, and Br_2 for recycle to the solar reactor.

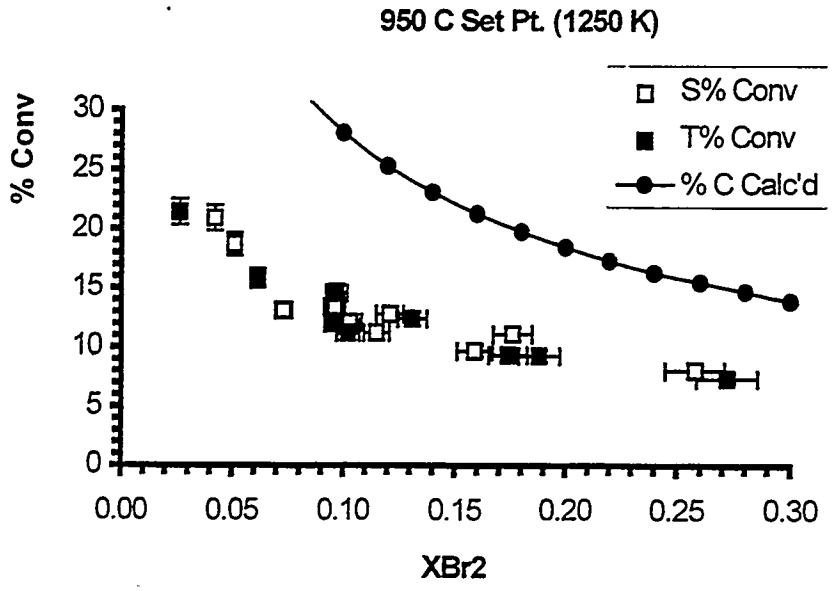


Figure 3. Comparison of solar (open squares), non-solar (dark squares) and equilibrium (circles) conversions for 950°C 1kW reactor temperatures.

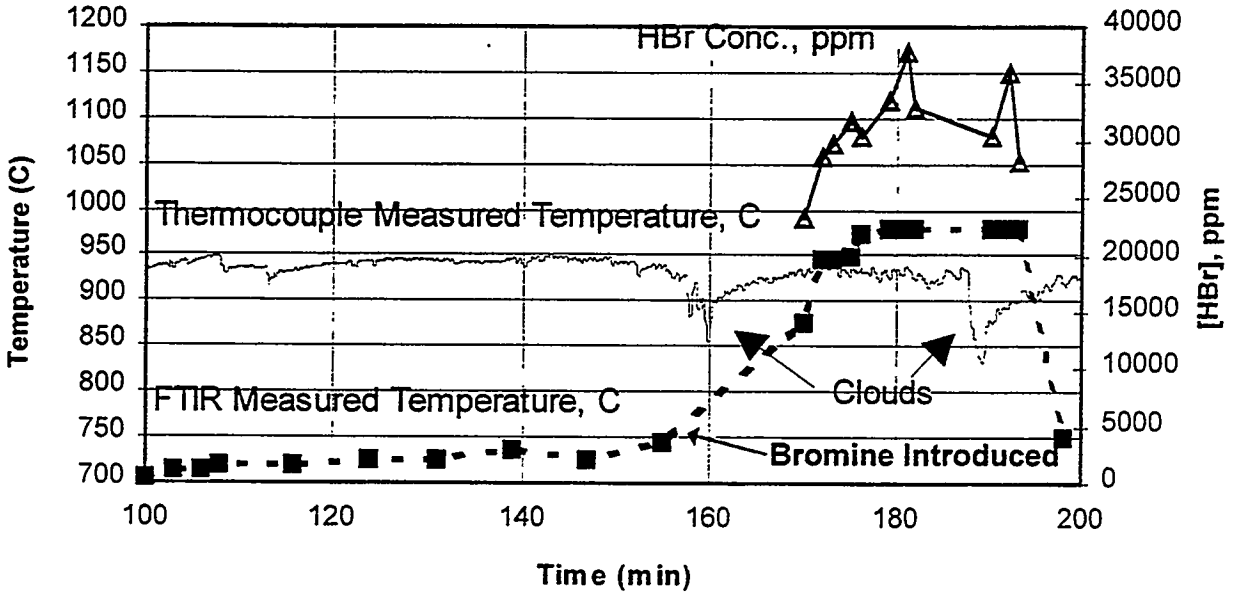


Figure 4. Note that the gas temperature, as measured by the FTIR was steady between 100 and 155 minutes, before bromine flow was started. When bromine flow commenced, gas temperature rose to a value greater than the reactor wall temperature, and HBr was found in the mixture. After bromine flow was stopped, the temperature of the gas recovered to the prior value.

BIOMASS-TO-HYDROGEN VIA FAST PYROLYSIS AND CATALYTIC STEAM REFORMING

E. Chornet, D. Wang, S. Czernik, D. Montané, and M. Mann
National Renewable Energy Laboratory (NREL)
1617 Cole Boulevard
Golden, CO 80401

Abstract

Pyrolysis of lignocellulosic biomass and reforming the pyroligneous oils is being studied as a strategy for producing hydrogen. Novel technologies for the rapid pyrolysis of biomass have been developed in the past decade. They provide compact and efficient systems to transform biomass into vapors that are condensed to oils, with yields as high as 75-80 wt.% of the anhydrous biomass. This "bio-oil" is a mixture of aldehydes, alcohols, acids, oligomers from the constitutive carbohydrates and lignin, and some water derived from the dehydration reactions. Hydrogen can be produced by reforming the bio-oil or its fractions with steam. A process of this nature has the potential to be cost competitive with conventional means of producing hydrogen.

The concept of hydrogen from biomass offers significant opportunities for novel research and development. Using a renewable resource feedstock is an alternative to conventionally producing hydrogen from petroleum and natural gas. As a consequence, the environmental benefit of zero net carbon dioxide emissions approaches a pollution-free energy system. An additional benefit is that a regionalized system of hydrogen production can be envisioned using this technology. Small and medium-sized pyrolysis units (<500 Mg/day) could provide the bio-oil to a centralized reforming unit to be catalytically converted to H_2 and CO_2. Therefore, storage and transportation problems associated with hydrogen production become less important in the economics of the process. The reforming facility can be designed to handle alternate feedstocks, such as natural gas and naphtha, if necessary.

Thermodynamic modeling of the major constituents of the bio-oil has shown that reforming is possible within a wide range of temperatures and steam-to-carbon ratios. Existing catalytic data on the reforming of oxygenates have been studied to guide catalyst selection. Tests performed on a microreactor interfaced with a molecular beam mass spectrometer showed that, by proper selection of the process variables: temperature, steam-to-carbon ratio, gas hourly space velocity, and contact time, almost total conversion of carbon in the feed to CO and CO_2 could be obtained. These tests also provided possible reaction mechanisms where thermal cracking competes with catalytic processes. Bench-scale, fixed bed reactor tests demonstrated high hydrogen yields from model compounds and carbohydrate-derived pyrolysis oil fractions. Reforming bio-oil or its fractions required proper dispersion of the liquid to avoid vapor-phase carbonization of the feed in the inlet to the reactor. A special spraying nozzle injector was designed and sucessfully tested with an aqueous fraction of bio-oil.

A process diagram for the pyrolysis and reforming operations is presented and discussed, along with initial production cost estimates. A window of opportunity clearly exists if the bio-oil is first refined to yield valuable oxygenates so that only a residual fraction is used for hydrogen production.

1 Introduction

Steam reforming of hydrocarbons, partial oxidation of heavy oil residues, and gasification of solid fuels to yield syngas (a mixture of H_2 and CO), followed by shift conversion to produce H_2 and CO_2, are well established processes. Renewable lignocellulosic biomass has been considered as a potential feedstock for gasification to produce syngas. However, economics of current processes favor the use of hydrocarbons (natural gas, C_2-C_5, and naphtha) and inexpensive coal. An alternative approach to the production of H_2 from biomass is the catalytic steam reforming of liquid streams generated from various biomass conversion processes such as pyrolysis, hydrolysis, and solvolysis that also yield valuable oxygenate products. This latter approach has potential to be cost competitive with the current commercial processes for hydrogen production.

The proposed technology for producing hydrogen would be comprised of two stages: fast pyrolysis of biomass to generate bio-oil and catalytic steam reforming of the oil or its fractions. Recent developments in pyrolysis processes allow for conversion of 75% of biomass into a liquid product (bio-oil). This bio-oil is made of oxygenated organic compounds [1,2]: acids, alcohols, aldehydes, ketones, furans, substituted phenolics and complex oxygenates derived from biomass carbohydrates and lignin. Very little ash and char are present in the bio-oil when appropriate filtration technology is used in the pyrolysis process [3].

An efficient steam reforming of the oil using no external heat can result in a hydrogen yield of 12.6 wt.% of dry biomass. This yield is similar to that from the biomass gasification/water-gas shift process (11.5 wt.%). The yield of hydrogen for the stoichiometric reaction between wood (poplar) and steam using externally supplied heat is 17.2 wt.%. These values were calculated using current yields for fast pyrolysis [4-6] and gasification [7] processes. An advantage of the pyrolysis process is that it is less severe and does not require an oxygen supply.

Our current objectives for the project are:

- To establish the proof of concept: can biomass-derived pyrolysis compounds be steam reformed?
- To determine H_2 yields from (a) model compounds and (b) pyrolysis oils or their fractions at reasonable severities and catalyst productivity.
- To identify technological hurdles and address them systematically to provide workable solutions.
- To develop a process flow diagram based on the data obtained during the research project.
- To assess the economics: under which conditions is our approach economically viable?

2 Fast pyrolysis: bio-oil yields and composition

Several fast pyrolysis technologies, at the pilot and demonstration levels, have been reported to give high yields of bio-oil, including fluid beds [4-6], transport reactors [8,9], and cyclonic reactors [10,11]. The common feature of all these technologies is rapid heating of the biomass particles at temperatures comprised between 450 and 550°C, and short residence time of the volatile products in the reaction chamber (a fraction of a second to a few seconds). For example, a 76 wt.% yield of bio-oil can be obtained from fluid bed fast pyrolysis of dry poplar ($CH_{1.47}O_{0.67}$) [4]. The organic fraction of the bio-oil represents 85 wt.% and its elemental composition is $CH_{1.33}O_{0.53}$. About 15 wt.% of the bio-oil is water from the dehydration reactions. Additional water will result from the moiture in the feedstock. The water is well dispersed within the organic fraction of the bio-oil due to the hydrophilicity of the carbohydrate-derived compounds that constitute the major fraction of the bio-oil.

Reliable values of oil, water, char and gas yields are limited in the literature; most published work contains unclosed and/or unreported material balances. The composition of bio-oil has been quantitatively reported from fluidized bed studies conducted at the University of Waterloo [4-6]. It is shown for several feedstocks in Table 1, together with the composition of the bio-oil derived from the cyclonic (vortex type) reactor located at NREL [11].

Variations in the composition of pyrolysis oil as shown in Table 1, should be expected as a function of raw material, pyrolysis treatment severity (temperature, residence time, and heating rate profiles) and using or not using catalysts during the pyrolytic step. However, the information presented in Table 1 indicates that the bio-oil is essentially a mixture of two acids (acetic and formic), numerous aldehydes and alcohols plus a significant fraction of lignin (denoted as pyrolytic lignin, a low to medium molecular weight material). The unidentified compounds range from a large number of carbohydrate-derived components [12] to monomeric lignin-derived products having alcohol characteristics [1].

3 Thermodynamics

Thermodynamic simulations of reforming model oil components as well as bio-oil have been performed in order to determine equilibrium yields of hydrogen. These simulations were performed on ASPEN Plus using model compounds representative of the bio-oil. The results are listed in Table 2, together with stoichiometric yields (moles and wt %). In general, the lignin-drived phenolics have a higher potential for producing hydrogen than the products from carbohydrates. This is because, for an oxygenated compound with a chemical formula of $C_nH_mO_k$, the stoichiometric yield of hydrogen is 2+m/2n-k/n moles per mole of carbon in the feed (eq. 1), and k/n is usually in the fractions for the aromatic phenolics from lignin, while k/n is close to 1 for most carbohydrate-derived products such as sugars.

Table 1. Pyrolytic oil compositions from different feedstocks/reactors

Process	Fluidized bed (UW)[c]			Vortex (NREL)[d]
Feedstock	poplar	maple	spruce	oak
Temperature, °C	504	508	500	650
Product	Yield (wt % of m.f. wood)			
acetic acid	5.4	5.8	3.9	5.0
formic acid	3.1	6.4	7.2	3.3
hydroxyacetaldehyde	10.0	7.6	7.7	4.3
glyoxal	2.2	1.8	2.5	3.0
methylglyoxal		0.65		
formaldehyde		1.2		2.2
acetol	1.4	1.2	1.2	1.8
ethylene glycol	1.1	0.6	0.9	
levoglucosan	3.0	2.8	4.0	3.8
1,6-anhydroglucofuranose	2.4			
fructose	1.3	1.5	2.3	
xylose				0.9
glucose	0.4	0.6	1.0	
cellobiosan	1.3	1.6	2.5	
oligosaccharides	0.7			
pyrolytic lignin[b]	16.2	20.9	20.6	24.9
unidentified	11.9	17.1	12.9	5.8
total oil[a]	65.8	67.9	66.5	55.3
water[a]	12.2	9.8	11.6	10.4
char	7.7	13.7	12.2	12.4
gas	10.8	9.8	7.8	12.2
mass closure	96.5	101.2	97.7	90.3

[a] Oil + water = bio-oil. [b] Material precipitated by addition of water. [c] From [6]. [d] Private communication.

$$C_n H_m O_k + (2n\text{-}k)\, H_2O = n\, CO_2 + (2n + m/2\text{-}k)\, H_2 \qquad (1)$$

Thermodynamic calculations indicate that the equilibrium yield of hydrogen (as percentage of the stoichiometric yield) under typical steam reforming conditions (750°C and S/C=5) does not vary much for these oxygenates, averaging around 85%. The small variation in this yield reflects the true ratio (5+k/n) of steam-to-carbon in the catalytic reformer: external steam supplied (S/C=5) plus that derived from the feed (S/C=k/n). A further water-gas shift (WGS) operation to convert all the CO formed in the reformer would improve the overall yield to about 97%. If coking could

Table 2. Hydrogen yields from steam reforming

Sample	Formula	Stoichiometric H_2 Yield		Equilibrium H_2 Yield	
		moles[a]	% (by wt.)[b]	% (of st.)[c]	(+ WGS)[c,d]
methane	CH_4	4.00	50.3%	85.6%	95.0%
methanol	CH_4O	3.00	18.9%	87.1%	96.8%
acetone	C_3H_6O	2.67	27.8%	85.2%	96.2%
ADP[e]	$C_{11}H_{14}O_3$	2.36	27.0%	84.7%	96.4%
guaiacol	$C_7H_8O_2$	2.29	26.0%	84.6%	96.5%
syringol	$C_8H_{10}O_3$	2.25	23.5%	84.8%	96.6%
lignin	$C_7H_9O_3$	2.21	22.1%	84.9%	96.7%
furfuryl alcohol	$C_5H_6O_2$	2.20	22.6%	84.9%	96.7%
poplar oil[e]	$CH_{1.33}O_{0.53}$	2.14	19.7%	85.2%	96.9%
poplar	$CH_{1.47}O_{0.47}$	2.07	17.2%	85.5%	97.1%
furfural	$C_5H_4O_2$	2.00	21.0%	84.6%	96.9%
5-HMF[e]	$C_6H_6O_3$	2.00	19.2%	84.9%	97.0%
xylan	$C_5H_8O_4$	2.00	15.3%	85.8%	97.3%
cellulose/levoglucosan	$(C_6H_{10}O_5)_n$	2.00	14.9%	85.8%	97.3%
HAc, HAA[e]	$C_2H_4O_2$	2.00	13.4%	86.3%	97.5%
formic acid	CH_2O_2	1.00	4.4%	87.7%	98.9%

[a] Moles of H_2 produced per mole of carbon in the reactant being reformed.
[b] Amount of H_2 formed divided by the sample molecular weight.
[c] Equilibrium moles of H_2 predicted at 750°C and S/C=5 divided by the stoichiometric yield.
[d] With additional moles of CO present under 750°C and S/C=5 to be shifted in a downstream water-gas shift (WGS) reactor.
[e] ADP: 4-Allyl-2,6-dimethoxyphenol; 5-HMF: 5-Hydroxymethylfurfural; HAc: acetic acid; HAA: hydroxyacetaldehyde. Poplar oil is on water-free basis.

Table 3. H_2 yields from steam reforming of poplar oil ($CH_{1.33}O_{0.53}$)

Temperature (°C)	Steam-to-carbon ratio (S/C)	% of stoi. H_2 yield at equilibrium (reforming only)
500	5	57.0%
500	10	76.3%
600	5	76.9%
600	10	90.4%
700	5	84.6%
700	10	92.8%
800	5	84.7%
800	10	91.7%
900	5	82.8%
900	10	89.9%

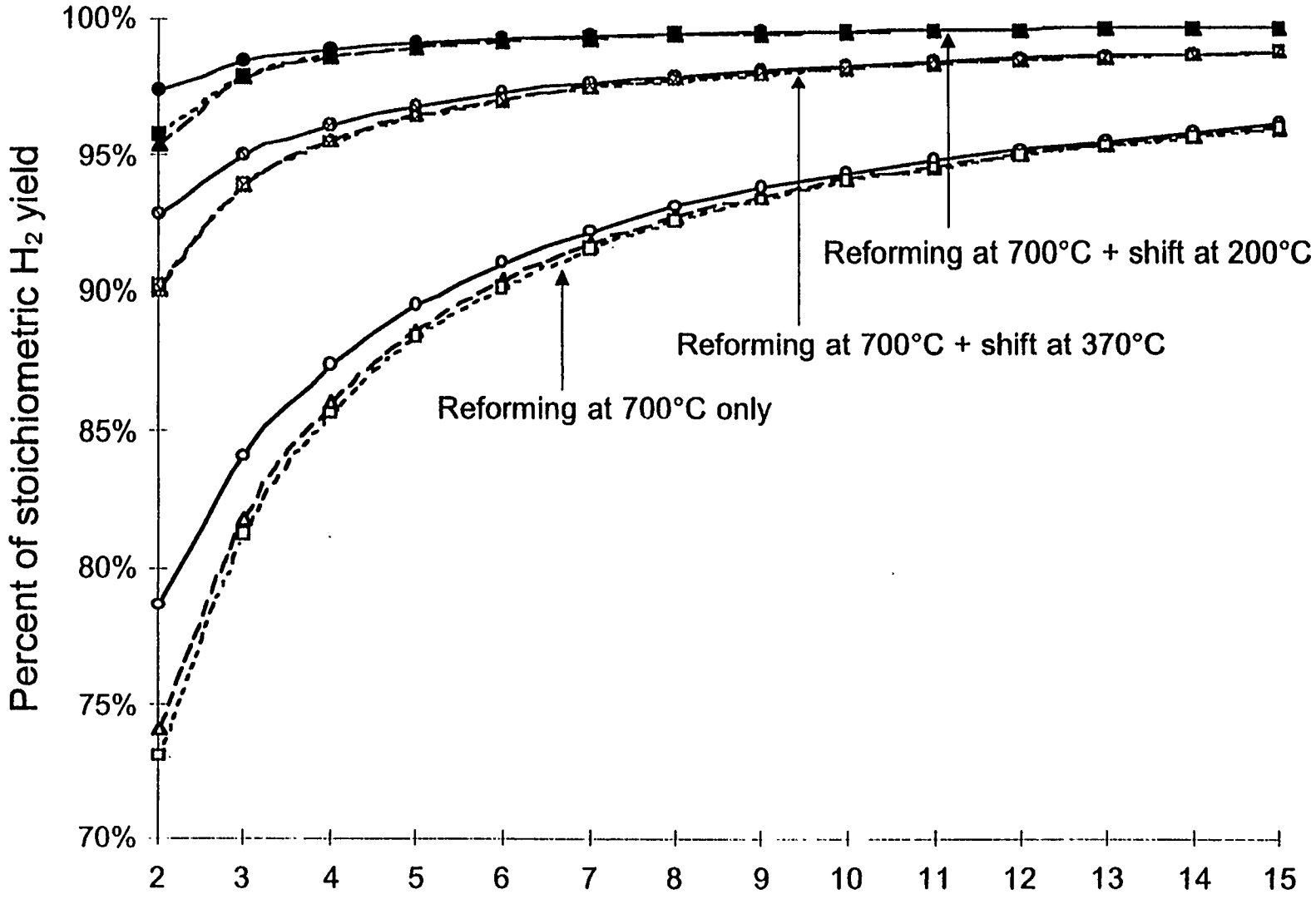


Figure 1. Thermodynamic equilibrium analysis showing the effect of steam-to-carbon ratio on the yield of hydrogen at selected reforming and shift conversion conditions. Feed: syringle (O), HAA (Δ), and furfural (□).

be avoided, the conversion of oxygenates to hydrogen would be almost quantitative through the combination of reforming and water-gas shift.

Figure 1 shows the approach to maximum stoichiometric yields of hydrogen as a function of S/C at a temperature of 700°C, which is in the lower end of temperatures used in current hydrocarbon reformers. The beneficial yield effect of the shift reaction is clearly established. The equilibrium yields of hydrogen from a typical bio-oil (of poplar) [4] as a function of temperature and steam-to-carbon ratios (S/C) were also calculated (Table 3). Results suggest that a wide range of combinations of the two key operating variables can be chosen to approach stoichiometric yields. Temperatures higher than 700°C and S/C greater than 5 are recommended for high efficiency conversion.

4 Catalytic reforming of oxygenates

4.1 Literature review

Processes of steam reforming C1-C5 hydrocarbons, naphtha, gas oils, and simple aromatics are well known and commercially practiced. When the objective is to maximize the production of H_2, the stoichiometry describing the overall process is:

$$C_n H_m + 2n\, H_2O = n\, CO_2 + (2n + m/2)\, H_2 \qquad (2)$$

In a hydrocarbon reformer, the following reactions take place concurrently:

$$C_n H_m + n\, H_2O = n\, CO + (n + m/2)\, H_2 \qquad (3)$$

$$CH_4 + H_2O = CO + 3\, H_2 \qquad (4)$$

$$CO + H_2O = CO_2 + H_2 \qquad (5)$$

At normal operating conditions, reforming of higher hydrocarbons (eq. 3) is irreversible [13], whereas the methane reforming reaction (eq. 4) and the shift conversion reaction (eq. 5) approach equilibrium. A large molar ratio of steam to hydrocarbon will ensure that the equilibrium for reactions (4) and (5) is shifted towards H_2 production.

The main problem in the steam reforming of hydrocarbons is carbon formation. Three types of carbon may be formed: whiskers, encapsulating deposits ("polymers"), and pyrolytic carbon [14]. The carbon formation is related to the kinetics, and hence the selectivity, of the catalyst. Significant improvements have been made in controlling coke formation by promoting the classical Ni-alumina or Ni-silica/alumina formulations with Ca and/or K and by the use of magnesia as magnesium-aluminum spinel [15].

The reforming operation requires relatively high steam-to-carbon molar ratios (S/C = 3.5 - 5.0 for methane), adequate temperature profiles in the tubular reactor (low inlet temperature increased along the tube length to a maximum of 750-775°C due to the structural constraints of the Ni-Cr alloys used), and a Ni-based catalyst (20-30 wt.% as NiO) on a refractory support having appropriate steam adsorption characteristics. The reforming operation is not very sensitive to pressure which is essentially dictated by the applications of the product H_2 [16]. Space velocities ($G_{C_1}HSV$, as volume of C_1 equivalent/h/volume of catalyst) used in tubular reformers are typically in the order of 1500-2000 h^{-1}.

Aznar et al [17] have demonstrated that steam reforming syngas obtained from the gasification of lignocellulosics is possible using commercially available Ni-based catalysts (Topsoe R-67 and RKS-1). Rapid deactivation of the catalyst takes place after a few hours only. Tars produced during gasification contain a high percentage of polycyclic aromatics, while pyrolysis oil is essentially a mixture of carbohydrate-derived fragments and lignin-derived phenolics [1].

Literature on the steam reforming of oxygenates falls within two categories: (a) reforming simple alcohols, such as methanol and ethanol; and (b) reforming oxygenated aromatics, i.e. cresols. A detailed review on this subject has been given elsewhere [18]. The steam reforming of methanol is a special case and a large body of information has been accumulated [19]. A variety of catalysts are capable of carrying out the conversion at low temperatures and the product slate is markedly affected by the type of catalyst and the experimental conditions used. A different mechanism intermediated by methyl formate was initially proposed by Takahashi et al [20] and based on the formation of methylformate ester on the catalyst surface between two adsorbed species, H_3CO and HCO. The ester is hydrolyzed to methanol and formic acid. The latter decomposes directly to CO_2 and H_2 with 100% selectivity, i.e. no CO is formed. Ethanol reforming has also been studied to produce acetic acid [21] and to hydrogen by Garcia and Laborde [22]. Steam reforming of oxygenated aromatics has been directed towards the dealkylation of cresol.

When considering the bio-oil composition shown in Table 1, it is clear that challenges in catalytic steam reforming will be linked to the ability to handle both the "pyrolytic lignin" fraction and the carbohydrate-derived fraction: acetic acid, aldehydes, sugars and anhydrosugars, and oligomers. It is likely that the oligomeric fragments, either lignin- or carbohydrate-derived, once condensed as bio-oil, cannot be revolatilized without significant char formation. Thus, our strategy will be either (a) to separate the "pyrolytic lignin" (which has a potential market of its own as a phenolics substitute for the production of adhesives) from the condensed bio-oil and steam reform the aqueous fraction which, while still containing some substituted, but monomeric phenolics, will predominantly be constituted of the carbohydrate-derived components; (b) to carry out a fractional condensation of the pyrolytic vapors to separate the oligomers and thus directly recover a "light" fraction comprised essentially of mixed monomers; or (c) try to reform the entire uncondensed vapors by coupling the reformer to the pyrolysis unit.

Given the chemical diversity of the bio-oil aqueous fraction, and according to the literature reviewed, Ni-based catalysts operating in the 700-800°C range ought to be able to carry out the steam reforming conversion. An appropriate temperature profile through the reactor will have to be developed experimentally to carefully control coke formation.

4.2 Rapid screening and mechanistic studies

A series of model oxygen-containing compounds, biomass and its main components (cellulose, xylan, and lignin), and bio-oil and its various fractions were screened under identical conditions using a commercial catalyst, G-90C, from United Catalyst Inc. (UCI). We also tested a number of research and commercial steam reforming catalysts and a WGS catalyst and determined H_2 yields using four model compounds (methanol, acetic acid (HAc), an aqueous solution of hydroxyacetaldehyde (HAA), and a methanol solution of 4-allyl-2,6-dimethoxyphenol (ADP)) under the same operating conditions. Methanol steam reforming was used as a standard test for checking the performance of the system as well as catalyst deactivation.

These experiments were performed in a vertical dual-bed microreactor coupled to a molecular-beam mass spectrometer (MBMS) [23,24]. This system has the advantage of simultaneously detecting, unconverted reactants, intermediates and products at the exit of the microreactor by rapidly sampling through a supersonic, free-jet expansion nozzle. This expansion cools the reaction products and forms a molecular beam that is ionized and analyzed by a quadrupole mass spectrometer. The microreactor was housed in a tubular furnace with four independently controlled temperature zones. The dual bed configuration of this reactor enabled us to study either the differences between thermolysis and catalysis or to compare the performances of two catalyst under the same temperature conditions. Mass spectra in the *m/z* range of 1-350 were obtained for pyrolysis and catalysis products with the MBMS operated under 25 eV EI ionization conditions. The detection limit of the MBMS corresponded to conversions of approximately 99.95% for most of the samples, i.e., from the sample signal without catalyst at more than 1.0×10^6 counts/s (cps) to less than the instrument lower limit of 500 cps (noise = ±250 cps) with catalyst. Among the most important parameters for steam reforming are catalyst bed temperature(s), molar steam-to-carbon ratio (S/C), gas hourly space velocity ($G_{C_1}HSV$, as defined above), and residence time (t, calculated from the void volume of the catalyst bed divided by the total flow rate of gases at the inlet of the reactor; void fraction = 0.4).

Under conditions of 600°C, S/C=10-13, $G_{C_1}HSV$ = 180-1680 h^{-1}, and t=0.1s (vapor residence time was similar because the feed flow rate was small compared with that of the helium carrier gas and steam), essentially complete conversion of all oxygenates was achieved, and in most cases, the yield of hydrogen was high, and close to stoichiometric values. However, there were several cases where the hydrogen yield was far below that predicted by stoichiometry and thermodynamic calculations, because of the formation of carbonaceous materials during vaporization or pyrolysis of the feed prior to entering the catalyst bed.

Other commerial and research catalysts tested were capable of reforming the model compounds and high conversions (>99%) were observed [24]. The H_2 yields for all catalysts and model compounds were high, averaging 90% (±5%) of the stoichiometric. Within our experimental error limit, there is no clear indication of one catalyst being better than the others. The yields were reproduced very well (typically within ±2-3%; the worst within ±5-6%). Among the different model compounds, we observed that methanol and HAA yield slightly more H_2 than HAc and ADP.

Among the various operating parameters studied, temperature has the most profound effect on steam reforming reactions. Methanol can be steam reformed at 300°C; HAc and HAA are reformed in high conversions (>99.95%) at above 350°C. The lignin model compound, ADP, was more difficult to reform with steam, requiring temperatures above 600°C for complete conversion. Within experimental error limits, varying residence time from 0.04 to 0.15 s and increasing S/C from 4.5 to 7.5 showed no significant effects on the yield of hydrogen under the conditions of 600°C and $G_{C_1}HSV = 1680\ h^{-1}$; however, it did on the yield of CH_4.

The microreactor-MBMS system also allows the study of reforming mechanisms through the continuous monitoring in real time of the intermediate products present in the gas phase at low conversions. Acids, ketones, alcohols and aldehydes were represented by HAc, acetone, ethylenediol, glycerol, and HAA. The phenolic series included phenol, anisole, cresols, resorcinol, 2,6-dimethylphenol, guaiacol, syringol, and ADP. The furan family of model compounds consisted of furan, 2-methylfuran, 2,5-dimethylfuran, 2-furfuraldehyde, furfuryl alcohol, 5-methylfurfural, and 5-hydroxymethylfurfural. A complete report on HAc and HAA has been published [25], and details of these studies are to be published in separate papers being prepared. HAc produced significant amounts of carbon on the catalyst during steam reforming. No intermediate was detected during steam reforming of HAA and phenol above 400°C. Phenol was the only intermediate detected at both 400 and 600°C from *o*-cresol steam reforming, while significant amounts of cresols, phenol, benzene, and toluene were observed from thermolysis of *o*-cresol at both 400 and 600°C. The results obtained for guaiacol and syringol are consistent with the weakening effect of MeO substituents.

The results obtained for these model compounds suggest that there are significant differences in steam reforming mechanisms of hydrocarbons and oxygenates. Most of the oxygenates found in bio-oils are thermally unstable. At the operating conditions of a typical steam reformer, these oxygenates undergo homogeneous (gas-phase) thermal decomposition, as well as cracking reactions on the acidic sites on the catalyst support. These reactions compete with the catalytic steam reforming reaction to hydrogen. However, a complete conversion of both the oxygenate feed and its decomposition products to hydrogen can be achieved with commerial Ni-based catalysts under reasonable operating conditions, if char formation prior to reaching the catalyst bed and coking on the catalyst can be eliminated, or at least controlled.

4.3 Bench-scale reformer studies

A bench-scale, fixed-bed reactor, shown in Figure 2, was used to establish the global and elemental mass balances and the carbon-to-gas conversion, to quantify the distribution of gas products under conditions of complete conversion of the pyrolysis oil feedstock, and to study the lifetime and regeneration of catalysts. It has been described in detail in our previous publication [24]. The reactor main body is a stainless steel tube (1.65 cm i.d. x 42.6 cm length) housed in a tubular furnace equipped with three independently controlled heating zones. Steam was generated in a boiler and superheated up to 850°C. The organic feed from a diaphragm metering pump was sprayed with ambient N_2 gas followed by mixing with superheated steam in a triple nozzle inlet. Products exiting the reactor were passed through a condensor. Every 4-5 min, the condensate (water in most cases) weight, volume and compositions of the permanent gas output were recorded. An on-line IR gas analyzer was used to monitor CO/CO_2 concentrationsand a MTI-QUAD GC was used to measure concentrations of H_2, N_2, O_2, CO, CO_2, CH_4, and other light hydrocarbons. The reformer system was interfaced with a computer to monitor temperatures and other important parameters (once every 30 s).

We initially used model compounds (methanol, acetic acid, syringol and *m*-cresol, both separately and in mixtures), then real bio-oil and its aqueous fraction. Most studies were carried out using the UCI G-90C catalyst; in several latest testings we used a dual-catalyst bed of 46-1 and 46-4 from ICI Katalco. The dual-catalyst bed configuration is detailed in Figure 3. Representative results are listed in Table 4 for the steam reforming of acetic acid, syringol/methanol mixture, a three-component feed made of acetic acid, *m*-cresol, and syringol, and an aqueous fraction obtained from a poplar pyrolysis oil. Profiles of the output gas composition are shown for the 3-component mixture in Figure 4 and for the bio-oil aqueous fraction in Figure 5.

Acetic acid: Results show that the temperature of the reforming section of the bed determines the extent of the carbon conversion to gas products. At temperatures below 500°C, only 73% of the carbon contained in the feed was converted to gas products. It was observed that a significant amount of carbon was formed during these experiments. Part of this carbon was entrained from the bed by the gas stream and was collected in the condenser. The accumulation of carbon in the bed caused the pressure at the reactor entrance to increase continuously during the experiment. An increase in temperature to 535°C in the reforming zone of the catalyst bed improved the recovery of carbon in the gas products up to 80% of that in the feed, and although carbon was still formed, it was not entrained by the gas but retained in the upper section of the catalyst bed. We observed that the carbon deposited in the catalyst bed during the steam reforming of acetic acid was gasified, at least partially, by steam and that after the steam treatment the pressure at the reactor entrance recovered the initial value. Further increase in the reforming temperature resulted in a lower extent of carbon deposition on the catalyst. Formation of carbon deposits was minimal when the temperature was raised to 665°C. At this temperature, the average carbon recovery was 98% and the pressure drop along the catalyst bed was stable throughout the experiment (90 min).

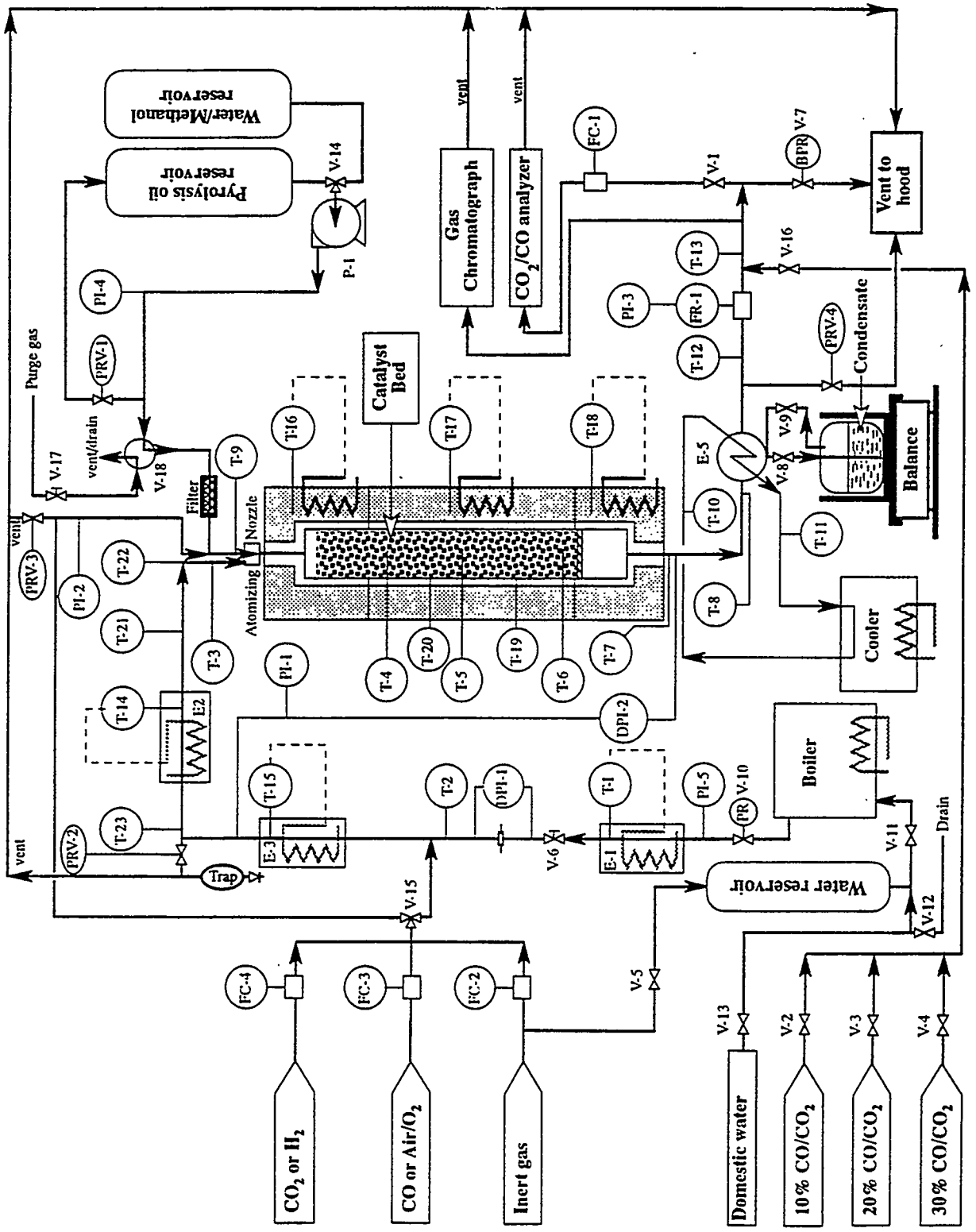


Figure 2. P&I diagram of the Fixed-Bed Catalytic Steam Reforming unit.

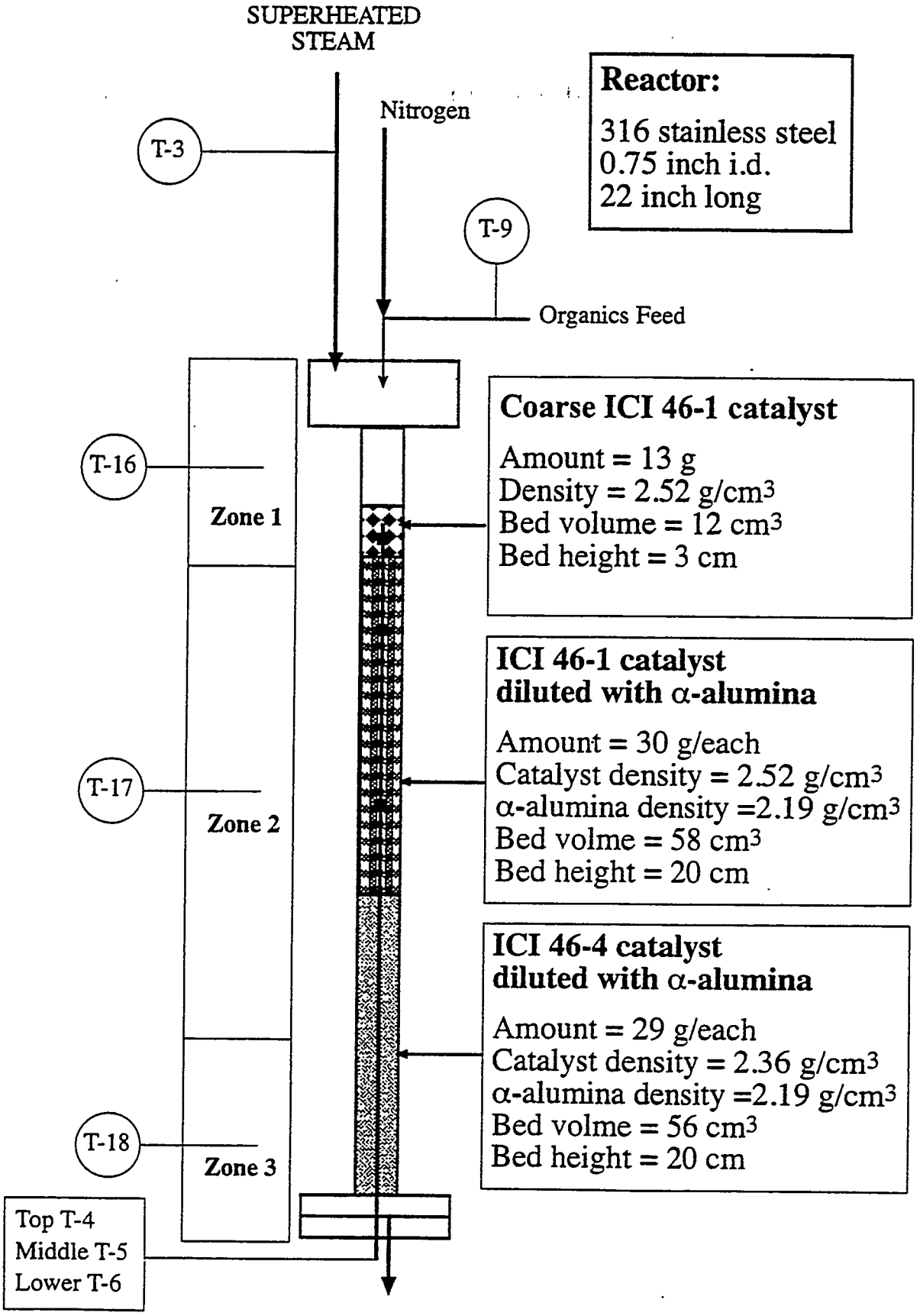


Figure 3. A schematic diagram detailing the dual-catalyst bed configuration.

Below 600°C, hydrogen yield grows with the rising in the reforming temperature due to the increase in the amount of carbon converted to gas products. Above 600°C, where carbon conversions approaching 100% are obtained, hydrogen yield tends to decrease as the temperature increases. This behavior is due to the thermodynamics of the reforming process, since WGS reaction (3) is displaced towards the formation of CO and water at high temperature. This results in a lower hydrogen concentration at the reformer exit. Thus, a unit for the steam reforming of acetic acid using commercial nickel-based catalysts does not differ conceptually from the process for the steam reforming of naphtha or methane, and must include high- and low-temperature shift reactors to obtain an optimal yield of hydrogen. In this context, higher temperatures in the reformer are favorable because they reduce not only the extent of carbon deposition on the catalyst bed but also the yield of methane, thus resulting in a higher yield of hydrogen after the conversion of carbon monoxide in the shift reactors.

Syringol: The steam reforming of syringol was studied at conditions similar to those employed for the reforming of acetic acid. Syringol was dissolved in methanol at a weight concentration ratio of 40:60, which corresponds to a mixture in which 53% of the carbon is provided by syringol. Methanol was selected since it was verified that this solvent was readily reformed in the range of experimental conditions to be tested without leaving any appreciable amount of carbon on the catalyst surface. As a general trend, syringol does not react as well as acetic acid during steam reforming using the UCI G-90C catalyst. At 670°C, the conversion of the carbon in syringol to gas products was estimated to be only 90%. Raising the catalyst temperature to 700°C and above resulted in almost complete carbon conversions (Table 4). Similar to the reforming of acetic acid, the increase in temperature during the steam reforming of syringol also results in the displacement of the gas composition: a decrease in the contents of methane, hydrogen and carbon dioxide, together with an increase in the amount of carbon monoxide.

Three-component mixture: Two long-duration runs using a 3-component mixture were perfromed in order to compare performances of catalysts from two manufacturers. This mixture contained approximately 67% acetic acid, 16% *m*-cresol and 17% syringol, to represent the components of the carbohydrate fraction and the lignin fraction in bio-oil. We observed some coke deposits on the top portion of the UCI G-90C catalyst bed. The overall mass balance (carbon, hydrogen, and oxygen) was 98.8% and the carbon conversion to gas was 96.1%. The other catalytst tested for steam reforming of the 3-component mixture was the 46-series from ICI Katalco (46-1/46-4). This dual catalyst bed (Figure 3) showed an excellent and steady performance without any coke deposition on the catalyst. Figure 4 shows the reactor temperature profiles, the output gas flow rate (very steady), and the gas composition, which remained constant throughout the whole run. The overall mass balance (including carbon, hydrogen, and oxygen) was 104.3%, and for carbon 105.1%, indicating that there may be a systematic error in our measurement. An excellent hydrogen yield of 85.6% was obtained, and the total hydrogen potential may be as high as 97.6% with a second water-gas shift reactor. These results confirm that both the UCI G-90C and especially the ICI 46-series catalysts can efficiently convert oxygenates to hydrogen.

Aqueous fraction of bio-oil: Steam reforming of bio-oil or its fractions was found to be more difficult than that of model compounds. The main problem that needed to be solved was feeding the oil to the reactor. Bio-oil cannot be totally vaporized; significant amounts of residual solids are often formed that block the feeding line and the reactor. Thus, the simple injection system used for model compounds had to be modified to allow spraying bio-oil and its fractions in to the catalytic reactor without prior char formation. Because the process economics favors the separation of lignin-derived phenolics as co-products (discussed below), we only used the aqueous, mostly carbohydrate-derived fraction to generate hydrogen.

Poplar pyrolysis oil generated in the NREL vortex reactor system was extracted using ethyl acetate and water (weight ratios of 1:1:1 for oil:ethyl acetate:water). The resulting aqueous fraction (55% of the whole oil) contained 25% organics and 75% water. It was successfully fed to the reactor using a triple-nozzle spraying system with minimal accumulation of char in the reactor inlet. A large excess of steam (S/C ~ 20 and 30 in the two runs) was used, together with a high flow rate of nitrogen, to allow for proper oil dispersion and heat transfer required to maintain a sufficiently high temperature (>500°) at the reactor entrance. The ICI 46-series catalysts performed satisfactorily with no coke formation. We observed a stable gas production rate and composition throughout the whole 4-hour-long experiment (Figure 5).

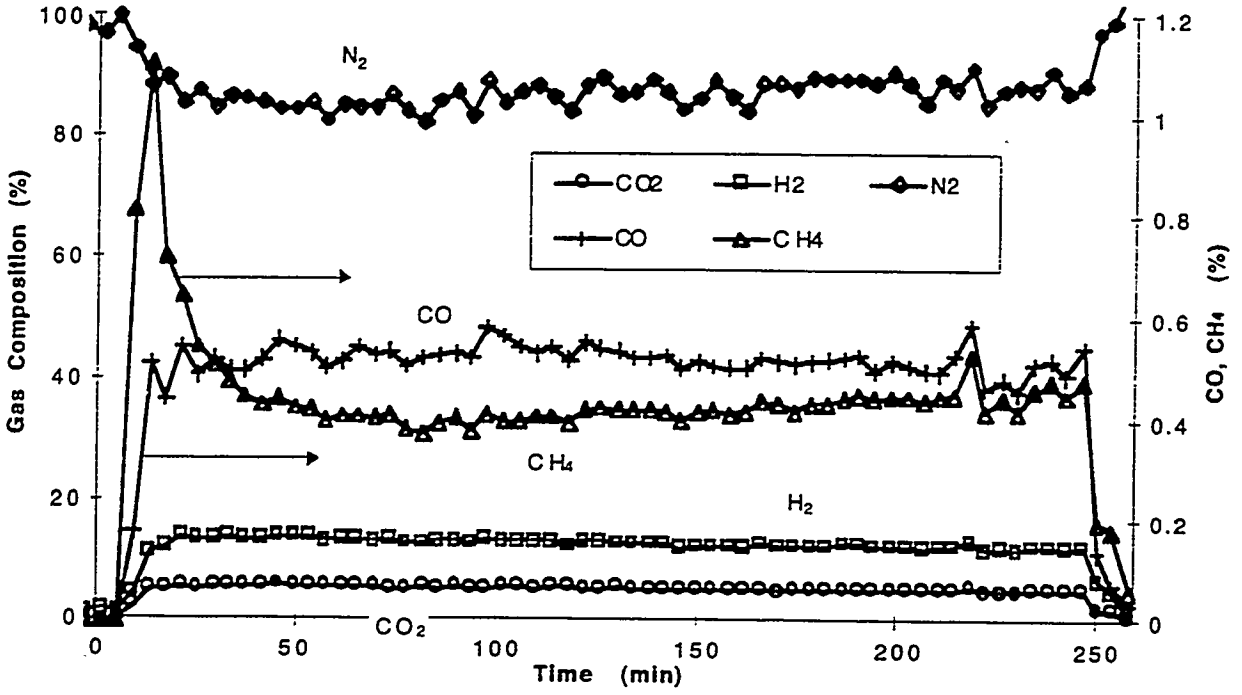


Figure 5. Composition of gaseous products during the steam reforming of bio-oil aqueous fraction using the ICI 46-series catalyst.

The carbon conversion of the aqueous fraction to gas products was almost quantitative in both runs that used the same catalyst bed (Table 4). We observed similar levels of mass balances as in the experiments using model compounds: global 99%, carbon 105%, and hydrogen 97% (assuming a formula of CH_2O for the organics in the aqueous fraction). The methane

concentration (with N_2 excluded) increased from 0.56% in the first run (2 hrs, t=0.03 s) to 2.2% in the second run (4 hrs, t=0.02 s), and both values were much higher than that (0.01%) obtained from the 3-component model compound mixture (17 hrs, t=0.09 s). This was likely caused by the shorter residence time forced by the large flow rate of steam and nitrogen used in the experiment, and also possible incomplete reduction or reoxidation of the catalyst.

Summary: It can be concluded that oxygenates present in bio-oil can be effectively steam-reformed using commercial catalysts under conditions similar to those used for the steam reforming of naphtha: S/C=5, >700 °C, and G_{C_1}HSV around 2000 h^{-1}. Excellent mass balances and high yields of hydrogen have been obtained in most cases. A catalyst formulation, such as the UCI G-90C and the ICI 46-series, used for the reforming of naphthas, can be effectively employed in converting bio-oil to hydrogen.

5 Process design and economics

Two scenarios for the production of hydrogen from pyrolysis oil can be envisioned:

(1) A regionalized system of hydrogen production with small and medium-sized pyrolysis units providing condensed bio-oil to a centralized reforming unit. At the reforming plant, the separation of the lignin-derived oligomers will generate a "clean" aqueous stream with simple carbohydrate-derived soluble organics which will be fed to the reformer.

(2) Transport the biomass to a larger pyrolysis unit and feed the uncondensed vapors directly to an integrated adjacent reforming unit located in the same plant premises. In this case, we can also condense the heavier fraction of the pyrolysis vapors via fractional condensation and feed the remaining uncondensed vapors to the reformer.

The first case has the advantage of the availability of cheaper feedstocks, which include biomass residues. In the integrated system, however, the costs of entirely condensing the vapors to produce the bio-oil and transporting it to the hydrogen facility are avoided.

A conceptual process design to make hydrogen from pyrolysis oil is shown in Figure 6. Because of the low sulfur content of biomass, a sulfur removal system is not likely to be required. Also, according to thermodynamic simulations and the screening results, a temperature reformer ramping up to 700-750°C will be needed.

In the process being evaluated, pyrolysis oil, its fractions or the uncondensed vapors are fed with steam into a catalytic reactor. Laboratory experiments will choose the most suitable catalyst and reactor configuration; the base-case will use a fixed-bed catalytic reactor. The reaction will occur at 700°C, and the ratio of steam to oil will be determined by experimental results and economic optimization, although it is clear that it will be in the 5 to 7 range. Since the overall reaction of pyrolysis oil to H_2 is endothermic, the char produced in the pyrolysis of the biomass will be

burned to produce heat and steam. Preliminary energy balances indicate that a fraction of the oil may also be used as a source of heat, especially in the centralized reformer supplied by satellite pyrolysis units. In the base-case design, a pressure swing adsorption unit will be used to purify the H_2 produced.

The purpose of performing technoeconomic, or systems analyses is several-fold. First, in a research environment, the economic feasibility of a given project can be assessed. Additionally, results of any of these levels of analysis are useful in guiding experimental planning. Finally, on-going analysis can be used to track the progress of research.

A determination of the selling price of hydrogen from this process has been made through a detailed technoeconomic analysis. The process analyzed (Figure 6) consists of fluid bed pyrolysis of biomass, water and ethyl acetate extraction to recover a phenolic substitute coproduct, and steam reforming to produce hydrogen in a process based on that used for natural gas reforming. The cost of the pyrolysis plant was taken from Beckman and Graham (1993). A pressure swing adsorption system is used to produce a hydrogen product pure enough to be used in fuel cells. Steam is produced through detailed heat integration and is intended to be sold as a by-product.

A combination of ASPEN Plus® and spreadsheet models was used to perform material and energy balances, sizing and costing of major pieces of equipment, and the life cycle cost of the process. The design assumes that a number of small pyrolysis operations, using biomass where it is available and thus at lower costs, supply bio-oil to a central extraction and reforming facility. Because biomass pyrolysis oil is similar to petroleum crude oil in that many fuels and chemicals can be derived from it, further coproduct options will be studied according to current economic and market conditions. The coproduct option was not studied to economically justify the pyrolysis-based process, but is meant to be an example of the opportunities available from biomass pyrolysis oil once a system of coproducts is developed.

The current selling price of H2 in industry is between $5/GJ and $14/GJ, depending on the size of the production facility. This range is for hydrogen as produced by the plant: purified, but not compressed or stored. The rationale for using this basis for deciding the feasibility of our process is that the end-use of the hydrogen, which is not appropriately specified at this time, will dictate the conditions at which it is shipped from the plant. The major assumptions used for the base case analysis are shown in Table 8. The economic feasibility of this process was studied using the discounted cash flow rate of return method. This method calculates the internal rate of return (IRR) that will be earned on the initial capital investment over the life of the project. Given this rate and a feedstock cost, the necessary selling price of the product can be calculated. Often, the IRR is specified as the minimum acceptable rate for an investor to finance a project. Therefore, the perceived risk of the project can be incorporated into the IRR. Because the process of producing hydrogen from biomass currently carries higher risks than conventional hydrogen-generating processes, the IRR specified in this study was 15% after tax, while the rate for

conventional processes is between 9% and 12%. For a 37% tax rate, a 15% after-tax IRR corresponds to a pre-tax IRR of 20.4%.

Results indicate that the necessary hydrogen selling price for the base case analysis is $7.70/GJ. Figure 7 shows the sensitivity of this price to different parameters used in the analysis. The line down the middle of the chart gives the base case scenario. Each parameter was changed relative to the base case and independent of the other parameters. Therefore, the selling price of hydrogen for one of the scenarios represents changing only that parameter (e.g., feedstock cost) relative to the base case. The current selling price of hydrogen is shown at the bottom for easy reference. This figure indicates quite clearly that the process to produce a phenolics substitute and hydrogen from pyrolysis via extraction and steam reforming has significant potential to be economically feasible. A high rate of return can be obtained and the process can sustain a high drop in coproduct selling price before the hydrogen becomes more expensive than current markets will allow. Relative to the market value of hydrogen, this analysis found that the process is able to sustain large changes in capital cost, hydrogen production capacity, and feedstock cost.

6 Conclusions and Future Work

Fast pyrolysis of biomass is an advanced technology to produce a bio-oil in high yields (70-75 wt.% of anhydrous biomass). This bio-oil is a complex mixture of simple aldehydes, alcohols and acids together with more complex carbohydrate and lignin derived oligomeric materials. Fractional condensation of the pyrolytic vapors could separate the simple monomeric materials, which comprise about one third to one half of the bio-oil from the complex oligomeric fraction. Steam reforming of the simple monomeric materials, the entire bio-oil or its fractions is thermodynamically and chemically feasible. Our screening tests have shown that such catalysis is possible using commercially available Ni-based catalysts. Improvements in their formulation may be needed to optimize the activity/selectivity/time-on-stream relationships when reforming the biomass-derived oxygenates. Results obtained at the bench-scale level on the steam reforming of model compounds and their mixtures, as well as bio-oil fractions have substantiated our findings at the microscale level. The challenge seems to be the adequate introduction of the bio-oil or its fractions to contact the catalyst prior to any gas-phase thermal decomposition which would result in unwanted char formation. In addition, progressively increasing the catalyst activity by either temperature ramping or catalyst formulation is an appropriate strategy to minimize coke formation on the catalyst. We have achieved a reasonable comprehension of the spray nozzle design and operating conditions to fulfill these goals.

The preferred implementation strategy consists of small- to medium-size regional fast pyrolysis units which will produce the bio-oil from either dedicated crops or plantations, or will use waste lignocellulosics as feedstocks. The bio-oil produced will be transported to a central separation/reforming unit serving a given region where H_2 and co-products will be produced. The process concept is simple: a desulfurization unit is not needed, and the bio-oil can be atomized in

a flow of steam which is then processed through a reforming unit. By a proper choice of conditions the near equilibrium design can be driven to maximize H_2 production. A pressure swing adsorption unit will purify the gas stream. An economic analysis of the process indicates that the necessary selling price of hydrogen is well within current market values. This analysis studied the co-production of hydrogen and a phenolics substitute for resin manufacture. The process studied was based on pyrolysis oil production at distributed locations followed by extraction and steam reforming at a centralized facility. Relative to the current market price of hydrogen, the economics of this process have been shown to be insensitive to changes in the assumptions made.

An alternate strategy, but less favorable economically, consists of transporting the biomass to a central conversion site where the fast pyrolysis and reforming operations can be conducted jointly. Fractional condensation of the vapors can be carried out in order to recover, for instance, the depolymerized lignin fraction which has value as a mixture of phenolics to be used in resin formulations.

The projected goals for future work are:

- To demonstrate the long-duration catalyst performance as well as its regenerability using bio-oil fractions.
- To determine optimum process conditions at the bench scale.
- To demonstrate the feasibility of alternative reactor configurations such as fluid bed (bubbling or circulating).
- To identify marketable co-products and separation methods.

7 Acknowledgments

We thank the US DOE Hydrogen Program for financial support of this research project under contract DE AC 36-83CH10093.

8 References

1. Elliott, D.C. (1988) Relation of reaction time and temperature to chemical composition of pyrolysis oils, in *Pyrolysis Oils from Biomass: Producing, Analyzing and Upgrading* (eds. E.J. Soltes and T.A. Milne), ACS Symposium Series 376, ACS, Washington, D.C. pp. 55-65.
2. Fagernas, L. (1995) *Chemical and Physical Characterization of Biomass-Based Pyrolysis Oils: Literature Review*, VTT Research Notes, No. 1706, Technical research Center of Finland, Espoo, Finland.
3. Diebold, J.; Czernik, S.; Scahill, J.; Philip, S. D. and Feik, C. J. (1995) Hot gas filtration to remove char from pyrolysis vapors produced in the vortex reactor at NREL, in *Proceedings of Biomass Pyrolysis Oil Properties and Combustion Meeting*, Estes Park, CO. pp. 90-108.
4. Radlein, D.; Piskorz, J. and Scott, D.S. (1991) *Journal of Analytical and Applied Pyrolysis*, Vol. 19, pp. 41.
5. Scott, D.S.; Piskorz, J. and Radlein, D. (1985) *Industrial Engineering and Chemical Process Design and Development*, Vol. 24, pp. 581.

6. Piskorz, J.; Scott, D.S. and Radlein, D. (1988) Composition of oils obtained by fast pyrolysis of different woods, in *Pyrolysis Oils from Biomass: Producing, Analyzing and Upgrading* (eds. E.J. Soltes and T.A. Milne), ACS Symposium Series 376, ACS, Washington, D.C. pp. 167-178.
7. Probstein, R. and Hicks, R. (1982) *Synthetic Fuels*, Mc Graw Hill, New York, pp. 235.
8. Graham, R.G., Freel, B.A. and Bergougnou, M.A. (1988) in *Research in Thermochemical Biomass Conversion*, (eds. A.V. Bridgwater and J.L. Kuester), Elsevier Applied Science, London, pp. 629-641.
9. Kovac, R.J., Gorton, C.W. and O'Neil, D.J. (1988) in *Proceedings of Thermochemical Conversion Program Annual Meeting*, Solor Energy Research Institute, Golden, CO, SERI/CP-231-2355, pp. 5-20.
10. Diebold, J. and Scahill, J. (1988) Production of primary pyrolysis oils in a vortex reactor, in *Pyrolysis Oils from Biomass: Producing, Analyzing and Upgrading*, (eds. E.J. Soltes and T.A. Milne), ACS Symposium Series 376, ACS, Washington, D.C. pp. 31-40.
11. Czernik, S., Scahill, J. and Diebold, J. (1995) *Journal of Solar Energy Engineering*, Vol. 117, pp. 2.
12. Antal, M.J. (1982) in *Advances in Solar Energy*, (eds. K.W. Boer and J.A. Duffield), Solar Energy Society, New York, pp. 61.
13. Tottrup, P.B. and Nielsen, B. (1982) Higher hydrocarbon reforming. *Hydrocarbon Processing*, March, pp. 89-91.
14. Rostrup-Nielsen, J.R. and Tottrup, P.B. (1979) in *Proceedings of Symposium on Science and Catalysis and its Applications in Industry*, FPDIL, Sindri, pp. 379.
15. Rostrupp-Nielsen, J.R. (1984) *Catalysis Science and Technology*, (eds. J.R. Enderson and M. Boudart), Springer-Verlag: Berlin, Heidelberg, Vol. 5, Ch. 1.
16. Patil, K.Z. (1987) Hydrogen, *Chemical Age of India* Vol. 38, No. 10, pp. 519-27.
17. Aznar, M.P., Corella, J., Delgado, J. and Lahoz, J. (1993) Improved steam gasification of lignocellulosic residues in a fluidized bed with commercial steam reforming catalysts. *Industrial Engineering Chemical Research*, Vol. 32, pp. 1-10.
18. Wang, D., Czernik, S., Montané, D., Mann, M. and Chornet, E. (1996) Biomass to hydrogen via fast pyrolysis and catalytic steam reforming of the pyrolysis oil or its fractions. (in preparation).
19. Jiang, C.J., Trimm, D.L., Wainright, M.S. and Cant, N.W. (1993) Kinetic mechanism for the reaction between methanol and water over a Cu-ZnO-Al_2O_3 catalyst. *Applied Catalysis A: General*, Vol. 97, pp. 145-158.
20. Takahashi, K., Takezawa, N. and Kobayashi, H. (1982) The mechanism of steam reforming of methanol over a copper-silica catalyst. *Applied Catalysis* Vol. 2, pp. 363-366.
21. Iwasa, N. and Takezawa, N. (1991) Reforming of ethanol - dehydrogenation to ethyl acetate and steam reforming to acetic acid over copper-based catalysts. *Bulletin of Chemical Society of Japan*, Vol. 64, pp. 2619-23.
22. Garcia, E.Y. and Laborde, M.A. (1991) Hydrogen production by steam reforming of ethanol: thermodynamic analysis. *International Journal of Hydrogen Energy*, Vol. 16, No. 5, pp. 307-12.
23. Evans, R. and Milne, T.A. (1987) Mass spectrometric studies of the pyrolysis of biomass. 1. Fundamentals. *Energy and Fuels*, Vol. 1, pp. 123-137.
24. Chornet, E., Wang, D., Montané D. and Czernik, S. (1995) Hydrogen production by fast pyrolysis of biomass and catalytic steam reforming of pyrolysis vapors, in *the Proceedings of the 2nd EU-Canada Workshop on Thermal Biomass Processing*, Toronto, Canada, May 8-9, pp. 246-262.
25. Wang, D., Montané, D. and Chornet, E. (1996) Catalytic steam reforming of biomass-derived oxygenates: acetic acid and hydroxyacetaldehyde. *Applied Catalysis A: General* (in press)
26. Mann, M. (1996) in *the Proceedings of 11th World Hydrogen Energy Conference*, Stuttgart, Germany, June 23-28.
27. Beckman, D. and Graham, R. (1993) in *Advances in Thermochemical Biomass Conversion*, (ed. A.V. Bridgwater) Blackie Academic & Professional, London, pp. 1314-1324.

Table 4. Summary of results for catalytic steam reforming experiments on the bench-scale reformer

Feed	Catalytst	S/C	$G_{C_1}HSV$	Temperatures (°C)			Yield (mol/100 mol of C fed)				C-to-gas	% st. yield	Run
				Top	Middle	Bottom	H_2	CO_2	CO	CH_4	conv.	H_2 (+WGS)	time, h
acetic acid	UCI G-90C	4.7	1973	685	716	833	145.8	50.3	49.7	0.055	101	73 (98)	6
	"	12.8	777	710	789	830	171.8	74.9	29.0	0.005	104	86 (100)	8
syringol (MeOH	"	6.3	2454	702	745	830	195.0	45.4	53.9	0.2	100	75 (96)	4
solution)	"	7.4	1985	750	803	863	197.3	46.0	54.9	0.1	101	76 (97)	4
3-comp.	"	6.5	1053	738	na	833	167.6	67.4	28.6	0.00	96	78 (91)	11
mixture	ICI 46-1/4	4.9	1053	782	753	834	187.8	79.8	27.4	0.03	105	86 (98)	17
poplar oil,	"	19.3	1110	480	730	818	206.7	85.2	9.6	1.7	97	103 (108)	2
aq. fraction	"	30.0	1000	530	744	821	205.8	86.6	8.4	6.9	102	103 (107)	4

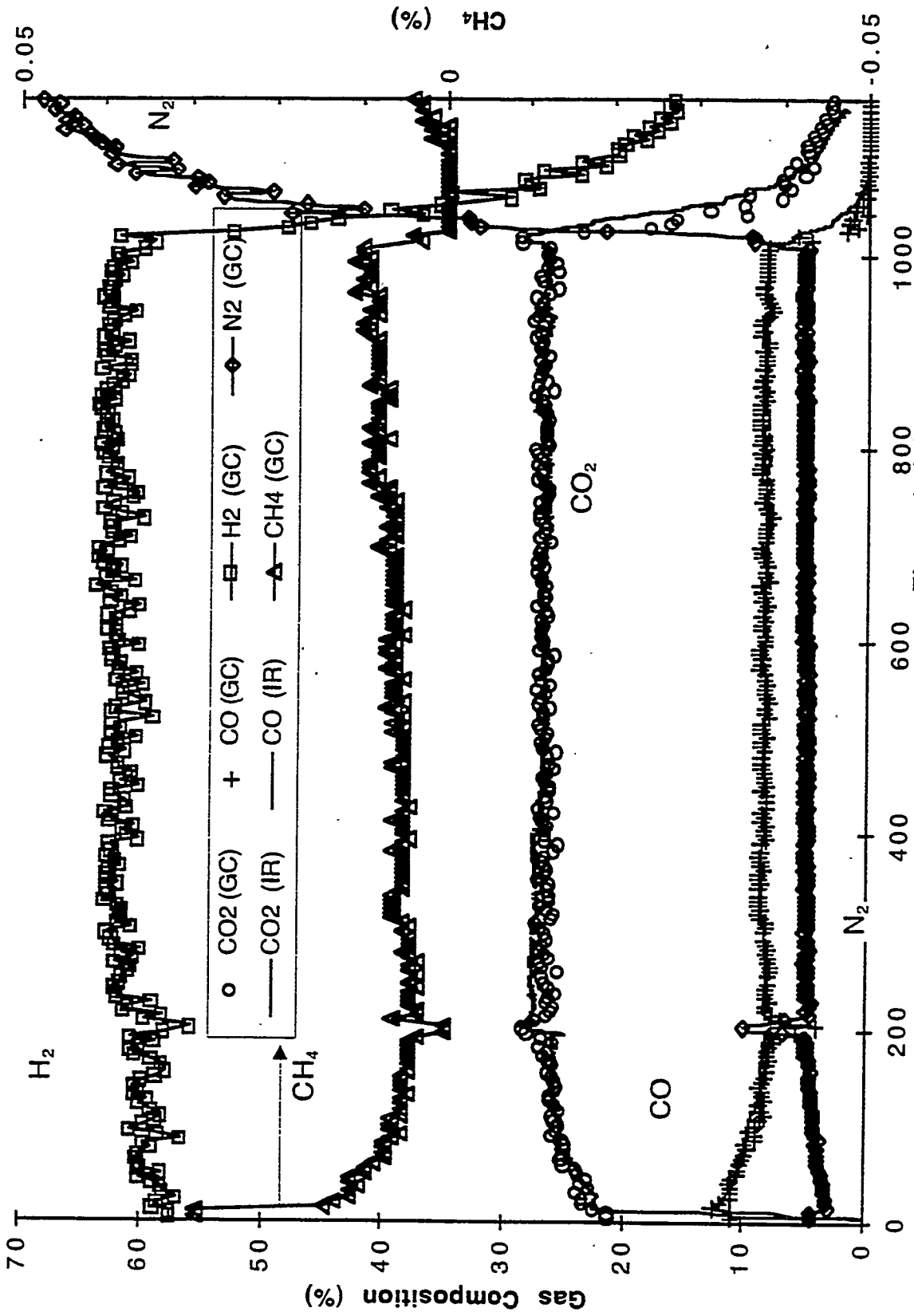


Figure 4. Composition of gaseous products during steam reforming of a 3-component mixture using the ICI 46-series catalyst.

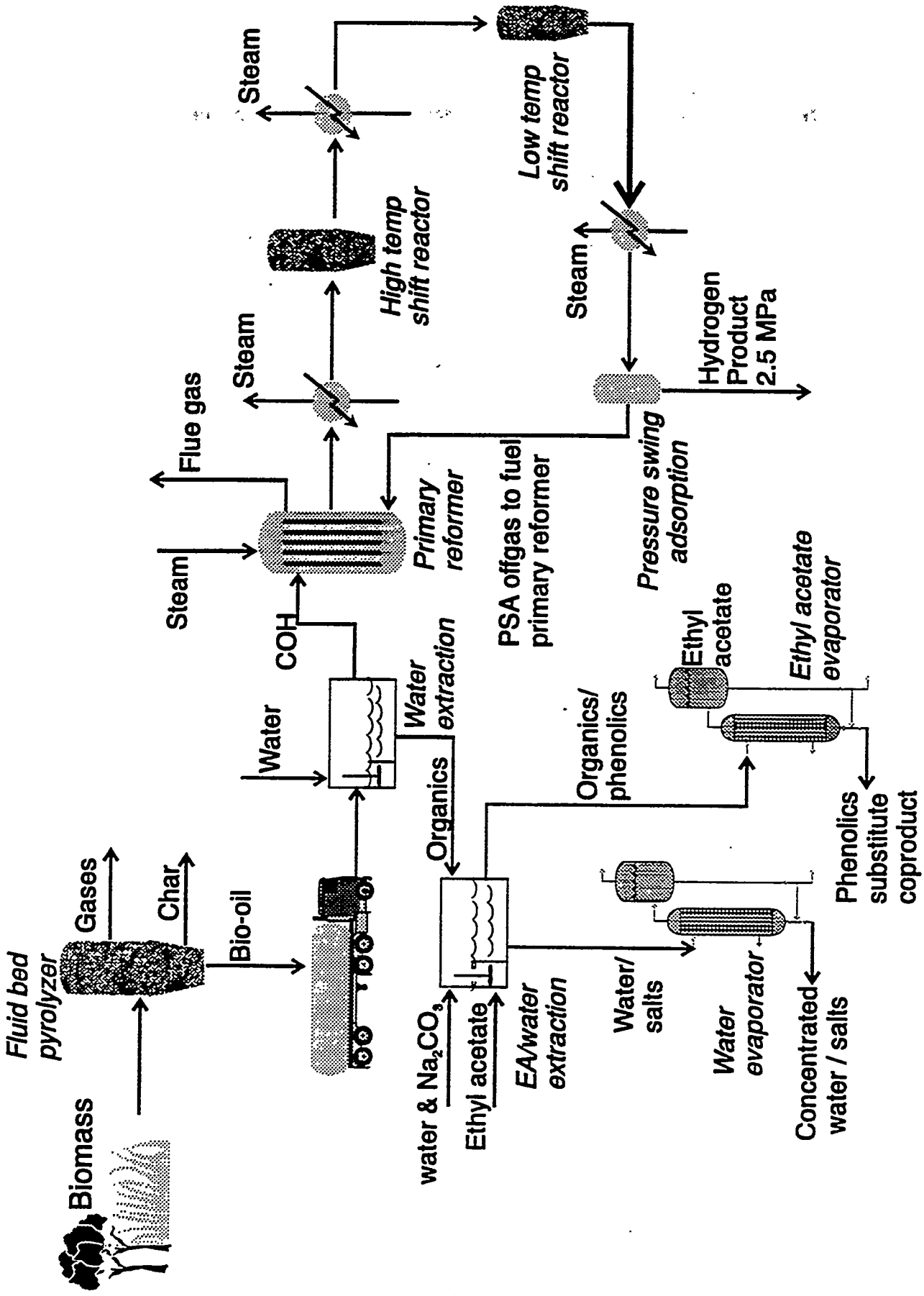


Figure 6. Process flow diagram for the fast pyrolysis and reforming of biomass.

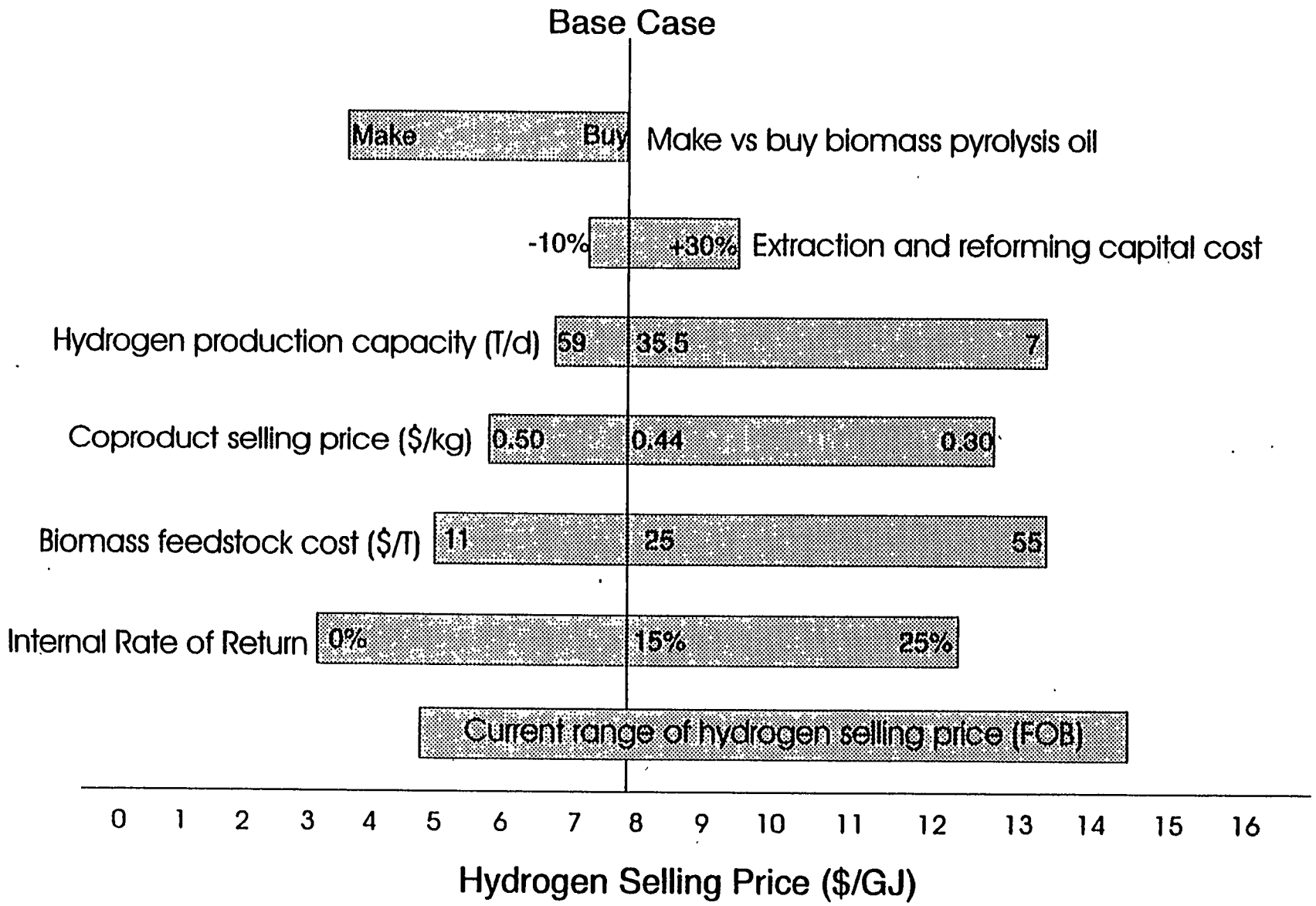


Figure 7. Incidence of the cost of pyrolysis oil (or its fractions) on the hydrogen production cost.

HYDROGEN PRODUCTION FROM MUNICIPAL SOLID WASTE

P. H. Wallman, J. H. Richardson, C. B. Thorsness
Lawrence Livermore National Laboratory
Livermore, CA 94551

T. F. Leininger, J. D. Klein, J. D. Winter, A. M. Robin
Montebello Technology Center
Texaco Inc.
329 N. Durfee Ave.
South El Monte, CA 91733

Abstract

We have modified a Municipal Solid Waste (MSW) hydrothermal pretreatment pilot plant for batch operation and blowdown of the treated batch to low pressure. We have also assembled a slurry shearing pilot plant for particle size reduction. Waste paper and a mixture of waste paper/polyethylene plastic have been run in the pilot plant with a treatment temperature of 275°C. The pilot-plant products have been used for laboratory studies at LLNL. The hydrothermal/shearing pilot plants have produced acceptable slurries for gasification tests from a waste paper feedstock. Work is currently underway with combined paper/plastic feedstocks. When the assembly of the Research Gasification Unit at Texaco (feed capacity approximately 3/4-ton/day) is complete (4th quarter of FY96), gasification test runs will commence.

Laboratory work on slurry samples during FY96 has provided correlations between slurry viscosity and hydrothermal treatment temperature, degree of shearing, and the presence of surfactants and admixed plastics. To date, pumpable slurries obtained from an MSW surrogate mixture of treated paper and plastic have shown heating values in the range 13-15 MJ/kg.

Our process modeling has quantified the relationship between slurry heating value and hydrogen yield. LLNL has also performed a preliminary cost analysis of the process with the slurry heating value and the MSW tipping fee as parameters. This analysis has shown that the overall process with a 15 MJ/kg slurry gasifier feed can compete with coal-derived hydrogen with the assumption that the tipping fee is of the order $50/ton.

Introduction

Our ultimate goal is to develop a commercial process for gasifying Municipal Solid Waste (MSW) to produce hydrogen for use as a premium fuel. This work is part of LLNL's systems approach to developing the critical technologies necessary to support the introduction of new transportation fuels, which would provide a sustainable, environmentally benign alternative to the use of imported petroleum.

Our approach is to couple innovative MSW preprocessing technology with Texaco's established gasification technology. A fundamental advantage of Texaco's high-temperature gasification is that it produces a glass-like slag byproduct which is expected to be non-hazardous even under conditions where the corresponding combustion-derived ash would be hazardous. Texaco's commercial gasification process includes gas product scrubbing that is applicable to the MSW feedstock case. However, an obstacle to feeding MSW to the Texaco gasifier is the lack of a preprocessing step for turning MSW into the high-energy content slurry that is required for efficient gasification.

This report describes work done jointly between Lawrence Livermore National Laboratory (LLNL) and Texaco. The focus is on the conversion of pre-classified MSW to a high-heating value slurry that can serve as feedstock to a conventional Texaco gasifier. To date the scope does not include initial MSW classification, but some initial results relating to this important part of the overall process have been documented elsewhere (Pasternak et. al., 1994).

Discussion

Pilot Scale Processing

Equipment

LLNL is renting a 6 ton/day Hydrothermal Treatment Unit (HTU) from Texaco. It has been described previously (Richardson et al, 1995). This facility was originally built to continuously process sewage sludges (Khan, 1993) and required modification for use in MSW testing. The main modification was the conversion to batch operation which was considered necessary for handling feedstocks containing plastics. As a consequence, changes to both the steam generator and the reactor pressure relief system were necessary. The batch hydrothermal treatment unit was shaken down in summer of 1995 with favorable results for waste paper feedstocks.

An early result from waste paper processing indicated that the hydrothermally treated material required further particle size reduction. For this purpose an off-line grinding pilot plant was built. This pilot plant consists of a pump-around loop including the option for convenient installation of different types of shearing devices. An initial grinding unit is mounted at the outlet of the feed tank which is used to prime the material for the diaphragm pump that feeds the main shearing device. This initial grinding unit is a commercial-grade garbage disposer (a common

household unit failed after 1 h of operation). To date, two main shearing devices have been tested: a commercial high precision flow-through grinder supplied by IKA-Works Inc., and a reverberatory device utilizing ultrasonic shear. Both devices produced significant size reduction of cellulose-derived solids at reasonable energy input; however, neither device tolerates large plastic particles because of narrow clearances.

Previous results from the hydrothermal processing of plastics proved that the plastic melts at treatment conditions, but then resolidifies on cooldown to its initial or to an agglomerated form. Hence, dispersion of hot molten plastic became desirable, and a hot blowdown system was installed on the HTU. This blowdown system consists of two 2-inch high-pressure slide valves with a pipe section in between, serving as a small lock hopper. The purpose of the blowdown is to utilize the energy of the high-pressure product to explosively shear the material resulting in particle and droplet comminution. The valves are provided with an automatic sequencing circuit, as well as safety interlocks.

Pilot-Plant Run Procedure

A typical HTU experimental run consisted of loading the 1.4-m^3 reactor vessel with 100-150 kg waste paper, heating the charge to reaction temperature by feeding in high pressure steam, soaking the charge at temperature for 1-2 h, letting down the pressure by venting steam and noncondensible gases, allowing cooldown of the charge, and finally removing the treated material from the reactor. The whole operation required several days mostly because of the slow cooldown. Based on early laboratory work, the treatment temperature was set at the plant maximum, or 275°C (Wallman, 1995). The corresponding reactor pressure was 6 MPa.

With the introduction of plastics feedstocks, the pressure let down procedure was changed to involve blowdown of the hot treated material from the bottom of the reactor into a receiving vessel. Initially, bridging at the reactor exit prevented a large fraction of the material from transferring to the receiving vessel. An impeller mixer installed in the reactor provided at least a partial remedy to the problem.

The HTU test runs provided material for the grinding pilot plant. Treated waste paper was successfully made into slurries in this unit. Series of shearing tests were conducted with energy input (time spent in the unit) as a parameter. Both the mechanical shearing unit and the ultrasonic unit seem to reach a final slurry consistency quickly, after which no change in slurry properties were seen. This "final" slurry had a particle size distribution extending from about 100μm down to 1μm with the mean particle size of 40μm (by weight).

Pilot-Plant Results

Two experimental runs with a paper/plastic mixture were carried out. The feed for the runs consisted of waste paper and 10 wt% plastic bags simulating the main plastic component of real MSW, Low Density Polyethylene (LDPE). Sampling of the blowdown product showed a significant size reduction of the plastic component. Particle size analysis on the plastic component (the two components can be separated by a sink-float technique) showed that approximately 1/3 of the plastic component in the blowdown product met the size specification

<1mm, and the oversize material was of the order 1mm-10mm. The plastic in the blowdown product was, therefore, very much reduced in size relative to the feed material that consisted of whole garbage bags.

Other results from the pilot plant units are covered under Laboratory Results.

Laboratory Scale Experiments

Experimental Approach

A Haake RV30 viscometer was used for this work. This viscometer uses a rotating spindle with a narrow gap between the spindle and the stationary wall which produces a Couette flow. The main reason for using this Haake RV30 viscometer was to obtain results that can be compared to earlier Texaco results using the same viscometer. Another type of viscometer, using flow through a sharp-edged orifice, was purchased and assembled for use with slurries of bimodal size distribution. Such slurries are encountered in the hydrothermal treatment of paper/plastic mixtures because the plastic component is of much larger particle size than the paper component. The purpose of the orifice viscometer addition is to allow future pump test results to be correlated to results from two different viscometers.

We have also performed some basic chemical kinetics studies on the carbonized cellulosic solids that are reported elsewhere (Reynolds, 1996).

Effect of Shearing on Slurry Properties

Figure 1 shows the shear stress/shear rate relationships (rheograms) for typical carbonized paper slurries with solids content as a parameter. Solids content is seen to have a very strong effect on the rheogram, thus, complicating the comparison of slurries in the parameter studies. The approach adopted in this work is to compare series of samples of varying solids contents rather than comparing just two slurries that may be of slightly different solids contents. Figure 1 also shows the Bingham plastic behavior of these slurries with significant yield stresses particularly for the low-solids cases. (The 31.5% and 33.8% slurries have a yield stress of about 30 Pa and a coefficient of rigidity of only 90 mPa·s.) An apparent viscosity can be obtained from the rheogram by drawing a straight line (Newtonian model) through the origin and the point on the rheogram at 100 1/s and determining the slope. The apparent viscosity as a one-parameter model can then conveniently be correlated to slurry properties such as solids content.

Figure 2 summarizes viscosity results obtained with slurries subjected to different levels of shear. All slurries are derived from the same HTU product, namely waste paper treated at 275°C for two hours. Several grinding techniques are included in Fig. 2, both laboratory scale and pilot scale. The viscosity results inside the band in Fig. 2 are referred to as "typical" slurries in this work. Three of the "typical" samples were analyzed for particle size and were found to be similar (40 μm mass median particle diameter). Addition of the ultrasonic device is seen to improve somewhat on the results obtained by disposer alone in pilot-scale grinding. The IKA grinding test included a correlation between grinding time (energy input) and viscosity. Only marginal improvement was found between the energy inputs 100kJ/(kg slurry) and 300kJ/(kg

slurry) implying that particle size reduction reaches maximum at a fairly modest energy input level in this grinding device. Fig. 2 also includes a laboratory slurry prepared by a Cusinart food processor showing the lowest viscosity of all the samples. This sample was run in the mixer for several hours, allowed to cool down and run for several more hours. Judging from the heat generated in the slurry the total energy input was high for this sample but quantification proved difficult. Whether this type of favorable result can be obtained by pilot- and full scale grinding equipment is a question for future work. (We have a contract with Professor Fuerstenau of the University of California at Berkeley to study both the fundamentals of the relationship between viscosity and particle size, and the issue of practical industrial-scale comminution units for these slurries.)

Results with Carbonized Paper Slurries with Additives

Figure 3 shows the rheograms of a carbonized paper slurry to which increasing amounts of surfactant have been added (percentage based on solids in the slurry). Some additional shearing in the laboratory sonicator was required to disperse the solid surfactant throughout the sample. The added surfactant has an effect on the rheogram similar to that of dilution of the sample by water (comparing Figs. 1 and 3). Hence, surfactant addition is an attractive way of maximizing solids content at the pumpability limit. This is quantified in Fig. 4 that shows the effect of solids content as well the effect of surfactant addition on apparent viscosity.

The results in Fig. 3 imply that one can raise the solids content at 1000 mPa·s viscosity (assumed pumpability limit) from 32% to 38% by adding 1 wt. % surfactant (percentage based on solids in the slurry) to the 275°C treatment product. Similarly, a 320°C treatment product shows that the solids content at the pumpability limit increases from 36 wt% to 42.5 wt% with the 1% surfactant addition. An additional 3-4 percentage points of gasifiable material is added to the solids content (numbers quoted in Fig. 3) when the soluble organic component is added for the heating value calculation (% organic material is the parameter that determines slurry heating value). With this credit the slurries with added surfactant would have a heating value of 11 MJ/kg slurry for the 275°C product and 12 MJ/kg slurry for the 320°C product.

Results with Carbonized Paper Slurries Containing a Plastic Component

Carbonized paper slurries with added polyethylene particles screened to a maximum size of 1 mm were studied in the laboratory with the objective of establishing the rheological properties of bimodal slurries. (The hydrothermal treatment of paper/plastic mixtures produced bimodal slurries in the HTU with the pressure blowdown option.)

Figure 5 shows the apparent viscosity of carbonized paper-polyethylene slurries. These results prove that slurry viscosity increases much less as a result of an increase in plastics content than as a result of an increase in carbonized solids content; the slope in Fig. 5 is about 0.04 while the corresponding slope in Fig. 2 is of the order 0.1. This implies that plastics, at least with the 100 μm -1 mm size distribution, is favorable to achieving a high solids content at the pumpability limit. The limiting solids concentration in Fig. 5 is about 45 wt% total solids (about half of the solids is polyethylene at this point). Such a slurry would have a heating value of 17 MJ/kg

slurry. Since MSW typically contains only 10 % plastics, this 17 MJ/kg slurry would require an additional waste plastic feedstock or other high-heating value cofeed.

Figure 6 shows the rheograms of carbonized paper/plastic slurries with added surfactant. Interestingly, these slurries appear to be almost Newtonian. This is probably more a result of the high level of surfactant addition (4 wt % based on solids) rather than a result of the polyethylene admix. These Newtonian-type slurries suffered from a much greater tendency to segregate than the more typical Bingham-type slurries encountered in this work. The Newtonian-type slurries segregated noticeably in a few hours; whereas, the Bingham-type slurries showed no noticeable change upon days of storage (over a week a heavier bottom layer developed even with the Bingham-type slurry).

Process Modeling

In order to help guide our process development work, a series of computer models has been developed (Thorsness, 1994, 1995a-d). The most recent work has involved an autoclave reactor model (Thorsness, 1995d) to interpret laboratory experimental results, a multidimensional steam heating model (Thorsness, 1995c) to describe batch hydrothermal treatment of MSW, and a preliminary economic evaluation of the proposed process options.

Autoclave Model

The autoclave simulation model was developed to allow the computation of autoclave pressures, as a function of time, based on vapor-liquid phase behavior in a confined volume along with temperature dependent decomposition kinetics. The model has been applied to data from our laboratory in which waste paper and water, in one case, and wood and water in a second case were heated to 350 °C. The model computations along with the experimental data are shown in Fig. 7. Also shown in the figure is the temperature/time profile and, for reference, the vapor pressure of water at the vessel temperature. In the calculations a simple first-order Arrhenius rate for the decomposition of the paper is assumed. The model uses a greatly simplified set of reaction products: a char solid, water, furfural, and carbon dioxide. The furfural is used as model compound to represent the gross behavior of the produced soluble organic components. The figure indicates the model does a fairly good job in matching the experimental data even though the resulting pressure curve deviates considerably from the simple water vapor-pressure curve.

The primary focus of the autoclave simulation effort was to determine kinetic parameters from the autoclave pressure history data. However, through the model we found that the shape of the curves were rather insensitive to details of the kinetics model, and consequently, discriminating between rate expression candidates was difficult.

Batch Hydrothermal Treatment Model

A general purpose packed bed model (Thorsness and Kang, 1986) initially developed for coal gasification systems has been modified to allow calculations relating to the hydrothermal treatment of MSW to be performed. The model (Thorsness, 1995c) addresses the batch treatment option by direct steam injection. The model can compute spatially resolved gas flows,

thermal evolution and decomposition reactions within a hydrothermal reactor. Through the use of artificial permeability changes the model is able to follow the evolving system through pressure changes of nearly two orders of magnitude. In some cases spatial variations in this artificial permeability were required to allow successful simulation of large scale systems with reasonable expenditures of computer time.

The model was applied to commercial and pilot scale systems. The pilot scale system, about 1 m^3 in volume representing the scale of our pilot experiments, was simulated for a time span of approximately 11 days. This computation required approximately 5.4 h of computer time on a P-9000/730 work station. The simulation indicated that velocities within the pilot reactor vessel would be low for the planned pilot operational scenario. Also, the pressure drops within the vessel would be small as long as the bed permeability remains at 23×10^{-12} m^2 (about 23 darcy) or higher. We saw no indication of large pressure differences within the pilot reactor during our experimental runs. In addition, simulation of the use of a small nitrogen bleed introduced to the vessel after the vessel pressure drops to 1 atmosphere during the blowdown operation indicated that the cooling time could be reduced from 10 days to about 4 days if the bleed was present. As a result a small bleed was used in the pilot runs and cooling times of 3-4 days were observed. The model also indicated a reasonably uniform heating of the reactor contents which was born out by our pilot scale experiments.

The commercial scale system simulated a hydrothermal reactor vessel size of 100 m^3. Simulations of systems representing a single bed system and multiple bed heat recovery system were performed. The multiple bed simulations required 2.3 hours of computer time to simulate the entire sequence of operations spanning about 170 minutes. The single bed system required 100 minutes of computer time to simulate the 140 minute operational time.

The commercial scale results indicate that in the absence of flow of liquid water the coupling between the reactor vessel contents and the thick metal walls of the vessel would be relatively small and, thus, would not degrade the system performance. On the other hand, the computed gas velocities are considerably larger than for the smaller pilot scale system and could potentially cause unwanted entrainment of liquid and solids, or could require processing times to be extended.

It appears that the model is capable of addressing some of the more detailed questions related to direct-steam heating of MSW. The model has difficulties in certain cases because of the large changes in system pressures present in typical hydrothermal reactor simulations. These problems are partially overcome in the model by the use of artificial permeability modifications. Based on current results, it appears that the model will prove to be a useful tool in our continued process development activities.

Economics

The project objectives are to demonstrate a technically feasible method of transforming MSW to hydrogen and to evaluate the economics of such a process. The economic evaluation of the process from a commercial perspective needs to await a better definition of operating parameters.

When these are available, Texaco will undertake a cost estimate. However, during the process development phase it is useful to perform order of magnitude economic estimates on an ongoing basis to help guide and focus our development work. As a result, LLNL has performed preliminary cost estimates for three process options currently under consideration for pretreatment of MSW prior to gasification. These include: 1) continuous hydrothermal processing; 2) batch hydrothermal processing by direct steam injection; and 3) a dry pyrolysis process option in which MSW is heated to 500 °C in order to decompose it into char, liquid and gaseous fractions.

Preliminary results indicate that all three pre-treatment options have similar costs. Estimated costs, depending of assumptions, currently range from $35-50 per ton of MSW processed. About half the cost is related to capital equipment. The process option with the highest estimated capital cost is dry pyrolysis, assumed to use indirectly heated rotary kilns, requiring an excess of 100M$ in equipment to process 30 kg/s of MSW. The final cost of the slurry is a function of the processing costs and the tipping fee obtained for disposal of the MSW.

To translate the cost of slurry into a final hydrogen cost, LLNL has developed a simple cost formula based primarily on the work of Larson and Katofsky (1992). They estimated hydrogen costs for production of hydrogen by gasification of biomass and presented results in simple formulas which include a linear dependence on feedstock costs. LLNL has extended the formula concept in several ways to fit our special needs. A factor explicitly accounting for the cost of oxygen in the gasification process is included in our analysis. The motivation for this is the fact that our objective is to estimate hydrogen costs for gasification of slurry feedstock that may be below the optimal slurry heating value for the gasification process. The main cost factor in considering non-optimal conditions is the increased oxygen consumption. Additionally, non-optimal conditions also lead to a greater gas throughput per unit of hydrogen production. This influence is harder to quantify. However, LLNL has chosen to approximate throughput effects by scaling the fixed part of the cost with a measure of gasification efficiency. Next, the amount of hydrogen produced per unit of feed to the gasifier is made a function of the quality of the feed, as measured by its heating value. Finally, the cost of the feedstock is broken down into two components, the cost of MSW derived slurry and the cost of a cofeed. This last modification is done in order to model the sensitivity of the economics to the addition of a cofeed.

The resulting formula for hydrogen cost is

$$P = 7.63\left(\frac{2.31}{\gamma}\right)^{0.6} + \frac{4}{\gamma} + \alpha[\eta S + (1-\eta)F]$$

Where P is the hydrogen cost ($/GJ-H2), S is the cost of the MSW slurry after pre-treatment ($/ton), F is the cost of cofeed ($/ton), and η is the fraction MSW slurry in the combined feed. The two other parameters are a function of the efficiency of the gasification process which in turn, to a first approximation, is a function of the overall effective heating value of the gasifier feed. α is the feed consumption parameter (ton/GJ-H2) and γ is the oxygen utilization efficiency (mol-H2/mol-O2).

Typical values of the efficiency parameters, as a function of overall gasifier feed heating value, were obtained from LLNL's gasification model (Rogers, 1994) and are shown in Figs. 8 and 9. Combining these curves with estimates of slurry and cofeed costs yielded the curves shown in Fig. 10. For slurries obtainable from MSW alone, estimated to have a maximum heating value of about 15 MJ/kg, the results indicate that hydrogen production costs can be competitive with those for coal derived hydrogen. For slurries with higher heating values, obtained by adding a cofeed, lower costs are possible. However, they remain significantly above the cost of hydrogen produced from natural gas, which is estimated to be approximately $6/GJ. As process development efforts continue, we hope to simplify the required pretreatment and, thereby, drive down the capital costs, which would translate to an improved competitive position for MSW-derived hydrogen.

Conclusions

In the half dozen Hydrothermal Treatment Unit (HTU) runs completed, we have shown that cellulosic feedstocks (wood and waste paper) can be adequately carbonized at 275°C with a reasonable treatment time. Based on laboratory work, a treatment temperature of 320°C improves the degree of carbonization, which is manifested by a higher solids content slurry at the pumpability limit. However 320°C implies a saturation steam pressure of 11MPa, a level that cannot be accommodated in the present HTU (6 MPa is the limiting steam pressure currently corresponding to a temperature of 275°C). Optimal pressure level is ultimately an economic decision to be addressed in the detailed economic study.

Results of HTU runs with 90% waste paper/10% polyethylene bags showed considerable size reduction of the plastic component in the blowdown scheme tested. However, only about 1/3 of the treated plastic product was below 1 mm in particle size (which is the specification for our slurry feedstock). We are currently investigating means to further develop the shearing of the plastic component by either improving the blowdown scheme, recycling oversize plastics to the reactor, or providing for a separate size reduction step for separated oversize plastics.

Laboratory work on HTU products and products from autoclave experiments has correlated slurry viscosity with HTU treatment severity, solids content, cellulose/plastic ratio, and level of surfactant addition. Using slurry heating value at the pumpability limit as a metric, the laboratory work has guided us to higher heating value slurries through a series of process measures. Grinding the HTU product down to a mean particle size of about 40 μm was shown to be favorable. Whether further size reduction continues the improvement trend will be determined in the near future. It is known from coal work that slurry viscosity starts to increase with reduced particle size when the mean particle size reaches a certain level. (However, this may be more a consequence of the particle size distribution becoming "too narrow" which will also be addressed in future studies.)

In laboratory work, we have shown that an inexpensive surfactant (a waste product of pulp processing) greatly reduces viscosity; addition of only 1 wt% surfactant based on carbonized solids in the slurry raises the heating value at the pumpability limit by about 20%. Typical

heating values for slurries with added surfactant are 11 MJ/kg slurry for the 275°C treatment product and 12 MJ/kg slurry for the 320°C product. Laboratory work has also shown that these carbonized paper slurries are excellent vehicles for carrying a plastic component in concentrations up to about 20 wt% of carbonized solids. Such slurries have heating values in the range 13-15 MJ/kg slurry (again depending on the treatment temperature for the cellulosic component). A high plastics-loading slurry has also been prepared having a 1:1 ratio between polyethylene plastics and carbonized cellulose. This slurry has a predicted heating value of 17 MJ/kg. In this case no surfactant was used to make the slurry more stable.

Our process modeling predicts hydrogen from MSW to be competitive with coal-based hydrogen at a tipping fee of $50/ton, resulting in a predicted cost of hydrogen in the range $10-12/GJ. This assumes a slurry heating value of 15 MJ/kg which is quite realistic. Although the model predicts the hydrogen cost to decrease with improvements in slurry heating value, the asymptote is still significantly above the predicted cost of hydrogen from natural gas estimated at $6/GJ. Significant cost improvements for hydrogen via our pre-classification/hydrothermal treatment/high-temperature gasification process would result from process simplification that translates into reduced capital cost.

Future Work

Our immediate plan is to prepare a 1-ton quantity of slurry product from waste paper and plastic for a gasification test at Texaco. The purpose of this test is not only to shake down the Texaco Research Gasifier Unit with a real slurry but also to confirm our process prediction with a slurry of 15 MJ/kg heating value.

We are pursuing several approaches to improving slurry properties. One activity is a more fundamental study of slurry rheological properties as a function of particle size distributions (bi-modal because the plastics-derived particles are much larger than the cellulose-derived particles) and surfactant additives. To carry out this task we have installed an orifice viscometer in our laboratory. We have also made a contract with Professor Fuestenau of the University of California to study our slurries from a more fundamental viewpoint. He will also address the question of scale up of the grinding process which is a challenging task because of the presence of plastics.

Another approach to higher-heating value slurries that we will investigate is the pretreatment of the MSW in a pyrolysis unit rather than in a hydrothermal unit. The pyrolysis approach has the potential of producing an improved gasifier feedstock but at the expense of requiring a fair amount of heat for the pyrolyzer. The pyrolysis option for pretreatment will be studied by modeling and then followed by a pilot-plant run using either the Laboratory's existing pyrolysis facility (which requires some modification because of the new feedstock) or a contractor's facility.

In FY97, we will make several slurry batches from increasingly more realistic feedstocks. One such feedstock will be a mixture of waste paper/waste plastic together with a representative

admixed ash component so that the slagging feature of the gasifier can be studied. Texaco will gasify these slurries for the purpose of determining mass and energy balances that will form the basis for the more detailed economic study. This study will be initiated in late FY97.

Acknowledgements

This work was performed under the auspices of the U. S. Department of Energy by Lawrence Livermore National Laboratory under contract No. W-7405-Eng-48.

References

Larson, E. D. and R. E. Katofsky, 1992. *Production of Methanol and Hydrogen from Biomass,* The Center for Energy and Environmental Studies, Princeton University, Report. No. 271.

Khan, M. R. 1993. *Clean Energy from Waste and Coal. ACS Symposium Series 515.* Washington, D.C. American Chemical Society.

Pasternak, A. D., J. H. Richardson, R. S. Rogers, C. B. Thorsness, G. N. Richter, J. K. Wolfenbarger, 1994. *MSW to Hydrogen* , Proceedings of the 1994 U.S. DOE Hydrogen Program Review NREL/CP-470--6431, 433, National Renewable Energy Laboratory.

Reynolds, G. D., A. K. Burnham, P. H. Wallman, 1996. *Kinetic Analysis and Characterization of Paper and Paper Residues Produced by a Hydrothermal Pretreatment Process for Municipal Solid Wastes.* Submitted to Energy and Fuels.

Richardson, J. H., R. Rodgers, C. B. Thorsness, P. H. Wallman, T. F. Leininger, G. N. Richter, A. M. Robin, J. H. Wiese, J. K. Wolfenbarger , 1995. *Conversion of Municipal Solid Waste to Hydrogen,* Proceedings of the 1995 U.S. DOE Hydrogen Program Review NREL/CP-430--20036, 731, National Renewable Energy Laboratory.

Rogers, R. III, 1994. *Hydrogen Production by Gasification of Municipal Solid Waste,* Lawrence Livermore National Laboratory, Livermore, CA, UCID-ID-117603.

Thorsness,C. B. and S. W Kang, 1986. *A General-Purpose, Packed-Bed Model for Analysis of Underground Coal Gasification Processes,* Lawrence Livermore National Laboratory, Livermore, CA, UCID-20731.

Thorsness, C. B. 1994. *Process Modeling of Hydrogen Production from Municipal Solid Waste* UCRL-ID-119231. Lawrence Livermore National Laboratory, Livermore, CA.

Thorsness, C. B. 1995a. *A Direct Steam Heat Option For Hydrothermal Treatment of Municipal Solid Waste,* UCRL-ID-120283. Lawrence Livermore National Laboratory, Livermore, CA.

Thorsness, C. B. 1995b. *Process Modeling of Hydrothermal Treatment of Municipal Solid Waste to Form High Solids Slurries in a Pilot Scale System,* UCRL-ID-119685. Lawrence Livermore National Laboratory, Livermore, CA.

Thorsness, C. B., 1995c. *A Multidimensional Model of Direct-Steam Heating of Newspaper and Municipal Solid Waste in a Hydrothermal Reactor,* Lawrence Livermore National Laboratory, Livermore, CA, UCID-ID-121991.

Thorsness, C. B., 1995d. *A Model for Simulating Autoclave-Reactor Pressure Histories,* Lawrence Livermore National Laboratory, Livermore, CA, UCID-ID-122947.

Wallman, P. H. 1995. *Laboratory Studies of a Hydrothermal Pretreatment Process for Municipal Solid Waste*, UCRL-ID-120296. Lawrence Livermore National Laboratory, Livermore, CA.

Figure Captions

Fig. 1 Rheogram of carbonized paper slurries.

Fig. 2 Effect of shearing method on slurry viscosity.

Fig. 3 Rheogram of carbonized paper slurries with added surfactant. Surfactant percentage based on solids content.

Fig. 4 Effect of surfactant addition on slurry viscosity.

Fig. 5 Effect of added plastic on carbonized paper slurry viscosity.

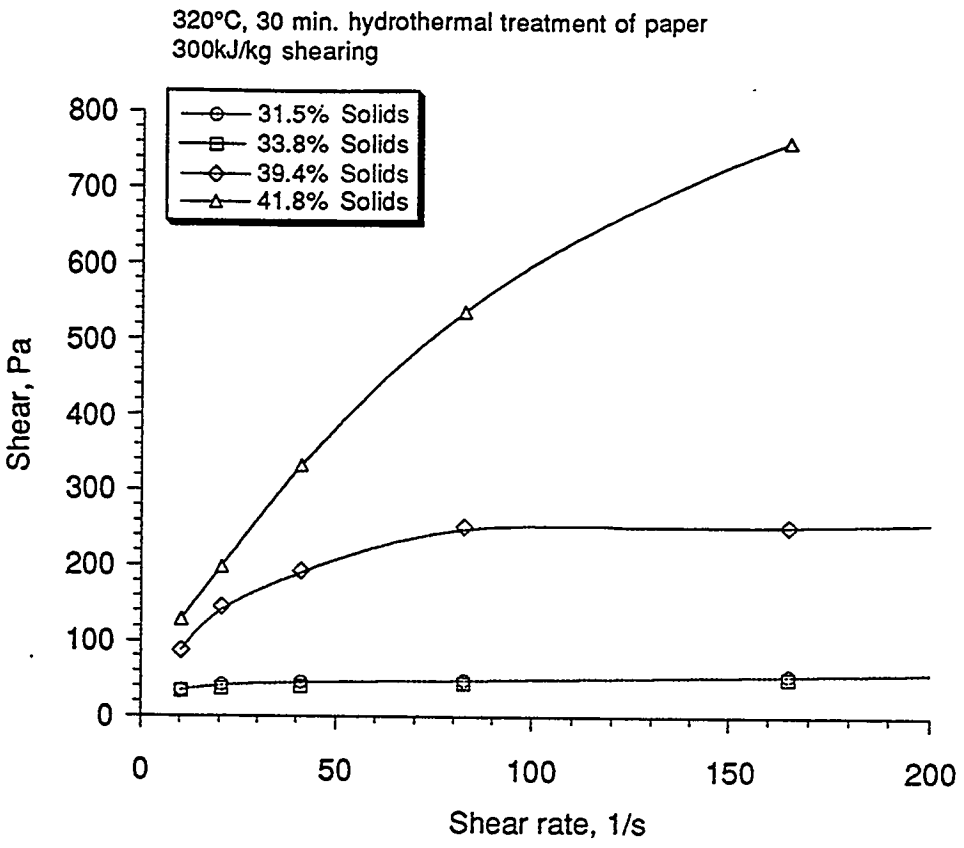
Fig. 6 Rheogram of additized carbonized paper slurries containing plastic (bi-modal size distribution).

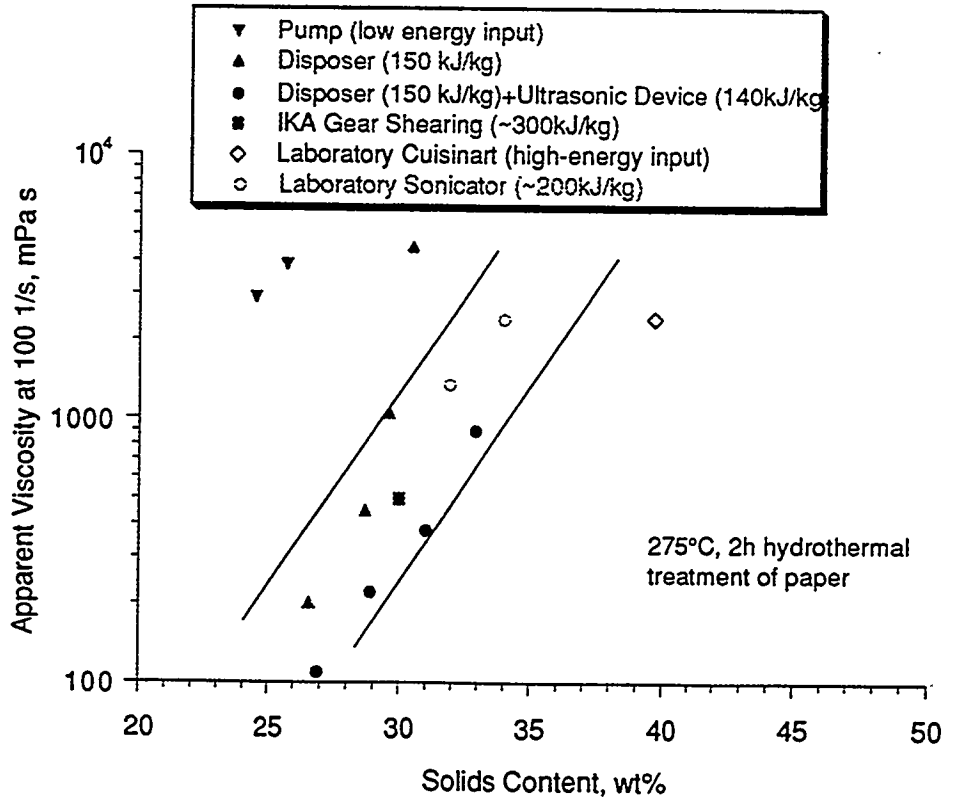
Fig. 7 Computed results from the autoclave model compared to experimental autoclave pressure data for (a) water/waste paper, and (b) water/wood .

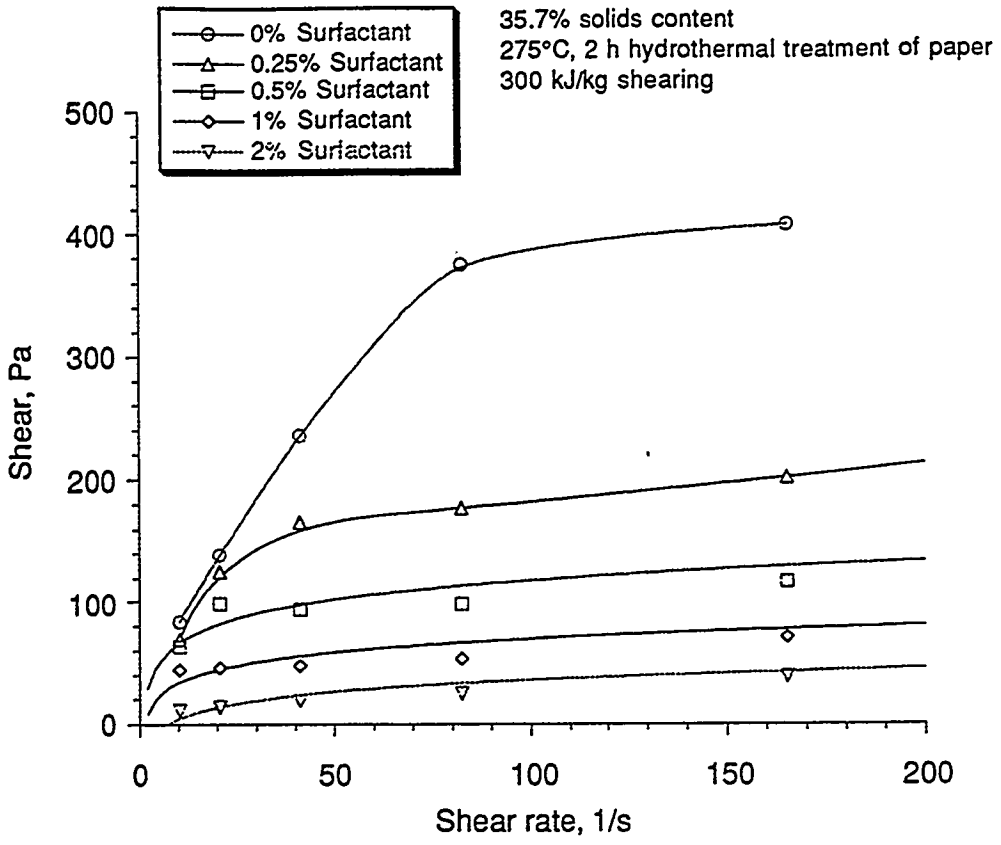
Fig. 8 Typical gasifier slurry consumption and overall efficiency as a function of slurry heating value.

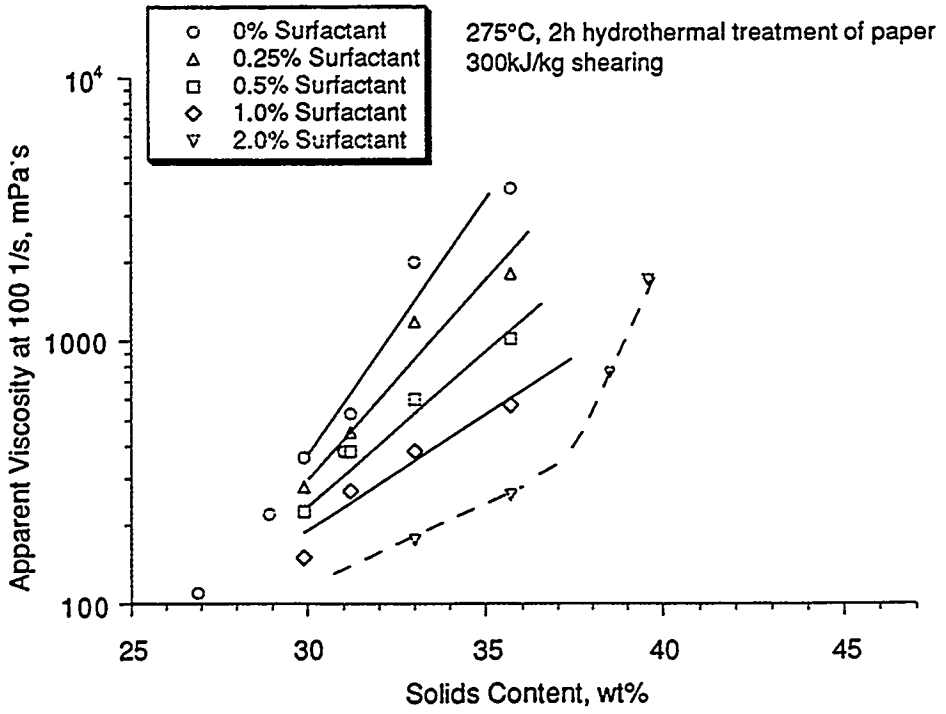
Fig. 9 Typical gasifier oxygen utilization as a function of slurry heating value.

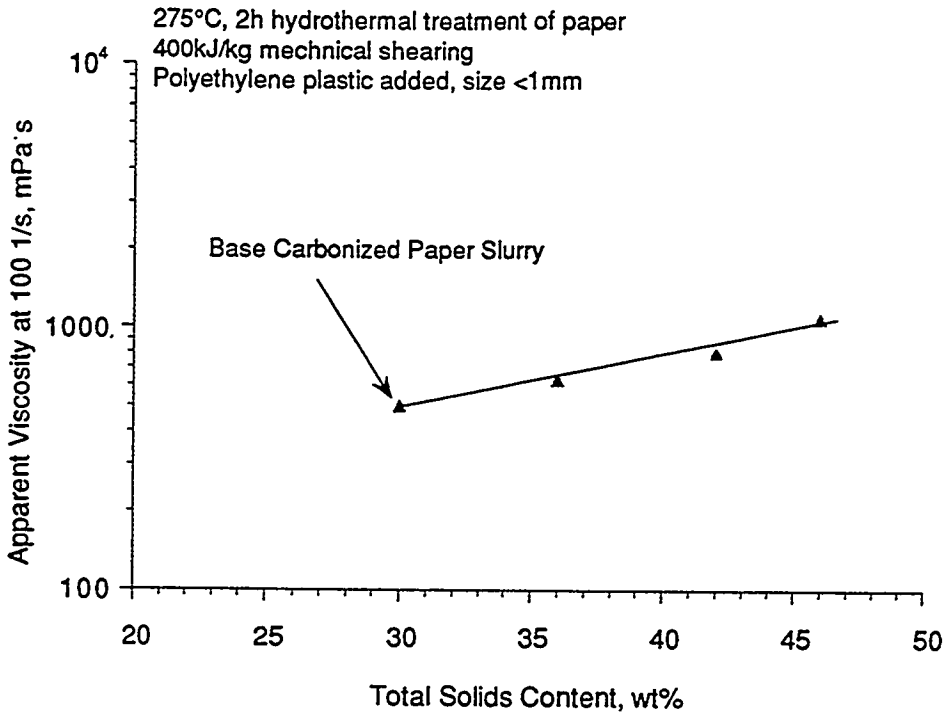
Fig. 10 Hydrogen cost estimate as a function of heating value of gasifier feed. A tipping fee of $50/ton for the MSW assumed. Upper and lower bounds for the estimate shown.

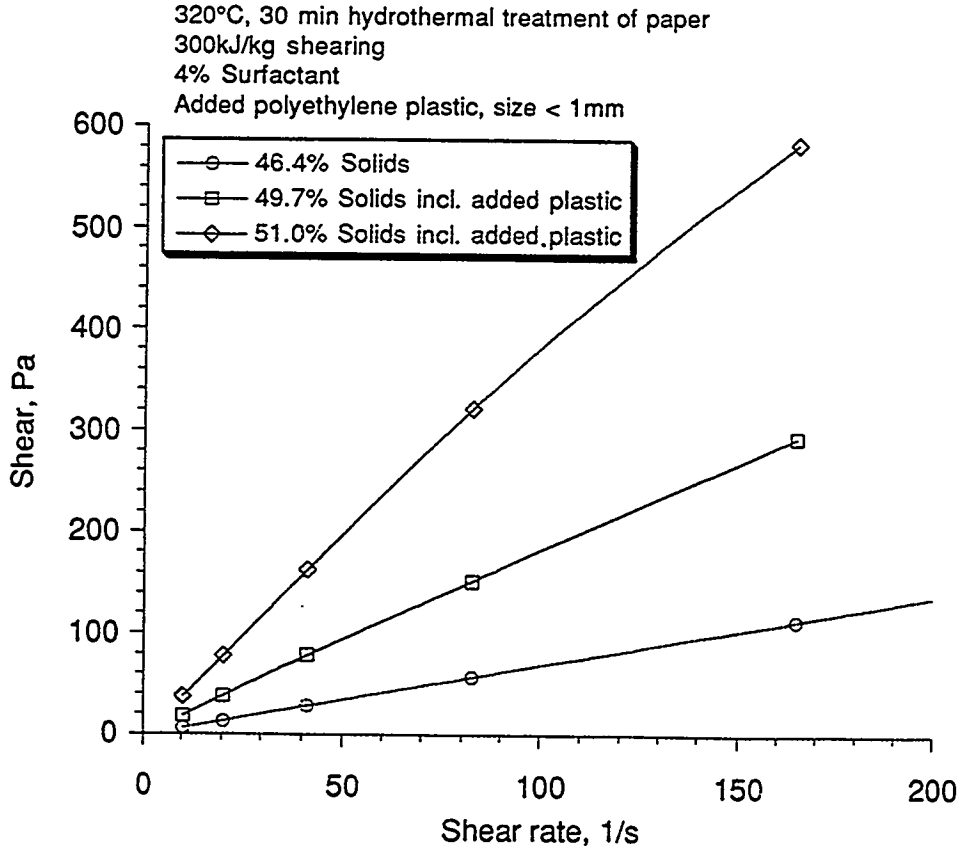

320°C, 30 min. hydrothermal treatment of paper
300kJ/kg shearing
31.5% Solids
33.8% Solids
39.4% Solids
41.8% Solids
Shear, Pa
Shear rate, 1/s
0
100
200
300
400
500
600
700
800
0
50
100
150
200

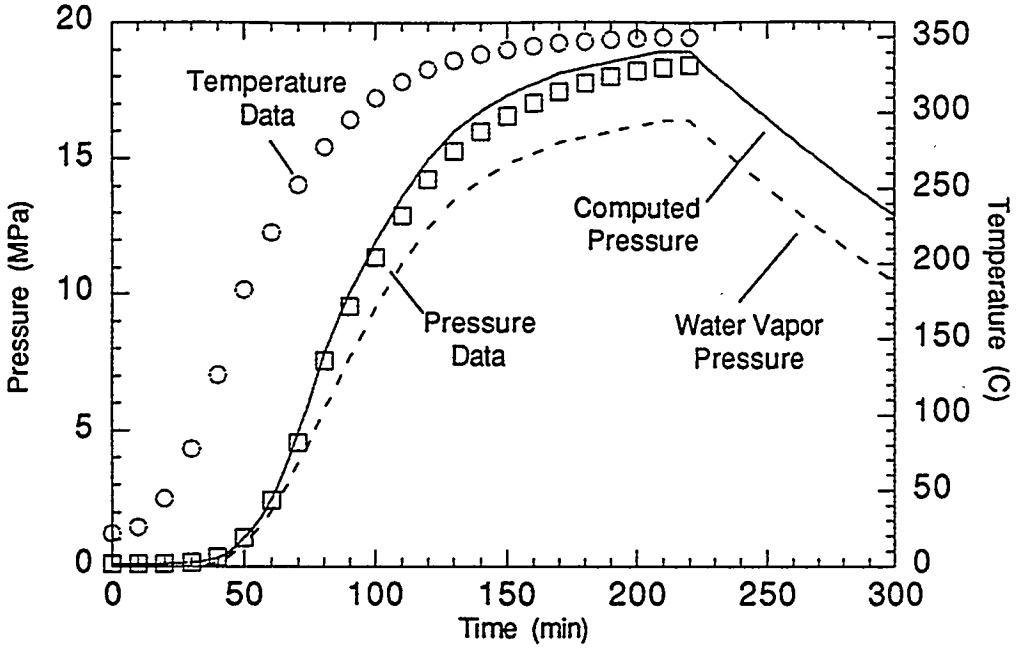

Pump (low energy input)
Disposer (150 kJ/kg)
Disposer (150 kJ/kg)+Ultrasonic Device (140kJ/kg
IKA Gear Shearing (~300kJ/kg)
Laboratory Cuisinart (high-energy input)
Laboratory Sonicator (~200kJ/kg)
Apparent Viscosity at 100 1/s, mPa s
Solids Content, wt%
10⁴
1000
100
20
25
30
35
40
45
50
275°C, 2h hydrothermal
treatment of paper


0% Surfactant
0.25% Surfactant
0.5% Surfactant
1% Surfactant
2% Surfactant
35.7% solids content
275°C, 2 h hydrothermal treatment of paper
300 kJ/kg shearing
Shear, Pa
Shear rate, 1/s
0
100
200
300
400
500
0
50
100
150
200

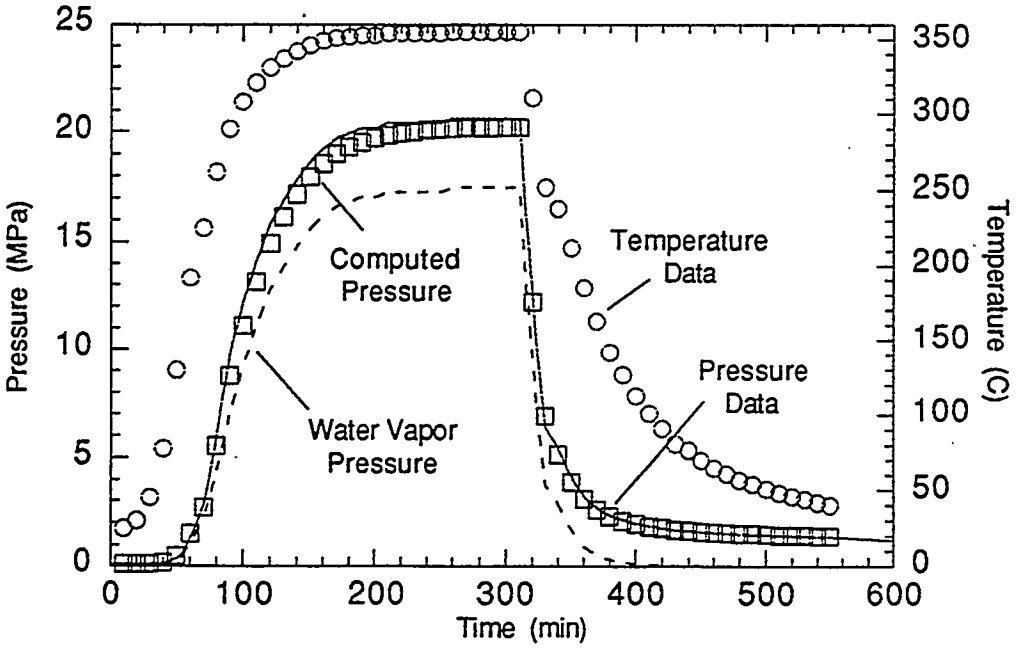

0% Surfactant
0.25% Surfactant
0.5% Surfactant
1.0% Surfactant
2.0% Surfactant
275°C, 2h hydrothermal treatment of paper
300kJ/kg shearing
Apparent Viscosity at 100 1/s, mPa·s
Solids Content, wt%
10⁴
1000
100
25
30
35
40
45


275°C, 2h hydrothermal treatment of paper
400kJ/kg mechnical shearing
Polyethylene plastic added, size <1mm
Base Carbonized Paper Slurry
Apparent Viscosity at 100 1/s, mPa·s
10⁴
1000.
100
20
25
30
35
40
45
50
Total Solids Content, wt%

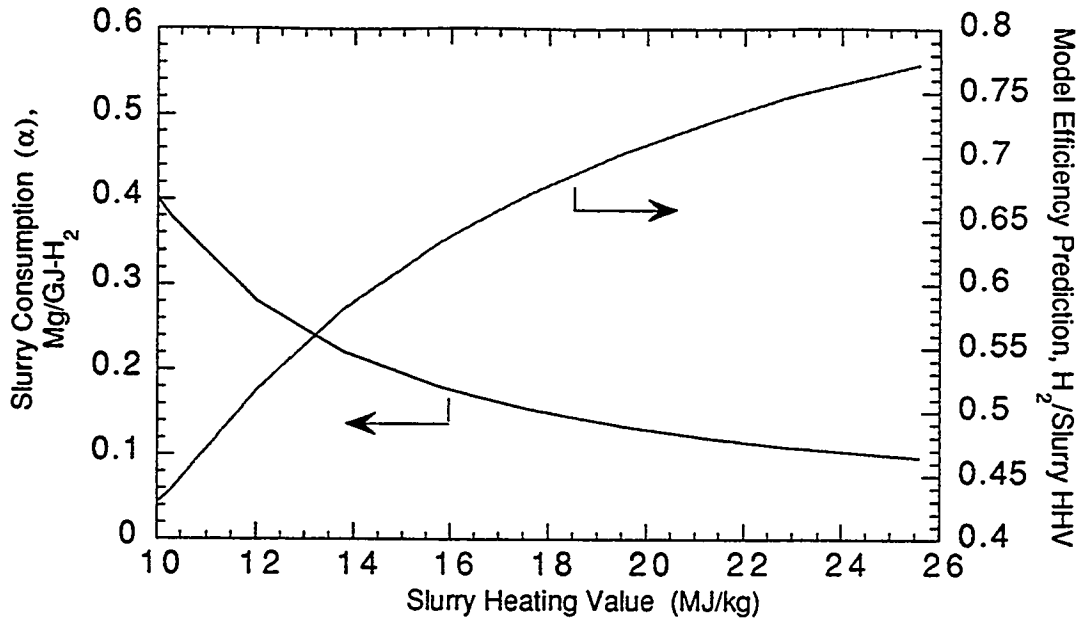

320°C, 30 min hydrothermal treatment of paper
300kJ/kg shearing
4% Surfactant
Added polyethylene plastic, size < 1mm
46.4% Solids
49.7% Solids incl. added plastic
51.0% Solids incl. added plastic
Shear, Pa
600
500
400
300
200
100
0
0
50
100
150
200
Shear rate, 1/s

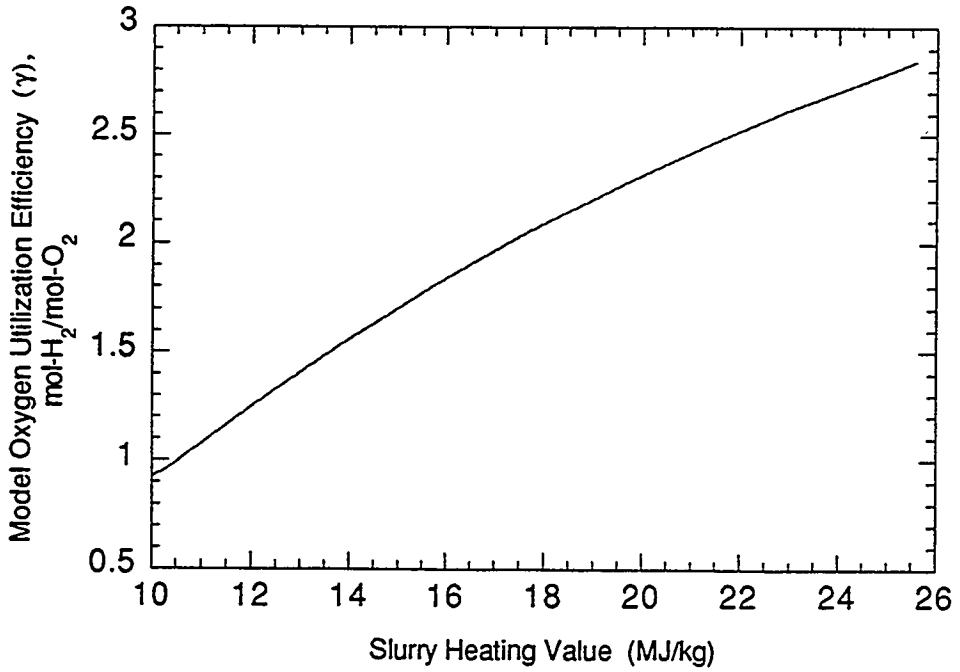

Temperature Data
Computed Pressure
Pressure Data
Water Vapor Pressure
Pressure (MPa)
Temperature (C)
Time (min)
0
5
10
15
20
0
50
100
150
200
250
300
350

(a)


Computed Pressure
Temperature Data
Pressure Data
Water Vapor Pressure
Pressure (MPa)
Temperature (C)
Time (min)
0
5
10
15
20
25
0
100
200
300
400
500
600
350

(b)


Slurry Consumption (α), Mg/GJ-H2
Model Efficiency Prediction, H2/Slurry HHV
Slurry Heating Value (MJ/kg)
0.6
0.5
0.4
0.3
0.2
0.1
0
0.8
0.75
0.7
0.65
0.6
0.55
0.5
0.45
0.4
10
12
14
16
18
20
22
24
26


Model Oxygen Utilization Efficiency (γ), mol-H2/mol-O2
Slurry Heating Value (MJ/kg)
3
2.5
2
1.5
1
0.5
10
12
14
16
18
20
22
24
26

HYDROGEN PRODUCTION FROM HIGH-MOISTURE CONTENT BIOMASS IN SUPERCRITICAL WATER

Michael J. Antal, Jr.(PI), Tadafumi Adschiri, Tomas Ekbom, Angela Garcia, Yukihiko Matsumura, Tomoaki Minowa, Frederick Nuessle, Makoto Sakurai, and Xiaodong Xu
Hawaii Natural Energy Institute, University of Hawaii at Manoa
Honolulu, HI 96822

Abstract

Most hydrogen is produced by steam reforming methane at elevated pressures. The goal of this research is to develop commercial processes for the catalytic steam reforming of biomass and other organic wastes at high pressures. This approach avoids the high cost of gas compression and takes advantage of the unique properties of water at high pressures. Prior to this year we reported the ability of carbon to catalyze the decomposition of biomass and related model compounds in supercritical water. The product gas consists of hydrogen, carbon dioxide, carbon monoxide, methane, and traces of higher hydrocarbons. During the past year we have: a) developed a method to extend the catalyst life, b) begun studies of the role of the shift reaction, c) completed studies of carbon dioxide absorption from the product effluent by high pressure water, d) measured the rate of carbon catalyst gasification in supercritical water, e) discovered the pumpability of oil-biomass slurries, and f) completed the design and begun fabrication of a flow reactor that will steam reform whole biomass feedstocks (i.e. sewage sludge) and produce a hydrogen rich synthesis gas at very high pressure (>22 MPa).

Rationale

Enough renewable biomass is available in the USA to produce more than 20% of its energy demand in the form of hydrogen. Currently, hydrogen is produced commercially by the steam reforming of methane (natural gas). Consequently, it is logical to examine the possibilities for using biomass as a feedstock for the steam reforming reaction. This approach has the attractive feature that water is required as a reactant in the steam reforming chemistry, and biomass is usually moist; hence the feedstock requires less pretreatment (drying) before conversion. When the reaction chemistry is conducted at high (supercritical) pressure, the gaseous products can be stored and transported without the need for expensive compressors. Note that the energy costs of compressing liquid water are negligible.

Past Results

Using glucose in water as a model compound for biomass, we (Yu et al., 1993) showed that temperatures above 600 °C and pressures above 22 MPa (the critical pressure) are sufficient to effect complete gasification of low concentrations of the feedstock in the absence of catalysts. But an economic analysis by Air Products Corporation revealed that the steam reforming process could be cost effective only if relatively high concentrations (ca. 20 wt % biomass) were gasified. Unfortunately, in the absence of catalysts, concentrated glucose in water solutions evidenced incomplete gasification (<80%, see Table 1) in supercritical water (Yu et al., 1993). Consequently, we initiated a search for effective steam reforming catalysts that survive in supercritical water. After a short time we learned that all kinds of carbons catalyze the gasification reactions of organic species in supercritical water (see Table 2). High concentrations (>20 wt %) of glucose in water were completely converted to a gas containing hydrogen, carbon dioxide, carbon monoxide, and some methane. Other feedstocks, including sewage sludge (see Table 3), were also completely gasified (Antal, 1995; Xu et al., 1996). We also found the carbon catalyst to be effective in the destruction of various Department of Defense wastes (see Table 4).

Current Year Results

During the past year we have: a) developed a method to extend the catalyst life, b) begun studies of the role of the shift reaction, c) completed studies of carbon dioxide absorption from the product effluent by high pressure water, d) measured the rate of carbon catalyst gasification in supercritical water, e) discovered the pumpability of oil-biomass slurries, and f) completed the design and begun fabrication of a flow reactor that will steam reform whole biomass feedstocks (i.e. sewage sludge) and produce a hydrogen rich synthesis gas at very high pressure (>22 MPa).

Catalyst Life

During the last Hydrogen Program Review Meeting an industrial representative commented that the carbon catalyst evidenced considerable deactivation after only a few hours of use (see Figure 1). We studied this problem and learned that deactivation was due to tar formation in the entry region of the reactor. By introducing swirl in the entry region heat transfer was improved, the heating rate of the feedstock was increased, and tar formation was considerably reduced. After

this modification to the equipment, the carbon catalyst showed almost no sign of deactivation after six hours of use (see Figure 2).

Shift reaction

The shift reaction is catalyzed by an (as yet) unknown agent in the reactor. Employing identical conditions, the yield of hydrogen is sometimes very high (and the yield of carbon monoxide very low); while at other times the yield of carbon monoxide is high and the hydrogen yield is low. Thermochemical calculations indicate that the yield of carbon monoxide should be very low when equilibrium is reached. This stratagem should enable us to produce a hydrogen rich gas containing only hydrogen, carbon dioxide, and some methane (the equilibrium mixture).

Carbon dioxide absorption

Experiments conducted in Honolulu indicate that considerable amounts of carbon dioxide can be absorbed by water at high pressure. Interaction parameters for the carbon dioxide, water, and hydrogen system have been calculated and a thermodynamic model for the two phase system has been developed (Matsumura et al., 1996a). By spraying about 19 volumes of (cold) water per volume of reactant into the (cold) gaseous product mixture, most of the carbon dioxide can be removed from the high pressure, gaseous product stream, thus producing purer hydrogen.

Rate of carbon gasification

The water gas reaction: $C + H_2O \rightarrow CO + H_2$ could cause a serious loss of catalyst, as well as acting as a spurious (and potentially misleading) source of hydrogen. We measured the rate of this reaction at conditions of interest (Matsumura et al., 1996b) and found it to be small (usually negligible).

Oil-biomass slurries

A thorough search revealed no commercial sources of pumps that could be used to deliver water-biomass slurries into our reactors at 34.5 Mpa. Also, we ourselves were unable to make pumpable water-biomass slurries that contained more than about 1 wt % biomass in water. However, we discovered that vegetable oils readily mix with biomass to make easily pumpable slurries. For example, slurries with as much as 39% by weight sawdust (0.14 mm avg. particle size) in palm oil flow through a syringe. We envision using slurries of dewatered sewage sludge and waste cooking oil (or engine oil) as feedstocks.

Reactor design and fabrication

Considerable effort has been made to design a reactor that will steam reform whole biomass feeds using only inexpensive, off-the-shelf parts. This design is now complete (see Figure 3), the components have been acquired and are now being assembled in the laboratory.

Future Work

We expect to complete the fabrication and shakedown of the new reactor system by July. Thereafter we will begin steam reforming studies of whole biomass feedstocks, emphasizing wood sawdust and sewage sludge in waste vegetable oil slurries. Attention will be given to water requirements, catalyst deactivation, and the development of promoters for the water gas shift reaction. We also plan to assist NREL with an economic assessment of the process.

Systems Analysis

We completed an energy balance of an idealized system (see Figure 4), including carbon dioxide removal by high pressure water (Matsumura et al., 1996a). A thermal energy efficiency of 70% was estimated (see Figure 5).

Goals

We hope to report the results of extended tests of wood sawdust or sewage sludge in waste oil gasification over carbon catalysts at the next Hydrogen Program Review Meeting.

Major Barriers

We must identify conditions and catalysts which reproducibly realize complete gasification of the feedstock and a high degree of shift. The catalysts must enjoy a long life.

Acknowledgments

We thank the Coral Industries Chair of the University of Hawaii, and the National Institute for Resources and Energy of MITI, Japan for partial support of this work.

References

Antal, M.J. 1995. "Catalytic Supercritical Gasification of Wet Biomass." *U.S. patent application no. 08/414,523.*

Matsumura, M., T. Minowa, X. Xu, F.W. Nuessle, T. Adschiri, M.J. Antal. 1996a. "High-Pressure Carbon Dioxide Removal in Supercritical Water Gasification of Biomass." To appear in *Advances in Thermochemical Biomass Conversion.*

Matsumura, M., X. Xu, M.J. Antal. 1996b. "Gasification Characteristics of an Activated Carbon in Supercritical Water." Submitted to *Carbon.*

Xu, X., Y. Matsumura, J. Stenberg, M.J. Antal. 1996. "Carbon Catalyzed Gasification of Organic Feedstocks in Supercritical Water." *Ind. Eng. Chem. Res.* In press.

Yu, D., M. Aihara, and M.J. Antal. 1993. "Hydrogen Production by Steam Reforming Biomass in Supercritical Water" *Energy Fuels*, 7: 574-577.

Table 1. Gasification of 1.2 M glucose in supercritical water at 600°C, 34.5 MPa with and without coconut shell activated carbon catalyst.

Catalyst	0.60 g	None
	WHSV = 22.2 hr^{-1}	Res. time = 34 s
Exp. date	4/18/94	12/4/92
Product	**Gas yield (mole of gas/ mole of feed)**	
H_2	2.24	0.56
CO	0.79	3.18
CO_2	3.09	0.29
CH_4	1.23	0.84
C_2H_4	0.00	0.03
C_2H_6	0.35	0.20
C_3H_6	0.00	0.00
C_3H_8	0.13	0.00
Carbon gasification efficiency	103%	80%

Table 2. Effect of various carbon catalysts on 1.2 M glucose gasification in supercritical water at 600°C, 34.5 MPa.

Catalyst type	Coal activated carbon	Coconut shell activated carbon	Macadamia shell charcoal	Spruce wood charcoal
WHSV	19.9 hr^{-1}	22.2 hr^{-1}	25.7 hr^{-1}	12.6 hr^{-1}
Date	4/11/94	4/18/94	4/22/94	7/21/95
Product	**Gas yield (mole of gas/ mole of feed)**			
H_2	1.48	2.24	2.71	3.86
CO	2.34	0.79	0.54	0.34
CO_2	1.45	3.09	1.09	3.72
CH_4	1.04	1.23	3.18	1.36
C_2H_4	0.002	0.0	0.002	0.0
C_2H_6	0.39	0.35	0.27	0.23
C_3H_6	0.002	0.0	0.003	0.0
C_3H_8	0.13	0.13	0.11	0.01
Carbon gasification efficiency	97%	103%	95%	99%
Unconverted TOC	N/A	N/A	N/A	0.9%
pH of liquid effluent	4	5	4	4

Table 3. Gasification of whole biomass feedstocks in supercritical water at 600°C, 34.5 MPa with coconut shell activated carbon catalyst.

Conc.	1.52 wt%	2.8 wt%
Feedstocks	Depithed bagasse liquid extract	Sewage sludge
WHSV	0.32 hr^{-1}	0.5 hr^{-1}
Exp. date	7/12/94	6/22/94

Product	**Gas yield (g of gas/ g of feed)**			
	Raw[a]	Corrected[b]	Raw	Corrected
H_2	2.4%	1.4%	2.7%	2.2%
CO	0.0	0.0	3.5%	3.3%
CO_2	90%	79%	66%	61%
CH_4	6.8%	6.6%	16%	1%
C_2H_4	0.2%	0.2%	0.05%	0.0
C_2H_6	1%	1%	7.7%	7%
C_3H_6	0.0	0.0	0.3%	0.3%
C_3H_8	0.0	0.0	1.7%	1.7%
Total gas yield	101%	89%	98%	77%
Unconverted TOC	N/A	N/A	0.28 g/L	0.28 g/L

[a] gas yield includes the gas generated by the coconut shell activated carbon catalyst.
[b] gas yield does not include the gas generated by the coconut shell activated carbon catalyst.

Table 4. Catalytic destruction of representative DoD wastes in supercritical water at 600°C, 34.5 MPa with coconut shell activated carbon catalyst.

Conc.	1.0 M		0.1 M		0.1 M		0.1 M		0.025 M	
Reactant	Methanol		Methyl ethyl ketone		Ethylene glycol		Acetic acid		Phenol	
WHSV	0.54 hr^{-1}		0.14 hr^{-1}		0.11 hr^{-1}		0.14 hr^{-1}		0.1 hr^{-1}	
Exp. date	8/15/95		8/15/95		8/15/95		8/15/95		7/14/94	
Product	**Gas yield (mole of gas/ mole of feed)**									
	Raw[a]	Corrected[b]	Raw	Corrected	Raw	Corrected	Raw	Corrected	Raw	Corrected
H_2	2.13	2.04	1.44	0.67	1.41	0.5	1.07	0.16	2.5	0.43
CO	0.04	0.04	0.0	0.0	0.0	0.0	0.0	0.0	0.55	0.17
CO_2	0.74	0.70	1.96	1.56	1.09	0.62	1.07	0.6	1.06	0.16
CH_4	0.05	0.04	0.77	0.74	0.35	0.32	0.55	0.53	0.35	0.22
C_2H_4	0.0	0.0	0.0	0.0	0.0	0.0	0.0	0.0	0.0	0.0
C_2H_6	0.0	0.0	0.08	0.08	0.02	0.02	0.0	0.0	0.05	0.05
C_3H_6	0.0	0.0	0.0	0.0	0.0	0.0	0.0	0.0	0.0	0.0
C_3H_8	0.0	0.0	0.0	0.0	0.0	0.0	0.0	0.0	0.0	0.0
Carbon gasification efficiency	84%	78%	72%	62%	74%	49%	82%	57%	35%	12%
Unconverted reactant	<0.3%	<0.3%	<0.3%	<0.3%	<0.3%	<0.3%	<0.3%	<0.3%	19.2%	19.2%
									7.5% benzene	7.5% benzene
Unconverted TOC	0.2%	0.2%	0.3%	0.3%	1.5%	1.5%	0.5%	0.5%	N/A	N/A

[a] gas yield includes the gas generated by the coconut shell activated carbon catalyst.
[b] gas yield does not include the gas generated by the coconut shell activated carbon catalyst.

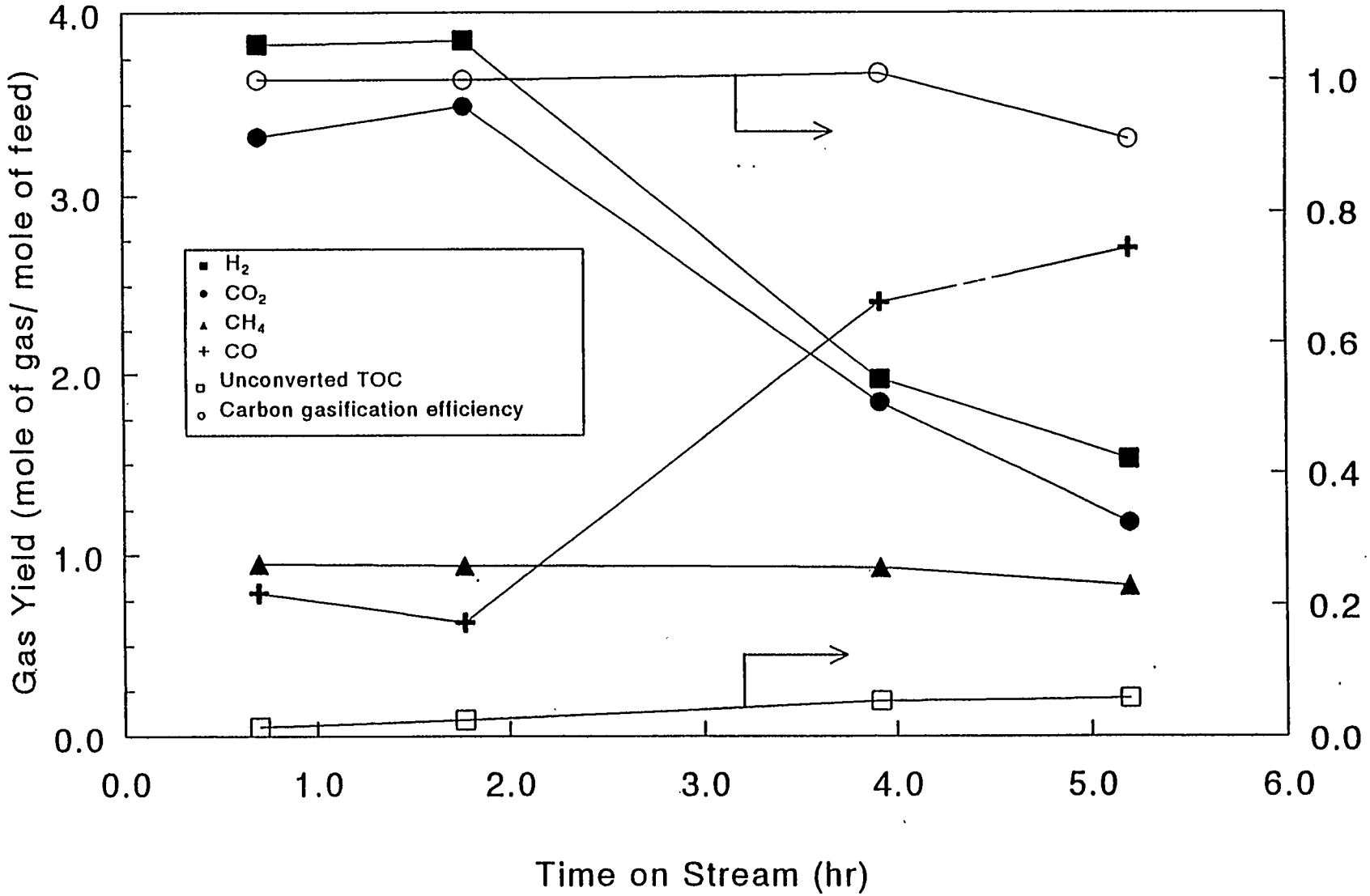


Figure 1. Deactivation of coconut shell activated carbon catalyst during 1.2 M glucose gasification in supercritical water at 600°C, 34.5 MPa without swirl, WHSV=19.9 hr^{-1} (exp. date: 5/4/94).

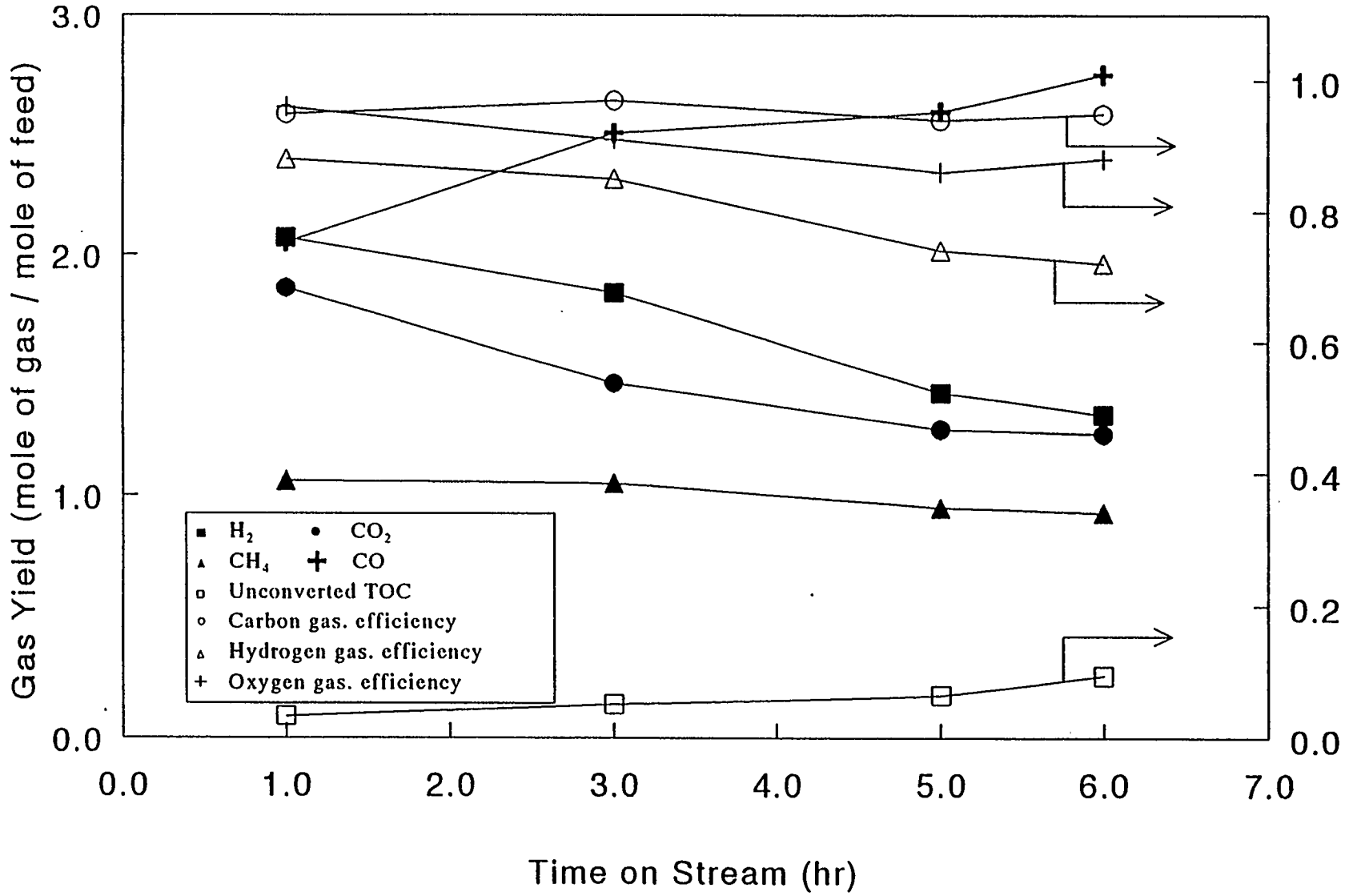


Figure 2. Gasification of 1.2 M glucose using coconut shell activated carbon catalyst in supercritical water at 600°C, 34.5 MPa with swirl, WHSV=17.1 hr^{-1} (exp. date: 7/13/95)

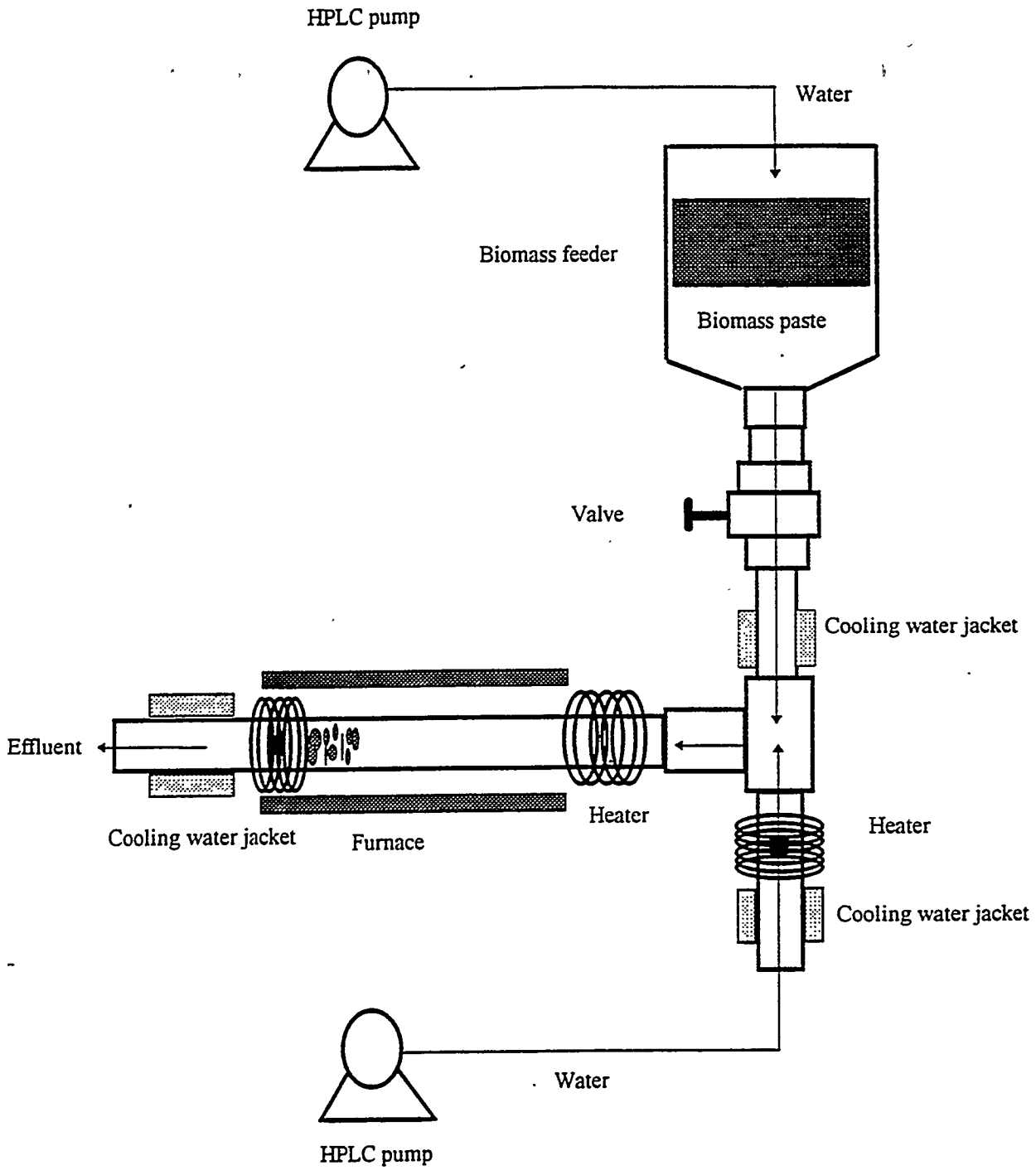


Figure 3. Supercritical flow reactor with a biomass feeder.

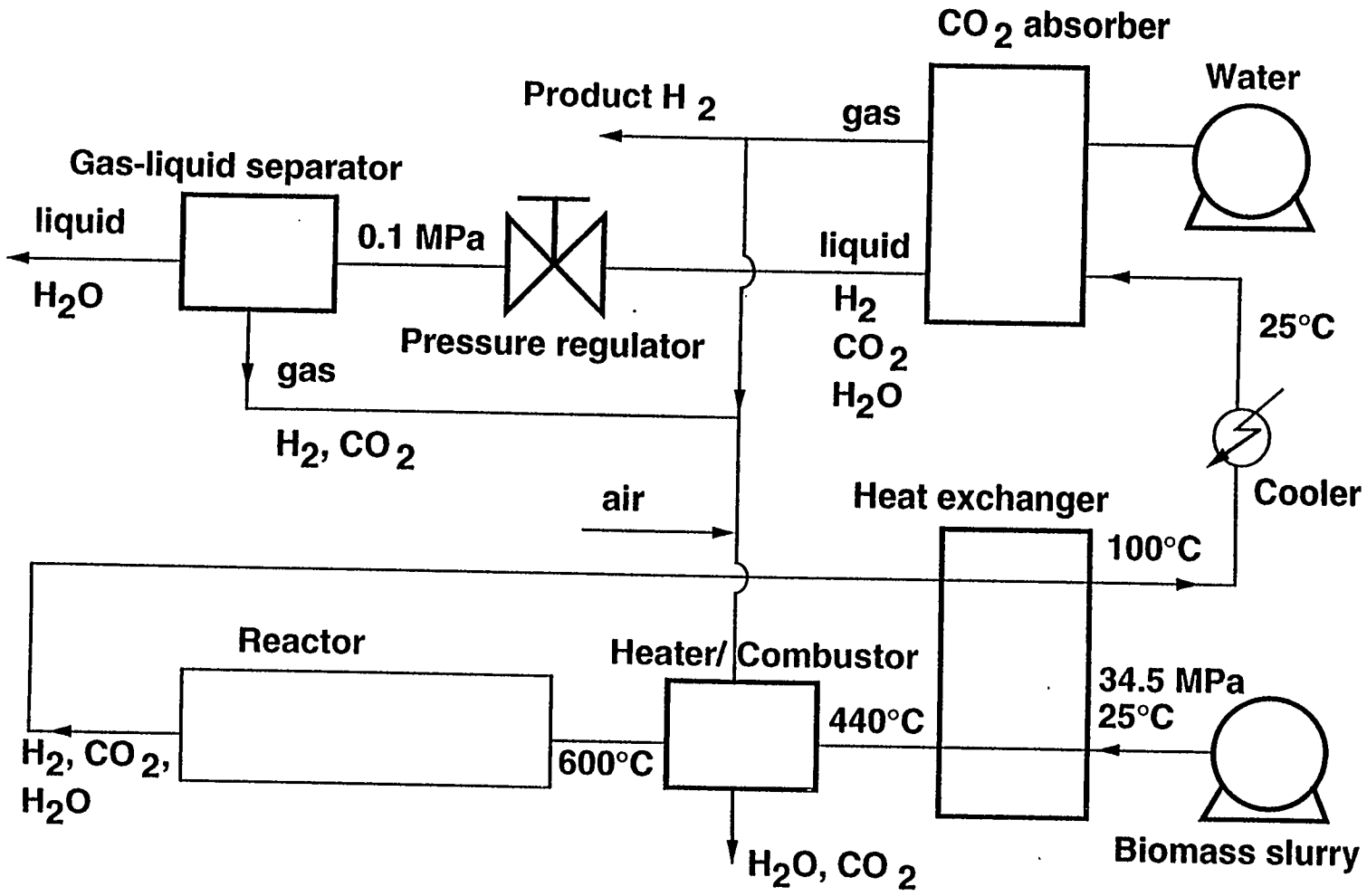


Figure 4. Biomass gasification process with carbon dioxide separation by adding water.

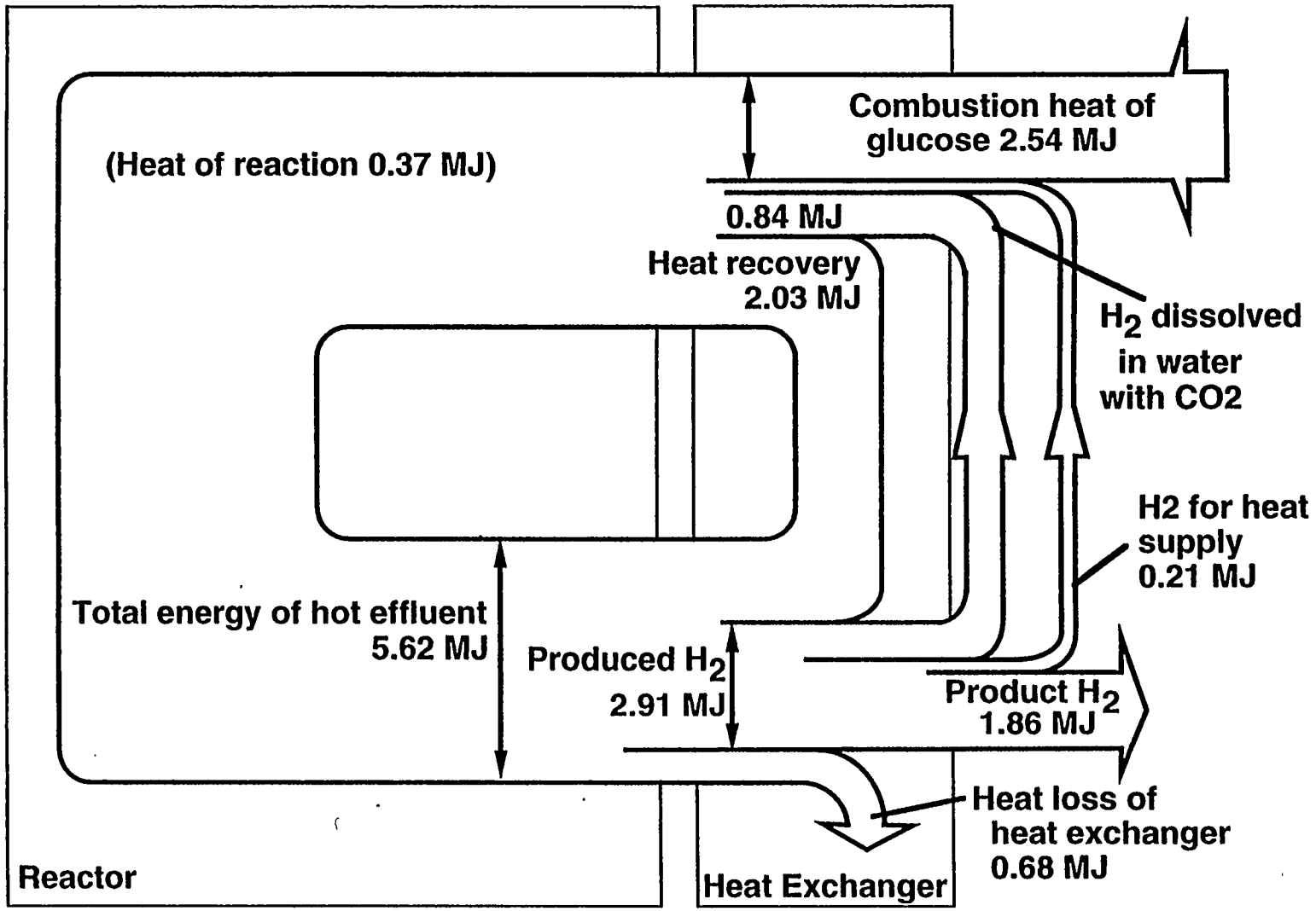


Figure 5. Energy flow analysis of the gasification system for 1 mol of glucose in a 1.2 M solution when the efficiency of the heat exchanger is 75%

PRODUCTION OF HYDROGEN BY THERMOCATALYTIC CRACKING OF NATURAL GAS

Nazim Muradov
Florida Solar Energy Center
1679 Clearlake Road, Cocoa 32922-5703

Abstract

The conventional methods of hydrogen production from natural gas (for example, steam reforming and partial oxidation) are complex, multi-step processes that produce large quantities of CO_2. The main goal of this project is to develop a technologically simple process for hydrogen production from natural gas (NG) and other hydrocarbon fuels via single-step decomposition of hydrocarbons. This approach eliminates or significantly reduces CO_2 emission. Carbon is a valuable by-product of this process, whereas conventional methods of hydrogen production from NG produce no useful by-products. Our approach is based on the use of special catalysts that reduce the maximum temperature of the process from 1400-1500°C (thermal non-catalytic decomposition of methane) to 500-900°C. Transition metal based catalysts and various forms of carbon are among the candidate catalysts for the process. This approach can advantageously be used for the development of compact NG reformers for on-site production of hydrogen-methane blends at refueling stations and, also, for the production of hydrogen-rich gas for fuel cell applications.

We extended the search for active methane decomposition catalysts to various modifications of Ni-, Fe-, Mo- and Co-based catalysts. Variation in the operational parameters makes it possible to produce H_2-CH_4 blends with a wide range of hydrogen concentrations that vary from 15 to 98% by volume. We found that Ni-based catalysts are more effective at temperatures below 750°C, whereas Fe-based catalysts are effective at temperatures above 800°C for the production of hydrogen with purity of 95% v. or higher. New reactor configurations to determine the catalyst activity have been designed, fabricated and tested; they included fixed bed, tubular and pulse reactors. The catalytic pyrolysis of liquid hydrocarbons (pentane, gasoline) over Fe-based

catalyst was conducted. We observed the production of a hydrogen-rich gas (hydrogen concentration up to 97% by volume) at a rate of approximately 1 L/min.mL of hydrocarbon fuel.

Introduction

All conventional options for hydrogen production from NG (e.g. steam reforming (SR), partial oxidation, autothermal reforming) involve CO_2 production at some point in the technological process chain, therefore, the main problem remains: how to produce hydrogen from NG without CO_2 emission. There are basically two alternative approaches to eliminating CO_2 emissions from methane use in hydrogen production:

- SR of NG with subsequent scrubbing of CO_2 from synthesis gas
- decomposition of methane into hydrogen and carbon

SR of NG is the most widely used among all present-day processes for hydrogen production. It is a complex multi-step process. The reforming reaction is a strongly endothermic, high temperature (800-870°C) process. Because of the energy intensive stages of SR process, the usage of NG as a fuel is almost equal to its usage as a chemical feedstock. As a result, the production of every cubic meter of hydrogen is accompanied by the emission of 0.5 cubic meter of CO_2. CO_2 can be removed from flue gas by several conventional methods, however, the real problem is what to do with accumulating volumes of CO_2 that are not released into the atmosphere. Several proposals have been discussed in the literature (Nakicenovic 1993) on CO_2 disposal (e.g. in the deep ocean, etc.), however, ecological consequences of the proposed solutions are not clear.

The thermal decomposition (TD) of methane is another option for CO_2-free production of hydrogen from NG.

$$CH_4 \rightarrow C + 2H_2 + 75.6 \text{ kJ}$$

There is a very valuable by-product of TD process, pure carbon, while SR produces no useful by-products. Unlike SR process, TD produces practically no CO_2 emissions. The decomposition of methane can be carried out plasmochemically. In a recent paper, Fulchery et al (1995) advocated a plasma-assisted decomposition of methane into hydrogen and carbon. It was estimated that up to 1.9 kWh of electricity will be consumed per one normal cubic meter of hydrogen produced.

Background

Thermal decomposition of methane is a well known process. The energy requirement per mole of hydrogen produced for TD is somewhat less than that for SR reaction: 37.8 and 41.2 kJ/mole H_2, respectively. The process is slightly endothermic, so only an insignificant amount of hydrogen produced could be used as a source of the thermal energy for the process.

Figure 1 depicts the thermodynamic data on the decomposition of various hydrocarbons (from methane to pentane) that constitute natural gas. It can be seen that the enthalpy of methane decomposition reaction is significantly higher than that of other hydrocarbons due to the strong C - H bond in the methane molecule. Equilibrium curves for methane decomposition reaction at 1 and 10 atmospheres are shown in Figure 2. Equilibrium H_2-CH_4 mixtures containing 47-90 and 90-98% by volume of hydrogen can be produced at the temperature intervals of 500-720 and 720-900°C, respectively. As discussed in the literature (Kelley et al 1980) the gaseous mixtures containing 20% v of hydrogen could be used as an ecologically acceptable transportation fuel without any changes in end use devices. Hydrogen rich gas (90-98% v.) could advantageously be used in fuel cells.

Attempts have been reported in the literature on the use of catalysts for the cracking of methane and light hydrocarbons. For example, Pohleny et al (1966) and Callahan (1974) used various refractory materials and metal oxide based catalysts for the catalytic decomposition of methane at 800-1100°C. . The carbon produced was then burned off the catalyst surface. In this regard, these processes exhibited no significant advantages over the conventional processes (for example, SR) because of high operational temperatures and large CO_2 emissions.

Our approach is based on the use of special catalysts that reduce the maximum temperature of the process from 1400-1500°C (thermal non-catalytic decomposition of methane) to 500-900°C. Transition metal based catalysts and various forms of carbon are among candidate catalysts for use in the process. This approach can advantageously be used for the development of the compact NG reformers for on-site production of hydrogen-methane blends at refueling stations and for the production of hydrogen-rich gas for fuel cell applications. The Table illustrates the process characteristics for hydrogen production by conventional processes and decomposition of NG.

Materials and Methods

The gases: methane (99.0%), nitrogen (99.999%) and hydrogen (99.999%) were used without further purification. Pt(1%) on alumina pellets was provided by Aldrich. Alumina-supported (9-16 mesh) Ni- and Fe-based (6-9% w) catalysts were prepared according to the procedure described by Richardson (1989). NiO-MoO_3/alumina catalyst was provided by Haldor Topsoe, Inc. The reduction of metal oxide catalysts into metallic form was carried out in the stream of hydrogen at 650°C. Several types of catalytic reactors were used in this work, continuous flow (packed bed and tubular) and pulse. Tubular reactors were made out of quartz, ceramic (alumina), stainless steel and metallic nickel. Figure 3 depicts the schematic diagram of the experimental set-up used for the catalytic decomposition of methane in fixed bed and tubular reactors. The experimental unit for the liquid hydrocarbons decomposition consisted of a syringe pump for metering and delivering of the hydrocarbon feedstock, a preheater for the evaporation of liquid fuel, a catalytic reactor, a flowmeter for metering the rate of hydrogen production and the analytical system (GC) for the product gas analysis. The products of methane decomposition/oxidation were measured gas-chromatographically (SRI 8610, N_2-carrier gas, TCD, silicagele column, and Varian 3000, He-carrier gas, FID, Hysep D_B column).

Table. Process Characteristics for Producing Hydrogen by Conventional Processes and Decomposition of Natural Gas

Process Characteristics	Steam Reform.	Partial Oxidat.	Thermal Decompos.	Plasmo-chemical Decompos.	Catalyt. Decomp.
Commercial Availability	+	+	+	-	-
Typical Capacity 10^3 m^3/h	12-120	36-120	N/A	-	-
Number of Steps	3(4)	3	1	1	1
Need for H_2 Purification	+	+	-	-	-
Special Requirements	Steam	Oxygen	-	Electricity 1.1-2 kWh/ m^3 H_2	-
Catalyst	+	-	-	-	+
Fuel Flexibility	Low	High	Moderate	Low	High
Tolerance to Sulfur in a Feedstock	Very low	High	High	Moderate	Moderate
Useful By-product	-	-	Carbon	Carbon	Carbon
CO_2 Emission	+	+	-	-	-
Efficiency*, %	78.5	80	N/A	95	92.8
Cost**, \$/1000 m^3	67.1	109.2	N/A	N/A	58.0***
Capacity of small scale units, 10^3 m^3/h	0.1-5.9	0.02-4.0	N/A	2.0	-
Power Density, kW/L	6.4	0.7 (el.)	N/A	~4	5.3

* - total efficiency

** - based on 118×10^3 m^3/h capacity (Steinberg 1988),

*** - after carbon credit taken

Results and Discussion

Thermocatalytic Decomposition of Methane Using Fixed Bed Reactor

We studied thermocatalytic decomposition of methane over various catalysts and supports in a wide range of temperatures, 200-900°C, and space velocities from, 200 to 1500 h-1, at atmospheric pressure. Preliminary tests were performed on the selection of materials for the catalyst support and catalytic reactor. It was found that among materials tested (quartz, ceramics, stainless steel) quartz demonstrated the least activity in the methane decomposition reaction at temperatures up to 1000°C. Stainless steel (SS) demonstrated noticeable catalytic activity at 750°C and higher. The activated alumina (9-16 mesh) was used as a catalyst support.

It was observed with all catalysts tested that at given pressure and space velocity the hydrogen production rate is a function of the temperature. Figures 4 and 5 depict the maximum concentration of hydrogen in the hydrogen-methane mixture produced in the presence of different catalysts at 750 and 850°C, respectively. It was demonstrated that Ni-based catalysts are more active than Fe-based catalysts at 75O°C; and conversely, Fe-based catalysts are more active than Ni-catalysts at 850°C and higher temperatures. Pt/alumina demonstrated moderate activity at 750°C. Unfortunately, no steady state hydrogen production was observed with all the catalysts tested. Figure 6 depicts the kinetic curves of hydrogen production over alumina-supported Fe, Fe_2O_3 and Pt catalysts at 750°C. We observed initial surge of hydrogen yield in the presence of Fe/Al_2O_3 catalyst which was followed by gradual decrease in the hydrogen production rate. In the case of iron oxide catalyst, there was a distinct induction period of 4-5 min. Apparently, the induction period corresponds to the reduction of iron oxide into metallic iron. GC analysis indicated that during the induction period the effluent gas was rich with carbon oxides. The Pt/alumina catalyst demonstrated quite different behavior. The maximum of the hydrogen yield was observed at the very beginning of the reaction followed by steep decline in the hydrogen concentration in the product gas. The shape of the kinetic curves of hydrogen production in the presence of alumina-supported NiO, $NiO-MoO_3$ and $CoO-MoO_3$ catalysts were identical to that of iron oxide, except the induction period was shorter. In the case of Ni-based catalysts the picture was more complicated because of the catalyst disintegration after 20-30 min into the run. As Figure 7 shows, the hydrogen concentration in the effluent gas in the presence of Ni/alumina slightly dropped during the first 5 min and then continuously increased until reactor was clogged by carbon. Similar behavior was demonstrated by NiO/catalyst except that there was short induction period corresponding to the reduction of NiO into metallic nickel. To prevent reactor clogging, we diluted Ni/alumina catalyst with bare alumina pellets of the same size in a ratio of 1:1 by weight. Figure 8 depicts the kinetic curve of hydrogen production in the presence of diluted Ni/alumina catalyst at 750°C. The catalyst activity drastically dropped during first 10 min, followed by slow decline in hydrogen production rate over several hours.

It was found that newly-reduced Ni/alumina and Fe/alumina catalysts exhibited very high activity in the methane decomposition reaction. For example, in the presence of Ni-catalyst the hydrogen was detected in the effluent gas at the temperature as low as 200°C. At 250°C the concentration of hydrogen in the hydrogen-methane mixture reached approximately one percent. The breakthrough temperature for the methane decomposition in the presence of Fe/alumina catalyst

was also 200°C. Unlike Fe/alumina, Fe_2O_3/alumina catalyst became active at temperatures higher than 600°C. Below this temperature the reduction of ferric oxide to metallic iron by methane is a very slow process. These experimental results supported the assumption that the induction period corresponds to the reduction of metal-oxide form of the catalyst into metallic form. Once the active metallic form of the catalyst was produced, the effective decomposition of methane on the catalyst surface with formation of hydrogen and carbon began. The carbon blocks the active sites on the catalyst surface which results in a limited reduction of the catalyst activity. Each catalyst is characterized by the maximum and steady state rate of hydrogen production as well as the time to reach the steady state.

Surprisingly, activated carbon demonstrated relatively high initial activity in methane decomposition reaction at temperatures above 800°C. As it is shown on Figure 9, hydrogen concentration in the effluent gas dropped from 78 to 60% v. during the first 10 minutes of the reaction and after several hours reached the minimum value. The data on the hydrogen production in the presence of activated alumina are also included in Figure 9. Alumina has negligible catalytic activity towards methane decomposition, however, as the process proceeds hydrogen yield increases due to the catalytic effect of carbon deposits on the catalyst surface. Hydrogen production rate reaches maximum and then slowly decreases over several hours and eventually stabilizes. The catalytic activity of various modifications of carbon is well documented. According to Tenser (1987), the rate constant of methane decomposition reaction over soot (k_s) is expressed by the following equation:

$$k_s = 1.8\times10^{-3} \exp(-272{,}000/RT) \text{ g cm}^{-2} \text{ s}^{-1} \text{ Pa}^{-1} \qquad \text{(at 700-950°C)}$$

Decomposition of Methane in a Tubular Reactor

We conducted a series of experiments on the decomposition of methane in a tubular reactor for the temperature range of 800-870°C. The tubular reactors were made out of quartz, ceramic (alumina), stainless steel and metallic nickel. The objective was to study the effect of carbon removal from the catalyst surface on its catalytic activity. Figure 10 depicts the results of the tubular reactor experiments. There was no or negligible yield of hydrogen using quartz and alumina reactor at 850-870°. Stainless steel tubes demonstrated relatively low catalytic activity at space velocities of 1500-2000 h^{-1} and 870°C. Nickel tube demonstrated the highest activity among the tested tubular reactors. After the first experimental run in the Ni reactor at 800°C, we mechanically removed carbon from the inner wall of the reactor, subjected the catalyst to methane flow at the same conditions (2nd run) and repeated the procedure one more time (3rd run). The results indicated that carbon can be removed from the reactor without effecting the catalytic activity. We observed that the rate of the catalyst deactivation was much higher for tubular reactors than for fixed bed reactors packed with alumina-supported catalysts. This can be explained by the effect of catalytic surface area.

Figure 11 summarizes our findings on the catalyst activity tests. Newly prepared or regenerated Ni- and Fe-based catalysts demonstrated the highest catalytic activity in methane decomposition reaction. The maximum hydrogen concentration in the effluent gas in the presence of alumina-supported Ni- and Fe-catalysts at the range of temperatures of 100-900°C are fairly close to the

equilibrium values of hydrogen concentration in H_2-CH_4 mixtures which is an indicative of very efficient catalyst. Experimental results indicate that Ni-based catalysts are suitable for the production of the hydrogen-methane blends with the hydrogen concentrations up to 85-90% v. at moderate temperatures 750°C and below. Fe-based catalysts can be used for the production of hydrogen with purity up to 95% and higher at temperatures of 800°C and higher.

Catalytic Pyrolysis of Liquid Hydrocarbons

The objective of this series of experiments was

- to study the catalytic decomposition of high alkanes, including pentane which is a minor component of natural gas

- to develop a process for the production of hydrogen-rich gas via single step decomposition of liquid hydrocarbon fuels (e.g. gasoline)

Figure 12 depicts the results of pentane decomposition (pyrolysis) over Fe/alumina catalyst at 880°C. Hydrogen-rich gas (H_2 concentration above 95% v.) was produced during the first 10 min of the process, followed by a steady decline in the hydrogen concentration. After 25 min, we observed the formation of ethane and ethylene. The yield of the hydrogen-rich gas reached up to 960 mL/min and, over one hour, dropped to 750 mL/min per mL of pentane.

Similar results were obtained with gasoline as the feedstock. The results of the catalytic pyrolysis of gasoline are shown in Figure 13 (a and b). After the first run, the carbon (coke) was burned off the catalyst surface by passing air through the reactor at 800°C. After the reactor was purged with nitrogen to remove air, the gasoline vapors were introduced into the reactor (2nd run). The procedure was repeated one more time (3rd run). The results of the 2nd and 3rd runs were similar to that of the 1st run. Figure 13b depicts the yields of hydrogen-rich gas during the three runs and it can be seen that the catalyst activity remains approximately at the same level after the three decomposition-regeneration cycles.

Conclusion

- The catalytic activity of various modifications of Ni-, Fe-, Mo-, Co- and carbon-based catalysts for methane decomposition reaction was determined. Variation in the operational parameters (temperature and residence time) makes it possible to produce H_2-CH_4 blends with a wide range of hydrogen concentrations that vary from 15 to 98% by volume.

- New reactor configurations to determine the catalyst activity have been designed, fabricated and tested. They included: fixed bed, tubular and pulse reactors.

- We found that Ni-based catalysts are more effective at temperatures below 750°C, whereas Fe-based catalysts are effective in a wide range of temperatures up to 900°C and

above for the production of hydrogen with purity of 95% v. or higher. It was demonstrated that the induction period of hydrogen production corresponds to the reduction of metal oxide to the metallic form of Ni- and Fe-catalysts.

- The catalytic decomposition of liquid hydrocarbons (pentane and gasoline) over Fe-based catalysts was conducted, resulting in the production of a hydrogen-rich gas with the hydrogen concentration up to 97% by volume at a rate of approximately 1 L/min.mL of hydrocarbon fuel.

Future Work

Optimize the process for the high yield of hydrogen and catalyst long term stability. Develop methods for efficient separation of carbon from the catalyst surface. Determine the catalytic activity of various forms of carbon in methane decomposition reaction.

References

Callahan, M. "Catalytic Pyrolysis of Methane and Other Hydrocarbons." *26th Power Sources Symposium,* 181-184, Red Bank, N.J.

Fulcheri, L. and Y.Schwob. 1995. "From Methane to Hydrogen, Carbon Black and Water." *Int. J. Hydrogen Energy,* 20: 197-202.

Kelley, J. and R. Hagler. 1980. "Storage, Transmission and Distribution of Hydrogen." *Int. J. of Hydrogen Energy,* 5: 35-54.

Nakicenovic, N. 1993. "Energy Gases: The Methane Age and Beyond, IIASA Working Paper WP-93-033, Laxenburg, Austria.

Pohleny, J. and N. Scott. 1966. U.S.Patent No 3,284,161 (UOP).

Richardson, J. 1989. *Principles of Catalyst Development.* NY: Plenum Press.

Steinberg, M. and H. Cheng. 1988. "Modern and Perspective Technologies for Hydrogen Production from Fossil Fuels." In *Proceedings of 7th World Hydrogen Energy Conference,* 699-730, Moscow, USSR.

Tenser, A. 1987. "The Kinetics of Pyrocarbon Generation." *Itogi Nauki i Tekhniki (Russian),* 16: 3-63.

Figure Captions

Figure 1. Thermodynamics of hydrocarbon decomposition reaction

Figure 2. Equilibrium data for methane decomposition reaction

Figure 3. Schematic diagram of continuous flow thermocatalytic system for methane decomposition

Figure 4. Maximum hydrogen concentration in the effluent gas at 750°C using different catalysts

Figure 5. Maximum hydrogen concentration in the effluent gas at 850°C using different catalysts

Figure 6. Kinetic curves of hydrogen production in the presence of alumina-supported Fe- and Pt- catalysts

Figure 7. Methane decomposition over Ni-based catalysts at 600°C using fixed bed reactor

Figure 8. Methane decomposition over Ni/alumina catalyst at 750°C

Figure 9. Catalytic decomposition of methane over activated carbon and alumina at 850°C

Figure 10. Methane decomposition using tubular reactors

Figure 11. Methane decomposition over Ni- and Fe-catalysts

Figure 12. Catalytic pyrolysis of pentane over Fe/alumina catalyst at 880°C

Figure 13. Catalytic pyrolysis of gasoline over Fe/alumina at 850°C.
a- products concentrations, b- gas production rate.

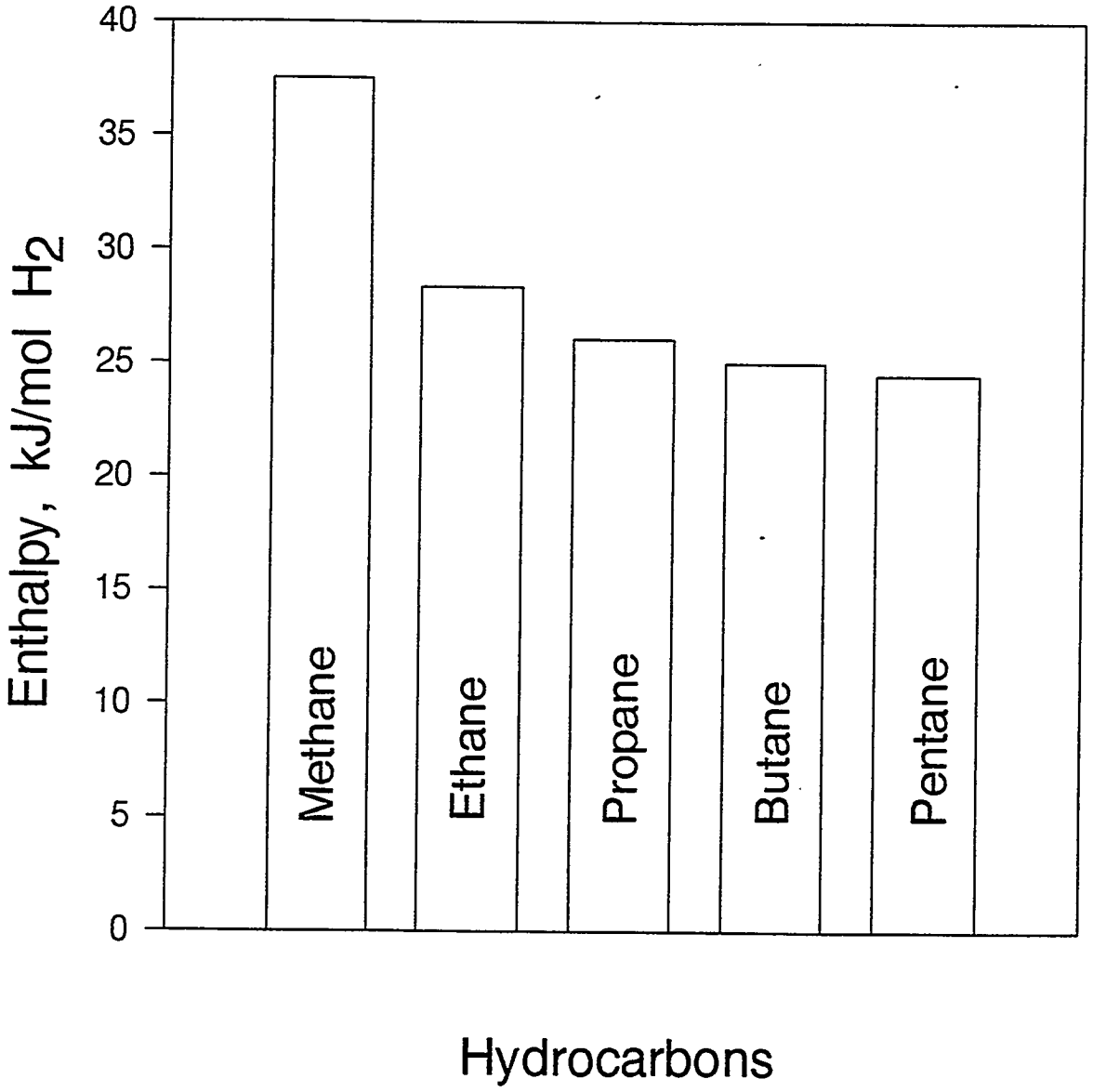

Enthalpy, kJ/mol H_2
40
35
30
25
20
15
10
5
0
Methane
Ethane
Propane
Butane
Pentane
Hydrocarbons

Figure 1.

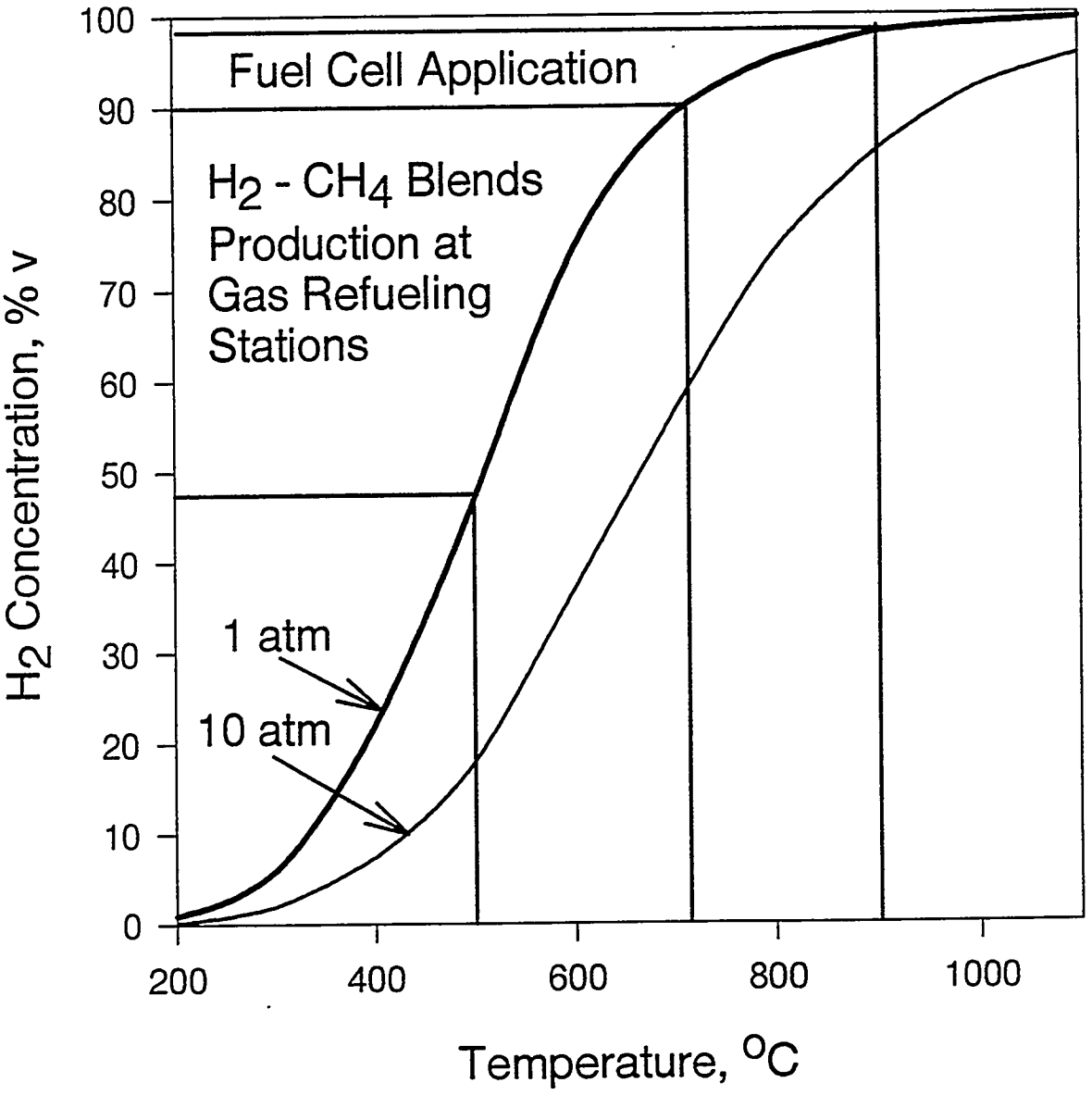

Fuel Cell Application
H_2 - CH_4 Blends
Production at
Gas Refueling
Stations
1 atm
10 atm
H_2 Concentration, % v
Temperature, °C
100
90
80
70
60
50
40
30
20
10
0
200
400
600
800
1000

Figure 2.

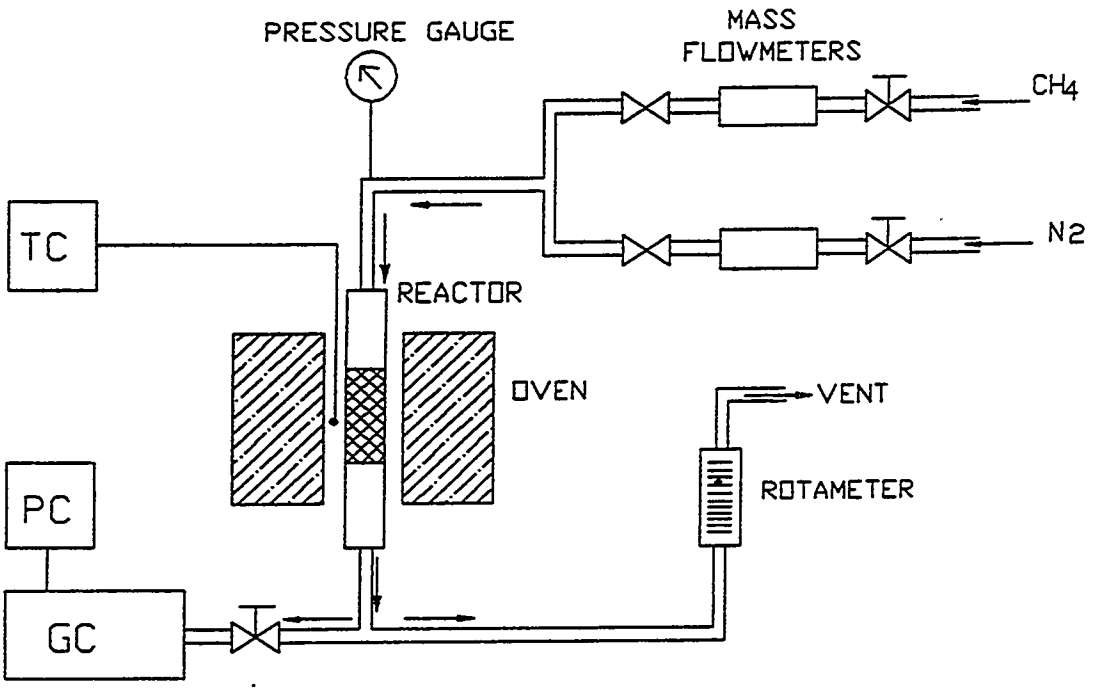

PRESSURE GAUGE
MASS
FLOWMETERS
CH4
N2
TC
REACTOR
OVEN
VENT
ROTAMETER
PC
GC

Figure 3.

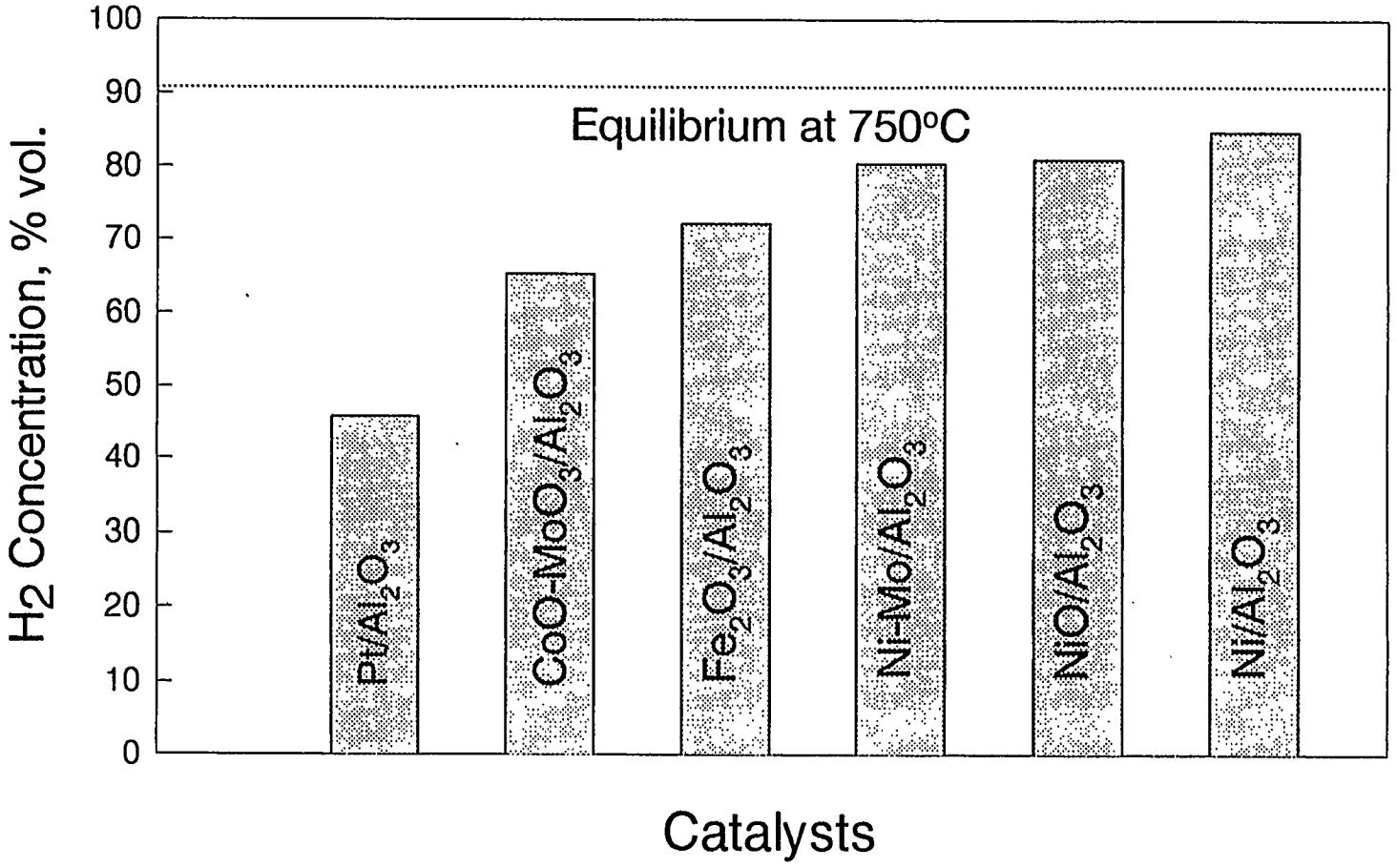

100
90
80
70
60
50
40
30
20
10
0
H2 Concentration, % vol.
Equilibrium at 750°C
Pt/Al2O3
CoO-MoO3/Al2O3
Fe2O3/Al2O3
Ni-Mo/Al2O3
NiO/Al2O3
Ni/Al2O3
Catalysts

Figure 4.

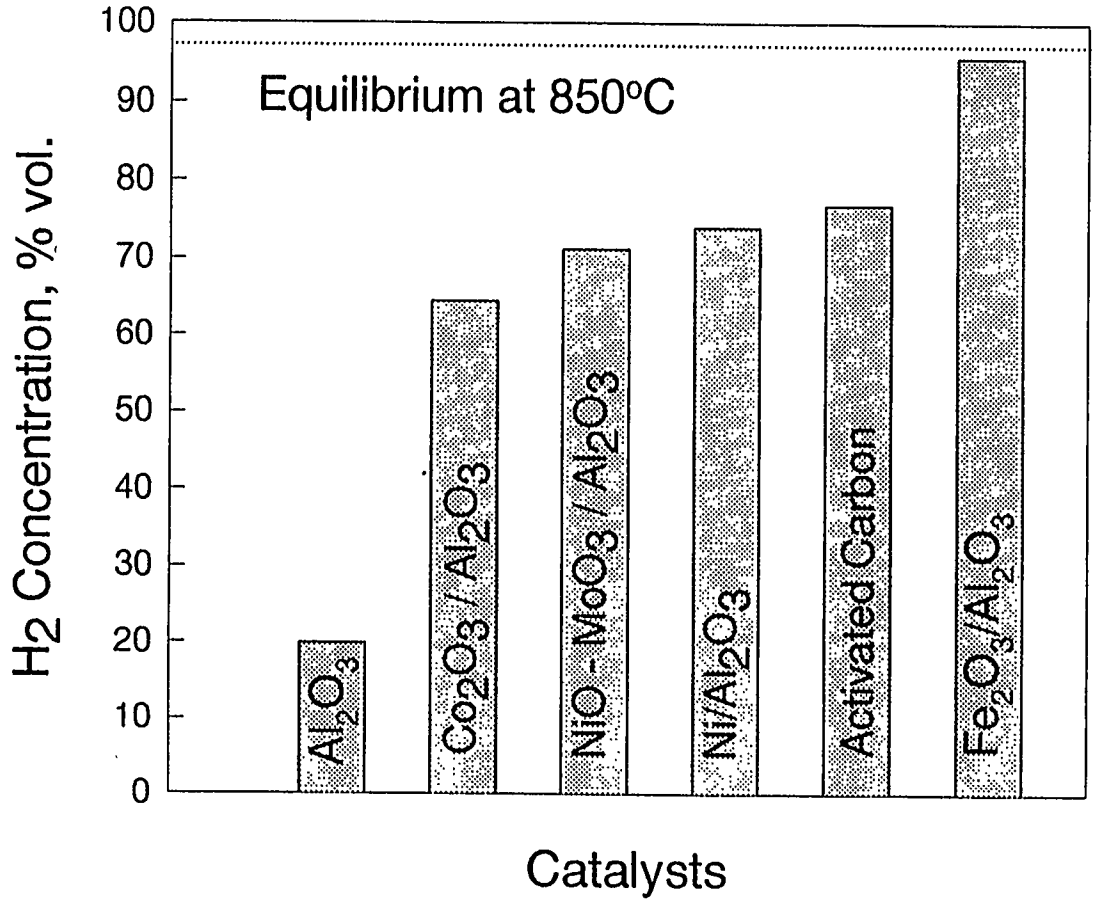

100
90
80
70
60
50
40
30
20
10
0
H2 Concentration, % vol.
Equilibrium at 850°C
Al2O3
Co2O3 / Al2O3
NiO - MoO3 / Al2O3
Ni/Al2O3
Activated Carbon
Fe2O3/Al2O3
Catalysts

Figure 5.

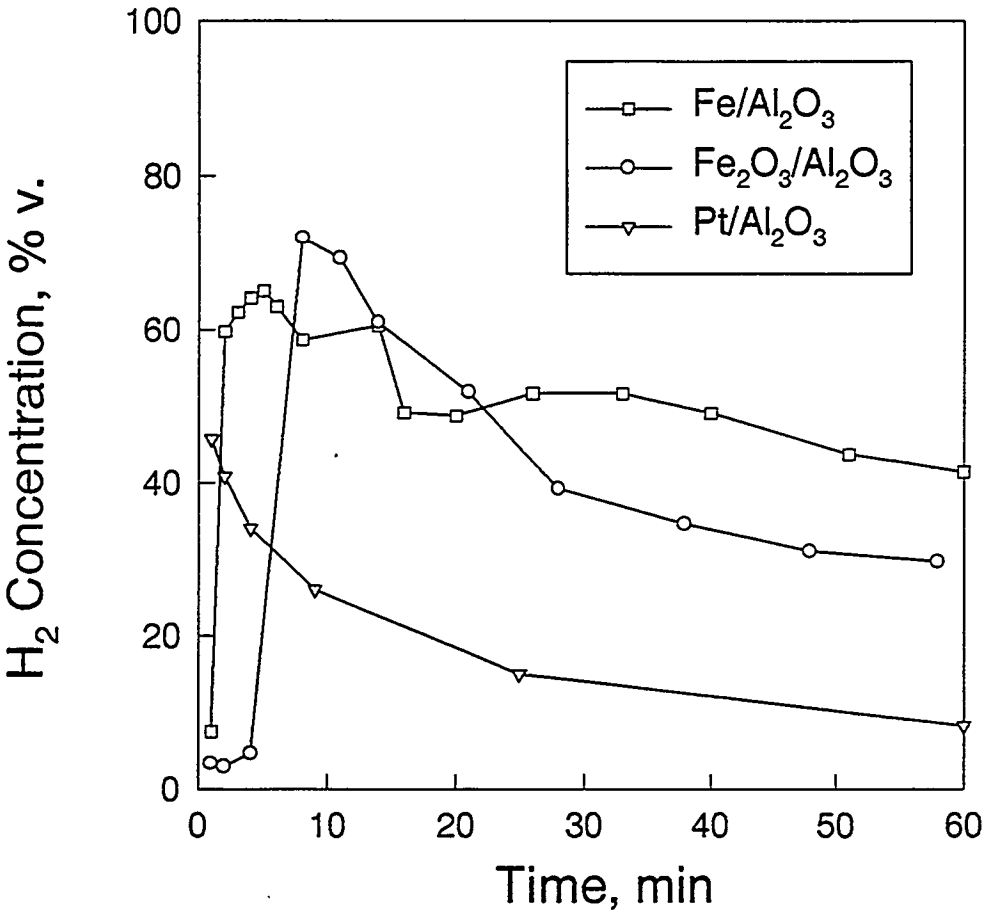

100
80
60
40
20
0
0
10
20
30
40
50
60
H_2 Concentration, % v.
Time, min
Fe/Al_2O_3
Fe_2O_3/Al_2O_3
Pt/Al_2O_3

Figure 6.

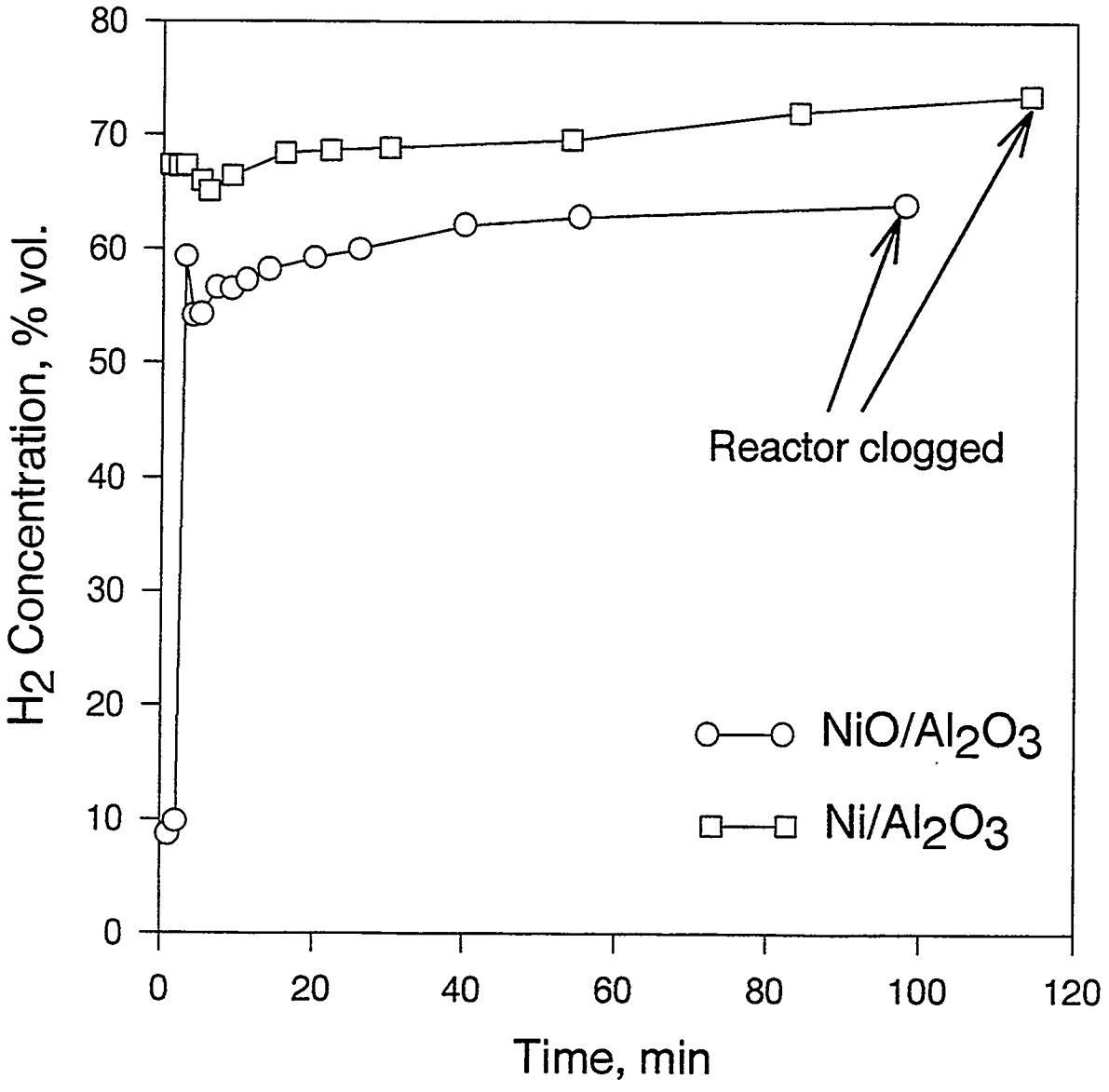

80
70
60
50
40
30
20
10
0
H_2 Concentration, % vol.
0
20
40
60
80
100
120
Time, min
Reactor clogged
NiO/Al_2O_3
Ni/Al_2O_3

Figure 7.

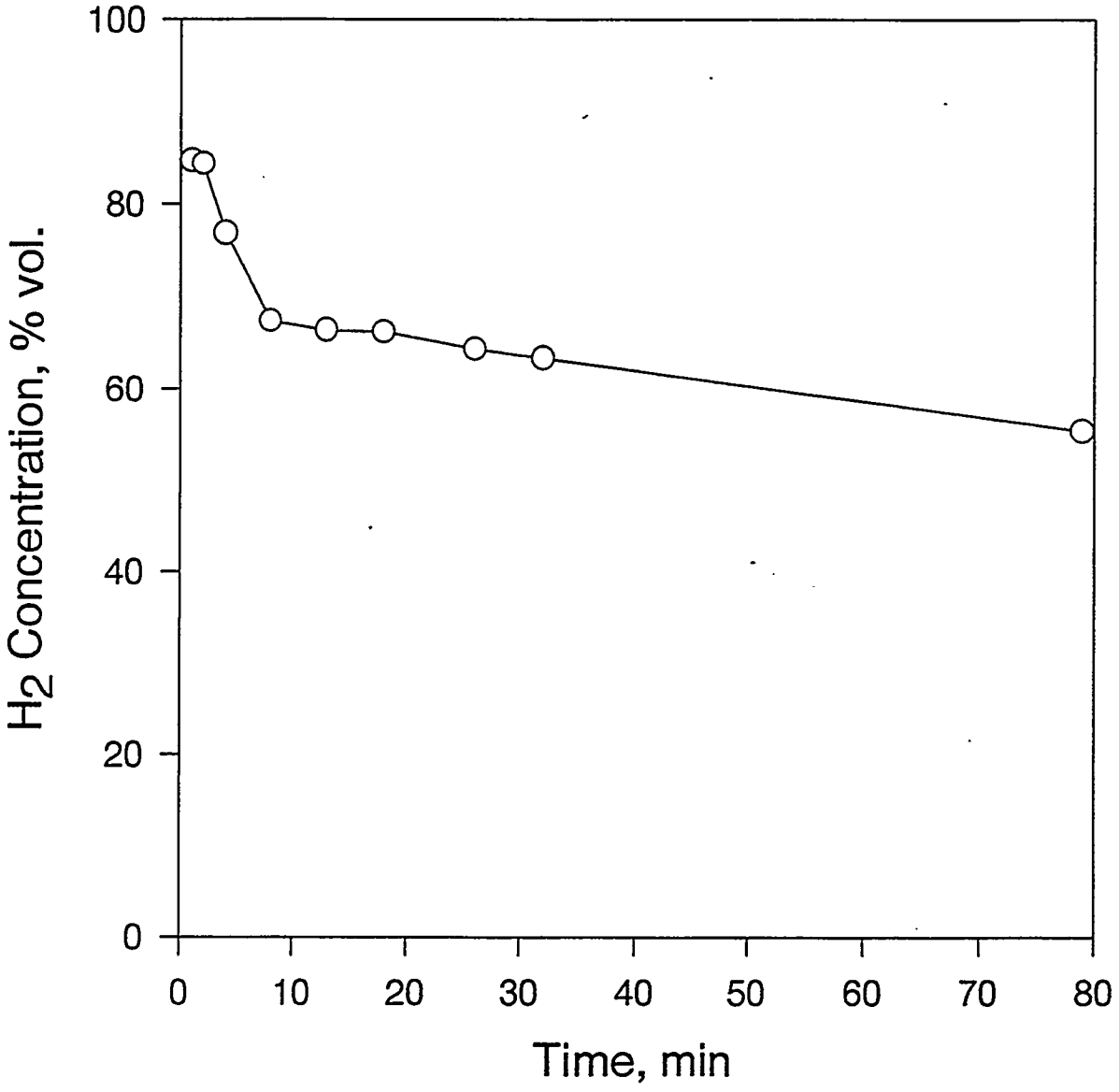

100
80
60
40
20
0
H_2 Concentration, % vol.
0
10
20
30
40
50
60
70
80
Time, min

Figure 8.

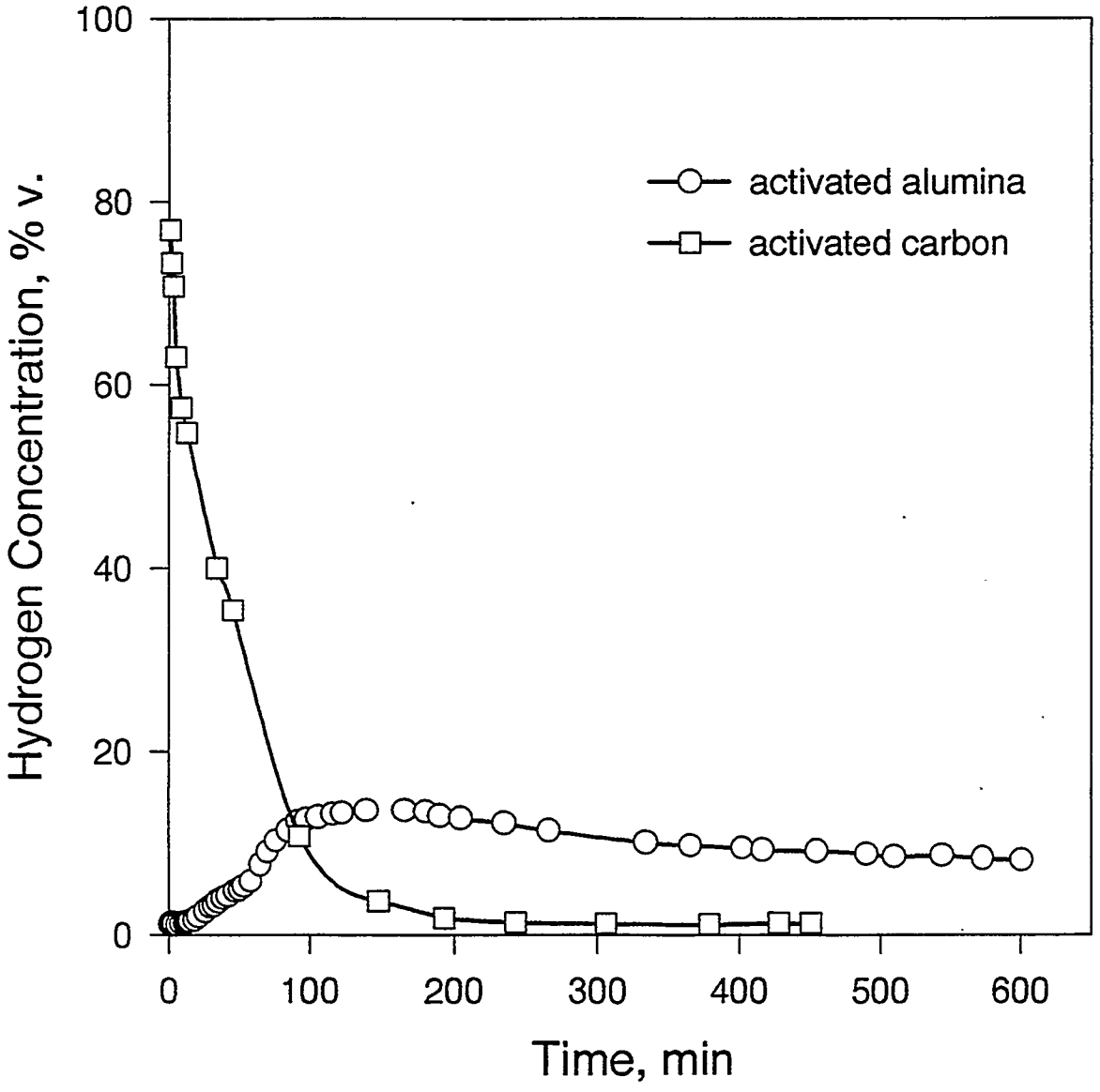

100
80
60
40
20
0
Hydrogen Concentration, % v.
activated alumina
activated carbon
0
100
200
300
400
500
600
Time, min

Figure 9.

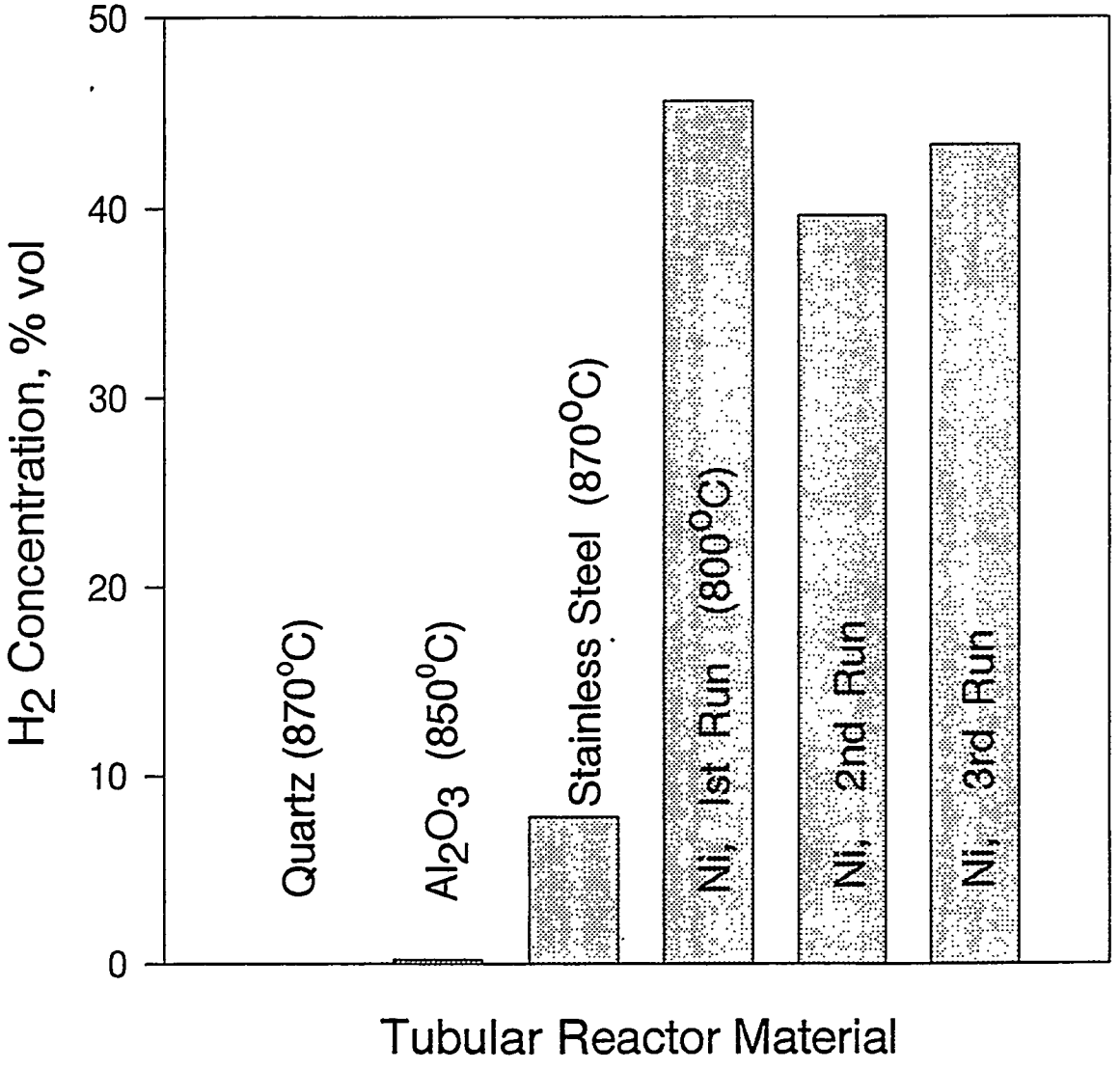

50
40
30
20
10
0
H_2 Concentration, % vol
Quartz (870°C)
Al_2O_3 (850°C)
Stainless Steel (870°C)
Ni, 1st Run (800°C)
Ni, 2nd Run
Ni, 3rd Run
Tubular Reactor Material

Figure 10.

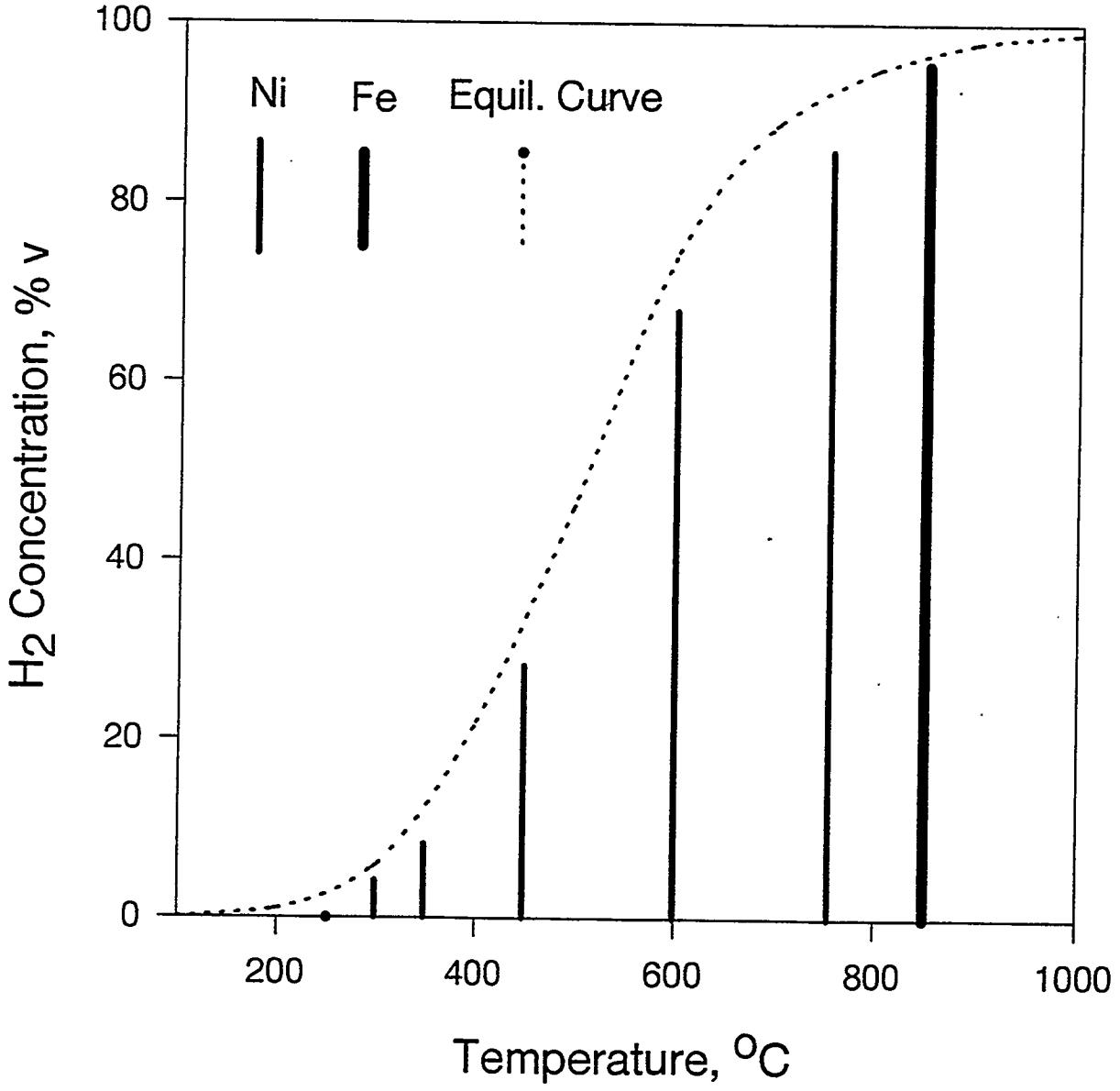
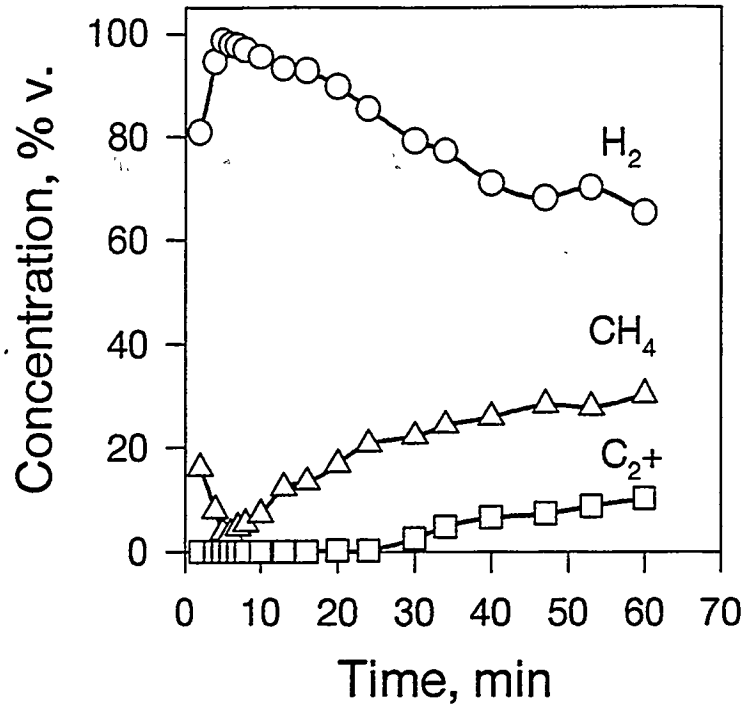

100
80
60
40
20
0
Ni
Fe
Equil. Curve
H_2 Concentration, % v
200
400
600
800
1000
Temperature, ^oC

Figure 11.


Concentration, % v.
100
80
60
40
20
0
H_2
CH_4
C_2+
0 10 20 30 40 50 60 70
Time, min

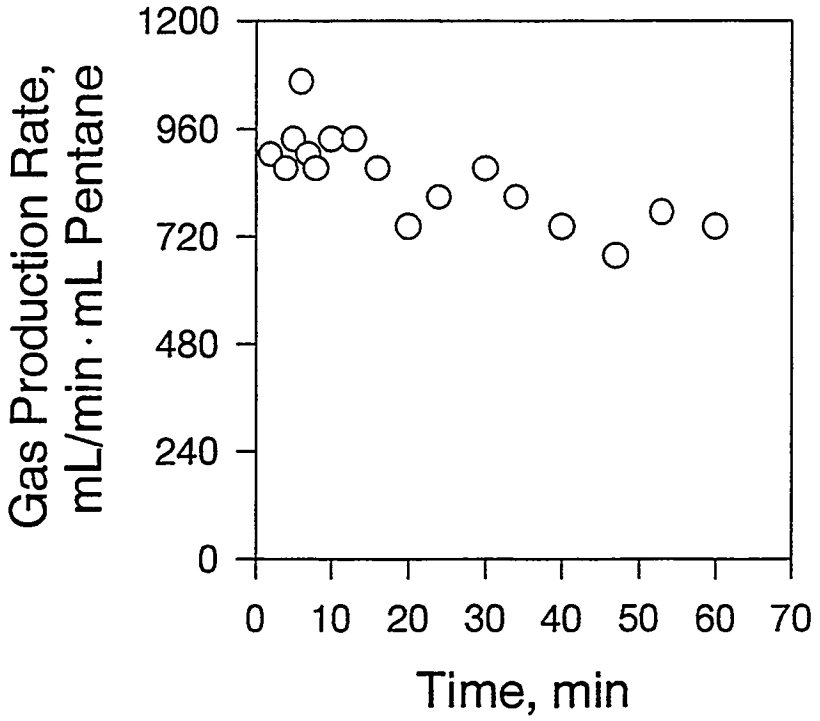

Gas Production Rate,
mL/min · mL Pentane
1200
960
720
480
240
0
0 10 20 30 40 50 60 70
Time, min

Figure 12.

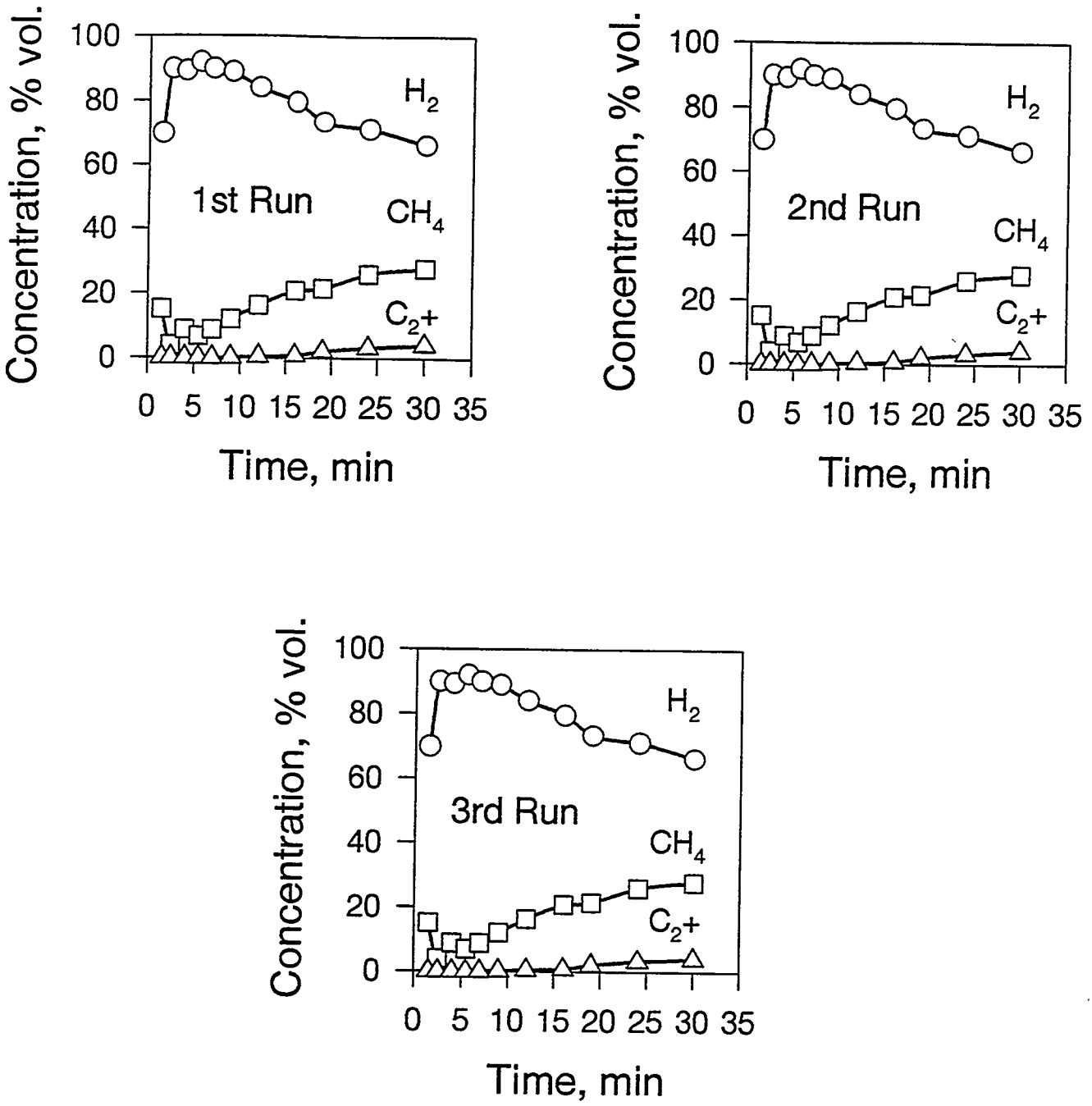

Concentration, % vol.
100
80
60
40
20
0
1st Run
H_2
CH_4
C_2+
0 5 10 15 20 25 30 35
Time, min
Concentration, % vol.
100
80
60
40
20
0
2nd Run
H_2
CH_4
C_2+
0 5 10 15 20 25 30 35
Time, min
Concentration, % vol.
100
80
60
40
20
0
3rd Run
H_2
CH_4
C_2+
0 5 10 15 20 25 30 35
Time, min

Figure 13 (a).

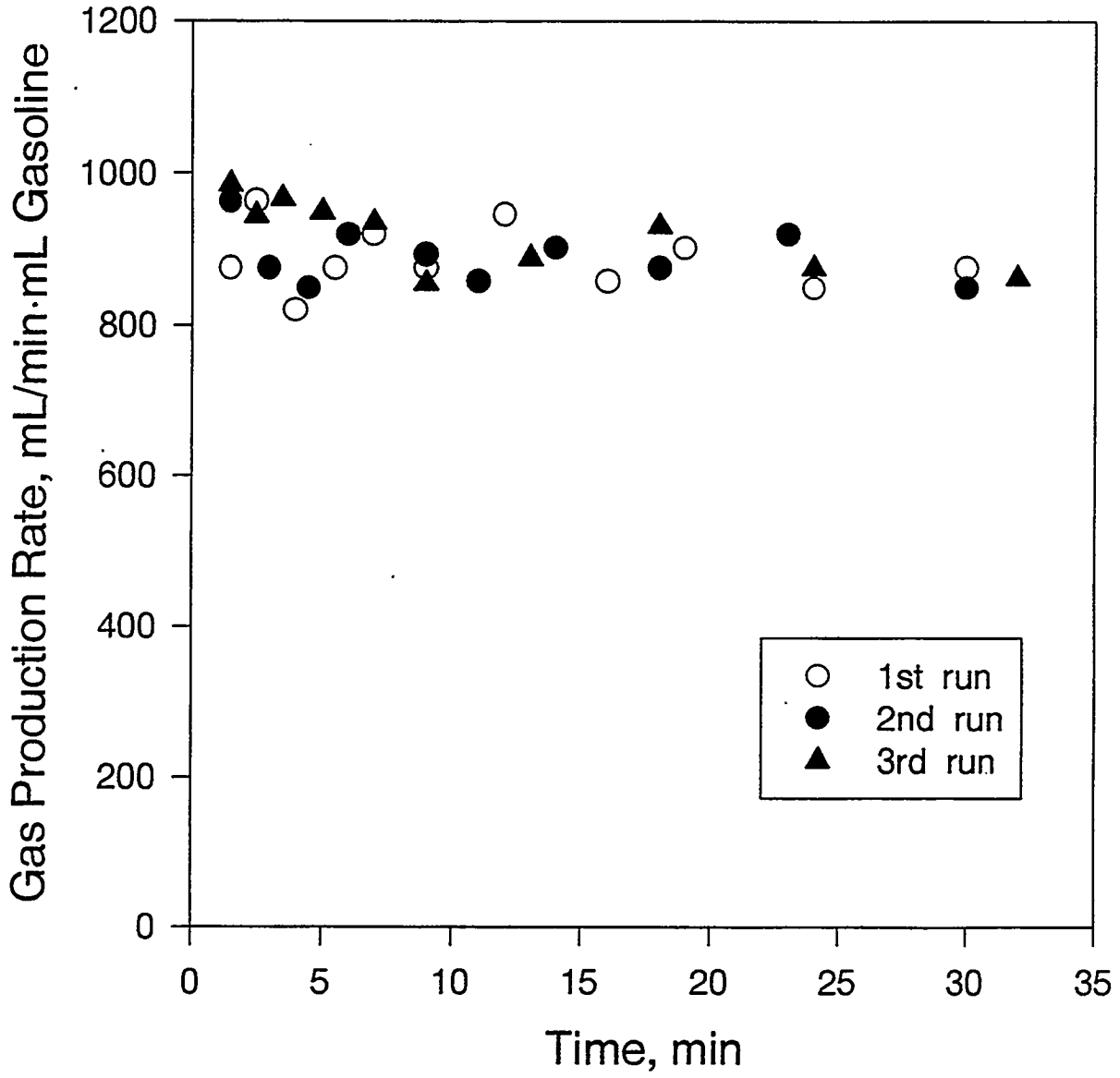

Gas Production Rate, mL/min·mL Gasoline
1200
1000
800
600
400
200
0
0
5
10
15
20
25
30
35
Time, min
1st run
2nd run
3rd run

Figure 13 (b).

SORPTION ENHANCED REACTION PROCESS (SERP) FOR PRODUCTION OF HYDROGEN

M. Anand, J. Hufton, S. Mayorga, S. Nataraj, S. Sircar, T. Gaffney
Air Products and Chemicals, Inc.
Allentown, PA 18195

Abstract

Sorption Enhanced Reaction Process (SERP) is a novel process that is being developed for the production of lower cost hydrogen by steam-methane reforming (SMR). In this process, the reaction of methane with steam is carried out in the presence of an admixture of a catalyst and a selective adsorbent for carbon dioxide. The key consequences of SERP are: (i) reformation reaction is carried out at a significantly lower temperature (300-500°C) than that in a conventional SMR reactor (800-1100°C), while achieving the same conversion of methane to hydrogen, (ii) the product hydrogen is obtained at reactor pressure (200-400 psig) and at 98+% purity directly from the reactor (compared to only 70-75% H_2 from conventional SMR reactor), (iii) downstream hydrogen purification step is either eliminated or significantly reduced in size.

The first phase of the program has focused on the development of a sorbent for CO_2 which has (a) reversible CO_2 capacity >0.3 mmol/g at low partial pressures of CO_2 (0.1-1.0 atm) in the presence of excess steam (pH_2O/pCO_2>20) at 400-500°C and (b) fast sorption-desorption kinetics for CO_2 at 400-500°C. Several families of supported sorbents have been identified that meet the target CO_2 capacity. A few of these sorbents have been tested under repeated sorption/desorption cycles and extended exposure to high pressure steam at 400-500°C. One sorbent has been scaled up to larger quantities (2-3 kg) and tested in the laboratory process equipment for sorption and desorption kinetics of CO_2. The CO_2 sorption and desorption kinetics are desirably fast. This was a critical path item for the first phase of the program and now has been successfully demonstrated.

A reactor has been designed that will allow nearly isothermal operation for SERP-SMR. This reactor was integrated into an overall process flow diagram for the SERP-SMR process and used for first pass economic evaluation. It was determined that SERP-SMR will produce H_2 at a significantly lower cost compared to the conventional SMR-PSA route of H_2 production.

Introduction

SER Background

The concepts based on Le Chatelier's principle that (a) the conversion of reactants to products, and (b) the rate of forward reaction in an equilibrium-limited reaction can be increased by selectively removing some of the reaction products from the reaction zone are very well known [Gluud et al., 1931]. Numerous applications of this concept using fixed bed, continuous countercurrent moving bed, and simulated countercurrent moving bed chromatographic reactors have been published. The detailed review of the literature is given elsewhere [Carvill et al., 1996].

The process concepts combining chemical reaction and adsorptive separation of reaction products in a single unit operation in conjunction with sorbent regeneration using the principles of pressure swing adsorption are generally called Periodic Separating Reactors [Vaporciyan and Kadlec, 1987, 1989] or Pressure Swing Reactors [Lee and Kadlec, 1989; Kirkby and Morgan, 1994]. Table 1 lists some of the key experimental studies reported in the literature under the general acronym of PSR.

Table 1. Experimental Evaluation of PSR Systems

Authors	Process Steps	Reaction	Sorbent	Products
Vaporciyan and Kadlec, 1989	Feed, delay, exhaust	$2CO + O_2 \Leftrightarrow 2CO_2$ feed diluted with N_2	5A Zeolite for CO_2	CO_2 distributed in both reaction effluent and desorption gas. Dilute CO_2 in both products.
Goto, Tagawa and Omiya, 1993	Feed, helium purge (or evacuate)	$C_6H_{12} \Leftrightarrow C_6H_6 + 3H_2$ feed diluted with helium	$CaNi_5$ for H_2	H_2 product obtained in mixture with helium as desorbed product. C_6H_6 product obtained as reactor effluent partly mixed with helium.
Han and Harrison, 1994	No process, feed only.	$CO + H_2O \Leftrightarrow CO_2 + H_2$ feed (CO_2, CO, H_2 and H_2O mixture) diluted with N_2.	Dolomite for CO_2	Dilute H_2 in N_2 obtained during feed step.

Two investigations especially relevant to this program are described below:

(i) Han and Harrison [1994] experimentally demonstrated that high conversion of carbon monoxide to hydrogen (larger than that dictated by thermodynamic equilibrium) could be achieved in the absence of a catalyst by the water gas shift reaction [$CO + H_2O \Leftrightarrow CO_2 + H_2$] when one of the reaction products (CO_2) was removed from the reaction zone by reacting with calcium oxide [$CaO + CO_2 \rightarrow CaCO_3$]. They used dolomite (~55% CaO + 45% MgO) as the sorbent at a reaction temperature of 550°C and at a total gas pressure of 15 atmospheres. No process scheme for regeneration of dolomite was disclosed.

(ii) Brun-Tsekhovoi et al. [1986] used a specially treated form of dolomite containing active CaO and chemically inert MgO as sorbent in a continuous fluidized bed reactor containing microspheres of nickel on alumina catalyst. Freshly regenerated particles of the sorbent were fed to the fluidized bed reactor in a direction countercurrent to reactant gas flow. Large sorbent particles were used so that they could travel under gravity through the fluidized catalyst particles towards the feed gas end of the bed. The size and density differences of the catalyst and the sorbent materials allowed complete separation between them at the gas inlet end. The sorbent particles were pneumatically carried to a thermal regenerator for desorption of CO_2. A very significant enhancement of CH_4 conversion to H_2 (compared to that achieved by catalyst alone) at pressure levels of 10–100 atmospheres and at a reaction temperature of 627°C was reported. The product gas leaving the fluidized bed reactor contained 92–96% H_2. A dust separator was required to clean the H_2 product gas. The proposed process scheme also included a gas turbine to recover power from the hot effluent gas exiting the sorbent regenerator. The turbine generated power to drive the pneumatic compressor for transporting the exhausted sorbent to the regenerator at the reaction pressure and temperature.

The above two studies are important because they show the use of metal oxides as sorbents for the application of the sorption enhanced reaction (SER) principle to (a) steam-methane reforming (SMR) and (b) forward water-gas shift reaction. The emphasis of the present work is very different. It carries out simultaneous reaction-separation in a single unit operation in order to obtain high conversion of CH_4 to H_2 at a much lower temperature while producing high purity H_2 at reaction pressure. This allows the use of stainless steel for material of construction of reactors, elimination or substantial reduction of subsequent H_2 purification process which results in lower cost of H_2 production. A detailed description of the novel SERP concept is described below.

Novel SER Process (SERP)

In the proposed SER process for H_2 production, the conventional steam methane reformation reaction,

$$CH_4 + 2H_2O \Leftrightarrow CO_2 + 4H_2$$

is carried out such that the reactants, steam and methane, are fed at 300-500°C and 200-400 psig into a reactor-sorber containing an admixture of reforming catalyst and an adsorbent for removing carbon dioxide at reaction conditions. A reactor effluent consisting of essentially pure hydrogen (98+%) is produced. The regeneration of the sorbent is carried out in situ by using the principles of pressure swing adsorption. We call this process the Sorption Enhanced Reaction Process (SERP) [Sircar et al. 1995]. Several patent application for the process and process integrations have been filed to the United States Patent Office by Air Products and Chemicals, Inc. [Anand et al., 1995, Hufton et al., 1996, Nataraj et al., 1996].

The key benefits of producing H_2 by the present concept are: (i) reformation at a significantly lower temperature (300-500°C) than conventional SMR (800-1000°C), while achieving the same conversion of methane to hydrogen, (ii) significantly lower capital cost, (iii) the product hydrogen is obtained at reactor

pressure (200-400 psig) and at 98+% purity directly from the reactor, (iv) downstream hydrogen purification steps are either eliminated or significantly reduced in size, (v) reduction/elimination of CO as a by-product, (vi) minimizing side reactions like coking, (vii) reduction of excess steam used in conventional SMR.

A comparison of the conventional SMR process and the proposed SERP-SMR process is shown in Table 2.

Table 2. SERP-SMR vs Conventional SMR for H_2 Production

	Conventional	SER Goals
Operating Temperature	800-1000°C	300-500°C
CH_4 to H_2 Conversion	80-85%	90+%
Reaction Product Composition	73.7% H_2+9.4% CO_2+ 12.0% CO+4.8% CH_4 (Dry Basis)	98+% H_2
Product Pressure	200-400 psig	200-400psig

The steps for the direct production of essentially pure H_2 by the cyclic SERP-SMR are shown in Figure 1:

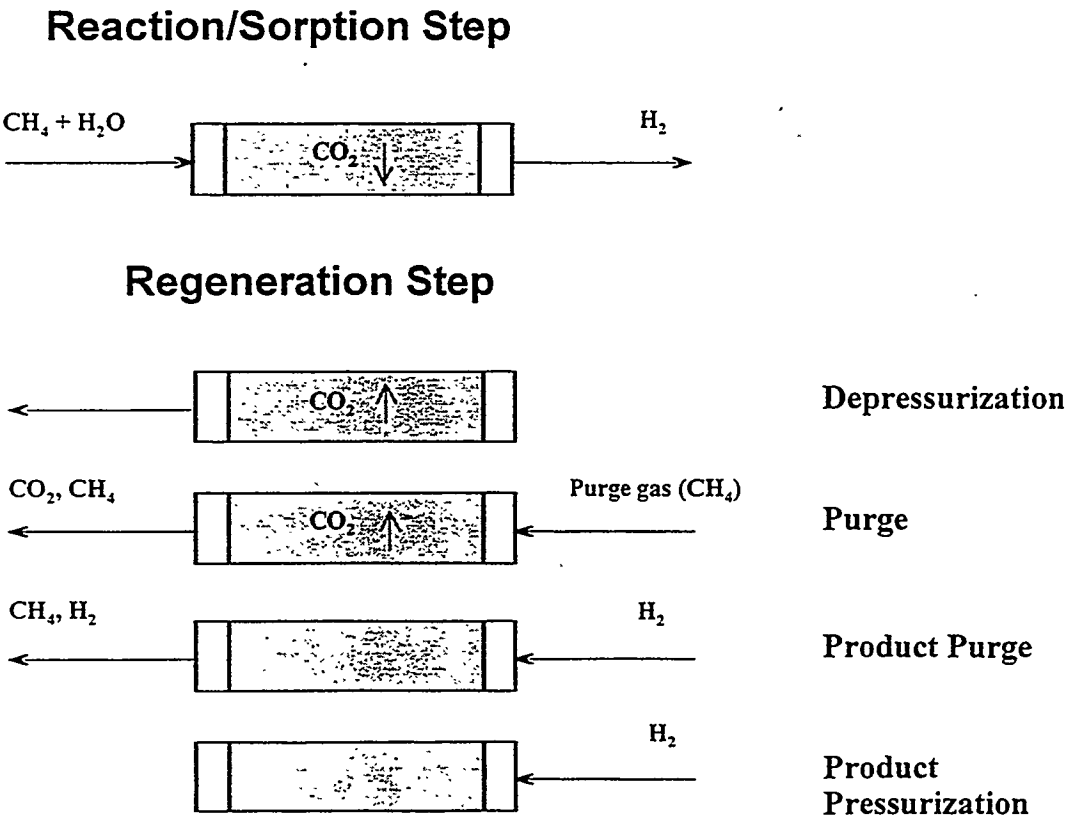


Figure 1. Process scheme showing the reaction and regeneration steps for SERP-SMR

1. Steam and methane at a ratio of 2:1 are fed into the reactor-sorber at the desired temperature and pressure. The reactor-sorber is presaturated with the product H_2 prior to introduction of the reactants.

2. An essentially pure H_2 product (>98% purity) is collected as the reactor-sorber effluent. The reaction step is continued up to the point when the H_2 purity in the product decreases to a preset level. The feed is then diverted to a second identical reactor-sorber.

3. The reactor-sorber is then countercurrently depressurized. The effluent gas can be recycled as feed to another reactor or used as fuel.

4. The reactor-sorber is countercurrently purged with a weakly adsorbing gas such as methane to desorb the CO_2. The desorption pressure may range between 0.2 and 1.1 atmospheres. The desorbed gas consisting of CH_4, CO_2, H_2 and H_2O is either separated for reuse of CH_4 as purge gas or used as fuel in the reformer.

5. The weakly adsorbing purge gas CH_4 is countercurrently displaced from the reactor-sorber with product H_2. The displaced CH_4 is recycled as purge gas or used as fuel.

6. Finally, the reactor-sorber is countercurrently pressurized to the reaction pressure with pure H_2. At this point, the regeneration of the reactor-sorber is complete and is ready to start a new cycle.

Program Goals and Milestones

The key program goals and milestones are shown in Table 3 along with the focus of the technical program for 1995-1997:

Table 3. Program Goals and Milestones

Program Goals	Milestones
Sorbent Development	1995-1996
SER Process Development	1995-1997
Economic Evaluation	1996-1997
Process Development Unit Test	1997-1998

The key goals for the first phase of the program (1995-1997) are:

(i) Development of a sorbent for CO_2 which is stable in the presence of high partial pressures of steam and maintains desired CO_2 capacity under cyclic pressure swing conditions at 300-500°C.

(ii) Modification of the existing laboratory scale experimental system for testing the SERP-SMR process.

(iii) Demonstration of the SERP-SMR concept in the laboratory scale process equipment.

(iv) First pass economic analysis to demonstrate the commercial attractiveness of SERP-SMR.

Experimental

The development of CO_2 sorbents for SERP-SMR for H_2 production has involved the synthesis, characterization and performance evaluation of a number of different families of sorbents. All promising sorbents are subjected to a battery of performance screening tests including: (1) determination of CO_2 working capacity under dry conditions and in the presence of low partial pressure of steam; (2) analysis of CO_2/N_2 cyclic stability; (3) evaluation of stability under static hydrothermal conditions utilizing the Hydrothermal Stability Testing Unit (HSTU); (4) measurement of CO_2 sorption capacity with a mixture of CO_2 and steam at partial pressures and temperatures (300-500°C) that are representative for H_2-SERP using the Binary Desorption Unit (BDU); and (5) analysis of CO_2 sorption-desorption kinetics with scaled up (1-3 kg) quantities of materials in a packed column in the laboratory process equipment.

The HSTU and BDU are new analytical equipment which are designed and built in-house exclusively for the evaluation of sorbent materials for the H_2-SERP. Figure 2 shows a simplified schematic diagram of the BDU.

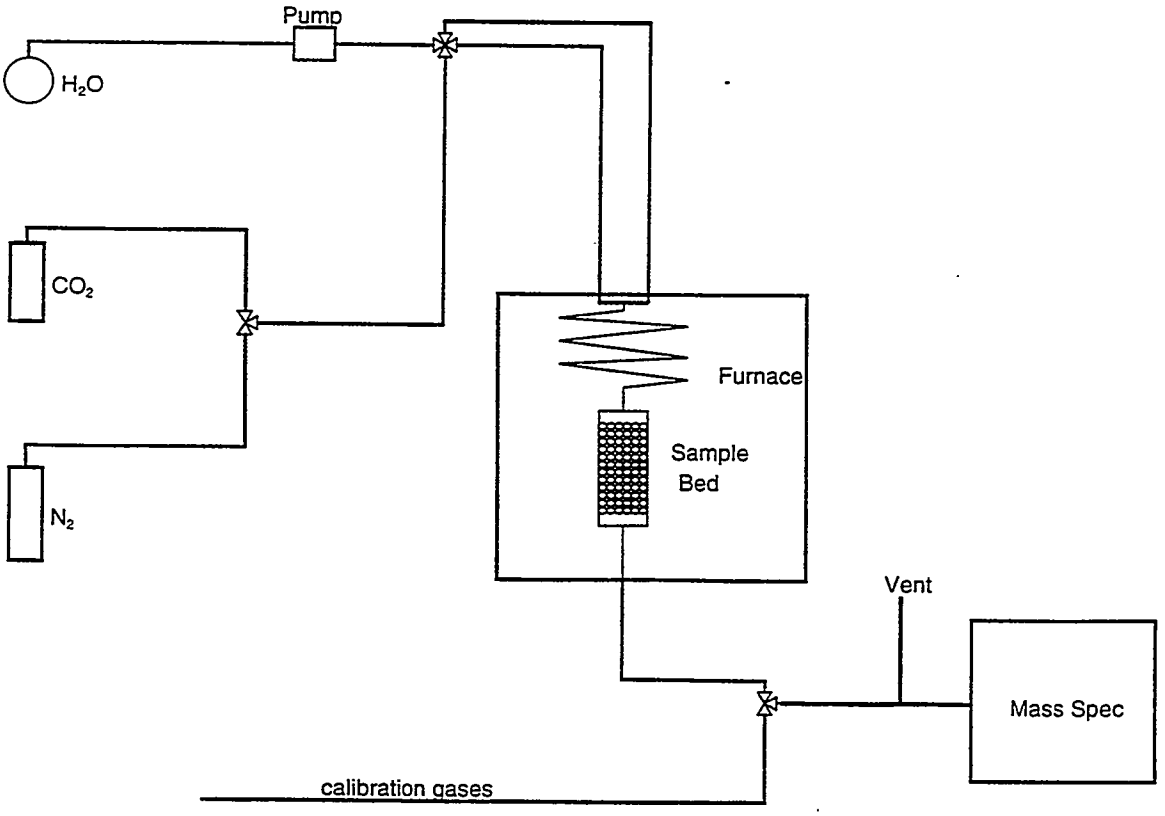
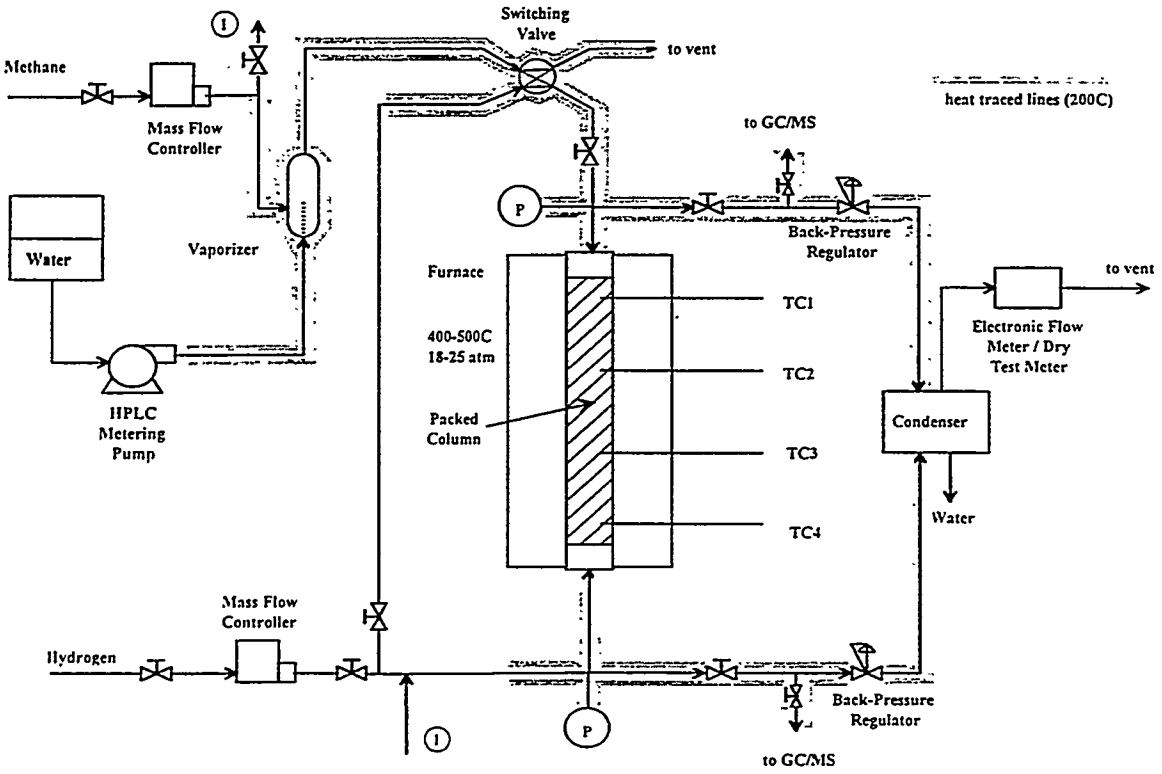


Figure 2. Schematic of Binary Desorption Unit

The modified lab process equipment for carrying out CO_2 sorption-desorption kinetic studies and for testing the SER-steam methane reforming reaction process is shown in Figure 3. Two sorption columns have been built: (a) 1.1cm ID, 213.4 cm long column for sorption experiments to test the performance characteristics of sorbents for CO_2 under SERP-SMR process conditions, and (b) 3.8 cm ID and 177.8 cm long column for investigating the SERP-SMR process steps.



Schematic of H2-SER Test Apparatus.

Figure 3. Schematic of Laboratory SER Reactor-Sorber System

Results and Discussion

High Temperature Sorbents for CO_2

The following criteria were developed for an acceptable CO_2 sorbent for performing steam-methane reforming by the SER concept:

(a) CO_2 working capacity > 0.3 mmol/g at 300-500°C in the presence of steam at high partial pressure (pH_2O) and at low partial pressures of CO_2 (pCO_2, 0.1 to 1 atm ; $(pH_2O)/(pCO_2) > 20$);
(b) Fast ad(de)sorption kinetics for CO_2 at reaction and regeneration conditions;
(c) Stable CO_2 sorption capacity after repeated sorption/desorption cycles;
(d) Adequate mechanical strength after cyclic exposure to high pressure steam;
(e) Readily scalable method for producing CO_2 sorbent in larger quantities;
(f) Environmentally benign sorbent and support.

Several families of CO_2 sorbents (both supported and unsupported) were prepared and evaluated with the screening tools listed above. A summary of the results is shown in Table 4. The data show that (i) most of the sorbents have adequate sorption capacity for CO_2 at low CO_2 partial pressures and in the absence of water, (ii) several of the materials lose the CO_2 capacity after multiple cycling between sorption and desorption steps; others have adequate reversible capacity after many cycles (iii) several supported sorbents with acceptable dry CO_2 sorption capacity have significant CO_2 sorption capacities in the presence of excess steam (pH_2O/pCO_2 ratios >20).

Figure 4 shows that the preferred sorbent, E4, exhibits stable CO_2 adsorption capacity even after weeks of exposure to high pressure steam.

Table 4. Summary of Materials Development Progress

	Reversible CO_2 capacity (mmol/g) at 400°C	Reversible CO_2 capacity (mmol/g) at 400°C	Cyclic Stability	Hydrothermal Stability at 400°C	Scale-up
Material	dry CO2 (TGA)	10 atm H_2O/ 0.30 atm CO_2 (BDU)	capacity loss under CO_2/N_2 cycling (TGA)	capacity loss after 1 day of steam** (BDU)	maximum scale produced (g)
MgO	0.20	-	loses 20% after 20 cycles	-	
CaO	0.05	-	-	-	
C3 (promoted Al_2O_3)	0.30 to 0.35	-	-	5% loss	200 g
C31 (promoted Al_2O_3)	0.25-0.30	0.08	loses 25% after 20 cycles	10% loss	
B2 (promoted Al_2O_3)	0.30-0.50	0.27	loses 40% after 60 cycles	30% loss	200 g
E4	0.50-0.60	0.53	stabilizes at 0.45 mmol/g after 20 cyc	no loss$^{\phi}$	3000 g

** 10 atm H_2O/0.30 atm CO_2

ϕ 30 day test

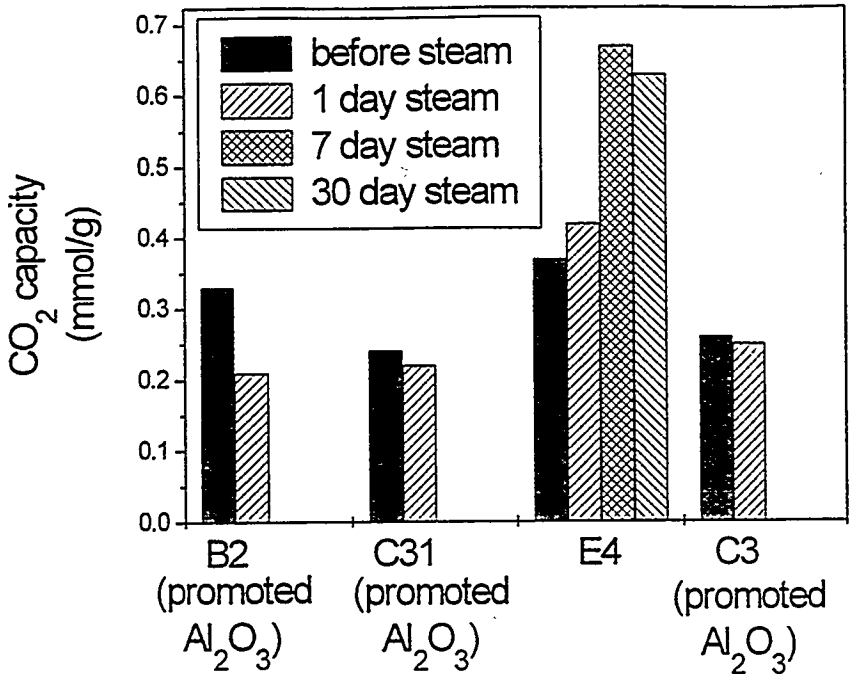


Figure 4. Hydrothermal Stability Test on HSTU

An initial criteria for stability was defined as (i) stable after >50 cycles of sorption/desorption in a thermogravimetric apparatus (TGA) and (ii) no loss in CO_2 sorption capacity after > 1 week exposure to 10 atm steam. Based on these criteria material E4 was selected for more detailed testing. Figure 5 shows that E4 loses some CO_2 capacity during the first 10 adsorption/desorption cycles, followed by a high and stable CO_2 capacity even after 60 adsorption/desorption cycles.

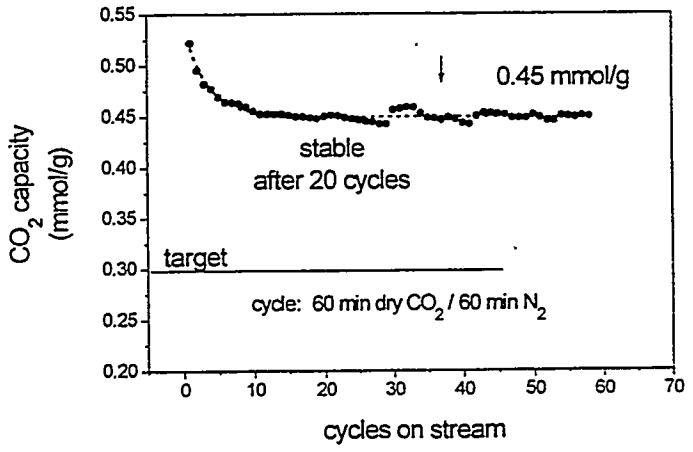


Figure 5. Sorption-Desorption Cycles of Material E4 with Dry CO_2 at 400°C on TGA

Figure 6 shows the adsorption isotherms for CO_2 at 400°C and 500°C in the presence of 10 atm steam.

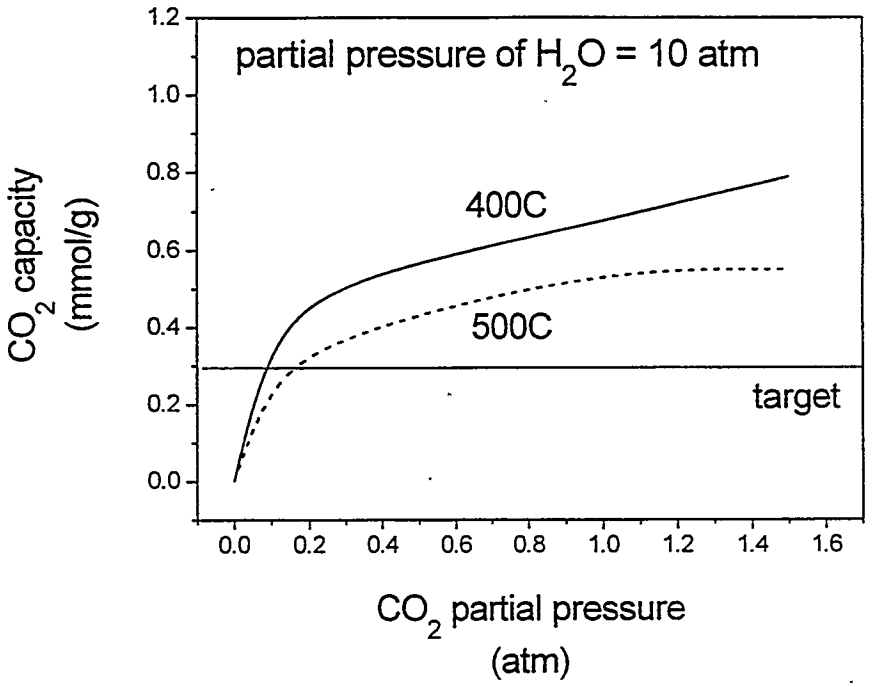


Figure 6. CO2 Isotherm Data for Sorbent E4 Collected on the BDU in the Presence of 10 Atmospheres of Steam

The data show that the reversible sorption capacity for CO_2 by E4 is above the target value at both temperatures for this application. Based on this work, E4 was selected for preparation in larger quantities. One kilogram quantity of E4 was prepared and packed into the laboratory adsorption column for evaluation of column dynamics.

Test of Sorption Properties in Lab Process Equipment

Carbon dioxide sorption column dynamics were conducted to evaluate the kinetics of CO_2 sorption. A sample of 159.3g of the sorbent E4 was packed into the 213.4 cm long stainless steel column. The column was maintained at 400°C and 1 atm during all experiments. The breakthrough experiments were conducted by flowing a feed mixture containing 65.7% CO_2 in N_2 at 1 atm and 400°C after thoroughly activating the sample at 400°C in nitrogen. The effluent CO_2 compositions were monitored as functions of time by a CO_2 infrared detector, and the flowrates were measured with an electronic flow meter. Both signals were directly fed to a computer acquisition system every 2 seconds. The adsorption run continued until complete breakthrough of CO_2 was observed. The column was then regenerated by flowing CO_2-free nitrogen at 400°C. The concentration of CO_2 and the flow rate of the effluent were continuously monitored during regeneration using the same analytical devices in order to study the desorption characteristics of CO_2. The length of the mass transfer zone (LMTZ) was calculated from the breakthrough data using a standard method (Sircar and Kumar, 1983).

A plot of the length of the CO_2 mass transfer zone (LMTZ) against the feed gas flow rate through the column (G rate) is shown in Figure 7. The mass transfer zone represents the length of column over which the CO_2 composition varies from the feed composition to essentially zero. Sharp mass transfer

zones are preferred in order to maximize the efficiency of the adsorption process. A MTZ length of only 28 cm was estimated for a typical industrial G rate of 5g mole/hr*cm^2. This is a relatively small value which indicates that the E4 material exhibits fast CO_2 sorption kinetics for use in the SERP-SMR process.

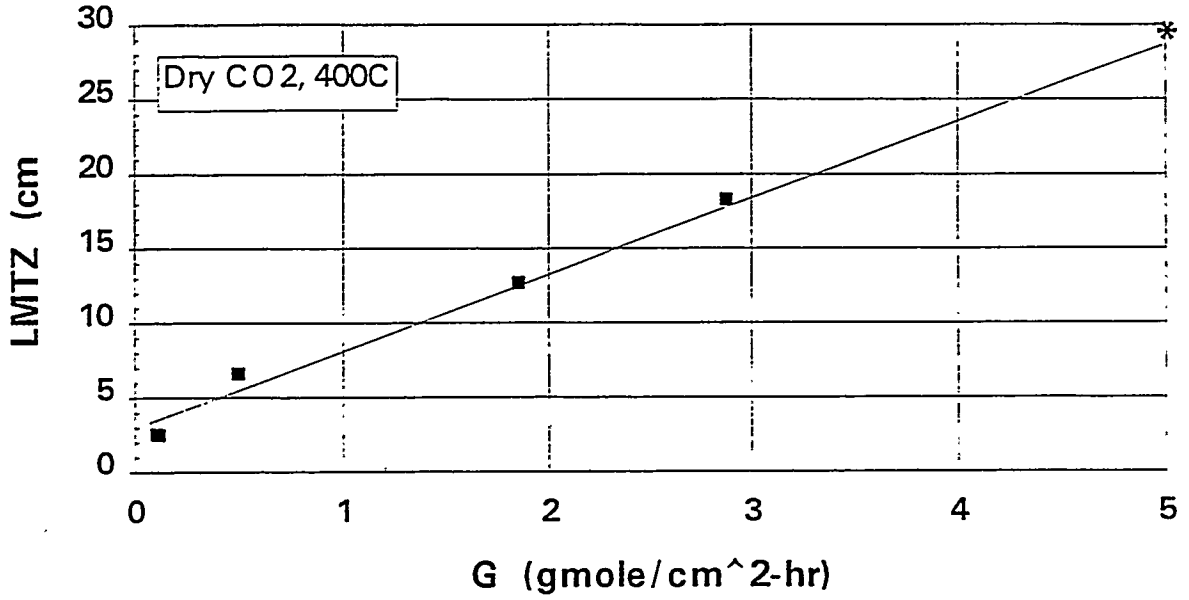


Figure 7. Length of Mass Transfer Zone as a Function of the Feed Rate

Desorption experiments were carried out by purging the sorption columns (saturated with pure CO_2 at 1.0 atmosphere and 400°C with pure nitrogen at different purge gas flow rates). Figure 8 represents the desorption curves at two different flow rates. They show the specific amounts of CO_2 removed from the column as functions of the total amount of purge gas effluent. The desorption characteristics are independent of purge gas flow rate which shows that the process is local equilibrium controlled. The solid line in Figure 8 is the calculated CO_2 desorption profile by local equilibrium theory (Sircar and Golden, 1996).

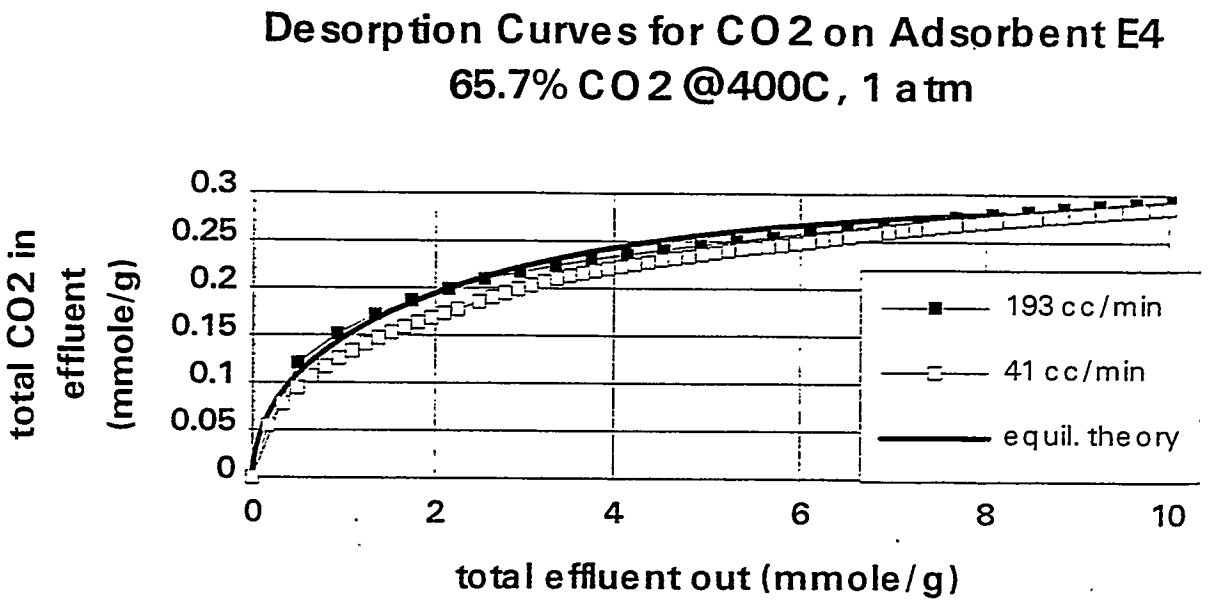


Figure 8. CO_2 Desorption Kinetics with E4 Sorbent in Laboratory Process Equipment

SER Reactor and Process Design

A novel reactor system for carrying out SERP-SMR concept has been designed (Figure 9). The concept will require a reactor/adsorber system which can (1) accommodate both the reaction medium (i.e., multiple packed columns (or tubes) containing admixture of sorbent and catalyst pellets) and the heat transfer system, (2) approximately maintain isothermal conditions (300-500°C) across equilibrated sections of the adsorption-reaction column, and (3) supply heat to the mobile adsorption-reaction transfer zones in the packed columns. During the reaction/sorption step of the SERP-SMR process, a reaction mass transfer zone (RMTZ) travels along the bed from the feed end to the product end, and energy must be supplied for the net endothermic reaction and adsorption process. Heat must also be supplied to the reactor during the endothermic desorption step (depressurization and purge). The device must also keep the packed column in intimate but indirect contact with the heat transfer fluid. Traditional methods of heat exchange based on the transfer of sensible heat are impractical for SERP-SMR since an infinite flow rate of heat transfer fluid is required to obtain nearly isothermal conditions along the column length. A novel shell and tube reactor system has been developed to meet these requirements. Reactant gas mixture or desorbed gases flow through the tubes which contain the admixture of catalyst and adsorbent. A recycled heat transfer fluid (HTF) vapor undergoes condensation on the shell-side to provide heat during the reaction/sorption step. Since the HTF always remains at its condensing temperature, the reactor tubes remain nearly isothermal. Also since condensation occurs only where the bed temperature drops (at the RMTZ), heat is only transferred into the section of the packed column where it is required.

Preliminary Design and Economic Analysis

A preliminary process flow diagram for the SERP-SMR has been completed with energy and mass balances. In addition, a first pass economic analysis has also been completed. The results clearly

indicate the potential for significant reduction in capital cost and H_2 production cost over conventional SMR process. A more thorough analysis will be carried out during the next year.

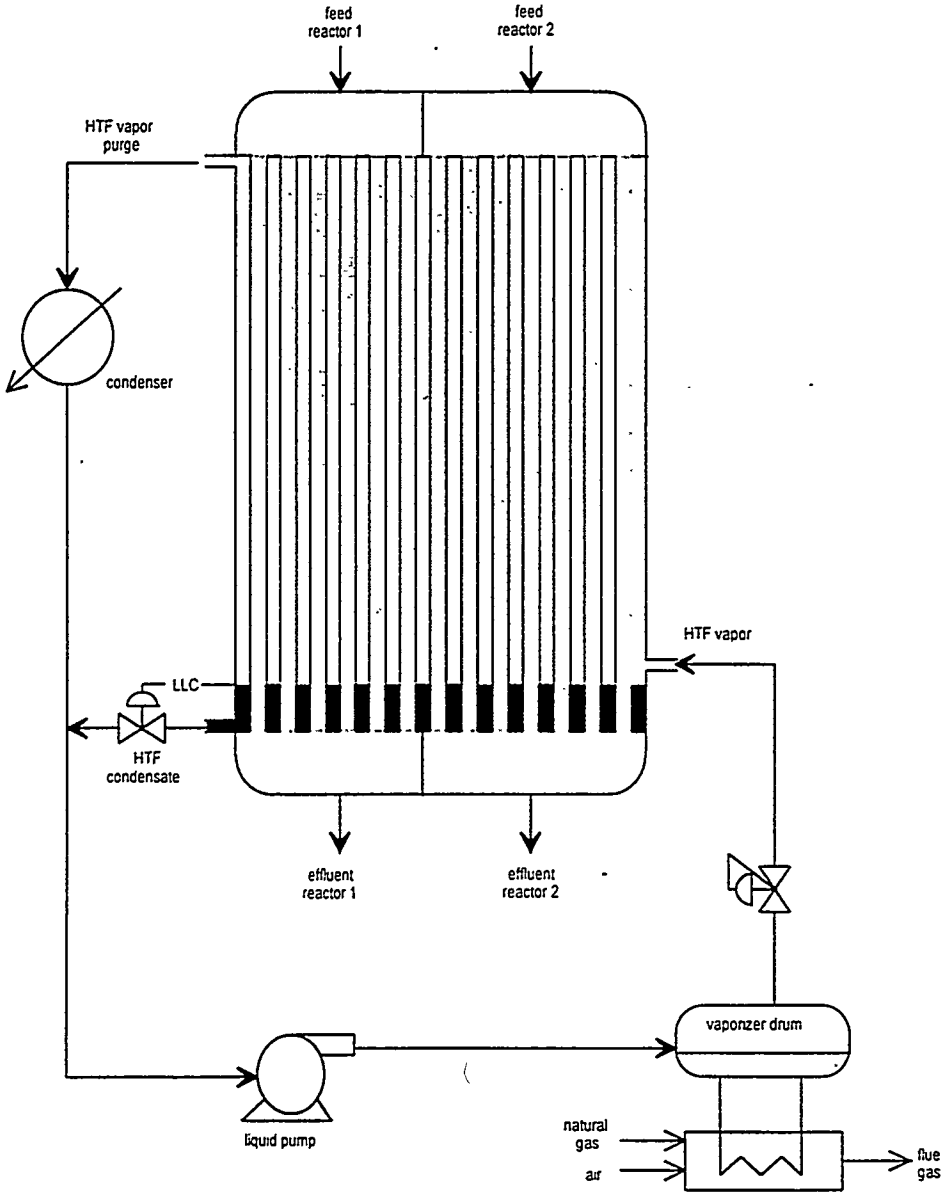


Figure 9. Shell and Tube Reactor-Sorber for SERP-SMR

Future Work

The following are the key goals to be completed for the remainder of the first phase:

1. Demonstrate SERP-SMR concept in the laboratory-scale apparatus.
2. Further optimize the preferred CO_2 adsorbent, E4, and prepare improved materials,
3. Develop laboratory scale data for more detailed process design and economic analysis.

Summary

Several families of sorbents which have CO_2 sorption capacity of larger than 0.3 mmol/g (target) at 300-500°C and in the presence of excess of steam have been identified. Several of these materials are stable after multiple adsorption/desorption cycles. One sorbent, E4, has been scaled up to three kilogram quantity and tested in the laboratory process equipment for evaluating CO_2 sorption-desorption column dynamics. The material has been found to have fast sorption-desorption kinetics for CO_2 which is desirable for this process.

A novel reactor has been designed for carrying out the SERP-SMR process under near isothermal conditions. A preliminary process flow diagram has been prepared by integrating this reactor into the SERP H_2 production scheme. A first pass economic analysis indicates that H_2 can be potentially produced at a significantly lower cost by using SERP-SMR concept compared to the conventional SMR-PSA route. The project is on track from a technical viewpoint and the goals and timetable do not need to be changed for the rest of the development program.

References

Anand, M., Sircar, S., and Carvill, B.T., "Processes for Operating Equilibrium Controlled Reactions," U.S. Patent Pending (1995).

Brun-Tsekhovoi, A.R., Zadorin, A.N., Katsobashvili, Ya.R., and Kourdyumov, S.S., "The Process of Catalytic Steam-Reforming of Hydrocarbons in the Presence of Carbon Dioxide Acceptor," *Hydrogen Energy Process VII, Proceedings of the World Hydrogen Energy Conference*, Pergamon Press, **2**, 885 (1986).

Carvill, B.T., Hufton, J.R., Anand, M., and Sircar, S., "Sorption Enhanced Reaction Process." AICHE J., in press (1996)

Gluud, W., Keller, K., Schonfelder, R. and Klempt, W., "Production of Hydrogen," U.S. Patent 1,816,523 (1931).

Goto, S., Tagawa, T., and Omiya, T., "Dehydrogenation of Cyclohexane in a PSA Reactor Using Hydrogen Occlusion Alloy," *Chem. Eng. Essays (Japan)*, **19**(6) 978 (1993).

Han, C., and Harrison, D.P., "Simultaneous Shift Reaction and Carbon Dioxide Separation for the Direct Production of Hydrogen," *Chem. Eng. Sci.*, **49**, 5875 (1994).

Nataraj, S.N., Carvill, B.T., Hufton, J.R., Mayorga, S.M., Gaffney, T.R., and Brzozowski, J.R., "Process for Operating Equilibium Controlled Reactions," U.S. Patent Pending (1996).

Hufton, J.R., Sircar, S., Baade, W.F., Abrardo, J.M., and Anand, M., "Integrated Steam Methane Reforming Process for Producing Carbon Monoxide," U.S. Patent Pending (1996).

Hufton, J.R., Sircar, S., Baade, W.F., Abrardo, J.M., and Anand, M., "Integrated Steam Methane Reforming Process for Producing Carbon Monoxide and Hydrogen," U.S. Patent Pending (1996).

Kadlec, R.H., and Vaporciyan, G.G., "Periodic Chemical Processing System," U.S. Patent 5,254,368 (1993).

Kirkby, N.F., and Morgan, J.E.P., "A Theoretical Investigation of Pressure Swing Reaction," *Trans. I Chem E.*, **72**, 541 (1994).

Sircar, S., Anand, M., Carvill, B.T., Hufton, J.R., Mayorga, S.G., and Miller, R.N., "Sorption Enhanced Reaction Process for Production of Hydrogen," *Proceedings of the1995 U.S. DOE Hydrogen Program Review*, **1** 815 (1995).

Sircar, S., and Kumar, R., "Adiabatic Adsorption of Bulk Binary Gas Mixtures: Analysis by Constant Pattern Model," I&E.C., Proc. Des. Dev., **22**, 271 (1983).

Sircar, S., and Golden, T.C., "Isothermal and Isobaric Desorption of CO_2 by Purge," I&E.C. Research **34**, 2881 (1995).

Vaporciyan, G.G., and Kadlec, R.H., "Equilibrium Limited Periodic Separating Reactors," *AIChE J.*, **33**, 1334 (1987).

Vaporciyan, G.G., and Kadlec, R.H., "Periodic Separating Reactors: Experiments and Theory," *AIChE J.*, **35**, 831 (1989).

List of Figures

Figure 1. Process scheme showing the reaction and regeneration steps for SERP-SMR

Figure 2. Schematic of Binary Desorption Unit

Figure 3. Schematic of Laboratory SER Reactor-Sorber System

Figure 4. Hydrothermal Stability Test on HSTU

Figure 5. Sorption-Desorption Cycles of Material E4 with Dry CO_2 at 400°C on TGA

Figure 6. CO_2 Isotherm Data for Sorbent E4 Collected on the BDU in the Presence of 10 Atmospheres of Steam

Figure 7. Length of Mass Transfer Zone as a Function of the Feed Rate

Figure 8. CO_2 Desorption Kinetics with E4 Sorbent in Laboratory Process Equipment

Figure 9. Shell and Tube Reactor-Sorber for SERP-SMR

HYDROGEN MANUFACTURING USING PLASMA REFORMERS

L. Bromberg, D.R. Cohn, A. Rabinovich
Plasma Fusion Center
Massachusetts Institute of Technology
Cambridge, MA 02139
and
S. Hochgreb, C. O'Brien
Department of Mechanical Engineering
Massachusetts Institute of Technology
Cambridge, MA 02139

Abstract

Manufacturing of hydrogen from hydrocarbon fuels is needed for a variety of applications. These applications include fuel cells used in stationary electric power production and in vehicular propulsion. Hydrogen can also be used for various combustion engine systems. There is a wide range of requirements on the capacity of the hydrogen manufacturing system, the purity of the hydrogen fuel, and capability for rapid response. The overall objectives of a hydrogen manufacturing facility are to operate with high availability at the lowest possible cost and to have minimal adverse environmental impact.

Plasma technology has potential to significantly alleviate shortcomings of conventional means of manufacturing hydrogen. These shortcomings include cost and deterioration of catalysts; limitations on hydrogen production from heavy hydrocarbons; limitations on rapid response; and size and weight requirements. In addition, use of plasma technology could provide for a greater variety of operating modes in particular the possibility of virtual elimination of CO_2 production by pyrolytic operation. This mode of hydrogen production may be of increasing importance due to recent additional evidence of global warming.

1. Current Year Results

In the first year of the program supported by the Advanced Utility Concepts Division, Office of Renewable Energy, Department of Energy, the following activities have been accomplished (O'Brien, 1996):

- Plasma reformer design concepts (including both arc plasma and microwave plasma technology for a range of applications).
- Chemical equilibrium and stability calculations for different modes of plasma reformer operation.
- Construction of experimental plasma reformer for gas and liquid reforming.
- Initial tests of experimental plasma reformer devices.
- Energy system analysis of methane plasma reforming with partial oxidation, steam reforming, and pyrolysis.

This report describes progress in these five areas and discusses directions for future work. The work during the first year has concentrated on the study of methane reforming. Methane is of interest because as a gaseous fuel it lends itself to easy operation. In addition, kinetic and thermodynamic processes are well known and easily modeled. Furthermore, reforming of heavier hydrocarbons involve quick decomposition of large molecules into smaller ones, the rate limiting step for reforming being their conversion to H_2. (Valibekov 1975; Kassel 1932)

2. Plasmatron Design

The initial plasmatron designs have been developed for partial oxidation reforming. A schematic diagram of the plasmatron used for the experiments is shown in Figure 1. The power supply is obtained from a commercial plasma cutting system (Thermal Dynamics Pak Master 25). The plasmatron consists of a commercial cathode, also from the plasma cutting system, a water cooled anode, and an insulator. The cathode is a steel rod with a zirconium insert at the tip. A swirl flow is generated by tangential gas injection coupled with helical groves in the cathode tip. In order to stabilize the arc, there is a step-like increase in the size of the anode. The anode root of the arc strikes the region just past the edge of the step. The net result is a rise in voltage and increased stability of the arc. The step has the additional advantage that the length of the arc is nearly independent of the flow rate, making it possible to independently vary the power and the mass flow.

The gap between the cathode and the anode is provided by a fiber reinforced epoxy (G-10) insulator. The insulator is cooled by the anode and has long life. The lifetime of the experimental plasmatron is determined by erosion of the cathode and, to a lesser degree, by the anode.

The device can be used to operate in oxygen-based gases (air, oxygen) and nitrogen. At the present time only air has been used. The discharge between the two electrodes generates large amounts of heat that raise the temperature of the gases to 10000-20000 K. The gas at this temperature is electrically conducting, a necessary condition in order to carry electrical current. The plasma is started (by breaking down the gas) with high voltage RF pulses generated by the same power supply. The plasmatron operates at 1-2 kW with flow rates less than 0.5 g/s.

The reactants (additional air and hydrocarbons) are injected downstream from the anode root. The air to hydrocarbon ratios and the total flow rate can be changed without affecting the arc characteristics (voltage, current and stability).

The air and fuel rates were measured by rotameters. The gas composition was determined using a gas chromatograph. The GC has two columns, one for separating hydrogen, oxygen, nitrogen, carbon dioxide and monoxide, and methane, and a second column to separated higher hydrocarbons (ethylene, acetylene and propane). The gas was analyzed through a water-cooled sampler that can be radially and axially displaced along the reactor.

It was determined that a fraction of the power dissipated by the plasma was removed through the cooling water of the anode (the only part cooled in the design). About 30-40% of the energy dissipated in the plasmatron is removed by the water-cooled anode. There are several possible reasons for the low efficiency. Most plasmatrons operate at power levels higher than 10 kW, while our initial plasmatron operates at much lower powers (1-2 kW). The low power results in a small plasma with large surface to volume ratio and therefore increased radiative losses.

The amount of energy removed by the cooling water depends on the reaction. For exothermic reactions with increased gas temperature, the losses are larger than for endothermic reactions., decreasing the overall reformer efficiency.

3. Experimental results

To-date, only experiments with partial oxidation of methane have been carried out. The source of oxygen has been air. A system has been assembled, but not yet tested, for investigating the reforming of iso-octane.

An initial set of experiments has been performed in order to determine the potential for plasma reforming. There are two major knobs, the air-to-fuel ratio and the specific energy input (power divided by flow rate). The air-to-fuel ratio can be characterized by the equivalence ratio λ, defined as the molar air-to-fuel ratio divided by the ratio at stochiometric combustion. For methane, partial oxidation occurs at $\lambda = 0.25$. The experiments covered a range of equivalence ratios from $\lambda = 0.15$ to $\lambda = 0.45$. The specific energy input was varied from 5 to 25 MJ/kg CH_4. The residence time in the reactor varied from 6 to 30 ms.

Figure 2 shows the output moles of H_2O and CO_2 (normalized to the CH_4 moles input) as a function of λ. The output of these compounds is nearly proportional to λ. This is due to the two-step nature of the partial oxidation mechanism. Partial oxidation consists of an initial rapid combustion of the fuel to CO_2 and H_2O followed by a slower reforming of the resulting mixture to H_2 and CO. Other species did not show strong variations with λ over the range investigated.

The conversion yields of methane a mixture of H_2 and CO shows a strong dependence on the specific energy input. This is consistent with the high activation energy of the reaction, with an exponential dependence on the reaction rate vs. temperature. Figure 3 shows the residual CH_4 and O_2 amounts decrease as the specific energy input is increased, and Figures 4 and 5 show the normalized yields of H_2 and CO under the same conditions. The hydrogen yield is about 0.5 moles per mole of CH_4. Methods of increasing the yield are being explored at the present time. These plans are discussed in section 5.

4. Modeling

Kinetic calculations have been performed in addition to thermodynamic equilibrium calculations. The evolution of a mixture reacting adiabatically at constant pressure has been considered. This analysis gives the product distribution as a function of residence time, and thus the minimum time required for conversion to the equilibrium composition. The minimum energy requirements for the ignition of the reaction within the reformer and the energy cost of H_2 production can then be determined for a simple physical model of the plasma reformer in the limiting cases of a plug flow and perfectly stirred reactor. These minimum energy requirements are quite different from the thermodynamic minimum energy input; they are associated with the energy required to overcome the reaction energy barrier and reflect the energy cost of performing the reaction within a finite time.

The results from the plug flow model are shown in Figure 6 for a specific energy input of 10 MJ/kg CH_4, corresponding to an initial temperature of the reactants of 1500 K. All concentrations are normalized to the initial amount of CH_4. There is a rapid change in concentration over a relatively short period of time accompanied by a sharp rise in temperature ("ignition"). The ignition delay decreases with increasing specific energy input (i.e., increasing initial temperature). After ignition, the composition of the reactants is not close to equilibrium. Instead, the composition changes slowly toward equilibrium. The rate of change also increases with increasing specific energy input. At 15 MJ/kg CH_4, the equilibrium is reached in about 100 ms.

The results for the perfectly stirred reactor (PSR) are shown in Figure 7. The residual amount of CH_4 and the reformed hydrogen (normalized to the initial CH_4) is shown as a function of the specific energy input. These calculations assume a one-step reaction mechanism and a residence time of 50 ms. The results are not very significantly affected by changes in the residence time, but are much more sensitive to the specific energy input. Again, it seems that a minimum of about 10 MJ/kg CH_4 is required in order to get the reaction to near completion.

5. System Analysis

Two activities were pursued on this topic during the first year: an assessment of the overall hydrogen production costs, and potential applications of the compact reformer in a reformer/fuel cell system.

5.1. Hydrogen costs

At the present time, it is expected that the energy consumption for methane is on the order of 10 MJ/kg CH_4. This is based on kinetic modeling and on previous results with liquid hydrocarbons. In addition, by utilizing heat regeneration (as described below) it is possible to decrease the energy consumption to about 4 MJ/kg. The initial experimental results indicate that for an energy consumption of 10 MJ/kg, the hydrogen yield is about 40-50% of the maximum expected. We expect that the poor results of these preliminary experiments are due to either heat losses in the reactor or incomplete mixing in the reactor channel. Utilizing a value of 4 MJ/kg CH_4 it is possible to determine the cost of hydrogen.

The cost of methane (assuming that methane is the hydrocarbon fuel) is about $2-4 /MMBTU. A methane-based partial oxidation reformer, followed by a water shift reactor, can convert into hydrogen over 80% of the available energy. With 4 MJ/kg as the specific energy input, and assuming that electricity is at $0.05/kWhr, then the electricity cost for hydrogen manufacturing is about $1.5 /MMBTU. The cost of the plasmatron system, (including power supply, flow system, plasmatron, and replacement parts) is small compared with the cost of the electricity. Therefore, the cost of manufacturing the hydrogen from methane is about 1/3 to 2/3 of the initial cost of the methane.

The above costing assumes that the carbon monoxide that is produced in the system has been reacted to produce additional hydrogen (via a water shift reaction). At the present time we are planning experiments to see if the water shift reaction can be achieved in the exhaust of the plasma reactor.

It may be possible to decrease the energy expenditure further. Several of the options that are being considered include the use of higher hydrocarbons (such as liquid ones), the use of a high temperature material to produce a packed bed reactor (to improve the mixing), and improved reactor design with increased efficiency.

5.2. Plasmatron/fuel cell systems

The performance of a plasmatron reformer/fuel cell system has been preliminarily evaluated from a system point of view. Operation with either partial oxidation, steam reformer, or pyrolytic decomposition has been investigated. Pyrolytic decomposition is attractive because hydrogen could be produced from hydrocarbon fuels with virtual elimination of CO_2. This capability is potentially important in light of increased evidence of global warming due to CO_2 production. A total energy pathway diagram showing where the inefficiencies and the emissions occur is being prepared.

A key feature of the plasma reformer/fuel cell system is that a modest fraction of the electricity produced by the fuel cell is needed to power the plasmatron. The overall system efficiency (conversion of chemical energy to electricity) is potentially high.

Of the several methods that will be investigated in this program (steam, partial oxidation, and pyrolysis), partial oxidation is the simplest, both from a modeling and experimental point of view. The experimental work and the chemical modeling during the first year have been exclusively dedicated to partial oxidation.

It is not required that all the energy required in the reforming process be provided electrically by the plasma reformer; a system analysis of the case of preheating the reforming gases using either the hot exhaust gases from the plasma reformer or the fuel cell or burning the fuel cell off-gas has also been preliminarily investigated.

The efficiency of the plasmatron/fuel cell system as a function of the reforming temperature in the reformer is shown in Figure 8, assuming that the fuel cell efficiency is 60%. There is no heat regeneration, and the calculations are performed using thermodynamical equilibrium, with partial oxidation reforming of methane. The maximum efficiency of the system is about 42%. At the low temperatures, the conversion is very poor while at the high temperatures, conversion is complete, but the plasmatron energy consumption increases. The overall efficiency, therefore, have a maximum at intermediate temperatures.

Kinetic calculations and the experimental results, however, have determined that close to complete conversion occurs at energy consumption of about 10 MJ/kg CH_4. The experiment also indicates that about 10 MJ/kg CH_4 are required for the reaction. 10 MJ/kg CH_4 corresponds to an equilibrium product temperature of 1500 K. At that temperature, the efficiency of the system is decreased from the maximum, which occurs at lower temperatures. The overall efficiency for T_{final} ~1500 K is about 36%.

With the use of a heat exchanger, the thermal enthalpy of the reformate can be used to preheat the air, methane or their mixture prior to injection into the plasmatron. In this way the net external heating requirements from the plasmatron can be reduced. Thus the net system efficiencies can be considerably higher. The net effect of using the preheating is that of reducing the plasmatron input power.

Heat regeneration can be modeled by assuming higher initial temperature of the inlet gases. The overall system efficiencies for reactor temperatures of 1500 and 1950 K, are shown in Figure 9 as a function of the initial temperature of the feedstock. The increase in the efficiency is approximately linear with the temperature. The maximum amount of regeneration from the reformate of the plasmatron in a heat exchanger is dependent on the maximum operating temperature of the heat exchanger.

It is possible to integrate the heat exchanger into the design of the plasmatron reactor. Figure 10 shows such an arrangement. The incoming gases are heated by the outgoing hot gases. The heat exchanger works such that the temperature of injection of the gases could be close to the reactor temperature. It is probably limited by the melting point of the material in the heat exchanger.

This analysis assumes that the entire feedstock mixture was raised in temperature. This may have the problem of the hot feedstock reacting prior to the reactor. Therefore, it would be preferable to heat exclusively the air, with the hydrocarbon injected separately at lower temperatures.

The above models can be used to estimate the overall efficiencies of a plasmatron/fuel cell system for different reforming technologies. The comparison presented here assumes methane reforming with equilibrium composition and with a fuel cell with constant efficiency ($\eta_{fc} = 0.6$). In reality, it is likely that different reforming technologies are better suited to different fuel cell technologies, with different efficiencies. Such a comparison will have to wait until the actual reformate composition is determined from kinetics modeling and from experiments. The issue is further complicated by the possibility of combining a plasma reformer with preheating the reforming gases by the exhaust gases from the plasmatron or the fuel cell or by burning the fuel cell off-gases.

In order to preliminarily compare the different methods of reforming, the efficiency of a plasmatron/fuel cell system is shown in Figure 11 for steam reforming, partial oxidation and thermal decomposition as a function of temperature of the reformate. The highest overall efficiency is for partial oxidation. The lowest temperature corresponds to the case where there is no additional input of heat, utilizing the energy from the exothermic reaction (adiabatic partial oxidation). Steam reforming is less efficient than partial oxidation. Pyrolysis is the least efficient, mainly due to the fact that the energy in the carbon is not used. However, as mentioned previously it has the advantage of virtual elimination of CO_2 production.

At the lower temperatures, the efficiency for all reforming methods is non-optimal because of incomplete conversion. As the temperature increases, the conversion increases. The heating value of the reformate increases faster than the energy expenditure. After the optimal temperature, the energy expenditure increases faster than the energy from the reformate, and the overall efficiency drops.

Since air is the source of oxygen for partial oxidation, it is necessary to determine the expected levels of NO_x in the products. Equilibrium calculations have indicated that only at the highest temperatures is the NO_x equilibrium concentration above 1 ppm. Just as the non-equilibrium effects help in the case of soot, they may hurt in the case of NO_x. However, NO_x will probably not be an issue because of the very fuel-rich operation. The kinetic calculations are required to address the NO_x issue. This has not been done yet.

6. Future Directions

During the first year of the program, a simple experiment has been designed, built and tested for methane. In addition, chemical kinetic and equilibrium models have also been employed in order to understand the process. In this section, the planned future work will be described.

6.1. Plasmatron

The plasmatron that has been initially used operates at about 1-2 kW. This is the smallest plasmatron that could be constructed with steady state operation. Although sufficient for the preliminary experiments, scaling to larger plasmatron powers will be necessary to understand the scaling of the process. Higher power should result in more efficient operation (since the losses are surface related). Operation at 10 kW followed by operation at 50-100 kW will be tested later in this program.

The design of plasmatron above 10 kW is fundamentally different from the small plasmatron in the first phase of this program. The small plasmatron does not require external means to prolong its life, with a gas vortex being sufficient. For the higher power plasmatron the presence of a magnetic field is required to spin the arc roots in order to minimize erosion of the electrodes. (Pfender, 1978; Camacho, 1988)

Additional experimentation with the design of the plasmatron could result in more homogeneous and more stable operation. This would result in lower energy consumption and increased gas utilization. Both of these would result in a lower cost of reformed hydrogen. In particular, tests with increased reactor size that result in increased residence time will be tested. Increased residence time can be achieved by partially insulating the gases from the walls or by increasing the temperature of the walls, such as by utilizing ceramic walls. .

In addition to power scaling, the present plasmatron cross sectional area increases substantially after the arc region in order to decouple the downstream gas addition from affecting the discharge parameters. This expansion results in fast-cooling of the gas, and the increased velocity reduces the residence time. Methods of stabilizing the discharge while at the same time maximizing the temperature will be investigated.

The plasmatron will also be modified in order to be able to operate with liquid hydrocarbons.

A small fraction of the effort will be spent investigating the characteristics of a microwave plasma. During the first year of this program a 1-2 kW microwave plasma was constructed. Testing of this plasmatron will continue in the second year. The microwave plasma produces larger, more uniform and stable plasmas at smaller powers than the DC plasmatron, although with reduced operation range (smaller flow rates, more limited composition, etc.).

6.2. Operating gases and liquids

During the first year of the program, the only hydrocarbon investigated was methane. The experiments have been run under partial oxidation conditions, with $\lambda = 0.1\text{-}0.5$. This is partially due to the need to prevent soot formation, which would accumulate in the gas sampling system used for GC operation. With FTIR operation this limitation is minimized, and testing under reducing conditions will be done in the near future. Plasma reforming with either steam reforming and thermal decomposition (pyrolysis) will be investigated.

One of the main advantages of the plasma reformers is their ability to process heavier hydrocarbons. This capability is due to the uncatalyzed thermal cracking. The problem of catalyst contamination by heavy hydrocarbon sludge or graphitic buildup would be eliminated. During the second year, heavier gaseous hydrocarbons (such as propane) and liquid hydrocarbons will be tested in the plasmatron. These hydrocarbons are easier to reform than methane and should reduce the cost of production of hydrogen. (Kaske, 1986; Muller, 1988)

The plasmatron has been tested with air as the plasmatron gas. Other gases will also be tested. Since only a small upstream gas flow rate is needed (compared with the amount of gas that can be introduced downstream), many gases, including hydrogen, could be used. In addition to hydrogen, water or light hydrocarbons can be used as the plasma gas. During the second and third year of this program, the effect of the ratio and composition of upstream vs. downstream inlet gases will be investigated.

One material, not a hydrocarbon, that is in the work plan is ammonia. This material has high hydrogen content and should be easily decomposed in the plasma reactor with relatively small energy expenditures. This material could be produced in substantial amounts in biofuels, and it is easily compressed to a liquid at room temperature. It is also easy to decompose.. Nitrogen and hydrogen gas are the products of the decomposition.

Finally, to maximize the energy utilization, the energy content of the hot plasma reformer products will be used in downstream reactors. In particular, the compatibility of a water-shift reactor downstream of a partial oxidation plasma reformer will be investigated.

6.3. Modeling

Equilibrium and chemical kinetic modeling have been performed during the first year. The modeling will be used to interpret the results and to indicate modifications to the experiment. The goal is to explore the tradeoffs between the purity of the hydrogen and the energy expenditure.

The equilibrium modeling of methane processing in partial oxidation has been completed. The equilibrium modeling of other hydrocarbons in the presence of other gases (such as air, steam, etc.)

will be completed in the second year of the program. This is also the case for other possible fuels (such as ammonia).

The kinetic model of methane under partial oxidation conditions has also been partially completed. The model agrees quantitatively with the experiment. More complete modeling for methane and modeling with heavier hydrocarbons will be performed in the second year.

The modeling of thermal cracking of hydrocarbons, including nucleation and particle growth models for soot formation, requires very large and sophisticated models. These models are not available at the present time.

6.4. System analysis

During the duration of the program, continuous investigation of the plasma reforming process will be performed. The energy requirement, the composition of the reformate, the gas conversion efficiency, etc., will be reviewed in order to identify the broadest possible applications, the performance with alternate fuels, and the overall cost of the process.

In addition, methods of total energy utilization need to be explored. This includes the high energy content of the plasma reformate and the exhaust hydrogen gas that is not consumed by a fuel cell (for the plasma reformer/fuel cell system).

These system issues have been identified in the first year of the program, and models are being developed to analyze them.

References

Gray, B.F., J.F. Griffiths and G.A. Foulds, *Natural Gas Conversion* II, Elsevier Science Publ., The Netherlands, p 13 (1994)

Camacho, S.L. "Industrial -worthy plasma torches: State-of-the-art" *in Pure & Appl. Chem.*, Vol. **60**, No. 5, pp. 619-632 (1988).

Kaske, G., Kerker, L. and Muller, R. "Hydrogen Production by the Huls Plasma-Reforming Process", *Hydrogen Energy Progress* YI, Vol. 1, pp. 185-190 (1986).

L. S. Kassel. *J.Amer.Chem.Soc.*, 54, 3949, (1932)

Muller, R. " The Use of Hydrogen Plasma Processes in the Petrochemical and Iron-Smelting Industries", *Hydrogen Energy Progress* YII, Vol. **2**, pp. 885-900. (1988)

O'Brien, C., A. Rabinovich, L. Bromberg, D.R. Cohn and S. Hochgreb, "Hydrogen Production via Plasma Reformers", in *31st International Energy Conversion Engineering Conference* (Aug. 1996)

Pettre, M., C. Eichner and M. Perrin, *Trans Faraday Soc* **43** p 335 (1946)

Pfender, E. " Electric Arcs and Arc Gas Heaters" in *Gaseous Electronics*, Vol. **1**, pp. 291-398. (1978)

Valibekov Yu.V., Volodin N.L., Vursel F.B. "Macrokinetics of hydrocarbons and chlorohydrocarbons pyrolysis in plasma," *Khimiya visokih energii*, v.9, 1, 1975, p.55-62. (in rus.)

Vernon, P.D.F., M.L.H. Green, A.K. Cheetham and A.T. Ashcroft, *Catalysis Letters* **6** p181 (1990)

Acknowledgments

This work is funded by the US Department of Energy under contract number DE-FG04-95AL88002.

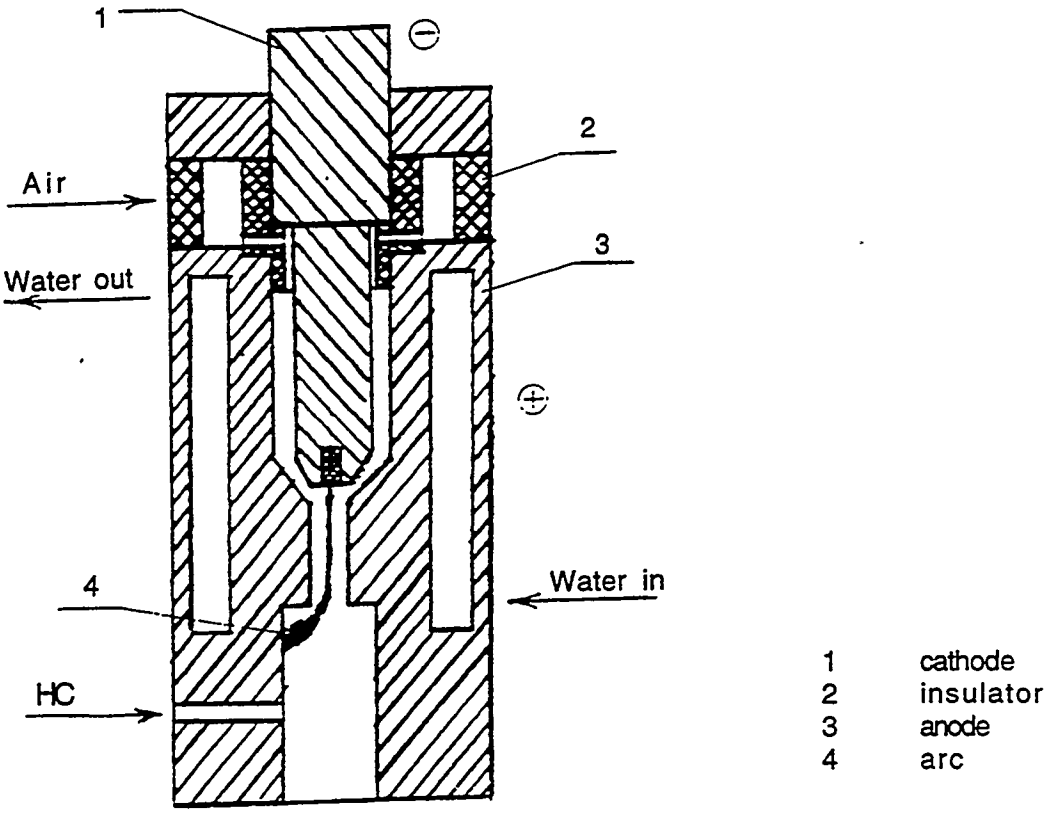


Figure 1. Schematic diagram of the experimental plasmatron

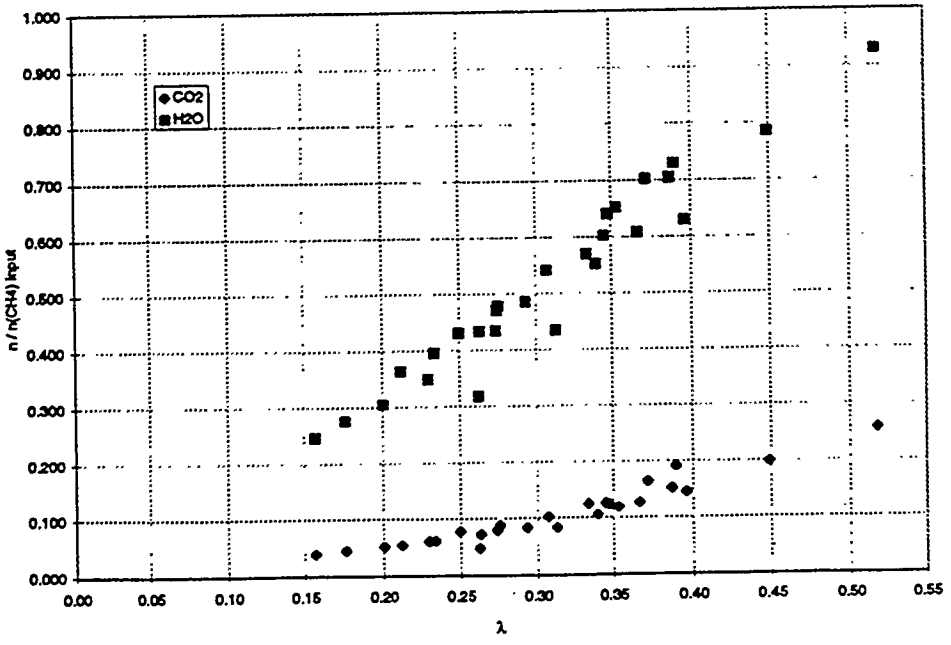


Figure 2. H_2O and CO_2 output vs equivalence ratio

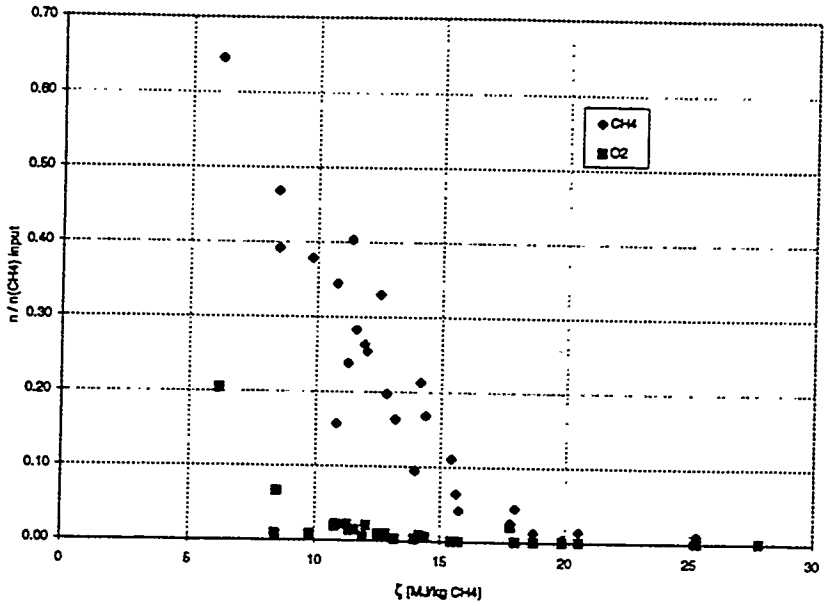


Figure 3. Residual CH_4 and O_2 (normalized to CH_4 input) vs. specific energy input

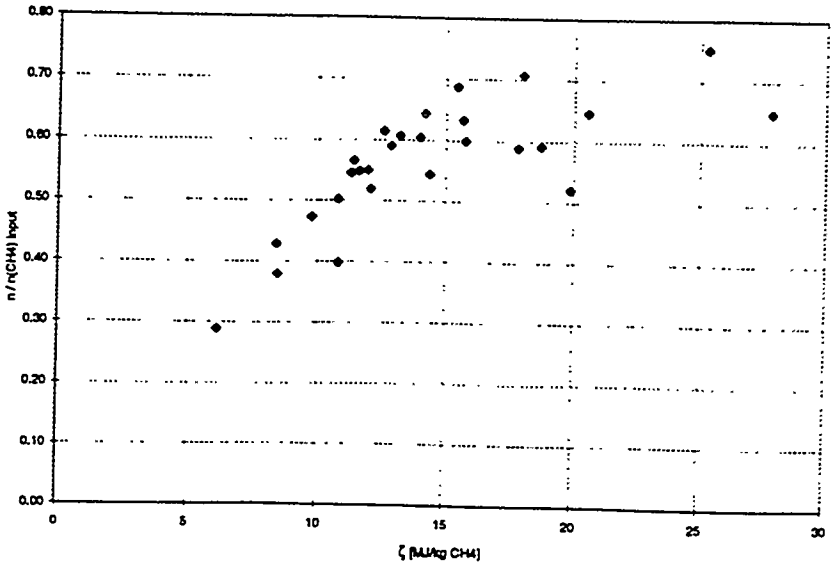


Figure 4. Output H_2 vs. specific energy input

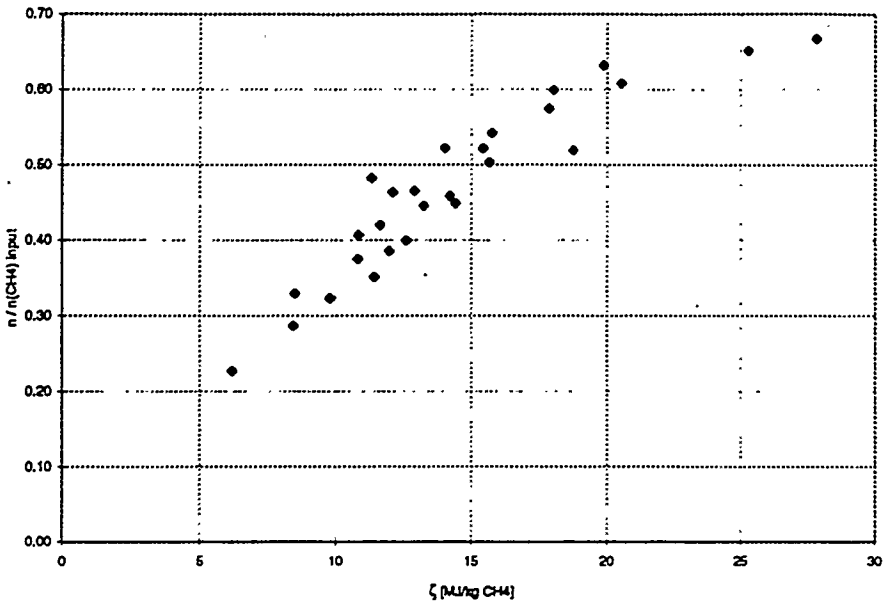


Figure 5. Output CO vs. specific energy input

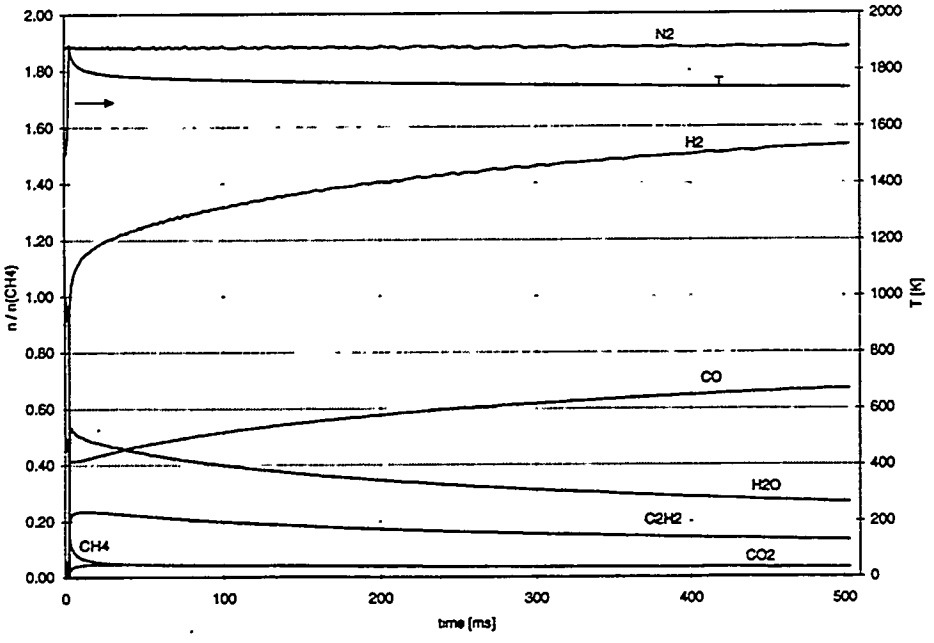


Figure 6. Normalized species concentrations and temperature as a function of time for a specific energy input of 10 MJ/kg CH_4 at 1 atm

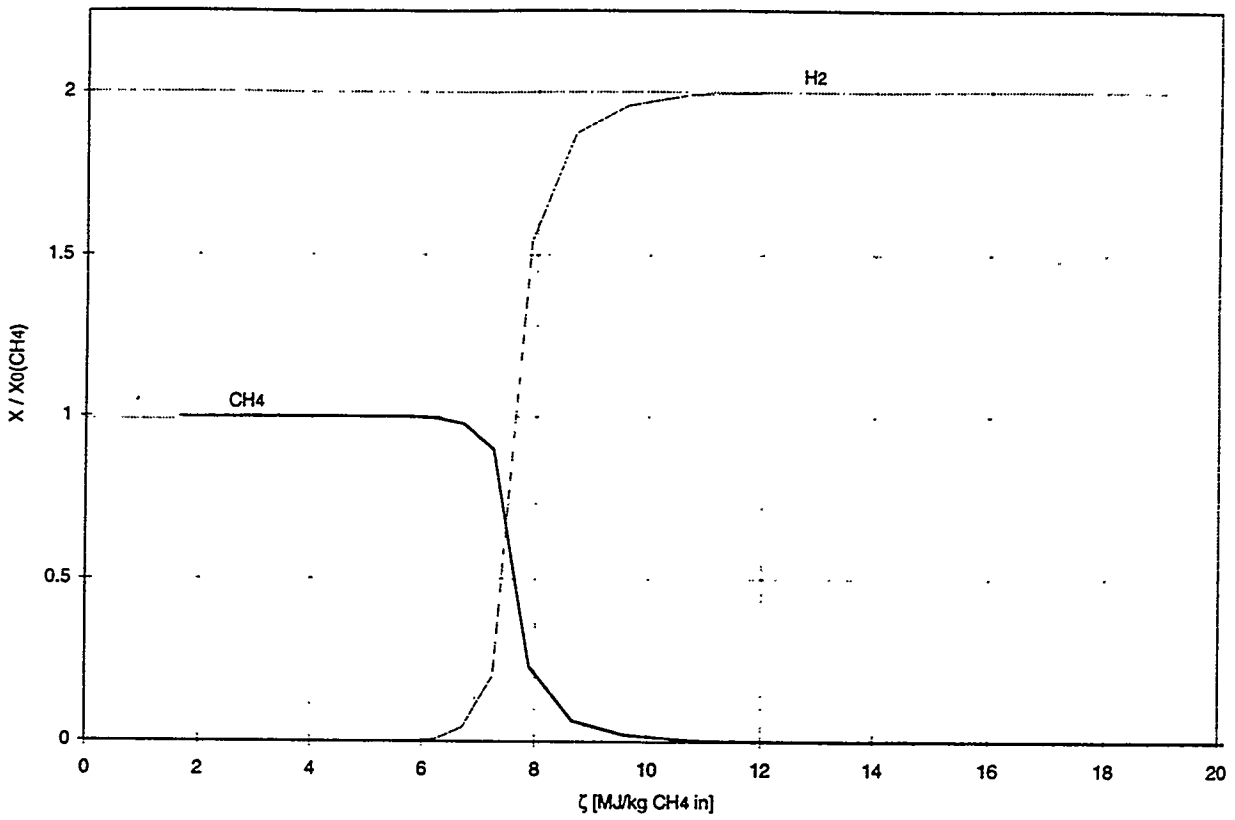


Figure 7. Normalized species concentrations as a function of specific energy input, at 1 atm

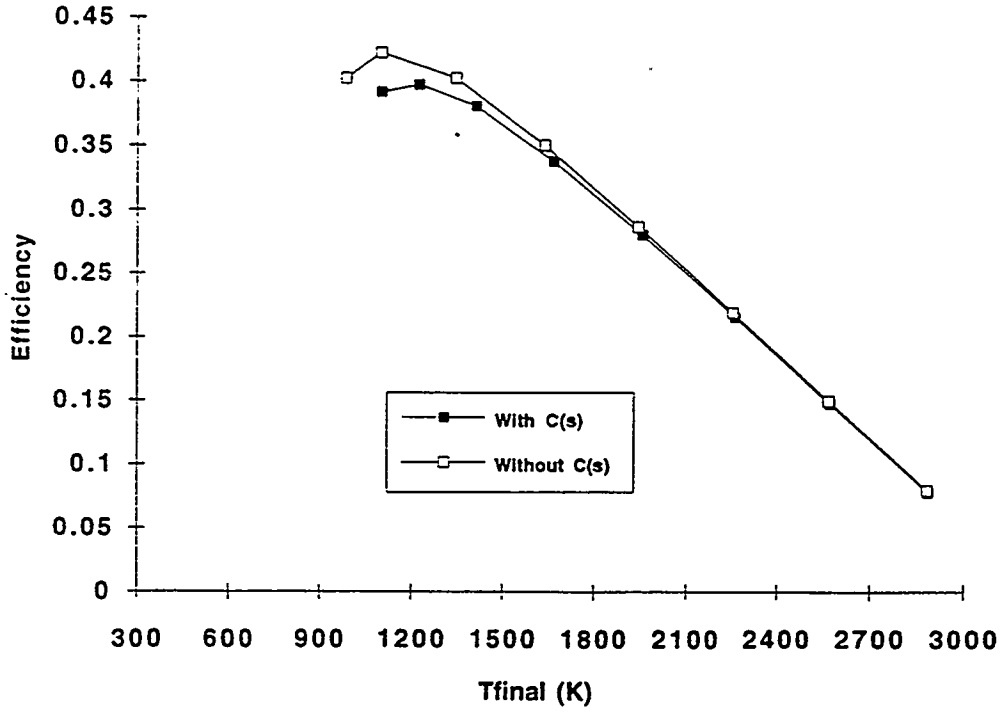


Figure 8. System efficiency η_s of the plasmatron/fuel cell system without heat utilization (partial oxidation of methane)

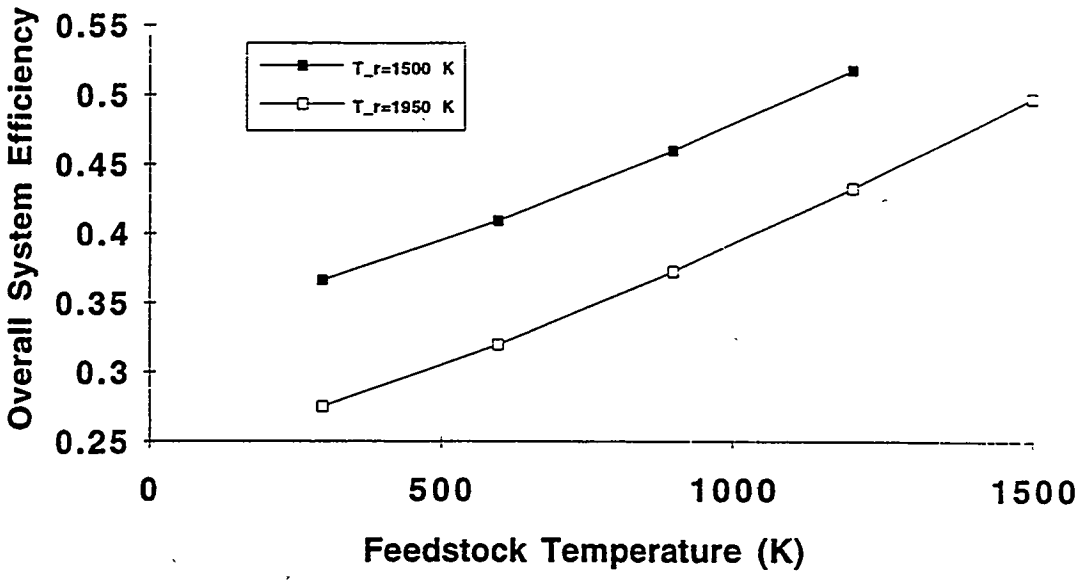


Figure 9. Overall system efficiency as a function of feedstock temperature in the case of preheating the stocks

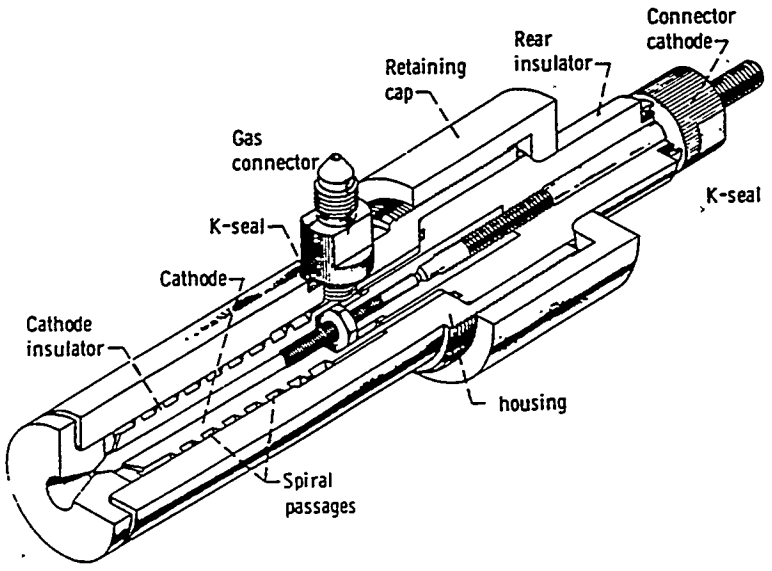


Figure 10. Regeneratively cooled arc jet

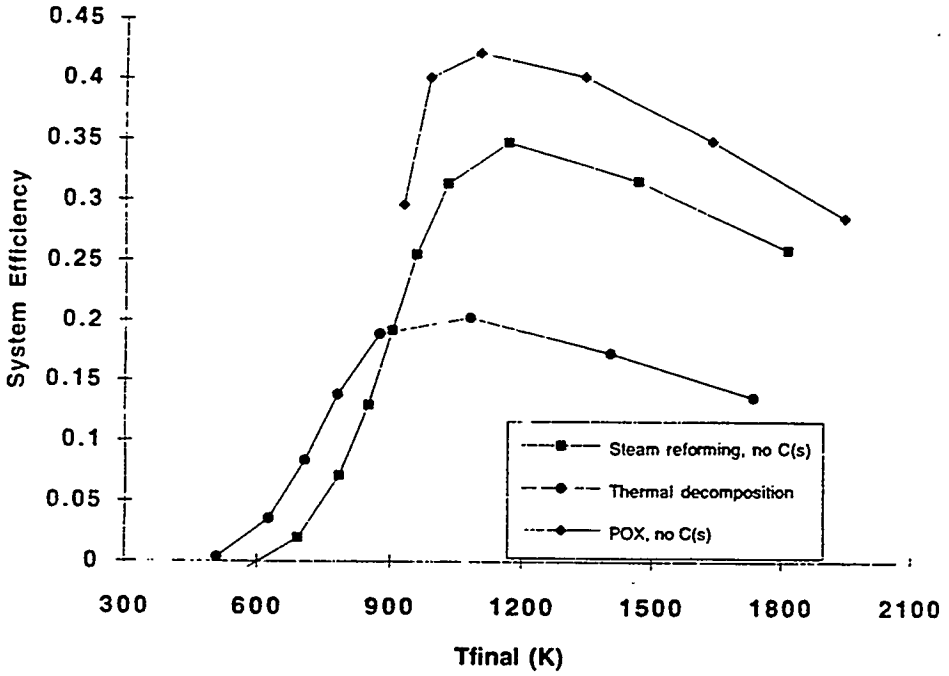


Figure 11. System efficiency η_s of a plasmastron/fuel cell system for several reforming technologies as a function of reactor temperature T_{final}, for methane at 1 bar, with $\eta_{fc} = 60\%$ and $\eta_p = 90\%$